ANNUAL REPORT
1994

CENTRAL LASER FACILITY

RUTHERFORD APPLETON LABORATORY

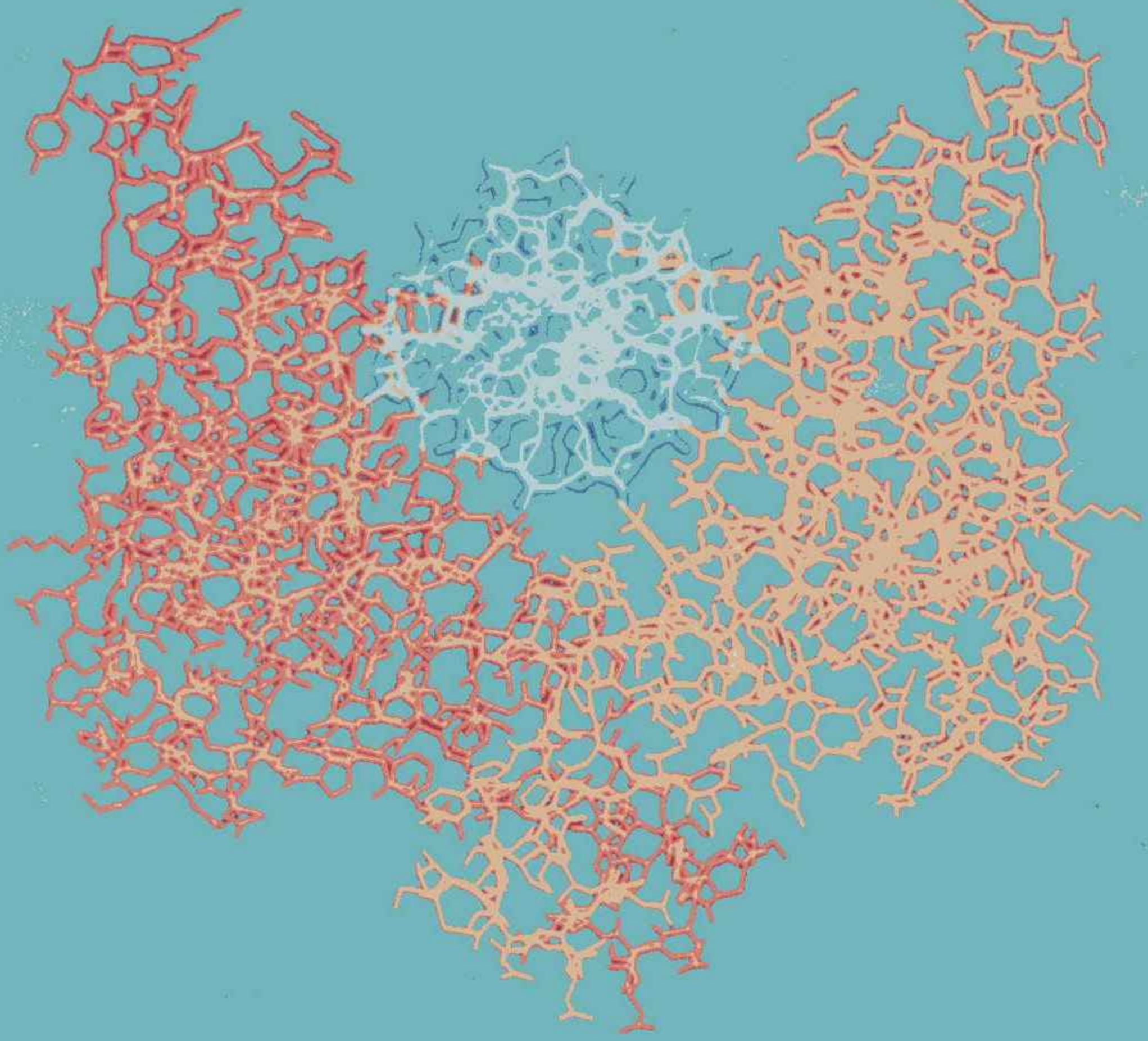

DRAL

Daresbury Laboratory
Rutherford Appleton Laboratory

ANNUAL REPORT TO THE

LASER COMMITTEE 1994

5 April 1993 to 4 April 1994

CENTRAL LASER FACILITY
RUTHERFORD APPLETON LABORATORY
CHILTON
OXON
OX11 0QX

Telephone 0235 821900
Telefax 0235 445888

Rutherford Appleton Laboratory Report RAL-94-042

The cover illustrates *ECO RV* restriction enzyme bound to the specific site of a DNA strand prior to genetic modification, see page 203.

ISBN 0902376055

DRAL is part of the Engineering and Physical Sciences Research Council

ACKNOWLEDGEMENTS

M H Key

This report is the product of a team effort.

The production was organised by Nic Allen, Chris Naboulsi and Katharine Hale with Chris Reason overseeing the technical specification.

The Chapter Editors were Peter Norreys, Mick Shaw and Bill Toner. Section Editors were Colin Danson, Edwin Divall, Chris Edwards, Chris Hooker, Graeme Hirst, Dave Neely, Dave Pepler, Steve Rose, Ian Ross, Waseem Shaikh, Phil Taday, Sue Tavender, Edmond Turcu and Barry Walsh. The important task of collecting publications was overseen by Chris Edwards with the help of Dave Neely, Mike Towrie and Chris Hooker.

Most of the text has been provided in camera-ready format by the Facility users and they deserve particular thanks for supplying their contributions to our production deadline.

The document has been produced by the RAL Reprographics Section.

PREFACE

M H Key

The most striking aspect of the year's work has been the completion of a two year project to provide ultra-bright beams on the Facility's high power lasers and the impact which this has had on the scientific programme of the users.

With 35 TW, 0.8 ps pulses at .1.05 μm generated by chirped pulse amplification and compression in vacuum and focused at 10^{19} W cm^{-2}, the Vulcan Facility has achieved an internationally outstanding capability for high power and intensity. The CPA method has been applied to the KrF laser, Sprite, giving 1 TW, 0.3 ps pulses at 248 nm, at the forefront of performance for short pulse and hihigh power in the UV. Sprite's previous Raman laser mode of operation was already giving uniquely high brightness in longer pulses and it has been upgraded to give a near to diffraction limited beam of 1 TW in 10 ps at 268 nm with focused intensity of 10^{19} W cm^{-2} unequalled by any other laser in the UV.

Significant progress was made during the year towards building a much larger KrF laser facility, Titania, by a task force which produced a final design of the system. Titania will begin operation in two years time and will help to maintain the CLF's high power lasers at the leading edge of performance.

The availability of 10^{19} W cm^{-2} with a substantial energy in ultra-short pulses has stimulated user interest and activity in high intensity interaction phenomena and the total number of high power laser experiments carried out during the year reached a record level of 21.

Highlights of the science arose from the first studies of ultra-high intensity interactions with gaseous and solid targets using the new facilities. Observations were made of high harmonic generation, frequency up shifting, self-focusing, stimulated Raman scattering and electron energy distributions in optical field ionised gaseous targets. Interaction with solid targets showed MeV ion emission and magnetically collimated plasma flow. Fusion research and X-ray laser research were both active areas with an apparent breakthrough to high gain in recombination lasers using a CPA driver for the first time, and important progress towards uniformity of drive pressure in laser-fusion research with a hybrid direct/indirect drive scheme.

Work with the diverse lasers of the Laser Support Facility has also been extremely vigorous during the year, exploiting to the full the wide range of capabilities from femtosecond pulses to high repetition rate pulsed X-rays. A particularly valuable achievement was the success of a bid by users and staff to upgrade the lasers of the LSF by replacing the stock of loan pool lasers and by capitalising on new OPO technology to improve the range of tunability and give synchronous 2-frequency output from the picosecond lasers. Work will begin in the coming year.

Outstanding scientific contributions from the LSF as usual span a very wide range and include further results from a major study of the ultra-low temperature kinetics of molecular and radical reactions, the first detailed thermodynamic analysis of the separation of a geminate ion pair in an electron transfer reaction, the first spectroscopic observation of the zinc ethyl radical ZnC_2H_5, photolithographic production of 0.18 μm features for silicon FET devices and the production of an intense soft X-ray beam from a laser plasma source.

One measure of the success of the scientific work is in individual and team prizes and honours awarded during the year as recorded in the news page following this preface.

A notable event was the formal start of high power laser operations in the CEC Large Installations plan with the first round of experiments selection completed in February. Operation of the high power lasers on behalf of European users is an exciting new development and it is hoped to extend the availability further to East European and former Soviet Union countries and to include access to the LSF lasers in the next phase.

A milestone for the future of the CLF was the decision in Autumn 1993 to initiate the third review of the Facility. These reviews at six year intervals consider the past record and future goals of the programme and are very important in setting the mid-term course of future work. It is vital for the continued funding of the CLF, that past performance and future plans measure up to the high standards required by the funding agency. This year with the change from SERC to EPSRC and a new set of directives for research contained in the Government's White Paper on science, the review will have added significance.

My thanks go to all who have contributed to this year's achievements, both users and staff and I look forward to a positive result from the Review process and to an even brighter future than has already been achieved this year with the ultra-bright laser beams! On a personal note I shall be spending a year from August '94 working at the Lawrence Livermore Laboratory. The CLF will be headed by W T Toner during my absence and I should like here to express my thanks to him and my best wishes to everyone for a successful year under his management.

INTRODUCTION TO THE CENTRAL LASER FACILITY

C B Edwards

LASER FACILITIES AVAILABLE FOR USERS AT THE CLF

Vulcan is a powerful, highly versatile, multi-beam Nd:glass laser. Up to 3 kJ of laser energy is available at 1 μm in a total of eight beams which can be configured in various geometries including cluster, line focus, and transverse and opposing beam configurations. Parallel operation is available in three main target areas, with an additional single beam area dedicated to the production of the high brightness X-radiation for applications in contact X-ray microscopy and instrumentation studies.

Pulse durations are available from 700 fs using Chirped Pulse Amplification techniques (CPA) up to 10 ns. Second harmonic frequency conversion to 0.5 μm is an option on all main beams, with a 3rd harmonic capability for probing.

Using the large aperture CPA beam, users are able to access new regimes of high intensity interaction physics. Power in excess of 35 TW can be delivered on target in a high quality subpicosecond pulse, producing a target irradiance up to 10^{19} Wcm^{-2}. This capability makes Vulcan the most powerful target irradiation facility of its type in the world.

Sprite is the world's brightest source of ultraviolet light. Pulse durations range from 300 fs (CPA at 249 nm) to 60 ps (Raman mode at 268 nm), at 1 TW power producing target irradiance up to 10^{19} Wcm^{-2} in a single near diffraction limited beam. Using the unique Raman amplification techniques which were developed at the CLF, ultra-high contrast laser radiation is delivered to target, enabling fundamental laser interaction studies to be performed in a pre-pulse free regime.

Based on electron beam pumped KrF excimer laser technology, the Sprite facility has a repetition rate of up to 12 full energy shots per hour, compared with the 3 shots per hour available from Vulcan.

The Laser Support Facility (LSF) operates a wide range of sophisticated, high repetition rate, table top laser systems which enable its community of users to pursue research in chemistry, biology, and photo-physics. Pulse durations span the range from 100 fs to 20 ns, with a wavelength coverage from the uv to the infra-red.

The Laser Loan Pool offers a choice of eight laser systems to University scientists for use in their home laboratories.

Visiting scientists to the CLF are supported by experienced scientific and engineering staff who assist at all stages of the work, from the initial planning through to the interpretation of data. The target fabrication group, for example, has wide-ranging capabilities for the manufacture and characterisation of complex targets. A suite of advanced instrumentation, and data analysis systems is provided, while the Theory and Computational Support Group assist with theoretical and modelling aspects of experiments.

ACCESS TO CLF FACILITIES

There are three calls per year for proposals for beam time at the CLF. Proposals are judged by one of three specialist panels (see Panel Membership), who report to the Laser Committee, and who make recommendations to the Head of the CLF on the scientific priorities and development issues. The Laser Support Facility Panel reviews applications for the use of the LSF facilities, the Loan Pool, and the high repetition rate X-ray source. Bids for the high power lasers Vulcan and Sprite are reviewed by either the High Power Laser Panel, or the European Panel (see European Access below).

Grant support for the scientific programme of the team applying to the Panels is normally a pre-requisite for success at the proposal review stage, but a small fraction of experimental time is available for trial experiments to enable better applications for grant support to be made. The facilities are over subscribed by a factor of two, ensuring that the scientific programme at the CLF typically is of the highest international standard.

EUROPEAN ACCESS TO THE CLF

In December 1993 a contract was awarded to the Central Laser Facility by the CEC to make beam time available to European researchers enabling European scientists to make direct applications for experimental time at the CLF. This will strengthen existing areas of investigation, stimulate new research themes, and promote the growth of new experimental groups and collaboration throughout Europe.

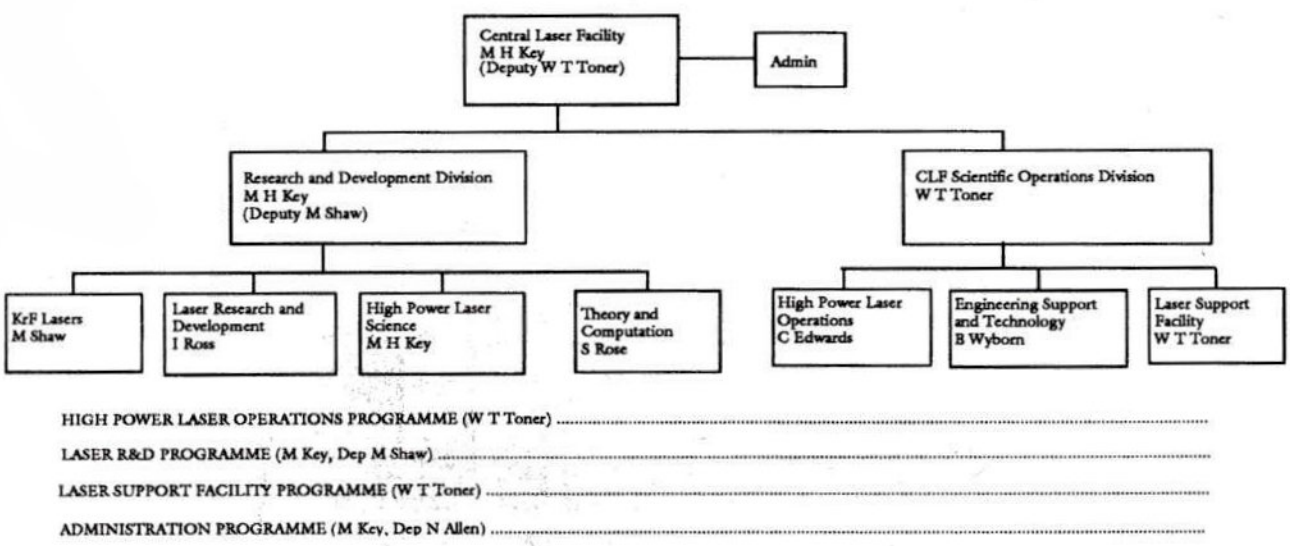

Figure 1. Divisional and Group Structure of the Central Laser Facility

FACILITY DEVELOPMENT

In order to maintain the competitiveness of its facilities on an international scale, the CLF is undertaking an ambitious programme of facility development and enhancement.

In the current year, the high power lasers have been substantially upgraded by the exploitation of CPA (Vulcan and Sprite) and the extension of the Raman architecture (Sprite). This work, made possible by the specially funded collaboration with laser development groups in UK universities, has made the CLF the world leader in the delivery of ultra-high brightness laser beams to target. As a result, proposals for experimental collaboration are being received from leading laser laboratories throughout the world.

The commitment of the CLF to the development of new facilities extends beyond the lasers currently in operation. The next generation of KrF lasers is already under construction at RAL. Titania, due to be commissioned in 1995, will deliver 400 J at 268 nm with peak powers in excess of 10 TW, pulse lengths from 100 fs to 10 ns, and target irradiance up to 10^{20} Wcm^{-2}. The LSF is to expand its operation with a substantial investment in new laser equipment over the next two years. A study on the exploitation potential of Vulcan has recommended a development strategy which will enable power of 200 TW to be delivered.

FACILITY MANAGEMENT

The programme at the CLF is managed by the Laser Committee, currently chaired by Professor W Sibbett, St Andrews University (see Committee Membership), which reports to the Facilities Commission. The divisional and group structure of the facility staff in the current reporting year is shown in Fig 1.

FACTS AND FIGURES

The total funding of the CLF in the current year was £4.1M, including the allocation to the high brightness Joint Project collaboration with universities (£310K). Funds were distributed as shown in Figure 2.

During the period covered by this report 27 experiments were scheduled on the high power lasers involving a total of 132 weeks of beam time. At the LSF 46 user experiments were performed over a total of 135 weeks, with an additional 15 loans of 3-6 month duration to support experiments carried out in University laboratories.

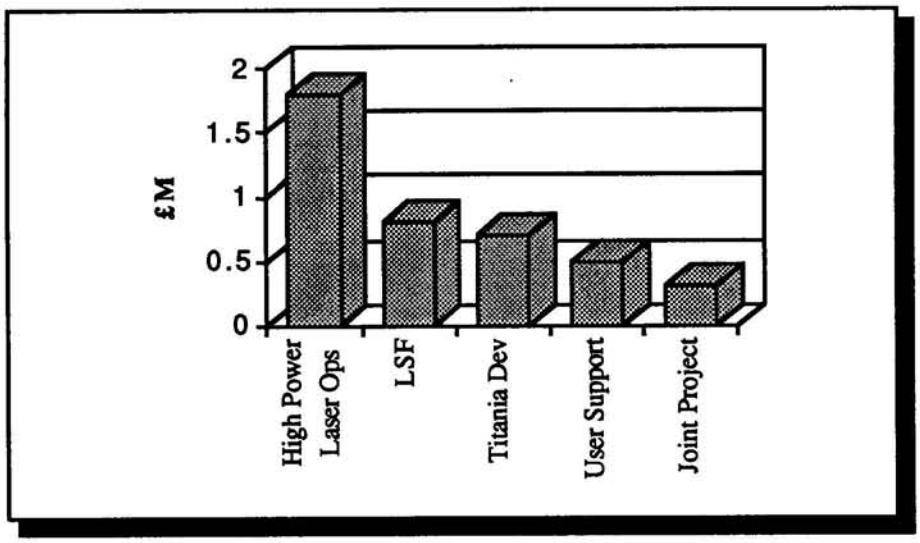

Figure 2. CLF Resources 1993/94

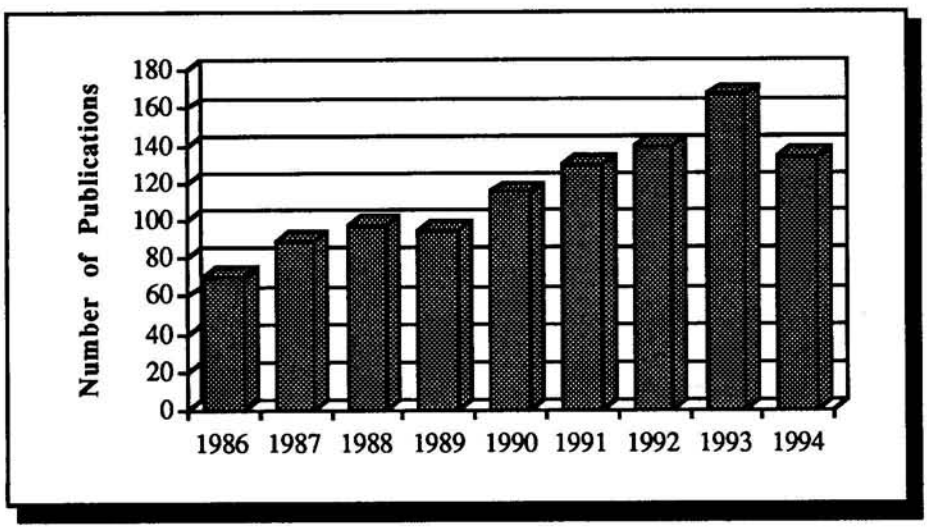

Figure 3. Refereed Publications and Published Conference Proceedings

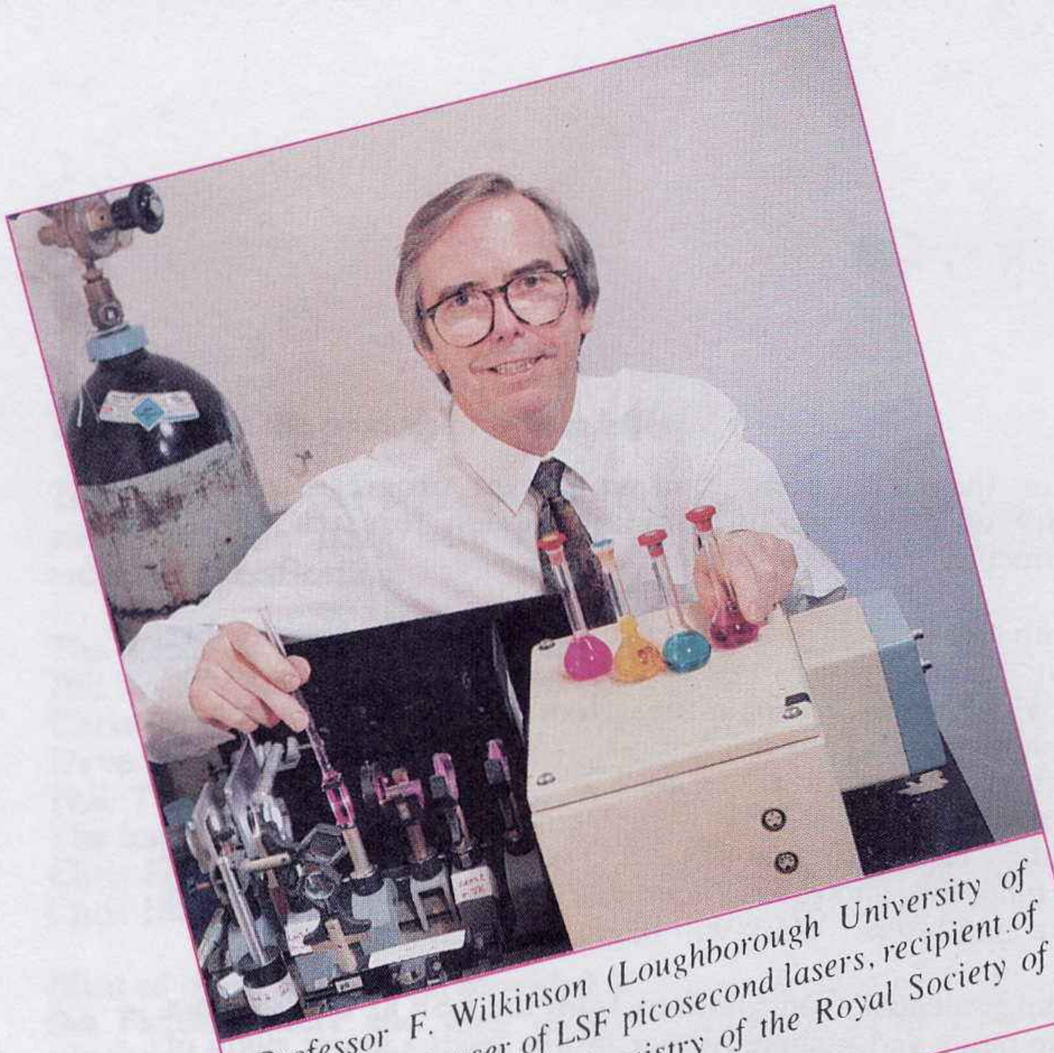

Professor F. Wilkinson (Loughborough University of Technology), user of LSF picosecond lasers, recipient of the Award for Photochemistry of the Royal Society of Chemistry.

Dr. A. Giulietti and members of his team from the Istituto di Fisica e Molecolare, Pisa with UK collaborators and CLF staff after the first experiment carried out at the CLF under the C.E.E.C. Large Installations Plan.

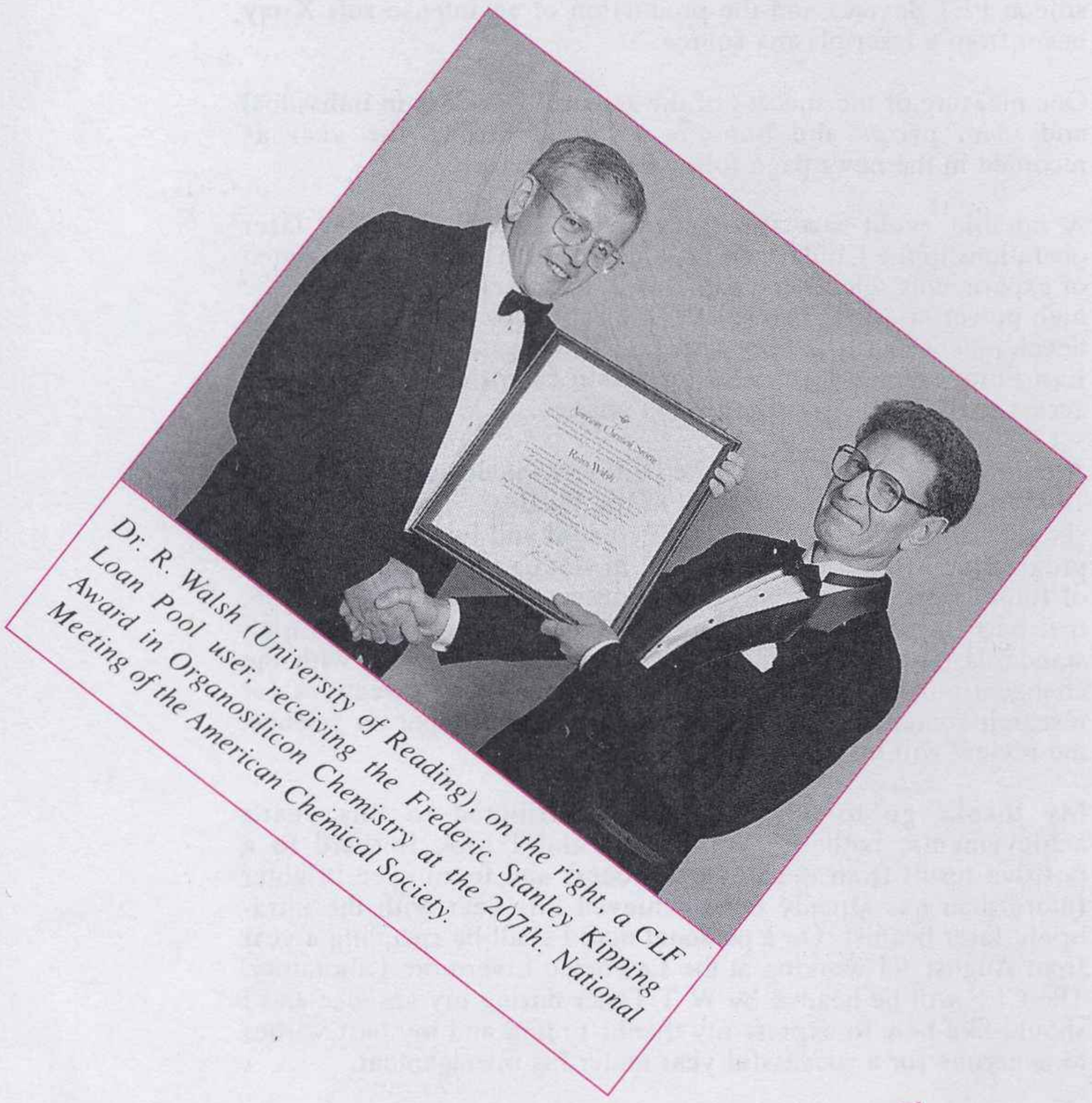

Dr. R. Walsh (University of Reading), on the right, a CLF Loan Pool user, receiving the Frederic Stanley Kipping Award in Organosilicon Chemistry at the 207th. National Meeting of the American Chemical Society.

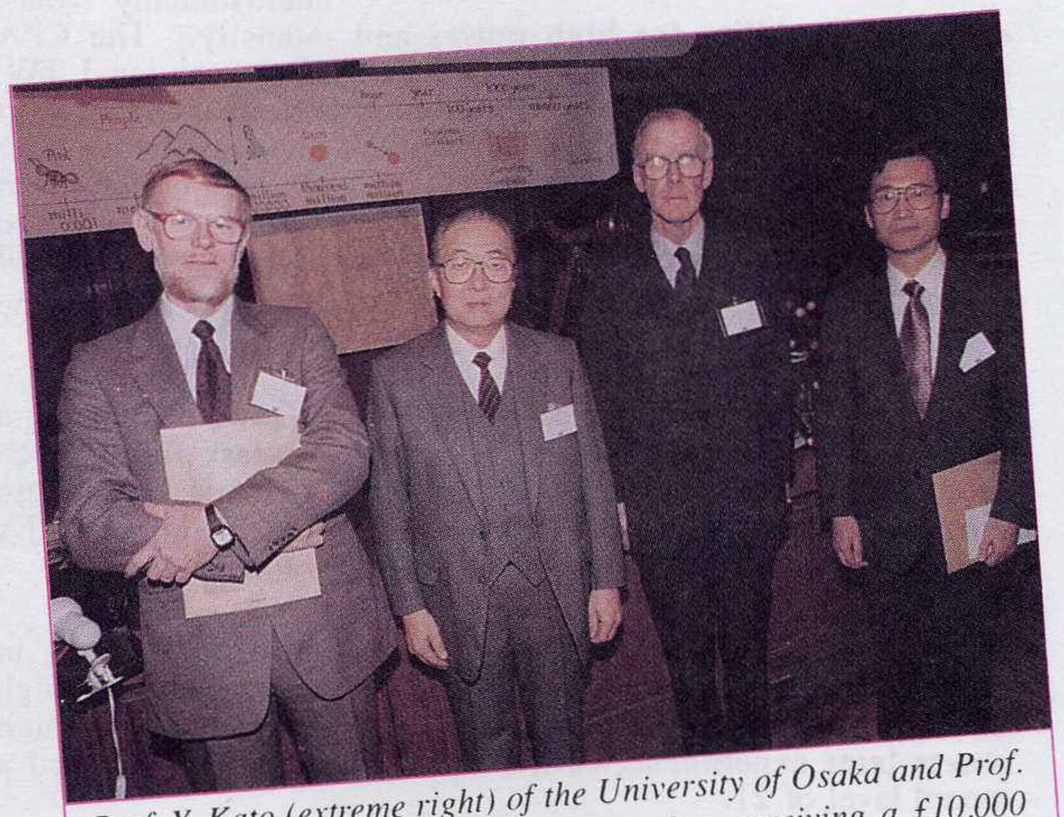

Prof. Y. Kato (extreme right) of the University of Osaka and Prof. M.H. Key of RAL at the Royal Institution, receiving a £10,000 Daiwa Award on behalf of Japanese and UK teams collaborating in X-ray laser research, presented by Mr. H. Kitamura, Ambassador of Japan and the Lord Adrian, FRS, trustee of the Daiwa Foundation.

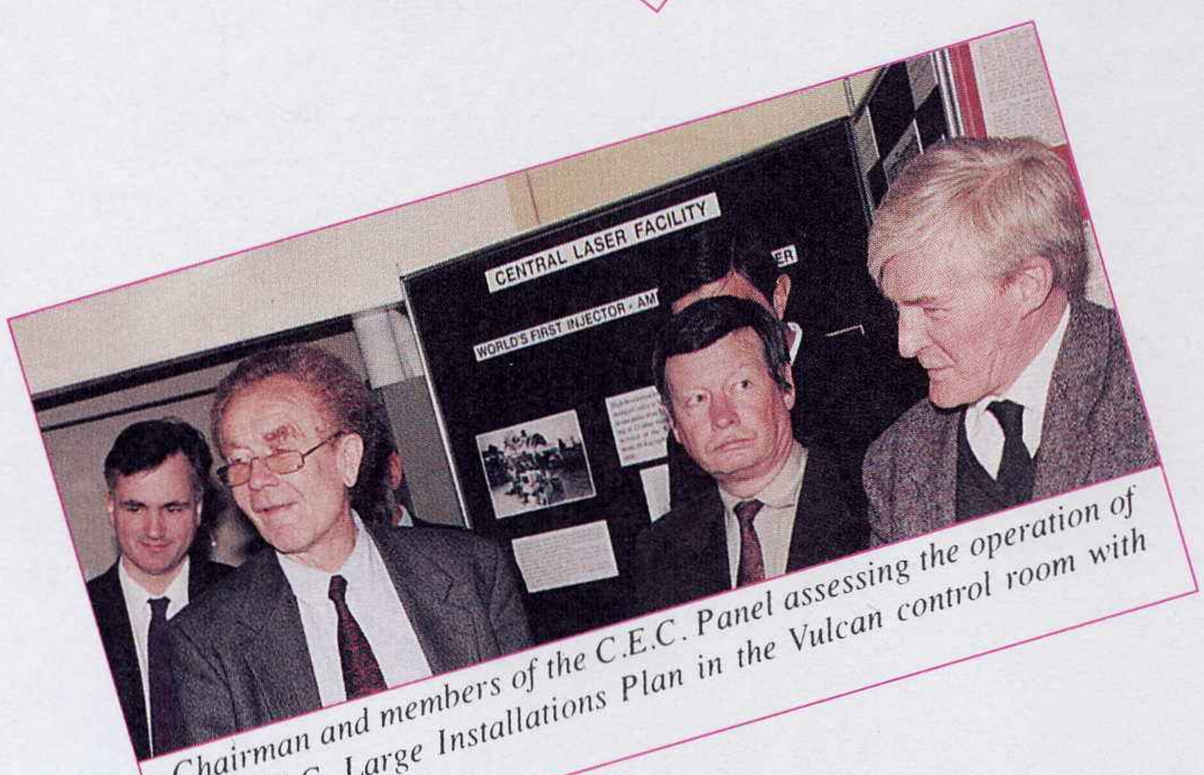

Chairman and members of the C.E.C. Panel assessing the operation of the C.E.C. Large Installations Plan in the Vulcan control room with W.T. Toner (right).

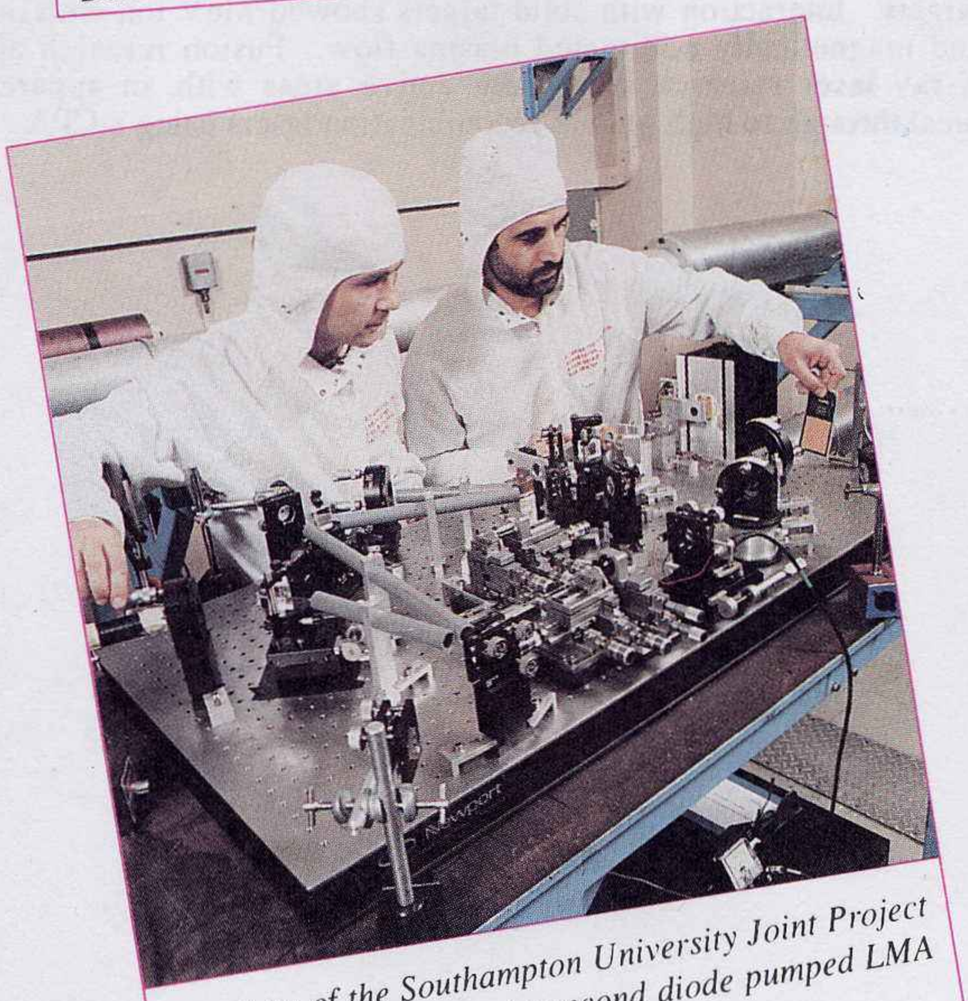

Members of the Southampton University Joint Project team setting up a sub picosecond diode pumped LMA oscillator for the Vulcan CPA system.

• CLF EVENTS AND PEOPLE IN THE NEWS

OBSERVATION OF HIGH GAIN RECOMBINATION X-RAY LASER AT 18.2 NM DRIVEN BY 2 PSEC LASER PULSES

J Zhang[1], M H Key[1,2], P A Norreys[2], C Danson[2], L Dwivedi[3], M Holden[3], P B Holden[4], C L S Lewis[5], A G MacPhee[5], D Neely[2], G J Pert[4], S A Ramsden[4], S J Rose[2], G J Tallents[3], F Walsh[2], Y L You[6]

[1] Department of Atomic and Laser Physics, University of Oxford, Oxford, OX1 3EU, UK
[2] Central Laser Facility, Rutherford Appleton Laboratory, Chilton, OX11 0QX, UK
[3] Department of Physics, University of Essex, Colchester, CO4 3SQ, UK
[4] Department of Physics, University of York, York, YO1 5DD, UK
[5] Department of Pure and Applied Physics, Queen's University, Belfast, BT7 1NN, UK
[6] Visiting Scientist from Institute of Nuclear Physics and Chemistry, Chengdu 610003, China

INTRODUCTION

One of the most important goals for x-ray laser research is to achieve saturated and diffraction limited laser operation in the water window spectral region. Adiabatically cooled recombination x-ray lasers appear to be a promising scheme to this end because in principle they require much lower driving energy for the same lasing wavelength than collisional excited lasers. A serious problem however has been the failure so far to produce a sufficient gain length product to reach saturation.

One way to tackle this problem is to seek to increase the gain coefficient by using shorter duration heating pulses[1]. Theory has predicted much higher gain coefficient on the C VI Balmer α transition at 18.2 nm when 7 μm diameter carbon fibre targets are irradiated by 2 picosecond laser pulses[1]. A newly available 2 psec, 20 TW chirped pulse amplification (CPA) beam of the VULCAN laser facility[2] (λ=1.053 μm) has offered the possibility of experimental verification of these ideas. We report here experimental results of the first observation of high gain C VI recombination x-ray laser driven by 2 psec laser pulses.

EXPERIMENTAL SET-UP

A schematic diagram of the experimental set-up is shown in figure 1. 2 psec, 20 TW laser pulses at 1.053 μm were generated using the Nd:glass laser VULCAN which was equipped with a chirped pulse amplification (CPA) system. The compressor was located inside the target chamber under vacuum. The recompressed beam of diameter 140x88 mm^2 was incident onto a partially reflecting turning mirror which allowed 5% of the recompressed pulse through for measurements of the laser pulse length, prepulse (contrast ratio), spectral distribution and focal spot aberrations. An off-axis parabolic mirror and an off-axis spherical mirror focused the laser beam into a 7 mm long, 20 μm wide line.

It is vital for recombination x-ray laser experiments to minimise prepulse and post-pulse to avoid pre-heating of the target and post-heating of the plasma. A background contrast ratio of between 10^{-6} to 10^{-7} was measured[2]. The pulse length was monitored during the experiment by an auto-correlator. 10 - 30 J of laser energy was incident on the line focus. The incident irradiation of the line focus varied from 3×10^{15} W/cm^2 to 1.0×10^{16} W/cm^2.

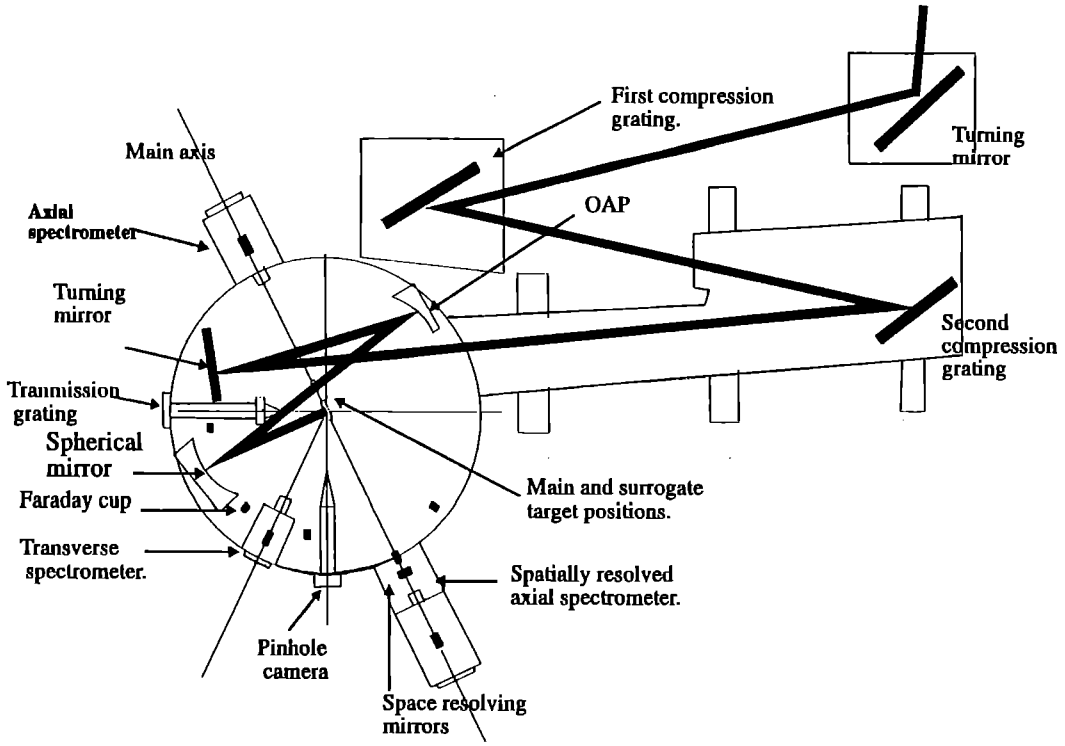

Fig. 1. Experimental set-up showing various diagnostics used in the experiment.

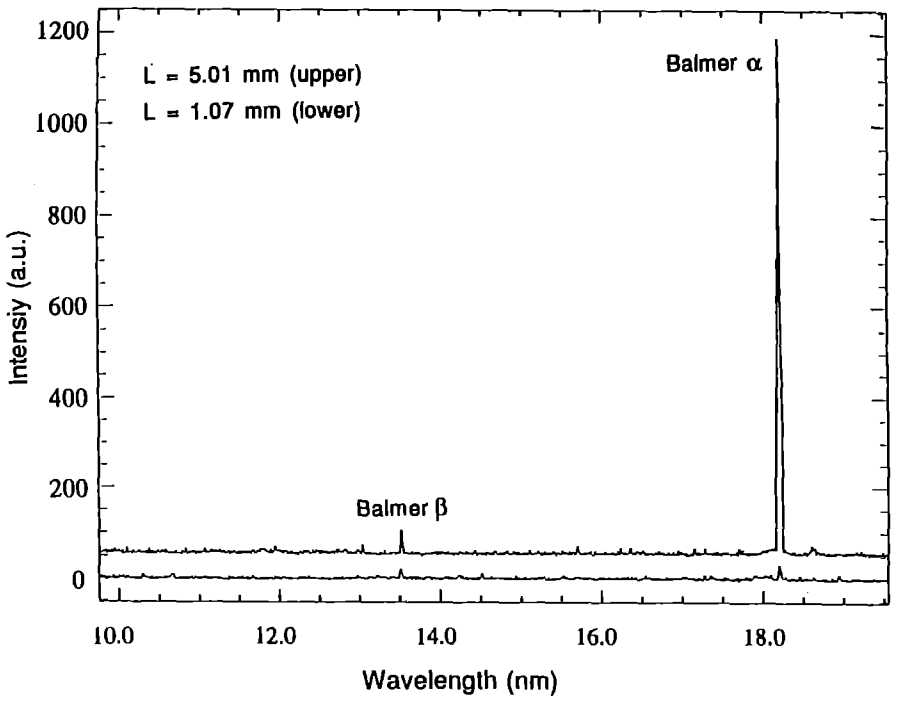

Fig. 2. On-axis spectra for a 1.07 mm long carbon fibre plasma (lower spectrum) and a 5.01 mm long plasma (upper spectrum). The wavelengths for the C VI Balmer α and Balmer β transitions are 18.2 nm and 13.5 nm respectively.

The targets used in the experiment were 7 μm diameter carbon fibres, which were self-supporting and remained straight for up to 1 cm. The fibre targets were supported horizontally at one end and positioned with better than ± 2 μm spatial accuracy and ± 1 mrad angular accuracy using a modified split-field microscope system. The irradiation of the fibre targets was accomplished by placing the fibres in the 20 μm wide focus. The free end of the fibre target was placed in a fixed position close to one end of the line focus with an overlap to avoid a cold plasma end. The irradiated length was varied by moving the line focus axially. The primary diagnostic on-axis was a flat-field spectrometer with a 1200 l/mm aperiodically ruled grating recording the spectral range 5.0 nm to 30.0 nm onto KODAK 101-04 film. A grazing-incidence optical system consisting of two cylindrical mirrors was installed in front of the entrance slit of the spectrometer to provide spatial resolution of the recorded soft x-ray emission[3]. The first cylindrical mirror with a radius of 3900 mm formed an image (x 2) of the source in the sagittal plane on the detector of the spectrometer to provide one-dimensional spatial resolution better than 30 μm. In the meridional plane the image of the plasma was focused by the second cylindrical mirror (r = 31.9 mm) onto the entrance slit In order to infer absorbed energy in the plasma and to diagnose the characteristics of plasma which could effect the soft x-ray lasing performance during adiabatic expansion, a 2400 l/mm flat-field grating spectrometer was used at 45 degree off the main axis to record the resonance emission from the H-like and He-like ionisation stages in the spectral range of 2.0 nm - 10.0 nm. The size and uniformity of the plasma were monitored using a transmission grating spectrometer and a pinhole camera. A group of Faraday cups were used to directly measure the energy distribution and the absorbed energy in the plasma.

RESULTS

Two spectra from the on-axis flat-field spectrometer are shown in Fig. 2. The lower spectrum is from a 1 mm carbon fibre irradiated at an intensity of 5.6×10^{15} W/cm^2. It shows the major features of the spontaneous emission spectrum from carbon plasmas. Above it is the spectrum from a 5 mm long carbon fibre target irradiated at a similar intensity of 6.5×10^{15} W/cm^2. The Balmer α transition at 18.2 nm and Balmer β transition at 13.5 nm in H-like ionisation stage are labelled on the figure. Comparison between the two spectra in figure 2 demonstrates the large enhancement in the on-axis signal for the Balmer α lasing transition as the plasma is lengthened. This is a strong indication of stimulated emission.

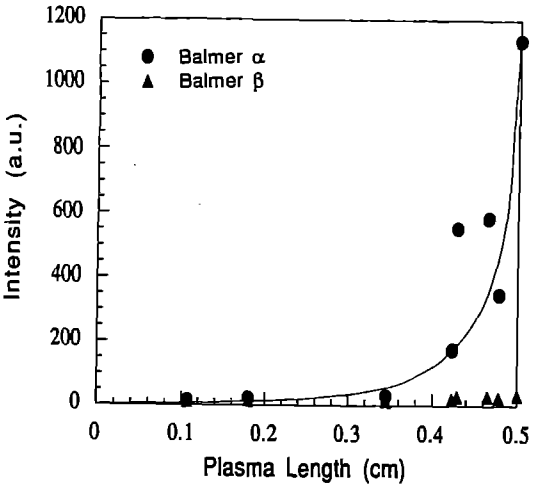

Fig. 3a. Intensity of the Balmer α lasing transition and the Balmer β spontaneous emission as a function of the plasma length. The solid dots represent the data for the Balmer α transition and the solid triangles stand for the data for the Balmer β transition. The Balmer α data was fitted by Linford formula of gain of 12.5 cm^{-1}.

During the experiment, an Al foil filter in the detector plane was used to attenuate the strong Balmer α emission relative to the Balmer β emission from plasmas in order to avoid film

saturation and to permit measurement of the intensity of the Balmer α relative to the Balmer β emission (this differential filtering gave approximately 25:1 differential attenuation between the two spectral lines).

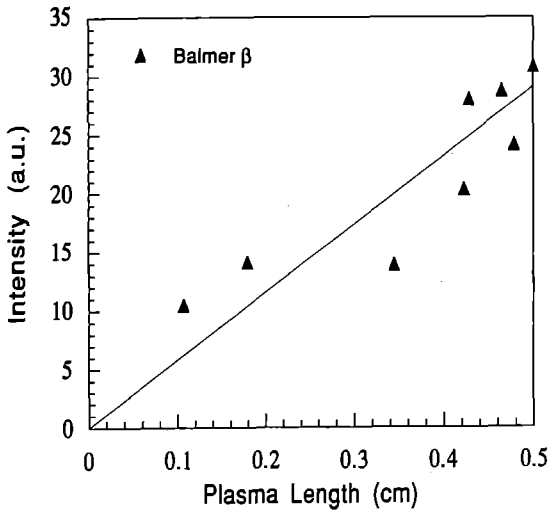

Fig. 3b. Intensity of the Balmer β transition as a function of the plasma length.

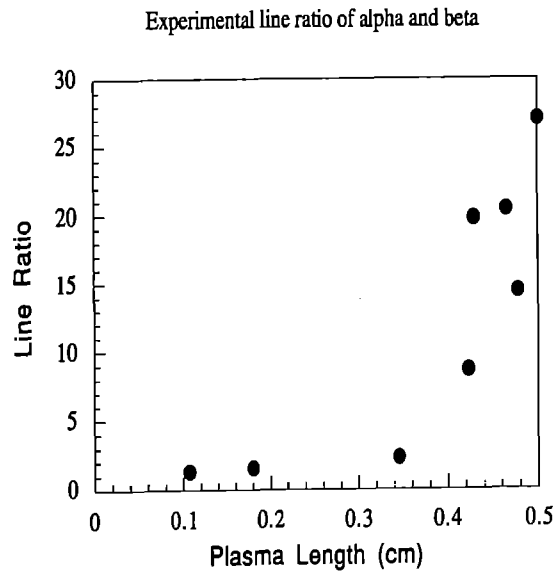

Fig. 4. Intensity ratio of the Balmer α to Balmer β transition measured in the experiment for different plasma length.

The photographic spectra were scanned by a digitising densitometer and the resultant film density values converted to intensity using a calibration curve[4]. The intensity of an individual line was then measured by subtracting the background continuum level and integrating over the line profile. The results of these measurements are plotted in Fig. 3a for the Balmer α and Balmer β lines. The Balmer α data have been fitted by the Linford formula[5]. Least-square fitting for the data gives a gain value of 12.5 ± 1.5 cm^{-1}. The procedure underestimates the highest gain which may be present in the best spatial and temporal source of the plasma. The uncertainty in the gain was calculated from the measuring error in the measurement of relative intensity values. The Balmer β line intensity increased linearly as the plasma length increased (Fig. 3b). This suggests the Balmer β line intensity is mainly due to spontaneous emission, which is the expected behaviour of an optically thin spontaneous emission.

The spatially resolved spectrometer on-axis showed that the spatial profile of the emission region was not larger than the 30 μm resolution. The peak gain value based on spatially resolved data could therefore be larger than the value from the integrated data. Simulations have predicted a 10 - 15 μm spatial region for the peak gain value. According to theoretical calculations, the gain length product needed to obtain saturation emission is about 12. It is therefore possible that we have already achieved saturation in very narrow gain region, but we need to greatly improve the spatial resolution to resolve the structure of the gain region.

The absorbed energy was deduced from measurements of the intensity ratio of resonance lines from adjacent ionisation stages[6,7]. It was inferred to be about 0.5 - 1.0 J/cm for most of the data used here. This value of the absorbed energy agrees with the direct measurements using the Faraday cups. The measurements of the slope of H-like and He-like carbon plasmas recombination continua gave an electron temperature of 10 ~ 20 eV during recombination. A similar value was inferred from the resonance line ratios. Details about the diagnostics using the resonance line ratio can be found in references 6&7 and in another paper in this report.

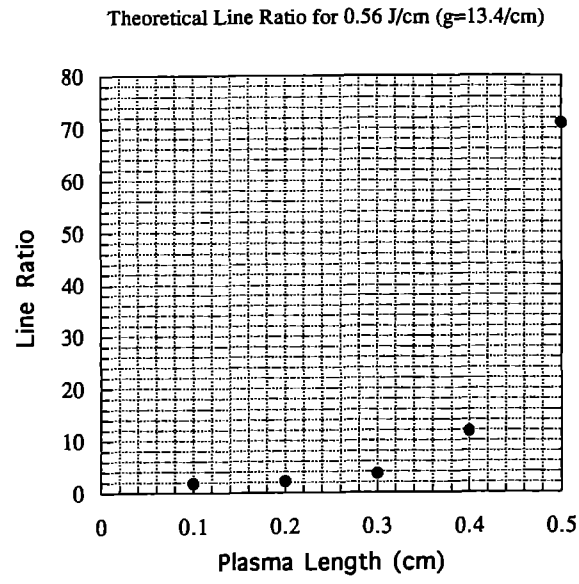

Fig. 5. Theoretically predicated intensity ratio of the Balmer α to Balmer β transition at different plasma length for an absorbed energy of 0.56 J/cm.

The enhancement of stimulated emission of the Balmer α transition at 18.2 nm over spontaneous emission of the Balmer β transition (n = 4 - 2) at 13.5 nm was measured in the axial direction. The measurements were based on the comparison of the intensities of the Balmer α transition and the Balmer β transition recorded for the same shot and allowed shot to shot variations in incident laser energy to be taken into account. The Balmer β transition has the same lower energy level and an upper level close to that of the Balmer α transition. Figure 4 shows the increase of the intensity ratio of Balmer α to Balmer β transition with plasma length. By comparing with the theoretical results for the same plasma length and absorbed energy, a separate determination of gain coefficient for each shot can be made. The theoretical results for absorbed energy of 0.56 J/cm, 0.76 J/cm and 1.08 J/cm are shown in figures 5,

6 and 7 and confirm the Linford-fitted measurements in figure 2.

A systematic large scale non-uniformity (fig. 8) was found along the line focus due to the spatial profile of the CPA laser beam. More incident energy than the calculated value was used in the experiment to compensate the mismatched space/time gain windows[8]. The output of C VI x-ray laser from the 5 mm long plasma is estimated to be about 1.5 kW from the energy density on the recording films and the duration of the lasing gain predicated by the simulation results.

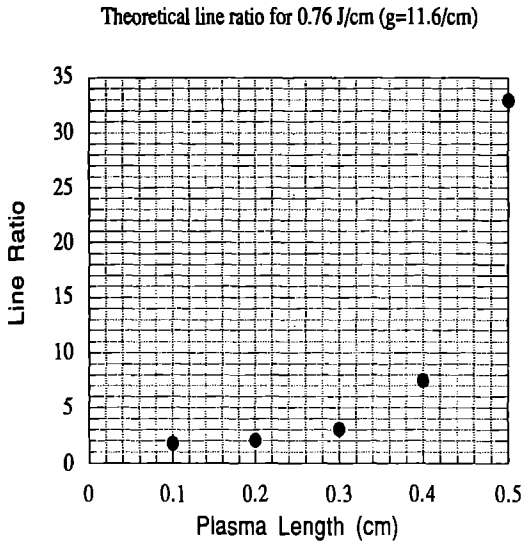

Fig. 6. Theoretically predicated intensity ratio of the Balmer α to Balmer β transition at different plasma length for an absorbed energy of 0.76 J/cm.

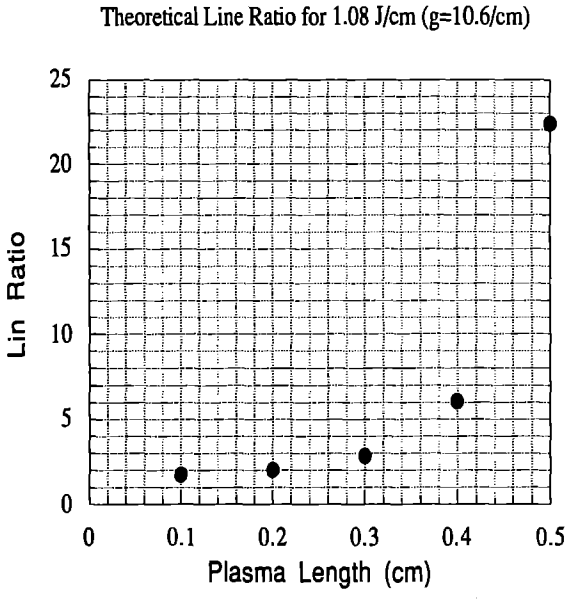

Fig. 7. Theoretically predicated intensity ratio of the Balmer α to Balmer β transition at different plasma length for an absorbed energy of 1.08 J/cm.

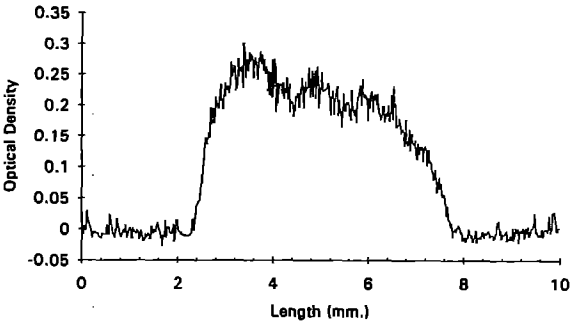

Fig. 8. Microdensitometer trace of soft-x-ray emission along the line focus.

CONCLUSION

In conclusion, we have demonstrated that high gain recombination x-ray lasers can be achieved by irradiating fibre targets with ultra-fast pulses. Our results give one of the most unequivocal measurements of a high ratio of the Balmer α to Balmer β emission and also the highest gain coefficient observed for the C VI x-ray laser. It is expected that a saturated C VI recombination laser at 18.2 nm can be achieved in the future.

ACKNOWLEDGEMENT

The authors would like to thank the VULCAN laser operations, the target preparation and engineering groups of the Central Laser Facility for their help and cooperation.

REFERENCES

1. J Zhang and M H Key, Appl. Phys., B58, 13 (1994).
2. C N Danson et al., Opt. Commun., 103, 392 (1993).
3. P Z Fan et al., Appl. Phys., 31, 6720 (1992).
4. B L Henke et al., J. Opt. Soc. Am., 1, 828 (1984).
5. G J Linford, E R Peressini, W R Sooy and M L Spaeth, Appl. Opt., 13, 379 (1974).
6. J Zhang, M H Key, P Norreys and G J Tallents, Opt. Commun., 95, 51 (1993).
7. J Zhang et al., *X-Ray Lasers 1992*, edited by E E Fill, (IOP publisher, Bristol, 1992) p.339.
8. M H Key, S J Rose, N Tragin and J Zhang, opt. Commun., 98, 95 (1993).

DIAGNOSTICS OF RAPIDLY RECOMBINING PLASMAS USING RESONANCE LINE RATIO

J Zhang[1], F Walsh[2], P A Norreys[2], C Danson[2], L Dwivedi[3], M Holden[3],
P B Holden[4], M H Key[1,2], C L S Lewis[5], A G MacPhee[5], D Neely[2],
G J Pert[4], S A Ramsden[4], S J Rose[2], G J Tallents[3], Y L You[6]

[1] Department of Atomic and Laser Physics, University of Oxford, Oxford, OX1 3EU, UK
[2] Central Laser Facility, Rutherford Appleton Laboratory, Chilton, OX11 0QX, UK
[3] Department of Physics, University of Essex, Colchester, CO4 3SQ, UK
[4] Department of Physics, University of York, York, YO1 5DD, UK
[5] Department of Pure and Applied Physics, Queen's University, Belfast, BT7 1NN, UK
[6] Visiting Scientist from Institute of Nuclear Physics and Chemistry, Chengdu 610003, China

INTRODUCTION

Significant improvements in the performance of recombination x-ray lasers has been predicted for plasmas driven by intense, picosecond laser pulses[1]. Recombination lasers have, to date, been studied under conditions far from ideal, in that the scale length of the plasmas studied have been relatively long and heating has occurred at densities around the critical density of the driving laser pulse[2-5]. Plasmas driven by picosecond laser pulses, however, have a sufficiently small scale length that heating occurs close to solid density, thus enhancing the volumetric expansion and adiabatic cooling of the plasma[6]. High gain operation of the C VI recombination x-ray laser requires an electron temperature and density of Te ~ 10 eV and Ne ~ $1x10^{19}$ cm^{-3} respectively during the peak of the population inversion. It is of great interest to study the conditions under which high gain recombination lasers operate in order to optimise their performance. We report here experimental measurements of absorbed energy, electron temperature, electron density and the fraction of fully stripped nuclei obtained by analysis of the ratio of the H-like to He-like resonance lines for rapidly recombining plasmas driven by 2 psec laser pulses.

EXPERIMENT

A 2 psec, 1.053 μm chirped pulse amplified beam from the VULCAN glass laser[7] facility with energies up to 30 J was focused onto 7 μm diameter carbon fibre targets. The intensity on targets varied from $3.0x10^{15}$ W/cm^2 to $1.0x10^{16}$ W/cm^2 for line focus lengths in the range of 4 - 7 mm. A grazing incidence spectrometer, incorporating an aperiodic (2400 grooves/mm average) flat-field grating of 5 m radius curvature, viewed the plasma in a transverse direction to record the Lyman series resonance lines (*np - 1s*) in the hydrogen-like ionisation stage and the *1snp - 1s*^{2} resonance transitions in the helium-like ionisation stage in the range of 2.0 nm - 10.0 nm. The spectra were recorded with a resolution of 0.03 nm on KODAK 101-04 film. The photographic spectra were scanned by a digitising densitometer and the resultant film density values were converted to intensities using a calibration curve[8]. The intensity of an individual line was measured by subtracting the background continuum level and integrating over the line profile. A soft x-ray pinhole-camera, filtered to 70 eV photon energy, recorded images of the plasma. The absorbed energy was directly measured with a group of Faraday cups.

RESULTS

When 2 psec laser pulses irradiate a fibre target, a plasma is formed with a high initial density that starts to rapidly expand and recombine. During the heating and early stages of recombination, when most emission occurs from resonance spectra, LTE is applicable for levels with quantum number n ≥ 3 and the population densities of excited states relative to the next higher ionisation stage are described by the Saha-Boltzmann equation. The resonance line emission from the n ≥ 3 levels of He-like ions is proportional to the population density of the ground state of H-like ions. For example the intensity of the *1s3p - 1s*^{2} transition of He-like ions is

$$I_\beta^{He} = h\upsilon_\beta^{He} A_\beta^{He} \left(\frac{\pi}{2}\right)\left(\frac{g_3^{He}}{g_1^{H}}\right)\sum_l\left[R^2(l+1) - R^2(l)\right]$$

$$\times N_e N_1^H \left(\frac{h^2}{2\pi m_e kT_e}\right)^{3/2} \exp\left(\frac{\chi^{He}(3,c)}{kT_e}\right),$$

Similarly the intensity of the hydrogenic resonance line is proportional to the concentration of bare nuclei, Hence the ratio of the resonance line intensity of H-like ions to that of He-like ions therefore gives the ratio of the concentration of bare nuclei to that of the ground state population of the H-like ions in the plasma. This relative abundance is determined by the absorbed energy in the plasma. If the absorbed energy is varied, the relative abundance will change and with it the electron temperature, electron density and the fraction of fully stripped nuclei of the plasma.

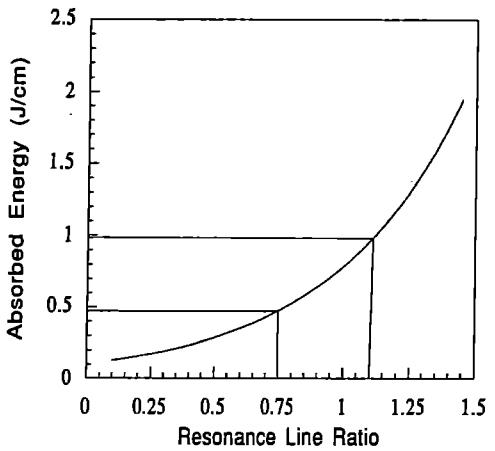

Fig. 1. Absorbed energy as function of line ratio of the Lyman β transition of H-like ions to the *1s3p - 1s*^{2} transition of He-like ions for 7 μm carbon fibre plasmas irradiated by 2 psec laser pulses.

Theoretical studies have shown that it is possible to infer the absorbed energy, electron temperature, electron density and the relative population of different ionisation stages from the measured ratio of resonance line intensities if we solve the coupled atomic physics, energy transport and hydrodynamic equations simultaneously[9,10]. MED101 is such a simulation code, which couples hydrodynamics, energy transport with atomic physics. This code (or earlier versions of it) has been tested extensively in cylindrical geometry in predicting the performance of plasmas in several previous experiments[11-13]. We have modified MED101 code to include calculation of the resonance line intensities in H-like ions and He-like ions.

Figure 1 shows the calculated relationship between the resonance line ratio and the absorbed energy in 7 μm diameter fibre targets irradiated by 2 psec laser pulses. Laser shots of different lengths with similar laser energy densities and relatively uniform x-ray emission

along the plasma were selected to deduce the C VI Balmer α gain[14]. The ratios of the intensity of the Ly β transitions of H-like ions to that of the $1s3p$ - $1s^2$ transitions of He-like ions were measured to be in the range of 0.75 ~ 1.1, which corresponds to the absorbed energy of 0.5 J/cm ~ 1.0 J/cm (see figure 1). This value agrees with the direct measurements using Faraday cups for these shots. The reason the ratio of the first resonance line pair ($2p$ - $1s$ and $1s2p$ - $1s^2$) in H-like and He-like ionisation stages was not used was that the opacity effects on these resonance lines could not be neglected. Opacity effects will invalidate the above discussion. The absorbed energy measurements were found to be in agreement only when the ratios of successive resonance line pairs had upper level $n > 2$.

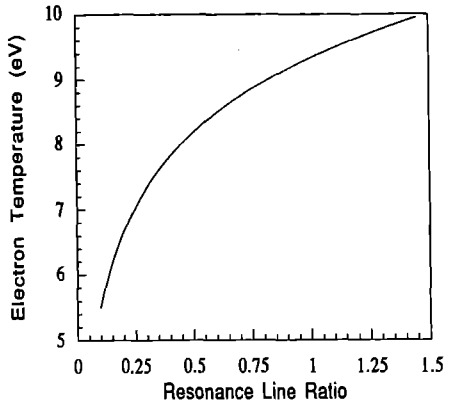

Fig. 2. Line ratio of the Lyman β transition of H-like ions to the $1s3p$ - $1s^2$ transition of He-like ions in carbon recombining plasmas for different electron temperature in the gain region at the lasing time for the same conditions as in fig. 1.

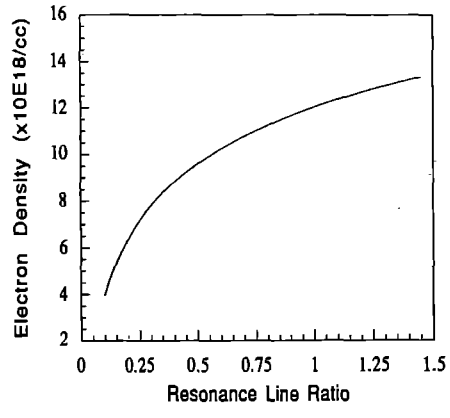

Fig. 3. The electron density in the gain region at the lasing time as function of line ratio of the Lyman β transition of H-like ions to the $1s3p$ - $1s^2$ transition of He-like ions in carbon recombining plasmas, for the conditions in figure 1.

The electron temperature, electron density and the fraction of fully stripped nuclei in the gain region at the lasing time are very important parameters for high gain operation. The inferred electron temperature for these shots were around 9 ~ 10 eV (figure 2). The measurements of the slops of H-like and He-like recombination continua gave a similar value during recombination. The electron density and the fraction of fully stripped nuclei in the plasmas are shown in figures 3 and 4. Dependencies of the electron temperature, density and the fraction of fully stripped nuclei on resonance line ratio can be well fitted by natural logarithmic functions. The fitted functions are $Y = 9.328 + 3.827 \log_e X$, $Y = 12.026 + 8.075 \times \log_e X$ and $Y = 0.674 + 0.614 \times \log_e X$ respectively. For the range of resonance line ratios of 0.75 ~ 1.1, the electron temperature, density and the fraction of fully stripped nuclei are all linearly dependent on variation of the line ratio. The electron density and the fraction of fully stripped nuclei for those shots are around 1.2×10^{19} cm^{-3} and 60% ~ 70% respectively. For the range of resonance line ratios smaller than 0.35, which corresponds to the energy threshold (0.22 J/cm see figure 1), the dependencies become very non-linear. The line ratio of 0.35 sets up a practical limitation for application of this diagnostic.

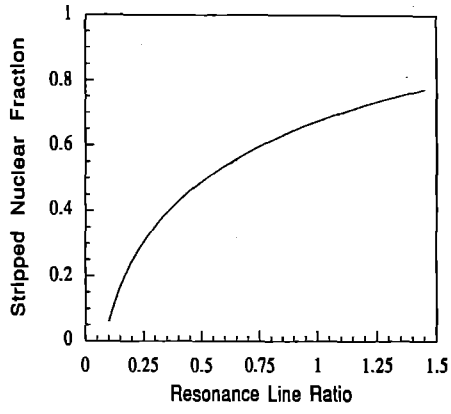

Fig. 4. The fraction of fully stripped nuclei in gain region at the lasing time as function of the line ratio of the Lyman β transition of H-like ions to the $1s3p$ - $1s^2$ transition of He-like ions in carbon recombining plasmas for the conditions in figure 1.

The inferred values of the electron temperature, electron density and the fraction of fully stripped nuclei are quite close to the optimised parameters for C VI recombination lasers[1]. These measurements explain the significant improvement in gain performance of C VI recombination x-ray lasers at 18.2 nm driven by 2 psec laser pulses[14].

CONCLUSION

It may be concluded that measurement of the intensity ratio of the Ly β transition of H-like ionisation stage to the $1s3p$ - $1s^2$ transition of He-like ionisation stage is a simple but effective diagnostic for inferring the absorbed energy in plasmas and for monitoring the production of the plasma suitable for high gain operation during adiabatic expansion.

ACKNOWLEDGEMENT

The authors would like to thank the VULCAN laser operations, the target preparation and engineering groups of the Central Laser Facility for their help and cooperation.

REFERENCES

1. J Zhang and M H Key, Appl. Phys., B58, 13 (1994).
2. P Jaegle et al., *X-Ray Lasers 1990,* edited by G J Tallents, (IOP publisher, Bristol, 1991) p.43.
3. M Grande et al., Opt. Commun., **74**, 309 (1990).
4. Z Z Xu et al., Appl. Phys. Lett., **63**, 1023 (1993).
5. J Steingruber and E E Fill, Appl. Phys., B58, 29 (1994).
6. D D Meyerhofer et al., Phys. Fluids, B5, 2584 (1993).
7. C D Danson, Opt. Commun., **103**, 392 (1993).
8. B L Henke et al., J Opt. Soc. Am., **1**, 828 (1984).
9. J Zhang, M H Key, P Norreys and G J Tallents, Opt. Commun., **95**, 51 (1993).
10. J Zhang et al., *X-Ray Lasers 1992*, edited by E E Fill, (IOP publisher, Bristol, 1992) p.339.
11. C Chenais-Popovics et al., Phys. Rev. Lett., **59**, 2161 (1987).
12. Y Kato et al., *X-Ray Lasers 1990,* edited by G J Tallents, (IOP publisher, Bristol, 1991) p.1.
13. G J Tallents et al., *X-Ray Lasers 1992*, edited by E E Fill, (IOP publisher, Bristol, 1992) p.101.
14. J Zhang et al., SERC CLF Annual Report (1994).

DEMONSTRATION OF SOFT X-RAY AMPLIFICATION OF POLARIZED EMISSION IN NEONLIKE GERMANIUM

B Rus[1,6], G F Cairns[2], P Dhez[1], P Jaeglé[1], M H Key[3,4], C L S Lewis[2], D Neely[3], A G MacPhee[2], S A Ramsden[5], C G Smith[4], A Sureau[1]

[1]Laboratoire de Spectroscopie Atomique et Ionique, URA 775 CNRS, Université Paris-Sud, Bâtiment 350, 91405 Orsay Cedex, France
[2]Department of Pure and Applied Physics, Queen's University of Belfast, Belfast BT7 1NN, U.K.
[3]Central Laser Facility, Rutherford Appleton Laboratory, Chilton, Oxon, OQ11 0QX, U.K.
[4]Clarendon Laboratory, University of Oxford, Oxford OX1 3PU, U.K.
[5]Department of Computational Physics, University of York, York YO1 5DD, U. K.
[6]on leave from the Department of Gas Lasers, Institute of Physics, Na Slovance 2, CZ-18040 Prague 8, Czech Republic

INTRODUCTION

There is a steady shift of worldwide soft x-ray laser research to control, and hence optimize various properties of the x-ray beam. One of these parameters, which may be of importance for a number of applications, is its polarization state. A scheme to produce polarized x-ray laser output, based on injecting polarized emission into an active medium and amplifying it to the desired intensity, is demonstrated in this work. Its first aim was to verify that a non-saturated ASE is unpolarized as concluded from simple arguments. The second objective was to demonstrate that a polarized x-ray beam can be amplified without a significant degradation of its degree of polarization (or without suffering "depolarization"). Finally, it was to show that an x-ray laser may deliver a linearly polarized beam and that polarization as an x-ray laser feature may be readily attained for applications.

POLARIZATION PROPERTIES OF ASE

The ions triggering the ASE are virtually uncoupled (correlation only over a distance of the order of one wavelength might be expected) and the orientations of their dipole moments as well as phases of their dipole oscillations are uncorrelated. Starting from an uncorrelated source, a definite phase and orientation of the macroscopic electric field vector over the beam area gradually build up during the propagation of the emission in the medium. The phase/coherence and polarization properties of the macroscopic radiation field are influenced by a number of processes taking place in the amplifying medium, such as collisions and the motion of the amplifying ions. As for the coherence, the ASE polarization will not be determined merely by the properties of the uncorrelated source having triggered it, but will depend on the character of the amplifying medium and the amplitude of the ASE field as well.

The interconnection of the coherence and polarization may be illustrated by considering collisions in the plasma. (The ion motion, leading to Doppler broadening, is assumed to influence the polarization properties to a much lesser extent.) The frequency of electron-ion elastic collisions is typically $\approx 10^{14}\ s^{-1}$ in relevant plasma conditions. This value is much larger than the A coefficient of the spontaneous emission, being typically $\approx 10^{10}\ s^{-1}$ as well as the rate of stimulated emission, which may be assessed as $\approx 10^{9}\ s^{-1}$ ($\tau_{stim} \cong 8\pi h\nu^3 \Delta\nu/(Ic^2A)$, where ν and $\Delta\nu$ are the emission frequency and the frequency linewidth, and I the intensity, taken here $\approx 10^5$ W/cm^2). The collisions thus intervene many times during the field-ion interaction: they randomly change the phase of the ion's dipole oscillations as well as the orientation of its dipole moment and their effects will manifest both in the coherence and the polarization. The situation is more complex if we distinguish effects of long- and short-distance collisions. The latter ones, considerably perturbing the energy levels and causing large disturbances of the oscillation phases, cause also large orientation changes of the dipole moments. The spectral wings thus undergo larger variations of the polarization state than the line center.

The phase of a quasimonochromatic radiation field of wavelength λ is maintained during the coherence time t_{coh} which may be evaluated via the spectral line width $\Delta\lambda$ [1]:

$$t_{coh} = \gamma\, \lambda^2/(c\Delta\lambda) \qquad (1)$$

where γ is 0.32 for a Lorentzian and 0.66 for a Gaussian profile. It is obvious that t_{coh} presents a useful estimate for the characteristic time during which a given polarization state of macroscopic field is maintained, especially in the case where the contribution of collisions to the line broadening is important. Measurements of the line profile at 206.4 Å in Se[2] suggest that homogeneous broadening is significant. Taking $\Delta\lambda \sim 20$ mÅ as an estimate for ASE at $\lambda \approx 200$ Å with a moderate gain-length product, (1) gives $t_{coh} \approx 0.3$ ps. As a typical x-ray laser pulse duration is hundreds of ps, it will accordingly consist of perhaps thousands of "wavetrains" each carrying a definite polarization state. Unless monitored by a detector with an extremely high temporal resolution, which could discern any one particular polarization state lasting for a time of the order of ≈ 0.1 ps, an unsaturated x-ray laser output should appear virtually completely unpolarized.

During the triggering of the ASE, different groups of atoms contribute to excite each of the transverse modes to a different extent (this contribution is given by the scalar product of the triggering field distribution with the mode field distribution). As a result, different modes will have different polarization states. To obtain a uniform direction of polarization across the whole beam, single-mode operation is necessary - or, equivalently, the Fresnel number $F=\pi a^2/(\lambda L)$ of the lasing medium (2a is the width of the gain region and L the plasma length) must be close to one. This is indeed the same requirement as to achieve perfect transverse coherence.

AMPLIFICATION OF POLARIZED EMISSION

We will describe the polarization properties of the x-ray laser beam in terms of the degree of polarization

$$D_p = I_p / (I_p + I_u) \qquad (2)$$

where I_p and I_u are the intensities of the polarized and unpolarized components.

In the scheme investigated, a plasma source of length l_s delivers an emission which is, following the above remarks about ASE polarization properties, considered to be completely unpolarized - i.e. its $D_p=0$. This emission is then polarized and further manipulated by x-ray optics having a total throughput R, and injected with a coupling efficiency C into an amplifying plasma of length l_a. Neglecting local spontaneous emission with regard to ASE in both the source and amplifier, the intensity emerging from the amplifier in below-saturation threshold regime is

$$I_{amp} = RCw \frac{j_s}{g_s} \frac{exp(g_s l_s + g_a l_a)}{\sqrt{g_s l_s + g_a l_a}} + w \frac{j_a}{g_a} \frac{exp(g_a l_a)}{\sqrt{g_a l_a}} \qquad (3)$$

where j_s, g_s and j_a, g_a are spectral peak emissivities and gain coefficients of the source and amplifier plasmas, respectively. The factor $w = \sqrt{\pi}\, \alpha\Delta\nu$ is due to the spectral line profile ($\Delta\nu$ is the intrinsic frequency linewidth and α a numerical factor ranging from 0.5 for a Lorentzian to ~0.6 for a Gaussian intrinsic profile). In deriving (3) we supposed that the line profiles were the same for both the source and the amplifier plasmas.

The first term in (3) represents emission being injected into the amplifier plasma and subsequently amplified; the second term is the proper ASE of the amplifier. Assuming that the gains and emissivities of the source plasma and the amplifier do not differ by

much, the quantity $g_s l_s + \ln(RC)$ must be at least of several unities in order that the amplified input dominates over the amplifier ASE. Supposing that the emission injected into the amplifier maintains its polarization state during the amplification, the degree of polarization of the first term in (3) will be identical to that of the emission entering the amplifier. On the other hand, the amplifier's own ASE contributes a totally unpolarized signal to the output. Labeling the degree of polarization of the injected beam D_p^{in}, the degree of polarization of the amplifier output D_p^{amp} will be

$$\frac{1}{D_p^{amp}} = \frac{1}{D_p^{in}} + \frac{j_a}{j_s}\frac{g_s}{g_a}\sqrt{\frac{g_s l_s + g_a l_a}{g_a l_a}}\, exp(-g_s l_s - \ln(D_p^{in} RC)) \quad (4)$$

One sees that even for moderate values of $g_s l_s + \ln(D_p^{in} RC)$, the influence of the amplifier ASE on the output polarization state will be very small. The processes which are, during amplification, able to partially "depolarize" this already polarized emission, will be assessed below.

X-RAY POLARIZERS

The devices used in the presented work, making it possible to polarize/analyze the soft x-ray emission of interest (lasing lines at 232 and 236 Å), were multilayer mirrors at a 45° angle of incidence. The ability of a 45° off-the-normal-incidence multilayer structure to act as a polarizer in the soft x-ray region[3] is based on reflection under Brewster's angle at a sequence of dielectric interfaces. The s-polarized wave, having its electrical vector parallel to the polarizer surface, is preferentially reflected. It should be noted that the reflectivity of the p-polarized wave cannot be simply brought to zero by minimizing the surface roughness, as the materials involved in the multilayer structure have a non-zero absorption.

The Mo:Si polarizers exploited in this work were produced by electron sputtering[4] onto superpolished fused-silica substrates and were tested with synchrotron radiation[5]. An *s*-reflectivity R_s near 24 % was found. The calculations suggest[4] that the ratio R_s/R_p should be typically ~7.4, i.e. the p-reflectivity R_p being ~3.25%. The calculations point to a fairly weak dependence of the ratio R_s/R_p on the surface roughness as well as on other fabrication parameters. As the degree of polarization depends on the measured data only by R_s/R_p, it gives us fair confidence in the precision of the presented experimental results.

Knowing the intensity and polarization state of the radiation before reflection on a polarizer ($R_s > R_p$), one may calculate the intensity and polarization state of the radiation after reflection, using e.g. Mueller matrix formalism. For instance, when a totally unpolarized wave of intensity I_{0u} undergoes two subsequent reflections on the polarizer, the reflected wave will consist of a linearly polarized wave of intensity I_p and an unpolarized wave of intensity I_u :

$$I_p = 1/2\left(R_s^2 - R_p^2\right) I_{0u} \quad \text{and} \quad I_u = R_p^2\, I_{0u} \quad (5).$$

Taking $R_s = 0.24(\pm 0.04)$ and $R_p = 0.03(\pm 0.01)$ we obtain for two successive reflections of an originally unpolarized wave $I_p \cong 0.0284\, I_{0u}$, $I_u \cong 0.0009\, I_{0u}$, and $D_p = 0.969(^{+0.021}/_{-0.046})$.

EXPERIMENTAL

The experiment presented in this work was conducted at the Rutherford Appleton Laboratory on the x-ray laser facility[6]. The layout of the experimental geometries for both the ASE polarization state measurements and the amplification of polarized emission is shown in Figure 1. The basis of the architecture in each case consists of a double-target amplifier which has been established as a routine part of the RAL experiments; from here on it will be referred to as 'injector'. In this experiment, its length was 22+22 mm and consisted of Ge glass-supported stripes 100±10 μm wide and 0.6 μm thick, displaced 225 μm laterally and 580 μm axially. The injector was driven by six 110 mm Vulcan laser beams each delivering ≈200 J at 1.06 μm in pulses of 650 ps FWHM. The typical irradiation intensity throughout the experiment was $\sim 1.6 \times 10^{13}$ Wcm^{-2} and the value of the gain coefficient is accordingly supposed to be[7] 3.5(±0.5) cm^{-1}.

The north-propagating injector ouput was manipulated using different x-ray optics depending on the kind of polarization experiment being carried out. (The south-going beam was blocked by an aperture stop so that it did not contribute to the output by a remnant signal.) The common x-ray optical component used throughout the experiment was a W:Si multilayer normal-incidence concave mirror with a focal length of 500 mm and with a reflectivity ≈10%. In the setup for the injector output polarization state measurements, this mirror simply relayed the x-ray beam towards the south, where the beam diagnostics were placed. Its distance from the injector's north exit was 740 mm. A triangular system of 150 μm thick crossed wires was placed 1930 mm downstream from the mirror and worked as a spatial and dimensional fiducial. The x-ray laser beam was analyzed by a pair of crossed multilayer polarizers. Due to the horizontal symmetry of the experiment, the task of viewing the whole x-ray beam in two polarizers is equivalent to the task of separately analyzing the upper and lower half of the beam; indeed, a precise alignment of such a configuration is essential. We arranged two polarizers in such a way that the first one intercepts and analyzes the lower half of the beam in the horizontal direction of polarization, while the second polarizer intercepts and analyzes the remainder of the beam in the vertical direction of polarization. As time-integrated recording media, two Kodak 104-02 film backs were used. They were protected by 0.8 μm Al filter to reject visible light. The films were placed so that the optical paths, and hence the magnification of the fiducial crossed wires system, were the same in both arms.

In the second arrangement, the injector emission was linearly polarized and subsequently seeded into the amplifier plasma. The north-going injector beam is reflected westwards by a multilayer

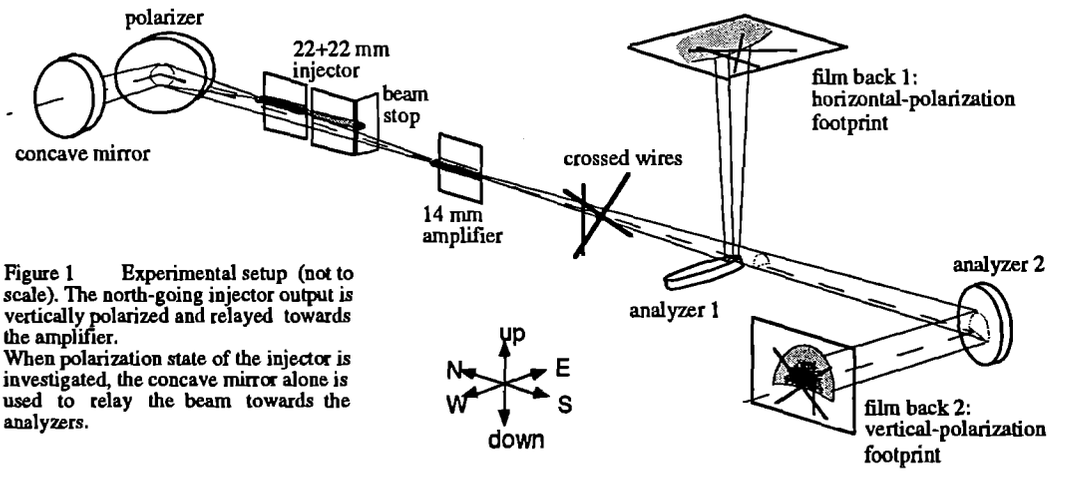

Figure 1 Experimental setup (not to scale). The north-going injector output is vertically polarized and relayed towards the amplifier.
When polarization state of the injector is investigated, the concave mirror alone is used to relay the beam towards the analyzers.

polarizer and reaches the normal-incidence concave mirror, which is that used in the injector ASE polarization measurements. The optical path between the injector exit and the mirror is the same as before -740 mm- so that regarding the beam propagation, the two arrangements are equivalent. After leaving the concave mirror, the x-ray beam experiences another reflection at the polarizer and is sent southwards. Supposing at this point that the injector output is unpolarized, the degree of polarization of the beam entering the amplifier is $\sim 0.97(^{+0.02}/_{-0.04})$ which is quite a high value. However, this polarized beam leaving the polarization/coupling optics is now $1/0.0284 \sim 35$ times less intense than the unpolarized beam leaving the concave mirror in the injector ASE polarization state measurements.

The amplifier plasma was produced by irradiating 14 mm-long Ge stripes of the same sort as the injector targets. The driving laser was one 150 mm beam of 1.06 μm light, delivering ≈400 J in ~1 ns and providing irradiation intensity of $\approx 1.3 \times 10^{13}$ Wcm^{-2}. The optical distance between the concave mirror and the amplifier north end was 1530 mm. The amplifier was shot at time 7.55 ns after the injector was fired. The overall set of irradiation parameters resulted in a net amplifier gain of [8] $2.5(\pm 0.5)$ cm^{-1}.

The polarized injector beam was imaged to ≈62 mm in front of the amplifier entrance plane. It was directed into the amplifier plasma at an angle of ≈3 mrad with an offset of ~70 μm relative to the target surface, so that center of the relayed beam matches the amplifer gain region. Here we define the geometrical coupling efficiency as the fraction of the injector beam overlapping the gain region at the amplifier entrance plane. This coupling efficiency equals approximately $C \approx M^{-2}$ assuming that the image plane of the injector output is close to the injector entrance. The magnification M is the ratio (distance between the mirror and the amplifier input) / (distance between the injector exit and the mirror). In this work, $M = 1530/740 \sim 2.07$ and hence the C~0.23. The actual fraction of the injector beam intensity, entering the amplifier gain region, is given by the product RC; for the vertically polarized emission, it amounts to $RC \approx 0.10 \times 0.0284 \times 0.23 \sim 6.53 \times 10^{-4}$.

RESULTS

In the first part of the experiment, devoted to the injector ASE output polarization state measurements, 11 shots of driving energy 570(±40) J per single injector target were fired. Care was taken to ensure that the exposed films from either arm were developed under identical conditions. Films were 2-D densitometered using a Perkin Elmer PDS densitometer and the obtained data were transferred onto a personal computer. The software processing of the images ("footprints") consisted of several steps. First, the background optical density was subtracted from each image. The images were then converted from optical density D into exposed radiation intensity (photons per square micrometer)[9]. A correction was done for the analyzer reflectivities and the attenuation of 0.8 μm Al filter, and a constant intensity value, obtained during a blank shot, was subtracted from each image. The two footprints from each shot were then finally composed into single image serving as a basis for the analysis.

A typical footprint image of the injector output is shown in Fig.2. At first sight it is obvious that the upper and lower halves of the beam, viewed by the two 90°-crossed analyzers, provide similar signals. However, one can also see that the x-ray beam is neither entirely symetrical nor perfectly centered with respect to the edge of the first polarizer and the cross-wire center; also, the beam shape and its position on the films fluctuate slightly shot by shot. As we are looking here for small differences between the signals from the upper- and lower- half of the beam footprint, interpretation of their relative intensity had to be carried out with a criterion independent of the exact beam position and/or its assymetry. One such criterion is to follow jumps in the composed footprint image intensity when passing from the bottom part of the beam, seen by the first analzer, to the upper part, viewed by the second one. As the beam is continuous, any such jump signifies that the beam

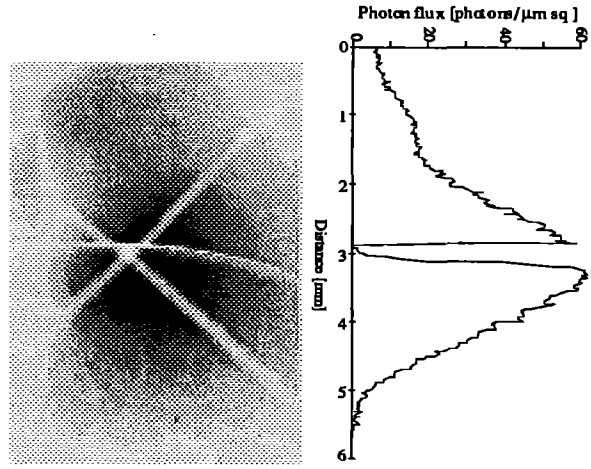

Figure 2 Footprint of the injector beam (#01-140993)

displays macroscopic polarization. Images obtained with the crossed wires removed were densitometered in several parallel traces, and an average value of the jumps in these individual traces was calculated. Based on the obtained results, we may state that:
i) Neither the upper- nor lower- half of the beam footprint were revealed to be systematically more intense than the other, which means that there is no preferred direction of polarization.
ii) The greatest observed magnitude of the difference between the s- and p- footprint signals, normalized to the beam intensity, was 0.08(±0.04), where the error is estimated as a typical value of the image noise. This maximal difference may be used as an upper estimate of the degree of polarization, being thus ~0.04(±0.02). Regarding the precision of the experiment, this value suggests that the macroscopic time-integrated degree of polarization of the x-ray beam is below the detectable threshold.

In the second part of the experiment, in which amplification of polarized emission was studied, 8 shots in total were taken. In addition, we performed a shot where the emission injected into the amplifier was not polarized (the arrangement was identical to that of Fig. 1 except that the concave mirror relayed the injector beam directly into the amplifier, without reflections on the polarizer).

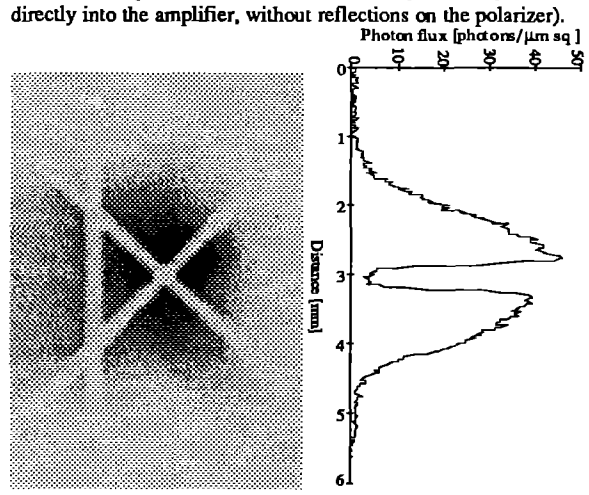

Figure 3 Footprint of the polarized amplifier output (#02-131093)

As a vertically polarized emission is injected into the amplifier, a "vertical" footprint (from the second analyzer) of the whole amplifer output beam was first taken. The result is shown in Fig.3; one may note a very high beam quality. This fact is made more evident from the vertical densitometry trace of this footprint. The first ("horizontal") analyzer was then mounted and films in both arms were exposed. A typical result is shown in Figure 4. One can see that the horizontal footprint contains virtually no signal; a high degree of vertical beam polarization is thus unequivocally demonstrated. Assuming that the x-ray beam is centered with respect to the crossed wires, the signal contained in the vertical footprint is $R_s I_{0p} + 1/2(R_s + R_p) I_{0u}$ and the signal in the horizontal

footprint $R_pI_{0p}+1/2(R_s+R_p)I_{0u}$; the quantities I_{0p} and I_{0u} are to be derived. We may then deduce $D_p=I_{0p}/(I_{0p}+I_{0u})$. Taking surfaces under the densitometry traces as the values of the overall signals, we obtain the degree of polarization of the amplifier output $D_p=0.98(^{+0.02}/_{-0.05})$. This value means that the amplified x-ray beam keeps the same degree of polarization as the injected beam and clearly indicates that no detectable depolarization effects took place during the amplification. Also, as the absolute response of the Kodak 104-02 films is known, the energy contained in the polarized beam was estimated as ~2 nJ.

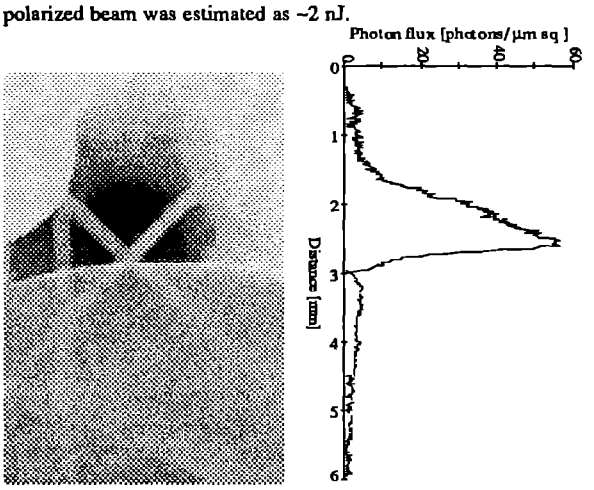

Figure 4 Polarized amplifier output viewed by two crossed analyzers (#04-131093)

The experiment was completed by verification shots. When the amplifier alone was fired, the vertical and horizontal footprints provided the same background signal. The 45°-mirror polarizing the injector output was then removed and the injector beam was coupled into the amplifier by the concave mirror only. The same footprints obtained in both arms provided another clear-cut proof that a polarized beam had been obtained in the other shots.

DISCUSSION

The results obtained in the first part of this work verify the basic validity of the given picture about ASE polarization properties. It is clear that the injector output beam was unpolarized within the limits of precision of the experiment carried out and that the small jumps between the signal of the upper and lower footprints may well be caused either by noise or by diffraction on the polarizer edges. The maximum degree of polarization deducible from the experimental data is $D_p=0.04$; this undoubtedly represents an upper bound of the real value. Two other facts should be further emphasized. First, due to the quite large bandpass of the polarizers, the footprints contain signals from both lasing transitions at 232 and 236 Å. We thus have an "overlap" of two beams whose polarization states are mutually uncorrelated - this even lessens the resulting degree of polarization of the whole beam. Secondly, the Fresnel number of the injector (22+22+0.5 mm long) is ~2 in the horizontal and ~7.5 in the vertical plane, assuming the gain region has a horizontal dimension of ~50 μm and a vertical dimension of ~100 μm. These are quite small numbers (although we are still far from a single-mode operating ASE) and show that the investigation has been performed under reasonable experimental conditions.

The central point of the results obtained when the injector output was linearly polarized and amplified is the observation that no detectable change of the polarization state took place during the process of amplification. In general, there are three possible processes able to "depolarize" the emission propagating down the below-saturation threshold amplifying medium: (i) contribution of the amplifier proper ASE, (ii) the Faraday rotation of the electric vector of the x-ray beam in the spontaneous magnetic field produced in the plasma, and (iii) collisions experienced by the amplifying ions, changing the orientation of their dipole moments. The contribution of the amplifier's own ASE to its output may be evaluated from the relation (4). Taking $D_p^{in}=0.97$, $g_s=3.5$ cm^{-1}, $l_s=4.4$ cm, $g_a=2.5$ cm^{-1}, $l_a=1.4$ cm, $RC=6.53\times10^{-4}$ and supposing that the emissivities of the injector and the amplifier are the same, we obtain $D_p^{amp}=0.969$. The effect (i) is hence negligible. The plasma-generated magnetic field B is here parallel to the propagation direction of the x-ray laser (the B is directed downstream in the above part of the amplifier plasma and counterstream in the bottom part), and the amplifier acts as a Faraday rotator for the linearly polarized beam. The rotation angle is[10] $\phi\approx(n_e/n_{cr})qB/(2m_ec)l_a$,where q and m_e are respectively the electronic charge and mass. Taking B≈50T, $n_e\sim3\times10^{20}$ cm^{-3} and $n_{cr}\sim2\times10^{24}$ cm^{-3} (for 236 Å), we get $\phi\sim1.77$ degrees. Again, the effect (ii) is not experimentally relevant. Although we do not have a quantitative assessment of (iii), the "depolarizing" short-distance collisions affect mainly the wings of the spectral profile, where gain is marginal. As this is further pronounced by gain-narrowing, the total depolarization due to the collisions is expected to be small - a fact indeed evidenced experimentally in this work.

CONCLUSIONS

In summary, the polarization state of two J=2-1 lasing lines at 232 and 236 Å in a neon-like Ge soft x-ray laser has been investigated in two experimental arrangements. Whereas in the first setup we studied the natural polarization properties of an ASE x-ray laser output, the amplification of a linearly polarized beam was examined in the second part of this work. For both of these cases we have presented rather simple background arguments making it possible to estimate the importance of the processes influencing polarization properties of the x-ray beam. These arguments suggest that one definite polarization state in a below-saturation ASE regime lasts a fraction of picosecond. The consequent expectation that a typical ASE output should appear virtually unpolarized in time-integrated diagnostics, was confirmed experimentally. The injector beam was observed neither to be preferentially polarized in any direction nor to show a measurable degree of polarization. The second experimental arrangement was designed to actively control the polarization state of the x-ray beam produced by a scheme injector-amplifier. To that end, only vertical polarization was selected from the injector beam prior to feeding it into the amplifier plasma. The measured degreee of polarization $D_p\sim0.98$ of the amplifier output beam has been found identical (within the experimental precision) to the degree of polarization of the injected beam. This result is consistent with the basic arguments suggesting that the depolarization effects should be fairly weak.

Producing a highly polarized x-ray beam of a good spatial quality is the major achievement of this work. Regarding the attained gain-length product of ≈12, another amplifier in future research would allow the polarized beam to reach the gain-saturation level.

REFERENCES

1. J W Goodman, Statistical Optics, J Wiley, New York 1985, Ch.5
2. J A Koch, B MacGowan, L DaSilva, D Matthews, J Underwood, P Batson, S Mrowka, Phys.Rev.Lett. 68(1992), 3291-3294
3. P Dhez, Nucl. Instr. and Meth. in Phys. Res. A 261 (1987), 66-71
4. The polarizers were designed and fabricated by J P Chauvineau team from the Institut d'Optique at Orsay.
5. The reflectivity tests were performed at NIST Physics Laboratory, Gaithersburg, by T Lucatorto, C Tarrio and R Watts.
6. G F Cairns, D M O'Neill, C L S Lewis, D Neely, A G MacPhee, C Danson, A Damerell, M H Key, D Rodkiss, R Wyatt, SERC Annual Report to The Central Laser Facility (1993), 131-134
7. D Neely, C L S Lewis, D M O'Neill, J O Uhomoibhi, M H Key, S J Rose, G J Tallents, S Ramsden, Opt. Comm. 87 (1992), 231-236
8. D Neely, C L S Lewis, G Cairns, A G MacPhee, M Holden, J Krishnan, G J Tallents, M H Key, P N Norreys, C G Smith, J Zhang, M T Browne, R E Burge, G E Slark, P B Holden, G J Pert, J Ploues, S A Ramsden, SERC Annual Report to The Central Laser Facility (1993), 3-7
9. J Krishnan, D Neely, C Danson, L Dwivedi, C L S Lewis, G Tallents, SERC Annual Report to The Laser Facility 1992, 22-23
10. J A Stamper, Laser and Particle Beams 9 (1991), 841-862

MEASUREMENT OF THE ASTIGMATISM INTRODUCED INTO AN XUV LASER BEAM BY AN XUV LASER AMPLIFIER

C G Smith[1], G Cairns[3], M H Key[1,2], C Lewis[3], D Neely[2], A MacPhee[3]

1 Clarendon Laboratory, Oxford University
2 Rutherford-Appleton Laboratory
3 Dept of Pure and Applied Physics, Queens' University Belfast.

INTRODUCTION

In previous work using the Vulcan laser facility at RAL, the Ge XXIII XUV laser has been developed as a high gain double plasma ASE generator[1] and with double passing has been driven to saturation[2]. More recently a beam from the double plasma source has been injected into a separate amplifier via an XUV mirror which, by coupling to the amplifier only a small fraction of the wavefront from the ASE source, reduced the beam divergence and increased the coherence of the injected beam[3]. The amplifier provided high gain but also introduced refractive bending and astigmatism with positive lensing perpendicular to the target surface, and negative lensing parallel to the surface, plus higher order aberrations[4]. Refractive deviation can be fully compensated by bending the target[5] and astigmatic lensing is also, in principle, able to be compensated.

In this work the magnitude of the astigmatism was measured for the first time.

EXPERIMENT

The experimental system is shown in Fig 1.

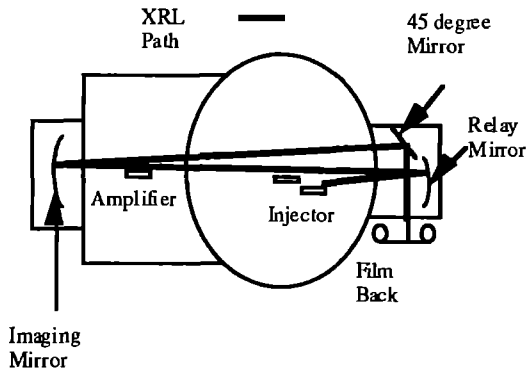

Figure 1 The experimental system.

The injector consisted of two 20 mm long slab targets with 100 μm wide germanium stripes. Each target was irradiated by three 1.05 μm wavelength beams from the Vulcan laser with overlapping 22 mm long line foci at an intensity of 1.5×10^{13} W cm^{-2} in a 650 ps pulse and the width of the optical focus on the target matched the Ge stripe width. ASE at the output from the injector was imaged by the relay mirror to a plane close to the input face of the amplifier target with 3-fold magnification. A single beam from Vulcan irradiated the 14 mm long amplifier producing 1.5×10^{13} W cm^{-2} on a stripe width of 150 μm. This plasma amplified the signal by approximately 70. Direct ASE from the injector to the amplifier was blocked and only the relayed beam reached the amplifier. The XUV beam at the amplifier was imaged by a 508 mm focal length XUV mirror at 4.2 x magnification. A film pack was used to record the images. Translation of the imaging mirror varied the image plane in the range ± 30 mm about the entrance face of the amplifier. Image resolution at the plane of the amplifier was 2.5 μm.

A series of beam images was recorded for variable position of the image plane. It was observed that the apparent shape of the beam changed consistent with the astigmatism of the amplifier. The beam images were digitised and converted to intensity using the response characteristic of the Kodak 101 film.

The most striking observation was that there was a minimum in the full width, half maximum (fwhm) of the beam profile about 10 mm downstream of the amplifier for measurements perpendicular to the plane of the target as shown in Fig 2(a). Conversely there was a minimum in fwhm in the plane parallel to the target, approximately 15 mm upstream of the target as shown in Fig 2(b). Pictures of the beam pattern at these two planes are shown in Fig 3(a) and (b) together with a typical trace of the intensity profile in Fig 3(c).

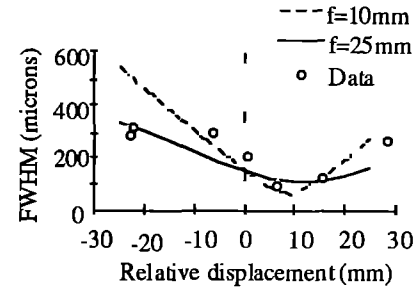

Figure 2(a) FWHMs measured perpendicular to the target face compared with model behaviour.

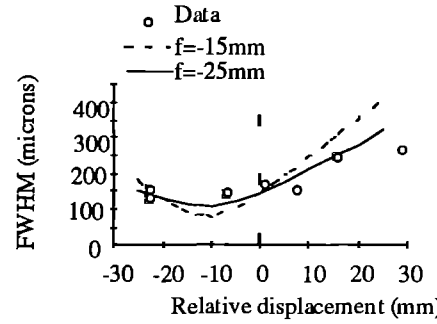

Figure 2(b). FWHMs measured parallel to the target face compared with model behaviour.

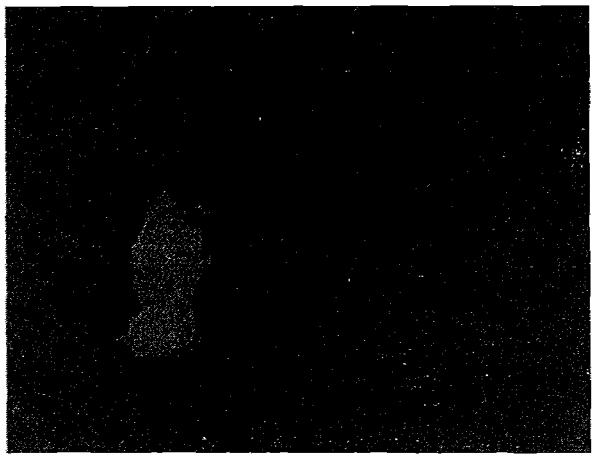

Figure 3(a). The beam profile 7mm downstream of the amplifier injection face.

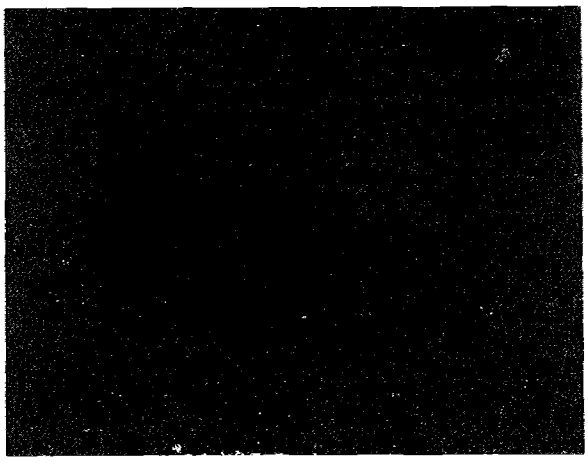

Figure 3(b). The beam profile 7mm upstream of the amplifier injection face.

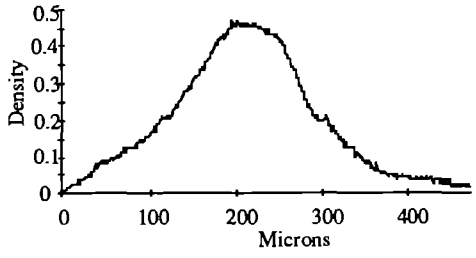

Figure 3(c). A trace parallel to the amplifier of shot 11171093.

MODEL

The behaviour of the beam in the amplifier was modelled in a simple way based on earlier analysis of the optical characteristics of the amplifier[3]. The amplifier was represented by distributed positive and negative lensing in the two perpendicular planes. The source was represented as an incoherent disc located at the furthest point of the injector, and having dimensions of 50 μm. Rays were traced from the incoherent disc source through the optical system to determine the full width half maximum of the image produced by the detection system.

The assumed positive and negative focal lengths of the lensing in the amplifier were varied to obtain a fit to experimental data. The results of the modelling also shown in Figs 2(a) and (b) indicate that the positive and negative lensing effects had focal lengths in the range + 10 to + 25 mm and - 15 to - 25 mm.

The coupling system reduced the beam divergence and increased the coherence of the injected beam but did not inject a fully coherent wavefront. The computed minimum diameter of the images was ~ 100 μm and comparable with the experimental measurement. An assessment of the higher order aberrations of the amplifier and of the ultimate limit to the coherence which can be produced in the beam from the amplifier, would require further experiments in which the injected beam had lower divergence and greater coherence. The present measurement is sufficient to estimate the astigmatism and to determine therefore the nature of the optical correction required to eliminate it.

CONCLUSION

The astigmatic behaviour of an X-ray laser amplifier has been studied for the first time. Agreement has been found between a simple model and experimental observation leading to a determination of the effective focal lengths of the positive and negative lensing in the amplifier. Correction of the astigmatism is possible in principle. The ultimate limits to beam quality from such an amplifier will be determined by higher order aberrations.

REFERENCES.

1 D M O'Neill, C L S Lewis, D Neely, J Uhomoibhi, M H Key, A MacPhee, G J Tallents, S A Ramsden, A Rogoyski, E A McLean, Opt Comm 75 406 (1990).

2 M H Key, A Kidd, P Norreys, R Kodama, H Z Chen, C Lewis, D Neely, D O'Neill, J Uhomoibhi, L Dwivedi, J Krishnan, G J Tallents, S Ramsden, G J Pert, J Zhang, A Carillon, P Dhez, P Jaegle, G Jamelot, A Klisnick, J P Raucourt., Physical Review Letters Vol 68 (no 19) pp 2917-2920 (1992)

3 D Neely, C L S Leis, G Cairns, A MacPhee, M Holden, J Krishnan, G Tallents, M H Key, P A Norreys, C G Smith, J Zhang, M T Brown, R E Burge, G Slark, P Holden, G Pert, J Ploues, S A Ramsden. RAL Annual Report 1993, p3.

4Optimisation of Brightness and Coherence in XUV Laser Amplifiers, M Key, C Smith, CLF Annual Report, 1993, p64

5 Y Kato, H Daido, R Kodama, K Murai, G Yuan, M Schulz, M Yamanaka, M Takagi, T Kanabe, S Nakai, D Neely, A MacPhee, C L S Lewis, G Slark, M Niibe, M Tsukamoto, Y Fukuda, H Tsunemi, S Nomoto, I Kodama, T Honda, K Shinohara, H Iwasaki, T Yoshinobu, SPIE Vol 2012 Ultrashort Wavelength Lasers II (1993)

PLASMA PROBING WITH A SOFT X-RAY LASER BEAM

A. G. MacPhee[⊗], G.F. Cairns[⊗], M.H. Key[×,*], C. L. S. Lewis[⊗], D. Neely[*], P. Norreys[*] and C. Smith[×].

(⊗) Department of Pure and Applied Physics, The Queen's University of Belfast, BT7 1NN
(*) SERC Rutherford Appleton Laboratory, Chilton, Didcot, Oxon OX11 OQX
(×) Clarendon Laboratory, University of Oxford, OX1 3PU

INTRODUCTION

Plasma probing with an XUV source, bright in comparison to the self emission of the object, is of considerable interest as a diagnostic for the ablative acceleration of targets both transverse and parallel to their direction of travel. For probing a target with a hot surface plasma and a thick, cold mass (typical of the initial conditions in inertial confinement fusion), produced either directly with an optical laser beam, or indirectly by the XUV emission from a laser plasma source, the probe brightness must be sufficient to overcome both the thermal emission of the object within the bandwidth of the detector system, and the high attenuation of the cold mass. Current XUV lasers with spectral brightness ~10^{31} photons cm^{-2} sr^{-1} s^{-1} in $\Delta\nu/\nu$ ~10^{-4} and pulse lengths down to ~50ps are suitably bright for this application. Results of a preliminary experiment are presented.

EXPERIMENTAL

A schematic of the XRL plasma probing geometry is shown in fig.1. The soft X-ray laser (J=2-1, Ne-like Ge, λ ~234Å: gl=14, duration of ~330ps) was generated by irradiating a 22mm × 100μm wide standard double target[1] at ~1.6×10^{13} Wcm^{-2}. The XRL beam was relayed with a 25cm focal length x-ray optic (Reflectivity=15%), to a point 90mm upstream of the probe site so as to provide a back-lighting disc at the interaction site of approximately 1mm diameter. Relative timing of the probe and drive beam was set to an accuracy of ± 50 ps using an optical streak camera. CH foils, 150μm diameter, 7 μm thick were ablatively accelerated by a normal incidence laser pulse (1μm, 1ns) at 6×10^{14} Wcm^{-2}. The accelerated foils were imaged onto 104-07 film via a 45 degree plane x-ray mirror, using a second spherical multi-layer mirror with 0.5m focal length, at a magnification of ~4·2.

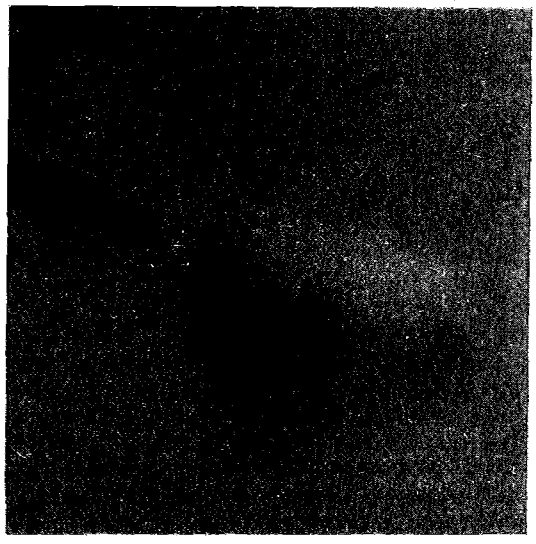

Fig.2 X-ray image of a CH foil 150μm diameter, 7μm thick, probed transversely at 1.5 ± 0.05 ns after the peak of the ablative drive pulse.

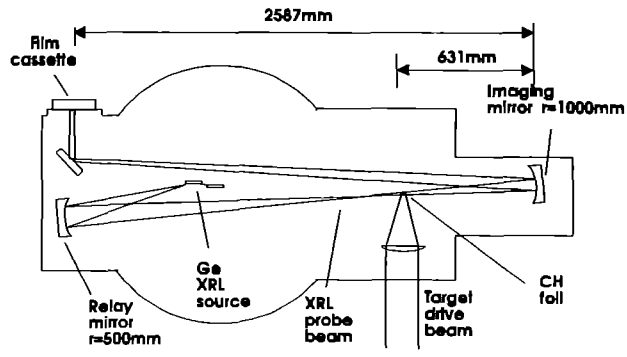

Fig.1 Schematic of the transverse XRL plasma probing set-up.

RESULTS

Intrinsic spatial resolution of 2·5μm was demonstrated over a 900μm diameter imaged area, based on the perceived width of the edges of lines in the x-ray image of an electron microscope grid (between the 10% and 90% transmission levels). The degree of spatial smearing observed in fig.2, corresponds to a minimum expansion velocity of ~2.10^5 ms^{-1} at the target centre.

CONCLUSION

Whilst imaging perpendicular to the ablation direction, it is necessary to constrain the probe pulse length to $\leq m\lambda/\theta v$ if temporal smearing is to be maintained below the diffraction limit of the system. To achieve this for typical parameters (beam divergence θ~10mrad, λ~200Å, magnification of the beam relay system onto the object m~3 and foil velocity v~$2\times10^5 ms^{-1}$), a ~30ps pulse is necessary. For probing *in line* with the foil velocity however, the spatial smearing parallel to the probe is eliminated. Smearing *transverse* to the ablation direction for in line probing and parallel to it for transverse probing, can then be reduced by employing a shorter probe pulse, such as the J=0-1 line of Ge at 196Å generated in recent pre-pulse experiments[2].

This work demonstrates the feasibility of such probing and possible future directions in this area will include in-line (or axial) imaging of ablatively accelerated Al foils, to study the seeding of Rayleigh Taylor instabilities due to small scale pressure variations on target. The resolution attained is suitable for observing the fastest growing Rayleigh Taylor modes in such foils, which have a spatial frequency of the order the foil thickness (~2-3μm) It is also possible to monitor spatial variations in the opacity of shocked targets, resulting from modulations in the drive beam intensity.

The 10^5:1 dynamic range of the new soft x-ray imaging system described separately[3] will provide for the increased contrast available in the recorded images for future experiments, due to the intrinsically low $\sqrt{N}$ noise of the X ray laser source.

REFERENCES

[1] D M O'Neill et al, Opt Comm 75 406 (1990).
[2] G F Cairns et al, this report.
[3] A G MacPhee, CLS Lewis, this report.

ENHANCEMENT OF THE J=0-1(19.6nm) LINE RELATIVE TO THE J=2-1(23.6nm) LINE IN THE GERMANIUM XUV LASER USING A PREPULSE TECHNIQUE

GF Cairns[1], CLS Lewis[1], AG MacPhee[1], D Neely[4], MH Key[2,4], C Smith[2], PB Holden[3], G Pert[3] and JA Ploues[3]

(1) Department of Pure and Applied Physics, Queens University of Belfast,BT7 1NN
(2) Clarendon Laboratory, Parks Road,Oxford
(3) Department of Computational Physics, York University, York
(4) Central Laser Facility, Rutherford Appleton Laboratory, Chilton

INTRODUCTION

The use of a low energy prepulse in the development of Ne-like XUV lasers represents another significant step in the 'subtle' manipulation of a plasma column for producing Amplified Spontaneous Emission, ASE. One of the anomalies in these schemes has been the relatively weak lasing observed on the J=0-1 transition compared to that observed for the J=2-1 transitions: the lasing observed on the J=2-1 lines at 23.6 and 23.2nm has been much stronger for the Ne-like germanium laser in all our previous experiments. This has been contrary to the modelling which predicts that a higher gain should be expected on the J=0-1 transition. It had been suggested that this might be due to the adverse effects of refraction, which tend to bend the ASE radiation out of the gain region; the gain region for the J=0-1 line lies in a higher density region where the density gradients tends to be larger.

Recent modelling(1,2) suggests that the use of a prepulse to pre-form the plasma before driving it with the main pulse, should help to relax the density gradients in the higher density regions and thereby reduce the effects of refraction. Nilsen et al(1) have observed the J=0-1 lasing line to dominate in Cr, Fe, and Ti using the prepulse technique. This led them to conclude that resonant photo-pumping was not a major pumping mechanism in the operation of the Ti XUV laser as originally proposed(1) but rather that refraction out of the gain region was reduced. Holden et al have specifically looked at the germanium lasing transitions and have suggested a significant increase in the ASE for the J=0-1 transition line can be expected with the use of the prepulse.

The experiment outlined here has given very promising results with the J=0-1 line being enhanced relative to the J=2-1 to become more intense than them. This may provide an alternative route for producing a highly coherent monochromatic beam, which is of particular relevance to application experiments, and forms one of our immediate goals.

EXPERIMENT

The experiment was carried out using 3 beams of Vulcan, the Nd-glass laser, which were arranged in the standard format, to give a line focus of ~25mm length and ~ 100μm wide(3). The targets consisted of germanium stripes, 100μm wide and lengths typically 22mm, coated onto glass substrates. Diagnostics included a streaked flatfield spectrometer at the north end and a time integrated flatfield spectrometer at the south, used for examining lasing emission. Resonance lines in the wavelength range 7.0-10.5Å were monitored on a spatially resolving time integrating bragg crystal spectrometer which had a CCD detector head, and on to a streak crystal spectrometer which gave time resolved spectra recorded onto HP5 film.

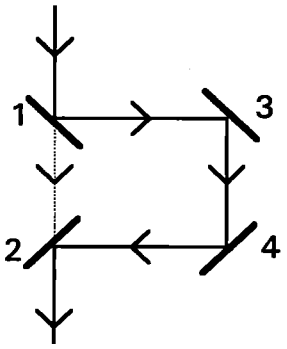

Figure 1 Dogleg for producing prepulse

The prepulse was produced by means of a dogleg using mirrors(figure 1), which was placed before the preamplifiers in the Nd-glass laser. The mirrors had a reflectivity of 99.7% and transmitted ~1.2% each. These were not ideal but were the only ones available for this 'look and see' trial. Consequently a low energy prepulse of approximately 0.02% of the total energy at target was

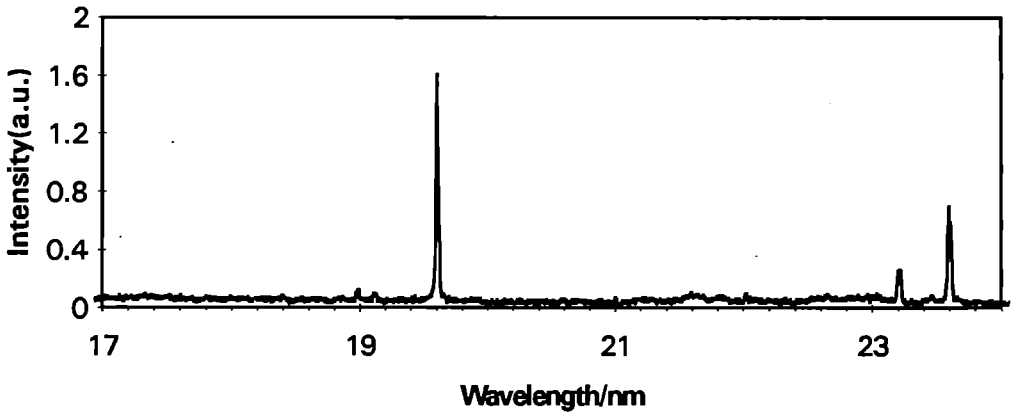

Figure 2 Spectral profile from time integrated data. #132910AS

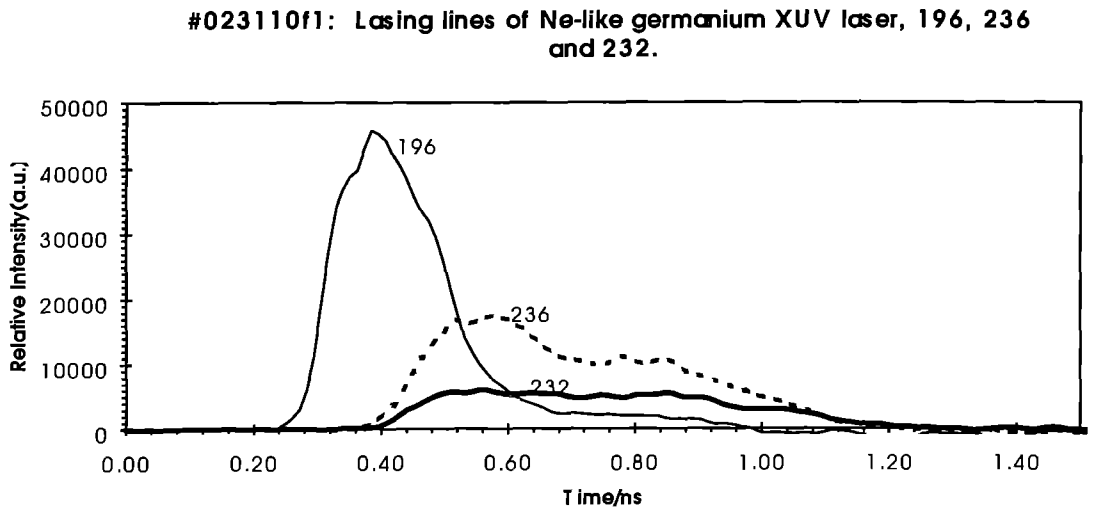

Figure 3 Temporal profile of lasing lines with prepulse

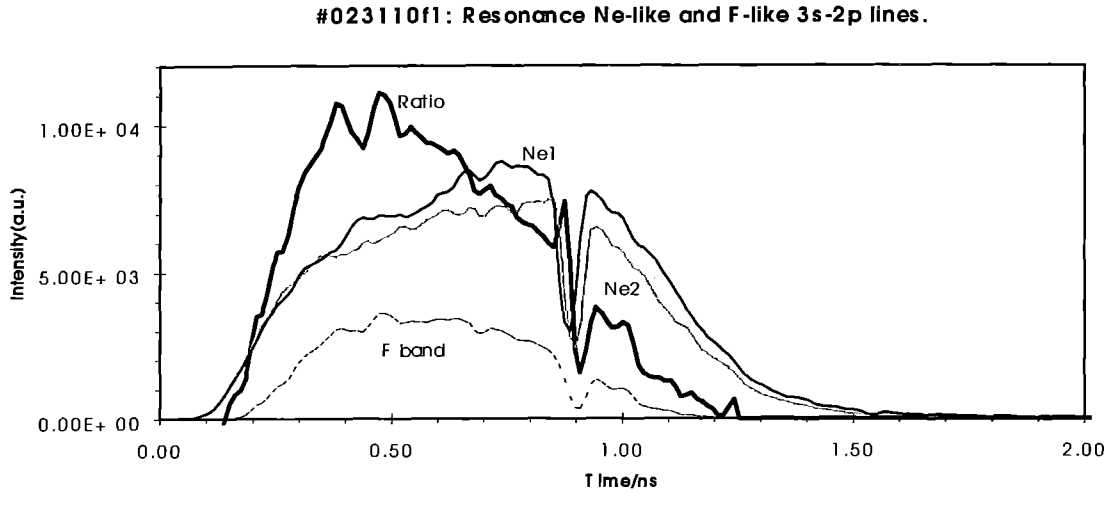

Figure 4 Temporal profile of resonance lines

produced and delivered 5ns early. The drive pulses were ~650ps FWHM at 1.06μm and gave irradiances of ~1.6×10^{13}W/cm^2 on target.

RESULTS AND DISCUSSION

A spectral profile is given in figure 2 showing clearly the dominance of the 19.6nm line in comparison to the 23.6 and 23.2nm lines for a typical prepulse shot. This trace was produced from a time integrated spectrum measured at 3.0 mRad from the main axis; this corresponded to the peak in the spatial profile for the 19.6nm line. Even though the J=2-1 lines peaked almost on axis their intensity was still significantly below the peak for the J=0-1 line shown in the figure.

Figure 3 shows a time resolved profile of the spectrally integrated intensities for the 19.6, 23.6 and 23.2nm lines. Again the dominance of of the 19.6nm line is evident. It tended to start lasing typically 150ps earlier than the J=2-1 lines and had a shorter FWHM pulse duration of about 150ps: the J=2-1 lines tended to lase twice as long. The Ne-like and F-like 3s-2p resonance lines were also time resolved. Figure 4 shows the resonance lines corresponding to the same shot as in figure 3. The noticeable dip in these lines is due to a reference line on the detector. Also shown in figure 4 is the ratio of the F-like(3s-2p) band at 9.439-9.553Å and the Ne-like lines at 10.01 and 9.762Å. This data indicates that the temperature reaches a peak earlier in time relative to the drive pulse . These results suggest, as expected, that the conditions for the J=0-1 line to lase requires higher temperature and densities.

To assess the effects of refraction on the ASE output, the angular deviation from the main axis of the lasing beams was considered. Figures 5 and 6 show the time integrated profiles for the three lines. Without the prepulse the intensity peaked off axis, as expected(5), at typically 8-10mRad. With the prepulse the deviation is significantly reduced. The 19.6nm line peaked at ~3-4 mRad off axis whilst the 23.2 and 23.6nm lines peaked almost on axis. This indicates that the density gradients tended to be relaxed in the gain regions with the use of the prepulse.

Three shots were taken under similar conditions with lengths 9, 14, & 22mm in order to provide an estimate of the gain on the lasing lines. The estimates were produced by applying a fit of the peak intensities from the time

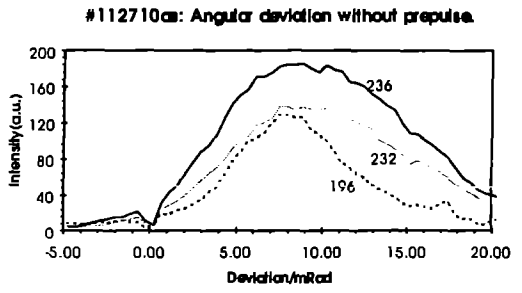

Figure 5 Deviation without the prepulse

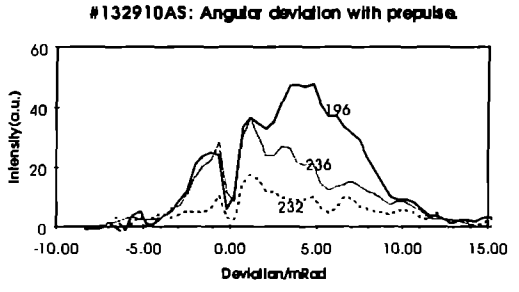

Figure 6 Deviation with the prepulse

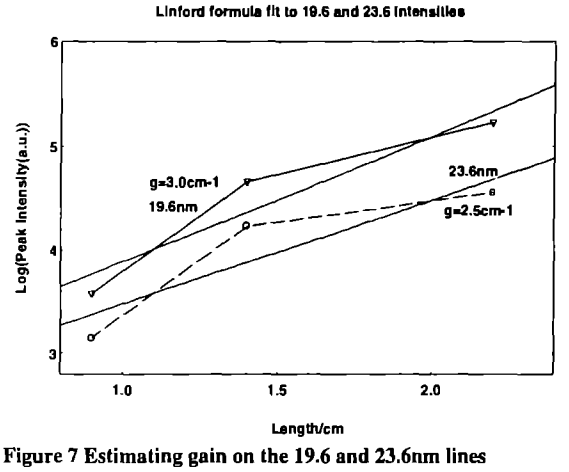

Figure 7 Estimating gain on the 19.6 and 23.6nm lines

resolved data to the Linford formula. Figure 7 shows the results with estimates of gain g=3.0cm^{-1} for the 19.6nm line and g=2.5cm^{-1} for the 23.6nm line. Values for the gain on these lines in previous experiments(3) have been measured as 2.7+/-0.1cm^{-1} and 3.8+/-0.3cm^{-1} respectively.

MODELLING

Modelling has been carried out for different prepulse strengths at 1%, 3% and 5% at York to try and predict the effects of such at different time intervals between the prepulse and main pulse. Figure 8 shows some of the results for a 1% prepulse at 5ns early, with beam and target conditions similar to those described for the experiment. They show how the temperature is increasing and the density gradient being reduced closer towards the surface of the target. Hence, the gain regions closer to the surface of the target and in higher density regions can conceiveably contribute more to the ASE beam. The deviation of the peak output from the axis is seen to be significantly reduced in agreement with the experiment. Although the prepulse in the experiment was smaller than 1%, there does seem to be good qualitative agreement with the modelling. Modelling for the 0.022% prepulse is currently being carried out. The low energy prepulse may explain the overall drop in intensity for the lasing lines with the prepulse.

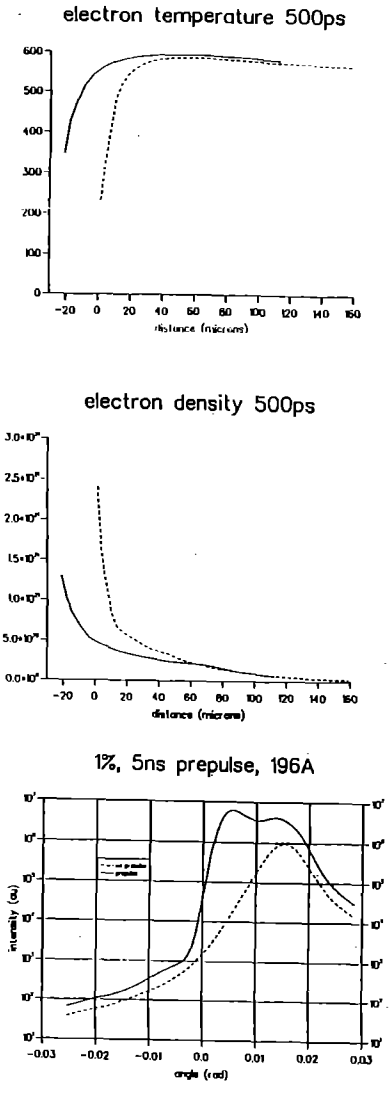

Figure 8 Some modelling results

CONCLUSION

The prepulse technique has been shown to work for the limited case outlined here and with a non-ideal intensity in the prepulse, in that as predicted the adverse effects of refraction can be overcome by preforming the plasma so as to relax the density gradients.However the overall brightness of the lines did decrease, especially the 236 and 232 lines which is contrary to predictions from the modelling which suggests these lines should also increase in intensity: the very low energy prepulse may explain why this is so. The experiment carried out had a limited number of shots available to it so that the main parameters such as timing and energy of the prepulse were only tried for the set of values indicated earlier. It is hoped in the near future to look more closely at the variation of these parameters with a view to optimising the output intensity of the 19.6nm line; this may provide an alternative route to a bright, monochromatic and highly coherent source so desirable for other experimental avenues such as microscopy and holography.

REFERENCES

(1) J Nilsen, BJ MacGowan, LB DaSilva, JC Moreno, Physical Review A, 48, 4682(1993)

(2) PB Holden, York, Private Communication

(3) DM ONeill, CLS Lewis, D Neely, J Uhomoibhi, MH Key, AG MacPhee, GJ Tallents, SA Ramsden, A Rogoyski, EA McLean and GJ Pert, Optics Comm., 75, 406(1990)

COHERENCE EXPERIMENTS WITH THE Ne-LIKE Ge X-RAY LASER

R E Burge, M T Browne and G E Slark

Physics Research, King's College London, Strand WC2R 2LS

INTRODUCTION

Considerable progress has been made in the development of diagnostic devices to determine the coherence and beam spread characteristics of the Ne-like Ge x-ray laser. Such studies are particularly relavant to exploring the potential advantages to be derived from the new injector-amplifier target configuration [1]. The diagnostic basically consists of pairs of Young's slits in which each slit is itself a narrow diffraction grating. Spectral dispersion separates the 23.2/23.6nm lasing lines from the background and allows their fringe visibilities to be studied independantly, Figure 1. The coherence function of the beam is related to the fringe visibility by the well known van Cittert-Zernike theorem. Preliminary investigation carried out with an early design of a Young's slits dispersive coherence diagnostic have already been described [2].

DIAGNOSTIC DESIGN

Initially two types of diagnostic were used; slits made out of PMMA and slits cut in gold, both on Si_3N_4 membranes. Analysis of the data from the first experiment established that although the PMMA gratings had a higher efficiency (because of the phase effect), there was an asymmetry between the diffraction envelopes from the two slits as a result of variations in the PMMA thickness. Gold gratings (which are purely amplitude gratings) were preferred in the second experiment in Aug-Sept 1993.

Another refinement was to fabricate two dispersive Young's slits pairs per membrane each with slightly different grating pitches to separate the fringe patterns on the film.

EXPERIMENT

The principal objective of the Aug-Sept experiment was to investigate the output beam characteristics of the Ge x-ray laser as a function of the target geometry and pumping conditions. Up to five diagnostic membranes were placed in the beam at a distance of 580mm from the amplifier target, Each membrane had two slit pairs with different separations enabling a good visibility envelope data set to be obtained on each shot. Each membrane had a 150μm slit separation and one other separation in the range 50μm to 250μm. The purpose of keeping one slit separation constant across the beam was to investigate the fringe visibility of the diffraction patterns as a function of beam position. The relative intensities of the corresponding diffraction patterns from the different membranes provides data on the intensity profile of the beam at any given wavelength. The entire set of membranes could be rotated vertically to allow the beam characteristics to be studied in the vertical plane. Hence, on a single laser shot, beam divergence and coherence could be established for each of the bright lasing and emission lines independently. Shot-to-shot stability and repeatability could be established by comparing results from several shots with the same target configuration and the variation in beam intensity distribution and coherence could be found as a function of the target geometry.

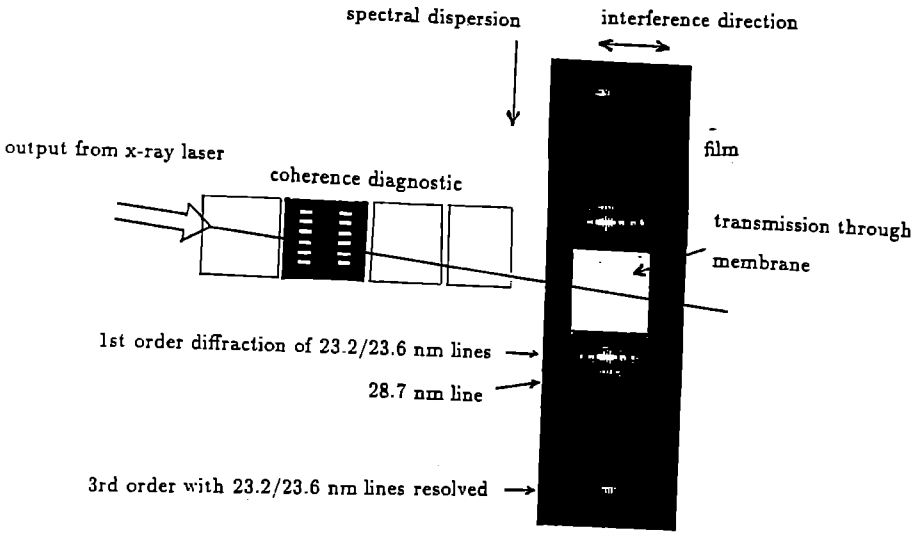

Figure 1

BEAM MODELLING

As a result of beam intensity limitations in the Ne-like Ge laser system it was not possible to perform the experiment under true far field (or Fraunhofer) conditions. The diagnostic to film distance was 770mm which does not satisfy the far field requirement. Consequently the experimental results have to be analysed on the basis of the more general Fresnel-Kirchoff diffraction theory. Physically, the main difference is going from a far to a near field system is that in the near field case there is an incomplete overlap between the diffraction patterns from the two slits. This restricts the allowable slit separations and complicates the determination of fringe visibility. To a certain extent the problem of establishing the source size is dependent on the assumption of a source intensity distribution. It is found from computer simulations that for relatively high visibilities the visibility envelope is the same for a range of source profiles. Only at rather low visibilities, corresponding to wide slit separations, $>200\mu$m, is there a strong dependence on source intensity profile. Unfortunately such wide slit separations give the poorest diffraction overlap from the two slits.

EXPERIMENTAL RESULTS

A total of approximately nine useful data shots were taken with the three target configuration, i.e the injector was a double Ge target and the amplifier was a single Ge target pumped by a one beam from VULCAN. The fringes were recorded on KODAK 104 film, digitized at King's College by a densitometer and the optical densities converted to intensities by the 104 calibration data. Unfortunately the flux levels were not high enough to obtain the third order diffraction fringes and therefore the 23.2 and 23.6nm lines could not be studied independently. Nevertheless, data were obtained on the variation of transverse coherence length (and therefore effective source size) with the position in the beam. In practice, of course, it cannot be assumed that the beam has a constant pointing direction. In fact the beam sweeps outwards from the target substrate as a result of diffraction in the amplifier target plasma which is a time dependent effect. The data therefore represent a time average at any point in space. Figure 2 shows the variation in beam intensity across the beam together with the change in the visibility of the first order fringes from the 150μm separation slits. These data were obtained on four laser shots with the slits ranges horizontally across the beam in order to investigate the horizontal source intensity distribution. It is fairly clear that there is a significant variation in transverse coherence length across the beam, with the coherence increasing away from the propagation axis. If the '88%' criterion is used to define coherence then the transverse coherence length varies from 65μm to 103μm in going from the east to the west sides of the beam. These visibility data can be used to establish an effective source size by fitting the visibility data to Fresnel-Kirchoff calculations with an assumed source intensity profile. For simplicity it was decided to assume a Gaussian profile sharply truncated on the substrate side. Under this assumption the effective source size ranges from 47.5μm to 26.4μm across the beam from east to west. In the vertical plane the data suggest a much larger effective source with a more sharply truncated intensity profile like a line source. The coherence length is $\sim 30\mu$m which corresponds to a 150μm line source. These data are to be compared with the actual physical size of the Ge target which is a thin strip, 22mm long on a glass substrate. The thickness is $\sim 1\mu$m, corresponding to the horizontal size and the width is 100μm, corresponding to the vertical size. The beam spread, evaluated from the intensity profile at the slits position, can be related to the intrinsic source coherence function via the generalized van Cittert-Zernike theorem [3]. It is found that the source coherence length iis very small, $\sim 1\mu$m, and that the source can therefore be considered to be simply a bright, incoherent source.

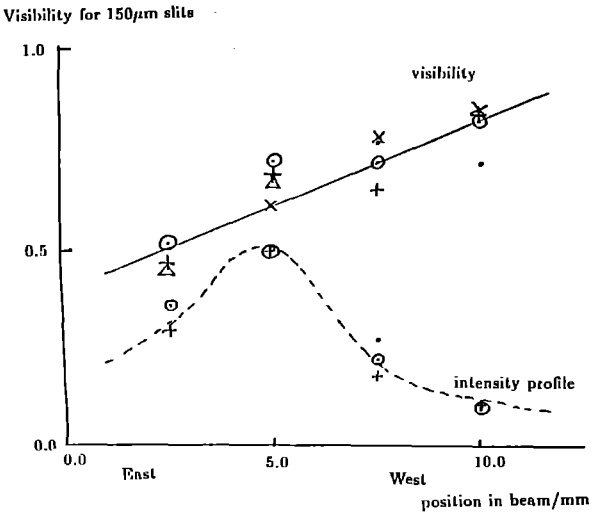

This conclusion is reinforced by data on the transverse coherence length of the 28.7nm line which exhibits a longer coherence length than the 23.2, 23.6nm lines simply because of its longer wavelength. Attempts to fit the experimental fringe data to a Fresnel-Kirchoff calculated diffraction pattern with an assumed source intensity distribution have led to the conclusion that, although to a first order the source has simply a localized Gaussian distribution, there are indications that there is also a much broader, lower intensity background.

CONCLUSIONS

A significant dependence of transverse coherence length on the position in the beam has been found by the use of a coherence diagnostic which is able to probe the properties of the Ne-like Ge x-ray laser output beam at several points in the beam. The source size in the vertical and horizontal directions, as calculated from the fringe visibilities, is roughly consistent with the Ge target size as determined from imaging experiments. Although the diagnostic techniques are in principle capable of revealing information about the source shape there was not enough flux to realizs such an experiment in practise. The variation of coherence length across the beam may be a result of the diffraction of the beam through the amplifier target plasma or may be due to the time dependence of the beam pointing direction. It is hoped that further experiments, perhaps with a streak camera, will be able to yield more information on these effects.

REFERENCES

[1] C L S Lewis et al; Collisionally pumped x-ray lasers, progress at RAL; IOP Conference series 125, p23-30, Ed E E Fill (1992)

[2] R E Burge, M T Browne,P Charalambous, G E Slark; Development of a coherence diagnostic for use on the Ne-like Ge x-ray laser, Central Laser Facility, Annual report (1993).

[3] A S Marathay, Elements of Optical Coherence Theory, Wiley (1982)

POLARISATION DEPENDENCE OF ENERGY ABSORPTION IN FIBRE TARGETS IN RECOMBINATION X-RAY LASERS

M G Holden[1], L Dwivedi[1], G J Tallents[1], M Key[2,3], J Zhang[2], D Neely[3], P Norreys[3], F Walsh[3]
C Lewis[4], A MacPhee[4]

[1]University of Essex, Wivenhoe Park, Colchester C04 3SQ
[2]Clarendon Laboratory, University of Oxford, Oxford OX1 3PU
[3]Rutherford Appleton Laboratory, Didcot OX11 OQX
[4]Department of Pure and Applied Physics,Queen's University of Belfast, Belfast BT7 1NN

INTRODUCTION

Gain in recombination x-ray lasers has been shown to be sensitive to the energy absorbed within the lasing plasma[1]. In this report, results are presented showing the role of the pump laser on the ion velocity distributions and absorbed laser energy measured using Faraday cups. In particular, large differences in the distribution were found for two different linear polarisations (s and p) of the driving laser.

EXPERIMENT

The measurements were taken during the recombination x-ray laser experiment performed in TAWest in Aug/Sep 1993. In this experiment, fibre targets (7μm diameter, 2-7mm length) were irradiated in a line focus geometery by the Nd:YLF VULCAN laser operating in CPA mode producing pulses of 30J in 1-2ps at a wavelength of 1.053μm giving irradiances up to 6 x 10^{15} Wcm^{-2} on target. The carbon fibre targets were held horizontally and the laser polarised vertically (s-polarised) or horizontally (p-polarised).

The ion velocity (and energy) distributions were determined using Faraday cup ion detectors. These consisted of two brass, cylindrical cups, one inside the other; the outer cup being earthed and the inner cup being kept at a potential of +60V. Meshes covered both cups so that only the positive ions entered the inner cup. Those ions were detected by a rise in potential of the inner cup.

The bias voltage was applied to allow fast recapture of any secondary electrons liberated by the ions hitting the cup walls. A folded metal sheet inside the inner cup also helped supress the escape of secondary electrons. The cups were placed at a distance of 41cm from the plasma and had a collection area of πcm^2.

The output of the cups was recorded on an oscilloscope with a time resolution of 1ns. The position of zero time (t=0) was deduced by the position of an x-ray spike due to the photoelectric effect.

RESULTS

Figure 1 shows the angular distribution of the ionic emission relative to the plane normal to the fibre axis. The distribution is approximately cylindrically symmetrical with a cone angle of 70°.

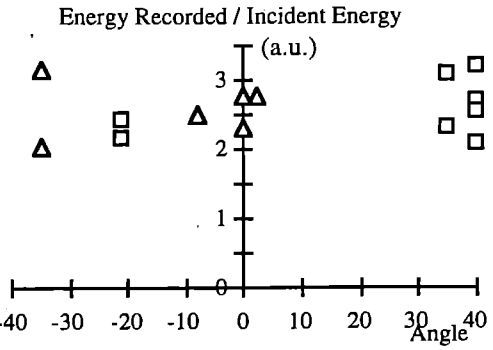

Figure 1 Angular dependence of emission. The angle here is relative to the plane normal to the fibre axis. The different symbols represent the different cups used.

Figures 2 and 3 show typical plots for s and p polarised pump laser irradiation. There is a significant difference in the structure of the two plots (note the different scales).

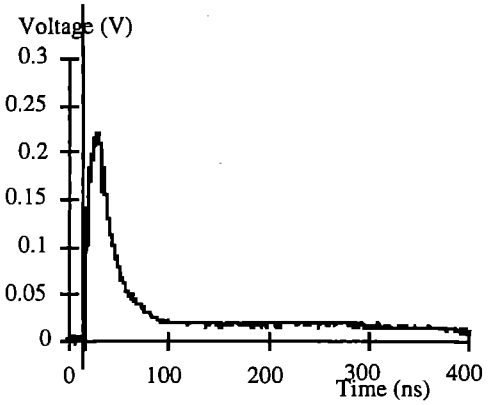

Figure 2 Typical plot for s-polarised light

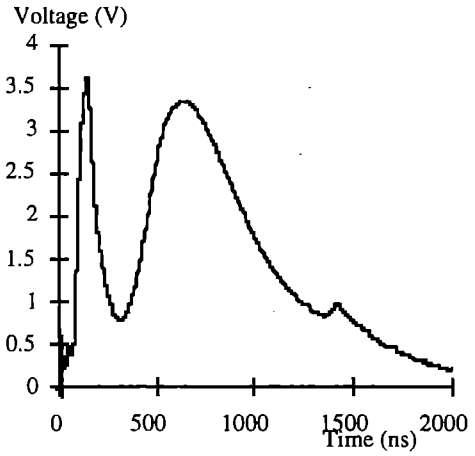

Figure 3 Typical plot for p-polarised light

Comparisons of the features of the two polarisations deduced from the Faraday cup signals are outlined in the table below.

	S-Polarisation	P-Polarisation
Absorbed Energy	2-7 J per cm 2-8 %	20-40 J per cm 20-50 %
Position of velocity Peaks	1.5 x 10^6 ms^{-1}	3 x 10^5 ms^{-1} 7.5 x 10^6 ms^{-1}

Table 1 Main differences between the two polarisations

CONCLUSION

The absorbed energy in the case of p-polarised pump irradiation is at least an order of magnitude greater than in the case of s-polarised light. A similar result has been found with sub-picosecond spot focus experiments on lollipop targets[2]. However evidence was not found for greater x-ray laser gain with the p-polarised irradiation.

REFERENCES

1. D Jacoby, G J Pert, L D Shorrock and G J Tallents
J. Phys. B 15, 3551 (1982)
2. U Teubner, J Bergmann, B van Wonterghem, F P Schafer, R Sauerbrey
Phys. Rev. Letts. 70, (6), 794 (1993)

IONISATION INDUCED BLUESHIFTING OF PICOSECOND LASER PULSES IN GASES

A Modena[1], A E Dangor[1], V Malka[2], J R Marques[2], Z Najmudin[3], P A Norreys[3], P F Taday[3]

[1]Imperial College of Science, Technology and Medicine, London SW7 2BZ, England
[2]Ecole Polytechnique, Paris, France
[3]Rutherford Appleton Laboratory, Chilton, Didcot, OXON, OX11 0QX, England

INTRODUCTION

With the pace of progress of laser technology over the last few years, short pulse, very high intensity laser shave become a common tool for different applications. With such high intensities available on target, lasers can now ionise gases in incredibly short times (as short as only a few cycles). The propagation and the coherence of the beam can be affected by this fast ionisation, since, as the short laser-pulse ionises the gas in which it propagates, so rapidly it can undergo an up-shift in frequency which can be related to the laser intensity and gas density. Here we report on the blueshifting of high intensity laser pulses propagating in low pressure gases.

EXPERIMENTS

The experiments were made using the Vulcan CPA laser in both the 3 ps and 600 fs configurations focused into static fills of gas. In the first configuration the pulse is focused by an f/4 off-axis parabola (OAP) into an elongated 15 x 50 μm focal spot, so with an average energy of 20 J in 3 ps giving on target intensities of 10^{18} W/cm^2. These intensities are much higher than the ionisation thresholds for the gases used (H, He, Ne) which implies that a very long-scale plasma was created especially for hydrogen (up to a few centimetres). Such high intensities mean that the ionisation occurs over a very long length. Close to the focal position, the ionisation occurs whilst the pulse is rising sharply so that the ionisation occurs very rapidly there.

The frequency up-shift of the beam is proportional to the ionisation rate, to the density and to the interaction length as can be seen from Eq (1).

$$\Delta\lambda = \frac{e^{2\lambda_0^3}}{8\pi^2\varepsilon_0 m_e c^3} L \frac{dn_e}{dt} \qquad (1)$$

where L is the ionisation length and dn_e/dt is the rate of change number density which is equivalent to the density of un-ionised atoms multiplied by the ionisation rate. With our ionisation length and ionisation rate (which is an exponential function of intensity) we observed significant shifts at very low pressures (three orders of magnitude less than in the work[1], where collisional ionisation begins to be important).

In the first configuration, because of problems in the chamber configuration, we could collect only part of the light with an f/9 lens that refocused it into a high dispersion spectrometer (with a resolution of 0.5 Å). The output was then recorded on a CCD

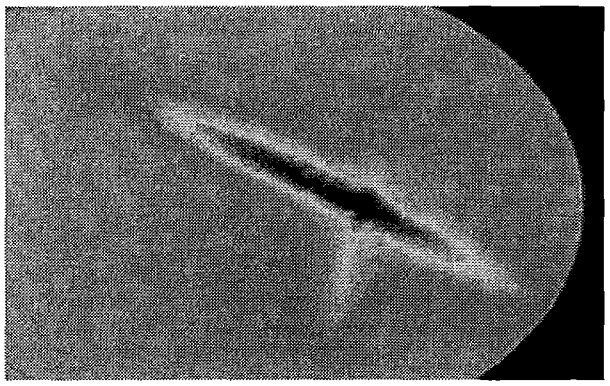

Figure 1 Plasma line-emission H_2 at 676 nm

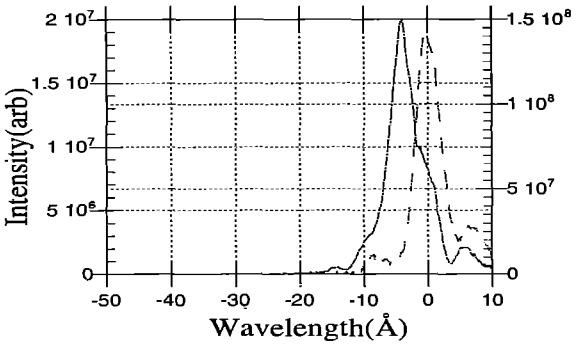

Figure 2 Transmitted spectrum through 1 Torr of hydrogen and vacuum shot

camera. In the second configuration an f/4 lens was installed in the chamber to collect the whole of the laser beam and a lower dispersion spectrometer (resolution of 4-8 Å) was used as the shifts expected and achieved were considerably larger. In both set-ups a pellicle was placed in front of the first collecting lens to reflect away up to 99% of the incident light. This was to prevent self-phase modulation in the lens which would corrupt our spectra.

RESULTS 3 ps

The amount of blue-shifting varied greatly with the different gases, which can be expected from the very different ionisation potentials that these gases have. The largest effect was observed in hydrogen where the shifted part starts to be observable, away from the expected laser bandwidth, at an low a pressure as 1 Torr (n_e = 6 x 10^{16} cm^{-3}), spreading to much more than 50 Å (our diagnostics limit) as the pressure was raised to 15 Torr (Figs 2, 3). It is interesting to note how that, even though the spectral width of the shifted part for the 15 Torr is much greater than for the 1 Torr case, the amount of energy in the non-shifted part of the pulse is roughly the same as in both the case. This is probably due to the fact that, even though the rise of the pulse is shifted much more at higher number densities (as expected from Eq (1)), the end of the pulse does not ionise in either case. However, the actual energy that gets shifted is considerably more than what would be expected from the simple consideration that as the second half of the pulse (ie after it reaches maximum) only focuses to the same intensities as the front part of the pulse, it can not do any ionisation (as it should have been already done by the front edge).

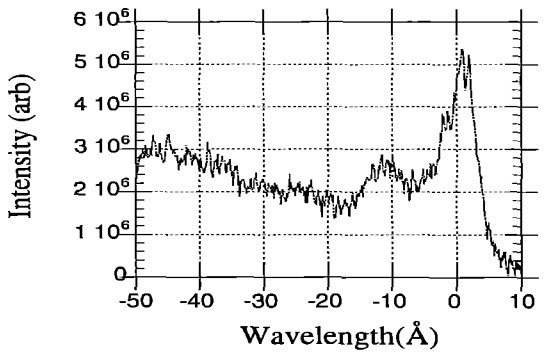

Figure 3 Transmitted spectrum through 15 Torr of Hydrogen with 3 ps pulse

So the amount of energy shifted should not much exceed 50% of the overall energy getting into the diagnostics. From the graphs one can imply percentages of more than 80% which does not vary much for the densities considered.

In neon the shifts were less pronounced at similar values of pressure (but of course higher number densities as our intensity was significantly higher than the threshold for the eighth ionisation stage in neon which is around 10^{17} W/cm^2). At the lower pressures the signals are qualitatively the same as for hydrogen (Fig 4). However at the higher pressures (Fig 5) the signal at the original wavelength was almost completely wiped out which suggests that ionisation occurred till well after the peak of the pulse (the apparent redshift is actually a residue of the spectral information in the elongated focal spot.).

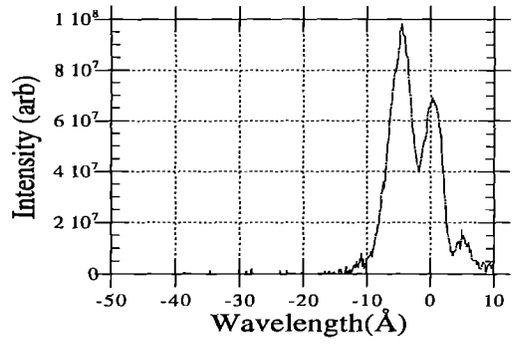

Figure 4 Transmitted spectrum through 3 Torr of Neon with 3 ps pulse

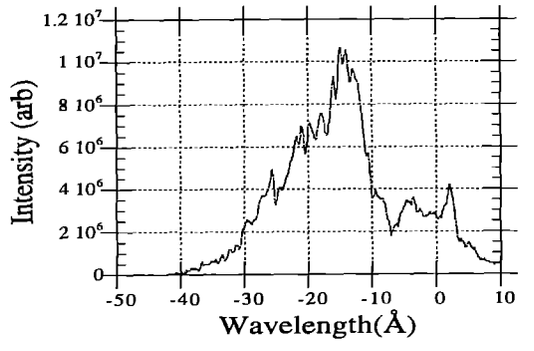

Figure 5 Transmitted spectrum through 14 Torr of Neon with 3 ps pulse

A possible explanation for the huge amount of energy shifted could be collisional ionisation, but at these densities one expects the collisional ionisation rates to be much smaller than the field-induced ionisation rates so that the effect should be negligible. This effect should be even less important with the shorter pulse-length yet in this case most of the energy is still shifted (see Fig 7). The shots in helium do not show such pronounced blue shifts, but this may be expected by the much higher ionisation potential of unionised helium compared to the other gases.

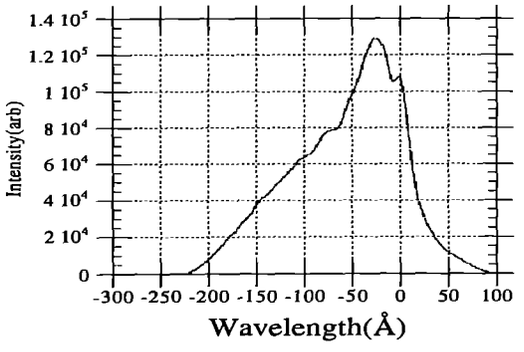

Figure 6 Transmitted spectrum through 14 Torr of Neon with 3 ps pulse

RESULTS (600 fs)

In the second set-up, with much higher intensities than previously, even the shots in helium showed very big shifts extending to more than 100 Å at the higher pressures (see Fig 6). According to a simple model the shifts should be inversely proportional to the cube or at lest to the square of the pulse length. This explains the reason for such shifts even in helium and also in neon as shown in Fig 7 where the comparison between the two different set-ups is clearly shown. This figure also shows once more, that most of the energy is shifted in neon with very little residual energy at the original laser wavelength.

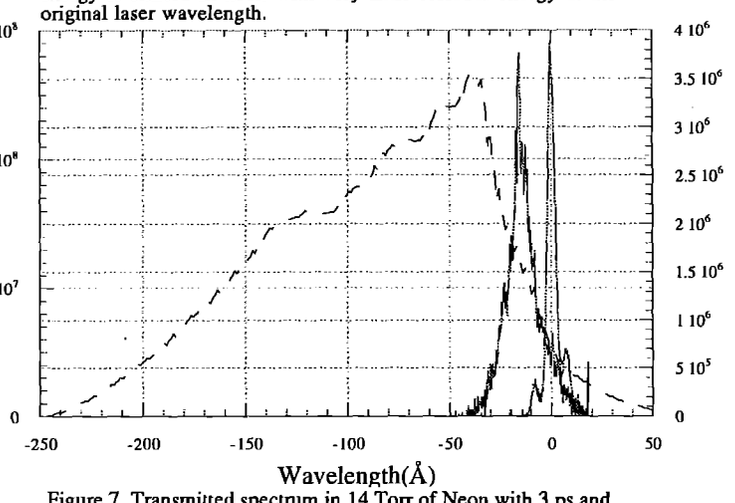

Figure 7 Transmitted spectrum in 14 Torr of Neon with 3 ps and 600 fs pulses and vacuum shot

REFERENCES

1. W M Wood, C W Siders and M C Downer
Measurement of femtosecond ionisation dynamics of atmospheric density gases by spectral blueshifting
Phys Rev Lett 67, 25 p3523 (1991).

OBSERVATION OF STIMULATED RAMAN BACKSCATTER IS UNDER-DENSE PLASMAS CREATED BY HIGH INTENSITY SHORT PULSE LASER

Z.Najmudin[1], A.E.Dangor[1], V.Malka[2], J-R.Marques[2], A.Modena[1], P.Norreys[3], P.Taday [3]

1) Imperial College of Science, Technology and Medicine, London
2) Ecole Polytechnique, Paris.
3) Rutherford Appleton Laboratory, Chilton

INTRODUCTION

Parametric instabilities have been studied extensively in the interaction of lasers with plasmas. The realisation that such instabilities can lead to significant beam power attenuation and to target preheating from electrons accelerated by the resulting plasma waves, meant that a great deal of attention was paid to these studies in particular in relation to laser ICF.

Recent advances in short-pulse lasers have allowed much higher laser intensities to be reached in the laboratory, and it has been matched by ideas for new applications such as particle acceleration in the laser Wake-field, and recombination X-ray lasers in the optical-field-ionised (OFI) plasma. As the growth rate of parametric processes increases with laser intensity, so the importance of these effects grows in this new high field limit of laser-plasma interactions. Hence the problems of beam attenuation (through the associated scattering) and significant plasma heating (from the thermalisation of the created plasma waves) are once more of interest.

The following report contains the results of studies of backscatter of intense short pulse laser light (@1μm) from underdense plasmas.

STIMULATED SCATTER FROM PLASMAS

Stimulated Raman Scatter is the process by which an electron plasma wave is resonantly excited by the interaction of an incident laser beam (of frequency ω_o) and scattered light at a frequency of (ω_o-ω_{pe}). Since the created plasma wave leads to further scattering at this shifted frequency, this results in a growth of both the plasma wave and the scattering. The process can be written as follows,

$$\omega_o \Rightarrow (\omega_o - \omega_{pe}) + \omega_{pe}$$
$$\text{photon} \Rightarrow \text{photon} + \text{plasmon}$$

A similar process can occur from ion-modes and is called Stimulated Brillouin Scatter (SBS). As, however, the characteristic growth time of these instabilities is of the order $1/\omega$, this is of much less importance in short pulse experiments, (where $\tau_{laser} < 1/\omega_{pi}$).

Stimulated scatter will be strongest in the direction opposite to the motion of the incident pulse, not only because the growth rate is greatest at 180°, but also because the interaction length between the scattered and incident pulse is greater than for sideward scattering. Indeed since ω_{pe} is dependant on number density and ω_{pi} is dependant on the plasma electron temperature, the backscattered signals can even be used as diagnostic tools. Of course this only applies if the plasma wave under consideration is not heavily (Landau) damped. This restricts SRS to the regime where $k\lambda_d \ll 1$. For $k\lambda_d > 1$ stimulated scatter is still possible, but

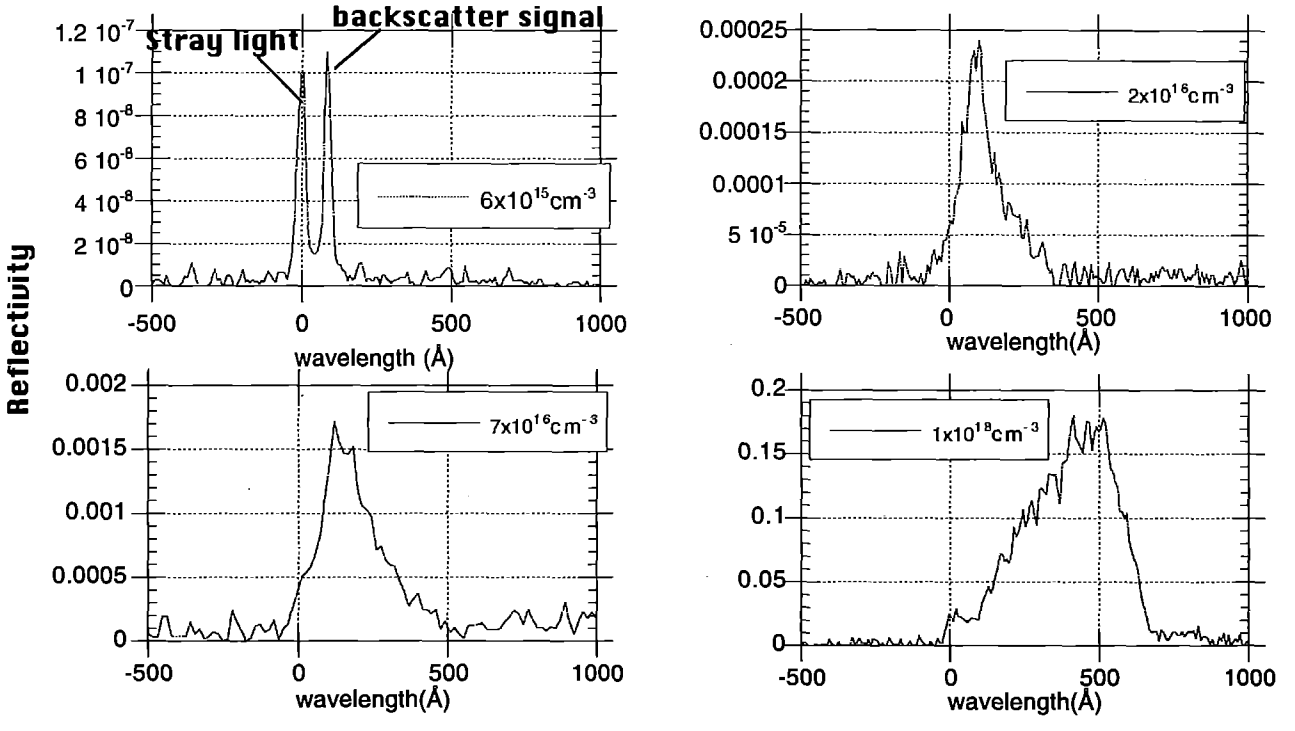

Fig. 2 Typical backscattered energy spectral profiles for 3ps pulse focused into various densities of static hydrogen plasmas.

it now grows off perturbations in the velocity distribution of individual electrons, rather than from the correlated movement of the electrons. This is then called Stimulated Compton Scattering, and is characterised by the large spectral width of the signal (compared to SRS), which is then an indicator of the Doppler velocities of the scatterers and hence of the plasma electron temperature.

However at the ultra-high intensities under consideration in the following experiments, the linear theory assumed in the preceding discussion no longer applies. For at high intensities the electron motion in the laser field approaches speeds close to the speed of light, and hence the resulting motion is highly non-linear. This leads to the possibility of exciting many more modes in the plasma, and making the maximum scatter now dependent also on the intensity of the incident light. In particular the largest growth rate is now expected for backscattered light with a frequency shift greater than that expected for purely linear waves. Provided that $v_o/c > (\omega_{pe}/\omega_o)^{1/2}$, where v_o is the quiver velocity of electrons due to the laser, the expected frequency shift of the maximum growth mode becomes;

$$\omega = (v_o/c)^{2/3}(\omega_o\omega_{pe}^2/4)^{1/3} \quad (1)$$

So although the corresponding analysis becomes more complicated, an idea can also be formed of the intensity of the interacting radiation.

EXPERIMENTAL SET-UP

The results that follow were taken from two dif ferent experimental runs on the Vulcan CPA laser. In the first the laser was configured to give up to 50J in a 3ps (fwhm) $sech^2$ pulse at 1.053μm which could be focused into an elliptical 15x50μm focal spot, by a 45cm focal length of f-axis parabola (i.e. ≈f4 optics). (see RAL reports by Danson, etc.). Focused intensities should then, be approaching 10^{18} Wcm^{-2}.
In the second experiment the laser was upgraded to provide 600fs (fwhm) pulses in a much more symmetrical 18x18μm spot, (focused by the same OAP), making focused intensities of 10^{19} Wcm^{-2} possible.

In both experiments the laser was focused into a static fill of gas, which on interaction with the high laser field is rapidly tunnel ionised. (The Keldysh parameter $\gamma << 1$ for all the ionisation levels considered). With a static fill of either hydrogen or helium, this then results in a relatively uniform, long scale length plasma, through which the laser beam must travel.

The backscatter is then extracted via the final turning mirror before the focusing parabola, (which is 5% transparent at 1μm). It is then passed through an infra-red filter, spectrally dispersed in a standard optical grating spectrometer and recorded on an S1 streak camera. The streak camera was set to between 100 and 30 ps/mm streak speed. This ensures that the signal of interest is separated in time from spurious reflections within the target chamber, though since the pulse is shorter than the time resolution available (maximum resolution is ≈5ps), it gives only limited information of the beams passage through its focal region. Absolute values of the reflected energy were obtained by comparing the total signal from the backscatter with a known reflection from a low energy shot, obtained by putting a mirror normal to the beam before incidence on the parabola.

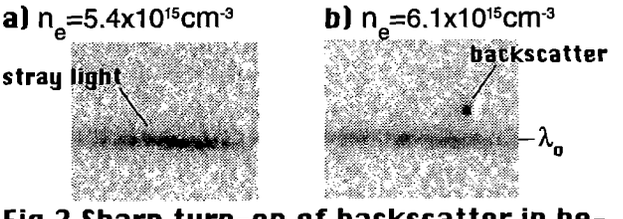

Fig.2 Sharp turn-on of backscatter in helium

RESULTS FROM 3PS EXPERIMENT

Some typical spectral profiles from the interaction of a ≈8TW 3ps pulse with a variety of pressures of hydrogen fill are shown in Fig. 1.
In all cases it shows scattering on the red (longer wavelength) side of the incident laser wavelength, with no corresponding signal on the blue side.

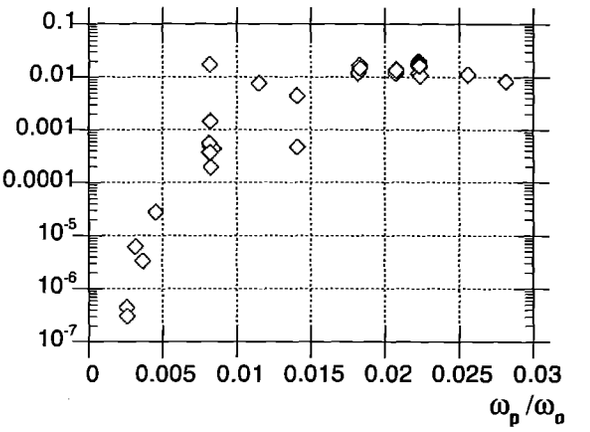

Fig.3 Fraction of energy reflected v. plasma frequency in helium

This is characteristic of stimulated scatter. At the low densities (of about $6x10^{15}$ cm^{-3}) the signal is very narrow (spectrally) and of low reflected energy. As the ambient pressure of the fill is increased, so the signal becomes broader and of greater reflectivity. In fact as can be seen from Fig. 2 the onset of signal is very sharp, the signal consistently disappearing for gas fills just 10% lower in pressure. This sharp turn on is evident in all the gases, as shown in helium in Fig.3. This plot also shows that the reflectivity seems to saturate at higher densities, though the maximum reflectivity in this case is very high (several % of incident in some cases). However even at these higher densities (>10^{17} cm^{-3}) the signals seem to be a mixture of a sharp peak sitting on a broader signal. This could well be mixing of signal from dif ferent parts of the laser beams path at differing intensities.

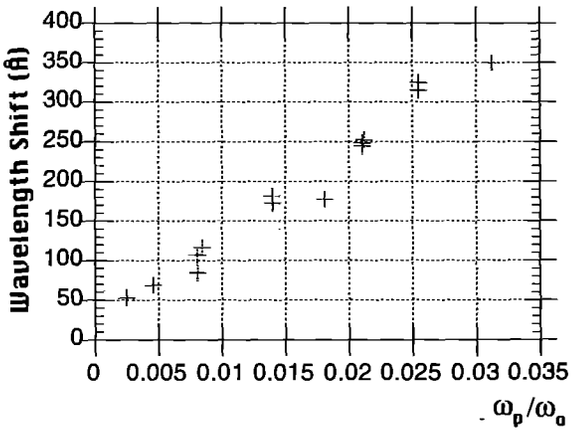

Fig.4 Wavelength shift of signal peak against plasma frequency in hydrogen.

Fig.4 shows that the spectral peak of the reflected signal is almost proportional to $(n_0e^2/\varepsilon_0m_e)^{1/2}$ i.e. to ω_p for cold (T_e=0) plasma waves. There is some discrepancy at both the highest and lowest pressures. In particular at the low pressures, the shift is much greater than this ω_p value. If this were just a result of the finite temperature correction (i.e. $\omega_{pe}^2=\omega_p^2+(3k_bT_e/m_e)k^2$) then this would imply plasma temperatures of only 3eV. This is not reasonable (temperatures in excess of 200eV are expected just from ATI heating) and would imply that the plasma frequency of the stimulated plasma wave has been strongly modified by the laser intensity. However using formula (1), this still only implies an intensity of around 1×10^{17} Wcm^{-2}. Also surprising is the spectral narrowness of this low density feature which would suggests a combination of both low intensity and low plasma temperature (i.e. conventional SRS).

The large width of the signal at the higher pressures, means that often it extends just to the blue side of the fundamental laser frequency. At the highest pressures, in fact, the signal seems to rise again, to a secondary peak at the fundamental wavelength, and this could be a signature of the on set of the growth of ion-modes (SBS).

Another notable aspect of this experiment was the similarity in signals observed from the different gases. In particular the threshold for the onset of SRS in neon, seems to be at almost the same ambient pressures, as for helium or hydrogen fills. This is even though one would expect, at close to focus (which is where one would expect the first signs of scattering to come from) the neon to be up to 4 times more ionised.

RESULTS FROM 600FS EXPERIMENT

Some typical spectral profiles from the second experiment, with 35TW in 600fs focused into helium are shown in fig. 6.
As can be seen these are noticeably different from the previous experiment. Though the peak of the scattering is always red-shifted, one can see that even at moderate pressures (≈10 ^{17}cm^{-3}) a good proportion of the signal is blue shifted. Indeed at the higher densities the spectrum extends on the blue side all the way to the cut-off of our detector at

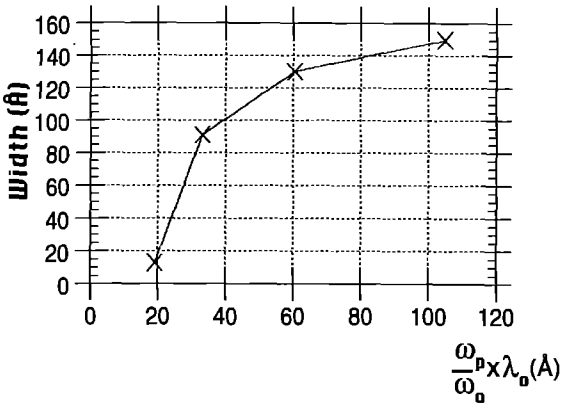

Fig. 5 Width of backscatter feature v. plasma frequency in hydrogen

≈990nm (i.e. a blue shift of nearly 600Å from the fundamental). This would seem initially to be rather surprising as for stimulated backscatter, one would normally only expect growth of modes which result in the emission of longer wavelength e-m waves. It cannot even be accounted for by the ionisation induced blue shifting of the transmitted beam (see RAL report by A.Modena) where the maximum shifting is only 200Å, though this will contribute. However the blue shifting can be explained (viz. Darrow et al.) by up shifting of the red-shifted scattered light as it passes through the refractive index gradient from inside to outside the laser pulse. (The refractive index inside the pulse being altered by the non-linear motion of the electrons in the high electric field.)

It is noticeable generally that the spectral width of the signals is much larger than in the previous experiment. However the observed shift still only implies an intensity, at which this interaction takes place, of about 6×10^{17} Wcm^{-2}. For helium the width of the signal seems almost to correspond to the separation of the peak of the signal from the fundamental (fig.7). This is as predicted by the theory of such "strongly modified plasma stimulated scatter" (Ref(1)). Also noticeable is that the shift from λ_0 of the peak of the signal is even greater at the lower densi-

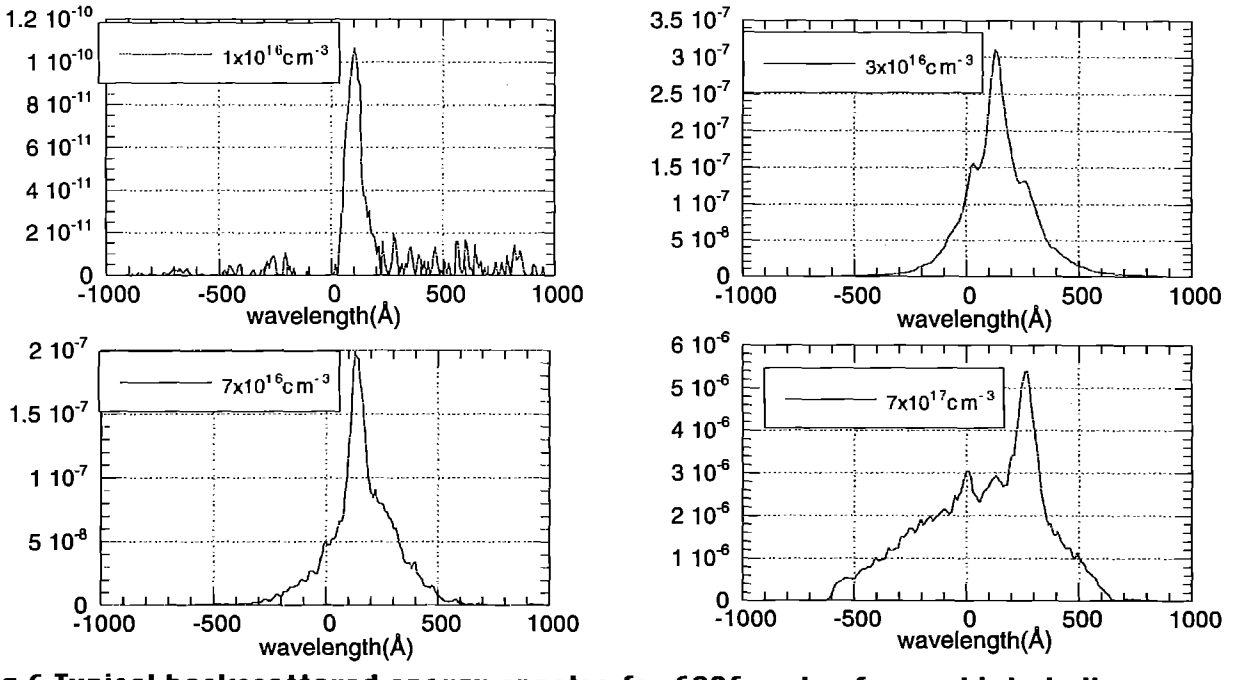

fig.6 Typical backscattered energy spectra for 600fs pulse focused into helium

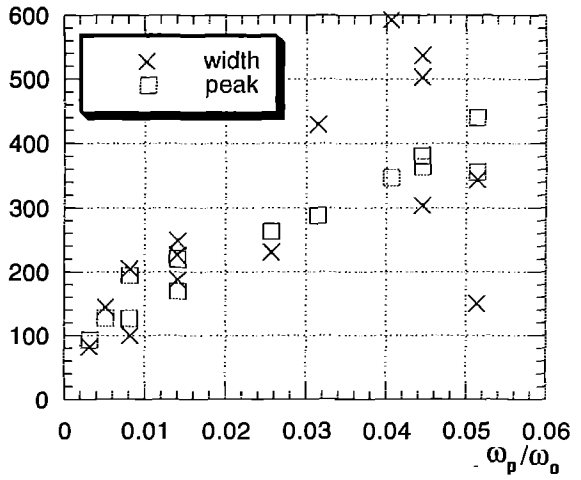

Fig. 7 Width and spectral-shift of back-scatter signal v. plasma frequency for 600fs pulse in helium.

ties than in the previous experiment and this seems to corroborate the role of the high laser intensity in modifying the plasma frequency . At the higher densities though this extra shifting becomes less and less apparent, until at the highest pressures, the shift is less than that expected for normal SRS. However this must also be tied in with the extra blue shifting incurred by the backscatter as it exits the region of high laser intensity.

Also very noticeable is the greatly reduced absolute reflectivity with these shorter pulse and tighter focusing in this experiment (Fig. 8). The difference is of the order of 100 times less for helium, and even more for neon. In fact whereas in the previous experiment the reflectivity was greater for neon, the opposite is true in this case. It is quite dif ficult to account for this change, but the shorter growth time would contribute. Also of issue may be plasma uniformity (the ponderomotive force would be appreciable for this experiment) and the coherence of the short pulse (it already has a larger bandwidth, and its coherence will be greatly modified by ionisation fronts). There are signs of a threshold similar to that of the previous experiment as seems also to be shown by the nar - rowing of the spectra of the backscatter at the lower densities.

The shots in neon show a considerable dif ference from the helium shots. In particular the spectral widths of the feature are much lar ger than those

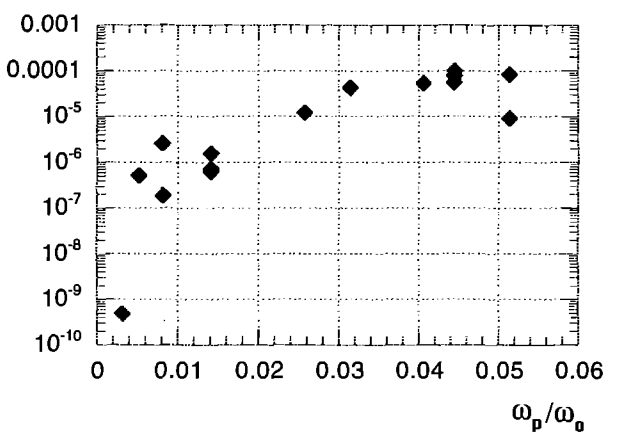

Fig. 8 Fraction of energy of 600fs pulse reflected versus plasma frequency

of helium, with correspondingly greater blue-shifts. Particularly inter - esting is the shots into 1torr of static neon which shows a harmonic structure on the blue-shifted side (Fig. 9).

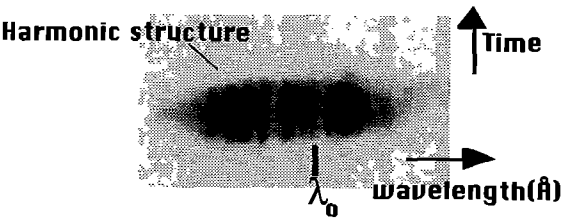

Fig. 9 streak camera image of 600fs pulse focused into 1 torr of neon, with harmonic structure on blue shifted side

SUMMARY

Observations have been made of stimulated Raman scatter over a wide range of static filled densities at high intensities, with either 3ps or 600fs pulses. The following main observations are evident;

Raman backscatter signals are observed in all gases over a threshold pressure of about 10 millitorr. The features are similar for all gases in the lower intensity experiment, but neon shots show much greater width in the 600fs experiment.

The backscatter signals are much greater for the longer pulse, lower intensity experiments, often reflecting back appreciable fractions of the incident laser energy at the higher densities (>10^{18}cm^{-3}).

The backscatter signals are much spectrally broader at the higher intensities, at a comparative density, correlating well to the frequency shift of the maximum growth mode, as predicted by the theory for scattering of high intensity beams. Indeed, particularly for the higher intensities, the backscattered feature extends well into the blue side of the spectrum, another indication of the high electron quiver velocities reached.

REFERENCES

1. J.F.Drake et al.
Parametric instabilities of electromagnetic waves in plasmas.
Physics of Fluids, 17, 4 (1974) p.778

2.C.Darrow et al.
Raman backscattering from subpicosecond lasers.
LLNL ICF Quarterly Report, 2,2 (1992) p.70

PLASMA TEMPERATURE AND ENERGY TRANSFERENCE TO MEV IONS FROM HIGH INTENSITY PICOSECOND LASER PULSE INTERACTIONS WITH SOLID TARGETS

A.P.Fews[1] P.A.Norreys[2] F.N.Beg[3] A.R.Bell[3] A.E.Dangor[3] C.N.Danson[2] P.Lee[3]

[1]Department of Physics University of Bristol Tyndall Ave.Bristol BS8 1TL
[2]SERC Rutherford Appleton Laboratory Chilton Didcot Oxon OX11 0QX
[3]Imperial College of Science Technology & Medicine Prince Consort Road London SW7 2AZ

The fast ion emission from high intensity, picosecond laser plasmas has been measured to give the hot electron temperature and the amount of laser energy transferred to ions with energies ≥100 keV/nucleon as a function of incident intensity. The plasma temperature varies from 0.2-1.0 MeV over the range $2.0x10^{17}$-$2.0x10^{18}$ W cm^{-2}. 10% of the laser energy is transferred into MeV ions at $2.0x10^{18}$ W cm^{-2}. A novel observation is a sharp cut-off in the energy spectra that scales linearly with laser intensity. The fast ions are shown to originate in an area that is similar in size and structure to the focal spot distribution, unlike the spot sizes associated with x-ray images which are extended due to lateral transport of energy.

At intensities of 10^{18}W cm^{-2}, the electron oscillatory velocity for 1μm radiation becomes relativistic and the radiation pressure reaches ~300 Mbars. Interesting new physical phenomena have been predicted in this regime, such as ultra-large self-generated magnetic fields, energetic ions in the MeV range and large amplitude plasma waves[1]. Applications include short pulse ignitors for inertial confinement fusion[2], short wavelength x-ray lasers and accelerator schemes.

The experimental conditions were similar to those reported earlier[3]. As before, one arm of the VULCAN laser delivered up to 30J of p-polarised, 1053 nm wavelength radiation. The pulse lengths ranged from 1.8 - 4.0 psec with 50% of the data points between 2.0 -2.8 psec. An off-axis parabolic mirror, located 44 cm from the targets, focused the radiation onto mylar (CH) disk targets of diameter 270μm and thickness 36μm which were placed at 30° to the incident laser light to protect the laser chain from back reflections. The focal spot was measured by an equivalent plane monitor to have dimensions of 15x50μm. The contrast ratio was measured[4] to be $1:10^6$.

The fast ion emission was recorded by CR-39 plastic nuclear track detector[5]. CR-39 records charged nuclear particles as tracks which are etched into the surface of the detector after the exposure. Each incident ion produces a separate etched track, the dimensions and depth of penetration of which enable the energy and atomic number of the atomic particles to be individually determined. The detector is sensitive to ions with energies > 100 keV/nucleon. The angular spread of emission can be determined from positioning the detectors around the target; and the total flux of ions can be measured simply by counting the number of tracks in the detectors. In all shots, one piece of CR-39 detector was placed in the normal incidence direction at a distance of 55cm from the target. The CR-39 was covered with array of 12 mylar filters that increased in thickness by steps of 2.5μm, and 8 steps of Al of thickness 25μm. Each step is sensitive to a different energy interval, giving an energy resolution of ~0.1 MeV in the range 0.1 - 6.0 MeV. At high flux levels where it not possible to analyse individual particles, the signal under each filter is averaged. In addition, ions with energies in the range 1-10 keV/nucleon were recorded by Faraday cups.

The technique of maximum entropy penumbral imaging was employed to image the ion emission[6]. The technique has previously been employed to measure the shape of implosion cores of inertial confinement fusion targets in three dimensions from alpha particle emission[7]. As the pulse length of the heating beam is so short, the spatial extent of the plasma is small during the interaction and the region of fast electron/ion production will be similar in spatial extent to the focal spot dimensions. A penumbral imaging camera was formed using a gold aperture of 80μm diameter aperture located 11.4mm from the target. The camera was at an angle of 35° from the normal in the vertical direction and 37° in the horizontal. Standard pinhole cameras recorded the plasma x-ray emission.

Figure 1 shows an example of a reconstructed image of the fast ion emission. In this shot, 30J of laser energy was incident onto the target in a pulse length of 1.8 psec. The image was formed from the highest energy ions to avoid problems with excessive particle fluxes and consequent blurring of the image due to space-charge effects. A significant non-uniformity in the emission can be observed, with a hot spot on one side of the image. Approximately 70% of the emission is contained within an area of 25x75μm in figure 1. This can be compared to a typical equivalent plane image of dimensions 15x50μm. We can therefore be confident that there is no systematic focusing error present in the experiment. Moreover, x-ray images from the pinhole cameras show that the heated region around the focal spot were never less than 60μm in the vertical dimension and increased with increasing laser energy[3]. These observations suggest that the extension of the focal spot dimensions measured in the x-ray images are due to radiation transport of energy away from the heated region.

The ion emission is predominantly from protons. In some cases, emission of carbon ions was also observed. Although in a few cases the maximum carbon energy was as large as half the maximum proton energy, the flux was much lower and no more than 10% of the energy was contained in non-hydrogenic ions. The spatial distribution of the emission was measured using an angular array of up to 7 detectors. Plasma confinement was observed, confirming the result of our earlier experiment. 50% of the ions were confined to a half angle cone of 20° to the target normal[3].

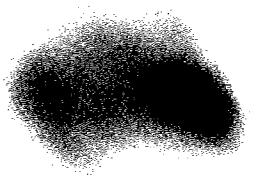

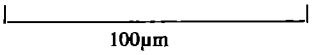

Figure 1 Reconstructed particle image showing the region of proton emission

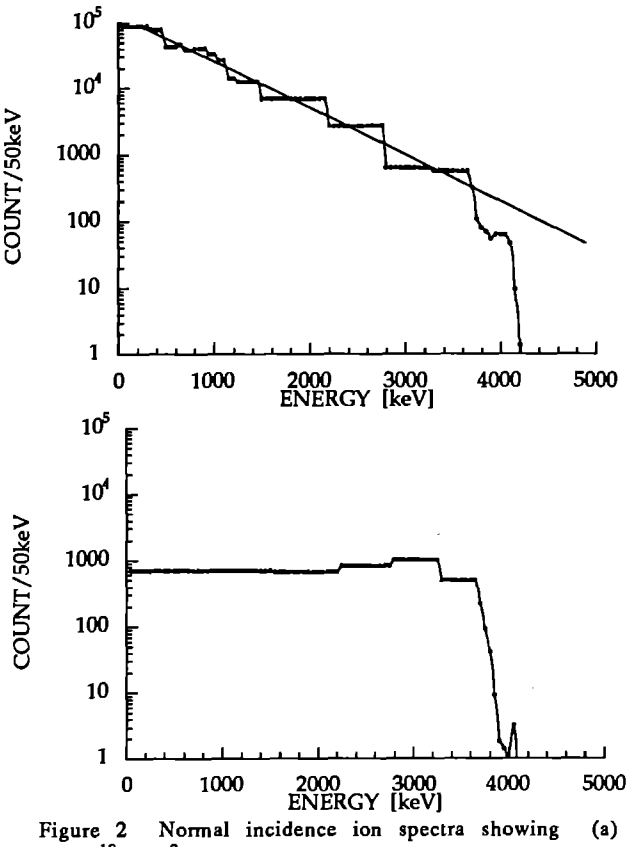

Figure 2 Normal incidence ion spectra showing (a) $1.9x10^{18}Wcm^{-2}$ incident intensity showing an exponential profile (b) $1.2x10^{18}W\ cm^{-2}$ incident intensity showing a non-exponential profile

Two typical ion spectra from the forward direction are presented in figure 2. The ion emission in Figure 2a shows an exponential decreasing profile with increasing energy followed by a sharp cut-off at 4.2 MeV. In this case 32J in 2.4 psec was incident onto the CH target at an incident intensity of $1.9x10^{18}\ W\ cm^{-2}$. This behaviour was typical of two thirds of the shots. The ion spectrum in figure 2b however, shows a quite different profile in that the decay with higher energies shows a distinct non-exponential behaviour. This was observed in one third of the extended data set. Here 24J in 2.6 psec was incident onto the CH target at an incident intensity of $1.2x10^{18}\ W\ cm^{-2}$. A variety of different shapes were observed for the non-exponential profiles, with many of them showing a gentle peak at higher energies as illustrated in figure 2b. The origin of this change in ion spectrum is not understood at present, but these differences may be caused by non-uniformities present in the focal spot structure. All of the data show a very sharp cut off energy and the particle detection threshold is two orders of magnitude smaller than the lower limit shown in figure 2. The emission falls monotonically with angle from the forward normal, suggesting confinement of the hot electrons.

Determination of the hot electron temperature of the plasma is straightforward. The characteristic ion energy is represented by the mean of the distribution. In the case of an exponential distribution (the case for two thirds of the data), this mean also corresponds to the characteristic temperature of the form exp(-E/kT). Provided that here is no electron energy lost to the cold solid target, the hot electron energy is transferred to the acceleration of the ions with a bi-Maxwellian form: a cold Maxwellian velocity for slow ions and a hot Maxwellian tail of fast ions. Hence the distribution of fast ions is representative of the hot electron distribution during the interaction. Figure 3 shows the scaling of the temperature of the particles in keV plotted against incident intensity. The triangles and the circles show the

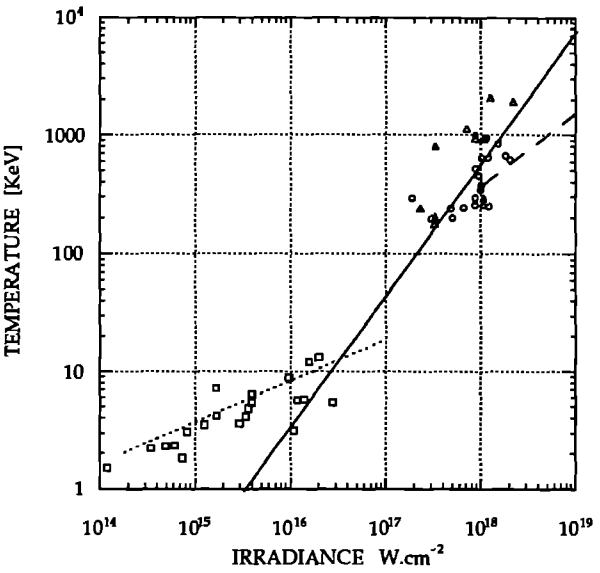

Figure 3 Temperature as a function of intensity. The circles and triangles show our data points and represent the exponential and non-exponential spectra respectively. The solid straight line is a least squares fit to our data. The squares are the data of Meyerhofer et al[8]. The dashed line the calculation of Wilks[11], and the dotted line the calculation of Gibbon and Bell assuming density scalelength of 0.1[9].

mean energy for the non-exponential and exponential spectra respectively. The two categories of spectra are not resolved from each other within the scatter of the measurements. A least squares fit to our data is $T_e = 4.210^{-18}[I^{(1.12\pm0.29)}/W\ cm^{-2}]$ keV and is shown as the solid line in figure 3.

The reported ion temperatures from Meyerhofer et al are also plotted, who made their measurements at lower intensities and with a measured contrast ratio of $2\text{-}3x10^{-6}$[8], below the threshold of plasma production. Gibbon and Bell [9] using a $1\frac{1}{2}D$ particle-in-cell (PIC) code have recently shown that the absorption mechanism changes from resonance absorption for density scalelengths of $L/\lambda>0.1$ to a form of vacuum heating when $L/\lambda\leq0.1$[10]. They also show that the hot electron temperature scaling with intensity is highly dependent on the density scalelength. The measurements of Meyerhofer et al are consistent with calculated temperatures when the density scalelength of $L/\lambda = 0.1$. These simulated temperatures from Gibbon and Bell are shown as dotted lines in figure 3. At much higher intensities, Wilks derived temperatures from $2\frac{1}{2}D$ PIC simulations assuming a small plasma created by the pedestal associated with the chirped pulse recompression[11] and are shown in figure 3 as the dashed line. The calculated temperatures at $1.4x10^{18}W\ cm^{-2}$ of 400 keV are within a factor of two of our measured value.

All the ion data show a very sharp cut-off in the ion energy spectra, as illustrated above in figure 2. This feature becomes progressively more prominent with higher intensity. The cut-off proton energy recorded in the CR-39 plotted against incident intensity is shown in figure 4. The circles and triangles represent the exponential and non-exponential spectral shapes respectively. Protons with energies up to 5.5 MeV were observed. It can be seen that the cut-off energy is roughly proportional to the intensity. There are two possible explanations for the existence of this cut-off energy. A sharp cut-off has been observed in harmonic generation experiments using short pulse lasers. In these experiments, the harmonic strengths show the following characteristics: a rather rapid decline in the first few harmonic

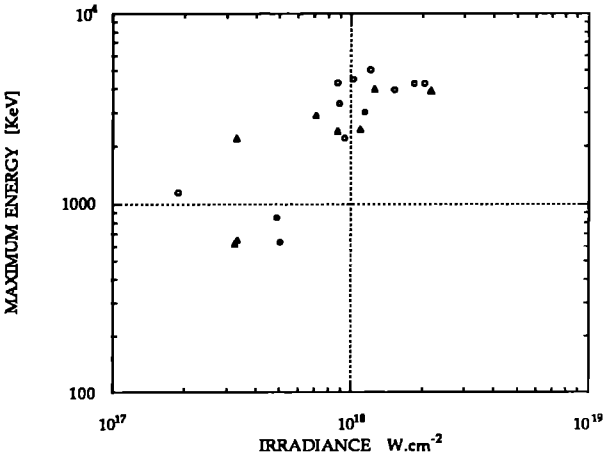

Figure 4 The ion cut-off energy as a function of laser intensity

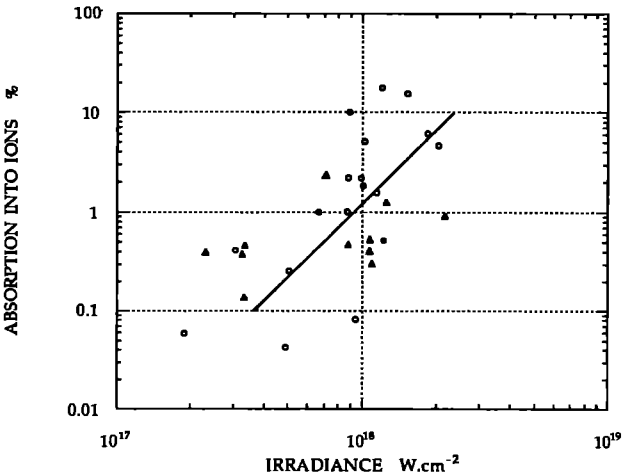

Figure 5 Percentage of incident energy emitted in the form of fast ions >100 keV as a function of intensity

orders followed by a plateau of constant intensity and then by an abrupt cut-off. The cut-off is governed by the ponderomotive energy of a free electron in the laser field and has been found to scale as $E_{max}=I_o + 3U_p$ where I_o is the field free ionisation potential and U_p is the ponderomotive energy of a free electron in the field and is given by $U_p = e^2E_o^2/4m_e\omega_o^2$ where E_o is the electric field in the light wave and ω_o is the laser frequency. A similar cut-off may be occurring in these conditions, which will vary linearly with the laser intensity. At $2x10^{18}$ W cm^{-2}, U_p~190 keV and E_{max}~570 keV. Non-uniformities in the laser beam can cause hot spots, which can clearly be seen in figure 1, and E_{max} can be of the same order as the measurements in figure 4.

An alternative mechanism is acceleration from rapidly changing magnetic fields. The maximum energy that an electron or proton can extract from a fast changing magnetic field can be derived from Maxwell's relationship $\nabla x E = -\partial B/\partial t$ and has been shown to scale as E_{max} ~eBcL, where B is magnetic field and L is the scalelength of the interaction[12]. If we take the interaction region to be the density scalelength and assume a density scalelength L/λ~ 0.5, and take B~30 MG at $2x10^{17}$ W cm^{-2} from Bell et al[3] and B~330 MG at $2x10^{18}$ W cm^{-2} from Wilks et al [13], then E_{max} varies from 450 keV to 4950 keV for this range of intensities.

Figure 5 shows the percentage of laser energy absorbed as a function of incident intensity. The circles and triangles represent the exponential and non-exponential spectra respectively. Half of the total fast ion emission was confined to a half angle cone of 20°. 10% of the laser energy is absorbed in MeV ions at $2.0x10^{18}$ W cm^{-2}. The percentage absorption into these fast ions represents an accurate measure of the fast ion component of the absorbed energy as the mean temperature of the Maxwellian distribution (0.2 - 2.0 MeV) is much higher than the detector threshold of 0.1 MeV. The scatter in the individual measurements is surprisingly large, and has also been observed at lower intensities by Meyerhofer et al[8]. The data we present here are for individual laser shots, with 66% of the data lying within a factor of 3 of the best fit line. The percentage of laser energy transferred into fast ions at lower intensities ($2x10^{17}$W cm^{-2}) is surprisingly small, especially given the absorption data reported by Wilks[11] who showed that ~20% of the incident laser energy is absorbed at similar intensities to those reported here. This suggests that at higher intensities, nearly all of the absorbed energy is transferred into the emitted fast ions. At the lower intensities, a significant proportion of the energy is transferred into other components. This is supported by our Faraday cup measurements which indicate that ~3% of the laser energy was transferred into ions of 1-10keV at $2x10^{17}$Wcm^{-2}, falling to ~ 0.3% at laser intensities of $2x10^{18}$ Wcm^{-2}.

In conclusion, we have shown that the fast ions originate in an area that is similar in size and structure to the focal spot distribution. The plasma temperature varies from 0.2 -1.0 MeV over the range $1.0x10^{17}$-2.010^{18} Wcm^{-2}. 10% of the laser energy is transferred into ions with an energy >100 keV/nucleon at $2.0x10^{18}$ Wcm^{-2}. The measured temperatures at ~10^{18} Wcm^{-2} are within a factor of two of $2\frac{1}{2}$D PIC simulations. A novel observation of a sharp cut-off in energy spectra which scales linearly with laser intensity has been presented. The origin of this cut-off could either be associated with the ponderomotive potential of a free electron in the laser field, or due to very fast changing magnetic fields.

The authors wish to thank Dr A Djaoui for useful discussions, and also the laser operations, target preparation and engineering groups of the Central Laser Facility for their help.

REFERENCES

1. W.L.Kruer, S.C.Wilks
Plasma Physics and Controlled Fusion 34(13), 2061 (1992)
2. G.Mourou, D.Umstadter
Physics of Fluids B 4(7), 2316 (1992)
3. A.R.Bell, F.N.Beg, Z.Chang, A.E.Dangor, C.N.Danson, C.B.Edwards, A.P.Fews, M.H.R.Hutchinson, S.Luan, P.Lee, P.A.Norreys, R.A.Smith,P.F.Taday, F.Zhou Physical Review E 48(3) 2087 (1993)
4. C.N.Danson et al Optics Communications 103, 392 (1993)
5. A.P.Fews, D.L.Henshaw, Nucl. Instrum. Methods 197 512 (1982); A.P.Fews Nuclear Instruments & Methods B 71 465 (1992); B 72, 91 (1992).
6. A.P.Fews, M.J.Lamb, M.Savage
Optics Communications 94 259 (1992)
7. A.P.Fews, M.J.Lamb, M.Savage, "Three dimensional alpha particle imaging of laser driven implosions" Lasers and Particle Beams (in press); A.P.Fews, M.J.Lamb, M.Savage, C.Regan Central Laser Facility Annual Report RAL-92-020 p 43 (1992).
8. D.D.Meyerhofer, H.Chen, J.A.Delettrez, B.Soom,.S.Uchida and B.Yaakobi Phys. Fluids B, 5, No.7, 2584, (1993).
9. P.Gibbon, A.R.Bell
Physical Review Letters 68(10), 1535 (1992)
10. F.Brunel Physical Review Letters 59(1), 52 (1987)
11. S.C.Wilks. Phys. Fluids B, 5, No. 7, 2603, (1993).
12. M.S.Longair, "High Energy Astrophysics" Cambridge University Press (1981) ISBN 0 521 28013 3. p387/8.
13. S.C.Wilks, W.L.Kruer, M.Tabak, A.B.Langdon
Physical Review Letters 69, 1383 (1992)

THOMSON SCATTERING MEASUREMENTS OF OPTICALLY IONISED PLASMAS - THE OBSERVATION OF HIGH Te/Ti RATIOS

J. S. Wark,[1] A. A. Offenberger,[1,2] W. J. Blyth,[1] M. H. Key,[1,3] S. G. Preston,[1] Z. Najmudin,[4] A. E. Dangor,[4] and A. Djaoui[3]

[1]Department of Physics, Clarendon Laboratory, University of Oxford
Parks Road, Oxford OX1 3PU.

[2]University of Alberta, Edmonton, Alberta, T6G 2G7, Canada.

[3]Central Laser Facility, Rutherford Appleton Laboratory, Chilton, Didcot, Oxon OX11 OQX.

[4]Blackett Laboratory, Imperial College of Science, Technology and Medicine
Prince Consort Road, London, SW7 2BZ.

INTRODUCTION

The production and diagnosis of optically ionized gases has attracted considerable interest in the past few years due to their potential to produce 'cold' plasmas that may be suitable media for XUV recombination lasers.[1-3] Such schemes rely on the rapid recombination of the cold, highly ionized plasma, and thus collisional ionization and the associated heating must be kept at a minimum. Measurements of electron temperatures, and the relative role of the various heating mechanisms, such as inverse bremsstrahlung, above threshold ionization heating, and stimulated Raman scattering, are therefore of considerable importance.

We have already reported preliminary results of Thomson scattering measurements from optically ionized plasmas, that have yielded temperature and density information about the resultant plasmas and the relative importance of the heating mechanisms.[4] Thus it is not our intention to reproduce those results in full here, but rather we wish to draw attention to one particular aspect of the recorded Thomson spectra that allows us to gain information about the ion, as well as electron temperatures, and to deduce that we have high electron-to-ion temperature ratios, as would be expected when the electron-ion collision time is significantly longer than the laser pulse.

EXPERIMENT

The experiment was performed using the high-power laser SPRITE. The 248 nm KrF beams from SPRITE were used to pump a Methane-filled Raman amplifier to produce up to 4 J of 268 nm light in a pulse length of 12 psec (FWHM), with a prepulse contrast ratio of 10^{-10}. The laser was focused by a 33 cm focal length parabolic mirror into static-fill and gas jet targets of H_2, He, Ne, and Kr. Approximately 50% of the energy of the beam was contained in a focal spot of 6.5 μm diameter, with all of the energy being contained in a spot of 20 μm diameter. The Thomson scattered light from the incident pulse was collected at 90 degrees to the beam and polarization vector, and dispersed by a monochromator (0.3 m, 1200 g/mm grating) onto a UV sensitive streak camera. The streak camera was used at a streak speed relatively slow compared to the pulse length (50 - 100 psec/mm) to discriminate the Thomson scattered light from the scattered stray light. Backscattered stimulated Raman and Brillouin spectra were also recorded, and details of these results will be presented elsewhere.

RESULTS

Typical Thomson scattering spectra are shown in Fig. 1.

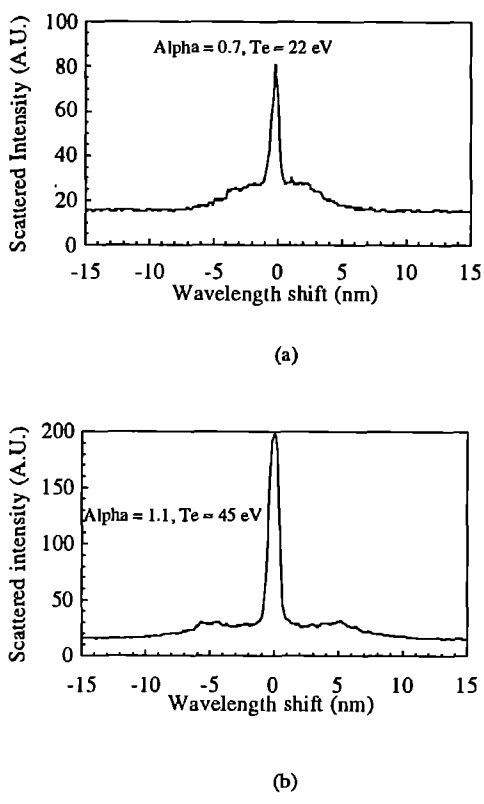

Fig. 1 Thomson scattering spectra from static-fill helium targets at a pressure of (a) 20 and (b) 100 torr.

The value of the parameter alpha (see equation (5)) is shown, along with the derived temperature, where the fitting corresponds to the thermal electron, high frequency part of the spectrum. Note that the symmetric nature of the curves confirms that this is not stimulated Raman sidescatter. A series of such measurements for a variety of pressures and gas targets has enabled us to study the roles of the various heating mechanisms.[4] In this paper, however, we shall concentrate on the information that can be extracted from the fraction of the energy in the high intensity central peak.

THOMSON SCATTERING IN THE HIGH Te /Ti LIMIT

The Thomson scattering factor, S(k,ω) for Maxwellian distributionfunctions is given by[5,6]

$$S(\mathbf{k},\omega)=\frac{2\pi^{1/2}}{ka}\left\{\frac{A_e}{|\varepsilon|^2}+\frac{A_i}{|\varepsilon|^2}\right\} \quad (1)$$

where

$$A_e=\exp(-x_e^2)\left[\left(1+\alpha^2 Z\frac{T_e}{T_i}Rw(x_i)\right)^2+\left(\alpha^2 Z\frac{T_e}{T_i}Iw(x_i)\right)^2\right] \quad (2)$$

$$A_i=Z\left(\frac{m_iT_e}{m_eT_i}\right)^{1/2}\exp(-x_i^2)\left[\left(\alpha^2 Rw(x_e)\right)^2+\left(\alpha^2 Iw(x_e)\right)^2\right] \quad (3)$$

and the plasma dielectric constant is given by

$$|\varepsilon|^2=\left\{\begin{array}{l}\left[1+\alpha^2\left(Rw(x_e)+Z\frac{T_e}{T_i}Rw(x_i)\right)\right]^2\\+\left[\alpha^2 Iw(x_e)+\alpha^2 Z\frac{T_e}{T_i}Iw(x_i)\right]^2\end{array}\right\} \quad (4)$$

The dimensionless frequencies and scattering parameter are defined as

$$x_e=\frac{\omega}{k}\left(\frac{m_e}{2\kappa_B T_e}\right)^{1/2},\quad x_i=\frac{\omega}{k}\left(\frac{m_i}{2\kappa_B T_i}\right)^{1/2},\quad \alpha=\frac{1}{k\lambda_D} \quad (5)$$

where $\lambda_D$is the Debye length. The real part of the plasma dispersion function, $Rw(x)$ is

$$Rw(x)=1-2x\exp(-x^2)\int_0^x\exp(p^2)dp \quad (6)$$

The imaginary part, which gives rise to Landau damping is

$$Iw(x)=\pi^{1/2}x\exp(-x^2) \quad (7)$$

It was first demonstrated by Salpeter that when Te ≈ Ti the spectrum takes a relatively simple form allowing the separation of electron and ion features, i.e. the scattering factor can be separated into the sum of two terms: one a function of x_e only, and the other simply a function of x_i.[6] However, in the experiments described here we expect the electrons to be considerably hotter than the ions, and the Salpeter approximation is no longer valid. In this case we expect the contribution from A_i to be small. Note however, that rather than make approximations, in the calculations that follow we have computed the solutions of equations (1) -(7) fully.

For large electron-to-ion temperature ratios the real part of the plasma dielectric constant (as given in equation (4)) vanishes in the vicinity of the ion acoustic frequency. This can be seen in Fig. 2 where we plot the scattering cross section as a function of wavelength for Helium at an electron temperature of 20eV, and a scattering parameter α of 1.0, for a range of temperature ratios. For all the plots given the laser wavelength is 268 nm scattered through 90 degrees. The increase in the ion acoustic resonance due to the decrease in the Landau damping of the ion waves as T_i is lowered can clearly be seen around 0.3Å from the central frequency. Of course, in the experiment the resonance itself is too narrow to be resolved due to the width of the instrumental broadening function (~0.7 nm), and a diagnosis of the ion temperature can only be inferred from the increase in the scattered energy into this central feature. It is the convolution of the instrumental broadening function with the narrow central peak of Fig. 2 which gives rise to the central features in Fig. 1.

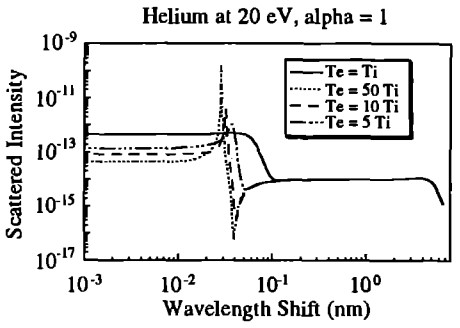

Fig. 2. The scattering cross-section as a function of wavelength shift from the central frequency for fully-ionised helium, with $\alpha = 1.0$, for various electron-ion temperature ratios, and with a fixed electron temperature of 20 eV.

The energy in this central feature is a strong function of the electron-ion temperature ratio. For values of the ratio not too far from unity the Salpeter approximation can still be used, and the ratio of the energy in the central feature to that in the rest of the spectrum, R, can be shown to be[5]

$$R=\frac{Z\alpha^4}{\left\{1+\alpha^2(1+ZT_e/T_i)\right\}} \quad (8)$$

However, in the limit of high temperature ratios, once the ion acoustic resonance is fully developed, this ratio simplifies to

$$R=\alpha^2 \quad (9)$$

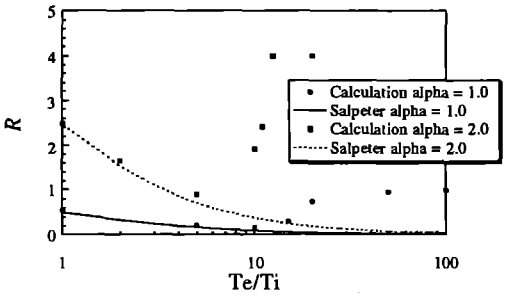

Fig. 3. Ratio of the energy in the central feature to that in the rest of the spectrum for helium as a function of the electron-to-ion temperature ratio. For alpha=1.0 the electron temperature has been taken to be 20 eV, and for alpha=2.0 it is 100 eV. Note the Salpeter approximation is valid for low Te/Ti, whereas at high ratios there is a limiting value of R of α^2.

In the intermediate regime R is a complex function of ZTe/Ti. This can be seen in Fig. 3 where we plot R as a function of the electron-ion temperature ratio for two different conditions. Also shown on the graph is the ratio predicted by the Salpeter approximation in each

case, which, as expected, is a good approximation when the electron and ion temperatures are of similar magnitude. It can be seen that in the limit of high temperature ratios equation (9) is obeyed. For an alpha of 1.0 we find that the transition from Salpeter to 'zero-damped' resonance behaviour occurs at approximately Te/Ti = 20, whereas for an alpha of 2.0 the ratio is closer to 10. Thus the fraction of the energy in the central portion of the Thomson spectrum can be used to gain information on the ion temperature.

COMPARISON WITH EXPERIMENTS

In Fig. 4 we plot the experimentally determined values of R as a function of α for several laser shots into static-fill helium targets. The variation in α from ~ 0.3 to 2 corresponds to a change in fill pressure from 20 to 400 torr. Also plotted on the figure are the values of the expected ratios for similar electron and ion temperatures (i.e. the Salpeter approximation of equation (8)) and for a high electron-ion temperature ratio (equation (9)). It can be seen that the experimental values are consistent with the high temperature ratio formula within the error bars.

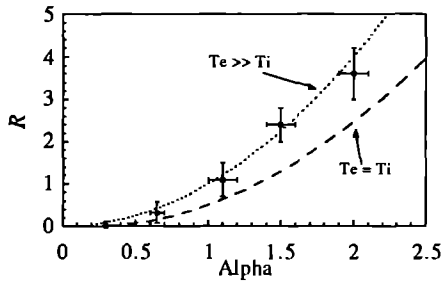

Fig. 4. The experimentally determined values of R as a function of α. Also shown are the expected values in the Salpeter and high temperature ratio limit.

The low observed ion temperatures can be explained by the long electron-ion collision times, which are estimated to be typically approximately 2 orders of magnitude longer than the laser pulse duration. A precise ion temperature cannot be inferred because, as can be seen from Fig. 3, once the ion acoustic resonance develops, the fraction of the energy in the central feature tends to α^2, and is no longer a sensitive temperature diagnostic. All we can infer is that the data are consistent with the resonance. For this to be the case we can conclude from calculations such as those shown in Fig. 3 that the temperature ratio must be at least of order 10-20 over the range of alphas shown.

CONCLUSION

Analysis of the central, low frequency region of Thomson scattering spectra from optically ionized gases shows that the fraction of the intensity in this region indicates the presence of 'zero-damped' ion-acoustic modes. Simulated scattering spectra show that this requires an electron-to-ion temperature ratio of at least order 10-20 for the helium spectra over the range of observed α. This result is consistent with the extremely long electron-ion collision times present compared with the laser pulse length.

REFERENCES

1. N. H. Burnett and P. B. Corkum, "Cold plasma production for recombination extreme ultraviolet lasers by optical field induced ionization", J. Opt. Soc. Amer., Vol. B6, pp. 1195-1199, 1989.
2. N. H. Burnett and G. D. Enright, "Population inversion in the recombination of optically-ionized plasmas", IEEE J. Quant. Elect., Vol. 26, pp. 1797-1808, 1990.
3. D. C. Eder, P. Amendt, S. C. Wilks, "Optical field ionized plasma x-ray lasers", Phys. Rev. A, Vol. 45, pp. 6761-6772, 1992.
4. A. A. Offenberger, W. Blyth, M. H. Key, J. S. Wark, Z. Najmudin, and A. E. Dangor, "Thomson scattering measurements in optically ionized gases produced by intense KrF laser radiation", Phys. Rev. Lett **71**, 3983 (1993).
5. D. E. Evans and J. Katzenstein, "Laser light scattering in laboratory plasmas", Rep. Prog. Phys., Vol. 32, pp. 207-271, 1969.
6. E. E. Salpeter, "Electron density fluctuations in a plasma", Phys. Rev., Vol. 120, pp.P 1528-1535, 1960.

MEASUREMENTS OF HEATING BY STIMULATED RAMAN SCATTERING IN OPTICALLY-IONIZED PLASMAS.

S.G.Preston[1], W.J.Blyth[1], A.E.Dangor[2], M.H.Key[3,1], A.Modena[2], Z.Najmudin[2], A.A.Offenberger[4], J.S.Wark[1].

[1]Clarendon Laboratory, Department of Physics, University of Oxford, Parks Road, Oxford OX1 3PU, UK,
[2]Department of Physics, Blackett Laboratory, Imperial College, London, UK,
[3]Rutherford Appleton Laboratory, Chilton, Didcot, Oxon, OX11 0QX, UK,
[4]University of Alberta, Edmonton, Alberta, T6G 2G7, Canada.

INTRODUCTION

The production of a plasma by rapid optical ionization introduces the possibility of creating an XUV recombination laser by producing a low electron temperature with a degree of ionization that is far from collisional equilibrium[1]. The use of UV laser pulses of extremely short duration (~100fs) is needed to minimise the electron temperature and maximise XUV gain.

Work has been carried out to measure the temperature, density, and heating mechanisms of such a plasma created by the SPRITE laser. Previous results have been reported using a 10ps Raman amplified beam [2-4]. We now report preliminary results using a 350fs CPA beam[5] incident on a high pressure gas target with densities up to 10^{20} atoms/cm^3 (lower pressures are discussed elsewhere in this report [6]).

THE EXPERIMENT

A 248nm CPA beam was used with a compressed pulse length of between 280 and 400fs (but typically 350fs), and energies up to 250mJ on target. An f/4 off-axis parabola focused the beam to a 10μm diameter spot with a mean intensity of 10^{18}W/cm^2 over a length of 100μm . The gas target was produced by a solenoid gas jet with a 1mm diameter nozzle placed 100μm below the laser focus with backing pressures up to 1000psi. The gases used were hydrogen, helium, and neon; although only results for neon will be discussed here.

DIAGNOSTICS

The primary diagnostics were optical spectrometers at 90° and 150° to the laser direction. An image in scattered laser light was relayed to them with 10x magnification by f/5 UV achromatic lenses. Each spectrometer was oriented with its axis of spectral dispersion perpendicular to the axis of the laser beam, thus relaying spatial and spectral information to an optical streak camera which was used to discriminate against stray light. The laser pulse was so short relative to the streak speed that there was effectively no temporal smearing. The intensified streak camera output was then coupled via a fibre optic bundle to a two dimensional CCD array. The gratings used were 300 and 600 l/mm at 90° and 600 l/mm at 150°. Spatial resolution was measured to be 20μm at 90°. Due to the aspect ratio of the beam at 150°, spatial resolution was relatively unimportant, but was essentially the same as the 90° channel.

Light scattered at 180° was collected by a 0.6mm thick quartz plate and relayed to a streak camera which was calibrated for absolute reflectivity. Stray light was eliminated using a filter which blocked all wavelengths below 300nm. Faraday cups were placed in the vacuum chamber to record time-of-flight spectra of charged particles ejected from the plasma.

STIMULATED RAMAN SCATTERING

Stimulated Raman scattering (SRS) is a particularly important heating mechanism because the frequency of the plasma wave can be as high as half the frequency of the incident laser frequency.

Although the wave starts as an ordered electron density fluctuation, electrons with velocities near the plasma wave phase velocity can be accelerated by the wave and draw energy from it (Landau damping). These 'hot' electrons later scatter and thermalise in the plasma. The extent of Landau damping depends on $\alpha = 1/k\lambda_D$ where k is the magnitude of the wavevector of the plasma wave, and $\lambda_D = (T_e\varepsilon_0/n_e e)^{1/2}$ is the Debye length (Te is in eV). When $\alpha < 1$ Landau damping of the waves is strong. Plasma waves produced by SRS have frequencies determined by the Bohm-Gross frequency,

$$\omega^2 = \omega_{pe}^2 + 3k^2 v_{te}^2$$

where $\omega_{pe}^2 = Ne^2/\varepsilon_0 m_e$ is the electron plasma frequency, and $v_{te}^2 = eT_e(\text{eV})/m_e$ is the electron thermal velocity.

RESULTS

Scattering signals at both 90° and 150° are shown in figure 1. Focusing the laser to 100μm from the nozzle exit produced electron densities of about 5x10^{20}cm^{-3}. The 90° signal generally consisted of one shifted peak (as shown), but occasionally two peaks were seen that were separated in both space and frequency. These separated features appear to be produced by scattering from different regions of plasma.

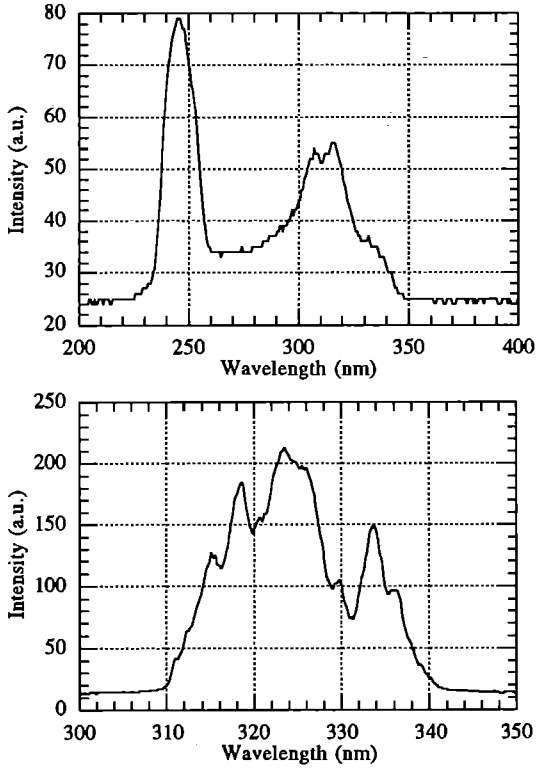

Figure 1 Stimulated scattering at 90° (upper) and 150° (lower) from the same shot (SN16087). The target was a neon gas jet with 500psig backing pressure and 100μm nozzle separation from the laser focus. Energy delivered on target was approximately 200mJ.

The 150° signal varied between one discrete frequency shifted peak and the extended scattering shown in the figure. Note the large bandwidth over which scattered light is shifted with mean

wavelength shifts of over 75nm with a spread of up to 30nm were seen. A possible explanation of this large bandwidth is filamentation of the focused laser beam, resulting in high intensity beamlets passing through regions of different densities in the gas target. Assuming a constant electron temperature of 1.5keV, this frequency spread comes from electron densities between $1.34x10^{20}cm^{-3}$ and $5.6x10^{20}cm^{-3}$. If the highest electron density corresponds to Ne^{8+}, then the lowest density is produced by Ne^{2+}.

Study of the variation in SRS reflectivity with laser energy, figure 2, indicates the rapid growth of the instability which increases by a factor of over 1000 when we double the laser energy, and reaches levels of over 2%. These enhanced reflectivities are well above the unstimulated Thomson scattering reflectivities of about 10^{-6}%. If we combine these reflectivities (~2%) with the frequency shifts recorded at 150° ($\Delta\omega$ ~ $1.8x10^{15}s^{-1}$) we see that the energy absorbed in a cylindrical focal volume estimated to be of 10μm diameter and 100μm length via SRS is 1.2mJ. If this is equally shared between electrons in the focus, at a density of $5x10^{20}cm^{-3}$, we arrive at an electron temperature of approximately 1.9keV.

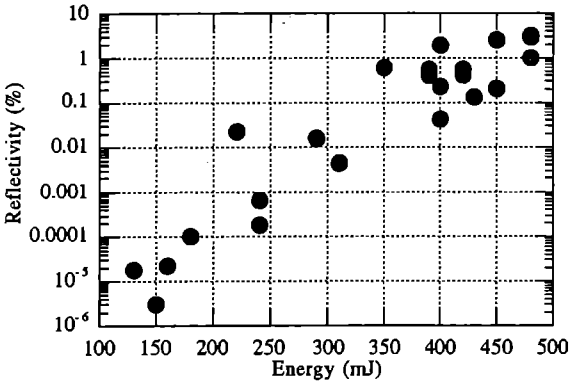

Figure 2 Growth rate of SRS backscatter reflectivity with laser energy from a 500psig neon gas jet 100μm below the laser focus. Note that the laser energies quoted are energies before the compressor gratings.

Evidence in support of the extremely high electron temperatures produced by our stimulated scattering comes from several sources. Firstly, we know that the frequency shift of the Raman scattered light is determined by the phase matching conditions of the incident light wave and the resultant plasma and light waves. The frequency shift of the scattered light is essentially the Bohm-Gross frequency (with a small correction to allow for the different refractive indices of the plasma and air). If both our 90° and 150° channels see scattering from the same region of plasma, the difference in frequency shift between the two directions tells us the thermal correction to the electron plasma frequency. Preliminary analysis of these thermal corrections indicate electron temperatures of about 2keV.

Secondly, if we assume that electrons heated by Landau damping are accelerated to the phase velocity of the plasma wave produced by the SRS[7] we see that 'hot' electrons are produced with energies of over 4keV. These hot electrons ejected from the focal region create a space charge which drags ions out of the plasma with the electrons. The ions and electrons then move away from the focus with equal momentum. Hence, the ions, by virtue of their much greater mass, acquire nearly all the kinetic energy initially associated with the electrons. A Faraday cup time-of-flight recording (figure 4) shows us the initial 'hot' electron energy distribution. We again infer that the 'hot' electron temperature is again about 4keV.

Finally, analysis of X-ray emission from the plasma, (figure 3), shows helium- and hydrogen- like recombination lines. The photon flux inferred from these is consistent with their being produced by collisional ionisation of neon by the SRS heated electrons.

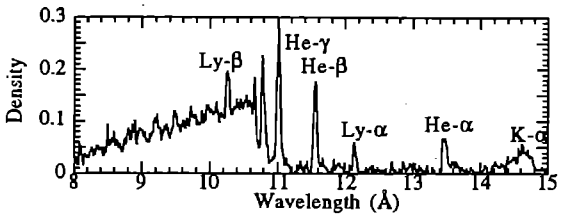

Figure 3 X-ray spectrum integrated over ten shots on 400psig neon at 100μm below the laser focus.

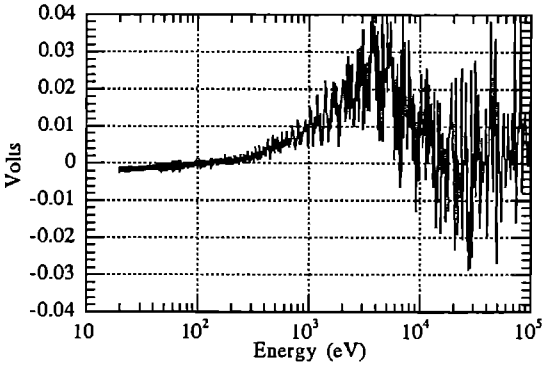

Figure 4 Faraday cup data from a neon gas jet with 400psig backing pressure and 100μm nozzle separation from the laser focus, showing the energy spectrum of ions ejected from the focal region. The energy on target was 150mJ (SN16437).

CONCLUSION

To produce XUV lasing in a lithium-like neon cold recombination scheme, electron temperatures must not be allowed to exceed about 40eV[1]. We have shown that at pulse lengths of 350fs and focused intensities of $10^{18}W/cm^2$ electron temperatures can be much higher than this due to SRS heating. Control of SRS is thus a key issue for such lasers.

The laser intensity used in this experiment is well above the threshold intensity for production of lithium-like neon, I_T~$3x10^{17}W/cm^2$. It is encouraging that SRS reflectivity levels fall so rapidly with decreasing laser energy. Reducing the intensity by altering our focusing optic to create a longer confocal length should significantly reduce SRS gain levels which are dependent on the intensity of the driving pulse. This reduced gain will not be countered by an increased length over which gain can occur as this is limited by the laser pulse length to about 100μm.

REFERENCES

(1) D.C. Eder, P. Amendt, S.C. Wilks. Phys. Rev. A, 45, 6761-6772 (1992).
(2) W.J. Blyth, S.G. Preston, A.A. Offenberger, Z. Najmudin, M.H. Key, J.S. Wark, A.E. Dangor, CLF Annual report to the laser facility committee, RAL-93-031 (1993).
(3) A.A. Offenberger, W.J. Blyth, M.H. Key, J. Wark, Z. Najmudin, B. Dangor, Proc. SPIE, (1993).
(4) A.A. Offenberger, W. Blyth, A.E. Dangor, A. Djaoui, M.H. Key, Z. Najmudin, J.S. Wark. Phys. Rev. Lett., 71, 3983-3986 (1993).
(5) I.N. Ross, A.R. Damerall, E. Divall, J.M. Evans, G.J. Hirst, C.J. Hooker, J.R. Houliston, M.H. Key, Z. Najmudin, P. Norreys, K. Osvay, J.M.D. Lister, Annual report to the laser facility committee, RAL-93-031 (1993).
(6) W.J. Blyth, S.G. Preston, Z. Najmudin, A. Modena, A.A. Offenberger, J.S. Wark, M.H. Key, A.E. Dangor, (This publication).
(7) W.L. Kruer, Laser-plasma interactions II, Scottish Universities Summer School in Physics, 185-204 (1982).

ELECTRON TEMPERATURE MEASUREMENTS OF OPTICALLY IONISED PLASMAS

W.J. Blyth[1], S.G. Preston[1], Z.Najmudin[2], A. Modena[2],
A.E. Dangor[2], M.H. Key[1,3], A.A. Offenberger[1,4], J.S. Wark[1],

[1] Clarendon Laboratory, Department of Physics, University of Oxford, Parks Road, Oxford OX1 3PU, UK
[2] Imperial College of Science and Technology, Prince Consort Road, London SW7 2AZ, UK
[3] SERC Rutherford Appleton Laboratory, Chilton, Didcot, Oxon OX11 OQX, UK
[4] Dept. of Electrical Engineering, University of Alberta, Edmonton, Alberta T6G 2G7, Canada

INTRODUCTION

The aim of these experiments was to measure the temperature of plasmas created by optical ionisation of gas targets with high intensity short pulse UV laser pulses. Optically ionised plasmas have been an area of great interest recently because of the possibility of producing a 'cold' recombination X-ray laser[1,2]. A parameter of key interest in these plasmas is the electron temperature, since this determines the maximum gain and efficiency of the proposed X-ray lasers.

In previous reports, we have presented data on the temperature measurements of optically ionised plasmas using the 12 ps Raman amplified beam of Sprite[3-5]. Here we present data from much shorter pulse experiments, which have a more direct relevance to the X-ray laser schemes. In these experiments, the laser used was the Sprite KrF beam used in the CPA mode. The pulse length was ~ 350 fs, energy 300 mJ, focused with f/4 optics to a 10μm spot with intensities in the region of 10^{18} Wcm^{-2}. The target chamber was filled with gas of pressures 5 - 200 torr to provide gas targets of density 10^{17} - 10^{19} cm^{-3}. The gases used were helium and neon.

The main diagnostic for the temperature measurements in these experiments was Thomson scattering of the incident laser. This allows the temperature to be measured during the pulse. The form of the Thomson scattering depends on the Debye length λ_D and k the difference in the wavenumber of the incident light and scattered light[6]. In the incoherent limit where the parameter $\alpha = 1 / k\lambda_D \ll 1$, Thomson scattering can be treated as scattering from individual electrons, and the spectrum of scattered light corresponds to the doppler broadening due to the thermal motion of the electrons. In the coherent limit, $\alpha \gg 1$, and the spectrum corresponds to scattering from plasma waves, and peaks occur in the spectrum which are shifted by the plasma wave frequencies. In these experiments, α typically has values of 0.3 - 1.5, so the spectra are between these two limits. The other feature of the Thomson scattering in these experiments is the prominant scattering feature near the laser wavelength. This is due to scattering from ion waves which are undamped because of the high electron temperature T_e to ion temperature T_i ratio. This is referred to as the ion feature, and the scattering at larger wavelength shifts is referred to as the electron feature.

RESULTS

The Thomson scattered spectra are shown in figure 1. The data is shown with theoretical spectra fitted which assume that $T_e / T_i \gg 1$. This is expected to be true since the ions are not expected to heat up on 350 fs time-scales. In these experiments we found that the measured spectra were asymmetrical, with more light scattered into the red-shifted side of the spectrum compared to the blue shifted side. This will be discussed further in the next section. For the moment, the blue and red shifted parts of the spectra are fitted separately, and different temperatures and α parameters are deduced for each part.

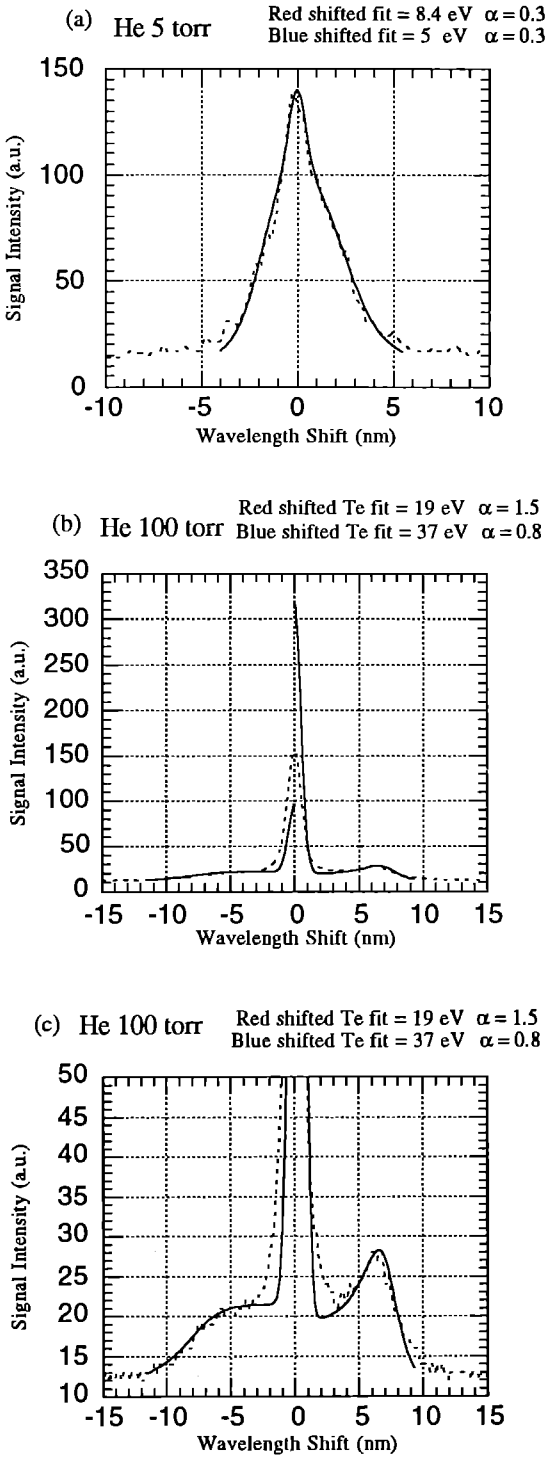

Figure 1 *Thomson scattered spectra in He at a) 5 torr, and b) &c) 100 torr. Figure 1c) shows a detail of the electron feature, and has the same fit as figure 1b). The dotted line shows the data, and the solid line is the fitted spectrum. The blue and red shifted parts are fitted separately.*

The temperatures measured in this experiment are summarised in figure 2. The temperatures deduced from the blue wing fits and the red wing fits are both shown, and the temperatures predicted by Medusa simulations are also shown.

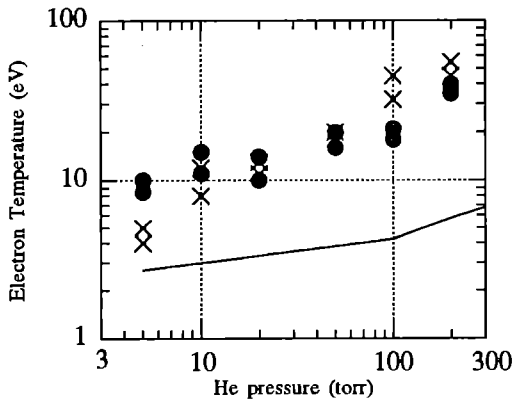

Figure 2 *Electron temperature vs pressure in Helium. The spots show the temperatures deduced from the red-shifted part of the spectrum, and the crosses show the temperatures deduced from the blue-shifted part of the spectrum. The solid line shows the temperatures predicted by Medusa simulations*

DISCUSSION OF RESULTS

There are several interesting features of these results that make interpretation complicated. Firstly, the scattering into the red-shifted part of the spectrum is enhanced compared to the blue-shifted part. Secondly, at the higher pressures, there is too much scattering in the ion feature to be consistent with the blue-shifted fit, and too little to be consistent with the red-shifted fit. Thirdly, the temperatures deduced from fits to both parts of the spectrum are significantly higher than those predicted by the Medusa simulations. There are various explanations of these features which partly explain some of the data, but as yet, a completely consistent explanation has not been found.

The first explanation is that SRS is occuring. This causes more light to be scattered into the red shifted part of the spectrum than the blue part. The growth time for SRS is less than the pulse-length, so it is physically reasonable to assume that SRS could start to occur. If the SRS were strong enough, this could also explain why the temperatures measured are greater than the Medusa simulations, since it acts as an additional heating mechanism. This has been observed at higher densities where SRS heating becomes very significant[7]. However, this does not explain all the features of the data. According to this argument, the plasma conditions should be deduced from the blue shifted part of the Thomson scattered spectrum, since the red shifted part is enhanced. This means that there is too much scattering in the ion feature, which suggests that SBS is occuring. This is not expected to occur however, since the growth time for the SBS instability is much longer than the laser pulse-length. Also, the amount of SRS measured at 150° is quite small. In order to account for the additional heating, the scattering at 180° would have to be a factor of about 10^5 times greater. This could possibly occur if the laser was self-focusing to create very narrow filaments, so that the gain length at 180° was much more than at 150°. However, self-focusing is not expected to occur at these densities. Therefore, if the enhanced scattering at 150° is due to SRS, it would not appear to be strong enough to be responsible for the level of extra heating observed.

The second explanation is that the pulse-length of the laser is so short, that the scattering does not occur from an equilibrium density fluctuation distribution in the plasma. In the coherent limit, the scattered spectrum is a measure of the density fluctuations in the plasma. In a thermal plasma in steady state, these tend to be dominated by plasma waves. However, when the plasma is created, it takes a finite time for the plasma waves to become established. In these experiments, the electron plasma wave period is in the region of 20 - 100 fs. This is approaching the regime where there are not many cycles of the plasma wave during the pulse, and so the thermal level of plasmons may not have been established. The possibility therefore exists that a photon incident on the plasma can create a plasmon, causing red-shifted scattering to occur, while the blue shifted scattering is essentially incoherent, since there are no plasmons to scatter from. Scattering into the ion feature would be determined by the level of the fluctuations in the gas before ionisation, since the ions are stationary on the time-scale of the pulse. This interpretation gives no explanation of the additional heating observed.

A quantitative analysis of this interpretation has not yet been made. The issue of scattering from a non-thermal plasma is a complicated one which requires further theoretical effort, and more time is required in order to develop an understanding of these results. However, it is apparent that the temperatures measured in these experiments are higher than expected, and this could have significant effects on future X-ray laser schemes using these optically ionised plasmas.

REFERENCES

(1) N.H. Burnett, P.B. Corkum.
Cold-plasma production for recombination extreme-ultraviolet lasers by optical-field-induced ionisation.
J. Opt. Soc. Am. B, 6, 1195 (1989).
(2) D.C. Eder, P. Amendt, S.C. Wilks.
Optical-field ionized plasma x-ray lasers.
Phys. Rev. A, 45, 6761-6772 (1992).
(3) A.A. Offenberger, W. Blyth, A.E. Dangor, A. Djaoui, M.H. Key, Z. Najmudin, J.S. Wark.
Electron temperature of optically ionised gases produced by high intensity 268 nm laser radiation.
Phys. Rev. Lett., 71, 3983-3986 (1993).
(4) A.A. Offenberger, W.J. Blyth, M.H. Key, J. Wark, Z. Najmudin, B. Dangor,
Thomson scattering measurements in optically ionized gases produced by high intensity KrF laser radiation.
Proc. SPIE, (1993).
(5) W.J. Blyth, S.G. Preston, A.A. Offenberger, Z. Najmudin, M.H. Key, J.S. Wark, A.E. Dangor,
Thomson scattering measurements of optically ionised plasmas.
Annual report to the laser facility committee, RAL-93-031 (1993).
(6) D.E. Evans, J. Katzenstein.
Laser light scattering in laboratory plasmas.
Rep. Prog. Phys, 32, 207-271 (1969).
(7) S.G. Preston, W.J. Blyth, A.E. Dangor, M.H. Key, A. Modena, Z. Najmudin, A.A. Offenberger, J.S. Wark.
This Publication, (1994).

HIGH HARMONIC GENERATION WITH A CPA KrF LASER

M. Zepf[1], W. Blyth[1], M H Key[1,2], M. Nakai[3], S.G Preston[1], J.S. Wark[1]

[1]Clarendon Laboratory, Department of Physics, University of Oxford, Parks Road, Oxford OX1 3PU, UK
[2]Rutherford Appleton Laboratory, Chilton, Didcot, Oxon. OX11 0QX,UK
[3] on leave from Institute of Laser Engineering, Osaka University, 2-6 Yamada-oka, Suita Osaka 565, Japan

INTRODUCTION

The generation of XUV harmonics of ultra short pulse lasers in the terawatt regime has drawn considerable interest because of the exciting properties of the emitted radiation. These are especially the short pulse length, the high spectral brightness and the possible tunability, which could be a basis for many applications.

The SPRITE CPA system lends itself to the generation of high harmonics, with good conversion efficiency for harmonics in the conversion plateau because it's short wavelength of 248 nm reduces dephasing by free electrons. Studies of harmonic generation from 1053 nm and 526 nm by Perry *et al.* have shown this advantage of a shorter wavelength of the primary laser quite clearly [1]. The maximum photon energy is given by $E_p=I_p+3U_p$ (I) (Where E_p is the photon energy, I_p the ionisation energy and U_p the ponderomotive potential which is proportional to λ^2).

EXPERIMENTAL SET-UP

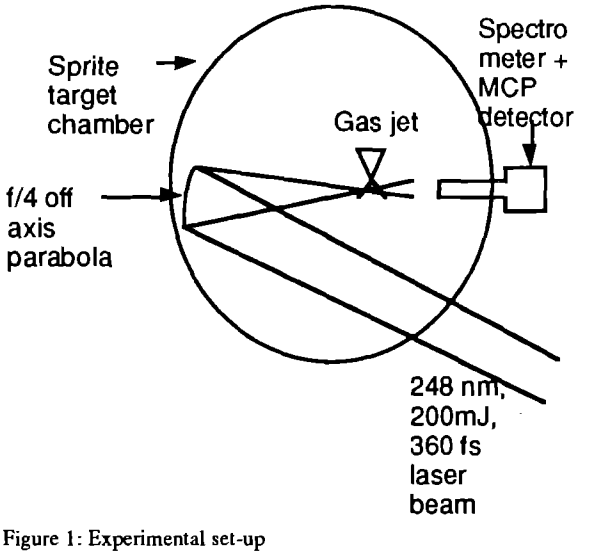

Figure 1: Experimental set-up

As shown in figure 1, the Sprite CPA-beam was focused into a pulsed 1 mm gas jet using an f/4 off axis parabola forming a 10 µm focal spot. The laser delivered about 200 mJ on target in approximately 350 fs resulting in an intensity of around 5 10^{17} W/cm^2 .The atom number densities used were between 5 $10^{17}$and 2 10^{19} cm^{-3}. We investigated the response of the noble gases He, Ne, Ar and Kr under these conditions. The harmonics were detected with a flat-field spectrometer using a 1200 line/mm grating and a microchannel plate (MCP).

The number densities and intensities were slightly higher in our experiment compared to those used by Sarakura *et al.* [2].

RESULTS

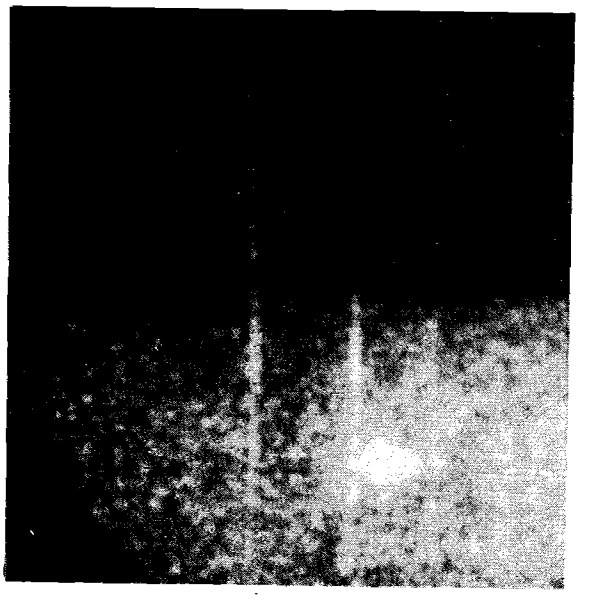

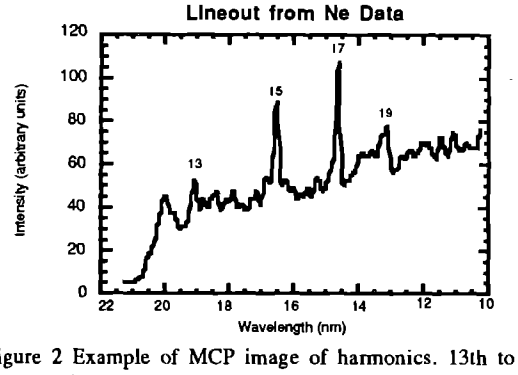

Figure 2 Example of MCP image of harmonics. 13th to 19th harmonic in Ne with split B/Al filter

The results obtained were very similar to those of Sarakura *et al.* [2]. A typical example of the spectra observed is shown in figure 2. We find relative intensities as illustrated in figure 3.

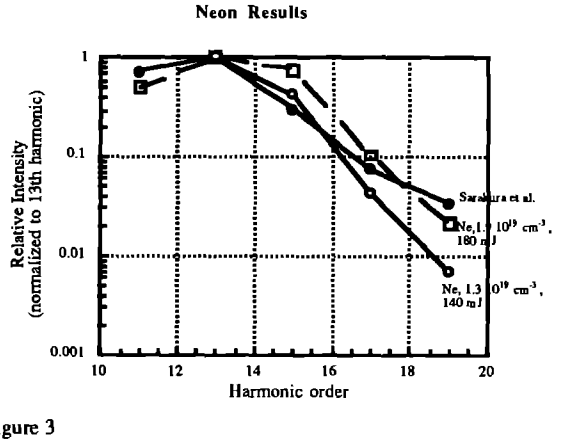

Figure 3

When the position of the gas jet in the focus was moved, harmonic yield was found to be largely independent of the position. The number density of atoms in the gas jet was also varied and it was found similarly that there was only a weak increase of harmonic intensity with number density. The harmonic yield was seen to be weaker in helium while results in argon and krypton were more difficult to interpret due to masking by strong plasma fluorescence, as seen in figure 4. Nevertheless we were able to record upto 19th harmonic in Argon.

DISCUSSION

The invariance of the harmonic yield, with position in the focus and gas density, suggests that the conversion is being limited by a short coherence length most probably due to the de-phasing introduced by free electrons [3,4].

It is therefore possible that the conversion is occurring outside the region of maximum intensity. The peak intensity within the focal region is such that simulations indicate a negligible fraction of neutral atoms present after the intensity reaches 0.2 percent of the peak intensity.

We were more concerned in the present study to examine effects of very high intensity and in particular to look for possible harmonic conversion through ions [5]. Due to their higher ionisation potential and higher ionisation threshold equation (I) suggests the generation of higher photon energies.

Our data shows a fall off in conversion efficiency beyond the 13^{th} harmonic to the 19^{th} though the high stray light level masks possible weaker conversion to higher harmonics (Our data extends only to 10^{-2} of the plateau intensity). Assuming the cut off is at the 19^{th} an analysis of the ionisation rate of neutral atoms gives an estimate of whether the observed harmonics are due to neutral atoms or ions.

An estimate with Up calculated at 10^{15} W/cm^2 (at which the population is reduced e-fold in 10 fs) gives a short wavelength limit of 32 nm according to equation (I) for the neutral cut off. Similarly we would expect a cut off of around 13 nm for Ne^+ and 5 nm for Ne^{++} The shortest wavelength observed is 13.7 nm which indicates that there must be a significant contribution of at least Ne^+ . We are presently engaged in a more detailed analysis of the possible ion response

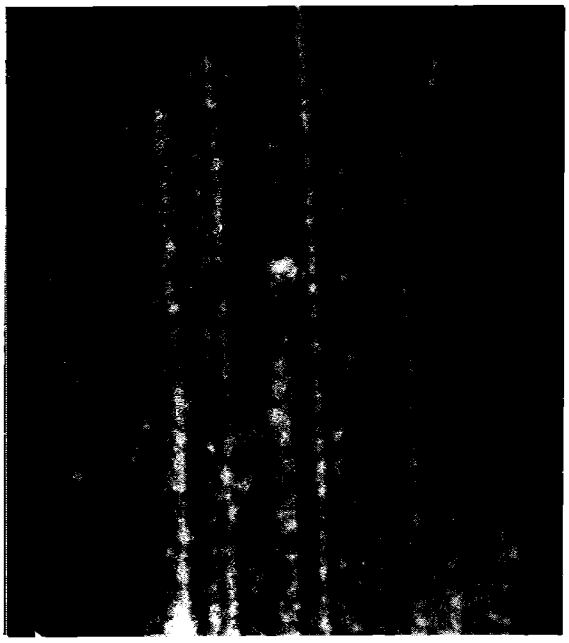

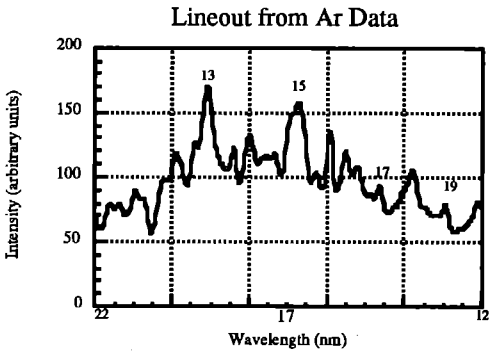

Figure 4:Ar shot showing fluorescence and harmonics

We have not determined the absolute conversion efficiency in these measurements but are in the process of doing so through a separate calibration of the MCP detector. We would in general expect that higher conversion efficiency would be obtained if the interaction intensity were optimised by using a much larger confocal parameter than that of our f/4 optics.

CONCLUSIONS

We have demonstrated for the first time, high harmonic generation using the new ultra short pulse CPA capability of the Sprite Laser Facility. Our aim was to examine harmonic conversion at high intensities. Our results are very similar to those previously obtained by Sarakura et al.. In our future work we shall be interested in the use of the short wavelength KrF laser to give higher conversion efficiency through reduction of de-phasing from the dispersive effect of free electrons.

REFERENCES

[1] Perry *et al.*
IEEE Transactions on Plasma Science, 21, 82 (1993)

[2] N Sarakura, K Hata, T Adachi, R Nodomi, M Watanabe, S Watanabe
Coherent soft x-ray generation by the harmonics of an ultra-high power KrF laser
Phys. Rev. A, 43, 1669 (1991)

[3] Anne L'Huiller, Phillipe Balcou, L.A. Lompre
Coherence and Resonance Effects in High-Order Harmonic Generation
Phys. Rev. Lett, 68, 166 (1992)

[4] Ph. Balcou and Anne L'Huillier
Phase-matching effects in strong-field harmonic generation
Phys. Rev. A, 47, 1447 (1993)

[5] J L Krause, K J Schafer, K C Kulander
High-Order Harmonic Generation from Atoms and Ions in the High Intensity Regime
Phys. Rev. Lett, 68, 3535 (1992)

TIME RESOLVED MEASUREMENT OF X-RAY EMISSION GENERATED BY 2 ps CPA PULSES

R Evans, T A Hall, J Ellison and A Djaoui*

Department of Physics, University of Essex
*Rutherford Appleton Laboratory

INTRODUCTION

An experiment was performed to observed the time resolved X-ray emission from various metal layer targets under irradiation by 2 ps CPA pulses from the VULCAN laser. The targets consisted of thin (1000-2000 Å) metal layers on a thick (~ 1 mm) plastic lollipop of diameter 250 μm. Some of the targets also had a 1000 Å or 2000 Å plastic overlayer to tamp the expansion during the laser pulse. The temporal evolution of the X-ray spectrum was monitored with a TlAP crystal spectrometer used in conjunction with a fast (~ 5 ps/mm) streak camera. A KBr photocathode, which has a high tempUniverstiy of Loughboroughs) compared to that of CsI, preceded the streak tube. The range visible was from 7 to 8 Å and contained the He_α and H_α resonance lines plus their respective satellite lines.

RESULTS

Two colour enhanced streak records from shots 0408 and 0111 are shown in figure 1. The data from 0408 was obtained using a 2000 Å Al target with no overlayer at 30° and there was 14.9 J incident. The 0111 data came from a 21.3 J shot incident onto a 2000 Å Al target over coated with 1000 Å of plastic. There is a marked difference in the resonance line histories between the two shots, a sudden quenching of the He_α and H_α emission is observed when an overlayer is present. Figure 2 shows a comparison of the lifetimes of the H_α resonance lines from shots with and without plastic overlayer. Shot 0408 2000 Å Al, 14.9 J incident, 30° angle of incidence, no overlayer. Shot 0910 1000 Å Al, 15.6 J incident, 30°, 2000 Å overlayer. Figure 2 demonstrates how the resonance line history differs from targets with and without a plastic tamping layer present over the X-ray emitting aluminium layer. Both lineouts are from similar incident energy shots which use the same angle of incidence. However, the temporal behaviour of the emission lines is very different. From the target with no overlayer, the FWHM lifetime of the H_α line is 30 ps, but from the equivalent shot with an overlayer present the FWHM duration is only 20 ps. As well as the FWHM lifetimes, the overall histories are quite different also. The risetime of both lineouts is fast (< 5 ps), but the decay of the emission from the shot with no overlayer is a slow exponential (with a 1/e folding time of ~ 20 ps), while the overlayered shot shows a very rapid quenching of the emission on a timescale similar to that of the rising edge. Other metal+plastic thicknesses gave results which implied that the duration of the X-ray emission was dependent on the presence of an overlayer and not on the thicknesses of the layer itself (within the ranges used here).

The other target materials, which only display continuum emission in the 7 to 8 Å range, exhibit no such shortening of the X-ray pulse, as was displayed by the aluminium resonance lines. The continuum lifetimes of germanium, copper and uranium targets without a tamping layer were all approximately the same as 15 ps (FWHM), thus figure 3 presents data from two uranium shots only. The results from two shots are displayed, each with similar laser energies and the same incident angle, shot 0711 with no overlayer and shot 0213 with a 1300 Å plastic tamping layer. The major difference between the two is the decrease, by around 50%, in the total X-ray output from the overlayered shot. This signal suppression is probably due to the lowering in the peak temperature attained in the aluminium when using an overlayer.

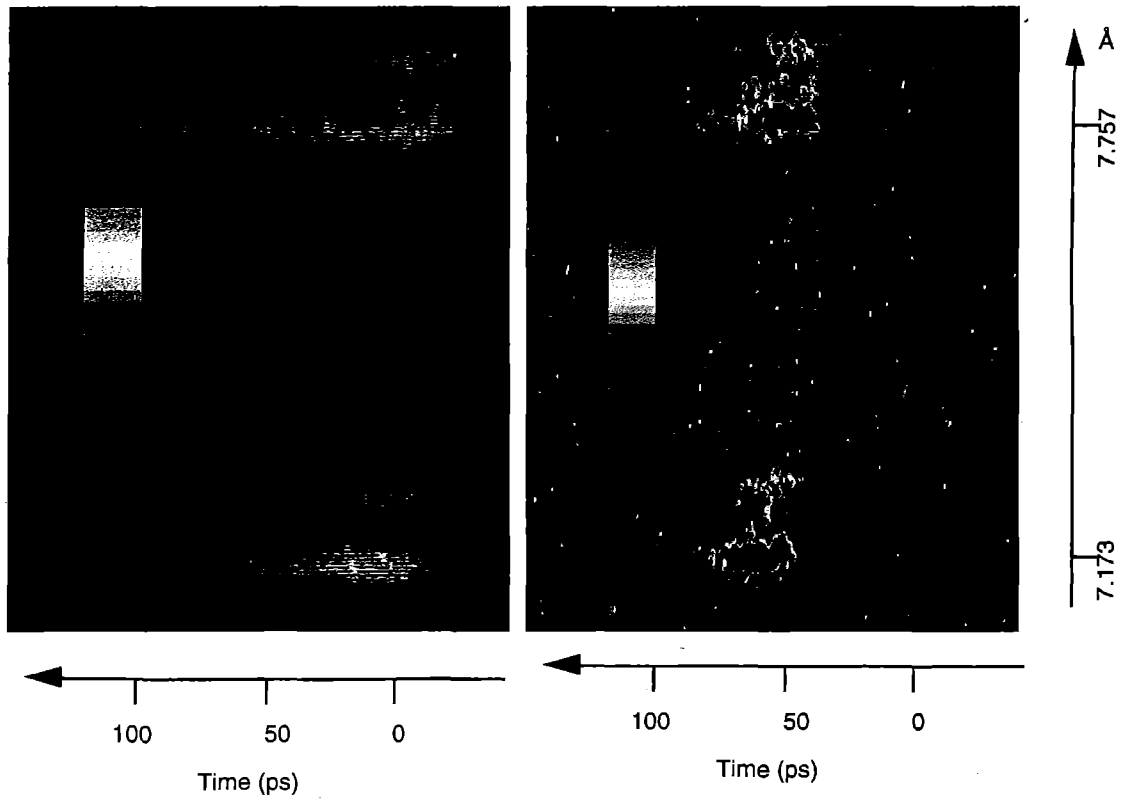

Figure 1 Colour enhanced streaked spectra from targets with and without a plastic overlayer. The image on the left is ~ 15 J incident on an un-tamped Al target, while the image on the right is k~ 20 J shot onto an Al target with a 1000 Å plastic overlayer

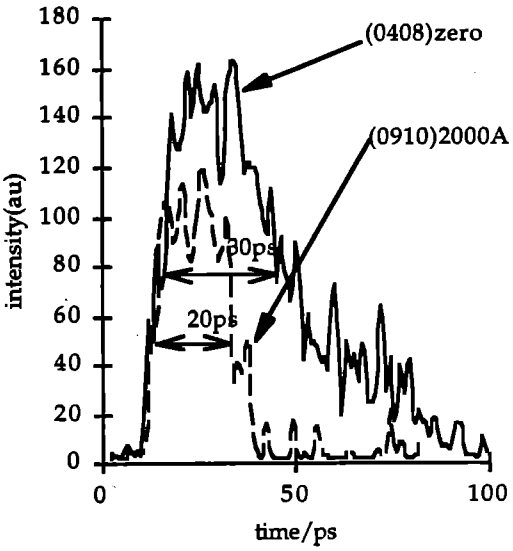

Figure 2 Comparison of the lifetimes of the H_a resonance lines form shots with and without plastic overlayer. Shot 0408 2000 Å Al, 14.9 J incident, 30° angle of incidence, no overlayer. Shot 0910 1000 Å Al, 15.6 J incident, 30°, 2000 Å overlayer

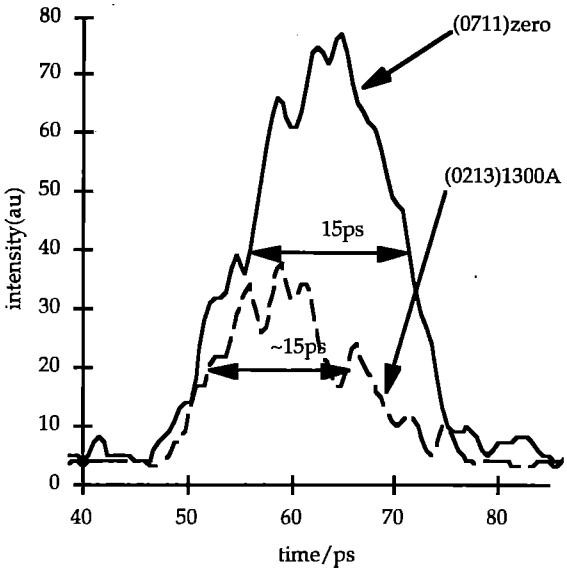

Figure 3 Comparison of continuum lifetimes from uranium targets with and without plastic overlayer. Shot 0711 1300 Å U, 15.7 J incident, 30° angle of incidence, no overlayer. Shot 0213 1000 Å U, 14.3 J incident, 30°, 1000 Å overlayer

The results of the resonance line lifetimes presented in figure 2 were modelled using the version of MEDUSA[1] which incorporates the effects of both velocity gradients and opacity on the transfer of line radiation through a plasma. Two simulations were undertaken to study the difference in the H_α resonance line history from targets with and without a plastic overlayer. The results are presented in figure 4. The peak of the laser pulse comes at 8 ps and the time meshing is 4 ps, which unfortunately is not fine enought to resolve the initial rise of the emission. Initially the behaviour of the two traces is almost idential. However, there is a significant divergence in the line evoluation at later times.

The un-tamped simulation shows the X-ray emission falling approximately exponentially with time after 15 ps, while the emission from the tamped model falls rapidly, actually going to zero after 32 ps. This is essentially the behaviour shown by the experimental data shown in figure 2.

DISCUSSION

Since strong H_a and He_a features are observed, the laser pulse must "burn through" to and probably beyond both the H-like and He-like ionisation stages, leaving the plasma in a state where many of the ions are fully stripped and the higher ionisation stage ions are mostly highly excited. Thus, during the laser pulse, the produced ionisation wave passes through the aluminium causing the nearly complete depopulation of both the H-like ion and the He-like ion ground state. At this time the amount of expansion is minimal and the density is still high, thus the population of the "forbidden" transition, is still possible. There will still be some residual ionisation after the laser pulse has finished, the timescale on which this will occur is related to the ion-electron collision time. The ion-electron equilibration timescale is formalised[4] and for T_e = 800 eV and n_e = 8 x

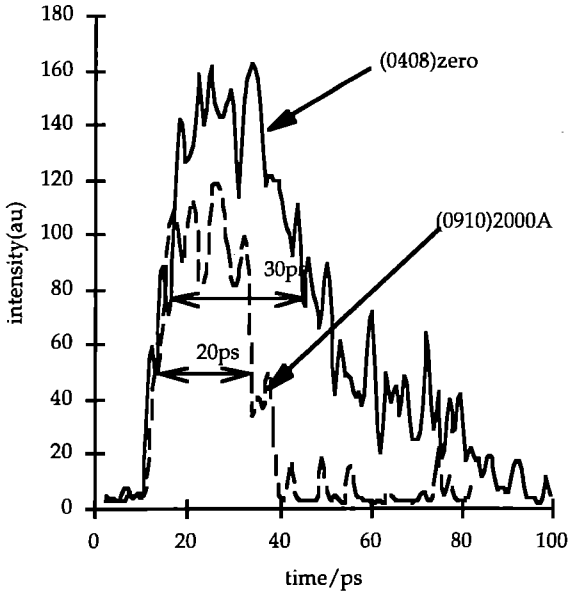

Figure 4 Predicted X-ray emission time history from targets with no overlayer and a 2000 Å plastic overlayer. Incident irradiance 10^{17}, aluminium thickness 2000 Å

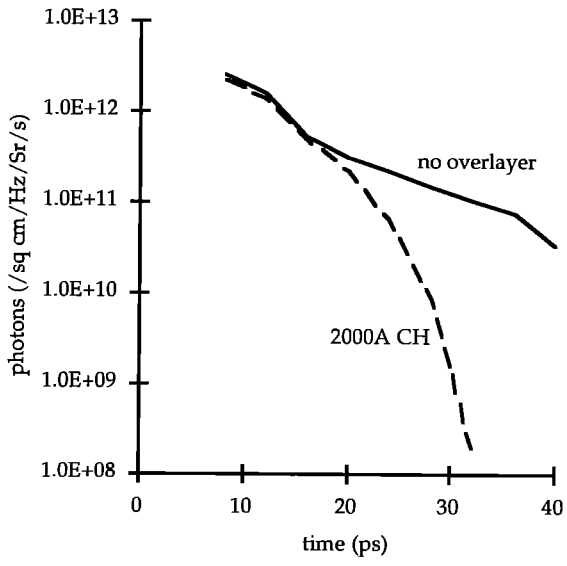

Figure 5 Predicted X-ray emission time history from targets with no overlayer and a 2000 Å plastic overlayer,. Incident irradiance 10^{17}, aluminium thickness 2000 Å

10^{22} cm^{-3} is ~2 ps. Once the ionisation has finished the excited electrons will cascade down into the lower energy levels emitting photons. The "forbidden" nature of the $1s2p\ ^1P$ level means it is impossible for it to be populated via photon only transitions, such as radiative decay, so when the ionisation stops so will the emission from the inter-combination transition. The decay time will be that given by the radiative lifetime and the collisional lifetime of the upper level, which is around 1 ps at a few times 10^2 cm^{-3}. It can no longer be collisionally populated since the density is decreasing.

However, the upper level of the H_α and the He_α transition can still be populated via the cascade process and hence the resonance lines will still be visible. The lifetime of the H_a simplicity being dependent on the cascade lifetime. If, for simplicity, the entire cascade process is approximated to only the radiative and three-body recombination routes, it is possible to calculate a transition rate and hence a decay time. Using the spontaneous radiative decay rate (C_{ci}) given[2] and the three-body recombination rate ($^3C_{ci}$) as used[3] and the peak simulated values of electron temperature and density from a non-overlayered shot (ie 800 eV and 8 x 10^2 cm^{-3}), we find that the three-body rate ($^3C_{ci}.n_e^2$) is 2.0 x 10^8 s^{-1} while the radiative ($C_{ci}.n_e$) rate is 5.3 x 10^{10} s^{-1}. The radiative rate is dominant giving a H_α decay time ($1/C_{ci}.n_e$) of ~ 20 ps which compares very favourably with the experimentally measured value.

For the case of an overlayered target where the history of he resonance lines is very different, the major physical differences seem to be the lower temperature and high density. Applying the same principles as above but using different plasma parameters (ie temperature 400 eV and density 5 x 10^{23} cm^{-3}), we find that the three-body recombination rate is 1.7 x 10^{10} s^{-1} and the radiative recombination rate is 5.0 x 10^{11} s^{-1}. The radiative rate still dominates but now not as strongly and gives a H_α resonance line decay time of ~ 2 ps. The increased density has the effect of rapidly de-populating the upper level of the H_α transition making the H_α X-ray pulse considerably shorter.

REFERENCES

1. A Djaoui, S J Rose and J Wark
   submitted to JSQRT January 1994.

2. L Spitzer
   Astrophysical Journal, 107, 6 (1948)

3. W Lotz
   Z Phys, 206, 205; 216, 241; 220, 486 (1969).

4. G J Tallents
   Optics Communications 37(2), 108 (1981).

SHORT PULSE X-RAY GENERATION USING 1.053 μm, 2 ps CPA PULSES

R Evans, T A Hall, J Ellison, A Badger, M H Mahdieh and A Djaoui*

Department of Physics, University of Essex
*Rutherford Appleton Laboratory

INTRODUCTION

Plasmas produced by short pules (ie ones of a few picoseconds or less) and high intensities (ie in excess of 10^{14} W cm^{-2}) constitute a novel form of hot, dense matter. Since the plasma has little to expand during the laser pulse, the extension of the plasma can be characterised by a scale length which is smaller than the laser wavelength. These plasmas are fundamentally different from those produced by long pulses for inertial confinement fusion. The observations of X-rays emitted from these plasmas have led to some interesting results, for example the spontaneous emission of X-rays up to energies of 1 MeV have been reported. Short pulse laser produced plasmas also show considerable promise as sources for time-resolved X-ray probing and backlighting (eg for microscopy and EXAFS) and as active media for X-ray gain and lasing.

EXPERIMENTAL SCHEME

An experiment was performed using the CPA facility on VULCAN, in which the angular dependence of the target reflectivity and its X-ray generating properties were observed. The targets for this experiment were 250 μm diameter plastic lollipops which were coated with 1000 Å or 2000 Å of X-ray generator material. The metals used were aluminium, copper, germanium and uranium. A number of the targets were also over-coated with a 1000 Å layer of plastic, so that the effect of restricting the plasma expansion could be observed.

A time-integrated spectrometer was used utilising an ADP crystal mounted at 45° t o the CCD detector plane, which was filtered from the plasma with 100 μm of Be. A streaked X-ray spectrometer using a TIAP crystal and a KBr photocathode was employed to observe the emission history. A 25 μm Be filter was used in conjunction with a 100 μm slit, which with a sweep speed of 5 ps/mm gives a temporal resolution of < 1 ps. Two photodiodes, one filtered (10 μm Be) to detect soft X-rays the other (100 μm Be) sensitive to harder X-rays, were used to measure the X-ray energy. The pinhole camera was used in a double aperture mode such that two images could be obtained simultaneously, (ii) through a 5 μm pinhole with a 25 μm Be filter and (ii) though a 10 μm pinhole using 125 μm of Be. The measurement of the angle-dependent reflectivity was achieved with an integrating cube detector which travelled on a circular beam surrounding the target. The cubes internal surfaces were coated with aluminium oxide (similar to the inside of an integrating sphere) and a photodiode sampled the light field within the cube through a 1.064 μm interference filter. The reflected light entered the cube thorugh a 150 mm x 100 mm opal glass window, since the input beam to the OAP is elliptical with dimensions 140 mm x 88 mm, the complex reflected beam should be detected.

RESULTS AND DISCUSSION

Figure 1 shows the reflectivity data as a function of angle of incidence. The results show that within the error bars the reflectivity is approximately constant with angle. Figure 2 presents the reflectivity data for aluminium targets oriented at 30° as a function of incident irradiance.

The reflectivity data agrees with that given by Baldis 1992 who shows that for p-polarised, 1.06 μm, 800 fs pulses in the incident irradiance range 10^{17} to 10^{18} W cm^{-2}, the specular reflected and the backscattered fraction of formvar (CH) are ~ 0.03, while the diffuse scattered fraction is large at ~ 0.8. These measurements imply an absorbed fraction of roughly 10%. Other workers using the VULCAN laser systems in both spot focus mode and line focus mode (eg Al-Hadithi et al, 1994) report measurements of the fast ion emission and heat from penetration at incident irradiances >10^{16} and have inferred similar values of absorption (up to a maximum of 10%).

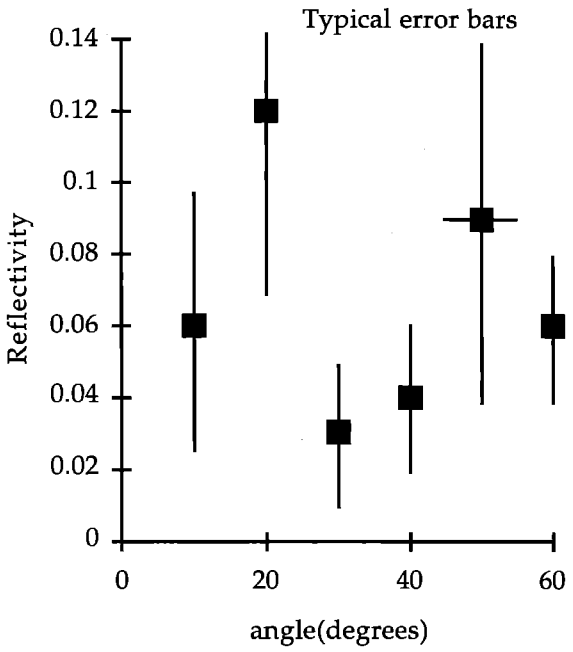

Figure 1 Reflectivity of aluminium targets as a function of angle of incidence

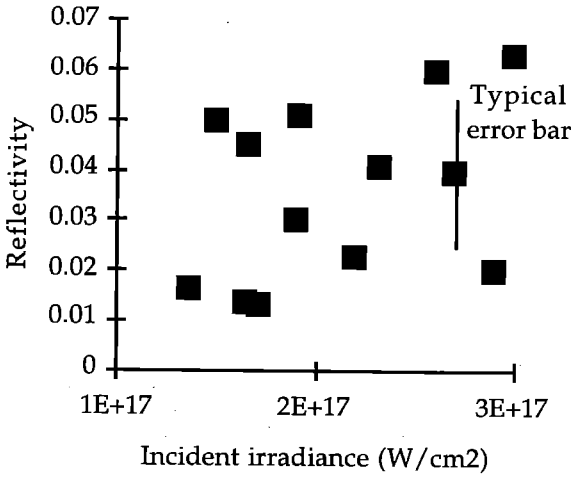

Figure 2 Reflectivity of aluminium as a function of incident irradiance for 30° angle of incidence. As in figure 1 the reflectivity error bars are due to statistical fluctuations in the measured reflected energy

The data showing the hard X-ray dependence on angle of incidence is presented in figure 3, while the data for different irradiances is given in figure 4. The yield shown in figure 3 peaks at around 30° where about 0.8% of the incident laser energy is converted into X-rays with energies above 1.5 keV. If we assume an absorption fraction of 10% this indicates that around 8% of the absorbed energy is used to create X-rays.

Using a constant absorption fraction of 10% for an angle of incidence of 30°, the data concerning X-ray conversion can be compared against the absorbed rather than the irradiance. The data presented shows a decreasing conversion efficiency with increasing irradiance (this was also the case for all other angles of incidence).

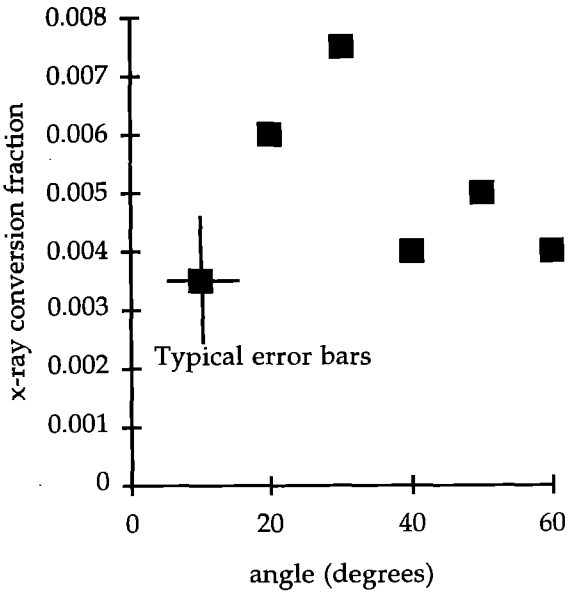

Figure 3 Hard (PD2) X-ray conversion, relative to the incident laser energy, of aluminium as a function of angle of incidence

For comparison with other workers a fit to the X-ray energy versus absorbed irradiance curve can be performed, which is plotted here in figure 5. The least squares fit to the data of other workers is usually of the form $X \alpha (I_{abs})^{\gamma}$ when both parameters are plotted on $\log_{10}$ axes[3] using KrF pulses and aluminium targets quotes $\gamma = 2.2 \pm 0.2$, whereas Kmetec et al[4] measured $\gamma = 1.5$ with visible light incident onto solid tantalum. Least squares fitting to the data presented in figure 5 yields a function with the same form but a slightly lower scaling parameter: $\gamma = 1.3$. With three independent measurements of γ at different wavelengths, a graph may be constructed allowing the comparison of the X-ray conversion from all three experiments. The comparison is shown in figure 6 and demonstrates that the X-ray energy increasing more rapidly with absorbed irradiance for shorter wavelength laser drivers. Since $n_{crit} \alpha \lambda^{-2}$, absorption should occur at higher densities for shorter wavelength drivers. Therefore, the amount ($\alpha \lambda^{-2}$) of bremsstrahlung emission (ie the broadband emission observed by the photodiodes) should increase. All of the data presented in figures 1 to 4 are for aluminium targets without an overlayer of plastic. The general trend shown in figure 5 is also seen for copper and germanium but with a slightly different gamma parameter. At absorbed intensities above 2×10^{16} W cm^{-2} all three (Cu, Ge and U) met also seem to give enhanced X-ray energies, but only by factor of ~2.

Applying a least squares fit to the data in figure 6 gives a power law trend of the form: $\gamma = \lambda^{-0.36}$, this law would appear to be almost independent of Z, laser pulse length and target parameters such as thickness.

The model [5] which includes both resonance absorption and "vacuum heating" concludes that the Brunel process dominates when $L/\lambda < 0.1$. (L is the plasma scale length, $L = n_e/\nabla n_e$

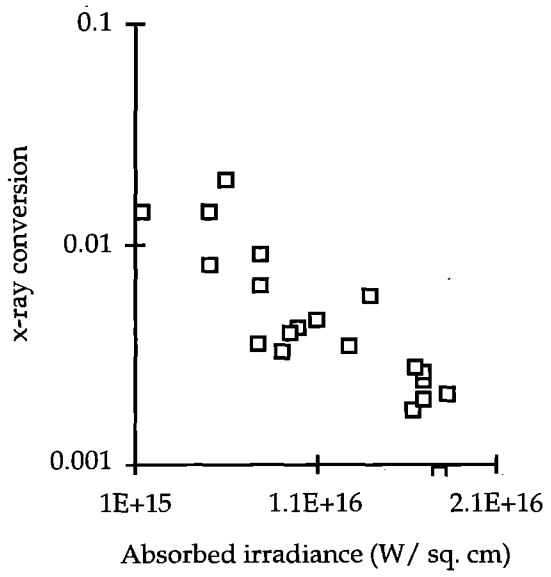

Figure 4 Hard X-ray conversion relative to the absorbed energy for aluminium at 30° as a function of absorbed laser irradiance (a constant absorption of 10% was used)

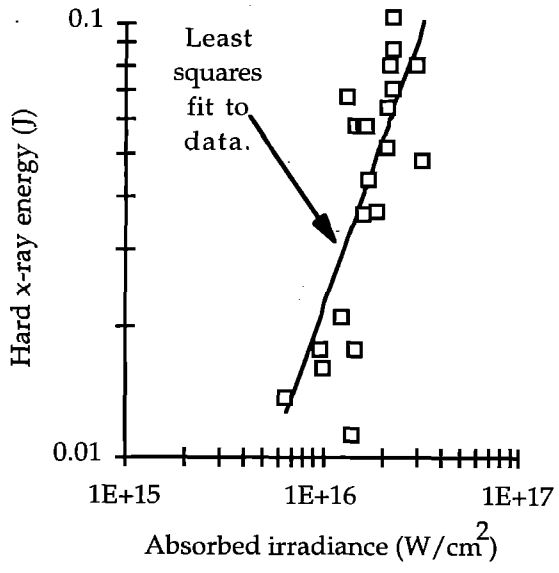

Figure 5 Hard X-ray energy for aluminium at 30° as a function of absorbed laser irradiance (a constant absorption of 10% was used)

where n_e is the electron density near the critical surface). They also predict that if $L/\lambda < 0.1$ and the incident irradiance is high ($I = 10^{17}$-10^{18}) the absorbed fraction is less than 20%. and more or less constant as the irradiance varies. They also predict the angular dependence of the absorption for different values of L/λ for $L/\lambda = 0.01$ the absorption is constant at < 10%, for $L/\lambda = 0.07$ there is a marked peak (up to 40%) at ~20°. This implies the dimensionless (L/λ) scale length of the plasma produced in this experimenter in the region of 0.1 to 0.01.

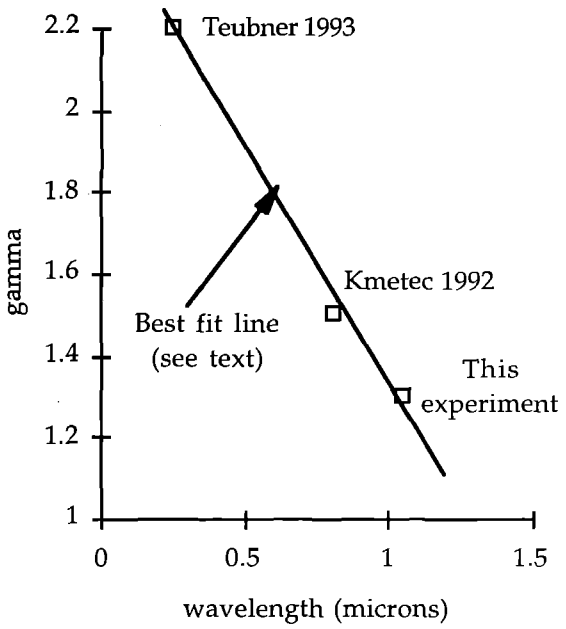

Figure 6 Comparison of gamma (ie the increase in X-ray yield with irradiance) for different laser driver wavelengths

REFERENCES

1. Y A Hadithi, G J Tallents, J Zhang, M H Key, P A Norreys and R Kodama
Submitted o Physics of Plasmas (to be published May 1994).

2. H Baldis
1992 presnted at NATO advanced study institute on "Laser Interactions with Atoms, Solid and Plasmas", Corsica, August 1992 (to be published).

3. U Teubner, J Bergmann, B van Wonterghem and F P Schäfer

Phys Rev Lett, 70(6), 794 (1993).

4. J D Kmetec, C L Gordon et al
Phys Rev Lett, 68, 1527, (1992).

5. P Gibbon and A R Bell, Phys Rev Lett, 68(10), 1535, (1992).

ENERGY TRANSPORT IN PLASMAS CREATED BY A FEMTOSECOND LASER

M G Holden[1], G J Tallents[1], P Fews[2], K Nazir[3], S Rose[3,4], P Norreys[4], J Zhang[5]

[1]University of Essex, Wivenhoe Park, Colchester C04 3SQ
[2]University of Bristol, Royal Fort, Tyndall Avenue, Bristol BS8 1TL
[3]University of Birmingham, Edgbaston, Birmingham B15 2TT
[4]Rutherford Appleton Laboratory, Didcot OX11 0QX
[5]Clarendon Laboratory, University of Oxford, Oxford OX1 3PU

INTRODUCTION

Energy transport processes in plasmas produced by a focussed laser are important in laser-plasma experiments, especially those relevant to x-ray laser research. The transport of the laser energy from the focal spot is characterised in two dimensions ('axially' in the direction of the laser into the target, and 'laterally' in directions along the surface of the target, orthogonal to the axial direction) and can occur due to several mechanisms[1].

In this report, preliminary results are presented showing the extent of axial and lateral transport in Iron (Fe) lollipop targets which were tamped with varying (0-0.4μm) overlay thicknesses of plastic (CH).

EXPERIMENT

In this experiment, tamped Iron lollipop targets (270μm diameter) with variable thickness plastic overlays, were irradiated in a spot focus geometery by the Krypton Flouride SPRITE laser operating in CPA mode producing pulses of 0.15J in 300fs at a wavelength of 0.248μm, giving irradiances up to 10^{18}Wcm^{-2} on target. The laser was focussed onto the surface of the overlay.

Initially during the experiment the contrast ratio between the pulse and a pre-pulse, due to amplified spontaneous emisson of the KrF amplifier, was measured at 10^9. This level of prepulse was above the threshold for plasma production and so was sufficiently intense to ablate the tamping overlay. The contrast ratio was consequently improved to 10^{10} during the experiment.

The extent of axial transport was deduced by analysis of x-ray spectra recorded using a minispectrometer with a TLAP crystal dispersing the spectra onto film.

The extent of lateral transport was deduced using a penumbral x-ray imaging technique. The focal area was imaged through an 80μm pinhole onto a CCD detector . The recorded image was deconvolved to produce an image with a spatial resolution of approximately 5μm.

RESULTS

The film used in the minispectrometer was analysed using a microdensitometer with matched optics of numerical aperture 0.25. Seven scans, orthogonal to the spectral lines were taken; each along a different part of the spectral lines. These scans were then averaged to reduce the signal to noise ratio of the spectra.

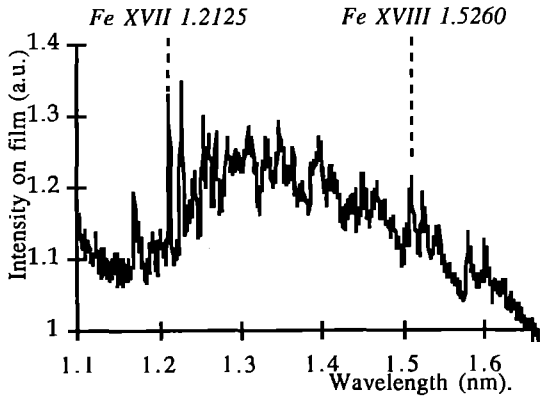

Figure 1 Typical Iron spectrum,. Here the target was an Iron lollipop with a 0.1μm overlay.

The calibration used to convert film densities to intensities on film was that of Henke et al.[2]

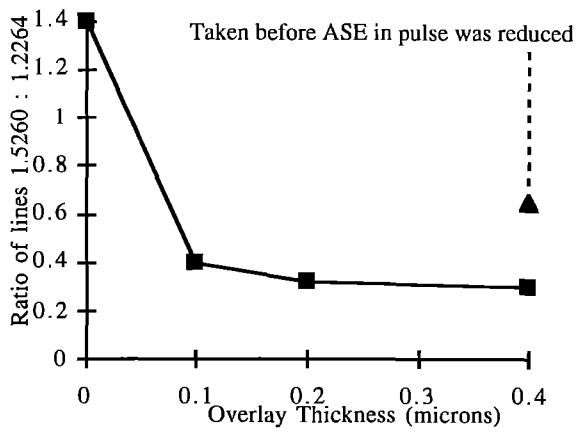

Figure 2 Ratio of most intense Fe XVIII to Fe XVII spectral lines plotted against overlay thickness. The triangular data point was taken before the pre-pulse contrast ratio was improved.

No systematic variation of emitting area size with overlay thickness was found. There was, however, a decline in emitted x-ray flux with overlay thickness (figures 2 and 3)

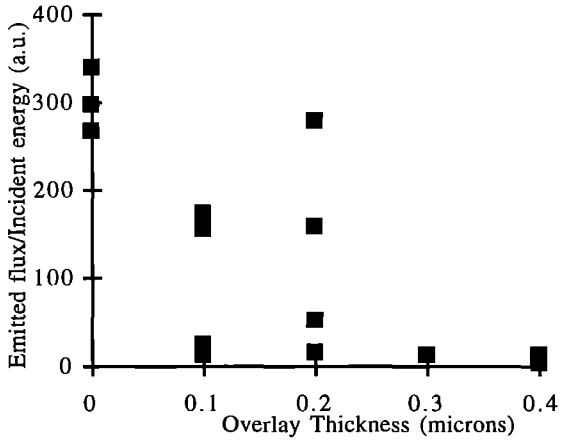

Figure 3 A plot showing the decrease of emitted x-ray flux (wavelength < 10 Å) with overlay thickness.

CONCLUSION

The extent of axial energy transport was greater than that reported by Al-Hadithi et al.[1]. It is likely that the level of pre-pulse was still above the threshold for plasma production. Further analysis of this experiment is proceeding

REFERENCES

1. Y Al-Hadithi, G J Tallents, J Zhang, M H Key, P A Norreys, R Kodama.
J. Plas. Phys. to be published (May 1994)
2. B L Henke, Y Y Uejio, G F Stone, C H Dittmore, F G Fujiwara.
J. Opt. Soc. Am. B3, 1540 (1986)

Observation of filamentary structures in the interaction of a 350fs KrF laser pulse with a Neon Gas jet target

A. J. Mackinnon, M. W. Jones, O. Willi
The Blackett Laboratory, Imperial College
London SW7 2BZ

INTRODUCTION

The production of plasmas produced by picosecond and subpicosecond lasers is currently the subject of a great amount of theoretical and experimental investigation. The short duration of the laser pulse coupled with the high intensities lead to plasmas where the ionisation stage is dominated by optical field induced (OFI) rather than collisional ionisation, leading to extremely highly ionised but relatively cold plasmas.

These plasmas are ideally suited for recombination X-ray laser schemes[1] where a rapid recombination cascade of electrons leads to a population inversion to the ground state of the ion. X ray lasing using this scheme has very recently been observed by Nagata et al in Hydrogen like Lithium at 13.5nm[2] using a KrF laser focussed to a 10μm spot and a 2mm confocal parameter. Other applications such as particle accelerators and high harmonic generation require similar conditions for optimum performance. Until now most work on low density targets have assumed a uniform interaction between laser and plasma.

At higher densities and intensities the uniformity will be affected by both relativistic and ponderomotive-charge displacement self focussing and filamentation [3]. Theories for the thresholds for these processes have been developed [4] and some indirect experimental evidence does exist for whole beam self focussing of a KrF pulse in Neon and Argon plasmas [3]. There is, to date, no experimental evidence, in the sub picosecond regime, of the the onset of filamentation for larger non uniform focal spots.

Experimental Arrangement

The experiment was undertaken on the SPRITE laser, which was operated in chirped pulse amplification mode. The compression gratings were located under vacuum in the target chamber. Typical operating parameters were a pulse duration 350fs (FWHM), 250-300mJ on target and a 10μm FWHM focal spot (with a F/5 off axis parabolic mirror focusing optic). This gave a maximum mean intensity of $2x10^{17}Wcm^2$. The main pulse was superimposed on a 20ns FWHM ASE pulse at an intensity of $1x10^{9}Wcm^2$. The plasma was diagnosed with a temporally independent probe pulse which was derived from a split off the main uncompressed heating beam. The duration of the uncompressed beam was less than 10ps. This pulselength was short enough to give a snapshot of the plasma density profile without any smearing arising from plasma motion. The Moire deflectometer used the probe to provide electron density gradient and density profiles at discrete intervals for times up to 2ns after the end of the pulse. The system has sub micron resolution and a magnification of 64x. The timing of the probe beam was accurate to 3ps.

Results

The parameters affecting the uniformity of the laser plasma interaction were investigated by varying the gas jet density and laser intensity. At low intensities and /or gas densities the laser was found to create a uniform channel with a diameter consistent with the diameter of the laser focal spot. Fig 1 shows a Moire deflectogram of a low density, high intensity interaction.

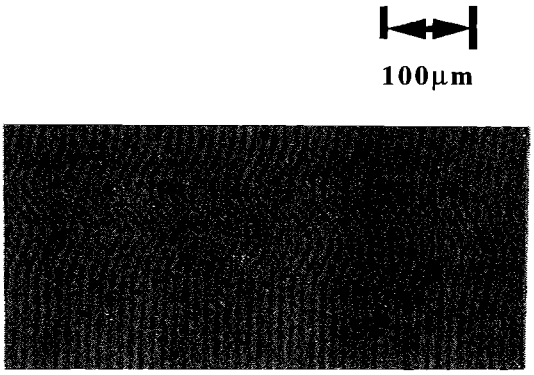

Fig 1 Moire Deflectogram at a density of $5x10^{17}$ atoms/cc and an intensity of $2x10^{17}$ Wcm^2 , showing the formation of a uniform channel .

When the laser intensity and/or gas jet density were increased above a threshold value of $1x10^{35}$ Wcm^2 atoms/cc filaments were formed along the axis of the channel. The diameters of the filaments were much smaller than the diameter of the laser focal spot. Fig 2 shows a shadowgram of a high intensity, high density interaction.

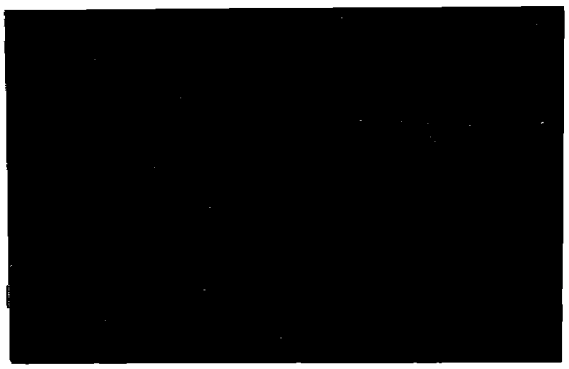

Fig2. A shadowgram of the interaction of a laser pulse with the gas jet at a density of $3x10^{18}$ atoms/cc and an intensity of $2x10^{17}$ Wcm^2

The Moire system was used to gain a quantitative measure of the density conditions present in the filamentary structures. Fig 3 shows a Moire deflectogram of a high intensity, high density interaction.

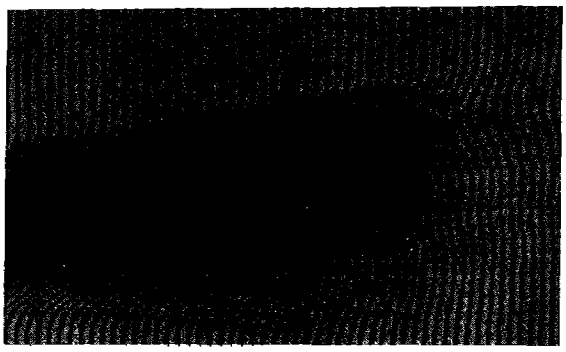

Fig 3 shows a Fig 3 shows a Moire deflectogram of a interaction at a density of $3x10^{18}$ atoms/cc and an intensity of $2x10^{17}$ Wcm2

The perturbations from the filaments can clearly be seen as fringe shifts of up to 1/2 a fringe. The background electron density has been obtained from preliminary abel inversion to be $2x10^{19}$ electrons/cc. The perturbation in the filaments corresponds to a density of approximately $1x10^{17}$ electrons/cc .

The threshold for filamentation was found by reducing the incident laser intensity and/or the gas density until all evidence of the filaments disappeared. It was found that if the density was reduced by a factor of 5 the filaments disappeared. The filaments also disappeared if the laser intensity was reduced by a factor of 5 keeping the gas density constant.

In order to be able to invoke laser filamentation as the mechansim producing these non uniformities it is important to know the range of hot spots present on the incident laser beam. The equivalent plane measurement of the laser focal spot provides this information. An equivalent plane image of the focal spot for the shot shown in fig 2 is shown in fig 4. The smallest scalelength present on the laser focal spot is found to be 2μm and so the features present in the density perturbation cannot have been directly caused by the laser hotspot but must have been caused by the hot spot filamenting to the sub micron scalelengths observed on the shadowgrams and deflectograms.

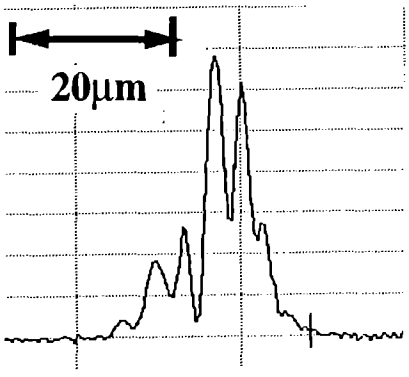

Fig 4 shows an equivalent plane measurement for the shadogram shown in shot 3

The mechanism responsible for this filamentation can be seen by comparing the ponderomotive force acting on electrons in a hotspot of 2μm diameter with the space charge limited force between the expelled electrons and the remaining ions. Simple order of magnitude estimates of the maximum density perturbation that would be produced when the electrons are expelled from a 2μm filament gives a perturbation of $1x10^{16}$-$1x10^{17}$ electrons/cc. In order to obtain a more accurate picture 2D Pic code simulations are being carried out to model this interaction. It was not thought that relativistic effects played a significant role in the filamentation mechanism as the mean intensity is two orders of magnitude lower than the relativistic limit of $4x10^{19}$W/cm2 . However the intensity within the hot spots can be between 10 and 100x the mean intensity, therfore relativistic effects will be more important within a filament and may tend to enhance the filamentation effect.

Discussion

This experiment investigated the uniformity of the laser plasma interaction when a 350fs, KrF laser beam was focussed at mean intensities up to $2x10^{17}$Wcm2, in a Neon gas target at atomic densities from $5x10^{17}$atoms/cc to $3x10^{18}$ atoms/cc. It was found that the interaction was uniform when the product of the laser intensity and gas atomic density was less than $1x10^{35}$Wcm2 atoms/cc and filamentary structures appeared when the product exceeded this threshold. These results have implications for applications where a high intensity laser interacts with a high density plasma Nagata et al [2] found that the optimum conditions for lasing were a pump beam intensity of $1x10^{17}$Wcm2 and an ion density of $2x10^{17}$atoms/cc. X ray lasing was found not to occur above an ion density of $5x10^{17}$atoms/cc, the authors suggested that defocussing of the high intensity interaction pulse by the electron density gradients was responsible for this limitation. As the X-ray laserintensity density product of $5x10^{34}$ W/cm2atoms/cc for a KRF laser of slightly longer pulse length. Comparing this limitation to our threshold for filamentation gives another possible intrepetation , that the X-ray lasing was not limited by defocussing but by plasma non-uniformity seeded by laser filamanetation.

References

1. P.Amendt,D.C.Eder,S.Wilks, Physical Rev. Lett. 66,2589,1991
2. Nagata et al Physical Rev. Lett. 71,23,1993
3. A.B.Borisov et al Physical Rev. Lett. 68,2309,1992
4. G.Z.Sun, E.Ott, Y.C. Lee, P.Gudzar, Physics of Fluids 30(2),526,1987

QUANTITATIVE MEASUREMENTS OF THE THERMAL SMOOTHING OF NONUNIFORM LASER IRRADIATION

M. Dunne, T. Afshar-rad and O. Willi

Imperial College of Science, Technology and Medicine, London, SW7 2BZ, U.K.

The presence of severe intensity nonuniformities in high power laser beams, even when partially smoothed using techniques such as ISI, SSD or RPP arrays, is detrimental to many laser-plasma applications. This is because any laser nonuniformities are reproduced on a target's surface, resulting in uneven heating and the possible seeding of a number of hydrodynamic, parametric and thermo-magnetic instabilities. In the absence of ultra-broad bandwidth lasers the only proven method for achieving a uniform thermal front in a laser-irradiated target is to introduce an initial plasma 'buffer', produced through the interaction of thermal x-rays. This hot plasma buffer acts to separate the absorption region from the ablation surface of the target, allowing the nonuniformly heated plasma to laterally diffuse before the solid surface is encountered.

This report presents the first quantitative measurements of thermal smoothing in an x-ray preformed plasma buffer. The behaviour of the ablation-to-critical surface distance (Dac) was monitored through the use of a third-harmonic interferometer, whilst uniformity levels in the super- and sub- critical plasmas were investigated using XUV radiography and Moiré deflectometry, respectively. Increased smoothing in the overdense plasma was observed as the modulation wavelength of the nonuniformities (λpert) was decreased, with 'complete' smoothing occuring when λpert was on the order of Dac, in accordance with intuition. Using an ISI/RPP smoothed beam, severe sub-critical nonuniformities were observed to persist simultaneously with a smooth super-critical plasma. In addition, an apparent coupling of the imposed modulation wavelength to shorter scalelengths was seen in the super-critical plasma.

The VULCAN glass laser system was used in a geometry shown shematically in Figure 1. Four frequency doubled (0.53μm) beams irradiated a thin gold layer, 1500Å thick supported on a 1μm thick plastic substrate. Thermal x-rays emanating from the rear of this foil were used to preform the main target, a 10μm diameter Copper wire. The x-ray intensity on target was varied between $5\text{x}10^{11}$ and $2\text{x}10^{12}$ Wcm^{-2}. This preformed wire was then irradiated by a delayed infra-red (1.05μm) beam with an imposed square-wave intensity modulation. The modulation wavelength was varied between 27 and 70μm, with a depth of 2:1 (Imax:Imin). In addition, on separate shots, this interaction beam was smoothed using RPP, and ISI/RPP techniques. Both f/10 and f/2.5 focussing optics were used in order to vary the characteristic speckle pattern wavelength from 10μm to 3μm.

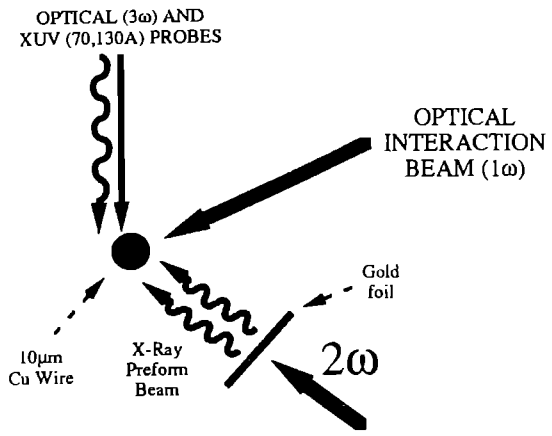

FIG 1 Target irradiation geometry

The initial x-ray interaction was characterised using a third harmonic (0.351μm) Wollaston interferometer. This provided the position of the critical surface for the infra-red interaction beam ($\text{Ne}\sim10^{21}\text{cm}^{-3}$) relative to the solid surface of the wire target. The density profiles obtained using two different x-ray intensities are shown in Figure 2 for a time 1ns after the start of the x-ray interaction. Typical values for Dac can be seen to be around 12μm. It should be noted that this represents the minimum distance between the absorption and ablation regions, since a relatively large degree of inverse Bremsstrahlung absorption is to be expected in the blowoff plasma. The quarter-critical surface is approximately 20μm from the solid surface for the low x-ray intensity case.

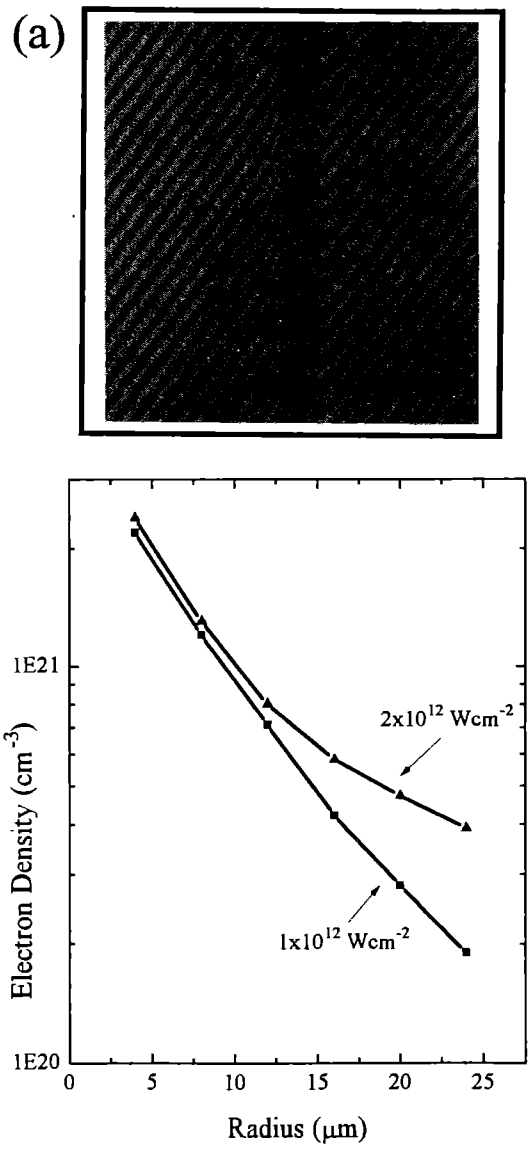

FIG 2 (a) 3ω interferogram of a 10μm Cu wire, 1ns after x-ray irradiation at $1\text{x}10^{12}$ Wcm^{-2}. (b) Abel inverted density profiles at 1ns after the start of x-ray interactions at two different irradiances. Zero defines the original solid surface.

The uniformity of the supercritical plasma when irradiated by an infra-red beam with a modulation wavelength of 27μm can be seen in Figure 3 for two sizes of preformed plasma. This shows the 2D absorption profile to a 50A probe. At this wavelength the absorption of the probe is a strong function of the temperatures and densities expected in the overdense plasma, providing a sensitive diagnostic of the plasma uniformity. The gating time of the detector is approximately 120ps. When the interaction beam follows 1ns after the start of the x-ray pulse, strong modulations (with a wavelength equivalent to that imposed on the beam) can be seen in the plasma. The uniformity of the plasma increases when the interaction beam is delayed by a further nanosecond, as more time is allowed for the plasma buffer to form and expand. Quantitative measurements of the degree of smoothing obtained in these two cases can readily be obtained from these images.

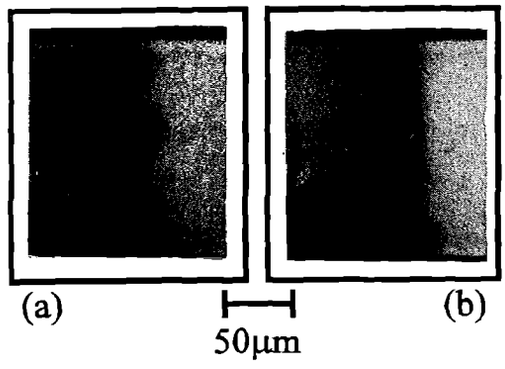

FIG 3 XUV (70Å) radiograms of an x-ray preformed 10μm Cu wire 1ns after the interaction of a modulated (λ=27μm) infra-red beam. The interaction beam was delayed relative to the x-ray pulse by (a) 1ns, and (b) 2ns.

A uniform overdense plasma, smooth to within the detection limit of the imaging system (which is sensitive to nonuniformities with scalelengths greater than approximately 5μm and which alter the absorption profile by 5% or more) can be produced through the interaction of an ISI/RPP smoothed beam with a preformed plasma buffer whose Dac is on the order of 12μm. The absorption profile of a target subjected to such an interaction is shown in Figure 4(a). For this interaction, the dominant perturbations have a wavelength on the order of the beam speckle size (approximately 10μm for an infra-red beam focussed through an f/10 lens). In this case the perturbation wavelength is slightly less than the distance between the absorption and ablation regions. A high degree of transverse (diffusive) thermal smoothing is therefore to be expected.

Moiré deflectograms were taken of these interactions using the third harmonic probe, set up to detect nonuniformities parallel to the target surface. For the interaction conditions of figure 4(a), jet-like nonuniformities were observed in the sub-critical plasma, as shown in Figure 4(b). These features were seen to persist for all irradiation conditions and at all times during and after the interaction. Removal of the ISI echelons resulted in these jet features becoming far more pronounced, extending many tens of microns away from the target surface. It is evident that, although nonuniformities and instabilities have been removed from the overdense plasma, there still remain strong instabilities in the underdense regions. It should therefore be possible to narrow down the type of instability which is being seeded in these plasmas; more specifically to determine whether simple hydrodynamic processes are responsible, or whether one of a number of thermo-magnetic instabilities are being seeded.
On a related note, it was observed that the plasma modulations in the overdense plasma (produced when λpert>Dac) initially reflected the modulation period imposed on the interaction beam, but then coupled into shorter scalelength modes later in the interaction, after the removal of the modulated drive. This is shown for the case of irradiation by a 70μm modulation period in Figure 5.

In summary, the temporal behaviour of the density profiles of Cu wire targets subjected to thermal x-ray irradiation has been quantitatively determined. This has allowed an accurate measurement of the degree of thermal smoothing of a nonuniform laser beam, when the characterised plasma was subjected to irradiation by a well defined intensity modulation. In addition, the production of a smooth overdense plasma has been demonstrated and that this plasma exists simultaneosly with strong filamentory modulations in the sub-critical plasma.

The data presented in this report are undergoing analysis and are currently the subject of a collaboration with LLE Rochester. Greatlful acknowledgement is given to Steve Craxton (LLE) for many helpful discussions and for work on 2D simulation of these results, which will be presented in a forthcoming publication.

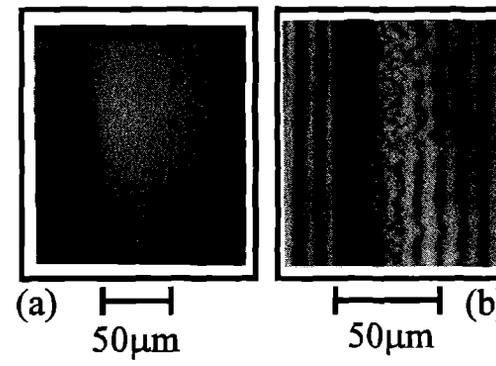

FIG 4 (a) XUV radiogram of an x-ray preformed 10μm Cu wire 1ns after the interaction of an ISI/RPP smoothed infra-red beam.
(b) Moiré deflectogram of the same target at the same observation time.

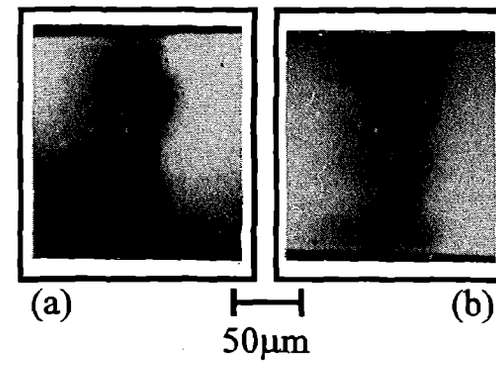

FIG 5 XUV radiograms of x-ray preformed Cu wire targets subjected to an interaction beam with a 70μm modulation wavelength. The images were taken at (a) 1ns, and (b) 2ns after the start of the optical beam. Note the change in modulation period at late time.

DETAILED OBSERVATIONS OF THE SUPERSONIC PROPAGATION OF IONIZATION FRONTS DRIVEN BY THERMAL RADIATION

M.Dunne, T. Afshar-rad, M. Desselberger, J. Edwards, J. M. Foster[1], D. Hoarty[1], M. W. Jones, S. J. Rose[2], P. A. Rosen[1], R. Taylor and O. Willi.

Imperial College of Science, Technology and Medicine, London, SW7 2BZ, U.K.

1) Atomic Weapons Establishment, Aldermaston, Reading, U.K.
2) Rutherford Appleton Laboratory, Chilton, Didcot, U.K.

The investigation of supersonic heat wave propagation in matter driven by thermal radiation is of fundamental interest in the study of radiation hydrodynamics in both laboratory and astrophysical plasmas. Examples can be found in the dynamics of gaseous nebulae and in the formation of ablation fronts as the intense radiation field from a hot star interacts with a remote interstellar cloud [1]. In addition there may be important terrestrial applications in laser driven Inertial Confinement Fusion (ICF), where the preforming of a plasma buffer could act to thermally smooth laser nonuniformities before they reach the ablation surface of an implosion capsule [2]. The production of this buffer through the passage of a supersonic x-ray driven wave would avoid the formation of preheating shocks which would otherwise result from the high x-ray intensities needed to form the required plasma scalelengths [3]. The implosion will thus be allowed to proceed along a lower adiabat. The propagation of radiatively driven supersonic ionization fronts is also of interest in ion-beam ICF, where the process may provide a means of decoupling the implosion process from non-uniform beam irradiation [4].

This report presents the first detailed measurements of the sustained propagation of a supersonic, radiation driven heat wave. A cylindrical low density foam target was irradiated by soft (<1keV) x-rays from a spatially separate gold converter foil. The position of the ionizing heat front in this foam target was observed using a high resolution, soft-x-ray, side-on radiographic imaging system using 2D gated and 1D streak detectors. This side-on detection system allowed the temporal development of the ionization wave to be studied for the first time. Our previously reported results used only the 2D gated detector and relied to some extent on computational analysis. We now present continuous, streaked information on the evolution of the ionization wave, providing direct evidence of the supersonic nature of the propagation. The experiment was modelled with a 1D Lagrangian radiation hydrodynamics code, resulting in good agreement. The supersonic nature of the ionization front was sustained for many hundreds of picoseconds, with the re-emission of x-rays in the heated target shown to play a crucial role in the dynamics of the front.

Seven frequency-doubled (λ=0.53μm) beams from the VULCAN glass laser system were used in a cluster arrangement (with a cone angle of 13^{o} including a beam at the centre of the cone) to irradiate a thin gold layer, 1500Å thick, supported on a 1μm plastic substrate. The soft x-ray pulse transmitted through the rear of this converter foil was used to irradiate a low density foam target, separated from the foil to ensure only x-ray heating of the foam occurred. This separation was set at 30μm and was monitored using a pair of high magnification telescopes, accurate to within 10μm. The pulse had a full-width-half-maximum (FWHM) duration of typically 1300ps and was focused to a focal spot of approximately 250μm diameter, producing laser irradiances of around 1x10^{15} Wcm^{-2}. The foam samples used were primarily triacrylate ($C_{15}H_{20}O_6$) chemically doped with a chlorine monomer ($C_9H_3O_2Cl_5$) to 25% by weight chlorine. These targets had a diameter of 160μm and lengths of up to 200μm, at a density of 50 mg/cm^3 (approximately 1/30th solid density). Cell sizes in the foam were less than 1μm in diameter, with a very high degree of homogeneity throughout the foam [13]. This was confirmed through the use of off-line, point source x-radiography and scanning electron microscopy [14]. The temporal behaviour and the absolute flux levels of the soft x-ray pulse produced from the gold converter foil were measured with a temporal resolution of better than 100ps using a calibrated, flat response vacuum x-ray diode. A rear side x-ray conversion efficiency of (4±1.5)% was observed, in agreement with previous measurements. This indicated an x-ray flux incident on the foam sample of (3.8±1.4)x10^{13} Wcm^{-2} (equivalent to a blackbody temperature of 138±12 eV). The optical burnthrough of the gold converter foils was monitored on separate shots to ensure that the drive foil remained super-critical throughout the experiment. It was confirmed that the burnthrough occurred late in time (after 1500 ps), well after all the wave propagation measurements, which were taken on the rising edge of the x-ray pulse. Additional experiments were performed in which lower x-ray fluxes and varying levels of Chlorine dopant were used, providing scaling characteristics of the wave propagation with drive flux and average Z, as will be discussed in a forthcoming publication.

The foam target was backlit by a soft x-ray source and imaged perpendicularly to the soft x-ray drive with a spherical multilayered mirror, as previously described [15]. For the chlorinated foams examined in the current study, the mirrors were coated to reflect at a central wavelength of 70Å (175 eV), with a bandwidth measured to be better than ±5Å. In this spectral region the dominant contribution to the radiative opacity is bound-free absorption, with no contribution from bound-bound transitions, as confirmed using XUV absorption spectroscopy. A 50 times magnified image of the cylindrical target was produced and recorded either on the slit of a soft-x-ray streak camera to provide continuous 1D information or on a two frame gated microchannel plate (MCP) intensifier with the target image placed across the two frames. This allowed information on the 2D response of the target to be monitored. The spatial resolution of the imaging system was found to be less than 1μm by the use of a ray tracing program which modelled the specific target geometry adopted, although the actual measured resolution in the streaked images was around 5μm, limited primarily by photocathode noise. The temporal resolution of the streak camera was 50ps and the gating time of the x-ray imager was approximately 120ps.

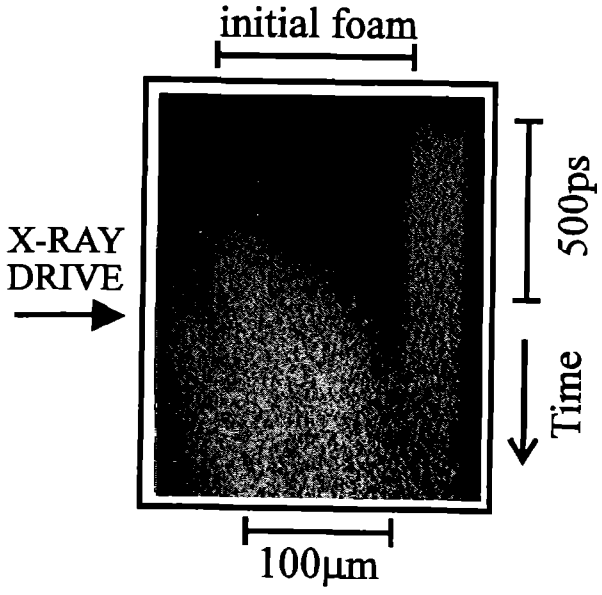

FIG 1 Soft x-ray (70Å) streaked radiogram of a 50 mg/cc, 135μm long foam. The probe starts 100ps before the arrival of the drive radiation, allowing the original extent of the target to be monitored. The passage of a supersonic ionization front is evidenced by the evolution of the transmission of the foam target.

A radiogram of a chlorinated foam target subjected to an intense radiation field is shown in Figure 1, demonstrating the evolution of the ionization wave as it propagates into the undisturbed foam. At early time, the foam is opaque to the monochromatic probe radiation since it is cold and unionized. As the x-ray drive pulse turns on, however, the opacity of the foam is reduced, so allowing the probing x-rays to pass through. For a target density of 50mg/cc and a probe wavelength of 70Å, the chlorinated foam is calculated to become 50% transparent at an electron temperature of 80eV, using the detailed configuration accounting opacity code, IMP [16]. The 50% transmission contour will be taken as being representative of the position of the ionization front. The initial velocity of this contour (essentially the 80eV contour since there is little perturbation of the target density), 300ps after the start of the x-ray drive is $(3.5\pm0.5)\times10^7$ cm/s. This velocity remains above 1.3×10^7 cm/s throughout the measurement. For these conditions, the maximum possible sound speed in the heated material is 10^7 cm/s, as discussed below.

In order to further assess the heating characteristics of the radiation field, 2D gated images were taken at various times in the evolution of the ionization front. A characteristic shot can be found in last year's annual report. A high degree of spatial uniformity was observed across the front. An important aspect of these data shots is that the diameter of the foam target at the position of the ionization front remains unchanged from its original value. This is an indication of the supersonic nature of the propagation and the consequent lack of significant material compression behind the front. Measurements taken at lower x-ray drive irradiances (approximately 10^{12} Wcm^{-2}), in which the heat front is preceeded by a shock front, resulted in a 'rolling-up' of the foam at the position of the shock front.

Simulations were performed using a 1D Lagrangian radiation-hydrocode [5] modified to take account of the geometrical coupling between the extended source and sample. The temporal behaviour and absolute levels of the x-ray drive were taken from the calibrated diode measurements, with the spectrum of the radiation assumed to be a blackbody defined by the ambient radiation flux. The use of this blackbody assumption has been shown to result in good agreement with experimental data in previous measurements where a similar converter foil geometry was used [5]. The drive spectrum was altered to take account of long mean-free-path x-rays originating from the gold M-, N- or O- bands, but this was found to have only a small effect on the wave propagation characteristics. The effect of electron thermal conduction was found to be insignificant except at very early time. Opacities were calculated from tabulated values generated using the detailed configuration accounting opacity code, IMP. A comparison of the measured and predicted propagation of the 50% transmission point of the data shot shown in Figure 1 can be found in Figure 2. The simulated foam transmission curves were obtained by post-processing the output of the hydro simulations with opacities generated from IMP. Good agreement on the extent and speed of propagation of the x-ray heating wave can be observed at all times in the evolution of the front, as may be expected if the supersonic nature of the radiation flow allowed a simple heating wave to propagate well ahead of any hydrodynamic response of the target. It was essential in these simulations to include target re-emission in the transport equations. The effect of neglecting this re-emission can be seen in Figure 2 (curve B).

When an intense radiation field is incident onto cold matter, the radiation penetrates about a photon mean-free-path into the material, which is consequently heated and ionized. The region where the unheated, unionized material is transformed into an ionized plasma defines an ionization front. If the x-ray flux is sufficiently high and the material density sufficiently low, as in the situation presented here, the propagation of such an ionization front can outrun any hydrodynamic motion which results from the large pressure differential between the heated and unheated material. That is, the upstream and downstream material in the region of the front can coexist at the same density despite the presence of large temperature and pressure gradients. The front is said to propagate supersonically with respect to both the heated and unheated matter. The development of global hydrodynamic motion in the plasma can be characterised by the ion sound speed, for which an upper estimate may be obtained by assuming a plasma temperature equal to the maximum x-ray drive temperature and ignoring reductions due to non-ideal gas behaviour. For the present conditions, this maximum possible sound speed is 10^7 cm/s, which is well below the propagation velocities observed. In reality any shock wave will propagate at lower velocities, primarily since the ambient plasma temperature will never reach the drive temperature due to the relatively low target Z. Even assuming this maximum sound speed, however, the ionization wave in the foam propagates supersonically for at least 600ps. This situation is reproduced in the simulations, which predict that density disturbances only catch up to the heat front after 1ns. A time sequence of temperature and density profiles in the foam target taken from the simulations is shown in Figure 3. This demonstrates the heat wave extending beyond the hydrodynamic motion which takes the form of a weak, ablative compression wave propagating behind the radiation heat front. The weak density disturbances seen at the position of the front can be understood from classical radiation hydrodynamics. If, for simplicity, we assume isothermal equilibrium in the downstream plasma then the density jump should be given approximately by $(1+(a/u)^2)$, where a is the sound speed in the heated material and u is the velocity of the ionization front. Taking the upper limit imposed on the sound speed and the measured propagation velocity of 3.5×10^7 cm/s, a final downstream density of 55 mg/cc is obtained, in agreement with the radiation hydrocode predictions. The production of a supersonic radiation heat front under these conditions can be readily understood by noting that the radiative flux (σT^4) is at least 7.5 times larger than the hydrodynamic energy flux (ρa^3).

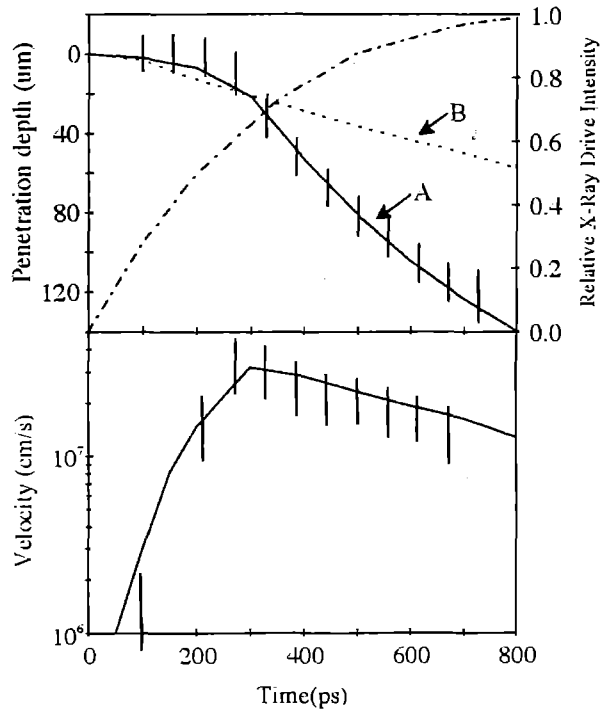

FIG 2 (a) A comparison of the observed and calculated propagation characteristics of the ionization wave observed in Figure 1. The experimentally measured propagation of the 50% transmission point (vertical bars) includes errors arising primarily from noise in the backlighter signal. 1D radiation hydrocode predictions (curve A) match the experiment well. The effect of allowing the target re-emission to escape without contributing to the driving of the ionization front is shown in curve B. Also shown is the measured x-ray pulse shape. (b) Velocities of the 50% transmission contour from the experiment (vertical bars) and the simulation (curve A).

In summary, we have observed the propagation of a sustained, supersonic ionization wave driven by thermal radiation for the first time in the laboratory. The side-on radiography technique adopted permitted a study of both the spatial extent and uniformity of the wavefront and the evolution of the velocity of the wave. The data were well reproduced by a 1D Lagrangian radiation hydrocode, which showed target re-emission to play a major role in the transport characteristics of the radiation wave.

Aside from its intrinsic interest, the technique of supersonically forming such plasmas may prove to be important in the elimination of laser nonuniformity imprint in the initial phase of laser driven implosions. It should be possible to tailor the size of the preformed, supercritical plasma to smooth the dominant laser nonuniformities whilst still allowing the production of high ablation pressures [3].

The authors would like to acknowledge the technical support of the CLF laser and target area staff, B. Evans (University of Reading) for supplying the multilayered mirrors, C. Horsfield (AWE), W. Nazarov and J. Falconer (Dundee University) for supplying the foam targets. Thanks are also due to C. Smith (AWE) for valuable comments and assistance.

REFERENCES

[1] W. I. Axford, Phil. Trans. Roy. Soc. (London) **A253**, 301 (1961).
[2] M. Desselberger *et al.*, Phys. Rev. Lett. **68**, 1539 (1992).
[3] M. Desselberger, M. Jones, J. Edwards, M. Dunne and O. Willi, to be published.
[4] A. R. Piriz and S. Atzeni, Plasma Phys. Control. Fusion **35**, 451 (1993).
[5] J. Edwards *et al.*, Phys. Rev. Lett. **67**, 3780 (1991); J. Edwards *et al.*, Europhys. Lett. **11**, 631 (1990).
[6] W. Schwanda and K Eidmann, Phys. Rev. Lett. **69**, 3507 (1992).
[7] T. Endo, H. Shiraga, K. Shihoyama and Y. Kato, Phys. Rev. Lett. **60**, 1022 (1988).
[8] T. S. Perry *et al.*, Phys. Rev. Lett. **67**, 3784 (1991).
[9] J. Foster *et al.*, Phys. Rev. Lett. **67**, 3255 (1991).
[10] R. Sigel *et al.*, Phys. Rev. Lett. **65**, 587 (1990).
[11] J. Edwards *et al.*, Phys. Rev. Lett. **71**, 3477 (1993).
[12] N.Kaiser, J. Meyer-teh-Vehn and R. Sigel, Phys. Fluids **B1**, 1747 (1989).
[13] J. Falconer *et al.*, J. Vac. Sci. Technol. **A8**, 968 (1990).
[14] C. Horsfield, AWE Aldermaston, Private Communication.
[15] M. Desselberger *et al.*, Appl. Optics **30**, 2285 (1991); O. Willi *et al.*, Rev. Sci. Instr. **63**, 4818 (1992).
[16] S. Rose, J. Phys. B **25**,, 1667 (1992)

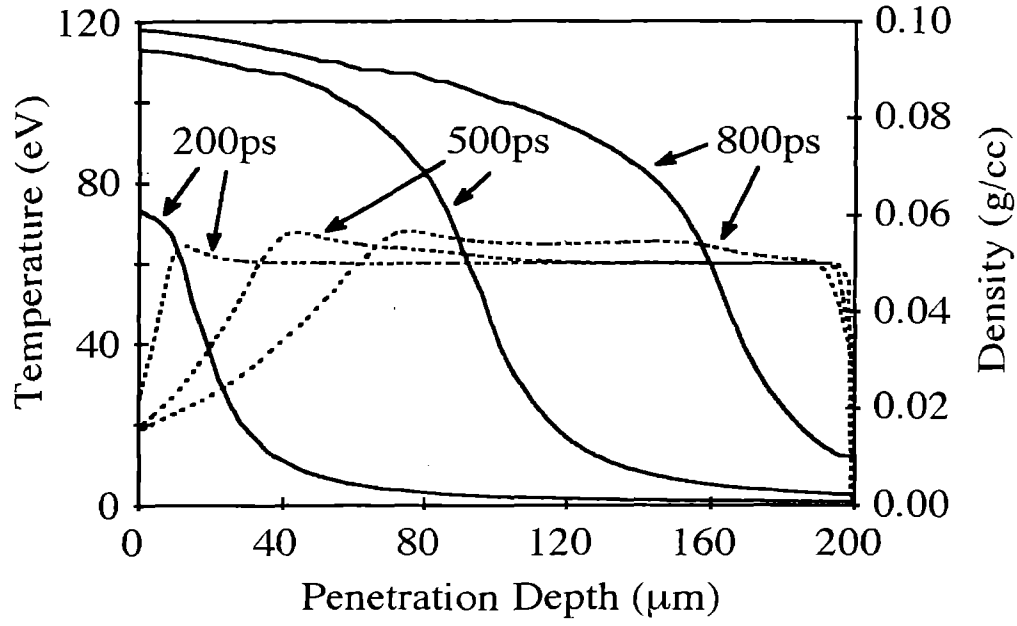

FIG 3 Calculated temperature (solid line) and density (dashed line) profiles in the foam target at three stages in the passage of the ionization front. The drive is incident from the left. The temperature wave can be observed to penetrate deep into the unshocked foam.

EXPERIMENTAL OBSERVATIONS OF THERMAL SMOOTHING AND HYDRODYNAMIC EFFICIENCY USING X-RAY PREHEATED FOAM BUFFER TARGETS FOR USE IN INERTIAL CONFINEMENT FUSION

M. Dunne, M. Borghesi, A. Iwase, M. W. Jones and O. Willi

Imperial College of Science, Technology and Medicine, London, SW7 2BZ, U.K.

A prime contender for a viable Inertial Confinement Fusion (ICF) driver is direct illumination by a large number of high power optical laser beams. Such a driver has the benefits of geometrical simplicity and potentially high overall energy efficiency. However, the wavefront of a high power laser beam suffers from severe and unpredictable intensity nonuniformities which induce nonuniform shock waves in the fusion pellet, leading to the seeding of many instabilities, premature target breakup and a drastic reduction in the achievable fusion yield. The development of a number of sophisticated beam smoothing techniques has so far proved inadequate in overcoming the imprinting of the remaining intensity nonuniformities in the early-time 'start-up' phase of the laser-target interaction. This imprinting arises due to the proximity of the absorption region to the ablation surface in the initial plasma, preventing any effective transverse thermal smoothing of the non-uniform shock before it reaches the ablation surface. The target response to the initial shock generated by these residual nonuniformities results in severe mass perturbations across the target, seeding hydrodynamic instabilities such as the Richtmyer-Meshkov and Rayleigh-Taylor instabilities, inducing premature target break-up. It has been demonstrated [1,2] that the presence of an x-ray preformed plasma buffer in front of the solid target surface can act to thermally smooth laser nonuniformities and result in a uniform ablation pressure as long as the distance between the absorption and ablation surfaces is greater than, or of the order of the intensity perturbation wavelength. The production of this preformed buffer by direct x-ray illumination of a solid target surface is, however, unsatisfactory for the purposes of ICF. The high intensity of the initial x-ray burst needed to form the required plasma scalelengths results in a compression shock wave being launched into the target. This shock and the inevitable presence of long mean-free-path x-rays act to preheat the inner, cryogenic DT fuel, forcing the implosion to proceed along a higher adiabat, dramatically raising the energy requirements of the main optical drive laser.

We propose a solution to this outstanding problem in which the x-ray burst is incident onto a thin, low density foam layer overcoated on the solid target surface. The x-ray heating can then occur through the passage of a supersonic ionization wave, thus preventing any shock waves reaching the solid surface prior to the thermal front induced by the main drive laser. The supersonic production of super-critical, homogenous plasmas from x-ray irradiated foam layers has already been demonstrated using a separated foil-foam geometry [3]. It now remains to establish the levels of thermal smoothing which can be expected for a given foam thickness, the effect this has on the hydrodynamic response of the target (and thus the implosion efficiency) and any possible increase in parametric instability generation in this preformed plasma buffer.

This report presents the first observations of the interaction of a laser with such a low density foam target. The foam targets were overcoated with a thin high-Z 'x-ray converter' layer and supported on solid plastic substrates for quantitative measurements of the target acceleration. The ability to produce a supersonic x-ray ionization wave in this 'overcoat' geometry was confirmed using streaked absorption images, as shown in Figure 1. The preforming x-ray wave can be seen to propagate well ahead of the thermal front, travelling at an average speed of $(1.0\pm0.1)\times10^7$ compared to $(0.7\pm0.1)\times10^7$ cm/s; approximately Mach 1.3. The simplicity of such a target design should allow a relatively easy conversion to spherical geometry.
A high degree of thermal smoothing was observed even in thin (50μm thick) foam layers, which retained a very high hydrodynamic efficiency and resulted in very low levels of stimulated Brillouin and Raman generation.

The VULCAN glass laser system was used in a second harmonic cluster configuration to irradiate the hybrid targets, with a central (axial) beam used both to drive and act as a backscatter probe. Typical irradiances on target were around 5×10^{14} Wcm^{-2}. A side-on XUV radiography technique was used to image the response of the target to the laser interaction, with a 2D gated XUV detector used to monitor the levels of thermal smoothing, and a 1D streak camera used to measure to target acceleration history. The irradiation geometry is shown schematically in Figure 2.
The backscatter channel monitored the absolute levels of the stimulated Brillouin (B-SBS) and Raman (B-SRS) instabilities (calibrated *in situ*), the spectrum of the B-SRS, the temporal history of the B-SBS spectrum, and the 2D spatial profile of the B-SBS (using a gated optical imager).
The targets used consisted of triacrylate (CHO) foam cylinders, 50mg/cc in density (approximately 1/30th solid density), 200μm in diameter, overcoated with 400Å Bismuth ($Z=83$, $\rho x=4\times10^{-5}$ g/cm^2) on the laser side and 12μm solid mylar (CHO) on the rear side. This plastic layer ensured that the rear surface always remained at solid density during the acceleration measurements, for direct comparison with simple planar foil targets.

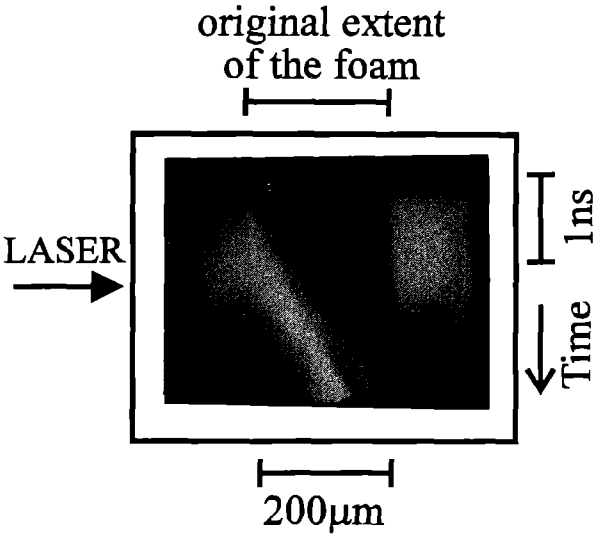

FIG 1 Streaked radiograph demonstrating that a supersonic, preforming, x-ray driven ionization wave propagates ahead of the thermal front in the current 'overcoat' geometry. The target was a 50mg/cc foam, 200μm in length, overcoated with 400Å Bi.

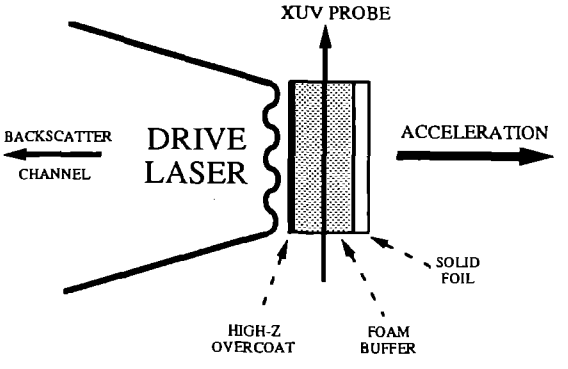

FIG 2 Shematic of the complete main target geometry

The thermal smoothing properties of the foam buffer layer are demonstrated in Figure 3, which shows 2D gated images (taken at 50 ±5Å) of the interaction of a nonuniform coherent laser beam with an x-ray preformed foam target and with a cold target where no preforming x-rays were present (i.e. no Bismuth layer was used). Three pairs of images are presented. Case 3(a) recorded the time-integrated self emission of the targets. In the absence of any x-ray preheat, intense filaments are seen to penetrate throughout the target; whereas for a preheated target these filaments are seen to laterally diffuse, producing a smooth intensity front towards the rear of the foam. Gated images were then taken, as presented in cases 3(b) and 3(c) to demonstrate that this smoothing effect is true at a given instant in the interaction and is not merely due to temporal smearing. Case 3(b) primarily recorded the gated self emission in the two cases, while case 3(c) recorded the targets' absorption profile to a 50Å probe. Once again, the difference between the two cases is clear, with the preheated target shown to produce a heat front which is smooth to within the resolution limit of the diagnostic used (able to detect nonuniformities on the order of 5μm). The smoothing is noticeable even at early time, as shown in case 3(b), where the heat front has only penetrated 20μm into the target. In the cold target case, the laser modulations are clearly reproduced in the target as a result of the well-understood laser imprinting onto the cold surface. The reduction in the level of target nonuniformity in the preheated foam arises as a result of the large distance between the critical and ablation surfaces, which is of the order of the thickness of the foam overcoat, throughout the interaction.

Such effective thermal smoothing is useless, however, if it compromises the hydrodynamic efficiency with which the target can be accelerated. For if the efficiency drops then the overall gain of an implosion will also drop unless the energy available from the drive laser is increased. Such a move would add substantially to the cost of the system and is therefore highly undesirable. Figure 4 demonstrates that the presence of a foam overcoat does not affect the degree to which a target can be accelerated. The streak record shows the thermal front propagating through a 50μm thick foam buffer and subsequent target acceleration as the shock front reaches the rear side of the foil. The efficiency of this acceleration is shown (in Figure 5) to be almost identical to that of a simple, directly heated solid planar foil even though the hybrid target contains 17% more mass. The slight difference in absolute position results from the increased shock transit time in the foam-foil target. This efficiency can be understood from the fact that in the interaction of the laser with a solid foil, the distance between the critical and ablation surfaces reaches a steady-state value on the order of 50μm in the first few hundred picoseconds of irradiation. The presence of the foam buffer, then, merely introduces this steady-state distance from the beginning of the interaction. For timescales of interest to ICF (tens of nanoseconds), the difference in energy transfer in this initial transient stage becomes irrelevant.

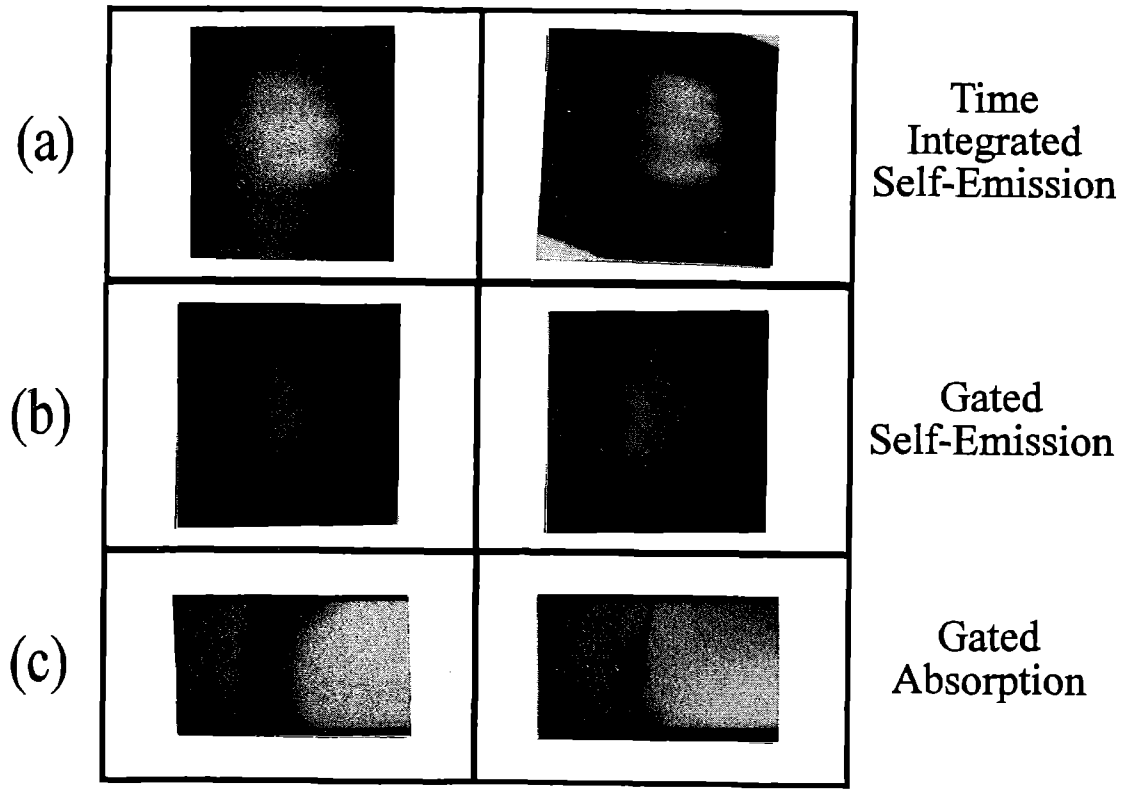

FIG 3 Demonstration of the thermal smoothing capabilities of an x-ray preheated foam layer (left column) compared to cold targets where no Bi (x-ray converter) layer was present (right column). Laser is incident from the right in all cases.
(a) Time-integrated record of the self emission
(b) Gated image showing self emission 250ps after the start of the interaction
(c) Gated absorption images 500ps after the start of the interaction.

The retention of hydrodynamic efficiency provides an indication that little energy is lost to parametric processes occurring in the preformed plasma. This was confirmed using calibrated, time-resolved diodes, which demonstrated that less than 1% of the incident laser energy was lost to B-SBS or B-SRS. No significant difference in the backscatter levels was seen between the irradiation of simple foil targets and Bi-coated foam hybrid targets. The backscattered light was shown to be concentrated in intense filaments within the focal spot profile, as expected in the underdense plasma.

In summary, we have demonstrated that an x-ray preformed foam buffer layer is capable of removing laser nonuniformities even from a coherent beam, without compromising the hydrodynamic performance of the target. Parametric instability generation has been shown to be insignificant under the current conditions.
These results appear to be extremely encouraging for conventional direct-drive ICF and it now remains to experimentally determine the reduction in the level of Rayleigh-Taylor growth that may be achieved using such hybrid targets under reactor-type conditions.

The authors would like to acknowledge the Los Alamos TRIDENT laser team for their collaboration in the initial experiment investigating the thermal smoothing properties of gold-coated foam targets, which will form the basis of a forthcoming publication.
Thanks are due to W. Nazarov, J. Falconer and G. Lyall (Dundee University) for supplying the foam targets, B. Evans for the XUV mirror coating, and to the laser, target area and target preparation staff for invaluable help during the experiment.

REFERENCES

[1] M. Desselberger *et al.*, Phys. Rev. Lett. **68**, 1539 (1992).
[2] M. Dunne *et al.*, 'Quantitative measurements of the thermal smoothing of nonuniform laser irradiation', this report.
[3] T. Afshar-rad *et al.*, submitted to Phys. Rev. Lett.; M. Dunne *et al.*, 'Detailed measurements of the supersonic propagation of ionization fronts driven by thermal radiation', this report.

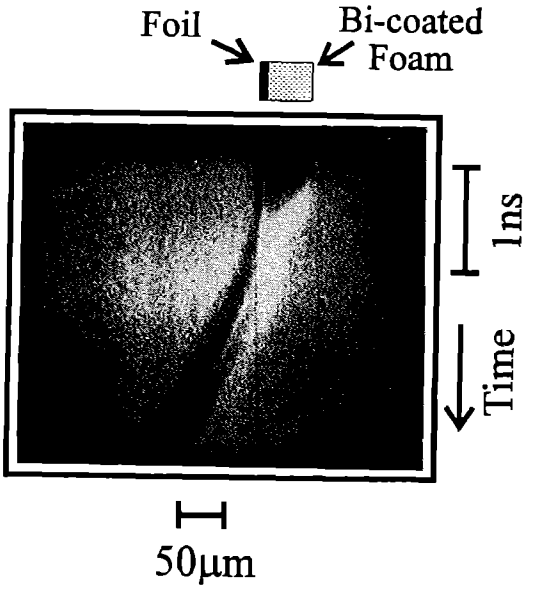

FIG 4 Streak record of an accelerating hybrid target. The target was a 50mg/cc foam, 50μm length, overcoated with 400Å Bi, supported on a 12μm mylar foil. The original target position is indicated at the top of the figure. Laser is incident from the right.

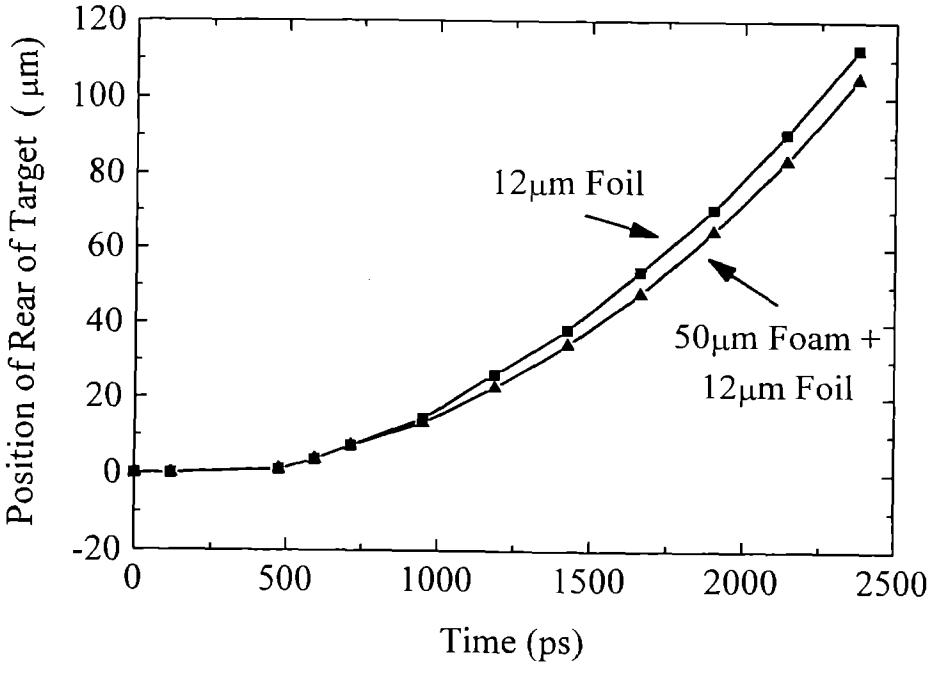

FIG 5 Temporal history of the rear side of the accelerating targets, for
(i) directly heated 12μm thick CHO foil, (ii) 50μm long foam+12μm foil (as shown in figure 4),
All points are accurate to within ±10μm. The errors arise primarily from photocathode noise.

IMPRINT OF LASER MODULATIONS ON SOLID TARGETS

M W Jones, M Dunne, A Iwase and O Willi
Imperial College, London

INTRODUCTION

The Rayleigh-Taylor hydrodynamic instability occurs in any system where the density and pressure gradients are antiparallel. In the case of inertial confinement fusion (ICF) experiments, the hot ablated plasma accelerated the colder denser target material, and is therefore susceptible to the RT instability. This instability is seeded by small perturbations on the interface between the two density regions. These could be caused by density non-uniformities on the target occurring during target manufacture, or as is being investigated here, by the imprinting of any laser spatial non-uniformities onto the target surface during the initial ablation phase.

THEORY AND SIMULATION

The growth of the amplitude of initially small perturbations to the interface between the different densities due to the Rayleigh-Taylor instability is given by :

$$A = A_0 e^{-\gamma t} \qquad (1)$$

where the growth rate γ is, to a first approximation,

$$\gamma = -\sqrt{gk\alpha} \qquad (2)$$

Here, g is the (constant) acceleration of the system, k is the wavenumber of the perturbation and α is the Attwood number.

So in the planar geometry that we are considering, if any process perturbs the front surface of the foil, then when the system accelerates, the perturbations grow, until the density variations are large enough for the transmission of the backlighter through the target to be visibly different across the target.

Figure 1 shows the transmission radiograph of a 12μm target which has preformed sinusoidal modulations with period 70μm and amplitude, ±2μm. The growth of the density perturbations is apparent by the increasing contrast of the lines in later time.

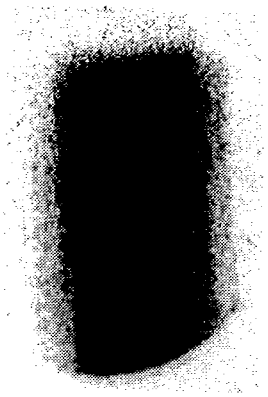

Figure 1 Transmission radiograph of a target with density modulations

Extensive computer simulations have been performed to investigate both the growth of the modulations of these RT targets, and also the effect of the laser imprint on targets [1].

Figure 2 shows the results of a simulation performed, to investigate the effect of a 7:1 sinusoidal modulation in the intensity of the interaction beam. The laser has wavelength λ=0.53μm, with an average intensity of $I=10^{14}Wcm^{-2}$ and has an imposed spatial intensity modulation of wavelength 30μm. The figure shows a density contour plot of the system at a time t=1500ps after the start of the laser pulse. The darker contours show the ablation surface, and critical surface respectively.

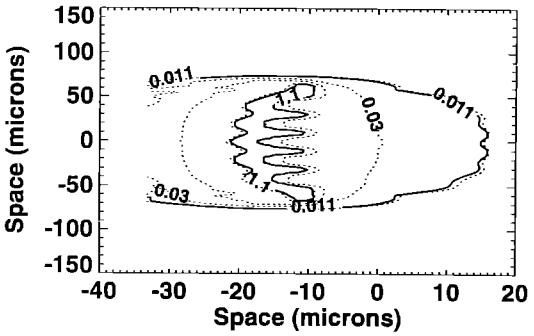

Figure 2 Computer simulation of laser imprint.

EXPERIMENT

To investigate the imprint, we utilised the cluster arrangement of TAE, with a target set-up as shown in Figure 3.

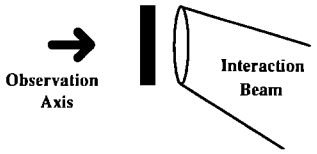

Figure 3 Experimental set-up

We used a transmission pinhole camera to observe the back of the foil, and a Mg backlighter with appropriate filtering to closely approximate a line radiation source. The main interaction beam came in through one of the 15° cluster ports, and its intensity profile was modulated spatially in one dimension using a mask consisting of an array of Neutral density filter strips, which provided us with an intensity modulation of approximately 6:1. The periodicity and size of the filter strips was varied, so that a number of interaction wavelengths could be studied. The backlighting was performed using 2 other beams, which were smoothed using RPP.

Both the interaction and backlighting beams had a wavelength of 0.526μm. The pulse duration of the driving pulse was 2ns, with a focal spot of approximately 350μm. This gave us an on-target intensity of approximately $2\times10^{13}Wcm^{-2}$.

In order to obtain quantitative results, the system had to be allowed to accelerate, so that the laser imprint could seed the RT instability which would then grow, and eventually become apparent in the transmission profile of the target.

Figure 4 shows the resulting radiograph of one of the imprint shots. It can be plainly seen that in later time, there is a distinct series of vertical lines appearing, which are indicative in this case of the RT growth of the initial density perturbations of the target caused by the imprint of the laser modulations.

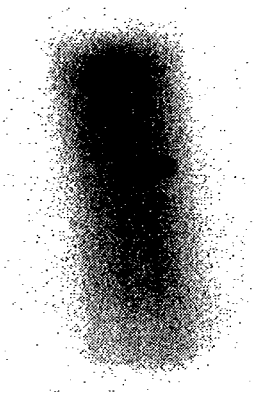

Figure 4 Transmission radiograph of laser imprint.

CONCLUSION

Good agreement has been found between the simulations and the experiment, and as a comparison, the laser imprint seems to have the same effect as an initial density modulation on the target of amplitude 0.06μm, an order of magnitude down from the control RT targets considered initially.

REFERENCES

1 M.Desselberger, M W Jones, and O Willi
Initial imprint of targets using coherent and incoherent laser irradiation
To Be Submitted.

THE EFFECT OF VELOCITY GRADIENTS ON X-RAY LINE TRANSFER IN LASER-PRODUCED PLASMAS

J.S.Wark[1], A.Djaoui[2], S.J.Rose[2,3], H.He[1], O.Renner[4], T.Missalla[5] and E.Foerster[5].

[1]Department of Physics, Clarendon Laboratory, Parks Road, Oxford, OX1 3PU.

[2]Rutherford Appleton Laboratory, Chilton, Didcot, Oxon OX11 0QX.

[3]Department of Physics and Space Science, University of Birmingham, Birmingham, B15 2TT.

[4]Institute of Physics, Czech Academy of Sciences, 180 40 Prague, Czech Republic.

[5]Max-Planck-Gesellschaft, University of Jena, D-O-6900, Jena, Germany.

During the expansion of high-power laser-produced-plasmas (LPPs) very large velocity gradients are produced of, typically, 10^9 sec^{-1}. These gradients increase the probability of escape of X-ray resonance line photons because of the Doppler-decoupling mechanism. This mechanism is an important contributor to the successful operation of recombination-pumped XUV lasers[1-8] because reabsorption of the resonance line photons pumps the lower laser level reducing the population inversion. Enhanced probability of escape due to high velocity gradients is also found in astrophysical plasmas, and many workers (starting with Sobolev[9-15]) have tried to calculate line transfer in this situation.

Previous workers have viewed LPPs parallel and perpendicular to the laser beam in the soft XUV regime, but these experiments are dominated by two dimensional effects, and no detailed comparisons with sophisticated radiation transfer models have been attempted. Data obtained observing parallel to the laser have yielded bulk Doppler shifts, but, again, little information on line transfer.[16-18] The effect of observation angle on relative intensity in the soft X-ray (keV) regime has also been investigated, but the resolution was insufficient to record the effect on lineshapes and positions.[19] More recently it has been noted that the range of Doppler shifts due to the velocity gradient in a LPP broaden and shift the peak of optically thick lines, though these XUV measurements were made with comparatively poor spectral resolution ($\lambda/\Delta\lambda$ ~ 1700), and no absolute shifts in the peak of the lines could be inferred.[20]

We describe here the first experiments to measure with high-resolution the lineshape, intensity, and position of an X-ray resonance line emitted by a laser-produced plasma as a function of observation angle. These line features can only be understood by considering the transfer of radiation through the plasma with its high velocity gradient. We have performed simulations showing that the combination of the velocity gradient (which alters the escape factor), the emission and absorption profile as a function of distance from the target surface, and the position-dependent line broadening mechanisms conspire to produce assymmetric lineshapes, the intensity and position of which are a strong function of observation angle. Experimental observations of these angle dependent features using a novel X-ray spectrometer show remarkable agreement with calculations. We describe first the experimental arrangement and results and go on to describe the numerical model used to simulate the experiment.

The measurements were obtained by use of the vertical dispersion variant of the double crystal spectrometer (DCS). The DCS, described in detail elsewhere,[21-23] is a two crystal instrument with extremely high spectral resolution and dispersion. For these experiments we calculate a spectral resolution of 6400, and a dispersion of 6.4 mÅ mm^{-1} at line centre on film at a distance of 10 cm from the source. The DCS also affords a degree of spatial resolution in a direction perpendicular to the dispersion plane, which in this case was 7 μm. More detailed information about the theory of the instrument can be found in the work of Renner.[21]

The experiment was performed using the Neodymium glass laser 'VULCAN'. A single beam containing 80 J of 0.53 μm light in a pulse of 1.2 ns (FWHM) was incident normally onto a 10 μm thick 500 μm diameter aluminum foil. The focal spot diameter on target was 200 μm, giving an incident intensity of 3 x 10^{14} W cm^{-2}. The experimental arrangement is shown schematically in Fig. 1. The DCS was fitted with two ADP crystals ($2d$ = 10.64 Å). It was mounted on a rotation stage whose axis of rotation was aligned with the centre of the aluminum foil to within ± 30 μm. The line shifts were measured in the following way. A series of laser shots was taken with a given laser energy and focal spot size. For each shot in the series, the angle between the DCS and the incident laser (the angle ψ in Fig. 1) was varied by rotating the instrument around the axis containing the target, and the X-ray film holder was moved transversely by approximately 2 mm, keeping the total target to film distance constant. The data were recorded on Kodak Industrex-C X-ray film.

Shifts in the recorded hydrogenic Ly-α resonance line ($1s\ ^2S$ - $2p\ ^2P$) due to errors in target-to-film distance are negligible due to the high dispersion of the instrument - a combination of the 30 μm difference between rotation axes, and an estimated maximum error of 200 μm due to film shift gives rise to an error of only 0.2 mÅ. Furthermore, for the final shot of each series of laser shots we returned the spectrometer to its original angle with respect to the laser beam. In every case no detectable difference between the line positions of the first and last shot was found.

Fig. 2(a) shows the spectra recorded from Al Ly-α for various angles of observation with respect to the laser beam. Film density has been converted to intensity by use of an unpublished calibration curve. The lineouts are taken from a 25 μm spatially resolved region in the centre of each of the emission profiles. The variation in laser energy over the shot series was measured to be less than ± 10 %. It can be seen that as the emission is viewed from angles where the plasma has a component of velocity towards the spectrometer (i.e. 30° and 60° with respect to the laser beam) there is an decrease in the wavelength of the peak of the emission consistent with Doppler motion away from the target. For the 150° and 180° data (i.e. observing the emission through the target towards the laser beam) the target was 1μm Al coated on 10μm plastic $(CH)_n$. For this data the reduction in intensity due to the X-rays passing through the cold, unablated portion of the target has been

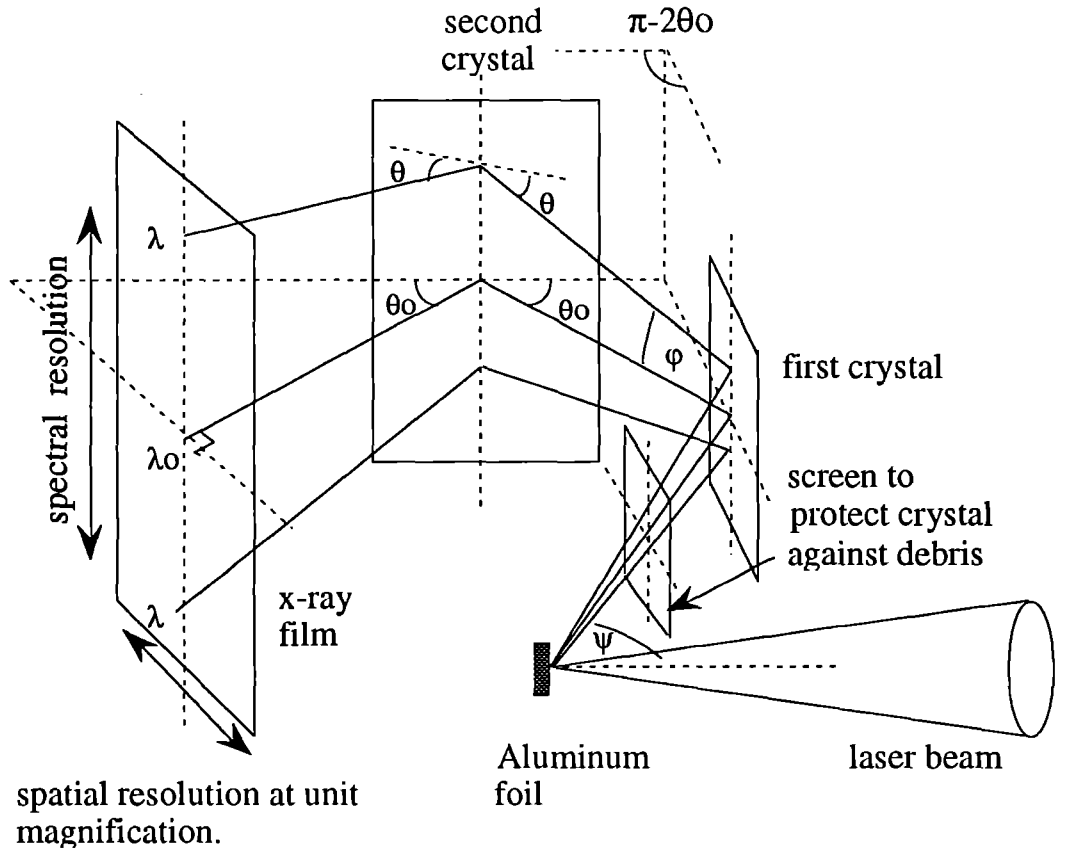

Fig. 1. A schematic diagram of the experiment. The DCS disperses the X-rays in the vertical direction, whilst yielding spatial resolution at unit magnification perpendicular to the dispersion direction. For each laser shot the instrument was rotated coaxially around the aluminum foil, altering the angle of observation with respect to the laser beam, ψ. The X-ray line, of wavelength λ, is recorded on both sides of a central point shown as λ_0, and is defined by $\lambda = \lambda_0 \cos\varphi$. Refer to Ref. 21 for further details of the instrument.

removed. The line is seen to be red shifted. Although the DCS does not record the absolute wavelength, the relative shifts and intensities shown in Fig. 2(a) are recorded accurately by the instrument. The absolute wavelength in Fig. 2(a) has been set by comparison with the simulated data described below.

Analysis of the spatially resolved emission away from the target surface shows it falls to a half intensity point at a distance ~ 0.5 of the focal spot diameter away from the surface, indicating that the data should be quasi 1-D. The numerical model used to simulate the experiment is based on a modified version of the 1-D Lagrangian hydrodynamic code MEDUSA which includes time-dependent average-atom non-LTE atomic physics.[24] The effect of optically thick line reabsorption on level populations is taken into account by use of escape probabilities which include the effect of the large velocity gradient[24] (an approximation which is in good agreement with detailed line transfer calculations[7]). This part of the calculation provides densities, temperatures, velocities and ionic populations in each Lagrangian cell. A detailed multifrequency line transfer model in the laboratory frame is then used to calculate the observed hydrogen-like Lyman-doublet line emission. Within each cell in which the photons originate, the model calculates the population in the $2p_{1/2}$ and $2p_{3/2}$ states from the average-atom populations using the technique described in ref. 24 together with the assumption of statistical equilibrium between all the n=2 levels. Absorption profiles in one cell are Doppler shifted relative to the emission profiles in a different cell because of the velocity difference between the cells. A Doppler profile is used for each component of the doublet with a width calculated from the ion temperature predicted by MEDUSA. Simulations show that the effect of using Voigt or Stark profiles, which include the effects of electron collisional lifetime and Stark broadening, is negligible. A more detailed description of this model is currently being prepared for publication elsewhere, although it is similar in principle to techniques used by others to predict realistic line shapes in laser produced plasmas.[20]

The results of the simulations at an absorbed irradiance of 10^{14} W cm^{-2} are shown in Fig. 2(b). The absolute predicted and observed intensities agree to within approximately a factor of two. It can be seen that there is remarkable agreement with the experimental data. The unshifted line positions of the doublet are shown. The code predicts the maximum ion temperature of the emitting plasma to be ~ 700 eV, leading to a thermal Doppler broadening of 2.8 mÅ (FWHM); the linewidths and shifts observed are much larger than this, demonstrating the importance of bulk Doppler motion. The simulations also show that for the front side emission (observation angles of 30° and 60°) the red side of the line is relatively independent of observation angle, whereas the blue

is not. Furthermore, the relative position, intensity, and degree of line reversal in the rear side (150° and 180°) data are also in excellent agreement. More detailed analysis of this data is the subject of further work, although the excellent agreement between code and experiment at this stage is encouraging. We believe the discrepancies between code and experiment in the slopes of the red side of the line are because the experiment is not purely one dimensional. This issue will be addressed more fully in the future.

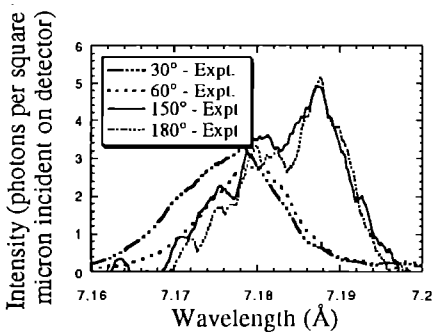

(a)

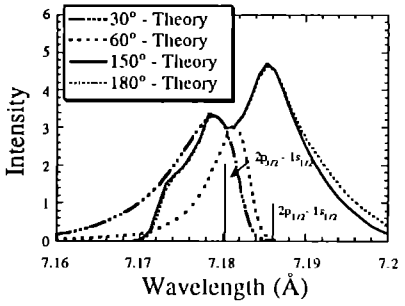

(b)

Fig.2. (a) The measured 1s ^{2}S - 2p ^{2}P spectral line of hydrogenic aluminum for various observation angles with respect to the laser beam and (b) MEDUSA simulations. The 30° simulated intensity has been normalised to the 30° data, although the two agree absolutely to within a factor of 2.

The code predicts that at the time of peak emission, at the unshifted position of the peak of the $2p_{3/2} - 1s_{1/2}$ component, the maximum optical depth normal to the target surface is 9 when absorption by the $2p_{1/2} - 1s_{1/2}$ component is included, and only 6 if not. If the Doppler decoupling is not taken into account the optical depth increases to 36. The predicted velocity gradient at this time in a direction normal to target surface is 4 x10^9s^{-1}. Simulations show that the angle dependent line shape and intensity are sensitive to the irradiance on target, and hence the resultant velocity gradient. Of the simulations performed, only those close to the experimental absorbed irradiance match both the experimentally observed intensity and lineshapes. Calculations for a static plasma show markedly different lineshapes from those observed. Thus the effect of velocity gradients is critical to the observations. Artificially setting the escape factor to unity in the average atom model results in a lower population of the upper level of the transition and a reduction in intensity by a factor of about 12, whereas the absolute experimental intensities are within a factor of two of the calculated values with the escape factor included in the calculation of the ionic populations.

In conclusion this work shows the first high-resolution spectra of line profiles and relative postions in an expanding laser-produced plasma as a function of observation angle. The peak positions, intensities, and salient features of the measured line profile, requiring experimental spectral resolution in excess of 6000, can only be simulated by accounting for the Doppler shift of the expanding material in the calculation of radiation transfer, and absolute intensities are consistent with the escape factor approximation; such results cannot be obtained by simply using models based on homogeneous slabs of plasma.

The authors are grateful for the assistance of the staff of the VULCAN laser. Three of the authors (O.R., T.M., and E.F.) were supported by a Science and Engineering Research Council Visiting Fellowship.

REFERENCES

1. J.P. Apruzese, J. Davis, and K.G. Whitney, J. Appl. Phys., **53**, 4020 (1982).
2. C.Chenais-Popovics, R.Corbett, C.Hooker, M.H.Key, G.Kiehn, C.L.S.Lewis, D.Pepler, G.J.Pert, C.Regan, S.J.Rose, S.Saadat, R.A.Smith, T.Tomie, and O.Willi, Phys. Rev. Lett., **59**, 2161 (1987).
3. J.P. Apruzese, P.C. Kepple, J. Davis, and J. Pender, IEEE Transactions on Plasma Science, **16**, 529 (1988).
4. M.Grande, M.H.Key, G.Kiehn, C.L.S.Lewis, G.J.Pert, S.A.Ramsden, C.Regan, S.J.Rose, R.A.Smith, T.Tomie, and O.Willi, Optics Comm. **74**, 309 (1990).
5. A.I.Shestakov and D.C.Eder, J.Q.S.R.T., **42**, 489 (1991).
6. G.J.Pert, J.Q.S.R.T., **46**, 367 (1992).
7. Y.T.Lee, R.A.London and G.B.Zimmerman, Phys.Fluids B, **2**, 2731 (1990).
8. D.C.Eder and H.A.Scott, J.Q.S.R.T., **45**, 189 (1991).
9. V.V. Sobolev, "Moving Envelopes of Stars", Harvard University Press, Cambridge (1960).
10. J.I.Castor, Mon. Not. R. Astr. Soc., **149**, 111 (1970).
11. L.B.Lucy, Ap. J., **163**, 95 (1971).
12. G.B.Rybicki and D.G.Hummer, Ap.J., **219**, 654 (1978).
13. D.G.Hummer and D.G.Rybicki, Ap.J., **254**, 767 (1982).
14. G.B.Rybicki and D.G.Hummer, Ap.J., **274**, 380 (1983).
15. D.Mihalas and B.W.Mihalas, "Foundations of radiation hydrodynamics", OUP, Oxford (1984).
16. F.E. Irons, R.W. McWhirter, and N.J. Peacock, J. Phys. B, **5**, 1975 (1972).
17. U. Feldman, G.A. Doschek, W.E. Behring, and Leonard Cohen, Appl. Phys. Lett., **31**, 571 (1977).
18. D. Santi, E. Jannitti, P. Nicolosi, and G. Tondello, Nuovo Cimento, **65B**, 198 (1981).
19. L.F. Chase, W.C. Jordan, J.D. Perez, and J.G. Pronko, Appl. Phys. Lett., **30**, 137 (1977).
20. J.C. Moreno, S. Goldsmith, and H.R. Griem, J. Opt. Soc. Am. B, **9**, 339 (1992).
21. O.Renner and M.Kopecky, Laser and Particle Beams, **10**, 841 (1992).
22. H.He, J.S.Wark, E.Foerster, I. Uschmann, O.Renner, M.Kopecky, W. Blyth, Rev. Sci. Instrum., **64**, 26 (1993).
23. J.S.Wark, H.He, O.Renner, T. Missalla, and E.Foerster, J.Q.S.R.T. (to be published).
24. A.Djaoui and S.J.Rose, J.Phys. B:Atom. Molec. Opt. Phys., **25**, 2745 (1992).

MEASUREMENT OF ELECTRON DENSITY DISTRIBUTION IN LONG SCALELENGTH PLASMAS

L.A.Gizzi, D.Giulietti, A.Giulietti, T.Afshar-rad[1], S.M.Viana[1], O.Willi [1].

Istituto di Fisica Atomica e Molecolare, Pisa, Italy.

[1] The Blackett Laboratory, Imperial College of Science, Technology and Medicine, London, UK.

INTRODUCTION

Interferometric techniques can be used to measure the electron density distribution of a plasma as well as its temporal evolution. A fringe pattern is generated by an interferometer which gives the phase shift induced on the probe beam by the plasma and integrated along the line of sight of the interferometer. With appropriate assumptions on the symmetry of the plasma, Abel inversion allows the density distribution to be obtained from the phase shift distribution. A detailed experimental investigation was performed[1] on long scalelength plasmas produced from laser irradiation of thin Al disks. A wide range of diagnostic techniques was employed in order to characterise the plasma in terms of electron density and temperature[2]. In particular, an extensive analysis[3] of interferometric measurements has been carried out using advanced techniques[4] based on the Fourier analysis and the results are summarised here.

EXPERIMENTAL SET-UP

The long scalelength plasmas were produced at the SERC Central Laser Facility using four 600 ps, 1.053 μm beams of the Vulcan laser, focused f/10 on a 400 μm diameter Al dot targets at an irradiance from 3 to 6×10^{13}W/cm^2 on each side of the target. A 100 ps (FWHM), 1.053 μm beam of the Vulcan laser was frequency doubled, delayed and used as a probe beam for interferometric measurements in a line of view parallel to the target plane. A Nomarski-like interferometer[5] was employed in order to measure the plasma induced phase shift at various delays relative to the peak of the heating pulses. It was found that, under analogous experimental conditions, interferograms were highly reproducible shot by shot. Fig.1 shows a representative interferogram taken 4.3 ns after the peak of the heating pulses.

INTERFEROMETRY: BASIC PRINCIPLES

The fringe pattern produced by the interferometer is the result of interference between a beam which has propagated through the plasma and an unperturbed reference beam, both beams originating from the same laser source. If the electron density n_e is much smaller than the critical density, n_c at the probe wavelength, one can assume that bending effects are negligible, that is the probe beam propagates through the plasma in a straight line. In this case the phase difference between these two beams in a given position (x,z) of an output plane of the interferometer perpendicular to the probe beam is

$$\Delta\varphi(x,z) = \frac{2\pi}{\lambda_p}\left(\int_{-L/2}^{L/2}(\varepsilon(x,y,z)-1)\,dy\right) \qquad (1)$$

where λ_p is the probe beam wavelength, ε is the plasma refractive index, L is the total path-length greater than the plasma extent along y.

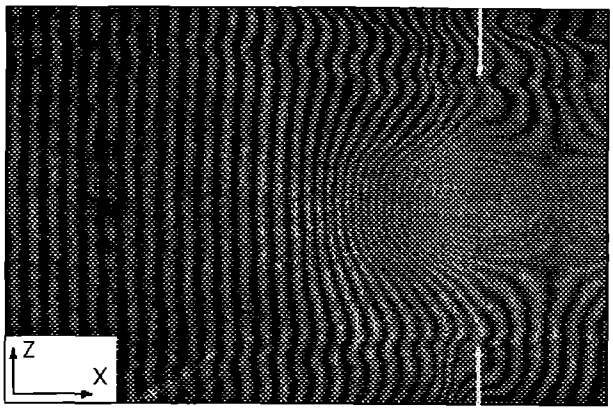

Fig.1. Interferogram of the preformed plasma taken 4.3 ns after the peak of the heating laser pulses. The intensity on each side of the target was 4.2×10^{13} W/cm^2. The position of the target is indicated by the arrows.

Considering that $n_e \ll n_c$, and assuming cylindrical symmetry of the plasma around the axis perpendicular to the target and passing through its centre, the phase shift can be written in terms of the radial co-ordinate, i.e. the distance from the symmetry axis

$$\Delta\varphi_{x_o}(z) = -\frac{e^2\lambda_p}{m_e c^2}\left(\int_z^{r_o}\frac{n_e(r)\,r\,dr}{\sqrt{r^2-z^2}}\right) \qquad (2)$$

where the usual symbols have been adopted for the electron mass and charge, and the speed of light. Eq.2 has the typical form of the Abel integral equation and can therefore be inverted to give

$$n_e(r,x) = -\frac{m_e c^2}{\pi e^2\lambda_p}\int_r^{r_o}\frac{\partial\Delta\varphi(x,z)}{\partial z}\frac{dz}{\sqrt{z^2-r^2}} \qquad (3)$$

which gives the radial distribution of the electron density in terms of the phase shift induced by the plasma, integrated along a direction perpendicular to the symmetry axis. In order to detect this phase shift a small angle is introduced by the interferometer between the probe beam and the reference beam so that, in absence of plasma, a pattern of parallel fringes is generated. The phase shift introduced by the plasma is then evaluated by measuring the displacement of the fringes from their unperturbed position. By counting the number of fringes crossed moving along z one can obtain a sampling of $\Delta\varphi$ for a given distance from the target plane. This set of data can be fitted and introduced in Eq.3 in order to calculate the electron density. However this procedure, typically used in the past, is subjected to a number of uncertainties introduced by the small number of data typically available to build $\Delta\varphi$ and by the particular choice of the fitting function. Moreover, the sensitivity of this technique is basically limited to one fringe shift which, as will be clear later, would strongly limit the effectiveness of the interferometric method itself,

capable of a much better resolution. The use of the Fourier transform method in the analysis of the interferograms allows a much more direct approach to the problem, free from the uncertainties evidenced above and easy to implement with simple numerical techniques.

FOURIER TECHNIQUE

The intensity of the fringe pattern produced by the interferometer on the output plane of the interferometer in presence of plasma can be written as

$$I(x,z) = a + b\cos[2\pi f_u x + \Delta\varphi] \qquad (4)$$

where a 1:1 plasma to image magnification has been assumed. In this equation $a(x,z)$ and $b(x,z)$ account for non-uniformities of the background intensity and fringe visibility, f_u is the spatial frequency of the unperturbed fringe pattern, i.e. the number of fringes per unit length on the output plane, $\Delta\varphi(x,z)$ is the phase shift induced by the plasma. It has been shown[6] that, by means of the Fourier analysis, the intensity $I(x,z)$ can be processed in order to directly obtain the phase shift. By expressing the cosine function in terms of the exponential function Eq.4 becomes

$$I(x,z) = a + [c\exp(2\pi i f_u x) + c.c.] \qquad (5)$$

where $c(x,z) = (1/2)\,b\exp[i\,\Delta\varphi]$ and its complex conjugate $c^*(x,z)$ carry all the information relative to $\Delta\varphi$. According to the definition of logarithm of a complex number one can verify that

$$\log c = \log[(1/2)b] + i\,\Delta\varphi. \qquad (6)$$

that is the phase shift can therefore be obtained taking the imaginary part of the complex logarithm of c. On the other hand, if we take the Fourier transform of Eq.5 with respect to x we obtain, for a fixed z

$$F_I(f) = F_a(f) + F_c(f - f_u) + F_c^*(f + f_u) \qquad (7)$$

where $F_a(f)$ is the Fourier transform of the background intensity along x and $F_c(f - f_u)$ and $F_c^*(f + f_u)$ are the Fourier transforms of the two terms containing $\Delta\varphi$. If the scalelength of typical non-uniformities of the background intensity along x is large compared to the fringe frequency, then the contribution of F_c to the total Fourier spectrum of Eq.7 will result well separated by the contribution due to the background intensity non-uniformities. In this case $F_c(f - f_u)$ can be extracted from the spectrum, shifted by f_u along the frequency axis toward the origin, in order to obtain $F_c(f)$, and inverse Fourier transformed to obtain c.

The interferogram of Fig.1 was digitised with the two scanning directions set along x and z respectively. The optical density of the film was converted into intensity and stored in a two-dimensional array. A fast Fourier transform (FFT) of the intensity distribution along the direction perpendicular to the fringes, i.e. along x was performed for each position along z. The three components of the Fourier spectrum given by Eq.7 are clearly visible in the image of Fig.2 where the modulus of the Fourier transform of the interferogram of the plasma of Fig.1, is shown as a grey-scale distribution.

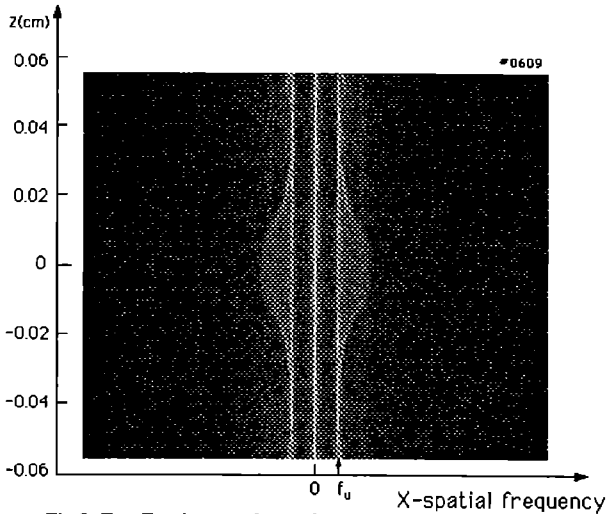

Fig.2. Fast Fourier transform of the intensity profile of the interferogram of Fig.1. The natural logarithm of the modulus is shown as a grey-scale image.

The two side components symmetric to the *zero* frequency are relative to the fringe pattern while the central, strong component accounts for the low spatial frequency variations of the background intensity.

According to Eq.6, the imaginary part of the complex logarithm of $c(x,z)$ will finally give the phase distribution $\Delta\varphi(x,z)$ that is still locally indeterminate by a factor of 2π resulting from the use of an inverse trigonometric function to obtain the argument of $c(x,z)$. However this indetermination can be solved by setting an appropriate algorithm able to detect and compensate jumps in the phase shift.

Fig.3 shows a 3D shaded surface of the phase shift distribution generated by the preformed plasma 4.3 ns after the peak of the heating pulses. According to Eq.3, the phase distributions of Fig.3 can be inverted to determine the electron density distribution.

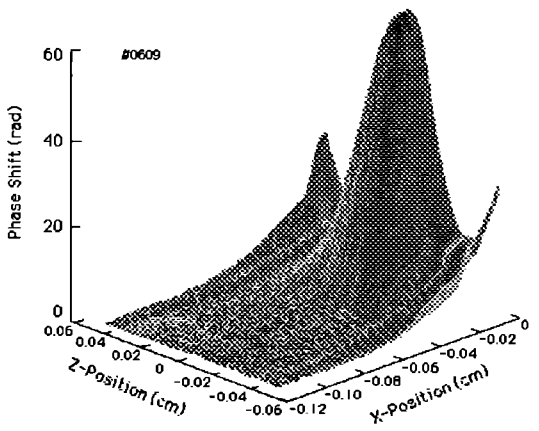

Fig.3. 3D shaded surface of the phase shift distribution obtained from the interferogram of Fig.1 using a Fourier based technique (see text).

The integral in the equation has been solved numerically using a corrected composite trapezoid rule. Due to the large amount of phase data points available, typically

512x512, the integral could be performed directly on the data itself, without polynomial fitting. A contour plot of the density profile obtained from Abel inversion of the phase shift of Fig.3 is shown in Fig.4. The contour levels are labelled in terms of the critical density at 1 μm. Consistently with the assumption of cylindrical symmetry, the Z-co-ordinate of Fig.3 has been replaced by the *radial* co-ordinate.

SENSITIVITY TO DENSITY INHOMOGENEITIES

The analysis of interferograms with the Fourier technique results in a substantial improvement of the sensitivity to small scale non-uniformities in the density distribution. The fringe shift recorded on film is the result of spatial integration along the line of sight of the interferometer, the sensitivity of our measurements to local density inhomogeneities depends upon their scalelength as well as their amplitude.

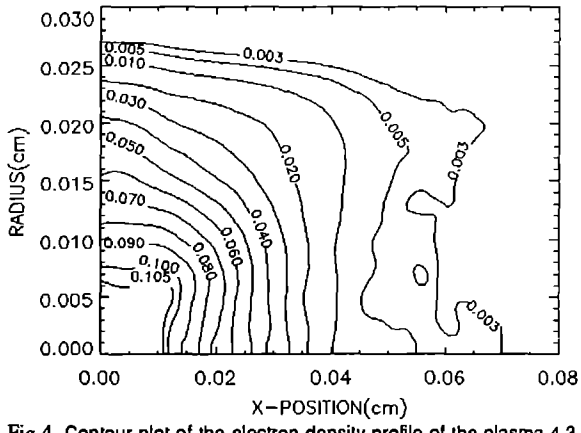

Fig.4. Contour plot of the electron density profile of the plasma 4.3 ns after the peak of the heating pulses as obtained from Abel inversion of the phase shift distribution of Fig.3. Contour levels are labelled in terms of the critical density at 1.053μm.

According to Eq.2 the phase shift induced by the plasma is linear with the density itself. The contribution of a local density inhomogeneity to the total phase shift $\delta\varphi$ has been evaluated assuming a density inhomogeneity along the line of sight at a given position (x_o, z_o) on the output plane of the interferometer given by

$$\delta n_e(x,y,z) = a\, n_{c@1\mu m} \exp(-y^2/w^2) \qquad (8)$$

where a is the amplitude of the density perturbation in units of the critical density at 1 μm, $n_{c@1\mu m}$ and w is the scalelength of the perturbation.

The phase shift $\delta\varphi$ must be compared with the minimum phase shift which can be experimentally detected. With the use of the Fourier technique described here the uncertainty in the phase shift arises from the non-linearity in the response of the detector used to record the interferogram. It has been shown in Ref.6 that such non-linearity would give rise to high frequency noise in the phase distribution. An estimate of the importance of this effect can be made from the contour plot of the phase shift of Fig.3 which is reported in Fig.5. It shows that the contour curves are perturbed by a high frequency noise. This effect leads to an uncertainty typically of the order of 0.5 rad that is less than one tenth of a fringe separation.

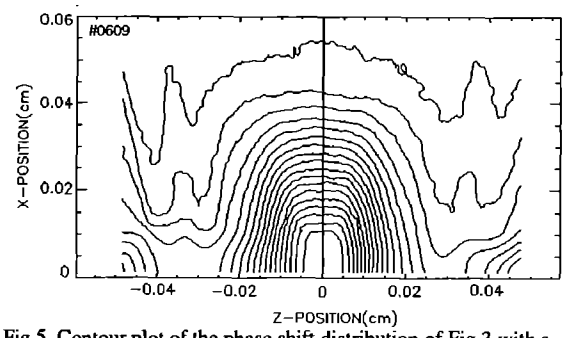

Fig.5. Contour plot of the phase shift distribution of Fig.3 with a contour interval of π, the uppermost curve corresponding to $\varphi=\pi$.

Consequently, according to Eqs.8, a single electron density perturbation along the line of sight with a scalelength of 20 μm will be detected as long as the corresponding amplitude of density fluctuation is greater than $0.01\, n_{c@1\mu m}$. This limit becomes $0.025\, n_{c@1\mu m}$ for a 10 μm scalelength perturbation.

Incidentally we observe that this procedure can also be used to determine the lowest electron density which can be detected for a given plasma extent along the line of sight of the interferometer. Assuming a plasma extent of the order of the target diameter, that is 400 μm, the uncertainty of 0.5 rad on the phase distribution mentioned above gives a lower limit to the detectable density of $\approx 10^{-3}\, n_{c@1\mu m}$ which is consistent with the measured limit given by Fig.4.

The sensitivity of the interferometric measurements to small scale density non-uniformities is a fundamental step for a correct interpretation of interaction experiments. From the point of view of the filamentation instability, for example, this study indicates that perturbations in the bulk of the plasma in the range of scalelengths of 10-20 μm, are typically characterised by $\delta n_e/n_e < 0.2$. The plasma studied here can be therefore be considered substantially free from density inhomogeneities which can efficiently initiate the instability.

REFERENCES

1 L.A.Gizzi, T.Afshar-Rad, V.Biancalana, P.Chessa, A.Giulietti, D.Giulietti, E.Schifano, S.M.Viana, O.Willi, RAL Annual Report, **RAL-92-020**, p.34, 1993.

2 L. A.Gizzi, T.Afshar-Rad, V. Biancalana, P.Chessa, A.Giulietti, D.Giulietti, E. Schifano, S. M. Viana, O. Willi, "22nd ECLIM", Paris, May. 10-14, 1993.

3 L.A.Gizzi, D.Giulietti, A.Giulietti, T.Afshar-Rad, V.Biancalana, P.Chessa, C.Danson, E.Schifano, S.M.Viana, O.Willi, accepted for publication, Phys.Rev. E (1994).

4 M.Takeda, H. Ina, S. Kobayaski, J. Opt. Soc. Am. **72**, 156 (1982).

5 M.G.Nomarski, Journal de la Physique et le Radium, **16**, 95 (1955); R.Benattar, C. Popovics, R. Siegel Rev. Sci. Instrum. **50**, 1583 (1979); O. Willi, in Laser-Plasma Interaction 4, Proceedings of XXXV SUSSP, St. Andrews, 1988.

6 Keith. A. Nugent, Appl. Optics **24**, 3101 (1985).

HIGH RESOLUTION IMAGES OF HYDRATED BIOLOGICAL SPECIMENS BY SOFT X-RAY CONTACT MICROSCOPY USING TA4

A.D. Stead[1], R.A. Cotton[1], A.M. Page[1], C.G. Steele[1], R. Bagby[2] & T.W. Ford[1]

[1]Department of Biology, Royal Holloway, University of London, Egham, Surrey, TW20 0EX, UK.
[2] Department of Zoology, University of Tennesse, Knoxville, Tennesse, TN 37996-0810, USA.

INTRODUCTION

Although several X-ray microscopy studies have reported very good resolution many of these measurements have been based upon "ideal" structures (eg gold particles or polystyrene spheres) which have little relevance to living biological material[1]. Even when biological material has been used it has often been chemically fixed[2]. Other frequently encountered specimens are diatoms[3,4]; these are silica-, not carbon-, based and, since they are dead, they are often imaged in vacuum. A more relevant test of the resolution of the technique is to determine the resolution within a living biological specimen where the contrast mechanism will be based upon minor differences in the carbon density. Using cells of the small green alga *Microthamnion* and cardiac muscle cells we have tried to determine the resolution of our current SXCM technique.

MATERIAL & METHODS

Liquid cultures of the green alga *Microthamnion* were maintained in minimal inorganic media and held in ambient conditions. A small drop of media and cells was placed onto a 1mm^2 100nm thick silicon nitride window. The photoresist (c.600nm thick polymethylmethacrylate spun onto a silicon wafer) was then placed on top and any excess liquid removed with a tissue. The environmental holder was tightened gradually and the specimen examined under a light microscope to ensure that the loading was satisfactory. The assembled holder was mounted in the target chamber installed in TA4 and exposed to soft X-rays generated from a laser plasma within 2-5 minutes. The laser energies used were typically 6-10J IR and the target material was yttrium or tungsten. This resulted in a soft X-ray fluence of up to 80mJcm^{-2} in the water window (2.3 - 4.4nm) on the window surface. Once exposed the photoresist was chemically developed in methyl isobutyl ketone (MIBK) and development monitored by interference light microscopy. Once properly developed the photoresists were examined by atomic force microscopy (AFM) using a Park Scientific Instruments BD2 microscope.

For transmission electron microscopy *Microthamnion* cells were fixed in glutaraldehyde (3%) in 0.1M phosphate buffer (pH 6.1) and post fixed in 1% aqueous osmium tetroxide. After dehydration through ethanol material was embedded in Taab resin.

RESULTS AND DISCUSSION

When examined under the transmission electron microscope the major structural feature observed is the parietal chloroplast which probably occupies the length of the mature cell. Internal to this is the nucleus, but since this is relatively small it is only seen in some transverse sections (Fig. 1). Several other smaller organelles such as mitochondria, endoplasmic reticulum and dictyosomes can also be identified in this conventionally prepared material.

In cells other than the tip cell the same organism the peripheral arrangement of the chloroplast and the basal nuclei are clearly visible (Fig. 2) in SXCM images, confirming the arrangement deduced from TEM studies. The carbon cell wall is also conspicuous and several small spherical structures are visible in Fig. 2. From our experience with other tissues we would suggest that these are mitochondria, although the position of these structures is not easily reconciled with the appearance by TEM (Fig. 1) However, these older cells are quiet thick and in consequence no internal structure has been seen within the organelles. The large spherical organelle seen towards the base of each cell in the SXCM images is thought to be the nucleus, the images of which raise two important questions. Firstly why should the diameter of the nucleus vary so greatly between cells? Secondly the spherical appearance of the nuclei suggests that organelle shape is determined, as could be anticipated, by the relative pressure of the organelle and its surroundings. However, in conventional TEM the shape of the nucleus, and other organelles, is rarely spherical. This indicates that considerable distortions to the shape of the nucleus, and presumably other organelles, has occurred during chemical fixation.

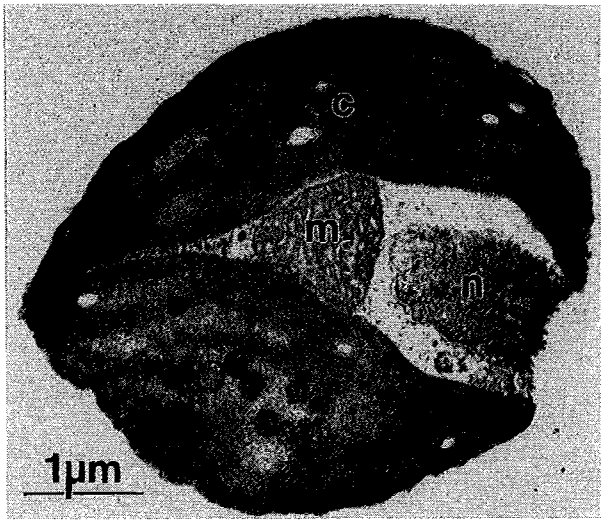

Figure 1 Transmission electron micrograph of *Microthamnion* showing the peripheral chloroplast (c), mitochondrion (m) and nucleus (n) and other organelles.

In tip cells of *Microthamnion*, the cell structure differs between those cells which are not branching (Fig. 3) and those which are (Fig. 4). In both there is an area at the very tip of the cell which would appear to be relatively carbon-dilute and thus the images in the photoresist are not as prominent. In the non-branching tips the parietal chloroplasts are clearly identifiable but these are less obvious in the branching cells. In these latter cells several fine structural details appear to have been imaged and, at higher magnification, some of these appear as a stack of overlapping discs. These three small discoid structure possibly correspond to a stack of thylakoids from within a chloroplast. Certainly the diameter of these structures (400nm) is similar to that recorded for thylakoid sacs[5]. The only contrast difference between each thylakoid would be the carbon-containing double membrane and possibly the internal contents of this disc-like structure. The height profile across this image (Fig. 6) clearly identifies the three separate structures and, using conventional edge analyses procedures, the resolution of this image approaches 30nm. Such a resolution is only possible when a AFM is used to observe the photoresist; scanning electron microscopy of these resists cannot achieve such a resolution.

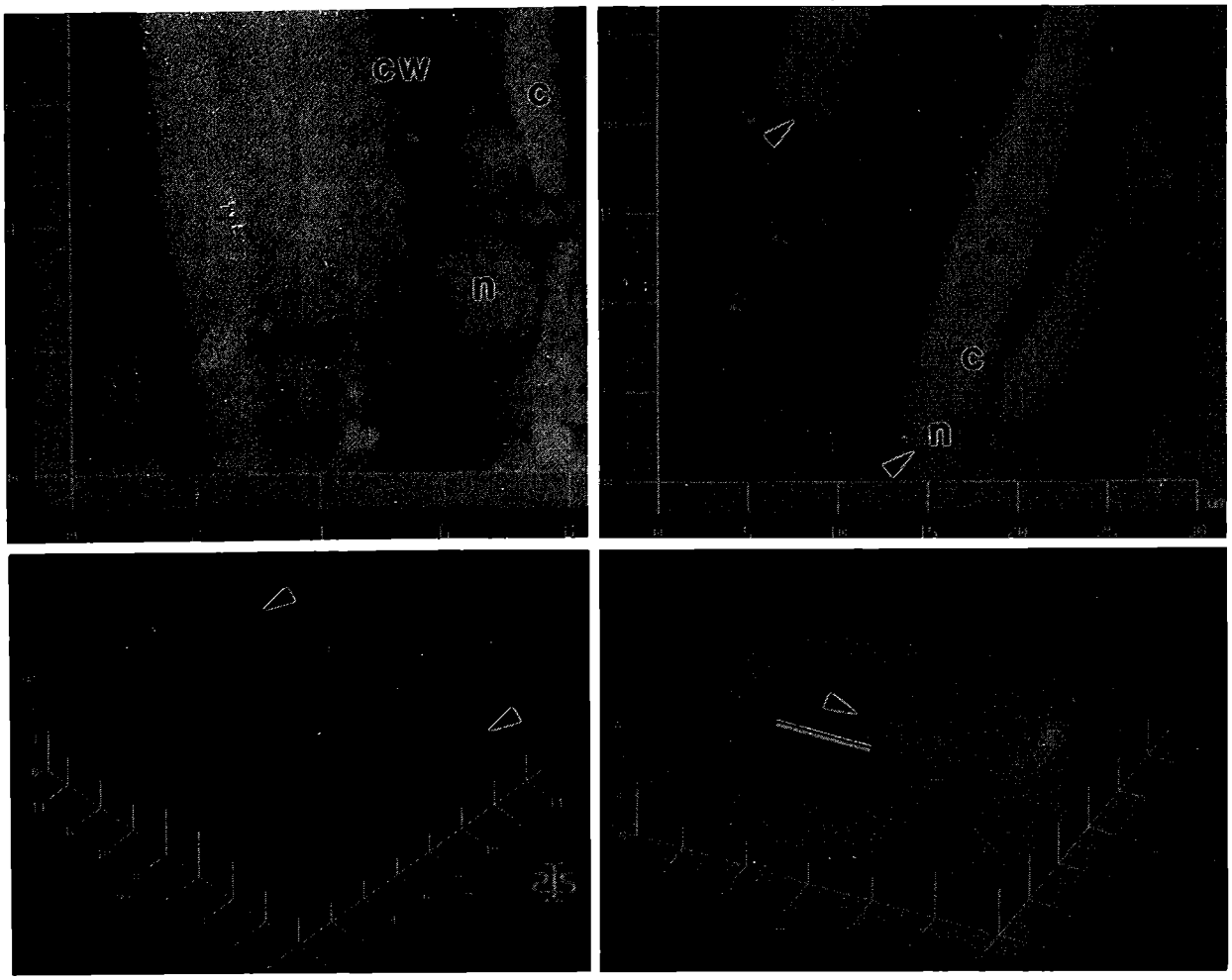

Figure 2 In the older, larger cells of *Microthamnion* the peripheral chloroplast (c) and basal nucleus (n) are clearly identifiable. Internal detail of these structures is not, however, visible as these cells are considerably larger and possess a much thicker carbon-containing cellulose cell wall (cw) than the tip cells.

Figure 3 Images of non-branching tip cells. The peripheral chloroplast (c) and nuclei (n) are clearly identifiable, the very tip region (arrows) does not contain any major organelles.

Figure 4 Image of a branching tip cell. The distal part of the cells are relatively carbon-dilute and hence the image of this area is less prominent (arrows). The remainder of the cell contains images of numerous small structural features.

Figure 5 AFM image of the developed photoresist showing the internal detail of one organelle. The edges of three overlapping discoid structures, probably thylakoids, have been imaged (arrows). The height profile across the image (position indicated by the line) is presented in Fig. 6.

It is also interesting to note that the chemical development time required to obtain the images varied; in the case of the older, denser cells 20-50 minutes development was needed (Fig. 2) but for the tip cells as little as 10s (Fig. 3) was needed. This difference cannot be entirely explained by differences in X-ray flux and must be mainly due the very much reduced carbon density in the smaller tip cells. In general however, images recorded using tungsten as a target required greater development than those using yttrium.

Images of biological specimens that have periodic structures of known size, with sufficiently small dimensions can provide excellent material to assess the capabilities of the technique. Like *Microthamnion*, cardiac muscle has many features which, if successfully imaged, provide information on the resolution which can be obtained. Fig. 7 shows an SXCM image of a living, hydrated single cardiac muscle cell. A single myofibril near the edge of the cell can be seen whose sarcomeres are 2.3μm long as measured between Z-lines.

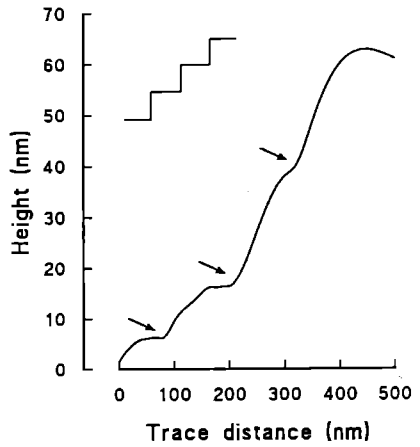

Figure 6 Height profile across the image in Fig. 5. The three discoid structures are clearly overlapping one another. The height difference between each successive stack is not constant due to the non-linearity in the response of the PMMA resist. Edge analysis indicates a resolution of approximately 30nm.

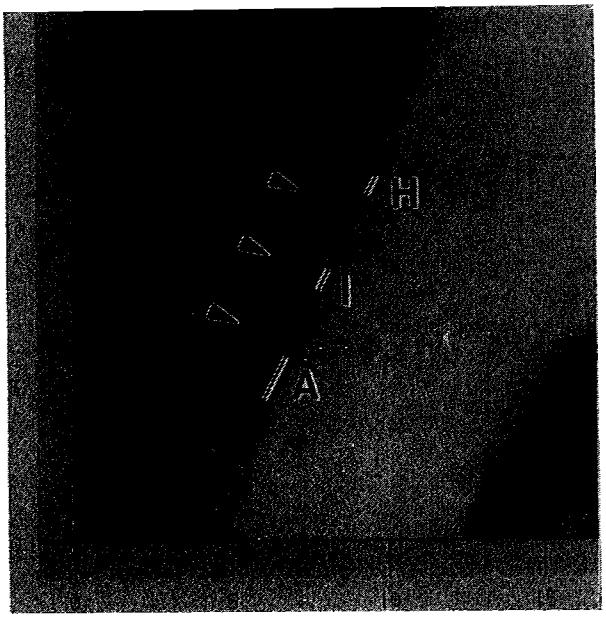

Figure 7 AFM image of a cardiac muscle cell, the banding pattern is clearly visible in the myofibril situated at the edge of the cell. For explanation of labelling see text.

On either side of the Z-bands are the more lucid I bands. The I-bands contain only thin filaments which are attached to the Z-lines and these extend longitudinally. In the middle of the sarcomeres are denser A-bands which contain thick filaments and the ends of thin filaments which are interspersed between the ends of thick filaments. In some A-bands there is a less dense zone bisecting the A-band usually referred to as the H-zone, which contains only thick filaments since the thin filaments do not always penetrate to the middle of the A-band. Deeper in the cell, myofibrils and their sarcomeres are not so clearly visible, but some dense longitudinal masses are found between the myofibrils which are probably mitochondria. The mitochondria are X-ray dense due to their inner membranes being packed with cytochromes which are composed of iron-containing proteins used in oxidative metabolism. Within these cells repeating structures smaller than 200nm (I-bands) are clearly discernable making these cells, or perhaps a single myofibril, excellent living specimens with which to study the factors which affect resolution. Myofibrils have indeed been extensively used in soft X-ray scanning microscopy[6] but the resolution obtained was comparable to the present study. The main advantage therefore in the use of soft X-ray contact microscopy is the ability to image the specimens rapidly, without the interference of radiation damage which has been demonstrated to occur when myofibrils are imaged by scanning X-ray microscopy[6].

ACKNOWLEDGEMENTS

This work was supported by a SERC grant (REF). One of us (RB) is indebted to Burrows-Welcome for the provision of a travel grant. We are grateful to Pete Anastasi (Kings College, University of London) for the manufacture of silicon nitride windows and photoresist materials; to the staff of the Electron Microscope Unit for the provision of electron microscope facilities and to Oxford University for access to the atomic force microscope. The cardiac muscle cells were kindly prepared by Dr. Terrar, Oxford University.

REFERENCES

1. R.A. Cotton, A.J. Jackson, A. Ridgeley, A.D. Stead and T.W. Ford. Annual Report to the Laser Facility Committee, Rutherford Appleton Laboratory. pp. 32-33, 1991.
2. K.S. Richards, A.D. Rush, D.T. Clarke and W.J. Myring. *Journal of Microscopy*, **142**, pp. 1-7. 1986.
3. T.W. Ford, A.D. Stead, C.P.B. Hills, R.J. Rosser, R.J. and N. Rizvi.*Journal of X-ray Science and Technology*, **1**, pp. 207-210, 1989.
4. R.J. Rosser, K.G. Baldwin, R. Feder, D. Bassett, A. Coles and R.W. Eason. *Journal of Microscopy*, **138**, pp. 311-319, 1985.
5. B.E.S. Gunning and M.W. Steer, *Ultrastructure and the Biology of Plant Cells*. Edward Arnold, London. 1975.
6. M. Bennett, G.F. Foster, C.J. Buckley and R.E. Burge. *Journal of Microscopy*, **172**, 109-119. 1993.

DIRECT OBSERVATION OF STRAIN RATES IN EXCESS OF 2 x 10^9 s^{-1} IN LASER-SHOCK CRYSTALS.

N.C. Woolsey & J.S. Wark

Clarendon Laboratory, Department of Physics, University of Oxford, Parks Road, Oxford OX1 3PU. UK

INTRODUCTION

Shock compression of solids is a violent process involving some of the most extreme physical processes known. Stress levels range from a few kilobars to several hundred megabars for durations from nanoseconds to microseconds. Solid materials are brought to unique states at strain rates far in excess of those encountered normally, and processes such as rapid dislocation nucleation, growth and material fracture occur.

Using time-resolving x-ray streak cameras we have made x-ray diffraction measurements from shocked single crystals on time scales comparable with dislocation generation time scales[1,2]. In this paper we report on the measurement of elastic strain rates in excess of 2x10^9 s^{-1} using x-ray diffraction measurements with time resolutions as short as 15 picosecond.

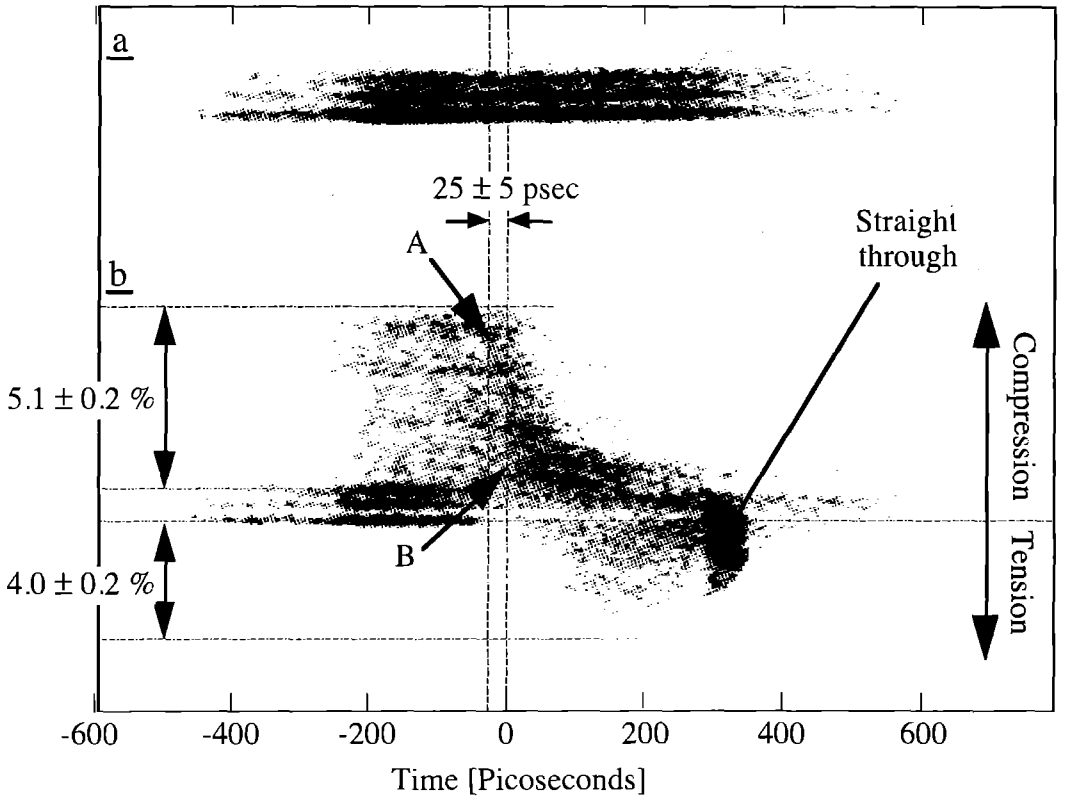

Figure 1 X-ray streak camera record of shock breakout from single crystal single shocked at 10^{10} Wcm^{-2} in a 66 psec FWHM Gaussian laser pulse.

EXPERIMENTAL

An example of a time-dependent x-ray rocking curve with strain rates close to 2x10^9 s^{-1} is shown in Figure 1. Experimental details are published elsewhere[3]. In this experiment the target consists of a 60 μm thick silicon crystal coated with a 1000 Å aluminium film overcoated with a 20 μm thick plastic layer. The plastic layer is transparent to 1 μm radiation up to irradiances around 10^{10} Wcm^{-2}, at these irradiances compressions of above 100 kbar are launched into the target, the plastic contines the ablating aluminium film increasing the duration and strength of the compression. The laser pulse duration was 66 psec FWHM Gaussian. A laser-produced-plasma titanium helium-alpha x-ray source ($\lambda = 2.6\text{Å}$) was used.

There are two spectra in Figure 1, spectrum a is recorded from an unshocked perfect silicon crystal, this streak serves as a temporal record of the strongly time-dependent nature of the titanium helium-alpha x-ray source. Spectrum b is recorded from a shocked crystal, initially identical to a. An artefact labelled "straight through" in Figure 5.11 is caused by x-rays passing straight through the streak camera to the image intensifier: a result of experimental geometry.

ULTRA-HIGH STRAIN RATES

The approximate uniform spread of diffracted x-rays at all angles between zero and peak compression seen in Figure 1 suggests x-rays probe all of the rarefaction following the shock and that the shock-front-rarefaction occupies a thin layer. The intensity of the shifted rocking curve increases as the shock approaches the crystal surface. At shock breakout an immediate and rapid fall in compression is observed as a tensile wave evolves. Bands at constant strain are observed in the compression part of the rocking curve, it is not clear how these bands originate, they may be related to structure on the shock front or rarefaction. Understanding the influence of the laser pulse length on time-

dependent rocking curves is provided through numerical simulation of shock compression and x-ray diffraction[4].

Close to shock breakout ultra-high strain-rates are observed. The measurement of these strain-rates is made by determining the change in strain with time of a feature in the rocking curve. A measurement is indicated by the points labelled A and B in Figure 1. During shock breakout peak compression is seen to decay by approximately 5 % in 25 psec giving strain rates close to $2x10^9$ s^{-1}. The previously highest reported strain-rate of $4.5x10^7$ s^{-1} were made by Gilath *et al.*[5] during laser-induced spallation studies in aluminium alloys. Strain rates of $2x10^9$ s^{-1} are in a new experimental regime.

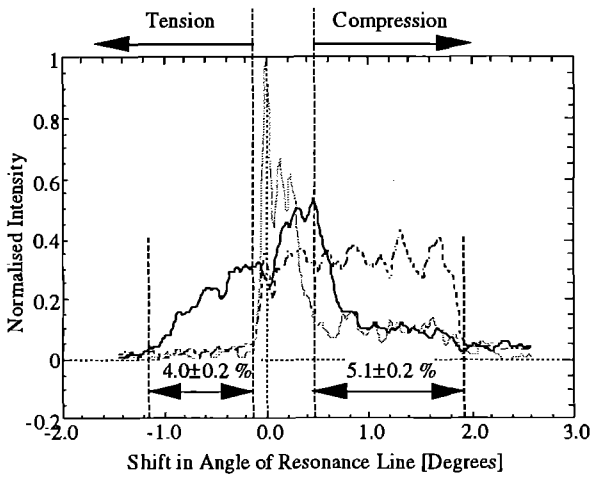

Figure 2 Cross-sections taken from Figure 1 showing the spectra at peak compression and peak tension.

ULTIMATE STRENGTH MEASUREMENT

At strain-rates close to $2x10^9$ s^{-1} and peak compression of ~5.2 % a large amplitude tensile wave develops, reaching maximum tensile strains of 4 % approximately 100 psec later. Cross-sections taken from Figure 1 are shown in Figure 2. Compression and tension is measured from the maximum shift in the spectra to high angle and low angle respectively. Due to the finite spectral width of the x-ray source, strain is measured from the lithium-like dielectronic satellites (centred 2.638 Å) for material in compression and from the resonance line (2.612 Å) for tensile strains. This process is clearly shown in Figure 1.

Data such as this provide a unique method of investigating the ultimate strength of solids[6]. As the strain rate increases the normal failure mechanisms which proceed through the effects of dislocations and cracks become less significant. A limiting strain rate is reached when a solid fails by pulling the lattice apart.

Grady and Lipkin[7,8] presented data and a theoretical model showing that the failure strength of brittle solids increases with increasing cube root of strain rate. Using this model the ultimate strength for silicon along [111] is expected to be reached at strain rates of $1.5x10^{10}$ s^{-1}. Strain rates of $2x10^9$ s^{-1} are below this but tensile strains of 4.0 % (approximately 7.6 GPa) are the highest tensile strains observed in large samples and are comparable to the tensile strains measured from a few micron diameter single crystal whiskers[9]. Recent Russian work[10] has shown the ultimate strength of molybdenum is reached within the current experimental range at strain rates of $5x10^8$ s^{-1}.

CONCLUSION

Using the x-ray diffraction technique ultra-high strain rates, almost 2 orders of magnitude above other report studies have been measured. This has led to the development of a novel technique for the measurement of the ultimate strength of solids. With further improvement in time resolution this technique could be used to study other ultra-high strain rate phenomena such as the the strain-rates encountered in the shock front. X-ray streak cameras can have temporal resolutions up to 1 psec[11] making shock front thickness measurements a serious proposition. At these resolutions measurements of the order a few tens of interatomic spacings can be made.

REFERENCES

(1) C.S. Coffey, Energy localisation in rapidly deforming crystalline solids. Phys Rev., B 32, 5335-5341 (1984).

(2) C.S. Coffey, A model for dislocation sources in a shock or impact enviroment. J. Appl. Phys., 62, 2727-2732 (1987).

(3) J.S. Wark, D. Riley, N.C. Woolsey, G. Klein, R.R. Whitlock, Direct measurements of compressive and tensile strain during shock breakout by use of subnanosecond x-ray diffraction. J. Appl. Phys., 68, 4531-4534 (1990).

(4) N.C. Woolsey, J.S. Wark, Time dependent simulations of x-ray diffraction from laser shocked crystals. This rep. (1994).

(5) I. Gilath, S. Eliezer, M.P. Dariel, L. Kornblit, Brittle-to-ductile transition in laser-induced spall at ultrhigh strain rate in 6061-T6 aluminium alloy. Appl. Phys. Lett., 52, 1207-1209 (1988).

(6) J.S. Wark, N.C. Woolsey, R.R. Whitlock, Novel measurements of high-dynamic crystal strength by picosecond x-ray diffraction. Appl. Phys. Lett., 61, 651-653 (1992).

(7) D.E. Grady, J. Lipkin, Criteria for impulsive rock fracture. Geophys. Res. Lett., 7, 255-258 (1980).

(8) D.E. Grady, The spall strength of condensed matter. J. Mech. Solids, 36, 353-384 (1988).

(9) R.J. Stokes In *Fracture*; H. Liebowitz, Ed.^Eds.; Academic Press: New York, 1972; Vol. VII.

(10) G.I. Kanel, S.V. Razorenov, A.V. Utkin, V.E. Fortov, K. Baumung, H.U. Karow, D. Rusch, V. Licht, Spall strength of molybdenum single crystals. J. Appl. Phys., 74, 7162-7165 (1993).

(11) O. Willi, Private communication. (1992).

INTERPENETRATION AND STAGNATION OF COLLIDING PLASMAS

RJ Taylor AJ MacKinnon R Mansukhani and O Willi

Imperial College of Science Technology and Medicine

INTRODUCTION

Plasma collisions occur in many situations where a laser is used to illuminate a target. The filling of a cavity with plasma will necessarily result in a collision between streams, and other applications such as double-foil x-ray laser experiments involve the collision between counter-streaming plasmas. Velocity gradients in the plasma blown-off from a planar target surface will also result in collisions as the lateral flows from neighbouring hot-spots meet. We report here experiments designed to isolate the processes involved though the collision of laser-accelerated foil targets.

Thin foil targets can be accelerated to velocities in excess of 100 km/s when subject to intense laser irradiation. If two such targets driven together at these velocities interact, significant ion heating will occur, as a large amount of kinetic energy per ion (>1.5keV) can be transformed into heat and ionisation through scattering. Alternatively, if the cross-section for interaction between the foils is low enough, they can stream through each other with little or no interaction, and hence without heating each other. The interaction cross-section is determined at high density by the ionic volume, since for material near solid density, the constituent atoms lie adjacent to each other, with the inter-nuclei space occupied by electrons, mostly in bound states. Ions at the velocities considered here are unable to penetrate such a wall. As material density decreases, however, the ions separate from each other, and at sufficiently low density, their physical size contributes little to the collision cross-section. If the material is ionised, the predominant mechanism for interaction with an incident ion of similar size is expected to be ion-ion coulomb collision. The mean free path (MFP) for scattering through this process is given by Berger et al.[1] as:

$$\lambda_{ii}=m_i^2|U|^4 / 4\pi N_i Z^4 e^4 \ln \Lambda \qquad (1)$$

where U is the combined velocity of the interacting particles. Thus, a low-density, high velocity interaction is necessary for interpenetration to occur on a scale comparable with density scalelengths, particularly if the material is ionised, due to the strong dependence of the MFP on Z, the ionic charge.

MODELLING PLASMA COLLISIONS

Conventional fluid codes assume an entirely collisional system, where λ_{ii} is small compared to the system dimensions. In such a system, no interpenetration is possible, and each part of the plasma retains its position relative to neighbouring regions. This enforces stagnation, with a shock front forming across the boundary between two colliding plasmas, and heating occurring due to the work done by the kinetic energy of the incoming material in compressing what is already there. When λ_{ii} is not insignificant when compared to the system's dimensions, however, this model is no longer valid, and explicit treatment of the interaction is required. This can be achieved with a particle-in-cell approach, which immediately lends itself to the modelling of partially collisional systems. Alternatively a kinetic treatment may be applied[2] or a modified fluid treatment that treats each plasma independently, and hence allows them to flow through each other, with an exchange of energy from one stream to the other. A two fluid model such as this has been developed[3], and was used to model the only published experimental data available on the conditions requisite for stagnation[4].

EXPERIMENT

An experiment was carried out in Target Area 2 of the Vulcan glass laser where thin, parallel Aluminium foils were irradiated on their outside faces, causing ablative acceleration which drove the foils together. The foils were irradiated at ~1E14 Wcm^{-2} for 800ps with green (2ω) light. The resulting collision was recorded through side-on XUV emission imaging, resulting in a spatial resolution of <5μm. The temporal evolution was recorded by streaking the emission along the axis of the two foils (the line along which they were accelerated). The multi-layer mirror forming the imaging element of the system was coated with a multi-layer stack providing a bandpass reflection at 100eV+/-5eV, a spectral region in which the emission from the targets used here is dominated by bremsstrahlung, as confirmed by spectroscopic measurements performed during the experiment. The level of bremsstrahlung emission is a strong function of density (N_i^2) and ionisation (Z^3), but a weak function of temperature.

In an attempt to observe both a collisional interaction, where stagnation is exhibited, and a collisionless interaction, where interpenetration is observed, foils of different thicknesses were used, such that for thicker foils, the laser did not burn through, but rather left a high-density region at the rear of the foil, ensuring a short MFP and hence a collisional interaction. This region will only have been heated by x-rays and shock transit at the point of collision, which will result in a pre-heat of only a few eV. Thinner foils were exploded by the laser, resulting in collision between two high-velocity, low-density plasma clouds, each with electron temperatures approaching 1keV. Equation (1) suggests that these conditions will result in interpenetration, and little or no interaction, and hence little ionic heating. This will result in a lack of heightened emission in the midplane at the point of collision, in contrary to the collisional case, where the increased ionisation produced through the extensive ionic heating will produce a greatly enhanced level of bremsstrahlung emission.

RESULTS

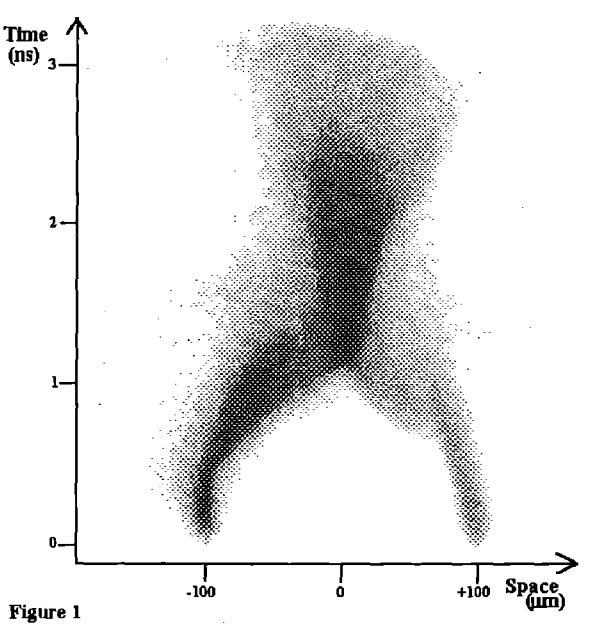

Figure 1

Figure (1) shows a streak image recorded for the collision of two thick (1μm) Aluminium foils. The combined velocity at the point of impact is 140km/s, and as expected, the foils did not burn through during the laser pulse. This is revealed through the continued high-intensity emission observed even after the 800ps pulse, betraying the high electron density present only prior to burnthrough. When the foils meet, a the formation of a shock front is observed, and very bright emission is recorded, suggesting a high level of ionisation. The material density can be estimated from the size of the emitting region,

and by assuming that approximately half of each foil is ablated during the acceleration, as predicted by hydrocode simulations. This suggests an average density of ~0.1g/cc 500ps after collision, and hence the Aluminium must have been several times ionised by the collision process to produce the observed emission, which is several times brighter than that observed during acceleration. This is consistent with the observed velocity with which the central region expands after collision: ~70km/s. For a conservative first estimate, we can assume that all ions in the central region move with this velocity, and that all these ions had a velocity of 140km/s prior to collision. This represents a conversion of 1.4keV per ion from kinetic energy, which must go into increasing the ion temperature and ionising the material.

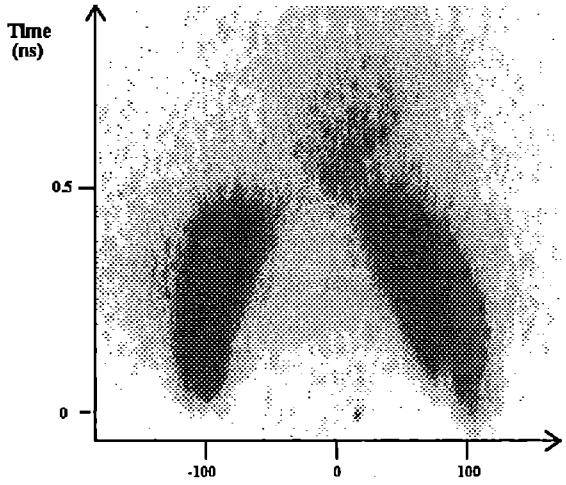

Figure 2

Figure (2) shows a streak for similar experimental conditions, but with 0.25μm foils in place of the 1μm pair. It can be seen that these foils are exploded by the laser illumination, and that the streams subsequently fly though each other with no evidence of significant heating, and no observable shift in their trajectory. The velocity of the streams prior to collision was 800km/s, which is in good agreement with hydrocode predictions. Taking the appropriate values from these simulations, the MFP as given by eqn (1) is several times the system dimensions, and hence we have directly observed interpenetration in support of the predictions made by Berger et al.

SIMULATION AND INTERPRETATION

The collision between the thinner foils is well modelled by assuming an entirely collisionless system. This assumption allows us to perform a simulation for a single foil, with the entire mesh mirrored about the midplane for comparison with the experiment. The extent of this agreement suggests that the collisionless assumption is valid, and hence that the streams interpenetrate with no significant interaction.

The collisional case, however, can be modelled by imposing a reflective boundary at the midplane and accelerating a single foil towards it. Such simulations have been performed with the 1-D hydrocode MEDUSA and the 2-D Eulerian code POLLUX. The 2-D simulation takes account of the $sinc^2$ beam profile used to drive the foils, and is in good agreement with the experimental observable prior to collision. After collision, however, the simulation falls down, since it allows the central region to decompress at a velocity close to that with which the foils met. This problem was also observed in MEDUSA unless explicit account of the energy lost to ionisation was taken into account with the time-dependant, non-local-thermodynamic-equilibrium ionisation package available in version 1.03[5]. This suggests that a significant fraction of the kinetic energy serves to ionise the plasma at collision, causing the inelastic collision observed experimentally. Figure 3 shows the density evolution as predicted by MED103 for the experimental conditions prevailing in the shot shown in figure 1.

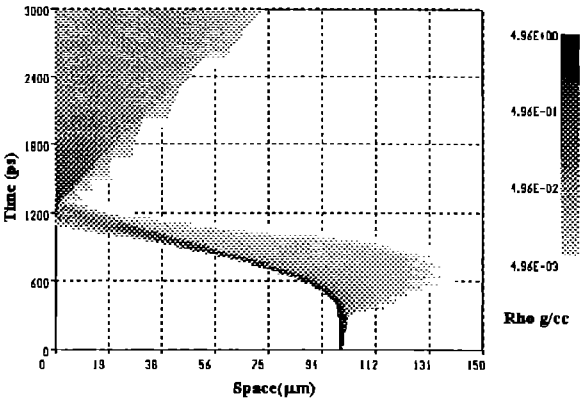

Figure 3: MED103 Simulation of the density evolution during collision between two 1μm Aluminium foils irradiated at $6x10^{13}Wcm^{-2}$. Darker regions indicate higher material density. Only one half of the collision is shown, symmetry about x=0 is assumed.

FUTURE WORK

The plasma formed by the high-density collision provides us with a high-density, large scale plasma at a higher temperature than attainable with other techniques, and promises to prove invaluable for opacity studies and for building more detailed models of the conversion of energy between kinetic and thermal forms. The interpenetrating plasmas observed with the thinner foils have prompted us to start a more detailed investigation of the processes at work, with experiments currently underway which aim to pinpoint the conditions requisite for stagnation to set in and interpenetration to cease, which has major implications in laser-plasma physics, particularly with regard to the uniformity of the plasma blown-off from a target surface. Should high velocity gradients be present, such as may be created by hot-spots in the beam or a non-uniform target surface, and the conditions for interpenetration not met, then a pile-up in density will occur between counter-streaming plasma regions. This will magnify under subsequent illumination, even if the drive is smoothed, seeding instability growth in the conduction region and precluding the possibility of uniform direct-drive without a perfectly smooth beam to drive the target, and a perfectly smooth target surface.

REFERENCES

1: R.L.Berger, J.R.Albritton, C.J.Randall, E.A.Williams, W.L.Kruer, A.B.Langdon and C.J.Hanna. Phys. Fluids B 3 (1), 3 January 1991

2: O.Larroche, Phys. Fluids B 5 (8), 2816, August 1993

3: S.M.Pollaine, R.L.Berger and C.J.Keane, Phys. Fluids B 4 (4), 989, April 1992

4: R.A.Bosch, R.L.Berger, B.H.Failor, N.D.Delameter, G.Charatis nd R.L.Kauffman. Phys. Fluids B 4 (4), 979, April 1992

5: A.Djoui and S.J.Rose, J.Phys B:At.Mol.Opt.Phys,25,2745 (1992)

LASER-PRODUCED PARTIALLY-DEGENERATE STRONGLY-COUPLED PLASMAS IN CONFINED GEOMETRY

G. R. Bennett[1], J. S. Wark[1], D. J. Heading[1], N. C. Woolsey[1], H. He[1], R. Cauble[2], R. W. Lee[2] and P. Young[2]

[1]Department of physics, Clarendon Laboratory, University of Oxford, Parks Road, Oxford, OX1 3PU, UK
[2]Lawrence Livermore National Laboratory, Livermore, CA 94550, USA

INTRODUCTION

The production of low-temperature high-density plasmas is of great interest to astro and plasma physicists alike. Such plasmas are generally strongly-coupled and partially-degenerate in character, and may be created in ion or electron beams, self-pinching discharges, laser fusion, capillary discharges, laser-produced plasmas etc. Strongly-coupled plasmas are predicted to have equation of state (eos) and transport properties quite different from those of classical plasmas, in addition, the various theories developed for such conditions differ quite dramatically in their predictions from one theory to another. Attempts by previous workers to measure such properties have always been limited by rather poor density and temperature uniformity, however, the plasma production method described below appears to overcome these uniformity limitations. This report describes the complete experimental investigations of the P, V, E equation of state and visible spectroscopy of the plasmas produced; also described are preliminary measurements of visible opacity and low-frequency resistivity.

The plasma is laser-produced and inertially confined between two quartz substrates which are separated by a well-defined micron-scale gap; and where one of the substrates forms a piezoelectric pressure transducer with nanosecond time resolution and a 1-40 kbar usable range. The target design is shown below in figure 1 and is described in other reports along with descriptions of the experimental details.[1-3] The results presented here were obtained from experiments carried out in the TA4 facility of the VULCAN laser during 1993.

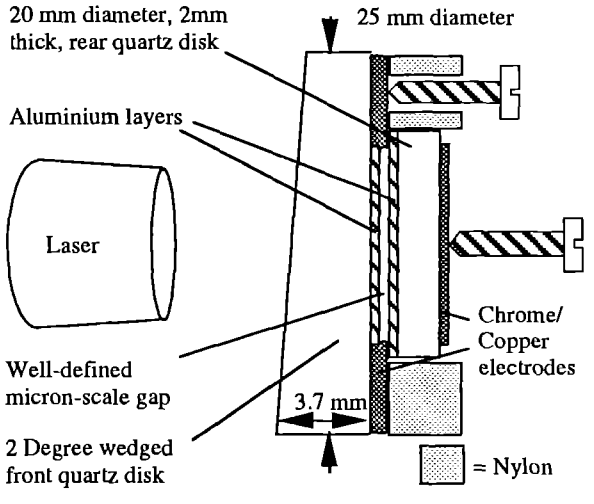

Figure 1 Target and target holder

EQUATION OF STATE

In the ideal-gas limit the plasma pressure is given by

$$P = \frac{2}{3}U \qquad (1)$$

where U is the energy per unit volume; however, for any real plasma the pressure is related to energy per unit volume by

$$\alpha = \frac{3P}{2U} \qquad 0 < \alpha < 1 \qquad (2)$$

where $1 - \alpha$ indicates the fraction of energy used in ionisation, latent heats of melting and vapourisation etc. It is useful to present the data as alpha versus pressure with alpha ranging from zero (a solid material) to one (an ideal gas). The data is compared - in figure 2 - with two eos models of the SESAME library; i.e. the Thomas-Fermi-Dirac (TFD) and Saha-Boltzmann (SB) models. The measured densities, as a fraction of solid aluminium, range from 0.46 % (low density) to 0.98% (high density) with both the TFD and SB models predicting intermediate densities to have alpha values resting between the high and low density curves. Two laser pulses of 1 or 4 nsec FWHM Gaussian were used throughout the experimental work. For the 2-20 kbar range the measured values of alpha are some what less than those predicted by TFD and SB; although for the 20-35 kbar range a good agreement with TFD is observed.

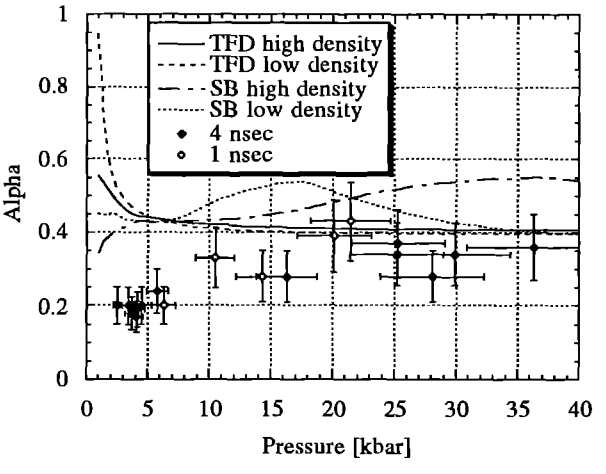

Figure 2 Data comparison with two eos theories

If one assumes the SESAME tables are correct, then the low α values are caused by energy leaking out of the plasma. The fractional absorbed energy which is lost appears to increase with decreasing pressure, and therefore the actual energy lost may be similar for all data shots. A certain amount of quartz is expected to melt implying there exists a surface of constant temperature at the molten/solid quartz boundary. The quantity of heat diffused into a semi-infinite strip of material - with one end held at constant temperature - is described by a very simple equation.[4] Indeed this simple heat diffusion model would explain the apparent similarity in values of *energies lost* over a wide range of pressures. This diffusion model and the SESAME equation of state subroutines were incorporated into a code developed to include:- energy deposition by a Gaussian laser pulse, and both effects of the compression of the confining walls: i.e. the changing plasma density and the PdV work done.
Simulations using this code explained very well the apparent deviation of data from theory in the 2-20 kbar region, and the good

agreement obtained in the 20-35 kbar range. A typical 20 kbar pressure shot is shown in figure 3 along with the pressure histories predicted by the TFD and SB models.

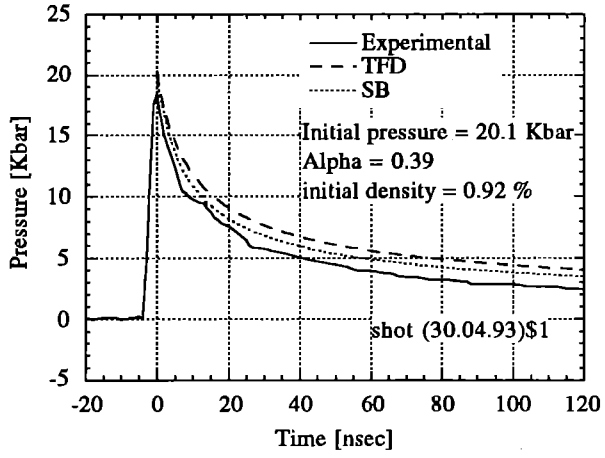

Figure 3 A 20 kbar pressure history along with two predicted pressure histories

Notice above the excellent agreement with theory. Such comparisons give confidence in the overall plasma uniformity and indeed the validity of SESAME itself. One would expect the temperature history predicted by SESAME to be equally valid and this is shown below for the same data shot.

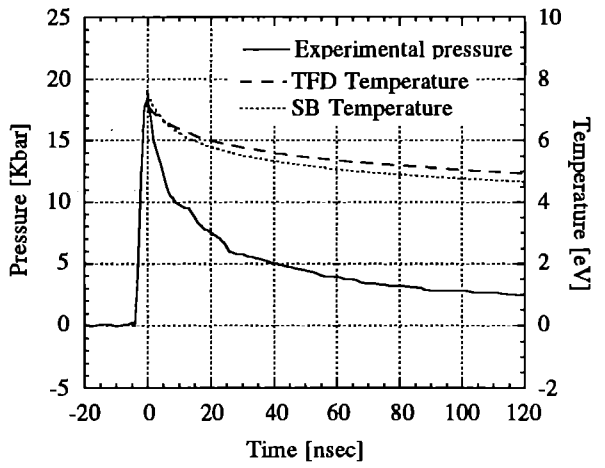

Figure 4 As figure 3 but with the predicted temperature histories

It is now clear that the production plasmas with parameters 20-35 kbar and 0.5-1.0% solid density can be reliably produced. Plasmas in the 2-20 kbar range are not as interesting due to their rather weakly-coupled nature.

VISIBLE SPECTROSCOPY

The visible spectroscopy of the 20-35 kbar well-characterised plasmas formed the next stage of the project. Each spectral line was expected to be very broad due to the high electron density, and therefore the relatively high dispersion of conventional grating spectrometers would be of little use. Furthermore, the comparatively low luminosity of the plasma itself and the low throughput of such spectrometers may result in a signal well below the detection level of the streak camera. A prism spectrometer overcomes these two limitations as it has a very high throughput and a very low dispersion. A visible prism spectrometer was built *in-situ* in TA4 with a 400-700 nm wavelength span. Glass achromatic optics were used throughout and a 10x de magnified image of the plasma was focused onto the entrance slits of the spectrometer. The spectrometer was coupled to an Imacon 500 streak camera fitted with reflective streak optics and two image intensifiers in tandem to increase sensitivity.

Many high-quality low-noise streaks were obtained (using 5 nsec/mm and 1 nsec/mm) with all streak showing no evidence of spectral lines. In contrast, streaks of unconfined aluminium foil showed many lines, and so the well-characterised plasmas were either optically thick and/or were emitting free-free Bremstrahlung radiation. The camera was triggered many 10s of nanoseconds after the laser pulse for the well-characterised plasmas and again no evidence of spectral lines was observed.

VISIBLE OPACITY

Measurements of the plasma opacity in the visible band were obtained by probing a plasma with a 1 nsec back lighter. This light source was obtained by splitting the TA4 beam in two, delaying by 3.5 nsec, and then focusing down onto a metallic block. The polychromatic light so produced was collected by the very large solid angle of an f/1 glass achromat (placed at its focal length distance from the block). This light was de magnified and collimated using a positive/negative lens system before being directed through the plasma. The light pulse was not quite bright enough to streak. However, because of its short 1 nsec duration, time resolving was not really necessary; and therefore the streak camera was used in focus mode - for which case the back lighter was bright enough. Preliminary analysis of the data indicates that a 3.25 micron thick, 1% solid density aluminium plasma of $\geq$ 10 kbar is optically thick at $\geq$ 400 nm. Opacity calculations for such plasma parameters and wavelengths suggest optical depths of around 2-3, and unitary optical depths at around 200 nm.

LOW-FREQUENCY RESISTIVITY

Possibly the most promising and simplest future experiments are the simultaneous measurements of the plasma low-frequency resistivity and its pressure. Several resistivity theories have been developed especially for the strongly-coupled regime, although they all display a wide variation of resistivity values for similar plasma parameters.

A trial resistivity experiment involved passing a constant current through a standard resistor in series with the aluminium foils that were to be vapourised. The voltages across the standard resistor and across the foils were monitored with the twin 1-$M\Omega$ dc-coupled loads of a Hewlett Packard 1-GSa/s digital scope. The resistor voltage gives the current history throughout the whole circuit; whereas the voltage history across the foils - in conjunction with this current history - allows the plasma resistance to be determined directly. The vapourised foils fill the *known* micron-scale gap whilst their length and width remains constant. Hence the rectangular strip of plasma with well-defined dimensions and the directly measured plasma resistance allows its resistivity to be determined. The experimental method works well and certainly deserves a thorough investigation in the future.

ACKNOWLEDGEMENTS

We are happy to acknowledge the assistance of:- the VULCAN laser staff (Rutherford Appleton Lab, UK), Chris Goodwin (Manager, Thin Film Facility, Department of Physics, University of Oxford, UK), and Ray Reed (Sandia National Labs, New Mexico, USA) for his very helpful discussions on x-cut quartz piezoelectric pressure transducers.

REFERENCES

1. RAL CLF 1993 annual report. pg 43-44
2. G. R. Bennett, J. S. Wark *et al* J. Appl. Phys. to be published
3. G. R. Bennett. D.Phil thesis. to be completed
4. J. M. Hill, and J. N. Dewynne: Heat Conduction, Blackwell Scientific Publications, ISBN: 0632017163.

OPTICAL SPECTROSCOPY OF DENSE METAL PLASMAS

D.J. Heading, G.R. Bennett, J.S. Wark

Clarendon Laboratory, Department of Physics, University of Oxford, Parks Road, Oxford OX1 3PU, UK

INTRODUCTION

The behaviour of dense plasmas is of great interest for fusion and stellar physics. A principle method of diagnosing plasmas is through the light emitted from them. At high densities and low temperatures the normal approximations used to calculate the spectral line shapes break down due to the strong correlation between the ions and also the breakdown of the impact approximation for the electrons. It is important to generate dense cool plasmas to examine the effect of the plasma environment on the radiators.

Previous attempts to generate plasmas at above 10^{17} electrons/cc have been made. However, the sources generally are small and inhomogenous, and may be optically thick. This leads to considerable problems with determining both the plasma and line shape (width and shift) parameters. These sources include z-pinches [1], rail-guns [2] and freely ablating plumes [3]. We present here a source for a laser produced plasma at high densities and low temperatures. Our plasma is optically thin under most circumstances and represents a considerable improvement in sources for the spectroscopy of dense plasmas.

To date there has been relatively little work on the spectroscopy of metal plasmas, due largely to the difficulty of introducing the sample into a discharge tube. Recent work on freely ablated plumes has provided data on plasmas at moderate densities and low temperatures [4]. We present here observations of an aluminium plasma at above 10^{19} electrons/cc and a few eV.

EXPERIMENTAL LAYOUT

The target consisted of a supporting quartz disk, a metal foil (in our case aluminium) and a quartz confining layer. The gap between the confining layer and the foil was set by layers of metal foil, 50 microns thick. The confining layer was transparent to the laser light. The laser beam was the Vulcan laser which gave up to 9J in a 4.5 ns pulse at 1.053 microns. The actual energy on target was calibrated using a Gentec ED-200 energy meter with calibrated neutral density filters. The energy on target was measured to be 2-3J.

The spectra were observed using a prism spectrometer constructed in situ. The optics consisted of an image transfer system observing the front of the plasma at a slight angle to the laser beam. The plasma was imaged onto a 37 micron slit and collimated onto a 30 mm 60 degree quartz prism (Spectrosil B). The dispersed light was then focused by a f=30 cm achromatic lens onto the entrance slit of an optical streak camera (Hadland Imacon 500), with a streak speed of 5 ns/mm. The output from the streak camera was observed by a CCD camera (Photonics Science Darkstar) and transferred to a computer for storage and analysis. The wavelength response of the system was calibrated using 10 nm bandpass optical filters and also a mercury discharge lamp in the object plane. The wavelength as a function of pixel was fitted using the known refractive index of fused silica for the dispersion, with a correction for the measured magnification and distortion of the optical system. The mercury lamp also gave the instrument width of the spectrometer system. This was found to be 0.75 nm. The intensity response was also calibrated using a tungsten lamp with a colour temperature of 3150 K. The intensity response of the system was also fitted using a polynomial.

A typical streak image is shown in figure 2. This is for a gap of 250 micron and an incident laser energy of 1.98 J on target. The early bright patch corresponds to the free ablation from the target foil. The plasma is largely optically thick at this stage. The second bright patch corresponds to the ablating plasma hitting the confining wall, and the subsequent heating. Thereafter, the plasma cools and recombines, this stage being characterised by the weakening of the emission from the higher ionisation stages and reduction in width of all the spectral lines observed.

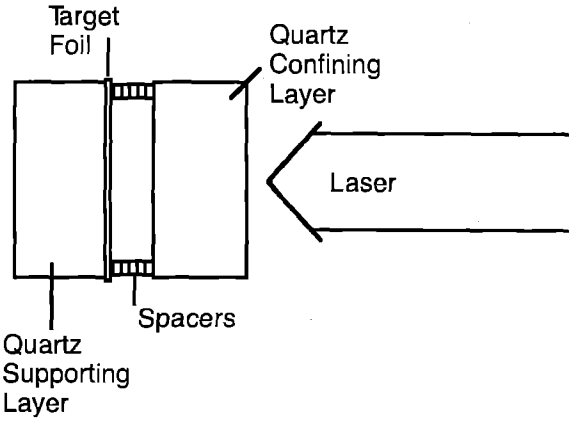

Figure 1 Dense plasma target design

An example of a spectrum is shown in figure 3, corresponding to a time about 60 ns after the laser pulse. Visible in the spectrum are the Al II 623 nm line ($3s4p\text{-}3s(^2S)4d$), and the Al III 452 nm (4p-4d) and 570 nm (4s-4p) lines. Also observable, although weaker are the Al I, 395 nm ($3s^23p\text{-}3s2(^1S)4d$), Al II 466 nm ($3p^2\text{-}3s(^2S)4d$) and Al III 490 nm (5d-7f). A particular problem of dense plasmas is exemplified by this spectrum. We observe that the lines are so broad that they merge into each other. Indeed, for this shot the blue wing of the 452 nm line is lost in other, weaker lines. This makes diagnostics difficult and shows the value of observing a large region of the spectrum.

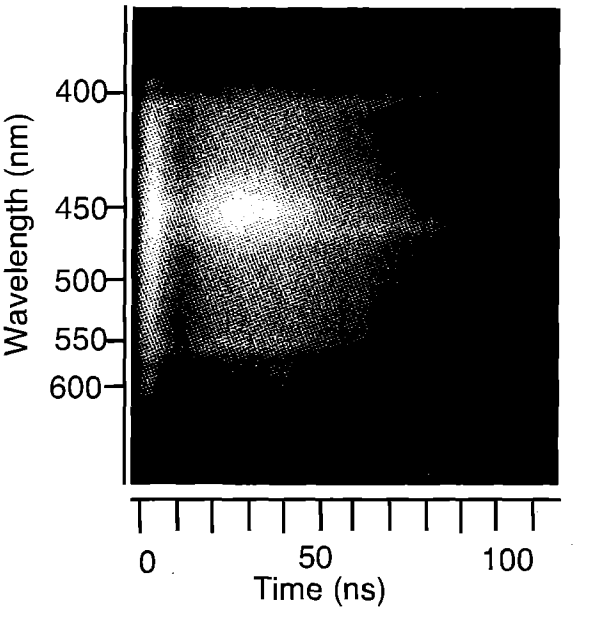

Figure 2 Typical streaked spectrum for a 250 micron gap target, laser energy of 1.98J.

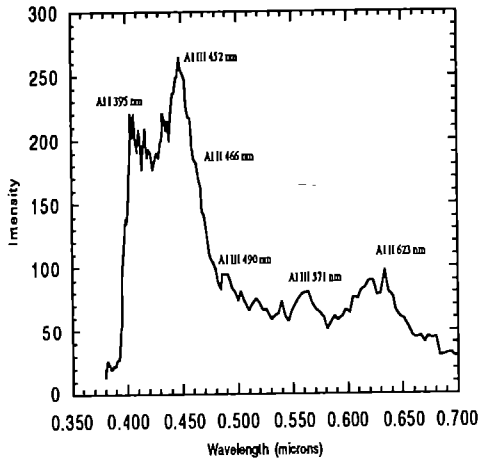

Figure 3 Typical spectrum for 250 micron gap, 6n ns after laser pulse

ANALYSIS

The problem of spectral lines merging calls for careful analysis. We must make allowance for portions of the observed lines underlying other features. For the temperature diagnostic, we may use the relative intensities of spectral lines from different ionisation stages[5]. The assumption of LTE is easily met in plasmas of this density. At various times during the time history we have Al I and Al II lines, or Al II and Al III lines observable at the same time. The relative ion abundances are varying rapidly in this temperature range, so the diagnostic is sensitive, and may be performed reasonably accurately, despite the difficulties described above. The time history of the temperature is shown in figure 4. Apart from the line merging and the difficulty of setting a continuum level, the major problem with this diagnostic is that for this target at times between 60 and 80 ns after the laser pulse the strong lines are all from Al II, both Al I and Al II lines themselves to be used s the diagnostic, and so we must accept larger systematic errors in the diagnostic at these times.

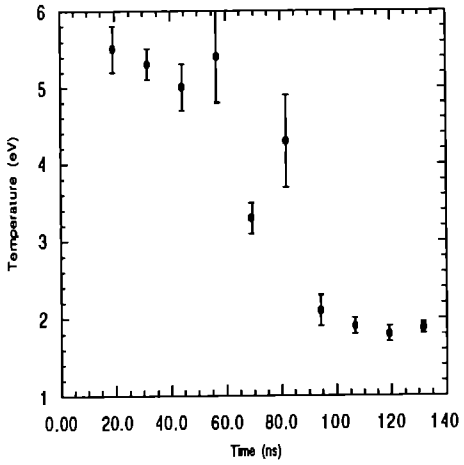

Figure 4 Temperature time history

For the density diagnostic, we use the widths of the lines present in the spectrum. Difficulties with this include problems with setting the continuum intensity and also wings from other lines underlying profile of interest. Nevertheless, using published results for the widths of the lines[2),6)] we can make reasonable estimates of he electron density from observed widths. The time history of the electron density is shown in figure 5. The densities were derived from all the visible lines in the spectrum which were found to agree reasonably well.

We can compare the results of our diagnostics with predicted results. We may expect one skin depth of the foil to be ablated by the incident laser pulse. We therefore know the density and internal energy of the plasma, and we can thus compare the observed values with those calculated. For the temperature, we may use the Sesame tables[7),8)]. For our density and temperature conditions, they give a temperature of 7.8 eV, which agrees well with the value observed 20 ns after the laser pulse of 5.5 eV as we have omitted the latent heats, reflectivity of the target, thermal conduction and diffusion in this calculation. For the electron density, the value of the mean ionisation given by the Sesame tables[9)] is 9.5, which is clearly too high. However, a calculation from the Saha equation gives an electron density of 2 10^{19} cm^{-3} which compares favourably with our results.

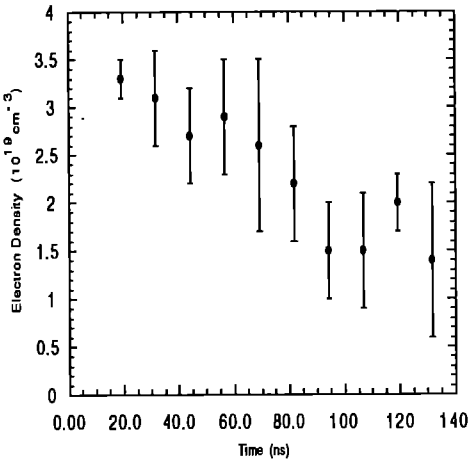

Figure 5 Electron density as a function of time

From our diagnosed conditions, we may use published line shape parameters to simulate the spectra. An example is shown in figure 6, at an electron density of 2.9 $10^{19}$$cm^{-3}$ which compares favourably with our results.

From our diagnosed conditions, we may use published line shape parameters to simulate the spectra. An example is shown in figure 6, an an electron density of 2.9 10^{19} cm^{-3} and temperature of 5.4 eV. Good agreement between the calculated spectrum and the Al III lines is seen. However, the calculated spectrum does not show Al II lines of the observed intensity. This may be due either to plasma inhomogeneities or to the approximations used in calculating the ionisation balance. The Saha model used included only the ground state of each ion stage in the partition function. As the plasma density increases, the excited states become more important and thus the partition functions particularly of the lower ionisation stages increase. This would tend to decrease the mean ionisation, and hence raise the relative populations in the lower ionisation stages. The inhomogeneities may be either along the line of sight s the plasma is not homogenous in the early stages, or at the edges of the target where the plasma will be cooler and less dense. It should be noted that the whole target was imaged. The matter of the plasma homogeneity and the behaviour of the Saha equation at high densities are both under investigation. In the calculation of the spectrum, shifts of the spectral lines are ignored. This is because they are believed to be small for all except the neutral line. A small shift of the calculated spectrum with respect to the observed can be seen in figure 6. This may be due to line shifts, or to the rather coarse wavelength calibration caused by the prism spectrometer.

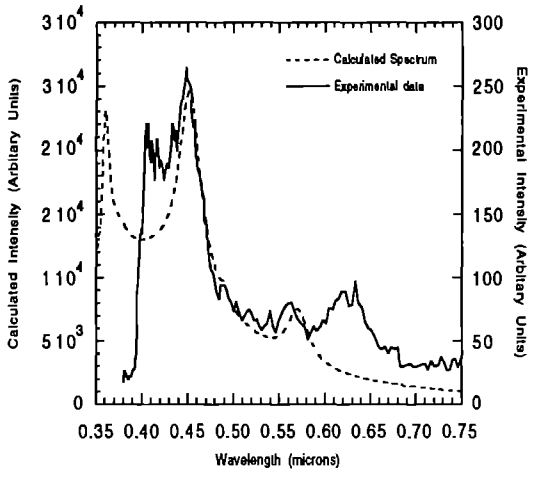

Figure 6 Comparison of observed and calculated spectrum

For all except the neutral line. A small shift of the calculated spectrum with respect to the observed can be seen in figure 6. This may be due to line shifts, or to the rather coarse wavelength calibration caused by the prism spectrometer.

We note that for an initial temperature of above 8 eV, the particles would take 25-30 ns to cross the 250 micron gap,. Thus, the likelihood of the plasma being completely homogenous 60 ns after the laser pulse is small. However, at longer times homogeneity should prevail, although at these times the plasma density and temperature would be much lower.

CONCLUSIONS

We have generated metal plasmas in a manner which they are both cool and dense. These targets are most promising for performing spectroscopic investigations f dense plasmas, at parameter ranges where the various normal approximations for the calculation of spectral line shape parameters begin to break down, and where ion correlations become important.

REFERENCES

1. D J Heading, J P Marangos, D D Burgess
Helium spectral lineshapes in a dense, cool z-pinch plasma,
J Phys B, 25, 4745-4753 (1992).

2. M S Dimitrijevic, Z Djuric, A A Mihajlov
Stark broadening of Al III and Cu IV lines for diagnostic of the rail gun arc plasma,
J Phys D, 27, 247-252 (1994).

3. J T Knudtson, W B Green, D G Sutton
The UV-visible spectroscopy of laser-produced aluminium plasmas,
J Appl Phys, 61, 4771-4780 (1987).

4. C Colon, G Hatem, E Verdugo, P Ruiz, J Campos,
Measurement of the Stark broadening and shift parameters for several ultraviolet lines of singly ionised aluminium,
J Appl Phys, 73, 4752-4758 (1993).

5. H R Griem
Plasma Spectroscopy; McGraw-Hill, NY (1964).

6. H R Griem
Spectral Line Broadening by Plasmas: Academic Press, NY (1974).

7. N G Cooper,
Sesame '83, Report on the Los Alamos Equation of State Library, Los Alamos Scientific Laboratory, LALP-83-4 (1983).

8. N G Cooper
An invitation to participate in the LASL Equation of State Library, Los Alamos Scientific Laboratory, LASL-79-62 (1980).

9. G A Rinker
Systematic calculations of plasma transport coefficients for the periodic table,
Phys Rev A, 37, 1284-1297 (1988).

THREE DIMENSIONAL SIMULATIONS OF LASER DRIVEN ICF TARGET IMPLOSIONS

B J Jones, R P J Town and A R Bell

Imperial College of Science, Technology and Medicine

The success of Inertial Confinement Fusion (ICF) as a viable power source is dependant on reducing the deleterious effects of various relevant hydrodynamic instabilities. The most important of which being Rayleigh-Taylor and Richtmeyer-Meshkov. Both instabilities are important at the outer surface of the target during the acceleration phase and at the inner surface during the deceleration phase. Most of the work performed, however, has been concerned purely with ablation surface instabilities during the acceleration phase. We have previously presented results of Rayleigh-Taylor evolution in the deceleration phase using PLATO, our three dimensional spherical implosion hydrocode [1].

We have now produced an upgraded version of PLATO with the addition of extra relevant physical phenomena. A diffusion equation solver has been written specifically for the geometry of the code allowing us to include thermal transport effects. Currently, we only consider electron thermal transport but the inclusion of other species would not involve excessive effort. A simple laser energy deposition routine has been added which calculates inverse bremstrahlung and resonance absorption along laser beamlets converging at the target centre. No ray-trace calculation is included. Previously the code was able to model just a single material but modifications have been made to the advection routines allowing the tracking of multiple materials. These modifications give us the ability to perform calculations of laser driven implosions, from the beginning of the acceleration phase to stagnation in three dimensional spherical geometry. However, a fixed eulerian mesh would be prohibitively expensive for modelling target implosions and so we have also added a sliding mesh option to the code. Each set of radial cell boundaries at a given radius is moved with a velocity dependant upon the mean radial velocity at that position. For a spherically symmetric problem the boundaries are moved at exactly the mean radial velocity and the code becomes essentially lagrangian but when there is deviation in the radial velocity the cell boundaries are effectively sprung apart to prevent the cells from emptying or gaining negative densities [2].

Preliminary results would seem to suggest that the code is behaving well with sensible shell trajectories and growth rates being observed. Most of the calculations performed to date have been with a uniform shell and a perturbed laser beam. The targets studied have been based upon those used by the Rochester group [3]: 5μm thick glass shells of radius 150μm containing various amounts of DT. These have been driven with 0.351μm laser pulses delivering a total energy of $\sim$1 KJ and having a 650ps FWHM half gaussian power envelope.

Initially, the laser induced shock travels through the shell and we see the perturbation amplitude on the outside grow rapidly from zero as the shell material is differentially burnt away. However, it is not until the shock reflects from the inside of the shell that the shell begins to accelerate and we see Rayleigh-Taylor growth. At the same time the rippled shock front imprints the perturbation on the pusher-fuel interface and the perturbation amplitude there jumps from zero to some finite value. These early test runs suggest an ablation surface instability growth rate of $\sim$60-70 % classical. At the same time, the inner surface is stable and we see an oscillation of the perturbation amplitude (gravity wave) with a frequency increasing as the shell acceleration increases.

Previously, we have identified the moment at which the shock running ahead of the shell reflects from the centre and collides with the incoming shell to be the point at which pusher-fuel instability growth starts but we have observed in these calculations that some growth occurs at an earlier time. We believe that this is due to a significant pressure building up between the shell inner surface and the shock front, a belief backed up by the fact that the shock begins to accelerate away from the shell. As yet, we have made no accurate calculations of the Rayleigh-Taylor growth rate at the pusher fuel interface.

1. B J Jones, R P J Town and A R Bell, Central Laser Facility Annual Report RAL-93-031 (1993)
2. D L Youngs, Private Communication.
3. See e.g. LLE Review 22 (1985) p.125 (Rep DOE/DP/40200-05)

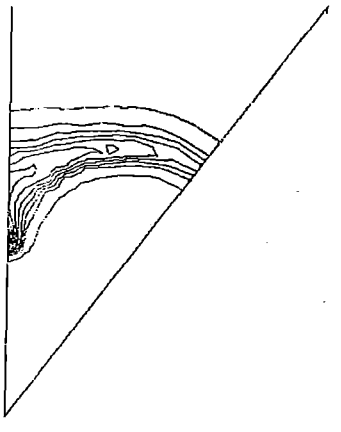

Figure 1. A 2-D slice through the target a short time before maximum compression showing contours of shell density. The shell radius has decreased by a factor of $\sim$30. The laser had a 5% perturbation.

MODELLING X-RAY EMISSION FROM ALUMINIUM TARGETS IRRADIATED WITH 12PS RAMAN AMPLIFIED PULSES FROM THE SPRITE LASER

D. Riley
The Blackett Laboratory, Imperial College
London SW7 2BZ

INTRODUCTION

A time dependent collisional radiative model has been used to study the evolution of ionic populations in a laser produced plasma. The hydrodynamic output from the MEDUSA hydrocode is post-processed to predict the populations in H, He and Li-like excited states. The effects of line trapping of a limited number of strong transitions, is included although radiation is not accounted for in energy balance. The code is used to investigate the K-shell emission characteristics of a laser plasma created with 12ps pulses from the SPRITE laser, incident on solid aluminium targets. The results show that strong population inversions of He-like and H-like excited states can be achieved. The Raman amplified pulses may therefore be a suitable driver for short wavelength recombination X-ray lasers. A brief description of the model is given below, followed by a discussion of some simulation results.

ATOMIC MODEL

The model includes a single ground state only for ion stages from neutral to Be-like. For the Li-like ion there are two ground levels i.e. the $1s^2 2s$ and $1s^2 2p$ levels. The other singly excited states ($1s^2 nl$, up to n=6) are averaged over principle quantum number up to n=6. The eight low lying doubly excited levels (1s2l2l') are also included. The He-like ground and singly excited states (1snl) up to n=7, are also averaged over principle quantum number, except for the case of n=2 which is split into the 1s2s ^{1}S, 1s2s ^{3}S, 1s2p ^{1}P and 1s2p ^{3}P levels. Six doubly excited levels (2l2l') are accounted for. The H-like ion has principle quantum number averaged levels to n=7.

The various rates needed to construct the collisional radiative model are taken from a wide range of sources in the literature. For the collisional rates, the work of Sampson and Co-workers[1-3] was heavily used. Radiative recombination rates were taken from Mewe[4], and Seaton[5]. Collisional ionisation was from the work of Lotz[6]. Autoionising rates were taken from Vainshtein and Safronova[7]. Three body recombination and dielectronic recombination, were calculated by the principle of detailed balance using the rates for collisional-ionisation and auto-ionisation respectively.

For the version with line trapping, we assume a Voight profile, which is determined by convolving the Doppler profile, with a Lorentzian profile which has a width determined by the sum of radiative and collisional deexcitation rates for the upper level. In this work only the strong He-like and H-like 1s-2p lines are considered. The line transfer is done with the core saturation method descibed by Peyrusse[8].

MODELLING HYDRODYNAMIC DATA

The density, electron temperature and size is printed out for each of the simulation cells from the MEDUSA code at various times. For simulations with line trapping, the ion temperature and flow velocity of each cell are included. In the following work 40 cells are used to describe the top 1.5 microns of the aluminium target.

A rate matrix is constructed, using the different rates connecting the levels. Continuum lowering means that some levels are not bound and these are not included. The matrix is solved using LU decomposition. The resulting populations are then used to calculate the electron density. This is used to update the continuum lowering and density dependent rates. The procedure is then repeated until convergence is achieved. The convergence criterion is that populations do not change by more than 1% between iterations.

APPLICATION

I have chosen to apply the model to the case of the Raman amplified pulses from the SPRITE laser, as considerable experimental data exists. This is at present being analysed for comparison with the code and a brief preliminary study will be presented. The specific conditions of interest are a 12ps 268nm laser pulse at $4x10^{15}Wcm^{-2}$ incident on a solid aluminium slab. The MEDUSA hydrocode is used to simulate the plasma evolution. The average ion model is used to calculate the average ionisation needed for energy balance (considerable amounts of energy may be used in ionisation). We then use the post processor to look in more detail at K-shell emission.

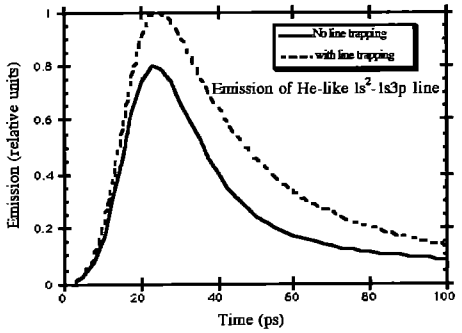

Figure 1. Emission history of Aluminium He-like $1s^2$-1s3p line both with and without line trapping of H and He-like 1s-2p lines.

In figure 1 we can see the predicted temporal history of emission for the He-like $1s^2$-1s3p line. We can see that there is a long tail of emission which is enhanced when re-absorption of the He-like $1s^2$-1s2p ^{1}P and H-like 1s-2p lines is included.

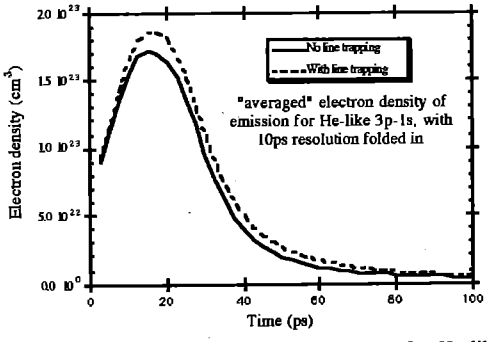

Figure 2. Weighted "average" electron density for He-like $1s^2$-1s3p line for $I=4x10^{15}Wcm^{-2}$. Both with and without trapping of resonance lines.

Figure 2 , above, shows the averaged electron density from which the emission originates. The line trapping does not seem to make much difference. In figure 3 below the emission history and electron density are shown for the H-like 1s-3p line. Again, there is enhancement of the emission tail due to line trapping.

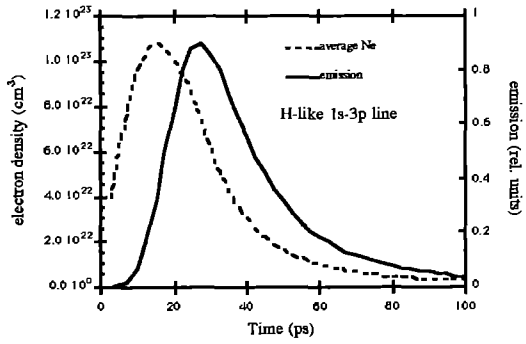

Figure 3. "averaged" electron density and emission history for the Al XIII 1s-3p transition with line trapping included.

For both these lines, the predicted electron density is in good agreement with the experimental results of reference 9. When instrument effects are folded in, and averaging over the focal spot is considered the agreement is expected to be better. The long tail of emission is in accord with the narrow lines seen in time integrated spectra. As can be seen from the simulations, a large fraction of the emission is expected to come late in time at low density. A further study over longer times would need to account for non-planar expansion, and well over half the emission may be shown to come from low density.

POPULATION INVERSIONS

I have looked at the population histories of the upper levels of the He-like and H-like ion species. The results show that strong population inversions can occur, but that these are reduced by the presence of line trapping. Figure 4 shows a graph of the small signal gain predicted for the H-like 4d-2p transition some 90ps after the peak of the laser pulse. It is assumed that population of the different angular momentum states just follows degeneracy within a principle quantum number level. For this calculation a Doppler linewidth was used. We can see that when line trapping is present, the gain is reduced by a factor of about two. For the He-like levels it was found that line trapping was quite effective in removing gain for the 4d-2p line.

This modelling does not account for realistic line profiles, trapping on other lines and non-planar expansion. However, the results show that there is the possibility that the SPRITE 12ps Raman amplified pulses may be a suitable driver for H-like aluminium X-ray lasers. The wavelength of the 4d-2p line is about 29 Angstroms, which is below the water window.

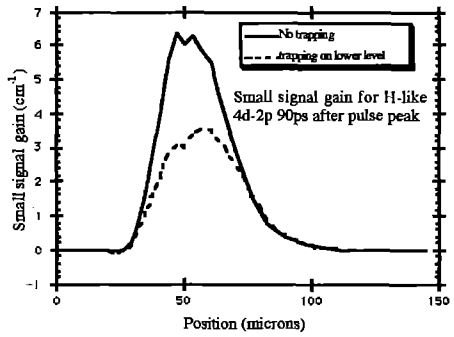

Figure 4. Predicted gain coefficient for H-like line at 29 Angstroms.. The presence of line trapping has a significant effect.

CONCLUSIONS

A post-processor code has been developed that is suitable for modelling the K-shell emission from short pulse laser produced plasmas with low to moderate Z. A detailed comparison with experimental data from the SPRITE laser is currently in progress. Other versions of the code deal with the effects of fast electrons in a two temperature approximation. It is intended to publish further results at a later date. The good agreement with previously published experimental results gives some confidence in the modelling of K-shell emission characteristics.

REFERENCES

1. D H Sampson et al, Atomic Data and Nuclear Data Tables, 28, 299 (1983)
2. H Zhang et al., Atomic Data and Nuclear Data Tables 35, 267 (1986)
3. S J Goett et al Atomic Data and Nuclear Data Tables 29, 547 (1983)
4. R. Mewe *Scottish Universities Summer School in Plasma Spectroscopy*, St Andrews (1987)
5. M J Seaton, Mon. Not. Roy. Astr. Soc. 119, 81 (1959)
6. W Lotz, Z.Physik 232, 101 (1970)
7. L A Vainshstein and U I Safronova, Atomic Data and Nuclear Data Tables 21, 49 (1978)
8. O. Peyrusse, Phys. Fluids B, 4, 2007 (1992)
9. D Riley et al Phys. Rev. Lett. 69, 3739 (1992)

ELECTRON - TEMPERATURE MEASUREMENTS FROM THE RATIO OF SPECTRAL LINE INTENSITIES

Y Al-Hadithi and G J Tallents
Department of Physics, University of Essex, Colchester CO4 3SQ, UK.

S Rose
Central Laser Facility, SERC Rutherford Appleton Laboratory, Chilton OX11 0QX, UK.

In this report, line ratios of hydrogen- and helium-like Na and F are investigated as temperature diagnostics using the RATION[1] code. Simulations using a code NIMP (Non-LTE Ionised Material Package) which calculates non-steady state ionisation shows that ionisation equilibrium occurs on a time scale of approximately 600 fs for the plasma conditions studied.

Spectral line intensity ratios can be accurate diagnostics of plasma electron temperatures because only relative (not absolute) intensity measurements are needed[2]. However, in laser-produced plasmas, problems can arise with line ratios as temperature diagnostics because of (i) departures of the quantum state populations from either simple coronal or LTE relations leading to the line ratios having a dependence on density and even perhaps a dependence on the density and temperature history of the plasma and (ii) opacity effects on the spectral line intensities. It is necessary to search for line ratios where these effects are negligible or the same for both lines so that cancellation of the effect occurs. Some sample ratios deduced using the RATION code (described in, for example, ref. 1) are plotted in figure 1.

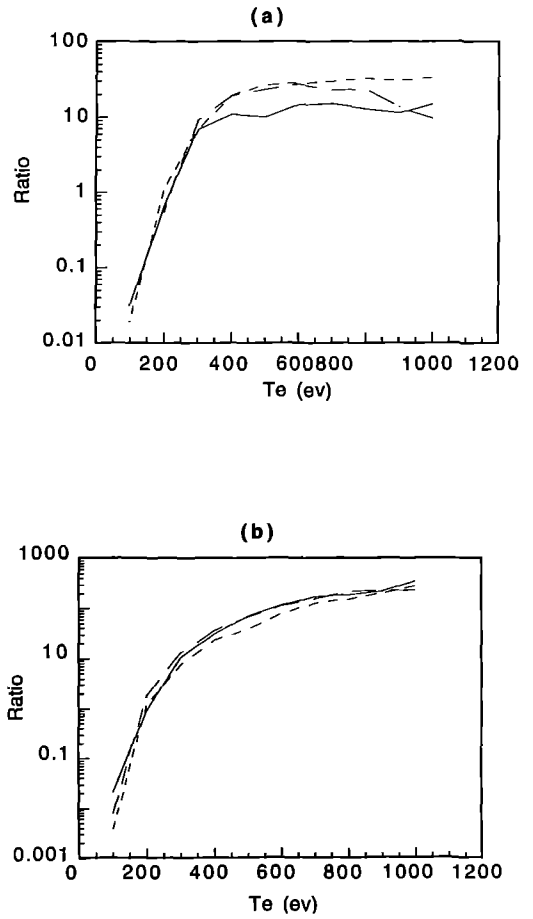

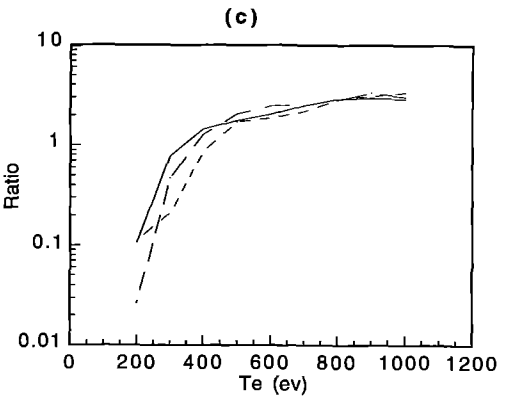

Figure 1
The ratio of emitted intensities for (a) NaX $1s^2$ -1s3p to FVIII $1s^2$ - 1s3p, (b) FIX 1s - 3p to FVIII $1s^2$ - 1s3p and (c) NaXI 1s - 3p to FIX 1s - 3p as a function of electron temperature for various electron densities (——— 10^{23} cm^{-3}, — — 10^{22} cm^{-3}, - - - - - 10^{21} cm^{-3}) as predicted by the RATION code.

It can be seen that over quite a range of parameters, these line ratios are potentially good temperature diagnostics as there is little variation with electron density. For areal densities corresponding to solid density and thicknesses up to ~0.25μm, RATION calculations show also that opacity has a negligible effect on the results for figure 1. Over the 100-500 eV range, the intensity ratios of figure 1 increase rapidly with temperature showing that the line ratios should be good temperature diagnostics over this range.

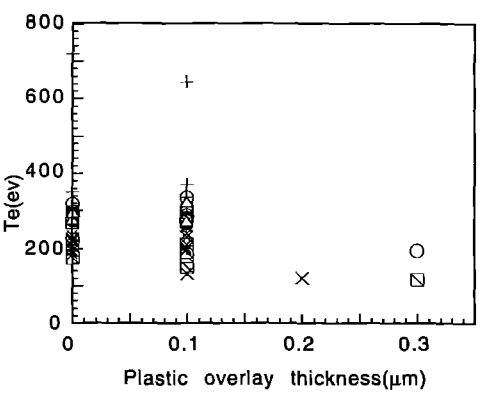

Figure 2 Electron temperatures as a function of plastic overlay thickness as determined from the intensity ratio of spectral lines and interpreted using the RATION code :O NaXI 1s - 2p to NaX $1s^2$ - 1s2p, ⊗ FIX 1s - 3p to FVIII $1s^2$ - 1s3p, × NaXI 1s - 3p to FIX 1s - 3p, ΔNaX $1s^2$ - 1s3p to FVIII $1s^2$ - 1s3p, ⊕ NaXI 1s - 3p to FIX 1s - 3p, * FIX 1s - 2p to FVIII $1s^2$ - 1s2p, + FIX 1s 3p to NaX $1s^2$ - 1s3p.

In an experiment, the high brightness krypton fluoride Raman laser SPRITE (wavelength 0.268 μm) generating 0.3TW, 12 ps pulses with 20 μrad beam divergence and a pre-pulse of less than

10^{-10} was focused to produce a 10 μm wide line focus (irradiances ~ 0.8-4 X 10^{15} Wcm^{-2}) on plastic targets with a diagnostic sodium fluoride (NaF) layer of thickness 0.25μm buried within the target[3]. The electron temperatures deduced from experimentally measured line intensity ratios from the NaF buried layer are plotted as a function of axial depth in the target in figure 2.

There is a reasonable agreement between the temperatures deduced from the different ratios, but a moderate scatter due to the shot-to-shot nature of the data collection and the steep slope of the intensity ratio/temperature curves.

Simulations using the average atom code NIMP (Non-LTE Ionised Material Package) which calculates non-steady state ionisation show that ionisation equilibrium occurs on a time scale of approximately 600 fs at solid density (see figure 3).

The effect of the electron density on ionisation equilibrium time is shown in figure 4. There is only a weak dependence on the electron temperatures.

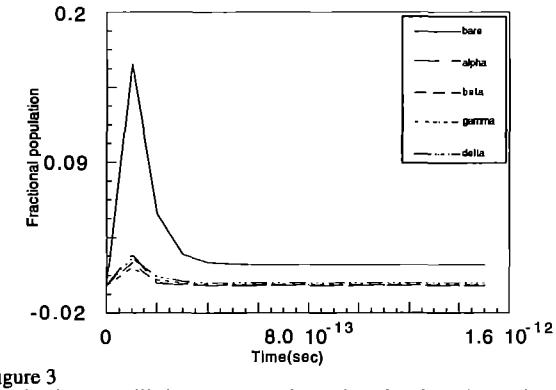

Figure 3
ionisation equilibrium time scale deduced using the code NIMP for electron density 7.2X10^{23} cm^{-3}. The labels bare, α, β, γ, and δ refer to the fully stripped fluorine and the ground state(n=1), 2nd excited state(n=2), 3rd excited state(n=3) and 4th excited state(n=4) respectively of helium like fluorine.

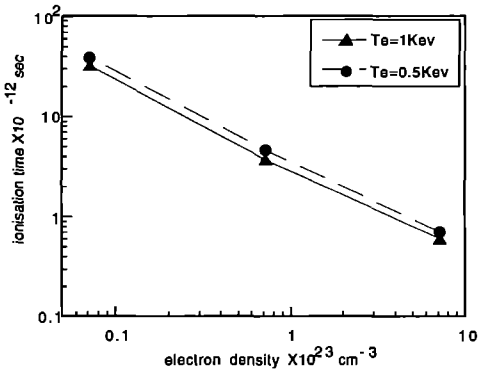

Figure 4
The effect of the electron density on ionisation equilibrium time (using the code NIMP) for helium-like fluorine. The figure shows the weak dependence on the electron temperatures.

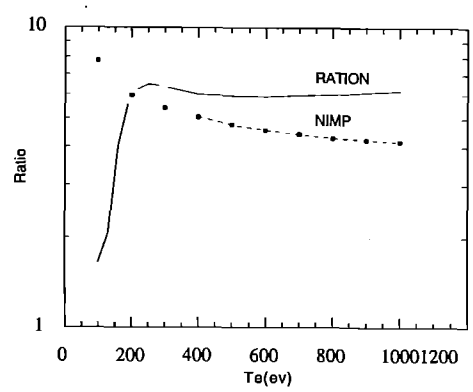

Figure 5
Comparison of RATION and NIMP FVIII $1s^2$ - 1s2p to $1s^2$ - 1s3p line intensities ratios. The results show general agreement of the line emission as a function of plasma electron temperature once steady state has been reached.

Comparisons of RATION and line intensities calculated by NIMP once steady state has been reached show general agreement of the line emission as a function of plasma electron temperature (e.g. figure 5).

REFERENCES

[1] R W Lee, B L Whitten and RE Strout J Quant Spect Radiat Trans 32, 91 (1984).

[2] R S Marjoribanks, M C Richardson, P A Jaanimagi and R Epstein Phys. Rev A46, R1747 (1992).

[3] Y Al-Hadithi, G J Tallents, J Zhang, M H Key, P A Norreys, R Kodama, S Rose, to be published in Physics of plasmas: May 1994.

FOKKER-PLANCK SIMULATIONS OF SHORT PULSE LASER PLASMA EXPERIMENTS

R P J Town[1], S J Rose[2] and A R Bell[1]

[1]Imperial College of Science, Technology and Medicine

[2]Rutherford Appleton Laboratory

The interaction of a short pulse laser with a solid target generates a solid density, keV plasma. At keV temperatures and densities the electron mean free path of the thermal electrons is approximately 0.05 μm. The scalelengths and the mean free path are, therefore, of the same order. Hence we would expect the heat flow to be poorly approximated by the classical Spitzer-Härm theory of heat transport [1] and for the electron distribution function to be strongly non-Maxwellian. During the short pulse interaction an initially cold, unionised solid is rapidly heated to a hot, ionised solid density plasma. Ionisation is, thus, an important mechanism in the time development of the plasma.

In last years report [2] we described simulations performed using the Fokker-Planck (FP) code in the intermediate intensity regime (10^{15} W/cm^2) where relativistic effects are not important. This regime is especially important for the generation of short pulse X-rays lasers by the recombination scheme [3]. We showed that the heat flow was poorly approximated by the Spitzer heat flow. A reasonable agreement to the FP heat flow was obtained in the body of the target with a flux limit of 0.3. We also showed that hydrodynamics could not be ignored. Results were reported using the NIMP (Non-LTE Ionisation Materials Package) [4]. This code post-processed the density and temperature of particular Lagrangian cells to obtain the ionisation state of the target. It was found that to achieve ionisation took a considerable time. For example, the cell closest to the laser took the rise time of the pulse to achieve the fully ionised state, whilst further into the target the plasma never reached full ionisation.

We have found that the dominant ionisation process in the interaction of a short pulse laser with a solid target is collisional ionisation and its inverse process, three body recombination. We will in this paper look in detail at the effect of the non-Maxwellian distribution function on the collisional ionisation rates.

In the simulations reported here a 0.4 μm thick fully ionised Carbon (Z=6) solid target was illuminated by a 350 fsec Gaussian KrF (λ=0.25 μm) laser pulse. The target was initially at solid density (n_e=3.0*10^{23} cm^{-3}) and at a temperature of 15eV. A step profile was used between the target and the vacuum. A uniform velocity mesh with 70 grid points extending to a maximum velocity of 40 times the thermal velocity was used. A non-uniform spatial mesh with a minimum physical cell size of 0.002 μm was found to be necessary to model the hydrodynamic response. An average absorbed intensity of 8.0*10^{14} W/cm^2 was used.

We have investigated the effects of the non-Maxwellian distribution function on the collisional ionisation rates. This was performed by multiplying the collisional cross-sections by the distribution function and integrating over all velocities then comparing the resulting rates with the rates obtained by using a Maxwellian of the same density and temperature. Work performed at Belfast [5,6] has derived the collisonal ionisation cross-sections as a function of incident electron energy in a simple analytic form, based on the best available experimental and theoretical studies.

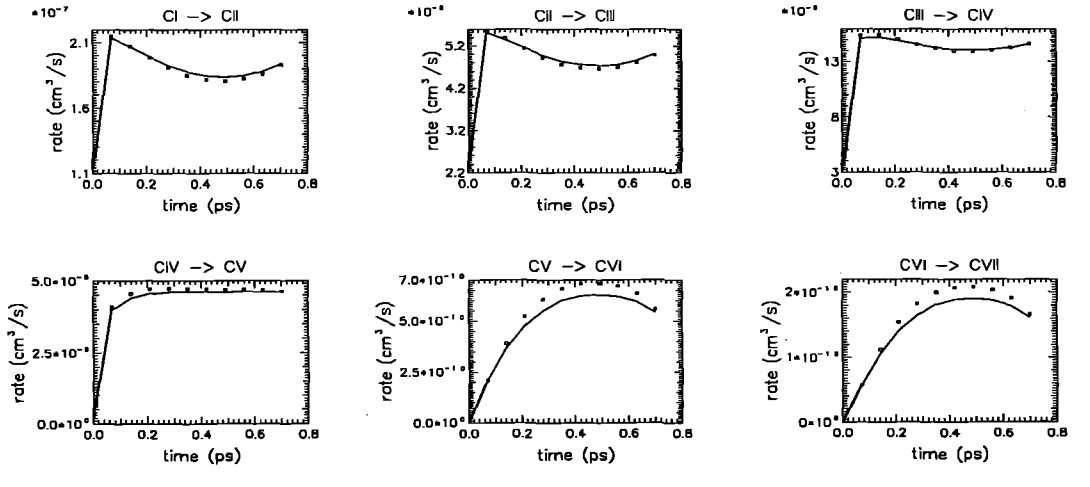

Figure 1: The collisional ionisation rates for all the ionisation transitions as a function of time for the outermost cell. The squares represent the rates calculated by the actual distribution and the solid line is the rates from the Maxwellian.

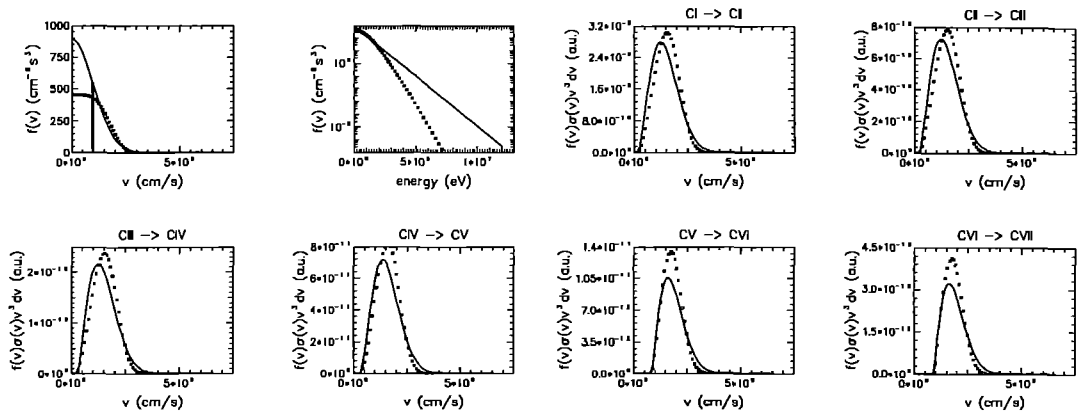

Figure 2: The distribution function, and the overlap between the cross-section and the distribution function as a function of velocity for the outermost cell at the peak of the pulse. The squares represent the non-Maxwellian and the solid line the Maxwellian result.

For certain key Lagrangian cells we output the density and temperature and the actual distribution function. We then plot the collisional ionisation rate for each transition as a function of time for both the Maxwellian and non-Maxwellian distributions.

Figure 1 shows the collisional ionisation rates for the outermost Lagrangian cells closest to the laser beam. The squares are the rates obtained by convolving the cross-sections with the actual distribution whilst the solid line are those obtained from the Maxwellian distribution. As can be seen the non-Maxwellian rates are very close to the Maxwellian rates (at most the rates are within 5% of each other). For the low ionisation transitions (up to CIV-CV) the non-Maxwellian rate is below the Maxwellian rate, for CV-CVI and CVI-CVII the rate for the non-Maxwellian case is higher. An examination of the distribution function and the product of the cross-section multiplied by the distribution function helps to explain these results. Figure 2 shows these curves for the outermost cell at the peak of the pulse. The actual distribution function (denoted by squares) is distorted by the Langdon reduction of the low velocity electrons [7]. The energy of the laser is taken up by the low velocity electrons, thus depleting this part of the distribution. When this distribution is multiplied by the cross-sections the product at low velocity is lower than the Maxwellian product. As the velocity increases so the Maxwellian falls below the actual distribution, thus leading to the cross-section product being higher for the actual distribution compared to the Maxwellian. At even higher velocities the Maxwellian product again dominates, but at these velocities the actual cross section is much smaller and thus contributes negligibly to the rate. The product of the cross-section and distribution has the same general shape, but the peak in the non-Maxwellian case is shifted to slightly higher velocities. As the ionisation energy increases, so the cross-section peak shifts to higher velocity, thus moving to the region where the non-Maxwellian distribution has a larger concentration of electrons, thus increasing the rate relative to the Maxwellian case. In general where the cross-section is peaked in energy the distribution functions are very close.

Further into the target there is practically no difference in the ionisation rates. Now the only difference between the Maxwellian and the actual distribution is at high velocity. At low velocities the bulk of the electrons are in a Maxwellian distribution. At high velocities the tail adopts the temperature of the heated region because these are the electrons originating from that region. However they play only a small role in determining the rate since the cross-section at these velocities is typically two orders of magnitude smaller than the peak.

In summary the difference between the rates obtained using the real distribution and the rates using a Maxwellian of the same density and temperature is quite small. Therefore, because of the law of detailed balance, the three body recombination rates would also only be marginally altered by using a Maxwellian rather than the actual distribution. This justifies the continued use of ionisation rates based on a Maxwellian velocity distribution in simulations of these experiments.

REFERENCES

1 L. Spitzer Jr. & R. Harm, Phys. Rev. 89, 977 (1953).

2. R. P. J Town, S. J. Rose & A. R. Bell, Annual Report to the Laser Facility Committee, RAL-93-031 (1993).

3 Jie Zhang & M. H. Key, submitted to Appl. Phys.

4. A. Djaoui & S. J. Rose, J. Phys. B: At. Mol. Opt. Phys. 25, 2745 appendix A (1992)

5. K. L. Bell, H. B. Gilbody, J. G. Hughes, A. E. Kingston & F. J. Smith, Phys. Chem. Ref. Data 12, 891 (1983).

6. M. A. Lennon, K. L. Bell, A. E. Gilbody, J. G. Hughes,A. E. Kingston, M. J. Murray & F. J. Smith, Phys. Chem. Ref. Data 17,1285 (1988).

7. A. B. Langdon, Phys. Rev. Lett. 44, 575 (1980).

MULTIPHOTON IONIZATION OF COMPLEX ATOMS IN INTENSE LASER FIELDS

P G Burke[1], C J Noble[2] and J Purvis[1]

[1] Department of Applied Mathematics and Theoretical Physics, Queens University, Belfast

[2] TCS Division, Daresbury Laboratory, Warrington

INTRODUCTION

The study of multiphoton ionization of atomic systems by intense laser fields has attracted considerable attention in recent years[1]. In the case of atomic hydrogen, there have been many theoretical studies both within the Floquet framework and also by solving the time-dependent Schrödinger equation numerically. However, most theoretical work for atoms and ions containing more than one electron has relied on the use of perturbation theory or the time-dependent Hartree-Fock approximation which includes only a restricted class of electron correlations. Recently, the present authors, in collaboration with colleagues in Belgium and France supported by an EC-HCM contract have introduced a new R-matrix-Floquet theory of multiphoton processors[2,3]. This theory is both non-perturbative, enabling it to be applied for intense laser fields, and also allows electron-electron correlation effects to be included for an arbitrary complex atomic or ionic target. The associated computer programs which have been developed have been shown to give accurate results for atomic hydrogen and are now being used to obtain multiphoton ionization rates for the inert gases and negative ions.

SUMMARY OF THEORY AND COMPUTER PROGRAMS

The R-matrix Floquet theory of multiphoton processes starts from the time-dependent Schrödinger equation describing the interaction of the laser field with a general atom or ion. The laser is assumed to be monomode monochromatic, linearly polarized and spacially homogeneous.

In accordance with the R-matrix method[4], configuration space is divided into an internal and an external region, in each of which the most appropriate form of the laser-atom interaction is used. The internal region is defined by a sphere centred on the atomic nucleus whose radius is chosen to just envelope the charge distribution of the target states of interest in the calculation. In this region electron exchange and correlation effects involving all the electrons are important. The external region is defined so that the ejected electron after multiphoton ionization lies outside of this sphere and the remaining electrons in the residual atom or ion are confined within this sphere. Since the ejected electron and the remaining electrons occupy different regions of space, electron exchange between them is negligible.

In order to solve the Schrödinger equation a Floquet-Fourier expansion of the wave function is adapted in both regions. Further in the internal region the dipole-length gauge is used to describe the interaction of the electron with the laser field, while in the external region the velocity gauge is adapted. The solution in the internal region then reduces to setting up and diagonalizing a large Hamiltonian matrix from which the R-matrix (logarithmic-derivative matrix) on the boundary between the regions can be determined. The solution in the external region reduces to solving a set of coupled differential equations. The solutions in these two regions are matched on the boundary through the R-matrix. For multiphoton ionization outgoing wave 'Siegert' boundary conditions are imposed at large distances. This involves an iterative procedure in the complex energy plane to obtain the relevant eigensolution, where the imaginary part of the corresponding energy eigenvalue gives $(-1/2)$ times the total multiphoton ionization rate.

A general computer program package has been developed for multiphoton ionization which implements the above theory for an arbitrary complex atomic or ionic target. This work has taken advantage of program packages developed at Queen's University Belfast over the last twenty years, which describe electron scattering by complex atoms and ions and single photon ionization[4]. This new package will also allow laser assisted electron-atom collision cross sections to be calculated.

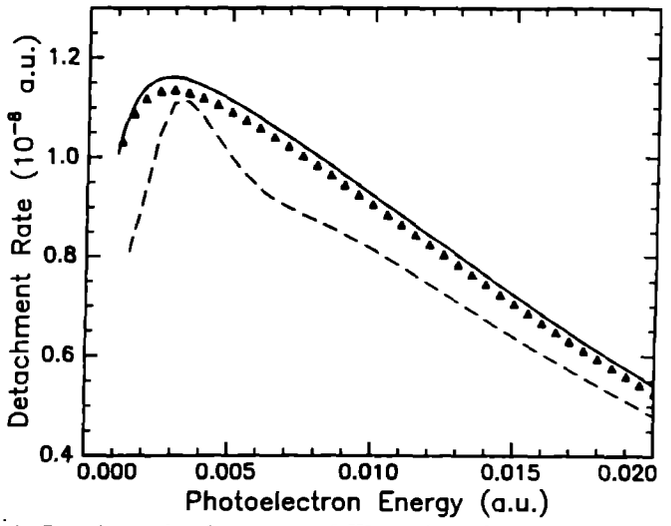

Fig 1. Two-photon detachment rate of H^- vs photo-electron energy close to threshold at an intensity of 10^9 Wcm^{-2}. Solid line, Present Calculations: Δ, Liu et al[5]; Dashed line, Proulx and Shakeshaft[6].

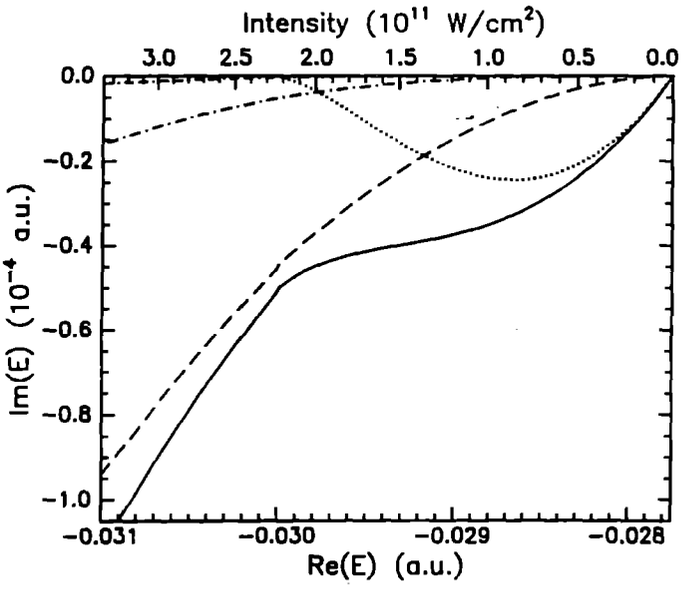

Fig 2. Trajectory of the H^- state in the complex energy plane as a function of field intensity for $\omega = 0.03$ au. Solid line, total width; dashed line, two-photon absorption width; short dashed line, four photo absorption width. The corresponding intensity is given on the top axis.

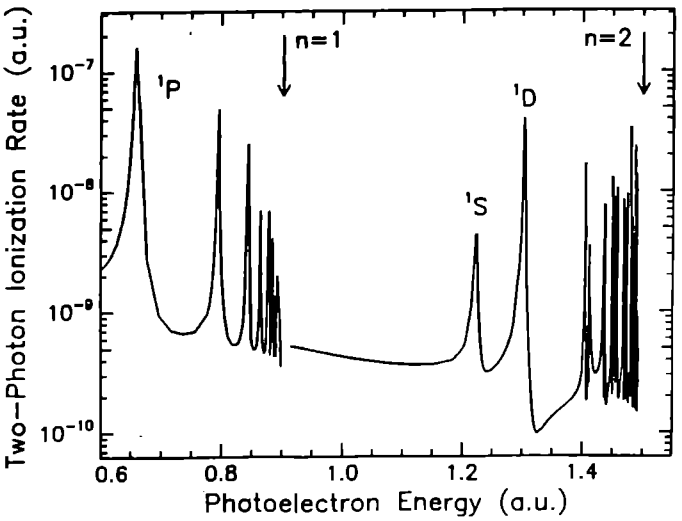

Fig 3. Two-photon ionization rate of He vs photoelectron energy at an intensity of 10^{12} Wcm^{-2}. The positions of the n = 1 and n = 2 thresholds are denoted by the arrows.

SOME RECENT RESULTS FOR H^- AND He

Results for multiphoton detachment of H^- are presented first. Fig 1 shows a comparison of the two-photon detachment rate in the perturbative limit (corresponding to a field intensity of 10^9 W cm^{-2}) with perturbation theory calculations of Liu et al[5] and Proulx and Shakeshaft[6]. The excellent agreement indicates that the R-matrix Floquet theory is giving a good representation of electron-electron correlation effects. At higher intensities perturbation theory is no longer applicable. As an example of this region the trajectory of the H^- state in the complex energy plane as a function of field intensity for a frequency w = 0.03 au is shown in Fig 2, also shown in the figure are the partial widths for ionization by one, two, three and four photons. In the zero field limit the corresponding eigenvalue lies on the real energy axis with E = -0.02775 au, the H^- attachment energy. As the laser is switched on, the eigenvalue moves into the lower half complex energy plane since H^- can then ionize by the absorption of one or more photons. The highly non-linear motion of the trajectory is an indication of the non-pertubative nature of the process.

Turning to mutiphoton ionization of He, Fig 3 shows the two-photon ionization rate versus photoelectron energy for He in a field of intensity 10^{12} W cm^{-2}. Two series of peaks are seen. The Rydberg series of peaks below the n = 1 threshold are $^1P^0$ one-photon bound state resonances in the intermediate channel. The series of peaks below the n = 2 threshold are composed of $^1S^e$ and $^1D^e$ autoionizing resonance in the final two-photon channel. It has been shown [3] that in the neigbourhood of the $^1D^e$ autoionizing resonances the total photoionization rate is dominated by one-photon absorption at intensities ~ 10^{12} W cm^{-2}, but as the intensity increases to ~ 10^{14} W cm^{-2} the two-photon rate dominates, showing again the importance of including electron-electron correlation effects.

CONCLUSIONS AND FUTURE WORK

The multiphoton ionization results for H^- and He show that the R-Matrix-Floquet theory is an approach which is both non-perturbative and also can accurately include electron-electron correlation effects for complex targets. The computer program package which has been developed can be used to obtain multiphoton ionization rates and laser assisted electron collision cross sections for any complex atomic system and results are now being obtained for Ne and Ar.

In the future, it is intended to extend the program package to treat harmonic generation and multiphoton ionization of diatomic molecules in order to interact with and support the experimental research programme on the CLF at DRAL.

This work was supported by EC-HCM Contract No. ERB CHRX CT 920013. In addition J P was supported by a Northern Ireland Department of Education postgraduate studentship.

REFERENCES

1. M Gavrilla, Ed. Atoms in intense laser fields, Advances in Atomic, Molecular and Optical Physics Supplement 1 (1992)

2. P G Burke, P Francken and C J Joachain, R-Matrix Theory of Multiphoton Processes, J Phys. B: At Mol Opt Phys 24 761 (1991)

3. J Purvis, M Dörr, M Terao-Dunseath, C J Joachain, P G Burke and C J Noble, Multiphoton Ionization of H^- and He in intense Laser Fields,Phys Rev Lett 71 3943 (1993)

4. P G Burke and K A Berrington, Eds, Atomic and Molecular Processes: An R-Matrix Approach, Institute of Physics Publishing (Bristol andPhiladelphia, 1993)

5. C R Liu, B Gao and A F Starace, Variationally stable treatment of the two- and three-photon detachment of H^- including electron-correlation effects., Phys Rev A46 5985 (1992)

6. D Proulx and R Shakeshaft, Two- and three-photon detachment of H^- by a weak field, Phys Rev A46 R2221 (1992)

PLASMA WAKEFIELD GENERATION BY MULTIPLE SHORT PULSES

D A Johnson R A Cairns[1] and R Bingham[2]

[1] University of St. Andrews

[2] Rutherford Appleton Laboratory

INTRODUCTION

The concept of plasma-based accelerators has received much attention in recent years since plasmas are capable of supporting large electric fields ($\sim$ 100GV/m)[1]. Such an accelerator relies on the generation of large amplitude longitudinal plasma waves with a phase velocity close to the velocity of light. The Laser Wakefield Accelerator scheme (LWFA)[2] uses a single high intensity short pulse of laser radiation to excite the plasma wave.

In this report we present an analysis of the interaction of a train of short laser pulses with an underdense plasma. The analysis shows that it is possible, by phasing the laser pulses correctly with respect to the plasma wave, to excite resonantly a highly relativistic plasma wave with correspondingly high field gradients in the plasma. This suggests that a given pulse energy may be used much more effectively in a series of pulses than as a single pulse to generate a wake plasmon.

THEORY

We base our analysis on a well-known model [4] which combines one-fluid, cold relativistic hydrodynamics with Maxwell's equations to simulate the plasma and laser pulse respectively. The model employs the 'quasi-static' and envelope approximations to obtain a set of two coupled nonlinear equations describing the self-consistent evolution of a_o, the vector potential of the laser pulse envelope, and Φ, the scalar potential of the plasma wake-field. The final equations are ,

$$\frac{\partial^2\Phi}{\partial\xi^2} = \frac{\omega_{p0}^2}{c^2}G \tag{1}$$

and

$$2i\omega_o\frac{\partial a_o}{\partial\tau} + 2c\beta_o\frac{\partial^2 a_o}{\partial\tau\partial\xi} + \frac{c^2\omega_{p0}^2}{\omega_o^2}\frac{\partial^2 a_o}{\partial\xi^2} = -\omega_{p0}^2 H a_o \tag{2}$$

where

$$G = \frac{\sqrt{\gamma_\parallel^2 - 1}}{\beta_o\gamma_\parallel - \sqrt{\gamma_\parallel^2 - 1}}$$

and (3)

$$H = 1 - \frac{\beta_o}{\gamma_a\left(\beta_o\gamma_\parallel - \sqrt{\gamma_\parallel^2 - 1}\right)}$$

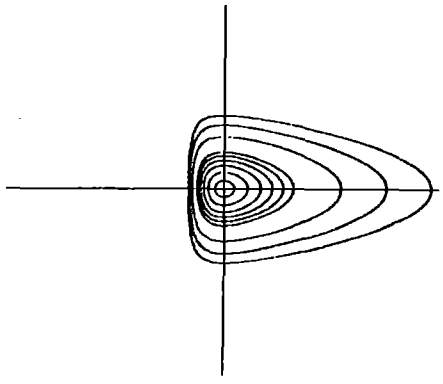

Figure 1 The trajectories in $u-\Phi$ space generated by equation (5) for varying values of the constant K. Notice the bunching of the trajectories as the minimum value of Φ is approached.

The model is valid for electromagnetic pulses of arbitrary polarization and intensities $|a_o|^2 \geq 1$.

To simplify the theory we use the approximation that the group velocity of the electromagnetic wave can be taken to be c, in which case the electrostatic potential is generated according to the equation

$$\frac{d^2\Phi}{d\xi^2} = \frac{1}{2}\frac{\omega_p^2}{c^2}\left\{\frac{\gamma_a^2}{(1+\Phi)^2} - 1\right\} \tag{4}$$

When $a = 0$, $\gamma_a = 1$ and a first integral of equation (4) is easily found, namely

$$u^2 + \frac{1}{1+\Phi} + \Phi = K, \tag{5}$$

where K is a constant and

$$u = \frac{c}{\omega_p}\frac{d\Phi}{d\xi} \tag{6}$$

The curves generated by equation (5) are illustrated in Figure 1. Now suppose that we can approximate a short pulse

by a δ—function,

$$\gamma_a^2 = 1 + 2A\,\delta(\xi - \xi_o) \tag{7}$$

where A is a positive number. The effect of such a δ—function pulse is to produce an impulsive change in u, of magnitude

$$\Delta u = \frac{A}{(1+\Phi)^2} \tag{8}$$

If we start from the equilibrium state $\Phi = u = 0$ and apply such a pulse, then we get

$$K = 1 + A^2 \tag{9}$$

and if $A \gg 1$, the maximum value of Φ is approximately A^2.

If, on the other hand, we use a series of pulses, each with a rather smaller value of A, we can exploit the Φ dependence of the impulses given by equation (8) and drive the system each time it passes through a minimum value of Φ. In this way each successive pulse produces a larger jump in u and there is a rapid increase in the maximum value of Φ. To show just how strong this effect can be, we note that for large K the maximum and minimum values of Φ are, approximately,

$$\begin{aligned} \Phi_{\max} &= K \\ \Phi_{\min} &= -1 + 1/K \end{aligned} \tag{10}$$

If we apply the impulse when the wave is passing through $\Phi_{\min}$, we get

$$\Delta u = AK^2 \tag{11}$$

and the new value of K is

$$\begin{aligned} K_1 &= A^2K^4 + K - 1 + \frac{1}{K} \\ &\approx A^2K^4 \end{aligned} \tag{12}$$

if A is of order 1 and K is large. Thus, once we get into the large K regime, there is the potential for extremely rapid growth of the electrostatic wave amplitude with successive pulses.

RESULTS

We now present some numerical results for the wake-fields generated by a particular combination of short pulses. The time for the simulation is scaled in terms of the plasma period, $T_p = \frac{2\pi}{\omega_{po}}$ and the spatial scale is the plasma wavelength, $\lambda_p = \frac{2\pi c}{\omega_{po}}$.The electric wake-field in the plasma is plotted as the normalised quantity $E_w = \frac{e|E|}{m_o c \omega_{po}}$.

The results in figure 2 show the effect of splitting the energy of a single 300fs pulse, with irradiance $I_o\lambda^2 \simeq 5 \times 10^{18} W/cm^2\mu m^2$, into two extremely short pulses to drive a larger plasma wave. The wake-field generated in the plasma is $E_w = 2.3$, which is a factor of 2.5 times higher than that generated by the single pulse. This phase diagram shows that in this case the impulse occurs at the point in the cycle where Φ is very close to its minimum value

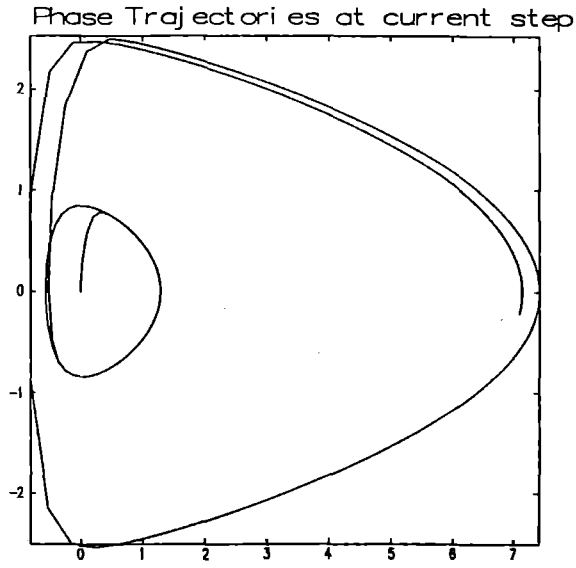

Figure 2 Simulation to illustrate the amplification of the electric wake-field when a trailing laser pulse is positioned such that it interacts with the plasma at the point where the electrostatic potential has a minimum. For each pulse, $|a_o^{in}| = \sqrt{10}$, $\sigma = 0.05\lambda_p$, $\omega_{po}/\omega_o = 0.05$ and $t = 6T_p$. The phase space trajectories show the two impulses given to the plasma electron oscillation. The orbits excited are those with K values 1.7 and 6.3

and imparts the maximum amplification to the wake-field oscillation.

We have presented an analysis and some numerical graphics to demonstrate the increased efficiency of using multiple laser pulses in the generation of relativistic plasma wake-fields. The maximum wake amplitude is obtained when ultrashort pulses are arranged in such a way that they interact with the plasma electrons at the local minimum of the electrostatic potential generated by the preceding pulse. The multiple pulse scheme demonstrates that several short pulses is better than one pulse with the same total energy.

REFERENCES

1. P. Chen, J. M. Dawson, R. W. Huff and T. Katsouleas, Phys. Rev. Lett. **54**, 693 (1985).

2. T. Tajima and J. M. Dawson, Phys. Rev. Lett. **43**, 267 (1979).

3. D. Strickland and G. Mourou, Opt. Commun. **56**, 216 (1985); P. Maine, D. Strickland, P. Bado, M. Pessot and G. Mourou, IEEE J. Quantum Electron. **24**, 398 (1988); M. D. Perry, F. G. Patterson and J. Weston, Opt. Lett. **15**, 1400 (1990).

4. U. de Angelis, Physica Scripta **T30**, 210 (1990).

MEDX: A RADIATION HYDRODYNAMICS CODE.

A. Djaoui

Rutherford Appleton Laboratory

INTRODUCTION

Intense x-ray radiation sources can now be generated by irradiating a high Z converter such as gold with a high power laser beam at intensities 10^{13} W/cm^2 - 10^{15}W/cm^2. Conversion efficiencies of up to a few percent are achievable[1]. X-ray fluxes of 10^{11}W/cm^2 - 10^{14}W/cm^2 or effective radiation blackbody temperatures of 30eV - 180eV approximately are therefore possible. These are of considerable interest as driving power sources for indirect-drive Inertial Confinement Fusion (ICF) or for creating hot dense materials of astrophysical interest having small temperature and density gradients. For high incident x-ray fluxes, high material temperature or low density, energy transfer by radiation is much more important than electron thermal conduction[2-3]. The momentum transferred from radiation to matter following photon absorption can also have a significant effect on the hydrodynamic motion of the material for high radiation temperatures. In order to calculate the behaviour of materials irradiated by intense sources of radiation it is therefore necessary to account for energy as well as momentum exchanges between radiation and matter in the hydrodynamic equations. For one dimensional flows the Lagrangian frame (co-moving frame) formulations has many advantages because it is the frame in which material properties are isotropic. The equations used here are restricted to the first terms in the expansion of the radiation hydrodynamics equations in the small parameter u/c (characteristic flow velocity / velocity of light) and are only valid for non-relativistic flows[3]. When the plasma velocity is much less than the speed of light, a photon travels one mean free path in a time much shorter than the time required for any significant changes in plasma temperature and density to occur. In this case there is an instantaneous distribution of radiation which can then be treated in a quasi-steady state approximation (the time derivative in the radiative transfer equation is set to zero). For low velocities, the Doppler shift between the point of emission and the point of absorption of a photon can also be neglected for the purpose of calculating radiative energy transfer.
In this work a radiation hydrodynamics code (MEDX) based on the 1D Lagrangian code MEDUSA[4] is implemented in both planar and spherical geometry. The algorithm requires externally generated local thermodynamic (LTE) Planck or Rosseland group opacities in a tabular form, from a model such as IMP[5]. MEDX is intended as a simulation tool for indirect drive implosions as well as different radiative transfer problems of current interest.

LAGRANGIAN EQUATIONS OF RADIATION HYDRODYNAMICS.

The free electron energy equation and the equation of motion for a non-radiating plasma in the 1D Lagrangian code MEDUSA (see reference 4 for details) are modified in the presence of radiation in the following way (SI units are used here).

Electron energy equation (or first law of thermodynamics):

$$\frac{dU(\rho,T_e)}{dt} + P_e\frac{dV}{dt} = S_e + H_R. \qquad \text{[W/kg]} \quad (1)$$

Equation of motion (Navier-Stokes equation):

$$\rho\frac{du}{dt} = -\nabla P + f_R. \qquad \text{[N/m}^3\text{]} \quad (2)$$

H_R represents the amount of radiative energy absorbed minus the amount emitted (per unit mass) by the plasma and f_R the radiation force on the plasma (per unit volume) resulting from the momentum of absorbed photons. Emission of radiation is isotropic in the plasma frame and contributes no net plasma momentum change. The net absorbed radiative energy and the radiation force are calculated from the radiation specific intensity $I_\nu(r,\mu)$ (ie amount of energy transported by radiation at position r per unit time, per unit area, per unit frequency ν, per unit solid angle). For a computational cell whose mass is dM and with a flux of radiation $F(r_l)$ crossing the left boundary (area A_l) and a flux $F(r_r)$ crossing the right boundary (area A_r,) the amount of energy absorbed is given by

$$H_R = \frac{F(r_l)A_l - F(r_r)A_r}{dM}, \qquad (3a)$$

where the radiation flux at a point r is given by

$$F(r) = 2\pi\int_0^\infty d\nu \int_{-1}^{+1} d\mu\ \mu I_\nu(r,\mu)\ . \qquad (3b)$$

The radiation force at a given point r where the opacity is $\kappa_\nu(r)$ is also obtained from the specific intensity at the same point and is given by

$$f_R = \frac{2\pi}{c}\int_0^\infty d\nu\ \rho\kappa_\nu(r)\int_{-1}^{+1} d\mu\ \mu I_\nu(r,\mu)\ . \qquad (4)$$

It is important to point out at this stage that equation (1) must be supplemented by an appropriate equation of state (EOS) which gives the internal energy U as a function of temperature T and density ρ. Such EOS should take into account not just the contribution to the internal energy from free electrons but also the contribution from the internal structure of the ions (ie excited states and ionisation/recombination). This is necessary because although some radiative processes directly affect the free electron energy (free-free processes for example) other processes such as bound-bound absorption do not affect the free electrons directly, but simply results in an ion being raised to a higher energy state. In formulating the opacity all processes involving radiation (including stimulated emission) are included in the calculation[5]. The opacity represents the total attenuation of a beam of radiation through the plasma resulting from all the radiative processes involving either ions or free electrons. A separate energy equation is used in MEDUSA for the ion temperature, with a perfect gas EOS which effectively consider the ions as point particles. This separation of the translational and internal properties of the ions is possible because in LTE the distribution over internal and translational states are statistically independent of each other. An example of an appropriate electron EOS for use in MEDX is the Thomas-Fermi model (with or without corrections) as this includes the effects of excitation and ionisation.

RADIATIVE TRANSFER EQUATION IN PLANAR GEOMETRY.

The method of solution of the radiative transfer problem and the level of approximation used is determined by the type of problem

we are interested in. In addition to the steady-state and LTE assumptions mentioned above, scattering is also neglected as it is usually not important. This changes the transport equation from an integro-differential equation in the general case of anisotropic and inelastic scattering to a simple differential equation. A powerful computational technique for solving the transfer problem is based on a second order form of the transfer equation which has the property of reproducing the diffusion limit at high optical depths and behaves correctly at small optical depths[3]. A mean intensity-like variable $j_\nu(r,\mu)$ and a flux-like variable $h_\nu(r,\mu)$ are defined as

$$j_\nu(r,\mu) = \frac{I_\nu(r,+\mu) + I_\nu(r,-\mu)}{2}, \qquad (0 \le \mu \le 1) \quad (5)$$

$$h_\nu(r,\mu) = \frac{I_\nu(r,+\mu) - I_\nu(r,-\mu)}{2}, \qquad (0 \le \mu \le 1). \quad (6).$$

A second order differential equation for $j_\nu(r,\mu)$ is then easily obtained from the standard radiative transfer equation (see reference 3 for details)

$$\mu^2 \frac{\partial^2 j_\nu(r,\mu)}{\partial \tau_\nu(r)^2} = j_\nu(r,\mu) - S_\nu(r), \qquad (7)$$

where $\tau_\nu(r)$ is the optical depth ($d\tau_\nu(r)=\rho\kappa_\nu(r)dr$) and $S_\nu(r)$ is the source function. In LTE this is given by the Planck function at the local temperature and is isotropic (no dependence on μ). Having solved for $j_\nu(r,\mu)$ in equation (7) (with the help of the boundary conditions from the next section) the flux-like quantity is then obtained from the following first order form of the transfer equation

$$h_\nu(r,\mu) = -\mu \frac{\partial j_\nu(r,\mu)}{\partial \tau_\nu(r)}, \qquad (8)$$

and equations (3b) and (4) can now be evaluated with the integration over μ restricted to the interval [0,1] only as

$$F(r) = 4\pi \int_0^\infty d\nu \int_0^{+1} d\mu \; \mu h_\nu(r,\mu), \qquad (9)$$

$$f_R = \frac{4\pi}{c} \int_0^\infty d\nu \; \rho\kappa_\nu(r) \int_0^{+1} d\mu \; \mu h_\nu(r,\mu). \qquad (10)$$

The numerical solution of equations (7) and (8) proceeds by integrating the equations in each frequency interval corresponding to the group structure for which the opacities are given. This then allows us to replace integrals over ν in equation (9) and (10) by sums over g where g=1..G (G=total number of energy groups) with the understanding that the group opacities are some suitably averaged (Planck or Rosseland for example) group opacities. The angular integrals are replaced by Gaussian quadratures which have the property of being exact for a polynomial in μ up to order 2M-1 for a quadrature of order M. The appropriate discrete directions μ_m, m=1..M and the corresponding weights W_m in the interval [0,1] are calculated from the [-1,1] interval values as given in reference 6.
The medium is also discretized in the spatial direction into L cells. In writing the finite difference form of the equations $j_{gm}(r)$ is assigned to cell centres and $h_{gm}(r)$ to cell boundaries. In the absence of scattering there is a separate tri-diagonal set of equations for each group and angular direction which can be solved by standard methods. The computational effort required to obtain a solution in planar geometry scales roughly as GML.

BOUNDARY CONDITIONS.

The system of equations (7) must be supplemented by left and right boundary conditions in order to get the same number of equations as unknowns thus allowing a solution. The right boundary condition at r_{L+1} should allow for an incident radiation intensity $I_g(r_{L+1},-\mu_m)=X_g^{in}(\mu_m)f(\mu_m)$ in each energy group with a degree of anisotropy given by $f(\mu_m) = \mu_m^{\,n}(n+2)/2$ (n=0 corresponds to the isotropic situation). The normalisation of the angular shape function ensures that as n is varied the total incident flux (power per unit area) in kept constant. The left boundary condition at r_1 is either free when $I_g(r_1,+\mu_m)=0$ or reflecting when $I_g(r_1,+\mu_m)=I_g(-\mu_m,r_1)$ and $h_{gm}(r_1)=0$. The free boundary case is used when the x-ray flux emerging from the back of a target is sought while the reflecting boundary case allows the simulation of symmetric illumination of a slab target.
The left and right boundary values $j_g(r_1,\mu_m)$ and $j_g(r_{L+1},\mu_m)$ are normally derived from a first order differential forms of the radiative transfer equation. We found that these however do not give the correct result in situations where the boundary cells are optically thick. To remedy this the formal solution of the transfer equation in integral form is used to close the system of equations (7). The results are

Left boundary:

$$j_{gm}(r_1) = j_{gm1}\frac{2\exp(-0.5\Delta\tau_{g1}/\mu_m)}{1+\exp(-\beta\Delta\tau_{g1}/\mu_m)} + S_{g1}\frac{[1-\exp(-0.5\Delta\tau_{g1}/\mu_m)]^2}{1+\exp(-\beta\Delta\tau_{g1}/\mu_m)}$$

where $\Delta\tau_{g1}$ is the optical thickness of the leftmost cell and β is equal to zero or one for the free and reflecting boundary respectively.

Right boundary:

$$j_{gm}(r_{L+1}) = j_{gmL}\exp(-0.5\Delta\tau_{gL}/\mu_m) + S_{gL}\frac{[1-\exp(-0.5\Delta\tau_{gL}/\mu_m)]^2}{2} + X_{gm}^{in}\frac{1-\exp(-\Delta\tau_L/\mu_m)}{2}$$

$\Delta\tau_{gL}$ is the optical thickness of rightmost cell. In deriving the above boundary conditions the opacity and source function are assumed to be constant across each boundary cell.

SPHERICAL GEOMETRY.

In curved geometries (ie spherical, the cylindrical case is not dealt with here) the transfer equation contains an angular derivative in addition to the spatial one. This derivative arises because during streaming, the direction variable of a photon changes continuously in spherical geometry (except for streaming through the centre). This problem is usually dealt with by use of discrete ordinate methods for which the computational effort scales as M^3 where M is the number of fixed angles used. For strongly anisotropic situations a very large M ought to be used in order to get adequate angular resolution and the computational expense rises rapidly. An alternative method which can deal with strongly anisotropic situations is the tangent-rays method. This consists in dividing the sphere in zones which are determined by the tangents to the cell boundaries (thick horizontal lines in figure 1). The angular quadrature for each boundary surface l in equations (9) and (10) is effectively split into a number of quadratures over angular intervals $[\mu_{li-1}-\mu_{li}]$ cut by a zone on boundary l. The number of rays j and the corresponding impact parameter p_j is determined by the gaussian quadrature order M and angles used in the angular interval. For most problem a single ray in each zone is sufficient since the effective number of angles used at each boundary l is equal to the number of zones into which they are divided (ie number of computational cells inside l). The boundaries of outside cells have therefore a higher angular resolution than the boundaries of

inner cells. The distance along the propagation ray s (with impact parameter p_j) at the point of intersection with boundary l having radius r_l is given by $s_{lj} = \sqrt{r_l^2 - p_j^2}$, while the angle made by the ray with the boundary is simply $\mu_{lj} = s_{lj} / r_l$. In each zone a quasi-1D planar problem is solved using equations (7) and (8) (with μ set to one) along the rays s and a reflecting left boundary condition. For every energy group and ray a tri-diagonal system of equations whith an order equal to the number of cells intercepted by the ray is solved by using the planar geometry procedure.

The tangent-ray procedure has however a disadvantage in that the computational cost scale as GML^2 where L is the total number of cells, and the method can be slow when the number of cells is large. Although a much simpler and faster algorithm such as multi-group diffusion or discrete ordinates is adequate in many situation, this procedure is very powerful in dealing with strongly anisotropic situations and is much simpler to implement than Monte-Carlo methods normally used in these cases.

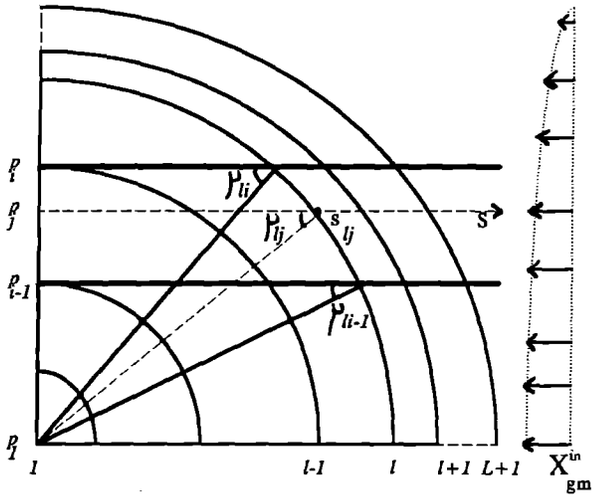

Figure 1: *Tangent-ray scheme. A sphere is divided into zones with boundaries determined by the tangents to the computational cells. A quasi-1D planar problem is solved for each zone. The incident flux as a function of angle X^{in}_{gm} is shown by the horizontal arrows to the right of the figure.*

APPLICATIONS

A few test cases are presented for different aluminium targets. The opacity data for these calculations was generated by S J Rose using the IMP code[5]. In order to show the behaviour of the method at small and large optical depths the emitted spectrum from a 1 μm Al planar target at a constant temperature of 100eV and constant density is calculated. It is seen in figure 2 that as the density of the target increases to 100 times solid density, the target becomes optically thick in all energy groups and a spectrum corresponding to a Planckian at 100eV is recovered. As the density decreases the spectrum starts to deviate from a Planckian case at high energies first since the opacity is smaller at these energies. At the lowest density (smallest optical thickness) some structure characteristic of line emission and bound-free edges is apparent in the emitted spectrum.

The full radiation hydrodynamics code is now used to simulate the behaviour of a 1μm radius Al sphere. The drive consists of a 100ev Planckian isotropic flux (constant in time). Figures 4 and 5 show the electron temperature and density as a function of computational cell number at different times in the simulations. Electron heat conduction in this situations is negligible compared to radiative heat transfer and at these temperatures and densities the radiation force is also negligible compared to the plasma pressure gradients. Ablation of the outside of the sphere results in a shock wave being launched toward the centre. The maximum compression is reached at about 30 ps in the simulation. Even before the arrival of the shock wave the centre of the sphere is heated by radiation (at 10ps and 20ps) to about 15eV.

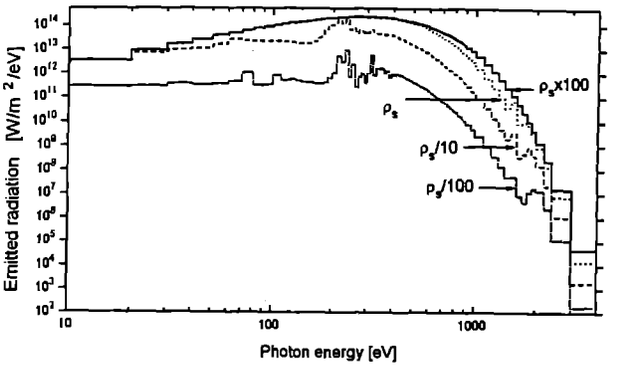

Figure2: *Emitted spectrum (Flux per unit photon energy) from 1 μm Al at a constant temperature of 100eV and four densities (ρ_s is the solid density=2.7g/cm^3). The full curve ρ_sx100 is not distinguishable from a Planckian spectrum of 100eV.*

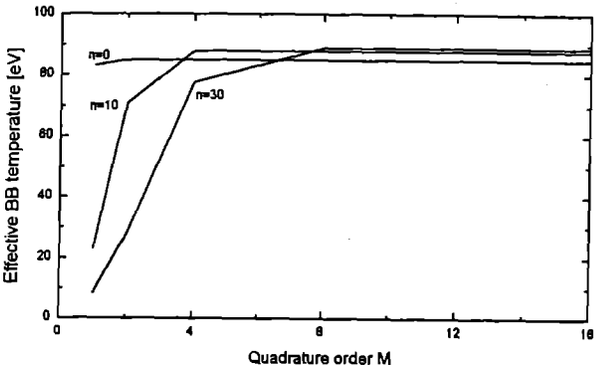

Figure 3: *Effective Black Body (BB) temperature of radiation flux emerging from left boundary of a 1μm Al foil at a density ρ_s/10 and a temperature of 10eV as calculated with different quadrature orders. The foil is irradiated from the right by a 100eV BB flux with varying degrees of anisotropy n.*

The question of what quadrature order to use is best illustrated by considering a 1μm Al foil at a density ρ_s/10 and a temperature of 10eV which is irradiated on the right hand side by a 100eV Planckian flux. From figure 2 it is seen that such target is partially optically thin to the driving radiation. The effective black body temperature of the emergent flux on the left boundary is plotted in figure 3 as a function of the angular quadrature order used and for different orders of anisotropy n. For an isotropic incident flux even M=1 is sufficient for a good angular resolution of the radiation. As the degree of anisotropy increases it is seen that M=4 or even 8 is necessary. However, these extremely anisotropic situations are rarely encountered and M=2 is often sufficient for planar problems. A similar calculation for 1 μm radius Al sphere at the same density and temperature showed that M=1 is sufficient for the calculation of the flux at the surface of the innermost cell (radiation is isotropic at the centre) as well as the outside boundary (where the angular resolution is high; the number of angles used being equal to the number of cells).

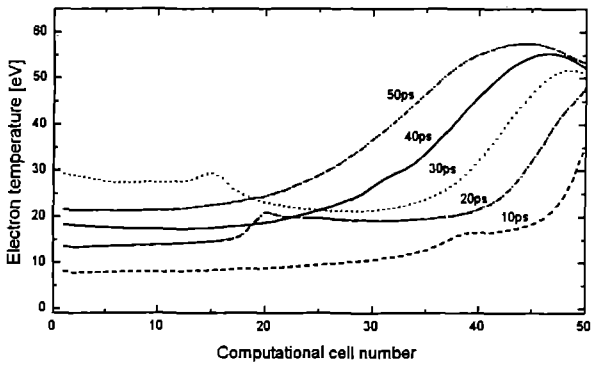

Figure 4: *Electron temperature as a function of cell number for different times in the simulation of a 1μm radius spherical target driven by a 100eV Planckian isotropic black body radiation field.*

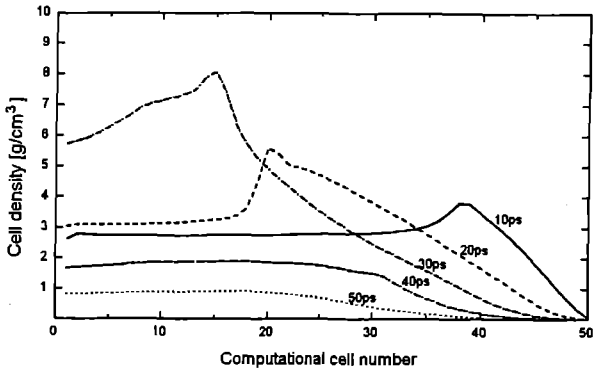

Figure 5: *Electron density as a function of cell number for different times in the simulation of a 1μm radius spherical target driven by a 100eV Planckian isotropic black body radiation field.*

CONCLUSION

A multi-group radiation transport algorithm is implemented in planar and spherical geometry and coupled to the hydrodynamics in a 1D Lagrangian code MEDX. Energy as well as momentum exchanges between radiation and plasma are taken into account. Tabulated group opacities as required by the code are generated by the IMP module. The radiation hydrodynamics equations are derived under the assumptions of LTE, no scattering and the neglect of the time derivative in the radiative transfer equation. A second order form of the transfer equation which reproduces the diffusion limit at high optical depths and behaves correctly at small optical depths is used. The curvature in spherical geometry is dealt with by using a tangent-ray scheme which is capable of dealing with very anisotropic situations. MEDX is intended as a simulation tool for radiation driven implosions of ICF targets and the study of the penetration and deposition of radiation into a plasma either in the diffusion or the transport limits.

REFERENCES

1. Michizuki, T. Yabe, K. Okada, M. Hamada, N. Ikeda, S. Kiyokawa and C. Yamanaka, *Phys. Rev. A*, **33**, 525 (1986).
2. Ya. B. Zel'dovitch and Yu. P. Raizer, *Physics of Shock Waves and High Temperature Hydrodynamic Phenomena*, (Academic Press, New York, 1966).
3. D. M. Mihalas and B. W. Mihalas, *Foundations of Radiation Hydrodynamics*, (Oxford University Press, Oxford, 1984)
4. J. P. Christiansen, D. E. T. F. Ashby and K. V. Roberts, *Compt. Phys. Commun.* **7**, 271 (1974).
5. S. J. Rose, *J. Phys. B: At. Mol. Opt. Phys.* 25, 1667, (1992).
6. M. Abramovitz and I. A. Stegun, *Handbook of Mathematical Functions*, Dover Publications Inc. New York (1970).

SOLUTIONS OF THE NON-LINEAR FOKKER-PLANCK EQUATION FOR ELECTRONS IN AN APPLIED ELECTRIC FIELD

M G Haines

Blackett Laboratory, Imperial College, London SW7 2BZ, England

ABSTRACT

An analytical approach to the solution of the non-linear Fokker-Planck equation under conditons when an applied electric field maintains a significant deviation from a Maxwellian reveals several interesting features' eg the leading term in electric field drives a term proportional to V^5 where V is the normalised velocity. Whether or not there is a connction with the Langdon effect is discussed. This work has applications to tokamaks as well as to laser fusion.

INTRODUCTION

Whilst the development of the theory in this paper was motivated by the need to explain a large electron heat flux up a temperature gradient in a tokamak plasma[1], the model and techniques hav wider application. Indeed the intiial method of expanding the distribution function in a tensor expansion[2] and truncating at f_1 with a non-Maxwellian f_0 was developed first in a laser fusion context[3]. We consider the simplified case in which an electric field $\underline{E}$ drives the distribution function to be non-Maxwellian.

The range of f_0 that is strongly distorted can be ascertained in an order of magnitude estimate as follows. Nothing that f_1 is related to f_0 by

$$\frac{\partial \underline{f}_1}{\partial t} = \frac{eE}{m}\frac{\partial f_0}{\partial v} - \nu_0 f_1 \frac{v_T^3}{v^3} \tag{1}$$

where n_0 is the electron-ion collision frequency for an electron with a mean thermal velocity v_T. In steady state and for a Maxwellian $f_0 = a_0 \exp(-v^2/v_T^2)$, f_1 becomes

$$f_1 = \frac{2e\underline{E}}{m\nu_0 v_T^3}\frac{v^4}{v_T^2} a_0 \exp\left(-\frac{v^2}{v_T^2}\right) \tag{2}$$

The condition that $|f_1| > f_0$ is $E > \frac{m\nu_0}{e v^4} v_r^5$ (3)

If we can write $\underline{E} = \eta \underline{J} = \frac{m_e \nu_\partial}{ne^2}.ne v_d$,

condition (3) becomes

$$\frac{1}{2}mv^2 > \left(\frac{v_T}{v_4}\right)^{1/2}\frac{1}{2}mv_T^2 \tag{4}$$

In contrast the Dreicer condition[4] for runaway electrons is

$$\frac{1}{2}mv^2 > \left(\frac{v_T}{v_4}\right)\frac{1}{2}mv_T^2 \tag{5}$$

NON-LINEAR FOKKER-PLANCK MODEL

We consider the self-consistent equation for the isotropic component of the distribution function f_0, given by

$$-\frac{1}{3v^2}\frac{\partial}{\partial v}\left(v^2 \underline{a}.\underline{f}_1\right) = \frac{\nu_{ee} v}{n_e}\frac{\partial}{\partial v}$$
$$\left[f_0 . 4\pi \int_0^v f_0 v^2 dv + \frac{v}{3}\left\{\frac{4\pi}{v^2}\int_0^v f_0 v^2 dv + 4\pi v \int_v^\infty f_0 v dv\right\}\frac{\partial f_0}{\partial v}\right]$$

where $\underline{a}\frac{\partial f_0}{\partial v} = \nu_{ei}\underline{f}_1$, $\underline{a} = \frac{e}{m}\underline{E}$, and $\nu_{ei} = \nu_0 \frac{v_T^3}{v^3}$

Integrating eq (6) and writing in dimensionless form we obtain

$$-\frac{A}{3}V^5\frac{\partial F_0}{\partial V} = F_0\int_0^v F_0 V^2 dV + \frac{V}{3}$$
$$\left\{\frac{1}{V^2}\int_0^v F_0 V^2 dV + V\int_v^\infty F_0 V dV\right\}\frac{\partial F_0}{\partial V} \tag{7}$$

where $A = \left(\frac{eE}{m}\right)^2 \frac{1}{\nu_0 \nu_{ee0} v_T^2}$ and $F_0 = \frac{4\pi v_T^3}{n_e f_0}$

Taking a series solution of the form $F_0 = \sum_{n=0}^{\infty} a_n V^n$ with $V^m F_0 \to 0$ as $V \to \infty$ for any finite m we can show that $a_1 = 0 = a_3$ while $a_2 = a_0$ and $a_4 = {}^1/_2 a_0$ consistent with a Maxwellian. However, a_5 is ${}^4/_5 A$ and is the first departure from a Maxwellian due to an electric field. a_6 is $-{}^1/_6 a_0$, but a_7 is $-{}^{19}/_{35} A$, while $a_8 = \frac{a_0}{24} - \frac{A^2}{a_0}$ has a higher order term. To describe F_0 to 1% accuracy for V=5, say, would require some 40 terms; but the expressions are explicit and straightforward to evaluate. The occurrence of the V^5 term as the leading effect due to the electric field has similarity to the Langdon effect [5] but this perhaps is just a coincidence. The self-similar solution of Langdon is obtained by ignoring electron-electron collisions and taking an oscillatory electric field with a frequency much greater than the electron-ion collision frequency. In this case our eq (6) is replaced by

$$\frac{\partial f_0}{\partial t} = \frac{\nu_0 v_T^3 v_0^2}{6v^2}\frac{\partial}{\partial v}\left(\frac{1}{v}\frac{\partial f_0}{\partial v}\right) \tag{8}$$

where $\frac{e\bar{E}}{m\omega} = v_0 \cos \omega t$. .Langdon found the self-similar solution

$$f_0 \propto \frac{1}{u^3}\exp\left(-\frac{v^5}{5u^5}\right) \tag{9}$$

where $u^5 = \frac{5}{6}\nu_0 v_T^3 v_0^2 t$ (10)

The $\underline{a}.\underline{f}_1$ term which both theories have in common is, however, rather different here because of the assumption of high frequency; instead of $\frac{\partial}{\partial v}\left(\frac{v^5 \partial f_0}{\partial v}\right)$ in eq (6), eq (8) has a term $\frac{\partial}{\partial v}\left(\frac{1}{v}\frac{\partial f}{\partial v}\right)$. The v^5 term here is, therefore, not related to the Langdon effect.

REFERENCES

1. T C Luce, C C Petty & J C M de Haas, Phys Rev Lett 68, 52 (1991)
2. T W Johnston, Phys Rev 120, 1103 (1960)
3. E M Epperlein, G J Rickard & A R Bell, Phys Rev Lett 61, 2453 (1988)
4. H Dreicer, Phys Rev 117, 329 (1960)
5. A B Langdon, Phys Rev Lett 44, 575 (1980)

RAYTRACING SIMULATIONS OF Ge SLAB TARGETS

J A Plowes, P B Holden, S B Healy and G J Pert

Department of Physics, University of York, York YO1 5DD, England

INTRODUCTION

Refraction of the X-ray laser beam by the high electron density gradients generated in collisional excitation X-ray lasers needs to be included in the modelling if such codes hope to reproduce experimental results. At York this is accomplished by using a 3D raytrace, including saturation effects, as post-processor to EHYBRID; a $1^1/_2$d langragian hydro/atomic code.

Parameters generated by EHYBRID, density, gain, etc are assigned to a triangular mesh in the radial transverse plane. The plasma is assumed homogeneous in the lasing direction. Rays are started across a spread of angles in each cell, each ray given a fraction of the spontaneous emission for that cell. The path of the ray is calculated and the ray is amplified accordingly as it passes through regions of gain. The near and far field parameters are built up by running successive rays.

Compensation of refraction by bending the target has been proposed by Lunney[1], and has recently been observed on targets bent along the lasing axis at Osaka University[2]. The effects of curvature are included in the raytrace code by modifying the ray angles at each cell exit. The following section shows typical results for both curved and flat targets.

RESULTS

Figure 1 shows a time integrated near-field pattern for a flat Ge target irradiated by a nanosecond driving pulse. The characteristic two lobe structure seen in experiment can be seen. Divergences, and the deflected angle of the beam measured from the far field are in good agreement with experiment.

Figure 2 shows the near-field pattern as the radius of curvature is decreased to 2 m. The dominant signal comes from a smaller area of the plasma which has a higher gain coefficient than for the previous case. This effect is accompanied by a narrowing angle of the lasing axis with respect to the target. This is caused by gain guiding of the X-ray laser beam, because some of the refraction effects have been compensated for and, therefore, the beams in higher gain dominate the signal.

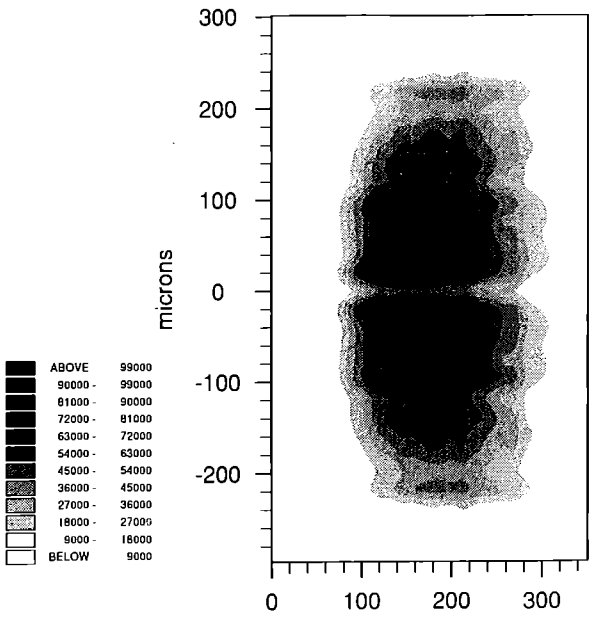

Figure 1 Near field, flat field

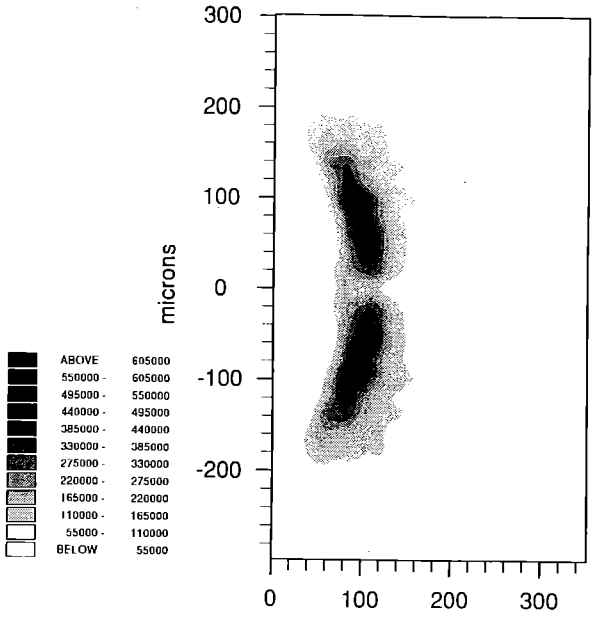

Figure 2 Near-field, curved target

REFERENCES

1. J G Lunney, Appl Phys Lett 48, 891 (1986).

2. Y Kato, Osaka University, Private communication.

SATURATION AND LINE PROFILE MODIFICATION IN ASE LASERS

G J Pert

Department of Physics, University of York, England

The saturation reduction of gain is an essential feature controlling the output from a steady state laser. In single pass ASE devices it plays a limiting role once the overall amplification determined by the gain length product is sufficiently high. The general behaviour has been well understood for over twenty years, and a useful model developed by Casperson and Yariv[1,2]. This model yields a description of intensity saturation, and line profile modification in uni-directional (travelling wave) and bi-directional (ASE) systems. In particular line narrowing with homogeneous broadening, and line re-broadening with inhomogeneous are clearly identified. Unfortunately, the model in its basic form does not give good agreement with the relatively limited experimental data available on line profile effects; in contrast to intensity measurements, which are relatively insensitive to the details of the model. We have therefore re-examined some of the details whilst retaining the essential framework of this approximation.

Casperson and Yariv[1,2] proposed a picture of an ASE laser in which only the emission within a specified solid angle is amplified, in a beam of constant cross section allowing beams to propagate both forwards and backwards. In order to simplify the analysis a number of assumptions were made, which we have removed[3].

Firstly the spontaneous emission is assumed to be reduced by the same factor as the gain, namely $1/[1 + I(\nu)/I_s(\nu)]$, whereas in fact the reduction is smaller namely $[1 + I(\nu)/I_s'(\nu)]/[1 + I(\nu)/I_s(\nu)]$ where $I_s'(\nu) > I_s(\nu)$. The Casperson-Yariv results correspond to $I_s'(\nu) >> I_s(\nu)$ and are valid provided the net spontaneous emissions rate is not too large, as indeed it is in experimental systems.

Secondly homogeneous broadening is treated by an approximation which neglects line narrowing. However the error involved is always small, and negligible once saturation sets in.

The third and most serious deficiencies in the earlier theory result from the treatment of the line broadening mechanism, in that the line is incorrectly assumed to be either completely homogeneously broadened with a Lorentz profile, or completely inhomogeneous with a Doppler. Once saturation is achieved these two mechanisms behave completely differently over the line profile. With a homogeneous line, the population depletion, strongest at line centre, is spread over the entire line profile, so that the gain profile is unchanged, and the gain uniformly reduced. Thus the line continues to be amplified with narrowing, but at a correspondingly reduced rate. On the other hand with an inhomogeneous line there is no redistribution of the depletion over the line, so that the gain is strongly reduced on line centre, remaining high in the wings. As a result the line re-broadens, eventually returning to the original small signal profile.

In fact, this differentiation is unsatisfactory for two reasons. Lasers are generally dominated by Doppler broadening with a relatively small underlying Lorentz component. In contrast to the tight Gauss distribution, the Lorentz has strong wings, whose effect is to re-distribute the gains over the profile, strongly inhibiting re-broadening (fig 1). More importantly collisional relaxation will redistribute the inhomogeneous profile to give a 'homogeneous' Gauss distribution. In the limit of strong collisional effects the line will have a homogeneous Voigt profile. Very strong collisions will give rise to Doppler narrowing.

We have investigated collisional relaxation in detail and show that a good approximation for the gain reduction is given by,

$$\frac{G'(\nu)}{G_o'(\nu)} = \frac{(1+\bar{I}/I_\tau)}{(1+\bar{I}/I_s)(1+\bar{I}(\nu)/I_\tau)}$$

where $G'(\nu)$ is the gain distribution associated with the inhomogeneous profile (and must be convolved with the homogeneous component to give the net gain), $\bar{I}(\nu)$ is the intensity convolved with the homogeneous component, and $\bar{I}$ the weighted intensity (i.e $\bar{I}(\nu)$ integrated over the gain profile). I_s is the usual saturation intensity, and I_τ the relaxation saturation intensity:

$$I_s = (\gamma_1\gamma_2 + \gamma_1 A_{21} + \gamma_2 A_{12})/(\gamma_1 B_{21} + \gamma_2 B_{12})$$

$$I_\tau = (\Gamma_1\Gamma_2 + \Gamma_1 A_{21} + \Gamma_2 A_{12})/(\Gamma_1 B_{21} + \Gamma_2 B_{12})$$

where $\gamma_1(\gamma_2)$ are the net rates from the lower (upper) laser states to other states and $A_{21}(A_{12})$ the rates from the upper (lower) to the lower (upper) state, and $B_{21}(B_{12})$ the corresponding stimulated emission absorption rate. The relaxation rates are simply given by $\Gamma_1(\Gamma_2) = \gamma_1(\gamma_2) + 1/\tau$ where τ is the relaxation time. In the limit $\tau \to \infty$, no relaxation, $I_\tau = I_s$ equation (1) is equivalent to purely inhomogeneous broadening; whereas $\tau \to \infty$, complete relaxation, $I_\tau \to \infty$, we obtain the homogeneous result.

The characteristics of an ASE laser may be calculated from the equation of radiative transfer for the individual frequency groups coupled through the frequency dependent gain coefficient, for either uni-directional or bi-directional propagation. The calculation is reasonably straightforward using finite difference methods, but must be iterated for the bi-directional case. In the fully relaxed homogeneous Voigt profile, case quasi-analytic methods may be efficiently used.

Experimental data on these devices is relatively limited. Koch *et al*[4] have measured line widths in selenium X-ray lasers at 206Å. The data is shown in fig 1. This is compared against the model for various conditions with a Lorentz profile FWHM 14mÅ and Doppler profile FWHM 36mÅ from Koch *et al*[4], the ratio of saturation to spontaneous emission intensity (which determines the onset of saturation) was taken to be 1.3×10^6 from our own simulation. It can be seen that under the experimental conditions the underlying Lorentz component, although relatively weak, markedly reduces the re-broadening from a purely Doppler profile (dotted line) even with no relaxation, $I_\tau/I_s = 1$, (line 1). Some level of relaxation clearly occurs, but it is not possible to identify its magnitude due to the experimental errors. Line (2) corresponds to $I_\tau/I_s = 10$, and line (3) to the fully relaxed case.

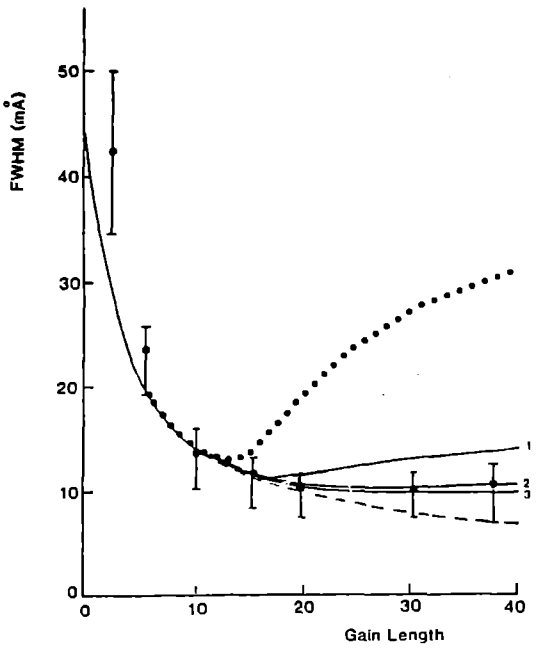

Fig 1.

Comparision of measures line widths for the selenium laser at 206Å versus gains length from Koch *et al*[4]. The curves (1), (2) and (3) are respectively unrelaxed, partially relaxed and full relaxed (totally homogeneous): the dotted line shows the line profile treated as totally inhomogeneous and the dashed without saturation.

A more comprehensive set of data was obtained by Schwamb and Smith[5] in a xenon laser with variable helium gas buffer pressures. Working at four different helium pressure line widths were measured as functions of ($G_o\ell$). The data does not fit well to either zero or complete relaxation. However, the introduction of a helium pressure dependent relaxation time, allows the data to be well re-produced by the model (fig 2). In this case the Lorentz component varied by 4-32 MHz compared to the Doppler width of 110 MHz as the helium pressure changed. Thus at the low pressure end the Lorentz background was relatively weak, and the effects of relaxation can be clearly identified.

To summarise the Casperson Yariv model of ASE lasers gives a good representation of the limited experimental data on line shape modification provided account is taken of the cross coupling effects associated with the overall Lorentz and Doppler components and with the relaxation within the inhomogeneous part due to collisions.

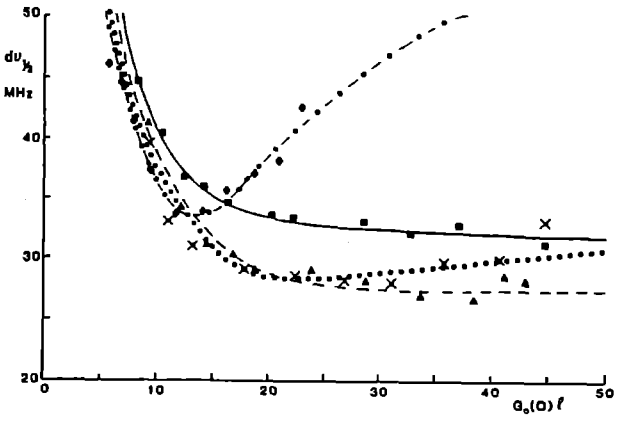

Fig 2.

Comparison of line width data from the xensor laser from Schwamb and Smith[5]. The lines are for different helium buffer pressures (○,- - -) 0 torr, (x, ...) 1.3 torr, (Δ, - - -) 2.5 torr and (□, —) 4 torr.

REFERENCES

1. L W Casperson and A Yariv.
I.E.E.E. J. Quant. Elec. QE-8, 80 (1972).

2. L W Casperson.
J. Appl. Phys. 48, 256 (1977).

3. G J Pert .
J.O.S.A. Pt B. in press.

4. J A Koch *et al.*
Spectral Line Shapes Vol 7 ed. R Stamm and B Talin.
(Nova Science Publishers) p.205 (1992).

5. D H Schwamb and S R Smith.
Phys. Rev. A21, 896 (1980).

NI-LIKE COLLISIONAL LASERS USING MODERATE POWER LASER DRIVERS.

P.A.Norreys, A.Djaoui
Rutherford Appleton Laboratory, Chilton, Didcot, Oxon OX11 0QX, United Kingdom

Significant progress has been made in recent years in the development of extreme ultaviolet (X-UV) lasers operating in the biologically important water window. This has been pioneered at the Lawrence Livermore National Laboratory (LLNL) using the NOVA laser facility by investigating Ni-like collisional lasers[1]-[6]. Gains of 3.6 cm^{-1} have been measured on the 4d - 4p, J = 0-1 transition at 4.48 nm in Ni-like Ta[7]. The major drawback, however, is the large pump power required to drive this laser to saturation (9 kJ, 0.53μm) using standard 1.0 nsec drivers.

One possible solution to this problem, as suggested by Key [8], involves heating and ionising the plasma to the Ni-like stage at high densities, thus increasing the gain coefficient significantly. This idea was further developed in a double pulse scheme by Maxon et al [9]. To obtain a high gain coefficient, the above scheme used a mixed target of $(LiH)_{0.85}Ta_{0.15}$ in the simulation which resulted in a peak gain coefficient of 49 cm^{-1}. These predicted gain coefficients are extremely large and offer an exciting possibility of obtaining saturated water window lasing with greatly reduced laser energy compared with the long pulse scheme.

We have examined the hydrodynamic behaviour of Ta exploding foils using a low intensity pre-pulse followed by a second high intensity heating pulse in detail. A modified version of the one dimensional Lagrangian hydrodynamic code MEDUSA [10] in planar geometry was used to investigate the scaling of Ni-like ions to a high gain regime. The atomic physics of excitation and ionisation is treated within the average atom approximation, as in Maxon et al's simulation. Previous comparisons of ionic fraction obtained from the average atom model and detailed configuration accounting calculations were in good agreement [11]. In this version of MEDUSA, the energy consumed in ionisation is taken into account in the free electron energy balance equation according to Djaoui and Rose [11]. A perfect gas equation of state and a flux limiter of 0.1 for the heat conduction are used in the simulations.

The laser energy is absorbed by inverse bremsstrahlung in the coronal region with 10% of the power reaching the critical density deposited there as resonance absorption. For a typical run, 60% of the laser energy is absorbed. Out of this about 50% is lost through radiative processes (mainly bound-bound) 10% in ionisation and the rest is shared between thermal and kinetic energy. In these calculations we assume that the plasma is optically thin to all radiation. This is a reasonable assumption for exploding foil plasmas where line radiation has an enhanced probability of escape as a result of Doppler decoupling due to large velocity gradients[12][13].

In our model, gaussian pulse shapes have been used (figure 1). These laser pulse shapes can be implemented on smaller glass lasers than the NOVA laser at Livermore, such as the VULCAN laser at the Rutherford Appleton Laboratory[14]. As MEDUSA is not able to calculate mixed targets at the moment, exploding foils of pure Ta with a density of 16.6gcm^{-3} and thickness 54nm were used. Foils with these parameters have already been used at LLNL in the original long pulse Ta experiments and can therefore be fabricated.

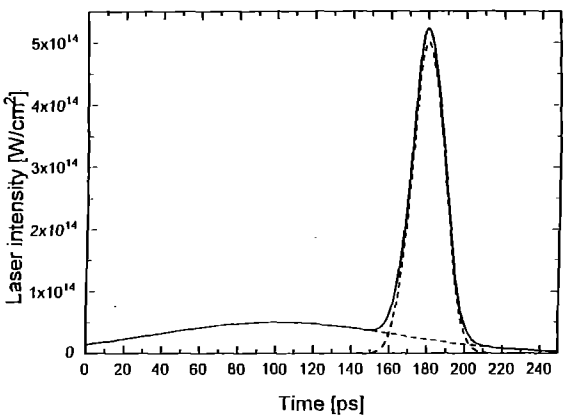

Figure 1. The temporal profile of the incident laser pulses showing the first low intensity pre-pulse ($5x10^{13}Wcm^{-2}$) followed by the second heating pulse ($5x10^{14}Wcm^{-2}$).

The timing between the two pulses was scaled to account for the increase in mass of the target by the simple relationship $t \propto I^{-2/3} \lambda^{2/3} m^{4/3}$ [15] where t is the time to transparency, I is the intensity, m is the target mass, and λ the laser wavelength. A 150 psec FWHM gaussian pulse of $5x10^{13}Wcm^{-2}$ was followed by a second gaussian pulse of 20psec duration and intensity $5x10^{14}Wcm^{-2}$. As expected, the time to transparency without any second heating pulse increased to 130 psec after the peak of the laser pulse to account for the larger areal density of the target. The timing of the heating pulse was varied with respect to the pre-pulse.

Figure 2 show the electron density profile as a function of space for (A) 10 psec before the peak of the heating pulse and (B) 10psec, (C) 25psec and (D) 40 psec after the peak of the heating pulse (corresponding to 170psec, 190psec, 205psec and 220psec in figure 1). At time (B) it can be clearly seen that a reasonably large flat density profile of $5x10^{21}cm^{-3}$ has been established of ~7μm half width at half maximum (HWHM). A uniform temperature of 2.0 keV (not shown in Figure 2) is also obtained at this time.

We are not at present able to accurately predict the gain coefficient that can be achieved due to a lack of atomic data for Ta. Nevertheless, it is possible to elucidate some properties of x-ray laser physics that can assist in estimating the value of the gain coefficient. The maximum total ion density in this simulation at 190 psec is $1.0x10^{20}$ cm^{-3}. Osterheld et al [16] calculated steady state gain coefficients from a detailed model of Ta and obtained values of 10-12 cm^{-1} for a total ion density of $2.0x10^{19}$ cm^{-3} and 1.0keV electron temperature. They also showed that the steady state gain is proportional to the electron density up to ~$1x10^{22}$ cm^{-3} after which it falls due to collisional depopulation. Hence we expect a high gain coefficient, similar to those predicted by Maxon et al (i.e. a peak gain of ~50 cm^{-1})[9].

It should be noted that the gain coefficient can be further increased with no extra cost of laser energy by irradiating an exploding foil target with a UV driver and achieving the flat density profile at even higher densities at the same temperature. Self-similar solutions to the heating of exploding foil targets performed by London and Rosen [15]

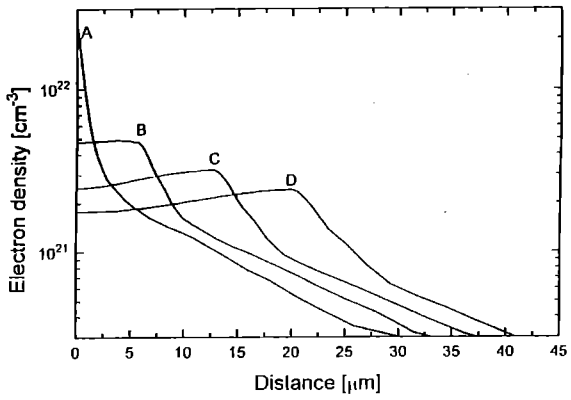

Figure 2. The electron density as a function of space for 530 nm laser irradiation of an exploding Ta foil at (A) 10psec before the peak of the second heating pulse (B) 10 psec (C) 25 psec (D) 40 psec after the peak of the second pulse.

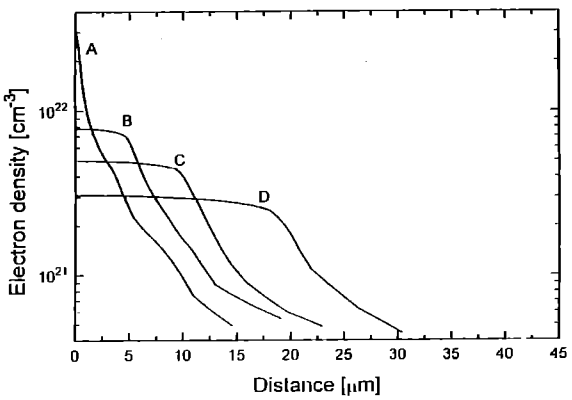

Figure 3. The electron density as a function of space for 268nm laser irradiation of an exploding Ta foil at (a) 10 psec before the peak of the second heating pulse and (b) 5 psec (c) 15 psec (d) 30 psec after the heating pulse.

show that before transparency the electron temperature scales as $T_e \propto I\ m^{-1}\ t$ (where I is the irradiance, m the mass of the target and t is the pulse length) and is independent of wavelength. A 268nm driver irradiates an exploding foil target with the same target mass as before, and the pulse length of the pre-pulse scaled to ensure that heating occurs before transparency. A 20 psec ($5 \times 10^{14} Wcm^{-2}$) heating pulse is super-imposed on a 80 psec FWHM ($5 \times 10^{13}\ Wcm^{-2}$) pulse. The second heating pulse peaks 40 psec after the peak of the first pulse. Figure 3 shows the density profile (A) 10 psec before the second heating pulse (B) 5 psec (C) 15 psec (D) 30 psec after the heating pulse. A flat electron density profile is established at $8 \times 10^{21} cm^{-3}$ electron density, a uniform 2.0 keV electron temperature, 400 eV ion temperature, 10 μm FWHM spatial profile and Ni-like ionisation. The electron temperature falls to 1.0 keV at point (D) still with a large proportion of Ni-like ions at $3 \times 10^{21} cm^{-3}$ electron density and a FWHM spatial profile of 34 μm. Thus a ×2 higher gain coefficient (approaching $100 cm^{-1}$) can be expected for these conditions.

It therefore appears that saturated emission can be achieved for laser energies ≤100J. If this is combined with developments in glass laser technology, such as high repetition rate slab lasers and pulse compression techniques, then the cost of producing affordable high repetition rate x-ray lasers in the biologically important water window is in sight. We suggest that it may be possible to vary the saturated energy output of the x-ray laser by irradiating a longer length than is necessary for saturation. If a post-pulse is then used to maintain the optimised electron temperature for efficient lasing of ~1.5 keV (together with multi-layer mirror optics), then the output energy can be increased by suitable matching of the post-pulse duration with the plasma expansion to maintain high gain length products.

In conclusion, the scaling of the collisionally excited Ni-like Ta laser to the water window using a pre-pulse and heating pulse has been numerically investigated. It has been shown that very favourable conditions for high gain lasing can be achieved for reduced laser energies than previously proposed by Maxon et al [9], provided that the heating pulse arrives before transparency. These reduced laser energy requirements should make it possible to realise saturated gain in Ni-like Ta lasing using optical drivers currently available at smaller scale facilities.

References

[1] P.L.Hagelstein, Phys. Rev. A **34**, 874 (1986).
[2] S.Maxon, P.Hagelstein, J.Scofield and Y.Lee, J. Appl. Phys. **59**, 293 (1986).
[3] B.J.MacGowan, S.Maxon, P.L.Hagelstein, C.J.Keane, R.A.London, D.L.Matthews, M.D.Rosen, J.H.Scofield and D.A.Whelan, Phys. Rev. Lett. **59** 2157 (1987).
[4] P.L.Hagelstein, S.Dalhed, Phys. Rev. A **37**(4), 1357 (1988).
[5] S.Maxon, P.Hagelstein, B.MacGowan, R.London, M.Rosen, J.Scofield, S.Dalhed and M.Chen, Phys. Rev. A **37**(6), 2227 (1988).
[6] B.J.MacGowan, L.B.Da Silva, D.J.Fields, A.R.Fry, C.J.Keane, J.A.Koch, D.L.Matthews, S.Maxon, S.Mrowka, A.L.Osterheld, J.H.Scofield, and G.Shimkaveg in *X-ray lasers 1990.* Institute of Physics Conference Series **116**, p221, Edited by G.J.Tallents, ISBN 0-85498-044-X (Institute of Physics Publishing, Bristol, United Kingdom, 1991).
[7] B.J.MacGowan, S.Maxon, L.B.Da Silva, D.J.Fields, C.J.Keane, D.L.Matthews, A.L.Osterheld, J.H.Scofield, G.Shimkaveg and G.F.Stone Phys. Rev. Lett. **65**, p420 (1990).
[8] M.H.Key in *X-ray lasers 1992.* Institute of Physics Conference Series **125**, p171. Edited by E.E.Fill. ISBN 0-85498-415-1 (Institute of Physics Publishing, Bristol, United Kingdom, 1992).
[9] S.Maxon, K.G.Estabrook, M.K.Prasad, A.L.Osterheld, R.A.London, and D.C.Eder, Phys. Rev. Lett. **70**, 2285 (1993).
[10] J.P.Christiansen, D.E.T.P. Ashby and K.V.Roberts Comp. Phys. Commun. **21**, 207 (1974).
[11] A.Djaoui and S.J.Rose, J. Phys B: At. Mol. Opt. Phys. **25**, 2747 (1992).
[12] I.N.Ross, M.S.White, J.E.Boon, D.Craddock, A.R.Damarell, R.J.Day, A.F.Gibson, P.Gottfeldt, D.J.Nicholas and C.J.Reason IEEE J. Quantum Electron. **QE-17**, 1653 (1981).
[13] T.W.Lee, R.A.London, G.B.Zimmerman and P.L.Hagelstein, Phys. Fluids **2**(11) 2731 (1990).
[14] D.C.Eder, H.A.Scott, S.Maxon and R.A.London, Appl. Optics **31**(24), 4962 (1992).
[15] R.A.London and M.Rosen, Phys. Fluids **29**, 3813 (1986).
[16] A.L.Osterheld, R.S.Walling, W.H.Goldstein, J.H.Scofield, M.H.Chen, B.J.MacGowan, S.Maxon, B.F.K.Young. Private Communication (1991).

HIGH GAIN RECOMBINATION X-RAY LASER AT THE WATER WINDOW

J. Zhang[1], M.H. Key[1,2], S.J. Rose[2,3], G.J. Tallents[4]

[1]Department of Atomic and Laser Physics, University of Oxford, Oxford, OX1 3PU, UK
[2]SERC Rutherford Appleton Laboratory, Chilton DIDCOT Oxon, OX11 0QX, UK
[3]Department of Physics and Space Science, University of Birmingham, Birmingham, B15 2TT, UK
[4]Department of Physics, University of Essex, Colchester, CO4 3SQ, UK

INTRODUCTION

X-ray lasers with wavelengths near 4.5 nm are optimum for making x-ray holograms of biological structures in living cells as the absorption contrast between carbon (protein) and oxygen (water) is greatest here[1]. The n = 3 - 2 (Balmer α) transition in the hydrogen-like magnesium ion is at 4.55 nm and so much effort has been dedicated to investing the hydrogen-like magnesium recombination x-ray laser. However, significant amplification on the Balmer α transition in hydrogenlike magnesium is still unproved[2-5]. Theoretical and experimental studies have indicated that high gain operation could be possible when shorter driving laser pulses and narrower targets are used[3,6-9]. The availability of psec and sub-psec pulse chirped pulse amplification (CPA) beam on several high energy Nd glass laser facilities now offers the possibility of further investigation of this lasing process[10,11].

In this paper we present a systematic theoretical study of the recombination x-ray laser operating on the Balmer α transition of hydrogen-like magnesium and show the potential advantages for the recombination x-ray laser driven by psec and sub-psec laser pulses. In particular, our theoretical investigations suggest significant improvement in gain performance of the recombination x-ray laser.

COMPUTER CODES

A one-dimensional Lagrangian hydrodynamic code MEDUSA coupled to an atomic physics code NIMP are used[12,13] to simulate the behaviour of the targets under irradiation. In the simulation, the laser energy is absorbed via inverse bremsstrahlung and resonance absorption. The resonance absorption fraction is set at each time step by calculating the scale length[12] at critical density. Twenty percent of the resonantly absorbed energy is assumed to be dumped at critical density. The rest is put into hot electrons which are transported in ten energy groups with an initial temperature at critical density. Energy transport by thermal electrons (including a 0.1 flux limiter taken from reference[14] to represent heat transport in regions of high temperature gradient), radiation cooling and recombination heating are treated.

The time dependent atomic physics of all ion stages are modelled in a non-LTE average atom (AA) description. Resonance line widths are Doppler except for H-like C where Stark broadening of the Balmer α line is calculated. Radiation transfer in the resonance lines is treated by using an escape factor, which accounts for Doppler decoupling[13]. The escape factor is applied separately to each Lagrangian cell with the average velocity gradient taken from the hydrodynamic simulation[13]. As Before[15,16], a maximum multiplier[13] of the optical depth in the escape factor is used in all these simulations to give a lower limit of results. For ultra-short pulse irradiation collisional absorption is weak due to the small depth of plasma at the critical density. Resonance absorption at the critical density is then the major absorption mechanism[13,17].

The code (or earlier versions of it) has been used extensively in cylindrical geometry to describe the recombination laser gain for fibre targets and it has also been tested in predicting the performance of experimental targets in several previous experiments[18,19], which used pulse length of 10 psec or greater. It has not been tested in the parameter space discussed in this article. However our present research mainly concentrates on the case of psec laser pulses case, which is close to the tested regime. The discussion on the sub-psec pulses poses an exciting challenge to the models in the code, and thus the results predicted for this regime should be taken with an appropriate amount of caution.

GAIN OPTIMISATION

Optimised conditions are calculated for 7 μm diameter fibres irradiated by short pulse drivers with various pulse lengths. It has been found experimentally that 7 μm diameter fibres are the thinnest which can be self-supporting and remain straight for lengths up to 1 cm[18]. Consequently such targets have the optimum practical diameter for x-ray laser action. The calculation is 1D and the energy incident at the target surface is varied to find optimum conditions giving the maximum gain. For each combination of the driving pulse length and wavelength, there is a corresponding optimum absorbed energy. For too small an absorbed energy, the plasma temperature is not sufficient to give the early predominant population of bare nuclei that is the necessary starting point of the recombination laser process. If the energy is too large, the LTE populations of the higher excited states are reduced by the increased temperature, which results in reduced population of the upper level and leads to a smaller gain. The optimum absorbed energy increases with increasing pulse length for both wavelengths. The optimum operation of the recombination lasers driven by the longer wavelength needs higher absorbed energy than that driven by a shorter wavelength with the same pulse duration. The value of the maximum peak gain increases as the pulse length is reduced.

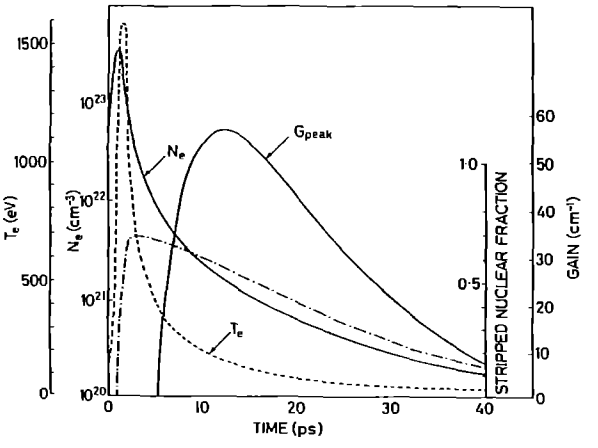

Fig. 1 Time evolution of the electron temperature, the electron density, the fraction of the fully stripped nuclei and the hydrogen-like magnesium Balmer α (4.55 nm) gain coefficient in the Lagrangian cell which gives maximum peak gain for a 7 μm diameter fibre target cylindrically irradiated by 1 psec 0.268 μm pulse driver with an absorbed energy of 21.9 J/cm.

Figure 1 shows a typical example for an optimised simulation of the time evolution of electron temperature (T_e), electron density (N_e), the fraction of fully stripped nuclei and peak gain for the hydrogen-like magnesium recombination laser at 4.55 nm in the Lagrangian cell, which gives maximum gain (both in time and space resolved). During the 1 psec interaction, there is a very rapid rise in temperature and very steep electron density gradients are produced. The electron temperature increases abruptly to a peak of 1.6 keV during the interaction and after the interaction the plasma expands quickly and the temperature drops rapidly to a plateau in a time less than 10 psec. The gain reaches the maximum when $N_e = 1.7 \times 10^{21}$ cm^{-3} and T_e = 158 eV. The FWHM (full width at half maximum) time duration of the gain region is about 21 psec with a maximum value occurring at 12.5 psec. Similar results are found for the corresponding calculations for a 1 psec 1.053 μm laser pulse.

The simulations show that longer driving pulses produce smaller peak gain with larger spatial FWHM. The spatial FWHM corresponding to the maximum peak gain (~ 10 cm^{-1}) produced by a 10 ps pulse with an optimised absorbed energy is about 60 μm.

COOLING CHARACTERISTICS OF RECOMBINING PLASMAS

The recombination rate and gain depend strongly on the plasma cooling rate. Increased cooling rate leads to reduced temperature at the optimised electron density and then to induce larger density of

inverted population for the Balmer α transition and consequently induce higher lasing gain. In order to illustrate the dependence of the cooling rate on the driving laser pulse length, the cooling time from the initial temperature to the temperature at x-ray laser time is shown against the driving pulse length (figure 2). It can be seen in figure 2 that the plasmas produced by the 0.268 μm wavelength laser driver cools more rapidly and that the difference between the cooling rates for 1.053 μm and 0.268 μm pulse drivers becomes the largest for the drivers with pulse lengths between 500 fsec and 2 psec.

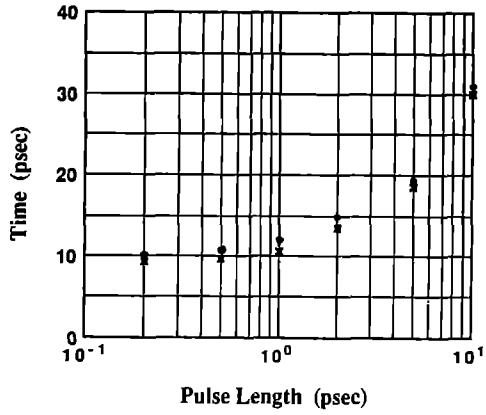

Figure 2 Variations of the cooling time taken from the initial electron temperature to the required temperature for optimum lasing operation with the driving pulse length for 1.053 μm "•" and 0.268 μm "x" wavelengths respectively.

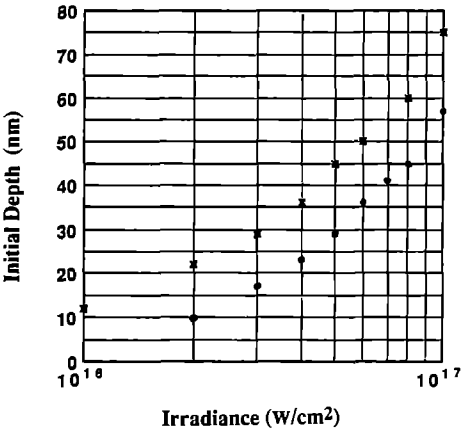

Figure 3 The initial depth of the optimum Lagrangian cell from the surface of the fibre target against the irradiance on the surface of the target irradiated by 1 psec pulse for 1.053 μm "•" and 0.268 μm "x" wavelengths respectively.

The initial depth of the optimum Lagrangian cell from the surface of the fibre target has been computed for different driving pulse lengths. An example of the dependence of the initial depth on the irradiance for 1 psec driving pulses is shown in figure 3. The Lagrangian cell, which is initially 30 nm from the target surface, with the optimum conditions of $N_e \sim 1.6\text{-}1.7 \times 10^{21}$ cm^{-3} and $T_e \sim 150\text{-}158$ eV at the X-ray laser time, mainly contributes to the amplification. The plasma, which comes from initial depths closer to the surface, expands too fast for attaining optimum density and temperature. Initial depths less than 10 nm do not contribute to the amplification. In contrast, the plasma initially too far from the surface can not reach a temperature high enough to achieve sufficient ionisation. For shorter driving pulse, the initial depth is smaller. The smallest optimum initial depth is 20 nm for sub-psec pulse drivers. For the longer pulse drivers, the optimum lasing operation requires greater initial depths for the 0.268 μm wavelength drivers than for the 1.053 μm drivers.

It is interesting to study the effects of increasing the cooling rate by substituting materials under the lasing layer producing plasma of higher conductivity. At the early time of heating, the plasma experiences very rapid heating. After the termination of the laser irradiation, rapid cooling can be divided into two stages dominated by thermal conduction and expansion cooling respectively. At the first stage of the cooling, thermal conduction predominates over expansion cooling because the sufficiently high initial temperature and small initial size of the plasma[20]. Thermal conductivity in the initial plasma can be orders of magnitude greater than that of a room temperature solid[21]. It is found that thermal electron conduction is effective in cooling the lasing magnesium and increasing the x-ray laser gain.

CONCLUSION

In summary, we have presented a detailed investigation of the hydrogen-like magnesium recombination laser driven by psec and sub-psec ultrashort pulses. Significant improvement of gain performance of the recombination lasers at 4.55 nm has been shown using the ultrashort pulse drivers. The optimised initial depth, which corresponds to the plasma cell where maximum gain occurs at later expansion period, from the surface of the fibre is found to be small (several tens nm) for the ultrashort pulse laser drivers. Cooling characteristics of the recombining plasmas are studied. Thermal electron conduction predominates over expansion cooling at early stages. Saturated gain operation requires a high gain-length product. This calculations presented here, however, do not include the effects caused by non-uniform irradiation along the plasma length. However our recent research show that increasing the irradiation intensity can avoid the production of absorbing zones along the plasma length and lessen the problem of mismatch of the space/time gain windows of the hydrogen-like magnesium recombination x-ray laser[22]. It would therefore be expected that a significant gain length product at water window might be achieved using this scheme.

REFERENCES

[1] L.B. Da Silva, J.E. Trebes, R. Balhorn, S. Mrowka, E. Anderson, D.T. Attwood, T.W. Barbee, Jr., J. Brase, M. Corzett, J. Gray, J.A. Koch, C. Lee, D. Kern, R.A. London, B.J. MacGowan, D.L. Matthews, G. Stone, Science, **258**, 269 (1992).

[2] H. Nishimura, H. Shiraga, H. Daido, T. Tachi, P.R. Herman, E. Miura, H. Takabe, M. Yamanaka, Y. Kato, G.J. Tallents, M.H. Key, *OSA Proc. Short Wavelength Coherent Radiation: Generation and Applications*, Vol. 20, Opt. Soc. Am., Washington DC, 137 (1988).

[3] M.H. Key, N. Tragin, and S.J. Rose, *X-Ray Lasers 1990*, G.J. Tallents ed., Bristol, IOP Publisher,163 (1990).

[4] R. Shepherd, D. Fields, L.B.Da Silva, C. Keane, B. MacGowen, D. Matthews, G. Shimkaveg, G. Stone, D. Eder, A. Osterheld, R. Walling, B.K.F. Young, A. Fry, M. Eckart, W. Goldstein, R. Stewart, G. Charatis, G. Bush, *X-Ray Lasers 1990*, G.J. Tallents ed., Bristol, IOP Publisher, 13 (1991).

[5] D.C. Eder, Phys. Fluids, B2, 3086 (1990).

[6] N.H. Burnett and P.B. Corkum, J. Opt. Am., B6, 1195 (1989).

[7] D.C. Eder, P. Amendt and S.C. Wilks, Phys. Rev. A**45**, 6741 (1992).

[8] E.J. Valeo and S.C. Cowley, Phys. Rev., E**47**, 1321 (1993).

[9] F.G. Patterson, M.D. Perry, R. Gonzales and E.M. Campbell, *SPIE Proceedings*, E.M. Campbell ed., **1229**, 2 (1990).

[10] C.N. Danson, L. Barzanti, Z. Chang, A. Damerell, M.D. Dooley, C.B. Edwards, S. Hancock, M.H. Key, R. Mahadeo, M.R.G. Miller, P.A. Norreys, C.E. Ollman, D.A. Pepler, D.A. Rodkiss, I. Ross, M.A. Smith, P.F. Taday, W.T. Toner, K. Wigmore, T.B. Winstone, R.W.W. Wyatt, A. Luan, F. Beg, A. Bell, A.E. Dangor, M.H. Hutchinson, P. Lee, I.P. Mercer, R.A. Smith. F. Zhou, A.P. Fews, *SPIE Proceedings*, H.A. Baldis ed., **1860**, 10 (1993).

[11] A.K. Dave and G.J. Pert, J. Phys. B. **17**, 4953 (1984).

[12] J.P. Christiansen, D.E.T.F. Ashby, and K.V. Roberts, Comput. Phys. Commun., **7**, 271 (1974).

[13] A. Djaoui and S.J. Rose, J. Phys. B: At. Mol. Opt. Phys., **25**, 2745 (1992).

[14] G.J. Rickard, A.R. Bell, and E.M. Epperlein, Phys. Rev. Lett., **62**, 2687 (1989).

[15] J. Zhang and M.H. Key, J. Appl. Phys. **74** 7606 (1993).

[16] J. Zhang and M.H. Key, Appl. Phys. B**58** 13 (1994).

[17] D.W. Forslund, J.M. Kindel, and K. Lee, Phys. Rev. Lett., **39**, 284 (1977).

[18] G.J. Tallents, L. Dwivedi, Y. Kato, M.H. Key, R. Kodama, J. Krishnan, C.L.S. Lewis, K. Murai, P.A. Norreys, G.J. Pert, S.A. Ramsden, H. Shiraga, C. Smith, J. Uhomoibhi, G. Yuan, and J. Zhang, *X-Ray Lasers 1992*, Bristol, IOP Publisher, 101 (1992).

[19] J. Zhang, M.H. Key, P. Norreys, and G.J. Tallents, Optics Commun., **95**, 53 (1993); J. Zhang, L. Dwivedi, Y. Kato, M.H. Key, R. Kodama, J. Krishnan, C.L.S. Lewis, K. Murai, P.A. Norreys, G.J. Pert, S.A. Ramsden, H. Shiraga, C. Smith, G.J. Tallents, J. Uhomoibhi, and G. Yuan, *X-Ray Lasers 1992*, E.E. Fill ed., Bristol, IOP Publisher, 339 (1992).

[20] N.H. Burnett and G.D. Enright, IEEE J. Quant. Electr., **26**, 1797 (1990).

[21] J.P. Matte and J. Virmont, Phys. Rev. Lett., **49**, 1936 (1982).

[22] M.H. Key, S.J. Rose, N. Tragin, and J. Zhang, Opt. Comm., **98**, 95 (1993).

MODELLING STUDY OF RECOMBINATION X-RAY LASERS DRIVEN BY ULTRA-SHORT PULSES

J. Zhang[1] and Y. Li[2]

[1]Department of Atomic and Laser Physics, University of Oxford, Oxford, OX1 3PU, UK
[2]Shanghai Institute of Optics and Fine Mechanics, Academia Sinica, P. O. Box 800-211, Shanghai, China

INTRODUCTION

It has long been known that shorter driving pulses are favourable for producing a high initial plasma density for high gain operation of recombination x-ray lasers[1,2]. Systematic simulations have shown that under intense irradiation of 2 ps ultra-short pulses, the gain coefficient produced from 7 μm diameter oxygen fibres can be as large as 100 cm^{-1} on the 3-2 Balmer α transition in hydrogen-like oxygen ions[3,4]. Although this result can be readily attributed to the fact that a higher initial density is produced by the shorter laser pulse, there still remain some details not fully understood. Simple models are therefore required for investigating the physics and for analysis over a large and important range of parameter space. In this paper we present a simple model based on the understanding of the special characteristics caused by the ultra-short pulse laser-plasma interaction in the near solid density regime besides the conventional hydrodynamic and radiation physics.

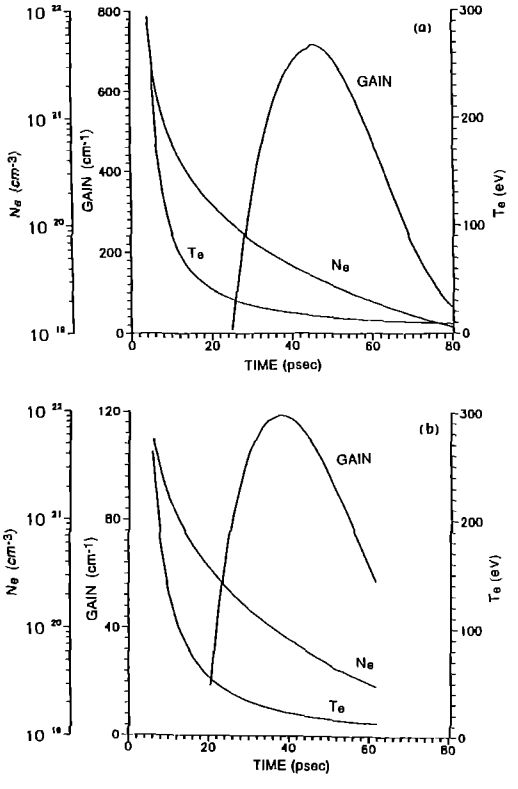

Fig. 1. Temporal histories of electron temperature, density and gain coefficient obtained from the model (a) and MEDUSA simulation (b) with τ = 2ps, R_0 = 3.5 μm, and optimised intensity I_{abs} = 5.6x10^{14} and 2.5x10^{14}W/cm^2 respectively, for Balmer α transition in oxygen.

THE MODEL

Generally speaking, plasma produced by a laser pulse can be divided into different regimes by examining the dominating physical process as well as the characteristics. In ultra-short pulse cases, most of the laser-plasma interaction is localised in the skin layer[5], which forms plasma and conduct expansion first. The rest of the energy deposited in the skin layer during the interaction is then transported into the solid portion under the skin layer by electron thermal conduction. The second part of the plasma is then created. We assume here the plasma produced from this skin layer play the most important role for high gain operation because they have the highest expanding speed and cool down fastest[6]. The electron temperature of this layer has been derived by solving the heat diffusion equation assuming a constant absorption intensity at the solid density surface prior to the hydrodynamic behavior[7,8] and also by solving the electron distribution function[6].

$$T_e = 1.331 \times I_{abs}^{4/9} \tau^{2/9} C_v^{-2/9} \kappa_0^{-2/9} \quad {}^{\circ}K \qquad (1)$$

where C_v, κ_0, I_{abs} and τ are the heat capacity at constant volume, heat conductivity, the absorbed laser intensity and the driving pulse duration. At an early stage, it is a good approximation to describe the hydrodynamic behaviour of the plasma by an isothermal expansion that takes place at the velocity of the ion sound speed $c_s = (\gamma Z_0 T_e / M_i)^{1/2}$ where M_i is the ion mass and γ=5/3 the specific heat ratio for an ideal gas[8,9]. When the laser heating ends, the density scale length is $c_s t$, and the average plasma density can be written by taking the volume ratio

$$N_e = Z_0 N_0 [R_0^2 - (R_0 - L_s)^2] / [(R_0 + c_s t)^2 - (R_0 - L_s)^2]. \qquad (2)$$

Equations (1)-(2) are solved together with collision-radiation equilibrium condition. The following free expansion can then be approximated by a self similarity process (with a immobile inner wall)[10-13] and the populations of the active levels can be related to the next highly ionised ions with a steady down flux model[12,13] and give the gain.

RESULTS

Fig. 1 gives comparison of model calculation (rectangular pulse profile) and simulation by MEDUSA[1,3,4] hydrodynamics code (Gaussian pulse profile) for Balmer α gain in a 7 μm diameter oxygen fibre irradiated by ultra-short pulses with 2 ps duration (λ_L = 1.053 μm). Both the simulation and the model calculation are optimised for the absorbed laser intensity. The model calculates temporal histories of the gain, the temperature and the electron density, agrees with the simulated results roughly. The gain coefficient from the model is about one order of magnitude higher than the simulation result, which may result from the incomplete atomic physics in the model. Simulation and model calculation give the same optimum atomic number for maximum laser operation. The optimised absorbed laser intensities are found by the model for pure carbon, oxygen and sodium fibre targets to be I_{abs} = 4.6, 5.6 and 11 x10^{14} W/cm^2, respectively, (Fig. 2); being comparable with the simulation results of correspondingly 0.4, 2.5 and 12.5 x10^{14} W/cm^2 of absorbed intensity.

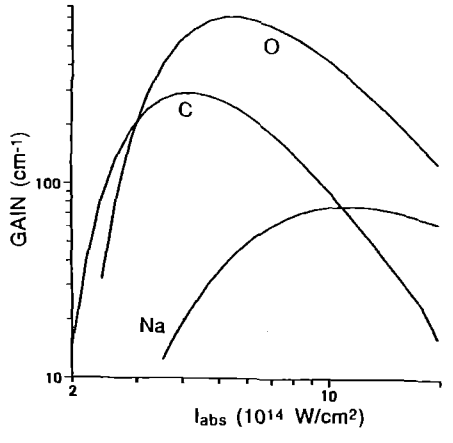

Fig. 2. Model calculated laser intensity dependencies of gain coefficient of carbon, oxygen and sodium fibre plasmas with τ = 2 ps, R_0 = 3.5 μm, and γ = 1.54, 1.6, 1.53 respectively. Optimum intensities are found to be 4.6, 5.6, and 11x10^{14} W/cm^2 for carbon, oxygen and sodium. Obvious the oxygen plasma shows the best performance.

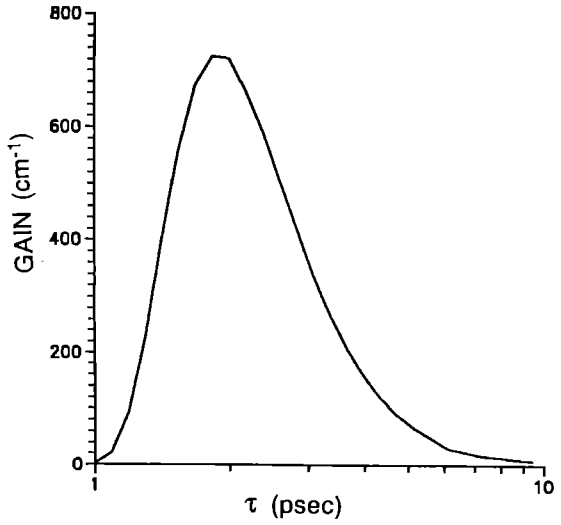

Fig. 3 Gain coefficient of oxygen fibre plasma as functions of driving pulse duration with I_{abs} = 5.6x10^{14} W/cm^2, R_0 = 3.5 μm. The intensity here is not adjusted to compensate for the pulse duration.

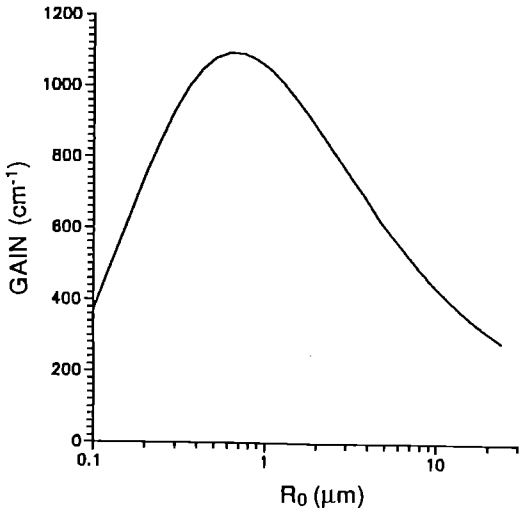

Fig. 4 Gain coefficient of oxygen fibre plasma as functions of fibre target radius with I_{abs} = 5.6x10^{14} W/cm^2, τ = 2 ps.

We have also calculated the dependencies of the gain upon the pulse duration and fibre radius (Fig. 3 & Fig. 4). It can be seen that a too thick fibre and too short pulse duration lead to very high initial density which will probably cause collisional quenching of the inversion, while too thin fibre and too long pulse duration will reduce the initial density of the active medium and hence the recombination efficiency. In those cases, the gain performance will be worse.

It is worth discussing the adiabatic exponent γ. In our model, γ is an integrated parameter of the hydro- and radiative dynamic motion. From the definition of the parameter $\gamma = C_p/C_v$ and $C_v = \partial\varepsilon/\partial T_e$, we can write $C_V = 3/2 + (1/N_e)\partial(N_b\chi)/\partial T_e$ in our case, where ε is the internal energy per ion, χ is the ionisation potential of hydrogen-like ions, and N_b is the number density of the bare nuclei written as

$$N_b = N_{b0}(V_0/V)\exp(-\int \alpha_3 N_e^2 dt).$$

γ is therefore a function of the initial condition and time. The use of γ as a constant can be tolerated when the plasma is far from the equilibrium state and means that the recombination reheating of the plasma is neglected. In figure 5 we give the best fit results from the MEDUSA simulation for sodium, oxygen, and carbon plasmas which are used in the model calculation here. Obvious rehashing can be observed for carbon, which might also be the reason for the unexpected behaviour in figure 2. For nitrogen and fluorine with the same radius and pulse duration, the best fit results for γ are 1.56 and 1.59 respectively.

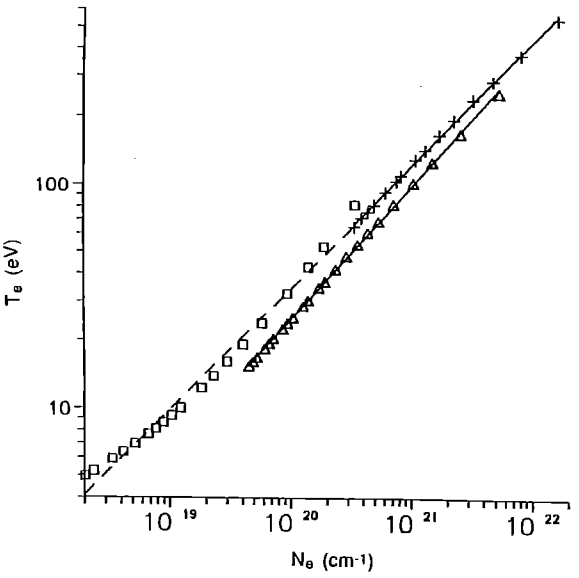

Fig. 5. Best fit adiabatic expansion trajectories for carbon, oxygen and sodium plasmas with τ = 2 ps, R_0 = 3.5 μm, and I_{abs} = 0.4, 2.4 and 12.5x10^{14} W/cm^2 respectively. The symbols and curves are the simulated results from MEDUSA and best fit results to the model calculation respectively.

CONCLUSION

The model is based on the two major assumptions, i.e., the skin layer assumption and the isothermal pre-expansion in the early stage. It should be noticed that the condition for both of the assumptions to be valid is that the density scale length of the plasma will not exceed the skin depth during the laser heating. This is actually a very restricted condition and results for an applicable pulse length of about 100 fs. Therefore our model will be more favourable for much shorter driving pulses other than 2 ps, although we make some detail comparison with the simulation for this relatively long pulse duration, where the laser absorption is described by different mechanisms in MEDUSA. A more accurate solution of this problem is related to the full understanding of plasma formation in the interaction range, which is dramatically different from the sub-ps range where the hydrodynamic motion can be entirely neglected, and the > 100 ps range where the steady ablative flux can be established. This will involve the full set of hydrodynamic and heat conduction equations and has not been solved.

REFERENCES

1. M.H. Key, N. Tragin and S.J. Rose, *X-Ray Lasers 1990*, G.J. Tallents ed., Bristol, IOP Publisher, 163 (1991).
2. M. Steyer, F. P. Schäfer, S. Szátmari, and G. Kühnle, Appl. Phys. B**50**, 265 (1990)
3. J. Zhang and M.H. Key, J. Appl. Phys., **74**, 7606 (1993).
4. J. Zhang and M.H. Key, Appl. Phys., B**58**, 13 (1994).
5. W. Rozmus and V.T. Tikhonchuk, Phys. Rev., A**42**, 7401 (1990).
6. J. Zhang, M.H. Key, S.J. Rose and G.J. Tallents, Phys. Rev. A**49** (1994) in press.
7. Y.B. Zel'dovich and Y.P. Raizer, *Physics of Shock Waves and High Temperature Hydrodynamic Phenomena*, Academic Press, New York, (1966).
8. R. Fedosejevs, R. Ottmann, R.Sigel, G. Kühnle, S. Szátmari, and F.P Schäfer, Appl. Phys. B**50**, 79 (1990).
9. O.L. Landen, D.G. Stearns, and E.M. Campbell, Phys. Rev. Lett., **63**, 1474 (1989).
10. G. J. Pert, J. Phys. B: Atom. Molec. Phys., **9**, 3301 (1976).
11. G.J. Pert, J. Opt. Soc. Am., B**4**, 602 (1987).
12. A.V. Borovskii, V.V. Korobkin and Ch.K. Mukhtarov, Sov. J. Quantum Electron, **17**, 1447 (1987).
13. N. A. Solovev and M. A. Fedotov, Opt. Spectrosc., **65**, 409 (1989).

AN ESTIMATE OF RESONANCE ABSORPTION OF ULTRASHORT LASER PULSES IN FIBRE TARGETS

W. Yu[1,2] and J. Zhang[3]

[1]Department of Physics, University of York, York, YO1 5DD, UK
[2]Shanghai Institute of Optics and Fine Mechanics, Academia Sinica, P. O. Box 800-211, Shanghai, China
[3]Department of Atomic and Laser Physics, University of Oxford, Oxford, OX1 3PU, UK

INTRODUCTION

Ultrashort pulse lasers have opened a regime of laser-plasma interaction where plasmas have scale lengths shorter than the laser wavelength and allow the possibility of generating near-solid density plasmas[1-4]. Recent studies have shown that near-solid-density plasmas of fibres irradiated by ultrashort pulses can significantly improve gain performance of recombination x-ray lasers[5,6]. Under intense irradiation of ultrashort laser pulses, the surface of fibre target will be ionised very rapidly, but the plasma created will not have time to ablate significantly while the pulse is incident. For the small scale length plasma thus formed, collisional absorption is highly inefficient and resonance absorption at the critical density is then the major absorption mechanism[3,4]. In this paper, we present a simple theoretical estimate of resonant absorption of ultrashort pulses in fibre targets in order to acquire a better insight into physics of the high gain operation of recombination x-ray lasers driven by ultrashort laser pulses.

CALCULATIONS

When linearly polarised, ultrashort laser pulses irradiate a solid target, the laser energy is mainly absorbed via resonance absorption in a thin layer of expanding plasma formed at the surface of the target. The scale length of the expanding plasma is

$$L = C_s t_L = 0.22 t_L \sqrt{T_e} \quad (\mu m), \qquad (1)$$

where t_L is the pulse length of laser in psec, T_e is the plasma temperature in keV, and $C_s = \sqrt{ZT_e / m_i}$ is the ion sonic speed. According to Kruer' model of resonance absorption[7], the absorbed energy flux at the angle of incidence θ is given by:

$$I_{abs} = \frac{1}{2}\Phi^2(\tau) I_L, \qquad (2a)$$

$$\Phi(\tau) = a\tau \exp(-2\tau^3/3), \qquad (2b)$$

where a = 2.3, $\tau = (k_0 L)^{\frac{1}{3}} \sin\theta$, $I_L = \frac{c}{8\pi} E_L^2$ is the incident laser intensity in free space, and $k_0 = 2\pi/\lambda$ is the wave number.

Figure 1 shows that the reduced absorption (I_{abs}/I_L) as a function of the argument τ. The dashed line in the figure 1 represents the calculation of equation 2 with a = 2.3. It can be seen that the absorbed energy flux peaks at $\theta_{max} = \sin^{-1}[0.8(k_0 L)^{-\frac{1}{3}}]$. The peak value of the absorption flux, up to $0.85I_L$, is somewhat overestimated (dashed line). More rigorous theories[8,9] suggest a peak value of $0.5I_l$. However, if we choose a = 1.76 in equation (2b), the accurate solution (thin solid line) presented in Ref. 8 can be well fitted by Kruer's model calculation (thick solid line). Hereafter, we shall approach our problem using the modified Kruer's model with a = 1.76.

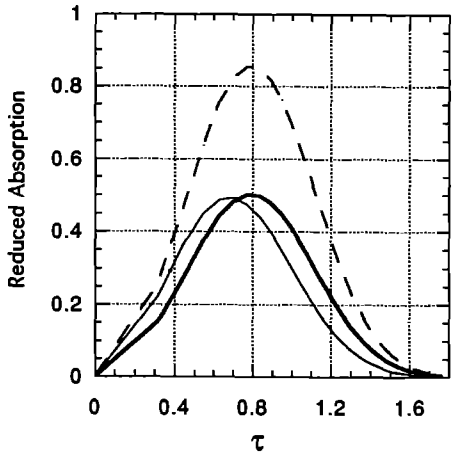

Figure 1. A plot of the equation (2), which characterises the efficiency of resonance absorption. The reduced absorption is defined as I_{abs}/I_L and τ is difined as $(k_0L)^{1/3}\sin\theta$. The dashed line represents the calculation with a = 2.3, the thin solid line for accurate solution and the thick solid line for a = 1.76.

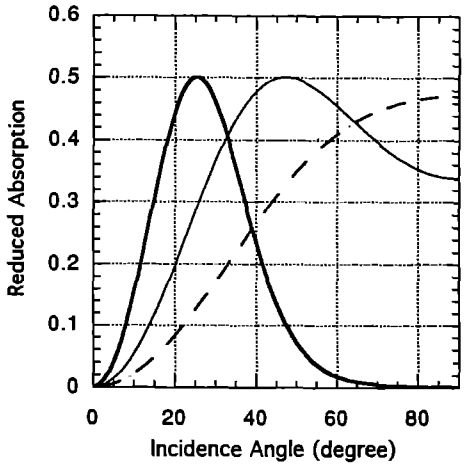

Figure 2. The reduced absorption as functions of incidence angle for different scale lengths. The thick solid line stands for the scale length of 1.0, the thin solid line for 0.2 and the dashed for 0.05.

Dependencies of the reduced absorption on the incidence angle of the laser pulse are calculated for scale lengths $L/\lambda = 1$ (thick solid

line), 0.2 (thin solid line) and 0.05 (dashed line) respectively (Fig. 2). A practical calculation can be done for the case of the recent C VI recombination x-ray laser experiment, where targets were irradiated by 2 ps, $3x10^{15}$ W/cm^2 laser pulses. The scale length in this case is about 0.5. The variation of the reduced absorption with the incidence angle is shown in figure 3. It is clear that the targets does not absorb the laser energy at the normal incidence angle. The absorption increases with increasing the incidence angle. The absorption reaches maximum at an incidence angle of 32.5 degree. For larger incidence angles, the absorption decreases as the incidence angle increases.

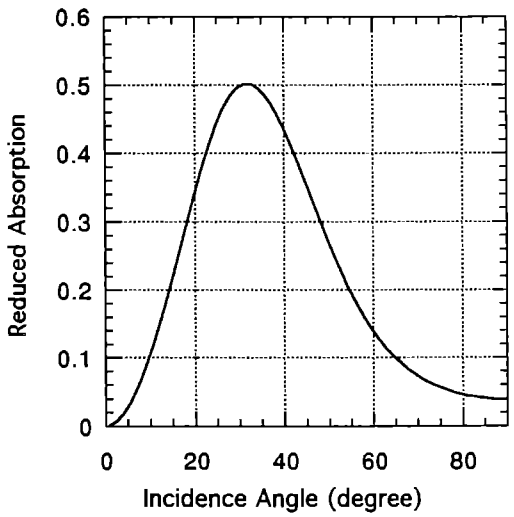

Figure 3. The reduced absorption as a function of incidence angle for 2 ps, $3x10^{15}$ W/cm^2 short pulse irradiation at 1.053 μm.

The total absorption of a fibre target with radius R, irradiated length X can be calculated by integrating the equation (2):

$$A = X\int_{-R}^{R} I_{abs}dy = \frac{1}{3}a^2RXI_L(k_0L)^{-\frac{1}{3}}\int_0^{k_0L}\exp(-\frac{4}{3}\tau^3)d\tau^3. \quad (3)$$

The total absorption coefficient is then given by

$$a_s = \frac{A}{I_L DX} = \frac{1}{8}a^2(\frac{2R}{D})(k_0L)^{-\frac{1}{3}}[1-\exp(-\frac{4}{3}k_0L)], \quad (4)$$

where D is the width of focused laser beam.

For a 7 μm diameter fibre placed in 20 μm wide focus, the dependence of the absorption coefficient on scale length is presented in figure 4. For the optimised experimental conditions of the C VI recombination x-ray laser of 2 ps, $3x10^{15}$ W/cm^2 laser pulse irradiation at 1.053 μm, the total absorption coefficient is about 9%, which well agrees with the measurement[10, 11]. From the Fig. 4, one can see that L/λ = 0.2 is the optimum value for a maximum absorption, which corresponds to a pulse laser with duration of 800 fs if the irradiance on the fibre target remains the same. For too large (L/λ = 10) or too small (L/λ = 0.01) scale lengths, the resonance absorption becomes insignificant.

CONCLUSION

It may be concluded that modified Kruer's model can give reasonable estimate of resonance absorption of ultrashort pulses in fibre targets. The optimum incidence angle is very dependent on scale lengths of plasmas. The model calculation has suggested that 32.5 degree is the optimum incidence angle to achieve the maximum absorption for 2 ps, $3x10^{15}$ W/cm^2 short pulse irradiation at 1.053 μm. In order to optimise C VI recombination x-ray laser operation, 800 fs pulse lasers might be more efficient as the driver than 2 ps pulse lasers.

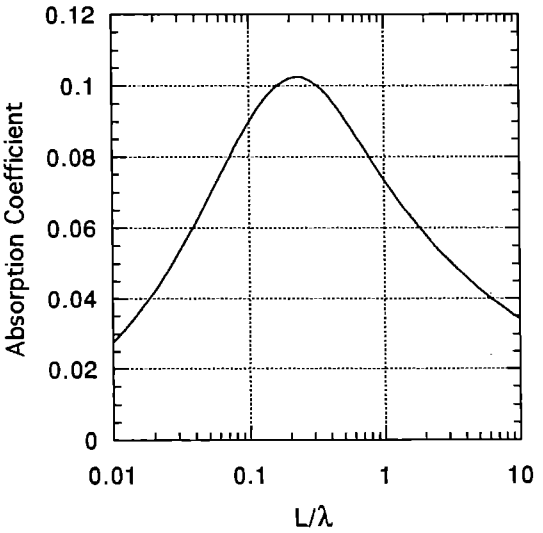

Figure 4. The total absorption coefficient as a function of scale length for a 7 μm diameter fibre placed in a 20 μm wide line focus of 2 ps, $3x10^{15}$ W/cm^2 short pulse irradiation at 1.053μm.

ACKNOWLEDGEMENT

One of the authors (WY) would like to thank the support of the Royal Society Sino-British Fellowship and the helpful discussion with Prof. G J Pert.

REFERENCES

1. J C Kieffer et al., Phys. Rev. Lett., **62**, 760 (1989).
2. H M Milchberg et al, Phys. Rev. Lett., **61**, 2364 (1988).
3. S C Wilks et al, Phys. Rev. Lett., **69**, 1383 (1992).
4. D D Meyerhofer et al, Phys. Fluids, **B5**, 2584 (1993).
5. J Zhang & M H Key, Appl. Phys., **B58**, 13 (1994).
6. J Zhang et al, Observation fo high gain recombination x-ray laser at 18.2 nm driven by 2 psec laser pulses, SERC CLF Annual Report (1994).
7. W L Kruer, *The Physics of Laser Plasma Interaction*, Addison-Wesley Publishing Company, California, 1987.
8. G J Pert, Plasma Physics, **20**, 175 (1978).
9. D W Forslund et al., Phys. Rev., **A11**, 679 (1976).
10. M Holden et al, SERC CLF Annual Report (1994).
11. J Zhang et al, Diagnostics of rapidly recombining plasmas using resonance line ratio, SERC CLF Annual Report (1994).

TIME DEPENDENT SIMULATIONS OF X-RAY DIFFRACTION FROM LASER SHOCKED CRYSTALS.

N.C. Woolsey & J.S. Wark

Clarendon Laboratory, Department of Physics, University of Oxford, Parks Road, Oxford OX1 3PU, UK

INTRODUCTION

Time-dependent, *in situ* x-ray diffraction from laser shocked single crystals is simulated with a combination of a hydrodynamics code, and an x-ray diffraction model. The hydrodynamics simulation was based on a published laser-plasma code MED101[1,2] modified to include solid state equations of state. A Mie-Grüneisen EOS was used for silicon and a Birch-Murnaghan EOS for the plastic layer. As complete dynamical and kinematic theories are computationally too intensive, a simplified x-ray diffraction model has been developed. This model is the perfect laminae approximation[3,4]. Improvement in computation efficiency is approximately 2 orders of magnitude, enabling time-dependent simulations to be calculated for the first time.
These simulations can be compared directly with experimental x-ray streak camera data.

THE SIMULATION

A simulation target is illustrated in Figure 1. A typical target consists of 176 cells, 150 cells in 25 μm thick silicon crystal, 1 cell for the 1000 Å aluminium layer, and 25 cells in the 20 μm thick plastic coating. A large number of cells are required for the silicon layer to suppress numerical instabilities.

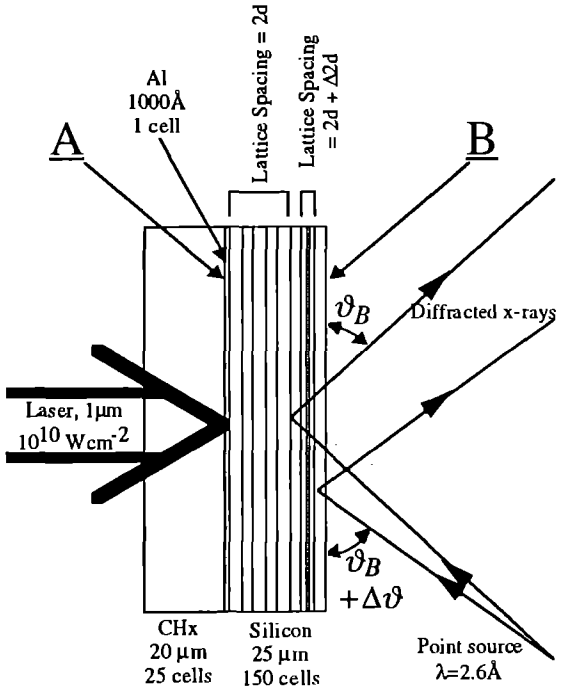

Figure 1 Simulation target, showing shift in diffraction angle with lattice compression.

At intensities below 10^{11} Wcm^{-2} plastic is transparent to 1 μm radiation, the coating acts as a confining layer increasing the peak pressure and duration of the compression pulse[5]. In confined ablation, the compression pulse is characterised by a rapid, almost discontinuous, increase in pressure with a relatively gentle release. The temporal development of this wave is illustrated in Figure 2. At early times t_1, the compression wave has clearly developed, due to absorption in the material between the compression wave and the free surface B diffraction from this part of the crystal is not observed. By t_2 the shock front has steepend, and should be close enough to the crystal surface to be seen. At t_3 the stressed state of the crystal is shown after shock breakout, both tensile and compressive states exist. At shock breakout a release rarefaction is created. As this free surface rarefaction crosses the rarefaction following the shock a tensile wave develops.

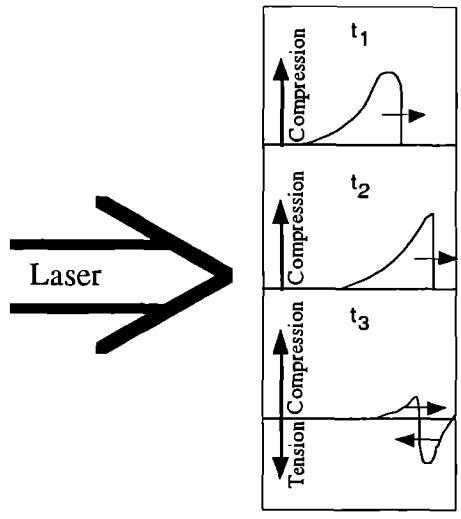

Figure 2 Development of a shock at shock breakout

Features such as shock breakout and the development of tensile states, their dependence on laser pulse lengths, and the role of x-ray absorption is clearly illustrated in the simulation results, Figures 3 to 6.
All simulations were along the [111] crystallographic direction in silicon, the x-ray source was titanium He_α with an approximate wavelength of 2.6 Å. In silicon, along the Bragg angle, the $1/e$ depth normal to the crystal surface is around 7 μm.

BASIC PRINCIPLES

A divergent, monochromatic x-ray source of wavelength λ, is positioned to diffract from the rear surface of a crystal, face B, from a set of crystallographic planes (h,k,l). These planes are assumed parallel to the crystal faces (Figure 1). The angle of diffraction, ϑ_B, for the unshocked crystal is given by Bragg's law,

$$n\lambda = 2d_H \sin(\vartheta_B) \qquad (1)$$

On launching a shock into face A, the crystal compresses with an associated change in lattice spacing $d_H(r)$, where d_H is now a function of depth r. Diffracting from these planes gives the elastic strain during shock compression as a function of the measured shift in diffraction angle. For small changes in the lattice spacing the change in diffraction angle is given by differentiating equation (1);

$$\frac{\Delta 2d(r)}{2d(r)} = -\Delta\vartheta(r)\cot\vartheta_B \qquad (2)$$

where $\Delta\vartheta(r) = \vartheta(r) - \vartheta_B$. The diffracted intensity as a function of $\Delta\vartheta$ gives the x-ray rocking curve. Diffracted intensity is determined by the volume of diffracting material at a given lattice spacing, and absorption processes on the incident and diffracted beams.

DESCRIPTION OF FIGURES

Depth dependent strain profiles from the modified MEDUSA simulations are shown in Figures 3 to 5 at 400 psec time intervals, before and after shock breakout. In each figure $t = 0$ is defined as shock breakout. A 10^{10} Wcm^{-2} peak intensity was used in the simulations with a Gaussian 60 psec, 300 psec and 600 psec FWHM pulse in Figures 3, 4, and 5 respectively. X-ray rocking curves calculated from these depth-strain profiles are shown in Figures 6, 7, and 8. Calculations were performed every 20 psec in Figures 6 and 8, and every 10 psec in Figure 7. The hydrodynamics, and rocking curve simulations should be compared to experimental data reproduced in Figures 9, 10 and 11.

The experimental images are distortion corrected intensity maps of time-dependent rocking curves recorded from 60 μm thick single crystal silicon using a titanium helium-alpha x-ray source. In Figures 9 and 10, two spectra are seen, one streak, a, is a record of the temporal nature of the x-ray source. The second, b, is the time-dependent rocking curve convolved with the x-ray source. Data in Figure 9 was shocked with a 66 psec FWHM Gaussian pulse, peak intensity 10^{10} Wcm^{-2}, Figure 10 with a 450 FWHM Gaussian pulse at ~10^{9} Wcm^{-2}, and Figure 11 approximately 1 nsec FWHM Gaussian pulse with an irradiance of 10^{10} Wcm^{-2}. Temporal resolution in these images is 40 psec.

HYDRODYNAMIC SIMULATIONS

Hydrodynamic decay, and numerical instabilities behind the shock front are quite pronounced in Figure 3. The hydrodynamic decay results from rarefaction over-running the shock front. Both the shock front and the rarefaction travel at the sound speed, the sound speed generally increases with pressure. Instabilities grow at the shock front-shock release boundary, these sort of instabilities are indicative of finite difference methods, they can be suppressed using artificial viscosity[6], but only at the expense of being able to accurately model shocks.

Shocks generated with longer pulse lengths (Figures 4 and 5) steepen more slowly than the short pulse shocks, they have a plateau of peak compression which is eroded by the faster moving shock rarefaction. The rarefaction reaches the shock front in Figure 5 at breakout, as in Figure 4 a tensile waves develops immediately. In Figure 6, where the rarefaction has not travelled through this plateau, a tensile wave forms about 100 psec later.

ROCKING CURVE SIMULATIONS AND COMPARISON TO EXPERIMENTAL DATA

The effects of hydrodynamic decay are apparent in the rocking curve, Figure 6, as a time-dependent fall in peak compression shift. The effect of numerical ripples are clearly seen as bands of decreasing strain in time. As short laser pulses generate shocks which occupy small thicknesses of crystal at any one particular time, x-ray diffraction from the whole volume occupied by the shock is observed, resulting in a continuous "smear" of diffracted x-rays from peak to zero compression. This is observed experimentally in Figure 9, and is markedly different to the simulations Figures 7 and 8 and data in Figure 10 and 11. Here longer driving laser pulse lengths are used, increasing the shock width to thicknesses larger than an x-ray absorption depth. Under current experimental arrangements diffraction from a shock front is not recorded. The shock front occupies a narrow region of crystal where strain gradients are large, as x-ray streak cameras

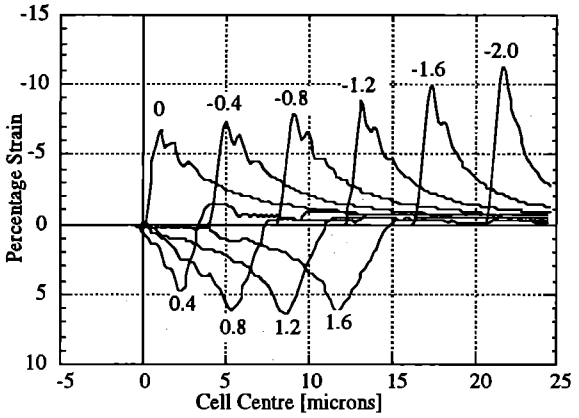

Figure 3 Depth-strain profile in silicon shocked with a 60 psec FWHM Gaussian pulse at 10^{10} Wcm^{-2}. Numbers above indicate time before/after breakout in nanoseconds.

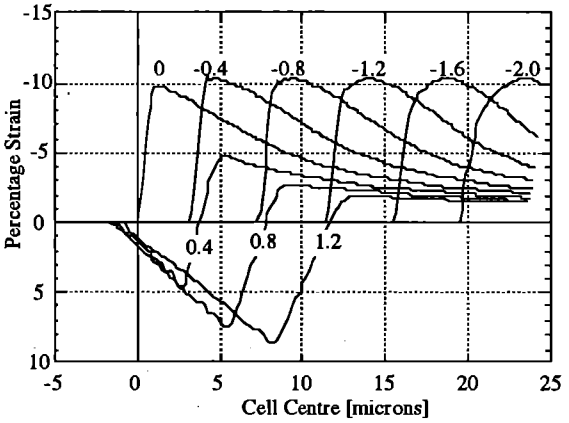

Figure 4 Depth-strain profile in silicon shocked with a 300 psec FWHM Gaussian pulse at 10^{10} Wcm^{-2}. Numbers above indicate time before/after breakout in nanoseconds.

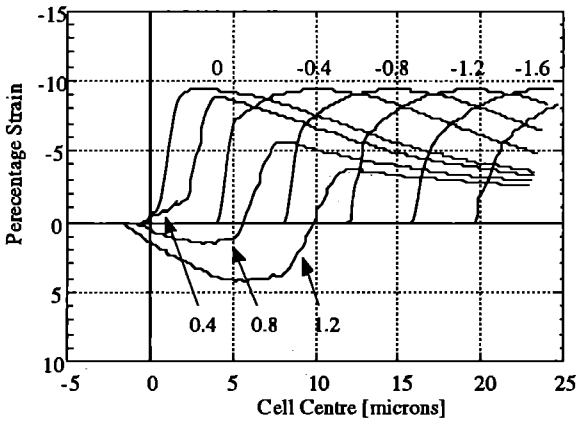

Figure 5 Depth-strain profile in silicon shocked with a 600 psec FWHM Gaussian pulse at 10^{10} Wcm^{-2}. Numbers above indicate time before/after breakout in nanoseconds.

have limited dynamical ranges diffraction from this region is not measurable. Observable diffraction occurs from behind the shock front. If the shock rarefaction tails far back into the solid, diffraction from material at low compression is not observed,

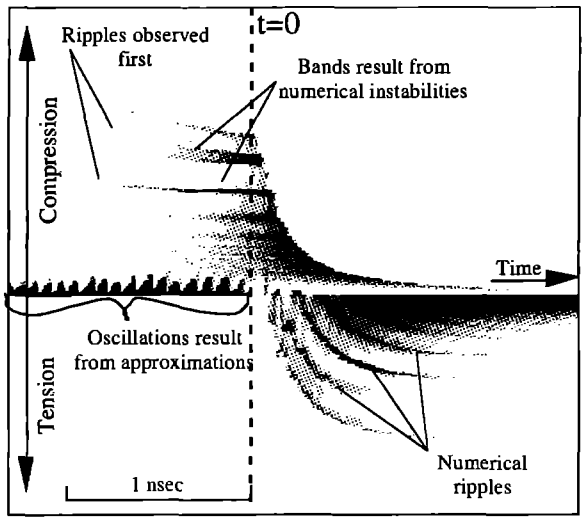

Figure 6 Simulated x-ray rocking curve, with 60 psec FWHM Gaussian, 10^{10} Wcm^{-2} laser pulse.

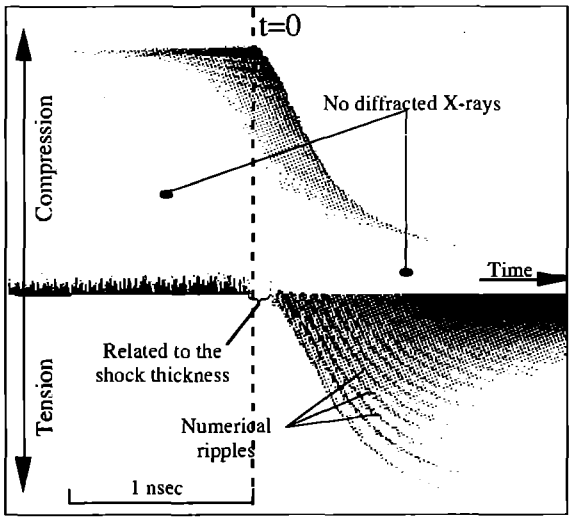

Figure 7 Simulated x-ray rocking curve, with 300 psec FWHM Gaussian, 10^{10} Wcm^{-2} laser pulse.

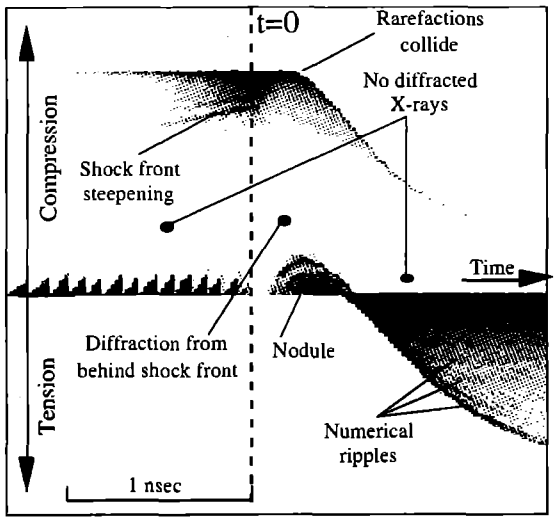

Figure 8 Simulated x-ray rocking curve, with 600 psec FWHM Gaussian, 10^{10} Wcm^{-2} laser pulse.

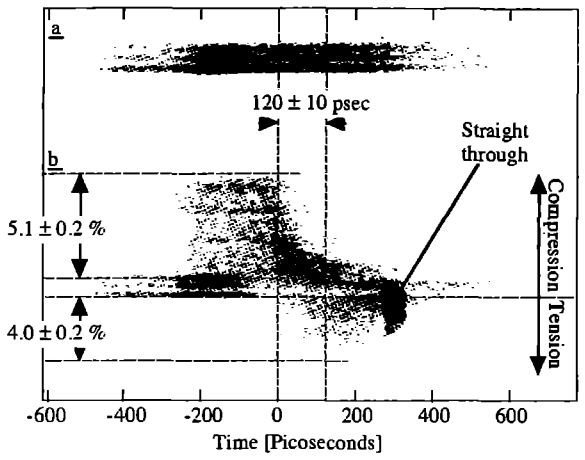

Figure 9 Short pulse (66 psec FWHM) experimental rocking curve.

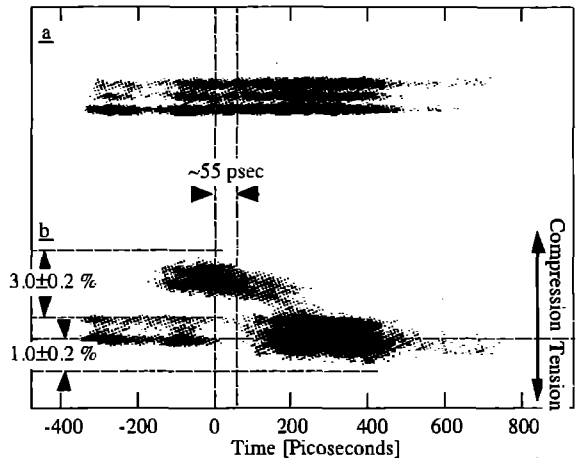

Figure 10 Short pulse (450 psec FWHM) experimental rocking curve.

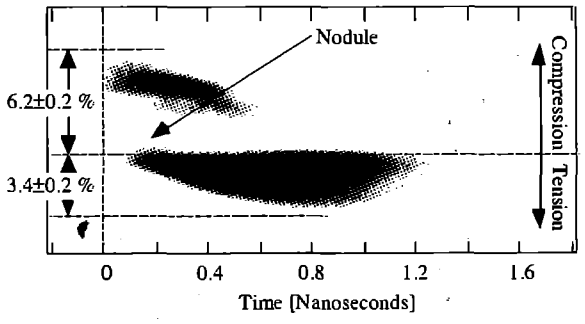

Figure 11 Short pulse (~1 nsec FWHM) experimental rocking curve.

leading to low or zero diffracted intensity at small angle changes. This situation is seen the simulations Figure 7 and 8, and in experimental data Figures 10 and 11.

Highlighted in Figure 7 is a region of no diffraction in the rocking curve at zero compression. This result is due to a finite shock front thickness in the simulations. A similar feature is observed experimentally in Figure 10. This feature exists for approximately 55 psec during shock breakout, and, if it can be interpreted as a

shock front thickness measurement, places an experimental upper limit of 0.5 μm on the shock front.

As already explained, with longer pulse irradiation, wide plateaux of peak compression are generated, the development of a tensile wave is delayed until the breakout rarefaction has travelled through this plateau and crosses the shock rarefaction. A delay of 100 psec is seen in Figure 8, which compares to approximately 100 psec in Figure 11. The simulation predicts a nodule in the time-dependent rocking curve, this is also seen in experimental data such as Figure 11. Contributions to this part of the rocking curve come from material between the free surface and the receding shock front. This nodule is marked in Figures 8 and 11.

CONCLUSIONS

Using our perfect laminae approximation it has become viable to calculated time-dependent rocking curves from hydrodynamic simulations. These simulations qualitatively predict differences seen between experimental rocking curves generated with different laser pulse lengths. The success of this work has encouraged the authors to pursue more quantitative simulations of shock compression. Phenomena such as elastic-plastic transition, and material rate-dependent properties need to be included. Finite difference codes suffer from the effects of numerical gridding and artificial viscosity this prevents the simulation of shock fronts and many rate dependent features. The authors are currently investigating the use of a characteristics computer code to eliminate these problems.

REFERENCES

(1) J.P. Christiansen, D.E.F.T. Ashby, K.V. Roberts, MEDUSA. A one-dimensional laser fusion code. Comp. Phys. Comm., 7, 272-287 (1974).

(2) P.A. Rodgers, A.M. Rogoyski, S.J. Rose, Med101: a laser plasma simulation code. User guide. RAL-89-127 (1989).

(3) N.C. Woolsey, J.S. Wark (1993)., Simulated x-ray streak camera data of in situ diffraction from laser shocked crystals. Shock Compression of Condensed Matter 1994, (1994).

(4) N.C. Woolsey, J.S. Wark, X-ray rocking curve calculation from shocked single crystals. Annual Report, RAL-93-031 (1993).

(5) J.S. Wark, R.R. Whitlock, A.A. Hauer, J.E. Swain, P.J. Solone, Shock launching in silicon studied with use of pulsed X-ray diffraction. Phys. Rev., B35, 9391-9394 (1987).

(6) J. von Neumann, R.D. Richtmeyer, A method for numerical calculation of hydrodynamic shocks. J. Appl. Phys., 21, 232-237 (1950).

FACTORS EFFECTING THE RESOLUTION OF SOFT X-RAY CONTACT MICROSCOPY

R.A. Cotton[1], E.Miura[2], A.D.Stead[1] & T.W.Ford[1]

[1]Department of Biology, Royal Holloway, University of London, Egham, Surrey, TW20 0EX, UK.
[2]Electrotechnical Laboratory, 1-1-4 Umezono, Tsukuba, Ibaraki, 305, Japan.

INTRODUCTION

To improve the resolution of soft X-ray contact microscopy (SXCM), it is necessary to investigate the factors which currently limit the resolution and attempt to quantify and reduce these factors. Using the soft X-ray microscope system in target area four (TA4) of the Vulcan laser system, initial studies have been made. Results of some of the experiments, imaging living biological specimens in TA4, are given in this volume[1].

For SXCM to play a significant role in microscopy for the life sciences, we believe that untreated, hydrated biological material must be imaged at a resolution of approximately 50nm on a routine basis. Although 50nm gold particles[2] and dry diatom frustules[3] have been successfully imaged at a resolution better than 50nm, these are ideal, high contrast specimens and structure on a 50nm scale has only been observed in a few hydrated biological specimens. For example, images of sperm have revealed what are believed to be the microtubular components of the flagella. In this case where the flagella have broken the individual microtubular doublets can be distinguished suggesting a resolution of 40nm[4]. Images of green alga *Microthamion* show considerable internal cellular detail and, in some images, what are thought to be granal stacks within the chloroplasts have been observed. If the individual thylakoids of these granal stacks is considered to represent a knife edge then the analysis of the edge profile implies a resolution of approximately 30nm[1]. Therefore, although the reality of sub-50nm resolution has been achieved, it is far from routine operation.

REQUIREMENTS FOR HIGH RESOLUTION

The final resolution obtained by SXCM is affected by a number of processes, ultimately limited by the wavelength of the X-ray source (~few nanometres) and by the inherent resolution of the photoresist which acts as the recording medium which is of order 10nm. However, other factors will limit the resolution to larger values. These include penumbral blurring, Fresnel diffraction, radiation damage and hydrodynamic motion[5], statistical noise in the photon flux and the readout of the image within the photoresist.

When interference light microscopy is used to examine the chemically developed photoresist the resolution will certainly be limited by the readout method. The use of scanning electron microscopy overcomes this problem, but because the photoresist has to have a metallic coating applied to provide electrical conductivity, this prevents further chemical development. Therefore the preferred method of examining the photresist is atomic force microscopy which offers exceptionally high resolution without the need to coat the photoresist.

Since not all of the specimen can be in complete contact with the recording medium, the image will be blurred because of the finite size of the X-ray source. This is known as penumbral blurring. However, from a simple geometric argument, it is clear that with the current parameters used for SXCM (source size ~100μm and source specimen distance ~7-10mm) penumbral blurring will not be a limiting factor if close specimen-resist contact is maintained.

The finite distance between the specimen and the resist will also lead to some degree of diffraction being recorded in the resist. From calculations of the Fresnel diffraction pattern created by a sharp opaque edge, illuminated by monochromatic radiation of wavelength λ, it can be shown that the first intensity peak occurs at a distance D from the edge given by $D \sim (\lambda s/2)^{1/2}$, where s is the specimen-resist distance. This gives an approximate resolution limit. For a feature in a specimen a distance 1μm from the resist illuminated with radiation of wavelength 3nm this implies a resolution limit of approximately 40nm. This would put a serious fundamental limit on the ultimate resolution of SXCM. However, the three assumptions of a sharp, opaque step being illuminated with monochromatic radiation are not valid when imaging hydrated biological specimens with radiation from a laser plasma source. Therefore, this limit may not be as severe. This is supported by absence of any diffraction effects being observed when imaging hydrated biological specimens under the present conditions.

X-RAY FLUENCE AND RESOLUTION

The image resolution can be limited by shot noise. The resolution limit is dependent on X-ray fluence and the contrast between various components within the biological specimen. Due to the variation in the absorption coefficients for protein, water and PMMA across the water window, the resolution limit will also depend on the spectral distribution of the X-ray flux. Because the X-ray photons arrive randomly and independently the actual number of photons per resolution area will be determined by a Poisson distribution. To distinguish a feature of transmission T_2 from the background with transmission T_1, assuming a detector quantum efficiency η_d and that we require that an overlap between the two Poisson distributions must only occur outside the 2 standard deviations limit, following the arguments of Spiller[6], we require

$$T_1\eta_d N - T_2\eta_d N > 2(T_1\eta_d N)^{1/2} + 2(T_2\eta_d N)^{1/2} \qquad [1]$$

where N is the average number of photons per resolution element. Therefore, the value of N required is

$$N = \frac{4}{T_1\eta_d(1-(T_2/T_1)^{1/2})^2} \qquad [2]$$

The number of X-ray photons absorbed by a resolution element δ is given by

$$N = E\frac{\lambda}{hc}A\delta^2 \qquad [3]$$

where E is the X-ray fluence on the specimen, (hc/λ) is the photon energy and A is the fraction of radiation absorbed in the resist. For a given thickness of resist d and an absorption coefficient α_{pmma}, A is given by

$$A = 1-\exp(-\alpha_{pmma}d) \qquad [4]$$

Combining these expressions, and making the assumption that we can resolve a feature that is of equal size to the resolution element, we obtain a final expression for the X-ray fluence required to resolve a feature of size δ

$$E = \frac{4}{T_1 \eta_d (1-(T_2/T_1)^{1/2})^2} \frac{hc}{\lambda} \frac{1}{(1-\exp(-\alpha_{pmma} d))\delta^2} \quad [5]$$

It is clear from equation 5 that the resolution will be dependent on the X-ray fluence incident on the specimen and the contrast between the specimen and background (eg water or buffer solution). It is thought that statistical noise in the X-ray flux is the limiting factor of resolution at the present time and hence will be improved by going to a higher X-ray fluence.

DEPENDENCE OF RESOLUTION ON X-RAY WAVELENGTH

The absorption coefficients of protein, water and PMMA in the water window region are shown in Figure 1. It is clear that the absorption coefficients decrease across the water window with decreasing wavelength. Considering equation [5], it is clear that not only is the wavelength included in the equation explicitly, but α_{pmma}, T_2 and T_1 are also wavelength dependent. It is therefore instructive to consider an idealised example of a square cylinder of protein of side 50nm in water, and calculate the X-ray fluence required to resolve this structure using X-ray photons at two separate wavelengths, either end of the water window region, say 2.5nm (case a) and 4.2nm (case b).

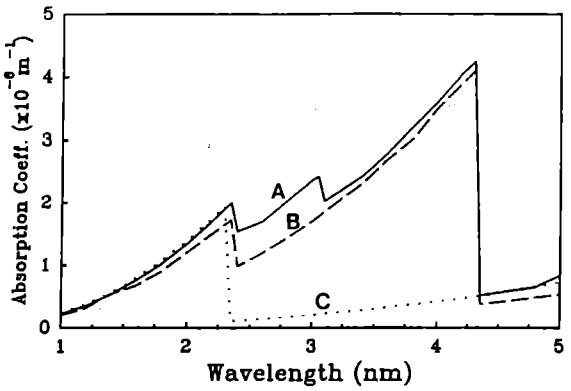

Figure 1. The absorption coefficients for A) protein, B) water and C) PMMA

Case a: For a wavelength of λ = 2.5nm, α_{pmma} = 1.1μm^{-1}, $\alpha_{protein}$ = 1.54μm^{-1} and α_{water} = 0.125μm^{-1} . This implies T_2 = 92.6% and T_1 = 99.4%. From equation [5], assuming a detector quantum efficiency of 100% and a typical development depth of 100nm, this implies that the an X-ray fluence of approximately E ~ 100mJcm^{-2} is required.

Case b: For a wavelength of λ = 4.2nm, α_{pmma} = 3.3μm^{-1}, $\alpha_{protein}$ = 3.0μm^{-1} and α_{water} = 0.467μm^{-1} . This implies T_2 = 86.1% and T_1 = 97.7%. From equation [5], this implies that the an X-ray fluence of approximately E = 7mJcm^{-2} is required.

The lower X-ray fluence required for radiation at 4.2nm is a direct consequence of greater absorption by the specimen (i.e. better contrast), greater absorption by the PMMA resist (i.e. more efficient use of X-ray photons) and a larger number of photons for a given X-ray fluence.

CARDIAC MUSCLE CELLS

To study the factors effecting resolution experimentally, it is necessary image biological specimens that have periodic strucfures of known size, with sufficiently small dimensions to test the technique. One such specimen is that of a living, hydrated single cardiac muscle cells, which have periodic structure ranging from a scale that is clearly visible by light microscopy to a scale beyond the theoretical limits of SXCM. Images of periodic structures with dimensions below 200nm have been observed with living cells in TA4. This work is described in this volume[1].

ACKNOWLEDGEMENTS

We would like to thank the support staff on the "Vulcan" laser at RAL for their help with this work. We are also grateful to Oxford University for access to AFM facilities.

REFERENCES

1. A.D.Stead, R.A.Cotton, A.M.Page, C.G.Steele, R.Bagby & T.W.Ford, This Volume.
2. A.D.Stead, R.A.Cotton, A.J.Jackson, A.Ridgeley, & T.W.Ford, Report to the Laser Facility Committee, Rutherford Appleton Laboratory, pp34-35, 1991.
3. T.W.Ford, A.D.Stead, C.P.Hills, R.J.Rosser, & N.Rizvi, *J.X-ray Sci.Tech*, **1**, pp207-210, 1989
4. T.Tomie, H.Shimizu, T.Majima, T.Kanayama, Y.Yamada, & E.Miura, *Proc.SPIE Conf.* **1741**, pp118-129, 1992
5. R.London, M.D.Rosen & J.E.Trebbes, Applied Optics **28** p3397, 1989
6. E.Spiller & R.Feder, "X-ray lithography", in "X-ray optics", Ed H.J.Queisser, Publ. Springer-Verlag **22**, p35, 1977.

ON THE EXAFS OF DISORDERED SYSTEMS

F.I. GORDON,

PHYSICS DEPT., ESSEX UNIVERSITY, COLCHESTER CO4 3SQ, ESSEX, U.K.

1. Introduction.

Extended X-ray Absorption Fine Structure (EXAFS) is an experimental probe of the local structure around a particular atomic species, and in monatomic samples allows information on the neighbouring shell positions and populations to be deduced. In a much-quoted paper on the limitations of the use of EXAFS for disordered systems Eisenberger and Brown(1979), hereafter EB, showed how the neglect of asymmetries in the model distribution function describing local atomic positions led to substantial errors in the determination of the nearest neighbour distance for hcp Zn in the c-direction. Their proposed alternative gave reasonable agreement with the known 0.05Å expansion of Zn at room temperature, found from diffraction experiments. Their analysis was based on fitting the experimental EXAFS phase difference between room and reference temperature data to a simple analytic function whose parameters yielded the relevant expansion distance ΔR. A similar approach was adopted by Crozier and Seary (1980) who concluded that the EB method was liable to overestimate the ΔR correction, although they studied higher temperatures in the region of melting for Zn. They also concentrated on the a-direction for the hcp structure, which is a less sensitive probe of the anharmonic effects than the c-direction.

We have repeated the EB / Crozier and Seary analysis for the EB phase data and find substantial deviations from the analytic form if the calculation of the extra phase difference as a function of wavevector k, $\Sigma(k)$, is done numerically and a realistic k-dependent mean-free path is used in the EXAFS equation. A constant mean-free path was used in the two above analyses. These differences are sufficiently large that the inferred expansion in R, ΔR is not the same as in EB and the 'degree of asymmetry' is roughly twice as much as in the original work, emphasising the inadequacy of the approximation implicit in the analytic fit.

2. Basic theory

An EXAFS spectrum is usually described by the normalised absorption coefficient $\chi(k)$, where $\chi(k) = (\mu - \mu_0)/\mu_0$, $\mu(k)$ being the real absorption coefficient measured, and $\mu_0(k)$ the absorption for a single atomic site. The normal EXAFS plane-wave single scattering formula is [Lee et al(1981), Stern et al(1975), Sayers et al(1971)]

$$\chi(k) = -\Sigma_j N_j \sin(2kR_j+\psi(k))\, e^{-2R_j/\lambda(k)}\, f(k,\pi) k^{-1} R_j^{-2} \qquad (1)$$

where a sum over atomic shells is made, the j-th shell of N_j atoms being at radius R_j. The backscattering amplitude is $f(k,\pi)$ and $\psi(k)$ is the total phaseshift from the scattering and central atoms [Stern et al(1975)]. $\lambda(k)$ is the photoelectron mean-free path which accounts for inelastic scattering losses [Gordon and Djaoui(1992)]. Single scattering implies that the photoelectron returns to the central atom after one back-scattering event- the complications of multiple scattering can be ignored here. Since equation (1) assumes all the atoms to be precisely at the distance R_j it takes no account of either thermal or structural disorder, thus requires to be modified for use with real data.

The common solution [EB, Bunker(1983), Crozier and Seary(1980)] is to introduce an integral over the distribution g(r)

$$\bar{\chi}(k) = -k^{-1} f(k,\pi)\Sigma_j \int_0^\infty g(r_j) r_j^{-2} \sin(2kr_j+\psi(k))\, e^{-2r_j/\lambda(k)}\, dr_j \qquad (2)$$

The use of a Gaussian probability distribution for g(r) with mean R_j and narrow width σ_j reproduces equation (1) with the addition of a damping factor $e^{-2\sigma_j^2 k^2}$, the so-called Debye-Waller term which accounts for thermal disorder by an averaging over the vibrational displacements of the atoms from their mean positions [Crozier et al(1987)]. The Debye-Waller factor σ_j^2 is the relative mean-square displacement for an atom in the j-th shell. This is valid provided $\sigma_j \ll R_j$, i.e. for low disorder. We henceforth concentrate only on the first shell of nearest -neighbour atoms so shall drop the j subscript on R and σ^2.

EB showed that equation (2) could be rewritten exactly as the following

$$\chi(k) = C(k)(A(k)^2+S(k)^2)^{1/2} \sin(2kR_j+\psi(k)+\Sigma(k)) \qquad (3)$$

where C(k) contains the backscattering amplitude and other factors unimportant here, and the antisymmetric and symmetric component functions A(k) and S(k) are given by the following expressions

$$A(k) = \int_0^\infty f(r+x) \sin(2kx)\, dx \qquad (4)$$

$$S(k) = \int_0^\infty f(r+x) \cos(2kx)\, dx \qquad (5)$$

with $$f(r) = g(r)e^{-2r/\lambda_r 2} \qquad (6)$$

where g(r) is the pair distribution for the absorbing atom and others in the sample. The value of the centroid of g(r) is $\bar{r}$. The function f(r) is the 'effective' distribution function and as emphasised in EB, is always asymmetric even though g(r) may be perfectly symmetric. The asymmetric function A(k) may therefore be non-zero and thus induces the extra phase shift

$$\Sigma(k) = \tan^{-1}(A(k)/S(k)) \qquad (7)$$

EB proceeded to give an analytic formula for S(k) for the case of a three-dimensional anharmonic distribution (see details in their paper) valid when $k^3\langle x^3\rangle < 1$ which is

$$\Sigma(k) = -2k\,\{2\langle x^2\rangle - \langle y^2+z^2\rangle/2\}(R^{-1}+\lambda^{-1}) - 8k^3\langle x^3\rangle/15 \qquad (8)$$

where $\langle x^N\rangle$ is the N-th moment of the distribution $g(\bar{r}+x)$. The extra phase as a function of wavevector is shown in Figure 1 (EB's Fig. 2b) and relates the phase at 10K (reference T) to that at T=285K. Thus by fitting their phase difference data to a function based on (8)

$$\Delta\varphi = \varphi_{10} - \varphi_T(k) = ak + bk^3 \qquad (9)$$

the value of the expansion ΔR could be deduced as in EB, and was found to be 0.05 Å, with the cubic term in k contributing significantly to this figure. A naive analysis without any consideration of the asymmetry of Zn would yield a non-physical contraction of 0.09 Å, clearly a large error.

3. Alternative approach.

We have re-analysed this problem, using the simplified version of the EB formula from Crozier and Seary(1980). In this model the Debye-Waller factor $\sigma_{//}^2$ for parallel vibrations is neglected, but $\sigma_\perp^2$ is retained. This can be shown to be a small error compared to the other two improvements which are

a) inclusion of a k-dependent mean-free path $\lambda(k)$

and b) numerical determination of $\Sigma(k)$ from (4),(5) and (7).

The data for the Debye-Waller factors as a function of temperature come from the work of Beni and Platzman(1976), which is related to the work of Sevillano et al(1979) who studied phonon modes contributing to vibrational motion in Cu, Fe and Pt. The theory is also appropriate for Zn. We use their theoretical predictions which are $\sigma_\perp^2$ (300K) = 0.032 Å^2, $\sigma_\perp^2$ (10K)=0.006 Å^2 (theory), and the experimental value quoted is $\sigma_\perp^2$ (300K) =0.04 Å^2.

We use a simple model 1-D as in Crozier and Seary(1980) with the form

$$g(\bar{r}+x) = \exp(-x^2 - hx^3)/2\sigma^2 \qquad (10)$$

so that parameter h quantifies the degree of asymmetry, The case h=0 corresponds to a symmetric Gaussian distribution which would yield the Debye-Waller factor and a shift of $4k\sigma_\perp^2 (1/R+1/\lambda)$. Note that even a symmetric case produces an extra phase shift which must be accounted for [Lee et al(1981), Crozier and Seary(1980), EB] which typically produces a small

change (~0.01 Å) in the distance determination. Using the theoretical curve data for $\sigma_{\perp}^2$ a best-fit is made to the phase-difference data (Figure 1) which yields the parameters a = -0.045, b=0.0018, ΔR = 0.048 Å, h=0.39 $Å^{-1}$ - this is essentially the conclusion of EB, and agrees with the known expansion of Zn.

We use the mean-free path data of Gordon and Djaoui(1992) derived for Al at normal density- this will provide an adequate description of the mean-free path for Zn. In the regime in question, λ(k) rises as a slow function of k but at lower k, there is a turnover near k~4 $Å^{-1}$.The best-fit using the numerical determinations of S(k) then is ΔR=0.025Å, h=0.70, which is clearly different, and not consistent with an expansion of 0.05 Å.

We also perform these fits with the experimental data of Beni and Platzman(1976). This gives

for the EB analytic case (equations (8) and (9)) ΔR = 0.056 Å, h= 0.28 $Å^{-1}$

and the numerical version with λ(k) gives ΔR = 0.045Å, h = 0.70 $Å^{-1}$.

This is a more satisfactory fit than that found using the calculated Debye-Waller factors and the approximately correct expansion is retrieved but the parameter h is much larger, emphasising the inadequacy of the analytic approximation. It could be argued that this approach underestimates the expansion, contrary to Crozier and Seary's ideas.

In all cases the goodness of fit is assessed using a 'chi-squared' figure defined as

$\chi^2 = [\Delta\varphi\ (exp) - \Delta\varphi\ (theory)\ ]^2$ which is minimised for the best-fit. These two numerical best-fit results are plotted graphically in Figure 1.

4. Conclusions

So we have shown that a more correct interpretation of the EB result requires the use of the experimental data for the Debye-Waller factors of Zn, a realistic k-dependent mean-free path and a numerical integration to find the components A(k) and S(k). This allows an expansion in R consistent with the known result to be obtained, whereas conclusions based on the use of other equations or the Beni-Platzman theoretical Debye-Waller curves are not as reliable.

Further improvements are strictly necessary involving the spherical wave theory of EXAFS as the plane wave equations outlined here actually give rise to an additional distance dependence, albeit weak, in the scattering amplitudge and phaseshifts when the problem is fomulated in terms of a plane-wave expresion like (1).

It would be desirable also to utilise the use of cumulant expansions following the work of Bunker (1983) and Brouder(1988) to detect asymmetry effects in model-independent ways.

Acknowledgements: The author gratefully thanks T. Hall and A. Djaoui for helpful discussions.

REFERENCES.

BENI, G. and PLATZMAN, P.W. (1976) Phys. Rev. B,**14**, No. 4, 1514

BROUDER, C. (1988) J. Phys.C **21**,5075

BUNKER, G. (1983) Nuclear Inst. Methods, **207**,437

CROZIER , E.D. and SEARY, A. (1980) J. Can. J. Phys.,**58**,1388

CROZIER, E.D., REHR, J.J. and INGALLS, J.E. (1987) in "Xray Absorption: Principles, applications, techniques of EXAFS, SEXAFS and XANES", Ed. Koningsberger, E. and Prins, D. (Wiley-Interscience)

EISENBERGER, and BROWN, (1979) Solid State Comms.,**29**,481

GORDON, F.I. and DJAOUI, A. (1992) Physics of Fluids B, **4**,12,3985

LEE, P.A., CITRIN, P. H., EISENBERGER, P. and KINCAID, B.M. (1981) Rev. Mod. Phys. , **53**, No.4,1

SAYERS, D.E., STERN, E.A. and LYTLE,F.W. (1971) Phys. Rev. Lett., **27**,1204

SEVILLANO, E., MEUTH, H. and REHR, J. J. (1979) Phys. Rev. **20**, No.12, 4908

STERN, E.A., SAYERS, D.E. and LYTLE, F.W. (1975) Phys. Rev. B.,**11**, No. 12,4836

Figure 1.

From Eisenberger and Brown(1979)'s Figure 2b, the experimental EXAFS phase at T=285K subtracted from that at T=10K as a function of wavevector k in $Å^{-1}$ (points, D) and the two best-fits found for the present numerical calculation, C) dashed line, with the Beni and Platzman(1977) calculated Debye-Waller factor σ = 0.179 Å, and h=0.70$Å^{-1}$, ΔR =0.025 Å and A) solid line, with the experimental Debye-Waller factors σ=0.200 Å, and h=0.70$Å^{-1}$, ΔR = 0.045 Å; both using wavevector dependent mean-free path.

Figure 1. Phase difference vs wavevector k

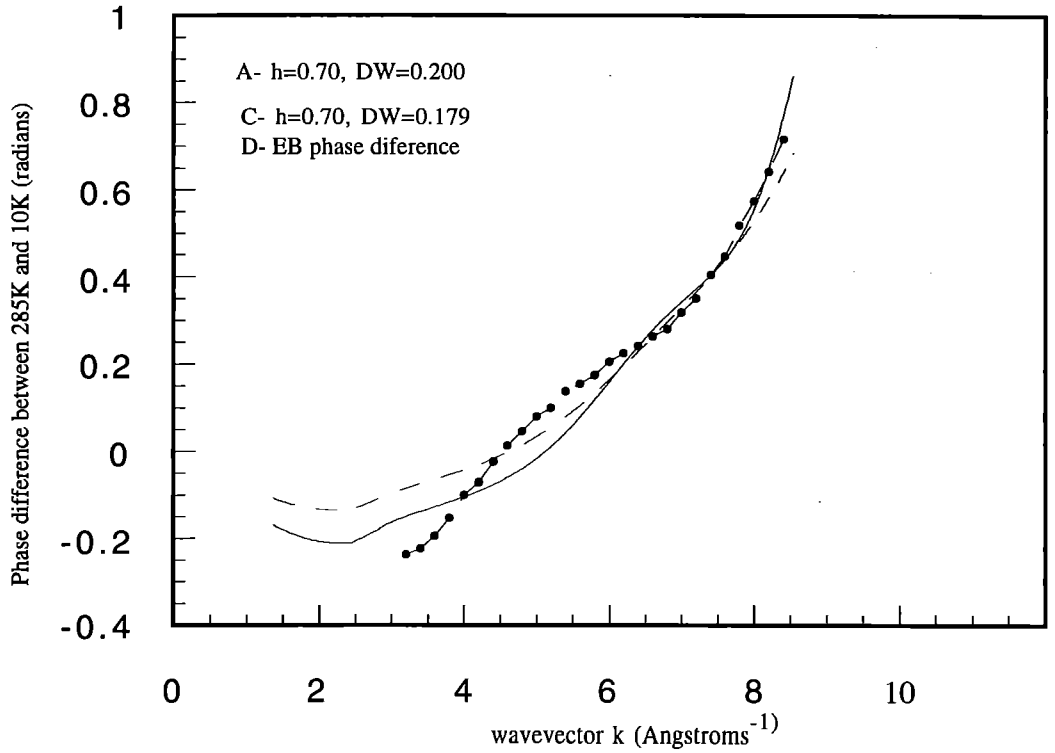

CALCULATION OF ATOMIC DATA FOR X-RAY LASER MODELLING

E Robertson, P Norrington and A Kingston

Applied Math. Dept., Queen's University of Belfast

The continuing interest both experimentally and theoretically in obtaining and applying lasing in the far X-UV and X-ray spectral regions has prompted the atomic calculations presented here. The successful demonstration and optimization of the 3s-3p lasing lines[1] in Ne-like Ge (Z=34) along with the successful modelling of this system[2] has led to an interest in Ne-like Y (Z=39) as a potential lasing medium. Also, in the longer term there is the possibility of Z scaling toward the Ni-like ions of systems such as Sm (Z=63) though such systems are at the technological limits of the CLF at present. This report presents atomic structure and electron collisional data for Ne-like Y calculated in the temperature region of interest as well as preliminary results of calculations on Ni-like Sm .

At QUB calculations have previously been carried out on the Ne-like ions of Ge and Se as part of the UK X-ray laser program. These calculations have used the non-relativistic R-matrix suite of codes[3] to solve the scattering problem with target functions obtained using the structure code CIV3[4] which is again non-relativistic. Using these codes it was possible to obtain collision strengths and therefore electron collision rates. Both of these codes use the non-relativistic version of the Hamiltonian and relativistic effects are included after the calculation of the Hamiltonian using the Breit-Pauli approximation. As the atomic weight and the degree of ionization of the ions under study increases, so we would expect the relativistic effects to increase in importance. This would make it more imperative to accurately calculate relativistic effects. The calculations described here were carried out using the atomic structure code GRASP[5] and the atomic scattering codes known collectively as JJMTRX[6]. All these codes are fully relativistic implicitly calculating the Dirac Hamiltonian and would therefore be expected to provide a more accurate estimation of atomic systems which have significant relativistic effects.

In the structure calculation for Ne-like Y we included the ground state plus the first 88 excited levels
ie $1s^2 2s^2 2p^6$
$1s^2 2s^2 2p^5$ 3s,3p,3d
$1s^2 2s^1 2p^6$ 3s,3p,3d
$1s^2 2s^2 2p^5$ 4s,4p,4d
$1s^2 2s^1 2p^6$ 4s,4p,4d

The energy levels for the first 27 energy levels produced by these configurations are shown in ***Table 1*** along with values calculated by Zhang and Sampson[7] for comparison. Also calculated using GRASP were the allowed electric dipole oscillator strengths between the 89 levels. ***Table 2*** shows those calculated oscillator strengths between the ground state and the first 26 excited states.

For the scattering calculation we used the JJMTRX suite of programs to solve the scattering problem for the Ne-like Y target ion. These programs employ the Dirac R-matrix method and are a relativistic generalization of the non-relativistic R-matrix method.

TABLE 1 Our calculated values for the energy levels compared with those calculated by Zhang and Sampson

level	configuration	Present (eV)	Zhang (eV)
1	$1s^2 2s^2 2p^6$	0.0	0.0
2	$1s^2 2s^2 2p^5 3s\ ^3P_2$	1996.98	1998.1
3	$^1P_1$	2000.44	2001.8
4	$^3P_0$	2055.28	2055.8
5	$^3P_1$	2057.73	2059.0
6	$1s^2 2s^2 2p^5 3p\ ^3S_1$	2075.67	2076.9
7	$^3D_2$	2076.20	2077.1
8	$^3D_3$	2076.95	2078.1
9	$^1P_1$	2078.74	2080.0
10	$^3P_1$	2080.67	2082.1
11	$^3P_0$	2100.51	2101.6
12	$^3D_1$	2136.29	2137.6
13	$^3P_1$	2146.61	2147.4
14	$^1D_2$	2149.64	2150.6
15	$^1S_0$	2153.46	2154.9
16	$1s^2 2s^2 2p^5 3d\ ^3P_0$	2154.71	2155.9
17	$^3P_1$	2155.19	2156.6
18	$^3P_2$	2156.79	2157.6
19	$^3F_4$	2158.00	2159.4
20	$^3F_3$	2158.20	2159.5
21	$^1D_2$	2161.07	2161.8
22	$^3D_3$	2162.00	2163.5
23	$^3D_1$	2175.76	2176.9
24	$^3F_2$	2232.68	2234.2
25	$^3D_2$	2237.35	2238.6
26	$^3F_3$	2238.93	2240.5
27	$^1P_1$	2246.97	2247.9

TABLE 2 Our calculated oscillator strengths compared to those calculated by Zhang and Sampson

upper level	configuration	Present	Zhang
3	$1s^2 2s^2 2p^5 3s^1\ ^1P_1$	0.134	0.125
9	$1s^2 2s^2 2p^5 3p^1\ ^1P_1$	0.085	0.080
14	$1s^2 2s^2 2p^5 3p^1\ ^1D_2$	0.004	0.004
23	$1s^2 2s^2 2p^5 3d^1\ ^3D_1$	1.746	1.719
27	$1s^2 2s^2 2p^5 3d^1\ ^1P_1$	1.815	1.793
31	$1s^2 2s^1 2p^6 3p^1\ ^3P_1$	0.101	0.103
33	$1s^2 2s^1 2p^6 3p^1\ ^1P_1$	0.309	0.318
39	$1s^2 2s^2 2p^5 4s^1\ ^3P_1$	0.025	0.021
47	$1s^2 2s^2 2p^5 4d^1\ ^3P_1$	0.001	0.001
53	$1s^2 2s^2 2p^5 4d^1\ ^1P_1$	0.504	0.512
63	$1s^2 2s^1 2p^6 4s^1\ ^3P_1$	0.000	0.000
71	$1s^2 2s^2 2p^5 4d^1\ ^3P_1$	0.316	0.317
79	$1s^2 2s^1 2p^6 4p^1\ ^3P_1$	0.040	0.039
81	$1s^2 2s^1 2p^6 4s^1\ ^1P_1$	0.101	0.103

The scattering calculation included the first 27 fine structure levels arising from the $1s^2 2s^2 2p^6$ and $1s^2 2s^2 2p^5$ 3s,3p,3d configurations. For the continuum electron values of the l quantum number up to l=14 were included. There were up to 109 channels opened for the given total J of this target ion. The dimension of the largest Hamiltonian matrix was 1750 for this system.

Collision strengths were calculated for continuum electron energies up to 4000eV. *Table 3* compares some of our results for collision strengths from the ground state to the excited states for an energy of 2070eV compared to those calculated by ref 7

In addition to calculating collision strengths at higher energies we also looked at energies between excitation thresholds and these showed significant resonance structure which can effect electron collisional rates produced from collision strengths. It is this ability to study resonance structure at lower energies which gives the R-matrix method an advantage over other methods such as the distorted wave method used by Zhang and Sampson which is more suited to higher energies.

TABLE 3 Our calculated values of collision strengths for transitions between ground and first 26 excited levels at an electron temperature of 2070eV

level	Present	Zhang
2	5.455(-4)	2.62(-4)
3	1.039(-3)	1.86(-3)
4	8.815(-4)	4.66(-4)
5	1.376(-3)	1.39(-3)
6	1.435(-3)	6.25(-4)
7	7.308(-4)	3.29(-4)
8	1.083(-4)	5.14(-5)
9	7.211(-4)	1.17(-3)
10	1.091(-3)	1.18(-3)
11	7.148(-3)	7.48(-3)
12	6.141(-4)	2.62(-4)
13	6.791(-4)	2.79(-4)
14	1.809(-3)	8.22(-4)
15	1.786(-3)	1.37(-3)
16	1.789(-3)	7.01(-4)
17	2.295(-3)	8.28(-4)
18	6.999(-4)	3.30(-4)
19	1.213(-3)	1.20(-3)
20	1.258(-3)	4.21(-4)
21	1.365(-2)	1.35(-2)
22	1.246(-3)	1.03(-3)
23	3.101(-2)	4.73(-2)
24	1.155(-3)	3.97(-4)
25	1.757(-3)	6.44(-4)
26	1.545(-3)	1.21(-3)
27	2.964(-2)	4.61(-2)

Using our calculated values for collision strengths collision rates for a number of different temperatures were then calculated. It was in the form of collisional rates that we supply the atomic data to X-ray laser modellers. Collision rates between the ground and the first 26 excited states are shown in *Table 4.*

In addition to the calculations of the Ne-like Y ion system so far carried out calculations on Ni-like Sm, another potential lasing medium, are also in the process of being carried out. This system, due to the higher degree of ionization, greater Z and large number of energy levels which would have to be considered, is a much larger problem requiring greater computational resources to solve. So far we have completed the structure part of the problem using GRASP and are presently working on the preliminary stages of the scattering calculation using JJMATRX.

TABLE 4 Shows calculated values of electron collisional rates between ground state and first 26 excited states for different temperatures

upper level	500eV	1000eV	1500eV
2	1.836(-14)	1.039(-13)	1.487(-13)
3	3.333(-14)	2.122(-13)	3.194(-13)
4	3.052(-14)	1.723(-13)	2.467(-13)
5	4.703(-14)	2.804(-13)	4.107(-13)
6	4.957(-14)	2.782(-13)	3.972(-13)
7	2.491(-14)	1.403(-13)	2.006(-13)
8	3.646(-15)	2.062(-14)	2.953(-14)
9	2.424(-14)	1.502(-13)	2.236(-13)
10	3.738(-14)	2.241(-13)	3.289(-13)
11	2.464(-13)	1.510(-12)	2.235(-12)
12	2.103(-14)	1.182(-13)	1.688(-13)
13	2.341(-14)	1.304(-13)	1.856(-13)
14	6.236(-14)	3.487(-13)	4.969(-13)
15	6.156(-14)	3.579(-13)	5.187(-13)
16	6.181(-14)	3.424(-13)	4.859(-13)
17	7.938(-14)	4.386(-13)	6.219(-13)
18	2.420(-14)	1.362(-13)	1.948(-13)
19	4.154(-14)	2.464(-13)	3.601(-13)
20	4.345(-14)	2.396(-13)	3.394(-13)
21	4.703(-13)	2.884(-12)	4.270(-12)
22	4.306(-14)	2.512(-13)	3.647(-13)
23	1.064(-12)	6.637(-12)	9.895(-12)
24	3.995(-14)	2.205(-13)	3.124(-13)
25	6.064(-14)	3.360(-13)	4.770(-13)
26	5.331(-14)	3.103(-13)	4.499(-13)
27	1.036(-12)	6.472(-12)	9.651(-12)

[1] D. Matthews et al, in 'X-ray Lasers 1990', G Tallents Ed (IOP, Bristol) p205 (1991)

[2] P Holden et al, 'A computational investigation of the neon-like germanium collisionally pumped laser' J.Phys.B,(in submission)

[3] K Berrington et al, Comput. Phys. Comm. **14** 367 (1978)

[4] A Hibbert, Comput. Phys. Comm. **9** 141 (1972)

[5] K G Dyall et al, Comput. Phys. Commun. **55** 425 (1989)

[6] J J Chang , J.Phys.B **10** 3335 (1977)

[7] H L Zhang and D H Sampson, Atomic Data and Nuclear Data Tables, **43** 1-69 (1989)

NON-LOCAL EFFECTS IN LASER PLASMAS

M G Haines

Imperial College, London SW7

It is now widely recognised that non-linear heat flow, in which the heat flux at a point is not simply proportional to the temperature gradient at that point but is dependent on the distribution of energy in a wide neighbourhood around that point, is an important and essential feature of laser-induced direct-drive inertial confinement fusion. The present work describes a review of the field and is contained in a recently published book. In contrast, the linear and local heat flux q is proportional to the local temperature gradient, ∇T which we can write as T/L where T is the temperature and L is a characteristic scale length. The heat flux can be written as

$$q = -\kappa \nabla T \tag{1.1}$$

or

$$|q| = \alpha \frac{\lambda_{mfp}}{L} nT(T/m)^{\frac{1}{2}} = \alpha \frac{\lambda_{mfp}}{\sqrt{2}L} \frac{1}{2} nmv_T^3 = \alpha \frac{\lambda_{mfp}}{L} q_{fs} \tag{1.2}$$

where κ is the coefficient for thermal conduction, λ_{mfp} is the mean free path, m is the particle mass, n the number density and v_T is the mean thermal speed defined by $k_B T = \frac{1}{2} m v \frac{2}{T}$, where k_B is Boltzmann's constant. There are three degrees of freedom for this fully ionized monatomic system. The flux q_{fs} is called the free streaming limit, and represents the heat flux associated with the mean thermal energy being transported at the mean thermal speed. The factor x is 3.2 for an ion charge Z of 1.

The heat flux can be considered more generally as an asymptotic series in powers of (λ_{mfp}/L), the first term being that relevant for linear, local heat flux. When early laser experiments failed to satisfy eqs (1) and (2), often termed Spitzer heat flow, it was because of some apparent heat flux inhibition. A convenient factor f, called the flux limit, was introduced so that for steep temperature gradients the heat flux was given by

$$|q| = f q_{fs} \tag{1.3}$$

A combined form of eqs (1) and (3) can be written as a harmonic mean,

$$q = -\left[\left(\frac{1}{\kappa|\nabla T|}\right)^s + \left(\frac{1}{f q_{fs}}\right)^s\right]^{-1/s} \frac{\nabla T}{|\nabla T|} \tag{1.4}$$

where s is a positive number, usually one, or, instead

$$q = \min\left(\kappa \nabla T, f q_{fs} \nabla T/|\nabla T|\right) \tag{1.5}$$

Comparison of typical experiments with computational modelling with different values of the flux limit led to values of f typically 0.03 to 0.1, (the low values of f are now largely discredited as being a misinterpretation of experiments in which two-dimensional effects in the form of lateral transport of heat were important).

However, in reality there is little or no theoretical justification for employing a crude flux limit, because when the mean free path is no longer small compared to the temperature gradient scale-length, local transport theory breaks down and indeed becomes non-local and dependent on the details of the distribution function up to several mean free path lengths away. The necessity to include the effects of the self-consistent electric field (to satisfy the condition of zero current in one-dimensional theory) and the corrections to the Rosenbluth potentials for a non-Maxwellian lowest order distribution function, make the theory non-linear as well as non-local. With new and fast Fokker-Planck codes operational, it should now be possible to compare experimental results with a more appropriate non-linear transport theory and the concept of a flux limit should be abandoned.

We examine linear transport theory and its limits of validity. Early experiments in laser - plasma interactions showed that the heat flux does not obey linear transport theory. Various explanations were put forward, which we will review, and eventually it has been accepted that the dominant effect is non-local, non-linear, but classical heat flux, i e, anomalous processes associated with electrostatic or electromagnetic turbulence are not present. The theory and simulations of this process are presented in various model situations. More careful experiments with time and space-resolved X-ray spectroscopy now permit a more detailed comparison. Results of an experiment scaled to low density so that Thomson scattering of a diagnostic laser beam can be employed, show other detailed features of the non-linear heat flux in a plasma. Attempts have been made to approximate the detailed Fokker-Planck simulations by simpler models, one of which relies on a convolution approach and is essentially linear. However, these have been overtaken by recently developed algorithms for the fast numerical solution of a truncated expansion of the Fokker-Planck equation coupled to the hydrodynamics which works efficiently in both one and two dimensions. The two-dimensional study of non-local transport is crucial for a quantitative understanding, and for an assessment of what spherical non-uniformities can be tolerated in inertial fusion. These non-uniformities can arise in either the laser-beam itself or in the imperfect fabrication of the target. However, the distribution function that typifies even one-dimensional non-local heat flow can be unstable to electrostatic ion-acoustic modes or to electromagnetic instabilities. There are as yet unexplained experimental phenomena of fine-scale (~ 10 μm) jets with associated magnetic fields which might be caused by electromagnetic instabilities. The instabilities have been studied theoretically in essentially three models: a thermal instability, which can be enhanced by radiation loss, a thermomagnetic instability, and the Weibel type of instability driven by the anisotropy in the distribution function. In keeping with the theme of this book, a non-local description of the collisional Weibel instability is included as the most definitive version so far of this mode. More recent work at Imperial College by A R Bell indicates that the jets could be caused by the well known $\nabla T x \nabla n$.

REFERENCES

1 M G Haines, Non-local effects in Laser Plasmas, in 'Spatial Dispersion in Solids and Plasmas' ed P Halevi, Elsevier Science Publishers B V, 1992.

RADIATIVELY COOLED RECOMBINATION LASERS

S B Healy and G J Pert

Department of Physics, University of York, Heslington, York YO1 5DD

Introduction

The recent demonstration of large gain-length products ($GL \sim 6$) at 182Åfor a carbon fibre irradiated with a high intensity $2ps$ pulse (Key et al) has led to renewed interest in recombination lasers. This paper briefly summarises the results of a computational investigation of radiatively cooled hydrogenic carbon recombination lasers, emphasising the inherent difficulties associated with these systems.

Physical Background

The important concepts of recombination lasers are well understood. The interaction of a high power pumping laser with the lasant material result in electron temperatures sufficiently high to fully strip the nuclei. If the free electrons cool rapidly, the subsequent recombination is predominantly into the high lying Rydberg states of the hydrogenic ion, which become preferentially filled. A population inversion occurs between the $n = 3$ and $n = 2$ levels as the upper state is populated by a collisional cascade, whilst the lower is depopulated by fast radiative decay. The cooling rate is of major importance in these systems as the three-body recombination rate, R_3, scales approximately with the electron temperature as $R_3 \propto T_e^{9/2}$. Therefore, faster cooling results in larger gain. Two approaches to cool the plasma have been considered. The first (Pert, 1976) allows the plasma to expand into a vacuum and cool adiabatically as thermal energy is converted into kinetic energy of the expansion. In the second approach (Suckewer and Fishman,1980), the plasma is confined in a magnetic field and cools as a result of radiative losses involving collisional excitation of bound electrons followed by radiative decay. These losses can be increased by doping the lasant with a heavy ion impurity. The aim of this work has been to investigate the possibility of combining both mechanisms, allowing a plasma doped with a heavy impurity to expand into a vacuum. Simulations of carbon doped with a selenium impurity have been presented by Nam et al.(1986) and Epstein(1988) with conflicting results.

The Computational Model

The model includes laser heating through inverse bremstrahlung and resonant absorption. The hydrodynamics of the mixed plasma are modelled with a self-similar expansion. The atomic physics of the lasant uses the collisional radiative model for the H-like and He-like ions with the remaining stages described with a modified form of Griem's model (Davé, 1984). The versatile average atom approach, based on the work of Locke and Grassberger (1977), is used for the impurity ions, enabling a wide range of impurities to be considered. The atomic physics and hydrodynamics are consistently in the solution of the free electron energy balance, which is subject to the 'energy limit' (Pert,1978) to damp oscillations in the free electron temperature.

Results and Discussion

The results presented refer to a $0.9\mu m$ fibre (noting that the self-similar model does not consider the remnant cold core) irradiated with a $70ps$ pulse. The total number of ions remains constant for all simulations and the impurity is seeded as a percentage of this number. Figure 1 summarises the peak gain, optimised with respect to the pumping power,

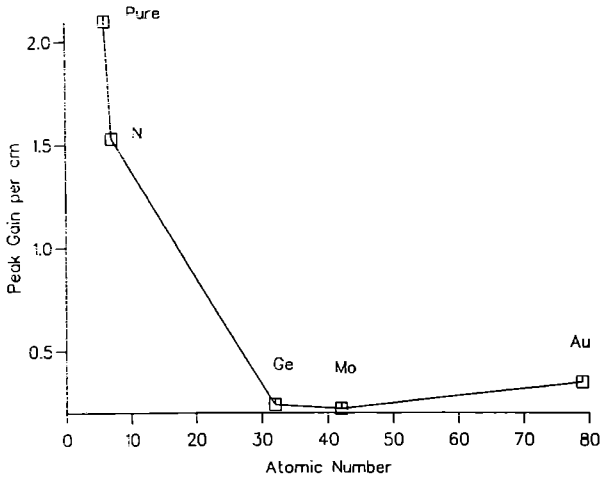

Figure 1: Optimised Peak Gain for pure carbon and 50/50 mixtures.

for the pure carbon simulation and 50% nitrogen, germanium, molybdenum and gold impurities. It is apparent that the mixtures result in lower gains and it is found generally that the gain falls as the percentage of impurity is increased, as shown in figure 2 for the germanium impurity. The simulations indicate that the impurities reduce the efficiency of a recombination laser and often result in a cooling rate slower than that due to the expansion of a pure carbon fibre, which will now be discussed.

The pumping power requirements are found to increase significantly both as the percentage of impurity is increased and as the impurities are scaled to higher z. This is due to increased radiative losses during the pumping pulse. Hence, more energy is required to ensure the plasma temperature is sufficiently high to fully strip the lasant. A second problem arises because the increased inertia of the impurity reduces the expansion rate as,

$$v_{exp} \propto ((z_{av} + 1)kT_e/m_{av})^{1/2} \qquad (1)$$

where m_{av} is the average atomic mass and z_{av} is the mean ionisation. As a consequence, the efficiency of the expansion cooling is reduced. Finally, the simulations have emphasised that the potential energy stored in excitation/ionisation E_{ion} must be considered in radiative cooling calculations. It is important to consider whether atomic processes result in a net cooling or reheating of the plasma and to note that radiative losses do not always reduce the free electron energy,

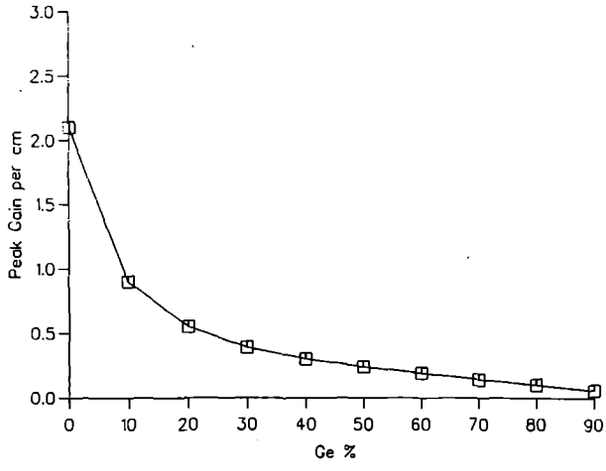

Figure 2: Variation of optimised peak gain with percentage of germanium impurity.

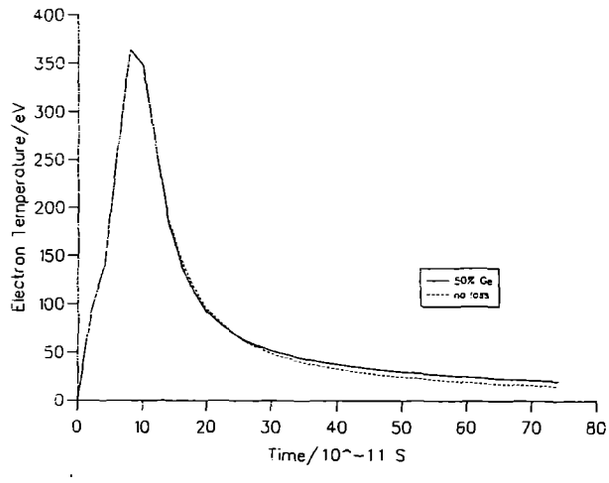

Figure 3: Comparison of electron temperature for 50/50 mixture for full simulation and when atomic physics is not included in the solution of the energy balance.

often only reducing E_{ion}. In fact, the change in free electron thermal energy ΔE_e over a timestep Δt due to atomic processes is given by,

$$\Delta E_e = -(\Delta E_{ion} + W_{rad}\Delta t) \qquad (2)$$

where W_{rad} is the radiated power and $\Delta E_{ion} > 0$ for upward transitions, if an electron is excited or ionised. Figure 3 shows the evolution of electron temperature for 50% germanium impurity when atomic processes are removed from the energy balance during cooling (denoted by 'no rad'). When this is compared with the full simulation, the cooling is rate of the former is clearly faster. Hence, this indicates that atomic processes, such as three-body recombination and collisional de-excitation, are resulting in a net reheating of the plasma.

Conclusion

Simulations indicate that doping a freely expanding carbon plasma with a heavy impurity does not lead to an increased cooling rate. Radiative losses during the pumping pulse, a reduced expansion rate and increased reheating due to recombining impurity represent major difficulties.

References

Key MH et al to be published
Pert GJ J. Phys. B. 9, 3301,(1976)
Suckewer S and Fishman H J.Appl.Phys 51,1922,(1980)
Nam CH et al J.Opt.Soc.Am.B 3,1199,(1986)
Epstein R Phys.Fluids B 1,214,(1988)
Locke WA and Grassberger WH LLNL Report UCRL 52276,(1977)
Pert GJ J.Comp.Phys. 27,241,(1978)

HIGH POWER LASER DEVELOPMENT AND OPERATIONS

M J Shaw

Rutherford Appleton Laboratory

INTRODUCTION

This year has seen the culmination of the Joint Projects for the enhancement of the high power laser facilities at the CLF. This RAL/University collaboration has been highly successful, being completed close to time and budget and leading to very significant improvements in the capabilities of the high power lasers at the CLF. These improvements place the CLF as the World leader in high brightness laser facilities.

GLASS LASER CPA

The RAL-Southampton-Imperial College collaboration on Vulcan CPA has pushed the performance to 35 TW at a pulse duration of 620 femtosecs. An irradiance on target of greater than 10^{19} W cm^{-2} has been obtained. The Nd-LMA oscillator was a vital part of this success in producing sub-picosecond pulses with extremely high reliability. New alignment techniques for the compression gratings have been developed which has resulted in the spot size being reduced to 15 μm diameter. Further improvements in performance can be expected after the installation of the Ti:sapphire regenerative amplifier which has significantly exceeded its design specifications in trial runs at Imperial College.

KrF CPA

1 TW, 300 fsec CPA operation on Sprite was made available to users after last year's development work and effort this year focused on reducing the pulse length. An absorption feature within the KrF gain band width has been shown to limit the pulselength so far obtained but a further two-fold reduction to use the full KrF laser band width is anticipated in future work. The issue of grating alignment is also addressed in this section together with better modelling of KrF pulse amplification using an improved kinetic plus ASE code.

KrF RAMAN

The enhancement of the Sprite Raman beam has led to a doubling of the power on target to 1 TW at a pulse duration of 10 ps. The maximum energy has increased from around 5 J to over 13 J at a pulse duration of 25 ps. This unique prepulse-free beam is capable of being focused to a near diffraction limited spot at more than 10^{19} W cm^{-2} irradiance at λ = 268 nm. A new 2D code has been developed at Imperial College which allows pump-to-Stokes phase and amplitude imprinting to be studied in detail. The possibility of Ultra-broad bandwidth generation using Raman scattering has been looked at theoretically in a collaboration between Imperial College and the Lebedev Institute, Moscow.

TITANIA

The Titania upgrade to the CLF's KrF capabilities is now well under way. A specification document for the new facility has been produced and construction of the shell of the new target area has already been completed. The Titania amplifier module is now close to its first laser shot. The laser triggered switches have demonstrated satisfactory performance and new I/V monitors have been calibrated. In the future, solid resistors are proposed for the Marx generators following successful tests reported here.

INSTRUMENTATION

The development of phase zone plates to produce smooth irradiation patterns continues to be one of the CLF's strengths. Analysis of a Fresnel zone plate is presented in this section. Also analysed in some detail is the use of 2-photon absorption as a means of measuring pulse duration and contrast ratio. This technique is particularly valuable in the UV where second harmonic crystals may not be available. A considerable advance in soft X-Ray imaging is reported which uses a high efficiency, small grain rare earth phosphor to convert X-Rays to visible photons which can be recorded by standard CCD techniques.

OPERATIONS

It has been another very busy year for the operations teams. Vulcan fired 1722 full disc shots to target in the main target areas and over 1000 low energy shots to TA4. Sprite delivered 1513 shots to target in both the CPA and Raman modes. Both the Vulcan and Sprite CPA beams were in high demand with experimenters keen to capitalise on the improved performance offered this year.

>10^{19} Wcm^{-2} OPERATION OF THE VULCAN HIGH POWER ND:GLASS CPA LASER FACILITY

C N Danson[1], J R M Barr[2], L J Barzanti[1], M D Ebbage[1], C B Edwards[1], M J Gander[1], D C Hanna[2], D W Hughes[2], M H R Hutchinson[3], M H Key[1], A A Majdabadi[2], I P Mercer[3], D Neely[1], P A Norreys[1], D A Pepler[1], S A Rivers[1], I N Ross[1], P F Taday[1], W T Toner[1], F N Walsh[1], T B Winstone[1] and F Zhou[3]

1 Central Laser Facility, Rutherford Appleton Laboratory, Chilton, Didcot, Oxon, UK
2 Opto-electronics Research Centre, University of Southampton, Southampton, UK
3 Blackett Laboratory, Imperial College, Prince Consort Road, London, UK

The recently commissioned chirped pulse amplification (CPA) facility on VULCAN[1] has been fully operational for the whole of the reporting year providing ultra-short pulses for laser/plasma interaction experiments. Recent developments have enabled shorter pulse operation (620 fs) with good focal spot quality giving 35TW in a single large aperture beam, with focused intensities on target in excess of 10^{19} Wcm^{-2}. This report describes these developments and characterises the amplification system for full power shots.

The system inprovements involved:

- Installation of a new diode-pumped Nd:LMA oscillator[2]. This device is capable of delivering pulses as short as 420 fs.
- Using the larger oscillator bandwidth of 2.6 nm to generate a longer stretched pulse which together with the optimisation of the amplification system and target area optics reduced the total B-integral of the system to <1.
- Alignment optimisation of the large aperture diffraction gratings using a novel technique which produced good focal spot quality (<3 times the diffraction limit).

OSCILLATOR

The oscillator, developed specifically for this work, used additive pulse modelocking (APM) of diode-pumped Nd:LMA. A minimum pulse duration of 420 fs was measured (assuming sech^2 pulse shape), and a time-bandwidth product of 0.32 indicating that the pulses were near transform limited. The maximum average output power from the modelocked oscillator was 115 mW at a repetition rate of 87 MHz , giving a single pulse energy of 1.3 nJ. A detailed description of this development work can be found elsewhere in this report (A Majdabadi et al).

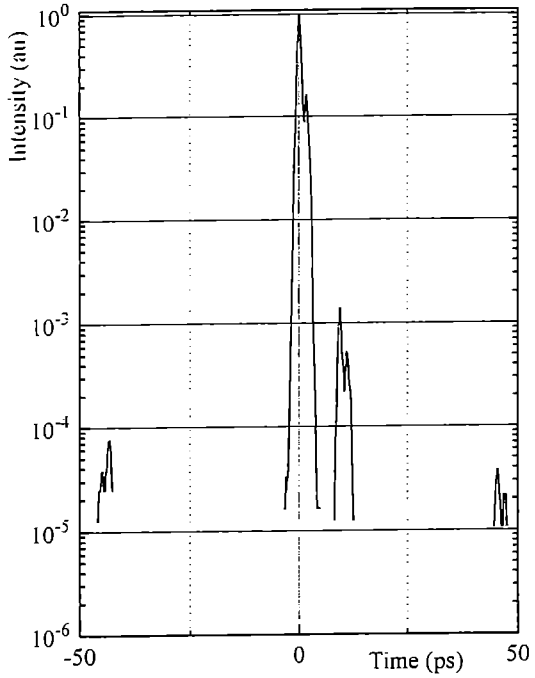

Figure 1. Contrast ratio measurements of the Nd:LMA oscillator

In previous experiments it was found that if the oscillator pulse contrast was good (~10^{-7}) then the contast (<10^{-6}) could be maintained to the system output. A third order cross correlator[3] was used to measure the contrast of the new oscillator, the results of which are shown in figure 1. The double pulse structure associated with each pulse is attributed to the instrumentation. A prepulse at the 2×10^{-5} level is evident at about 50 ps, and post pulses at 12 ps and 45 ps. These are attributed to reflections which are currently being investigated.

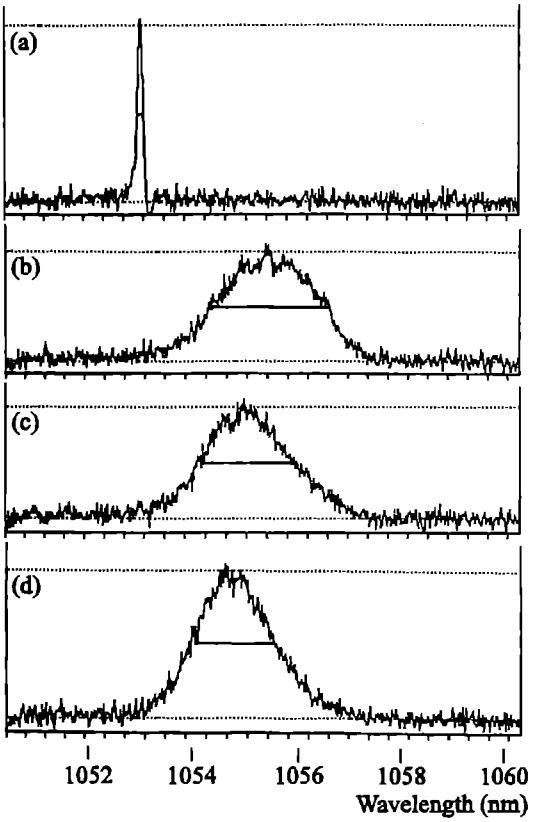

Figure 2. Spectral characterisation of the CPA pulse through the VULCAN amplification system

AMPLIFICATION

As the pulse was amplified through the system a spectral shift of the pulse to shorter wavelength was observed. This occurred because the peak of the oscillator lies ~ 1.4 nm to the long wavelength side of the peak of the gain bandwidth, producing preferential amplification of the shorter wavelengths. This is illustrated in figure 2 where the central maximum for the amplification envelope is ~ 1054 nm. Trace 2(a) shows the spectrometer output with the continuous wave

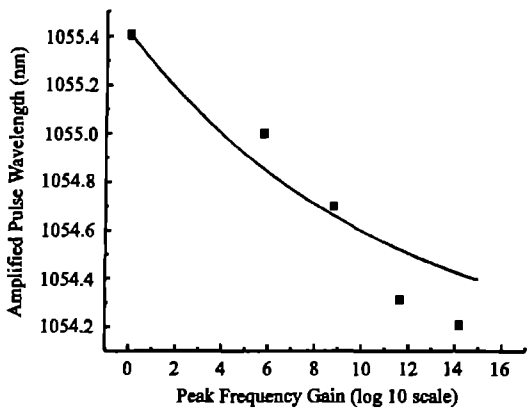

Figure 3. Spectral walking with increased gain

Nd:YLF laser passing down the system, this was used as a calibration with the peak of the spectrum at 1053.0 nm. Trace 2(b) shows the CW Nd:LMA oscillator output at the same point with the centre of the spectrum being at 1055.4 nm. Trace 2(c) shows the peak of the spectrum lying at 1055.0 nm for a gain of ~6.3×10^5. This is further accentuated when the gain is increased as can be seen in trace 2(d), where with a gain of ~5.7×10^8, the peak of the spectrum is at 1054.7 nm.

To measure the spectral characteristics of high power shots a spectrometer was also used after recompression in the target area. At net system gains of 4.5×10^{11} and 1.5×10^{14} peak spectral positions of 1054.3 and 1054.2 were measured respectively. These data points are plotted in figure 3 showing the spectral shift with gain. The curve on the graph is a theoretical output assuming all the glass in the system has the same gain characteristics and line shape. This simple model shows surprisingly good agreement with the measured values.

PULSE RE-COMPRESSION

The grating separation was optimised by taking a series of test shots at low energy, and measuring the compressed pulse duration with a single shot auto-correlator. A distinct minimum was found in the pulse duration as shown in figure 4. The gratings were then set to this separation.

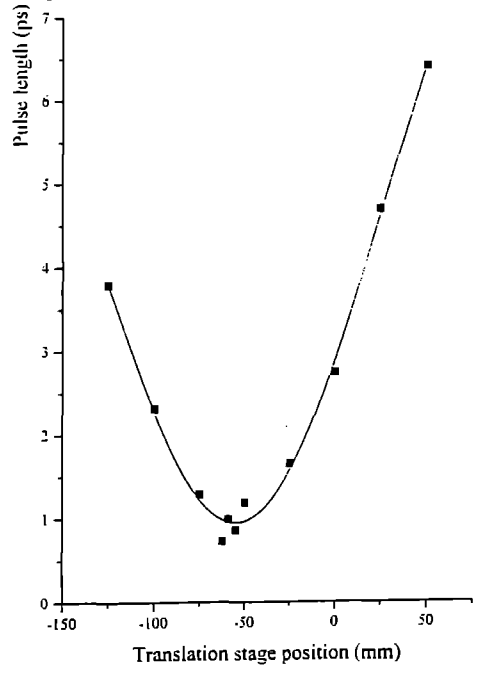

Figure 4. Optimisation of the grating separation

In previous experiments (1) it was observed that the focal spot of the re-compressed pulse was elongated in a direction parallel to the gratings, significantly reducing the maximum target irradiance. This problem was attributed to a slight misalignment error between the recompression gratings. A novel alignment method was devised using two CW alignment beams described in more detail elsewhere in this report (D Neely et al). The grating alignment was therefore optimised to eliminate any residual dispersion.

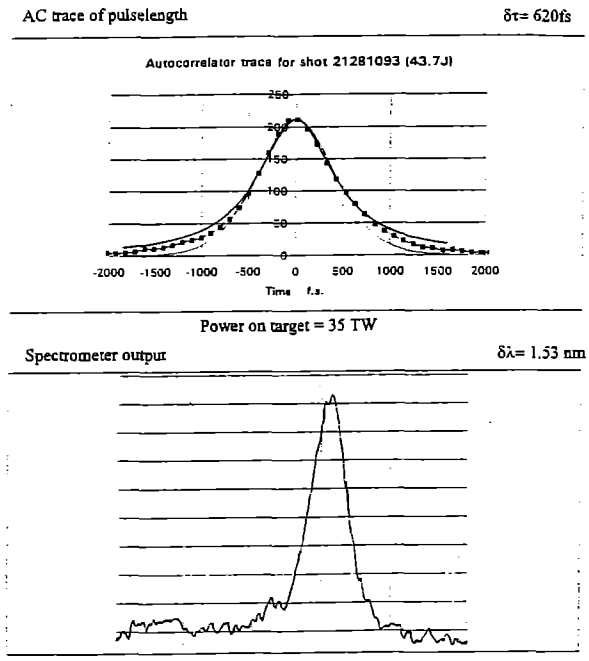

Figure 5. Diagnostic outputs for a full energy CPA shot

The pulsewidth and spectral data for a high power shot are shown in figure 5. The incident energy onto the gratings for this shot was 44 J, with losses due to diffraction efficiency and mirror reflectivity at ~ 50%, giving an energy on target of 22 J. The pulsewidth was measured at 620 fs (sech^2 profile), and the bandwidth of this pulse measured to be 1.53 nm (figure 5), giving a delivered laser power to target of 35 TW. Using the measured focal spot size of ~ 15 μm diameter for the shot this gives an irradiance on target of $>10^{19}$ Wcm^{-2}.

CONCLUSION

With the successful commissioning of a new APM diode-pumped Nd:LMA oscillator and improvements to the relay/transport optics, the Vulcan system has been used in high power 35 TW, 620 fs operations in a CPA mode onto target. Improved grating alignment techniques have allowed us to obtain focal spot sizes less than three times the diffraction limit giving target irradiances of $>10^{19}$ Wcm^{-2}.

During the reporting year almost 500 CPA disc shots have been delivered to experiments. In the coming year we will be installing the recently developed regenerative amplifier, allowing even shorter pulses to be generated.

REFERENCES

[1] C N Danson et al, Optics Communications, 103 (1993) 392-397
[2] D W Hughes et al, OSA Topical Meeting on Advanced Solid State Lasers, paper AMC3, New Orleans, USA (1993)
[3] S Luan et al, Meas.Sci.Technol. 4 (1993) 1426-1429

A SUB-PICOSECOND, LASER DIODE PUMPED, Nd:LMA OSCILLATOR .

A. Majdabadi, D. W. Hughes and J. R. M. Barr,
Optoelectronics Research Centre,
Southampton University,
Southampton,
U.K.

INTRODUCTION

We report the generation of pulses as short as 420 fsec at 1054.5nm from a laser-diode-pumped additive-pulse-modelocked Nd:LMA ($Nd_xLa_{1-x}MgAl_{11}O_{19}$ or LNA) laser using a dipersively compensated Michelson interferometer as the laser output coupler. The technique of mode-locking using a nonlinear external cavity (additive pulse mode-locking, APM) has achieved much success in the field of ultrashort pulse generation. In a variety of laser systems, the technique has permitted pulses approaching the bandwidth limit to be generated eg Nd:YAG[1] and Nd:YLF[2]. By combining this technique with laser-diode-pumping, it is possible to obtain highly efficient, reliable, stable and compact all solid state sources of mode-locked pulses[1-3]. Our motivation for the investigation of short pulse generation at 1054 nm is the development of a reliable all solid state source, capable of generating sub-picosecond pulses, to be used as an oscillator for chirped pulse amplification (CPA) experiments being carried out on the VULCAN Nd:glass laser at the Rutherford Appleton Laboratory.

Nd:LMA is a laser material whose use was first reported in the mid 1980s[4]. Its cw operation has previously been reported with a variety of pump sources, including argon ion lasers[4], Ti:Al_2O_3 lasers[5] and laser diodes[6,7]. Mode-locked pulses in the picosecond regime have been reported using passive mode-locking of a pulsed, flashlamp-pumped Nd:LMA laser[8] (where pulses of 10 psec duration were obtained) and active mode-locking of laser-pumped systems[9,10] (14 psec pulses from FM mode-locking of a laser-diode-pumped Nd:LMA laser[9] and 70 psec from FM mode-locking of a Ti:Al_2O_3 laser pumped Nd:LMA laser[10]). However, the fluorescent linewidth of this material (centred at 1054 nm) is 1.3 THz, which indicates that the Nd:LMA laser should be capable of supporting pulses as short as 250 fsec assuming a hyperbolic secant temporal pulse profile. Continuous wave passive modelocking of Nd:LMA using APM has been reported where a Ti:Al_2O_3 laser pumped Nd:LMA laser generated 550 fsec pulses[11] and a laser diode pumped Nd:LMA laser produced 420 fsec pulses.[12] Both of these reports used a Fabry-Perot configuration for the nonlinear arm, in this paper a Michelson configuration was adopted since it exhibits better stability and greater useable output power.

EXPERIMENT

The experimental apparatus is shown in figure 1. The pump source was a 3W laser diode array (SDL 2482). Its wavelength was temperature controlled around 800nm using a thermoelectric cooler to ensure good absorption of the pump beam in the active medium. It should be noted here that the same laser diode can be used to pump Nd:YLF and Nd:glass lasers to produce ultrashort mode-locked pulses at 1054 nm. The laser diode output was collimated in the plane perpendicular to the junction using a compound lens of focal length 6.5 mm and numerical aperture (NA) 0.615, anti-reflection (AR) coated at 800 nm. In the plane parallel to the junction, an AR coated 15 cm focal length cylindrical lens was used to collimate the laser diode output. The beam was then split into two. The beam labelled number 2 was passed through a half-wave plate WP before being recombined to exactly overlap with the beam labelled number 1 at the polarizing beamsplitting cube PBC. The combined beams were then focused onto the Nd:LMA rod using an AR coated 3.2 cm focal length lens. It was found that the pump beam and the lowest order Nd:LMA laser transverse mode had to be matched in size very carefully to obtain single transverse mode output. Even if the pump beam was significantly smaller than the laser mode (ie a regime where single transverse mode operation is usually readily obtained), multi-mode operation was observed, with the mode structure changing as the pump power was changed. This effect has been attributed to thermal lensing within the laser rod.[11]

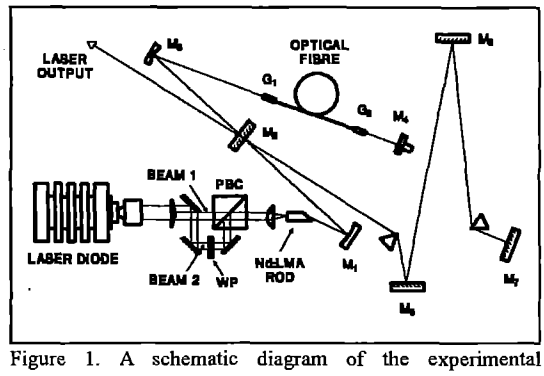

Figure 1. A schematic diagram of the experimental arrangement.

The purpose behind the splitting and recombination of the pump beam was to improve the quality of the pump beam near the focus. The spot size at the focus of the 3.2 cm lens was monitored using a beam analyzing system (Big Sky Corporation). It was observed that the minimum spot size obtained parallel to the plane of the junction (the non diffraction limited plane) was approximately 200 μm when the beam was unsplit, and 150 μm when the beam was split into two and recombined (the calculated average spot size in the laser crystal was 204 μm by 116 μm). This implies that the divergence of the pump beam near to the focus has been reduced by a factor of greater than two. By doing this the average size of the pump beam along the length of the crystal is reduced, which should result in both a lower laser threshold and a higher slope efficiency, due to a better match of the pump beam and the laser mode throughout the length of the crystal. Clearly, this procedure can only be carried out because the laser diode array is only partially spatially coherent and because Nd:LMA, when pumped along its c-axis, has an isotropic absorption. The performance of the laser for the pump beam both split and unsplit is shown in figure 2. This data was recorded with a 10% transmission output coupler at the end, rather

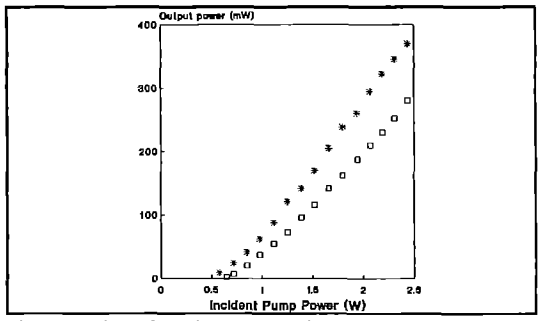

Figure 2. The points (*) represent the split performance while the points (□) represent the unsplit performance.

than in the middle of the cavity. It can be seen that the optical slope efficiency for the split case (20%) is significantly higher than for the unsplit case (15%).

The active medium was a plane-Brewster rod of Nd:LMA (Nd doping level 9% wt.) supplied by LETI (Laboratoire d'Electronique de Technologie et d'Instrumentation), Grenoble, France. It was 9 mm long and 5 mm in diameter, and was cut with its c-axis along the axis of the rod. The plane end of the rod was coated to give high transmission at the pump wavelength and high reflectivity at the lasing wavelength, 1054.5 nm. This crystal absorbed 90% of the pump light. The cavity was designed to compensate the astigmatism produced by the intra-cavity Brewster surface.[13] The off-axis turning mirror M_1 had a radius of curvature (ROC) of 30 cm. The laser output was taken through a 10% transmitting mirror M_2 placed a distance of 36 cm from the curved turning mirror. The linear arm of the Michelson interferometer was formed between this mirror and a plane high reflector M_7. A pair of Brewster angled SF10 prisms was incorporated into this arm, separated by 87 cm, to provide dispersion compensation for the net positive dispersion inherent in the APM scheme. In addition, two plane high reflectors M_5 and M_6 were used for increased compactness of the system. The laser was set up so that the beam passed through the prisms as close as possible to the apexes. The threshold pump power was 1.5 W incident on the crystal and the slope efficiency was 12.4% (this is calculated using the combined output power from both beams). The maximum output power was 88 mW in the beam going to the nonlinear arm, and 71 mW in the other beam. The output from the laser was at all times single transverse mode.

The nonlinear arm of the interferometer was formed between the 10% transmitting mirror and the high reflector M_4. A curved mirror M_3 (high reflector at 1054 nm, ROC 750 mm) was used to focus the beam into the GRIN lens G_1. By placing the GRIN lens a distance of 28 cm from the curved mirror it was found that a significantly higher launch efficiency could be obtained than when the curved mirror was substituted by a plane high reflector (78% as opposed to 26%). The input GRIN lens G_1 was a 3 mm diameter, 0.25 pitch lens (supplied by NSG, Belgium) and was uncoated at both ends. A GRIN lens (0.23 pitch) was also used to couple light out of the fibre. Index matching was accomplished at each of the GRIN lens to fibre interfaces using a drop of paraffin. The optical fibre used was a single mode (at 1054 nm) fibre (Newport F-SY) with core diameter 6.7 μm and NA 0.11. The fibre length used in these experiments was 39 cm. The nonlinear arm of the interferometer was completed by the high reflector M_4 mounted on a piezoelectric stack to enable active stabilization of the system to the correct relative phase of the two cavities for APM to occur.

In this set-up the nonlinear arm of the Michelson interferometer was the same optical length as the linear arm. Assuming hyperbolic secant temporal pulse profile, the pulse duration was measured to be 420 fsec, a typical intensity autocorrelation trace is shown in figure 3. The corresponding optical spectrum has FWHM of 750 GHz. The time-bandwidth product is hence 0.315, exactly the theoretical value for hyperbolic secant pulses. The maximum useful average output power in this case was 115 mW at a repetition rate of 87MHz, yielding a peak power of 3.3 kW, and a pulse energy of 1.3 nJ. The optical spectrum of the mode-locked laser shows no structure or modulation. However, in order to achieve this, very careful adjustment of the phase mismatch between the two cavities was required. Away from the phase mismatch at which no structure was observed on the optical spectrum, the optical spectrum exhibited a spike, the amplitude of which increased as the phase mismatch was detuned from its optimum position. We have attributed this spike to the presence of a cw component in the laser output, which was also seen to exist in the Ti:Al_2O_3 pumped Nd:LMA laser which we have reported previously.[11]

CONCLUSION

In conclusion, we have demonstrated the efficient, stable performance of an all solid state mode-locked laser operating at

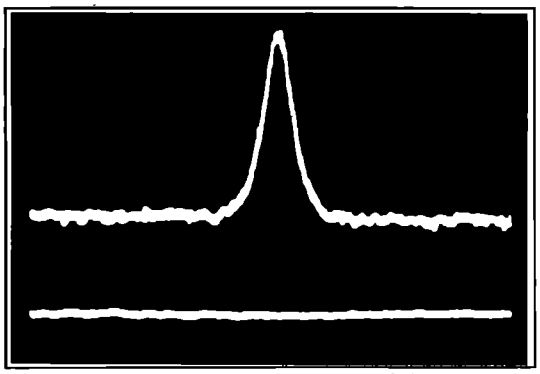

Figure 3. Intensity autocorrelation trace of the pulse. The width of the trace is 9.7ps and the pulse duration is 420fs.

1054.5 nm and capable of operating for many hours without user intervention. The pulses can be as short as 420 fsec which is still 1.7 times greater than the bandwidth limit of 250 fsec for this material, so in principle further decreases in the pulse duration are possible at this wavelength. The system is reliable, stable and compact, and has found use as a seed source for a Nd:phosphate glass amplifier chain. During these experiments the seed laser operated for 12 hours a day over a period of two months indicating the reliability of laser-diode-pumped APM systems in a laboratory environment. This work was supported by a Science and Engineering Research Council (SERC) funded collaboration with the Rutherford Appleton Laboratory. A. Majdabadi acknowledges financial support from the Ministry of Education, Iran.

REFERENCES.

1. J. Goodberlet, J. Jacobson, J. G. Fujimoto, P. A. Schul z and T. Y. Fan, Opt. Lett.**15**, 504 (1990).
2. G. P. A. Malcolm, P. F. Curley and A. I. Ferguson, Opt. Lett.**15**, 1303 (1990)
3. D. W. Hughes, M. W. Phillips, J. R. M. Barr and D. C. Hanna, IEEE J. Quantum Electron.**QE-28**, 1010 (1992).
4. L. D. Schearer, M. Leduc, D. Vivien, A. M. Lejus and J. Thery, IEEE J. Quantum Electron.**QE-22**, 713 (1986).
5. T. Y. Fan and M. R. Kokta, IEEE J. Quantum Electron.**QE-25**, 1845 (1987).
6. J. Hamel, A. Cassimi, H. Abu-Safia, M. Leduc and L. D. Schearer, Opt. Commun.**63**, 114 (1987).
7. J. J. Aubert, Ch. Wyon, A. Cassimi, V. Hardy and J. Hamel, Opt. Commun.**69**, 299 (1989).
8. M. I. Demchouk, V. P. Mikhailov, A. K. Gilev, A. M. Zabaznov and A. P. Shkadarevich, Opt. Commun. **55**, 33 (1985).
9. D. W. Hughes, A. Majdabadi, J. R. M. Barr and D. C. Hanna, Applied Optics, **32** 5958 (1993).
10. Y. Shi, J. P. Ragey and H. K. Haugen, IEEE J. Quantum Electron.**QE-29**, 435 (1993).
11. M. W. Phillips, Z. Chang, J. R. M. Barr, D. W. Hughes, C. N. Danson, C. B. Edwards and D. C. Hanna, Opt. Lett.**17**, 1453 (1992).
12. D. W. Hughes, A. Majdabadi, J. R. M. Barr and D. C. Hanna, OSA Topical Meeting on Advanced Solid State Lasers, paper AMC3, New Orleans, USA (1993).
13. H. W. Kogelnik, E. P. Ippen, A. Dienes and C. V. Shank, IEEE J. Quantum Electron. **QE-8**, 373 (1972).

DOUBLE-SIDE PUMPED TI:SAPPHIRE REGENERATIVE AMPLIFIER OPERATING AT 1.053 μm WAVELENGTH

F Zhou, I P Mercer and M H R Hutchinson

Blackett Laboratory, Imperial College, Prince Consort Road, London, UK

Recent rapid progress in high power, short pulse technology has made it possible to attain focused intensities in the 10^{18} W/cm^2 regime, allowing a variety of experiments involving the interaction of matter with ultra-bright and ultra-short light pulses to be performed in a new fundamental regime[1]. Flashlamp pumping combined with the large saturation fluence of Nd:glass enables the production of high energy and high peak power pulses. The amount of energy that one can extract from a solid-state laser material with a short pulse is in general limited by the nonlinear effects in the gain medium. However, these problems can be avoided by resorting to the technique of chirped pulse amplification (CPA)[2]. This technique makes it possible to amplify short pulses to energies near the amplifier saturation level while maintaining power densities below the beam spatial and temporal distortion limits in the amplifier chain.

Although it is now very well developed for the amplification of an optical pulse, the single or double pass Nd:glass pre-amplifier of the usual "master-oscillator power-amplifier" system is inefficient and has a restricted bandwidth which gives rise to spectral narrowing and consequently pulse lengthening. To amplify a low-energy pulse, numerous amplification stages with successive amplifiers of increasing diameter may be required since it is necessary to boost the output from an oscillator at the nJ level to the mJ level before injection into the rod amplifiers. In the regenerative amplifier[3], the pulse to be amplified is rejected into a cavity containing the amplifier and extracted when saturation is reached. This is usually achieved by placing the gain medium in a high-Q, stable TEM_{00} optical cavity. When the gain saturation is approached after the desired number of round trips, the injected pulse is switched out of the resonator. It is also necessary to Q switch the cavity simultaneously with the injection of the pulse, so that the gain is not lost by amplified spontaneous emission before pulse amplification.

Current Nd:glass amplifier chains used in conjunction with a Ti:sapphire pre-amplifier are an excellent system for producing terawatt femtosecond pulses. The Ti:sapphire regenerative amplifier presents several advantages. Firstly, the gain bandwidth is broad enough to support high amplification factors for pulses with bandwidths corresponding to less than one hundred femtosecond in duration without any spectral narrowing. It has recently been reported that 250 fs pulses at 1.053 μm had been amplified to 100 μJ with a Ti:sapphire regenerative amplifier longitudinally pumped by 80 mJ of the second harmonic of a multimode Q-switched YAG laser[4]. Secondly, it can be tuned to match perfectly the wavelength of any oscillator around 1 μm. Thirdly, the high repetition rate operation is possible which will be indispensable for the alignment of the compression gratings and diagnostics. Finally, this scheme exhibits a good spatial mode determined by the mode of the regenerative amplifier cavity, and a stability and reproducibility resulting from a stable laser pump and an all-solid-state design. These make the Ti:sapphire regenerative amplifier an ideal front end for high power Nd:glass systems.

Although the operating wavelength at 1.053 μm of this regenerative amplifier is far from the peak of the gain profile of a Ti:sapphire crystal, we have shown that Ti:sapphire is suitable for amplification of ultrashort pulses at this wavelength up to millijoule level. If the pump energy density is increased, not only does the extraction efficiency increase, but the system is less sensitive to loss at the laser wavelength. Due to the reduced gain coefficient at around 1 μm, a relatively high pumping energy (~ 120 mJ) is required. To prevent optical damage to the Ti:sapphier crystal, it is pumped from both ends.

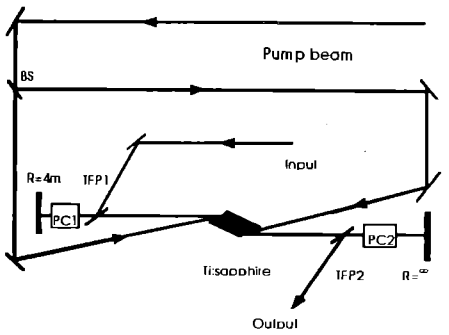

Figure 1 The configuration of the Ti:sapphire regenerative amplifier operating at 1.053 μm wavelength. BS, 50:50 beam splitter at 532 nm; PC, Pockels cell; TFP, thin film polariser.

The configuration of the regenerative amplifier used in this experiment is illustrated in Fig. 1. The resonator consists of one concave mirror (radius 4.0 m) and one flat mirror, spaced at a distance of 1.8 m to provide a Gaussian mode diameter of 2.0 mm on the flat mirror and 2.3 mm on the concave mirror. This choice of cavity decreases the misalignment sensitivity of the resonator, and produces large beam sizes on critical elements, thereby minimising optical damage. These two end mirrors are coated dielectrically for high reflection centred at 1.053 μm. Two KD*P Pockels cells, PC1 and PC2, and two broadband thin film polarisers, TFP1 and TFP2, are used to switch a pulse into and out of the resonator. A 2.0 cm long Ti:sapphire rod doped at 0.1 Ti_2O_3 wt% with an absorption coefficient of 1.5 cm^{-1} at 532 nm and with both ends cut at Brewster's angle is placed near the centre of the cavity.

The pump source is a Q-switched, frequency doubled Nd:YAG laser (Spectron Laser Systems Ltd.) which produces 150 mJ, 7 ns pulse at 532 ns. The polarisation of the pump beam is horizontal, along the optic axis of the crystal to avoid the reflection on the Brewster angled surfaces of the Ti:sapphire rod. The output from the pump laser is directed through a tunable attenuator to control the amount of energy

delivered to the regenerative amplifier. The pump beam with a Gaussian radial profile is incident at a 1.6 degree angle from the cavity axis on both ends of the rod at a repetition rate of 10 Hz. The internal angle between the pump and the lasing axis is approximately half this value, due to the high refractive index of sapphire. This provides a substantially co-linear end-pumping geometry. The pump beam spot size is estimated to be 2.4 mm in diameter on the rod end which is slightly larger than the cavity TEM_{00} mode spot size so that the cavity is relativelyinsensitive to the pump beam steering variation. This pump results a smooth, Gaussian-like gain region serving as a soft aperture for the cavity to achieve the reliable TEM_{00} operation. No damage on the crystal was observed for a full pump energy up to 75 mJ at 532 nm on each side although typical pump energy for the regenerative amplifier is 50 - 60 mJ. The pump fluence is estimated to be 2 J/cm^2 on the crystal. The amplifier lasing wavelength is tuned to 1.053 μm by rotating the two polarisers.

The regenerative amplifier may be operated as a pulsed Ti:sapphire oscillator, without the rejection of input optical pulses. The relaxation oscillation builds up from spontaneous emission in this configuration. The natural build-up time between the arrival of the pump pulse to the maximum developed intensity is 1.5 μs when the cavity is aligned optimally and other losses are at a minimum. We have tested this regenerative amplifier with chirped pulses from a diode pumped additive pulse mode locked Nd:YLF oscillator producing 2 ps pulses at 1.053 μm[5]. After temporal stretching with a 1740 grooves/mm grating pair to 200 ps, the s-polarised pulses are sent to the Ti:sapphire regenerative amplifier through a Faraday isolator to prevent any of the regenerative output being fed back into the Nd:YLF oscillator.

A significant consideration in the design of a preamplifier is the shot-to-shot variation in the pulse output energy due to fluctuations in the output energy of the pumping Nd:YAG. This is particularly severe if the regenerative amplifier is operating in the small gain regime. However, if the amplifier is allowed to saturate, the variation in output pulse energy is very much smaller. A numerical model of the system shows that there is an optimum output switching time for the regenerative amplifier when the output energy is essentially independent of the pumping energy. Fig. 2 shows the envelope of a pulse train in the amplifier for different pumping pulse energies.

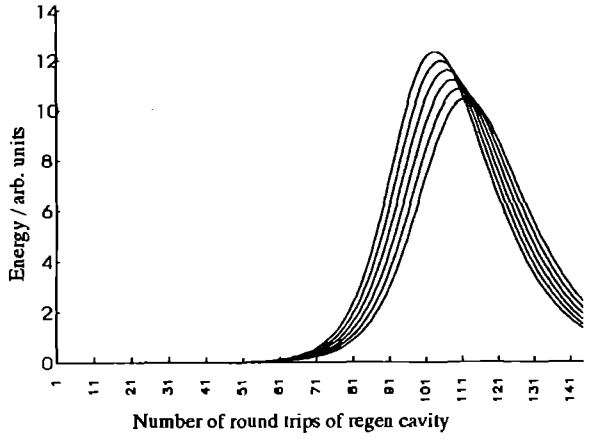

Figure 2 Calculated shot-to-shot variations as a function of different pumping pulse energies.

At a time after the peak of the intracavity intensity, the envelopes cross and this is the preferred time for switching the pulse from the resonator. The corresponding results obtained experimentally are shown in Fig. 3 and agree well with the model.

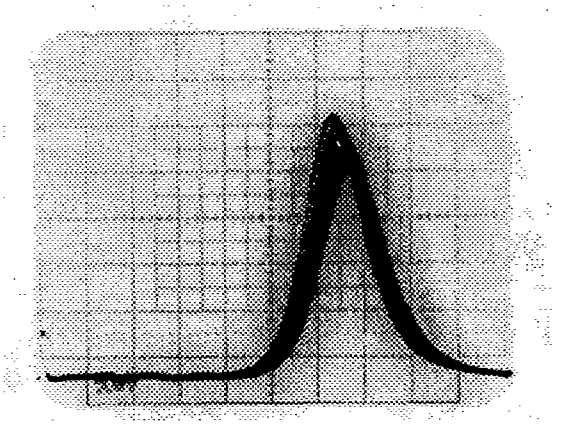

Figure 3 Measured shot-to-shot variations as a function of different pumping pulse energies.

The arrivals of the pump laser pulse and optical switch trigger signals in the regenerative amplifier are synchronised to an accuracy of ±1 ns relative to the input pulse train from the oscillator which is detected with a fast photodiode. The Pockels cells are driven by avalanche transistor circuit delivering voltages of $v_{\lambda/4}(-3.2\ kv)$ to each cell to provide complete switching on a double pass. This is configured in order to simplify the switching electronics required for the Pockels cells and to reduces the jitters. When the green pump pulse reaches the Ti:sapphire rod, the switch-in Pockels cell (PC1) is switched on rapidly to select a single pulse in a 130 MHz train. By switching it off in a time which is less than the 12 ns oscillation period of the regenerative cavity, the pulse is trapped inside the cavity. The seeded pulse is overlapped in time with the Q-switch pump to minimise amplified spontaneous emission. The regenerative amplifier boosts the seeded pulse energy to the gain saturation limit in a number of passes determined by the small signal gain and by the input pulse energy. The delay between the switch in and switch out can be changed so that the amplified pulse is picked out near the peak of its amplification.

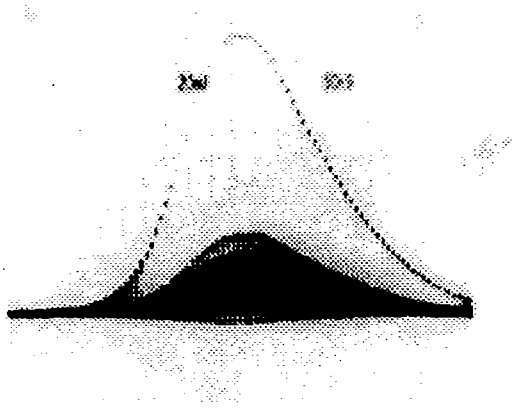

Figure 4 Build-up of the regenerative amplifier when seeded with a 1 nJ pulse.

For this system, 100 to 110 round trips are necessary for the gain saturation. At this point, a $\lambda/4$ voltage is abruptly applied to the switch-out Pockels cell (PC2). The amplified pulse is then rejected by the switch-out thin film polariser (TFP2) after double passing through PC2. Fig. 4 shows the build-up of the regenerative amplifier when seeded.

When the maximum pulse energy is obtained by switching out at the peak of the amplified intensity, this gives rise to significant fluctuations in output energy. By switching after the peak, i.e., after the system has saturated, these fluctuations are significantly reduced. The output energy fluctuations are examined by switching the pulse out of the resonator after different numbers of round trips. When switched out at the peak intensity, the output energy of the regenerative amplifier reaches 5.0 mJ in single-pulse mode, corresponding to an extraction efficiency of approximately 5 % at 1.053 μm wavelength. The minimum shot to shot variation are found to be ± 5.0 % from peak to peak when switched out at 118 round trips while the output energy is 4.3 mJ.

In summary we have demonstrated a stable and reliable Ti:sapphire regenerative amplifier operating at 1.053 μm wavelength at 10 Hz repetition rate with net gains up to 10^6. This amplifier is designed for use in terawatt subpicosecond lasers based on chirped pulse amplification. With such a system one should be able to amplify 100 fs pulses to the mJ level at 1.053 μm with an excellent stability.

REFERENCES

[1] A.R. Bell et al., Phys. Rev. E, 48, 2087 (1993)

[2] D. Strickland, and G. Mourou, Opt. Comm., 56, 219 (1985)

[3] W.H. Lowdermilk, and J.E. Murray, J. Appl. Phys., 51, 3548 (1980)

[4] C. Rouyer, E. Mazataud, I. Allais, A. Pierre, S. Seznec, C. Sauteret, and A. Migus, Opt. Lett., 18, 214 (1993)

[5] I.P. Mercer et al., Opt. Comm., 107, 77 (1994)

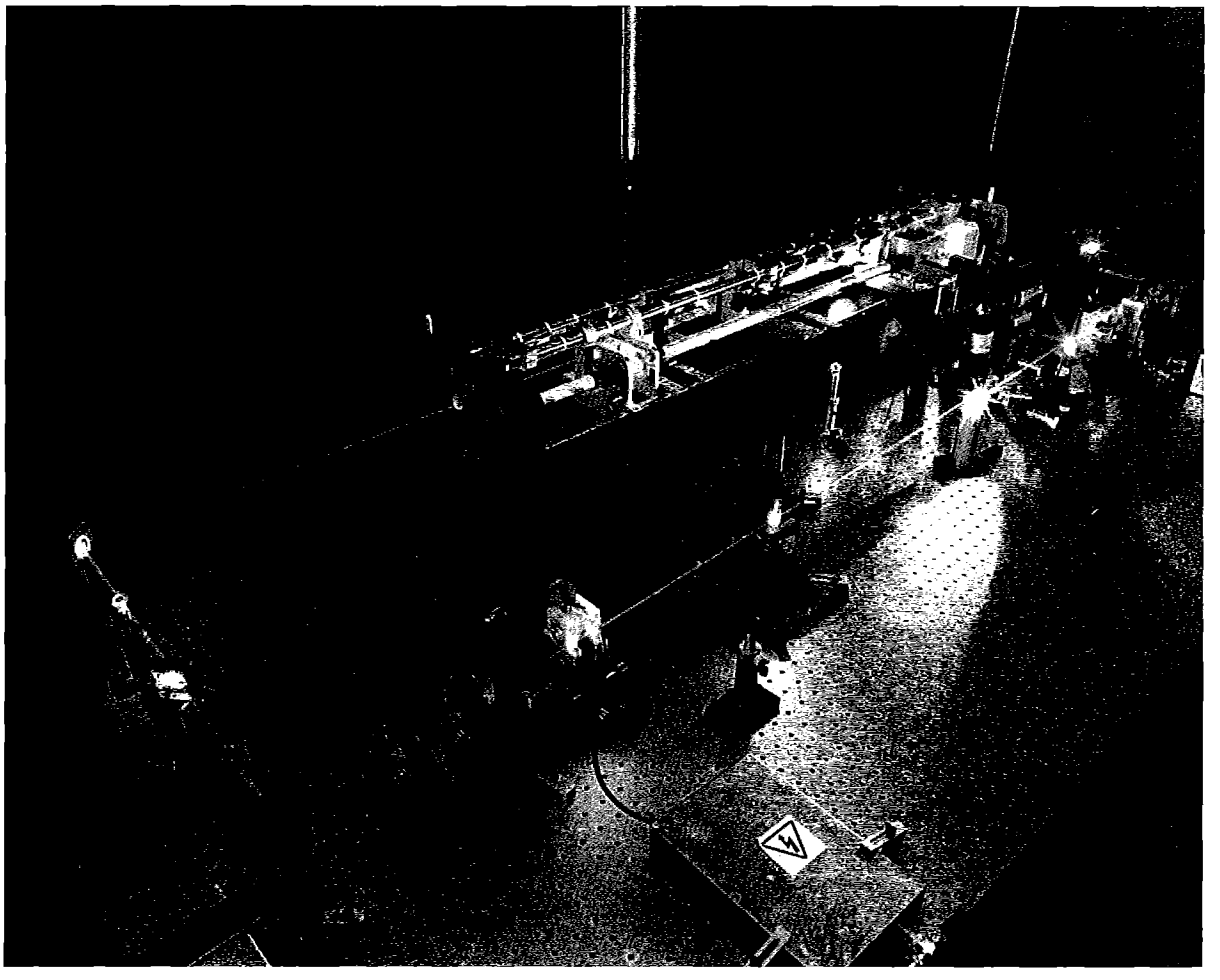

Ti:Sapphire regenerative amplifier showing the double-sided pump configuration

OPTIMISATION OF COMPRESSION GRATING ALIGNMENT FOR VULCAN CPA OPERATIONS

D Neely, C N Danson, C B Edwards, D Pepler, D Rodkiss, I N Ross, P Taday and F Walsh.

Rutherford Appleton Laboratory, Chilton, Didcot, Oxon, UK

This paper describes techniques to optimise the alignment of the CPA compression gratings on the VULCAN glass laser system allowing focused intensities of $>10^{19}$ W cm^{-2} to be achieved on target. The compression gratings are of large aperture, separated by 2.8 m and one of them is housed in a vacuum vessel where access is difficult. All of these factors conspire to make it difficult to align the gratings to the required parallelism. An alignment method was devised where two CW laser beams were used to produce accurate grating parallelism to the ± 0.5 mrad level. Also discussed are alignment errors that can be introduced by spectral differences between the CW alignment beam and full power shots, which act to reduce the throughput of the recompressor system.

GRATING ALIGNMENT

Alignment of the gratings essentially consisted of two operations. In the first, the grating surfaces and the grooves were constrained to lie in the vertical plane to an accuracy of better than 1 mrad. This was attained by monitoring the zero and first order reflections of an unexpanded 632 nm HeNe beam from each grating. The gratings were adjusted until the input beam, the reflected and the diffracted beams were all horizontally coplanar.

A second alignment technique was then used to set the grating surfaces parallel in the horizontal plane. It used two lasers of different wavelengths injected colinearly into the compression gratings. If the gratings are not parallel then the two beams will exit from the grating pair with some residual dispersion. Therefore the gratings are aligned when the two wavelengths emerge colinearly. A schematic of the alignment technique is shown in figure 1. The two wavelengths used were the 1053.0 nm CW Nd:YLF Vulcan alignment laser and a 1064 nm laser diode pumped Nd:YAG. To ensure that the 1064 nm beam traversed the double grating pair it was necessary to inject this beam close to one edge of the first grating, (see fig 1) since it's exit angle was much larger (2.4 degrees) than the shorter wavelength Nd:YLF beam. A retro- reflecting mirror was placed after the second grating to double pass the beams through the system. The grating parallelism was then optimised by adjusting the gratings until the double passed output alignment beams were collinear.

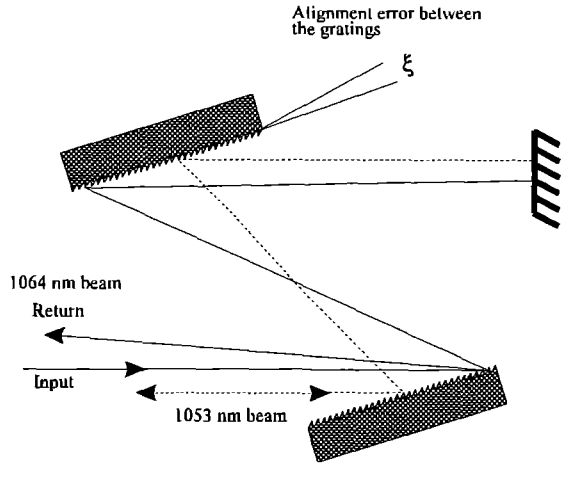

Figure 1 Schematic showing the set-up used to accurately align the gratings in the dispersion plane.

If two collinear laser beams of wavelengths λ and $\lambda + \Delta\lambda$ are incident onto the first grating of a recompression pair at an input angle θ_i then, after passing through the recompression grating pair the output pointing difference ψ between the beams can be expressed as

$$\psi = \xi \frac{\cos\theta_o - \cos\theta_{o,\lambda+\Delta\lambda}}{\cos\theta_i} \qquad (1)$$

$$\psi \approx \xi \Delta\lambda np \frac{\tan\theta_o}{\cos\theta_i} \qquad (2)$$

where θ_o is the output angle, n the diffraction order, p the number of grooves per m and ξ is the misalignment error (difference from parallel) between the grating pair. For VULCAN, λ = 1053.0 nm, $\Delta\lambda$ = 11 nm, θ_i = 73.0°, and the recompression gratings have 1.74 x 10^6 lines/m which gives $\psi \approx 0.124\xi$. Retro-reflecting the beams through the grating system effectively doubles the angular separation between the two beams. The maximum wavelength that can be propagated through the gratings when they are aligned centrally for 1053 nm operation is 1065.8 nm. The 1064 nm laser is ideal since it operates near to this limit and therefore gives close to the maximum possible alignment sensitivity in the present grating configuration.

For the VULCAN glass laser the focal spot size is typically m times the diffraction limit in the infrared where m lies in the range $1<m<4$. The maximum recompression grating misalignment error which can be tolerated without significantly effecting the focused beam intensity is designated ξ_m. This limit is reached when the spot size in the focal plane due to residual spectral dispersion caused by grating misalignment is equal to half the diffraction limit. For a grating of length L which is completely filled we obtain the condition

$$\xi_m \approx \frac{m\lambda}{2\Delta\lambda_B npL\tan\theta_o} \qquad (3)$$

For a 3.5x diffraction limited beam incident onto gratings of length L = 300 mm and a pulse bandwidth of $\Delta\lambda_B$ = 1.6 nm (i.e. a high energy shot), this gives the maximum tolerable recompression grating misalignment error of $\xi_m \approx 1$ mrad.

RESULTS

The focal spot size was measured both before and after grating alignment using medium energy ≈ 0.2 J, 2 nm bandwidth CPA pulses on an equivalent plane monitor. The results shown in figure 2 are scaled to represent the horizontal intensity distribution that would be achieved at the target plane using a 0.45 m focal length focusing optic. A theoretical fit is also shown on figure 2. The fit was generated assuming a 3.5x diffraction limited minimum spot size and a residual dispersion component as described by equation 2. The estimated alignment accuracy of the dual wavelength system used was ± 0.5 mrad which is a factor of two better than required. The accuracy of the dual wavelength system was limited by the poor collimation of the 1064 nm diode pumped injection laser. Once aligned, full energy shots verified the improved performance of the full system. Figure 3a shows data from a full energy shot from a previous experiment[1] using a 2 ps 0.5 nm CPA pulse, which showed considerable elongation in the dispersion plane. Figure 3b shows a 1.7 nm bandwidth full energy shot taken after alignment. The horizontal focal spot size is now only 3.5x the diffraction limit and proved ideal for use in experimental studies.

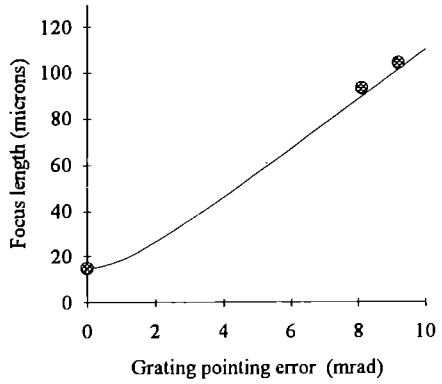

Figure 2. Graph showing the measured and calculated horizontal focal spot size as a function of misalignment error between the recompression gratings.

5 m. The second grating was rotated and the displacement d of the output beam set such that

$$d = \frac{fnp\Delta\lambda}{\cos\theta_o} \qquad (5)$$

The first grating of the pair was then rotated until the spot on the monitor moved back to its starting position. This operation maintains grating parallelism and beam pointing whilst ensuring maximum geometrical throughput for full energy shots. Since this operation changes the input and output angles of the grating pair it must be carried out prior to the optimisation of the grating separation for minimum recompressed pulse duration.

CONCLUSION

A series of simply implemented alignment procedures for the optimisation of a recompression grating pair have been demonstrated. These procedures overcame the problems of limited access to the gratings and ensured optimum possible performance of the system.

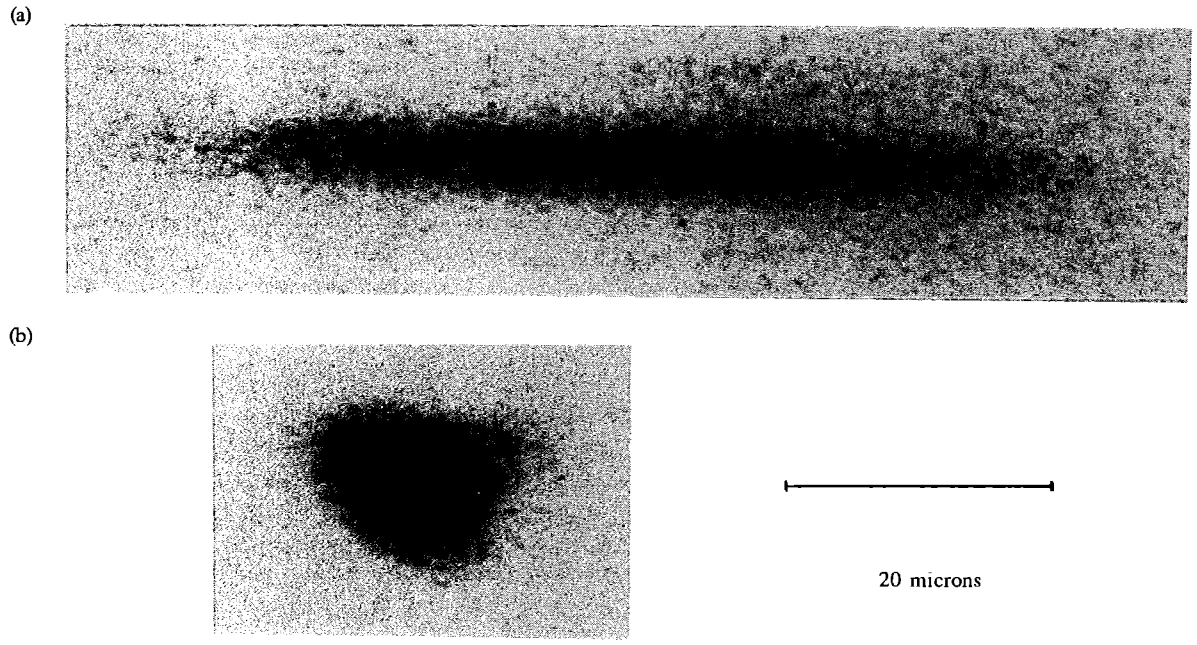

Figure 3. Comparison of the focal spot quality before and after grating optimisation

COMPENSATION FOR SPECTRAL SHIFT BETWEEN THE ALIGNMENT BEAM AND FULL SHOTS.

Alignment of the grating pair was initially carried out using a CW beam at λ = 1053 nm. Since the amplified CPA beam is centred at a different wavelength of $\lambda+\Delta\lambda$ beam walk off will occur on the second grating reducing the throughput of the pair. The beam will be displaced by a distance k on the second grating where

$$k = s\cos\theta_o\,[\tan\theta_{o,\Delta\lambda} - \tan\theta_o] \qquad (4)$$

and s is the separation between the gratings. For the present case where s = 2.8 m this gives k (mm) $\approx 21\Delta\lambda$ (nm). Since the difference between the CW alignment beam and a full power shot is 1.7 nm this corresponds to a reduction in the throughput of the system of $\approx$ 10%. To compensate for this a simple alignment technique was used which overcame the problem of limited access to the second grating in the recompression system. A far field monitor of the output beam from the diffraction grating pair was set up using a lens of focal length f =

This has allowed the Vulcan glass laser to deliver a 620 fs chirped pulse amplified beam of 3.5 times the diffraction limit at intensities on target of > 10^{19} W cm^{-2} for experimental use.

References

1 C. N. Danson, L. J. Barzanti, Z. Chang, A. E. Damerell, C. B. Edwards, S. Hancock, M. H. R. Hutchinson, M. H. Key, S. Luan, R. R. Mahadeo, I. P. Mercer, P. Norreys, D. A. Pepler, D. A. Rodkiss, I. N. Ross, M. A. Smith, R. A. Smith, P. Taday, W. T. Toner, K. W. M. Wigmore, T. B. Winstone, R. W. W. Wyatt and F. Zhou.
High contrast multi-terawatt pulse generation using chirped pulse amplification on the Vulcan laser facility.
Opt. Comm. 103 p392-397 (1993)

AN INVESTIGATION OF SPECTRAL EFFECTS IN A SHORT PULSE KrF LASER

I N Ross, C J Hooker, J M D Lister, P Matousek, ^K Osvay, M J Shaw, +P Simon,
*S Szatmari,

Rutherford Appleton Laboratory, Chilton, Didcot, OXON, OX11 0QX, England
*Max Planck Institute, Gottingen
^JATE University, Hungary
+Laser Laboratorium, Göttingen

INTRODUCTION

There is an increasing demand for laser systems to be designed for maximum power and minimum pulse duration. The technique of chirped pulse amplification (CPA) has been widely applied to laser systems[1)-3)] to provide access to the stored energy without the intensity limitations imposed by nonlinear processes in the system. Thus high energy pulses of duration determined only by the gain bandwidth are possible. KrF is an interesting candidate for CPA because its large gain bandwidth (~ 400 cm^{-1}) suggest that pulse durations well below 100 fsec are possible. The first implementation of a full CPA and recompression scheme on KrF has been described[4)]. This yielded TW pulses with pulse duration limited to 300 fs, a factor of two longer than was anticipated. This restriction was shown to result from a stronger than expected spectral narrowing in the KrF amplifiers. We report here further investigations which have been carried out to investigate this effect to try to understand its cause and hence to reduce its effectiveness or eliminate it entirely.

Figure 1 demonstrates the spectral anomaly in KrF[5)]. The fluorescence curve shows a smooth gaussian distribution with a FWHM of 400 cm^{-1} and would be expected to represent the gain distribution of the medium. The amplified fluorescence or gain narrowed fluorescence curve shows an anomalous dip to the long wavelength side of the peak, which has the effect of reducing the FWHM of the spectrum. At the high gain present in most high power lasers the resulting output spectral width is ~ 60 cm^{-1} with an approximately gaussian distribution, and this limits the pulse duration to at best 250 fs.

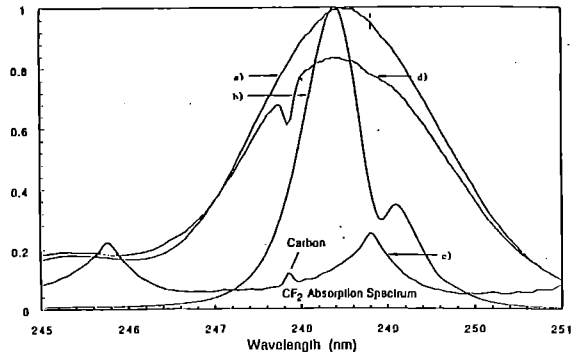

Figure 1 Spectral distribution curves for KrF.
a) Fluorescence curve, b) Gain narrowed fluorescence curve, c) Absorption spectrum for CF_2, d) Fluorescence curve in presence of CF_4

Figure 1 also demonstrates one explanation for the spectral anomaly. This is an absorption feature for the radical CF_2 which is generally present due to the breakdown of an impurity CF_4 in the pumped region and which has a spectrum well matched to the dip in the gain curve. This is the only explanation that has been proposed but the literature evidence is not conclusive. The strength of the feature appears to have varied greatly in reported experiments but is not consistent with it being due either to contamination (CF_4) or to an intrinsic effect in KrF (excited state absorption perhaps).

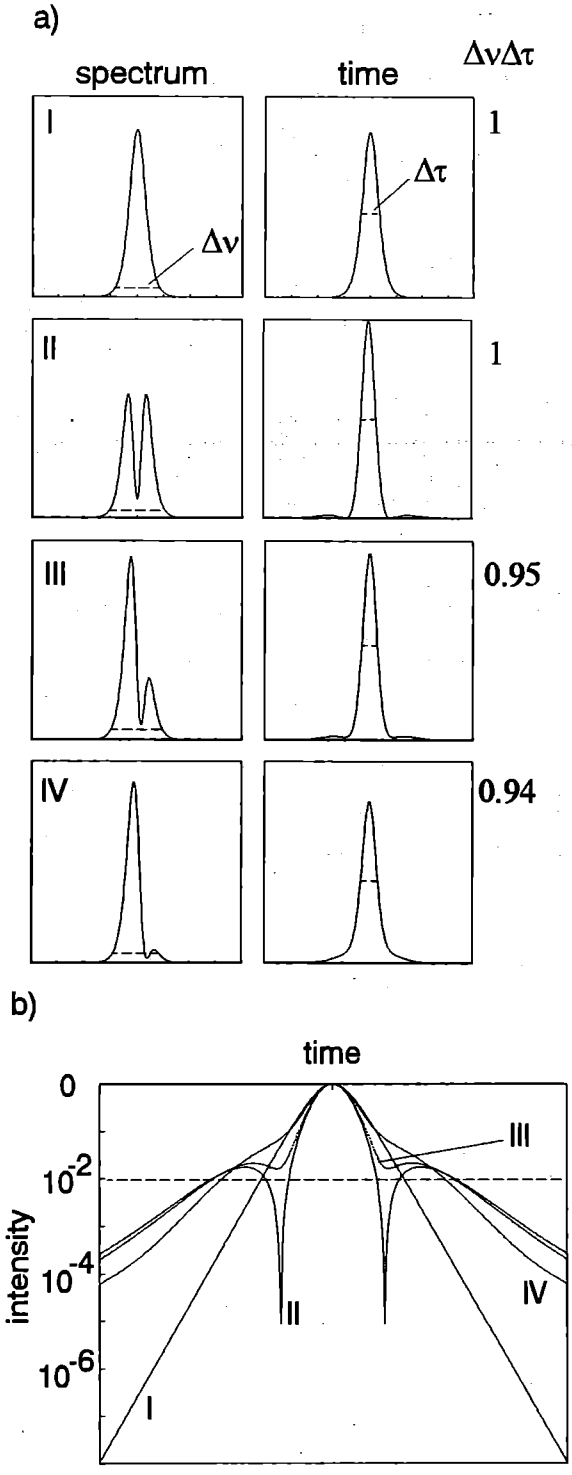

Figure 2 a) Spectral profiles and their corresponding pulse temporal profiles calculated by Fourier transformation.
b) Calculated temporal profile curves of figure 2a) showing the changes in pulse contrast.

THEORETICAL CONSIDERATIONS

It is instructive to look a little more closely than is often the case at the relationship between spectral and temporal distribution in the 'transform limit' as this will provide clues as to what is required of the spectrum in order to achieve the pulse durations required. This will indicate what is more important and what is less important in the spectral distribution as regards the pulse parameters such as FWHM, pulse contrast ratio, and pulse rise time.

Fourier transforms have been calculated for a wide variety of spectral and temporal distributions and we can draw a number of conclusions as follows:

a) For most distributions that are likely to be met in practice, the product of spectral and temporal width is approximately independent of pulse shape if these widths are measured at 6% level (in contrast to the normal 50% level). An extension of this is the product of autocorrelator and spectral width which is also approximately independent of pulse shape for transform limited pulses if measured at ~ 11% level, and is consequently a good measure of how close a pulse is to the transform limit.

b) Since the pulse duration at the 50% level is of more general interest, it is useful to assess what feature of the spectral distribution is most important in its determination. The conclusion is that the wings of the spectrum, rather than the central distribution, most strongly influence the temporal FWHM. This is illustrated in figure 2 where it is demonstrated that for an overall $(sech)^2$ profile the pulse duration at FWHM is only determined by the spectral width at the 4% level and not by the distribution within that width. In particular, for a spectral anomaly as observed for KrF, short pulses are achievable so long as the subsidiary spectral peak does not fall below the 4% level. In a real laser system this implies that either the gain is kept below a critical level or that, for high gain systems, the effect of the anomaly must be reduced (but not to zero).

c) Figure 2b) demonstrates that the wings of the pulse are much more sensitive to the spectral distribution than is the pulse duration at FWHM. Generally, any disruption of the spectral profile from its best form ($(sech)^2$ in the examples shown) will lead to increased energy in the wings of the pulse beyond the few % level. The contrast ratio of the pulse is decreased and this may have serious consequences in some experimental applications.

d) The application of spectral filtering[6] can reduce the pulse duration. An example of amplitude filtering to increase the effective spectral width is shown in figure 3. In this case, at the expense of a factor 10 in overall energy, the resultant pulse duration is decreased by 30%. This is close to the practical limit of what is achievable by this technique since the pulse duration is determined by the width in the wings of the spectrum and this is very insensitive to the attenuation at the peak of the spectrum.

Alternative more effective spectral filtering would be to amplify the wings of the spectrum or to redistribute the spectral distribution from the centre into the wings by, for example, self-phase-modulation.

e) Spectral filtering which includes phase control can control the intensity distribution to give an asymmetric pulse with, for example, a faster rising leading edge. This is, for a given symmetric input pulse, usually accompanied by an increase in the pulse width at FWHM. Figure 4 shows an example in which the 10% to 90% risetime is reduced by 30% by the imposition of a phase shift across the spectrum of $-\pi/2$ to $+\pi/2$ with a 'tan' profile.

SPECTRAL MEASUREMENTS

An arrangement was set up for the measurement of KrF spectral gain curves under a variety of circumstances in order to acquire data on the spectral anomaly which could supply clues as to its origin and which could lead to a reduction of its effect. Figure 5 shows the arrangement schematically. A short pulse distributed feedback dye laser generated pulses of ≈ 500 fs at 497 nm[7] which were amplified and focused into a short length of optical fibre. Self phase modulation and group velocity dispersion in the fibre led to a strongly chirped broad bandwidth (~ 400 cm^{-1}) and stretched (a few picoseconds) pulse. A grating pair pulse compressor and BBO crystal enabled seed pulses at 249 nm to be generated with varying

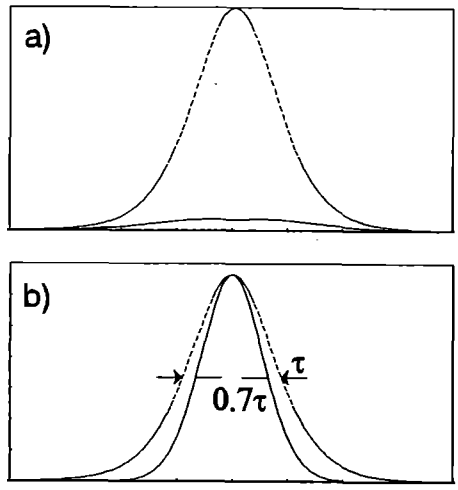

Figure 3 Calculated reduction in pulse duration resulting from spectral filtering using purely attenuation to increase the effective spectral width.

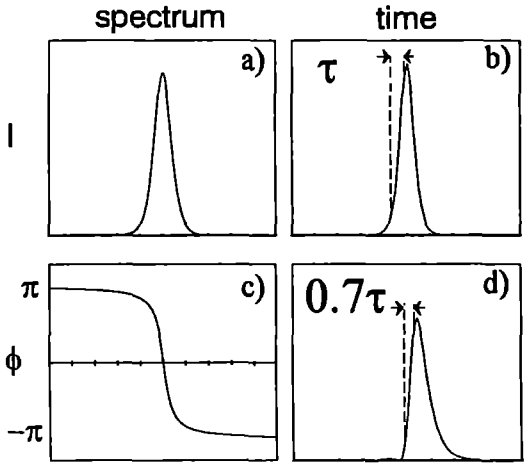

Figure 4 Calculated reduction in pulse risetime resulting from spectral filtering using a purely phase filter

amounts of chirp. A typical seed pulse spectrum is shown in figure 6. This pulse was amplified in a discharge KrF amplifier and its output spectrum measured. This output spectrum, normally very much narrower than the seed pulse was a good measure of the gain narrowed spectral gain distribution of the amplifier. Measurements were also made on the amplified spontaneous emission (ASE) spectrum which, although long pulse and time averaging, had the advantage of better consistency of spectrum. Direct comparisons of ASE and amplified pulse spectra demonstrated that they were, as far as was measurable, the same. In addition pulse spectra recorded for amplification at different times within the amplifier gain window showed very little change other than variations in gain. Consequently it was concluded that ASE spectra can be taken to show the spectral effects of amplified short pulses where there is no gain saturation and negligible non-linear effects.

Spectra were recorded under a wide variety of parameter values. The principal parameters which were varied were:

a) Gain. This was changed by changing the
   - (i) off-axis angle in the amplifier
   - (ii) number of amplification passes
   - (iii) charging voltage
   - (iv) gas mixture
   - (v) timing
   - (vi) age of the gas mixture.

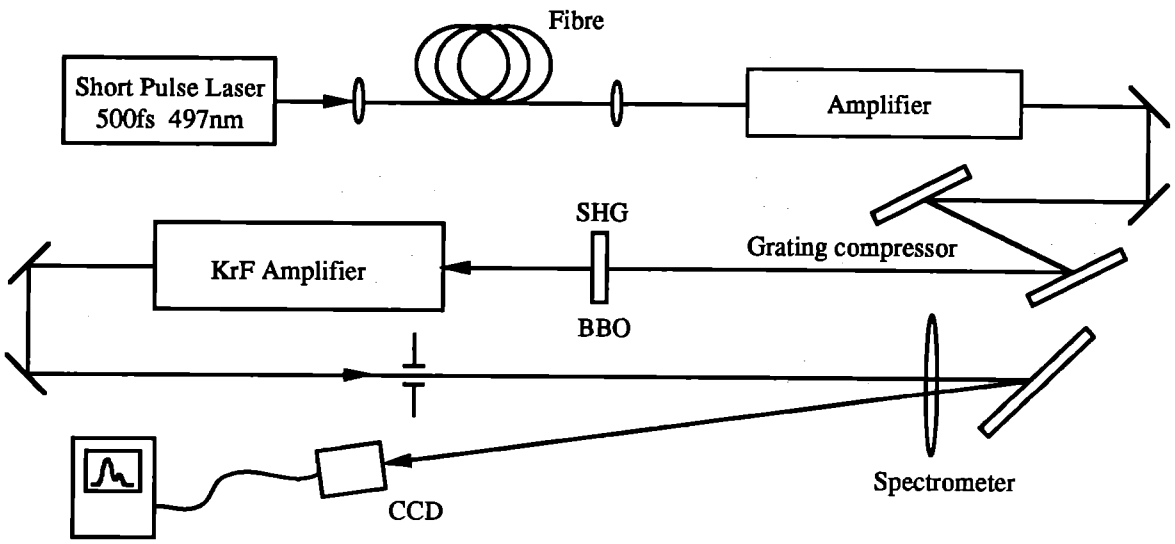

Figure 5 Schematic of experimental arrangement to measurement broadband spectral changes occurring in a KrF amplifier

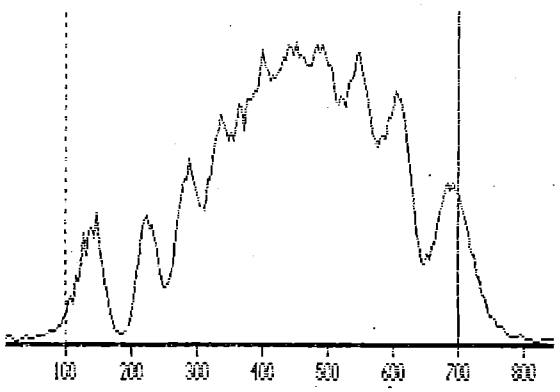

Figure 6 Seed spectrum at 249 nm resulting from frequency doubling of a chirped and stretched short pulse from a dye laser

b) Gas contamination. This was changed by changing the
- (i) fill pressure of the constituent gases to change the quantity of impurities coming in from the gas supplies
- (ii) shot age of the gas mixture
- (iii) pump out and refilling procedure
- (iv) vacuum pump with an oil free pump
- (v) purity at the fluorine gas by placing a liquid nitrogen trap in the fluorine inlet line
- (vi) temperature of the laser chamber.

c) Amplifier gain saturation. This was adjusted by changing the input seed pulse energy and the amplifier gain.

A selection of both ASE and amplified pulse spectra are shown in figure 7. One primary objective was to try to eliminate from the analysis the spectral changes due to gain narrowing, and in some way to normalise with respect to gain the anomalous dip in the curve. This was important because i) measurements were made over a variation of gain from a few to a few thousand, ii) a crucial question is to determine whether the 'loss' in the spectral dip is or is not proportional to the gain because, if it is, then the anomaly is more likely to be an intrinsic feature of KrF. The loss to gain ratio was determined as follows:

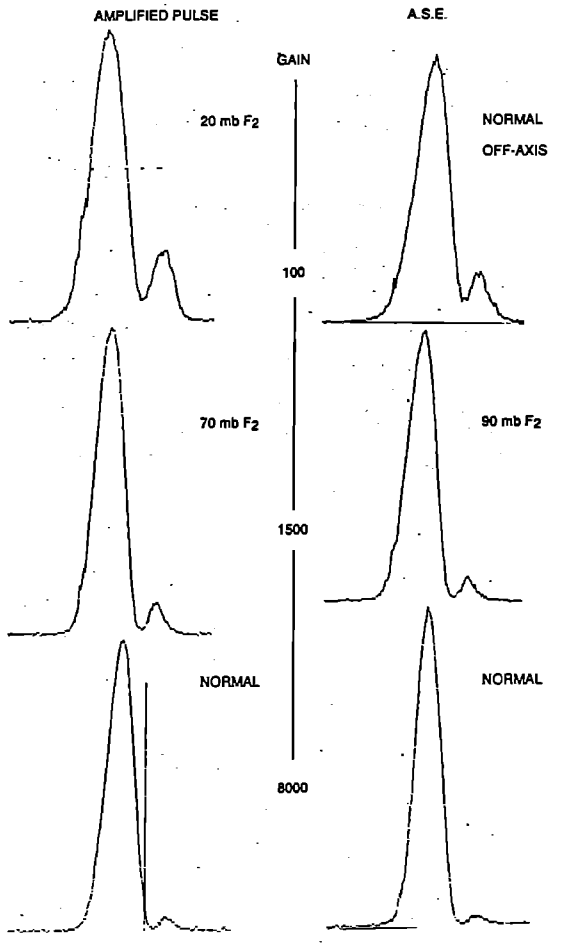

Figure 7 A selection of spectra for amplified short pulses and amplified spontaneous emission, demonstrating the dependence of the anomalous dip on the amplifier gain

Oil based pump					Oil-free pump			
	Short pulse	ASE			Short pulse	ASE		
		Standard	F_2 weak	Kr weak		Standard	F_2 weak	N_2 trap
No	7	21	11	7	31	14	9	9
Mean	0.48	0.48	0.47	0.50	0.46	0.43	0.45	0.42
σ	0.03	0.04	0.05	0.04	0.04	0.03	0.06	0.03
	Overall mean - 0.48				Overall mean - 0.45			

Table 1 Average values of α / g_0 for the spectral anomaly in a KrF discharge amplifier

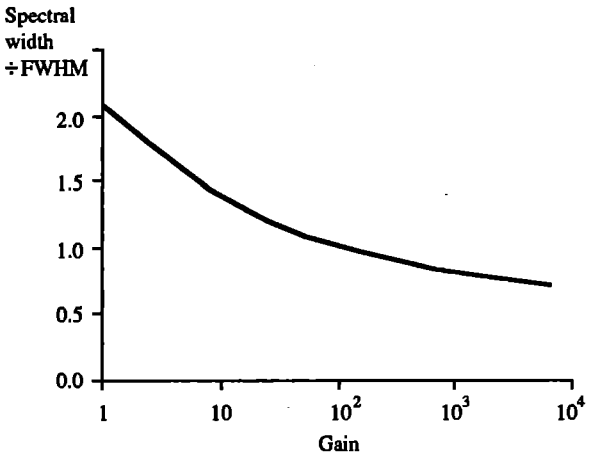

Figure 8 Calculated dependence on amplifier gain of the full width at 5% of the peak of the amplified spontaneous emission spectrum

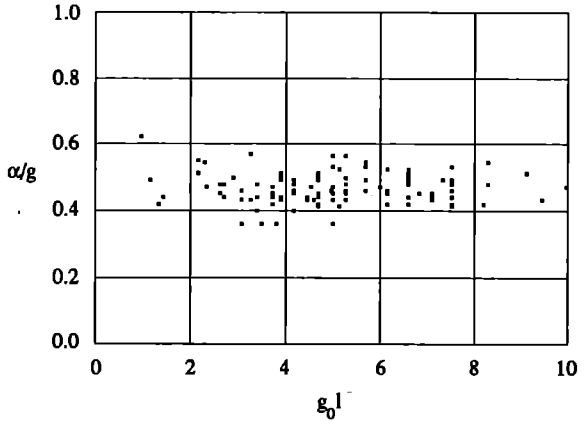

Figure 9 The variation with gain of the anomalous loss to gain ratio as calculated from a large number of experimental spectra recorded for both amplified pulses and ASE, and taken under a variety of amplifier parameter values. Amplifier gain is $\exp(g_0)$

Taking measurements from a spectrum, if the heights of the two main peaks and the dip are h_1, h_2 and h_3 respectively, then the loss exponent (α) was taken to be approximated by $\ell n\left[(h_1 + h_2)/2h_3\right]$. The gain was calculated from the spectral width at the 5% points, this width being assumed to be unaffected by the anomaly. Assuming a Gaussian gain spectral distribution with FWHM width of 2.5 nm, the shape of the gain narrowed distribution is given by:

$$S(\Delta\lambda) = F \exp g_o \left[1 - \exp - \left(\frac{\Delta\lambda}{\Delta}\right)^2\right]$$

where

$\Delta = e^{-1}$ half width

g_o = peak gain exponent

F = input spectral shape $\left[= \exp - \left(\frac{\Delta\lambda}{\Delta}\right)^2 \right.$ for ASE]

Figure 8 shows how the calculated spectral width at the 5% level depends on the gain. Measurements of this spectral width can consequently be used to estimate the gain exponent (g_0).

Figure 9 plots the loss to gain ratio α / g_o against the gain g_o for a large number of spectral curves taken with a large range of parameter values under conditions of small signal gain. The principal conclusion is that the loss to gain ratio is independent of gain and is largely unaffected by any changes made to the amplifier. Although the spread of values is quite large so also is the number of points and we may extract a little more from the data by looking at mean and standard deviation values. These are presented in Table 1. These values suggest one further result, that the 'loss' associated with the anomaly was somewhat improved after the change to the oil free pump.

DISCUSSION

Preliminary analysis of the KrF spectral anomaly data suggests that there is a very close link between the 'loss' dip and the gain and that in consequence it would be expected to be an intrinsic property of the KrF system. However, there was some evidence to support the 'contamination' theory since some improvement was observed after the change to an oil free pump, and there is of course no appearance of an anomalous dip on any purely fluorescence curves. More detailed analysis of the data is expected to shed more light on the source of the anomaly, as also are similar measurements on different KrF modules having different levels of contamination.

REFERENCES

1. D Strickland and G Mourou, Opt Comm, 56 219, (1985).
2. C Royer et al, Opt Lett, 18 214, (1993).
3. C N Danson et al, Opt Comm, 103, 392 (1993).
4. I N Ross et al, Opt Comm, in press.
5. N A Kumit et al, 3rd Workshop on KrF Laser Technology, B01, (1992).
6. A M Weiner, J P Heritage, E M Kirschner, JOSA (B), 5, 1563 (1988).
7. S Szatmari, F P Schäfer, Opt Comm, 68, 196, (1988).

A GENERAL ANALYSIS AND ALIGNMENT TOLERANCES OF A GRATING PAIR PULSE COMPRESSOR

K Osvay* and I N Ross

Rutherford Appleton Laboratory
* On sabbatical from JATE University, Szeged, Hungary

INTRODUCTION

Since Treacy demonstrated short pulse compression with a pair of gratings[1] the technique has been used in various arrangements for pulse shaping[2]. In these cases the authors assumed their laser/compressor system to be aligned well enough so that they could neglect any perturbation due to compressor alignment. This assumption might be satisfactory for some lasers but should be revised for high power-high energy systems based on chirped pulse amplification (CPA) techniques. To our knowledge there has been little attempt made to investigate practical limits in real situations (as regards for example tolerance of grating alignment) apart from the case of finite beam size by Martinez[3]. In the report which follows exact analytical formulae are presented for the residual angular dispersion due to a grating compressor with gratings having arbitrary orientation. From these formulas a numerical example is given relating to the alignment of the compressor in SPRITE CPA.

DIFFRACTION ANGLES AND ANGULAR DISPERSION

The position of a grating plane with respect to a light ray falling on it is fully determined by two angles α and β, where α is the inclination angle of the input ray to the Y-Z plane and b is the angle between the projected ray on the Y-Z plane and the Z axis (Fig.1). In what follows, however, we need to give the position of the incident beam by other pairs of angles as well, like γ,δ and τ,σ (Fig.1). The relationships between these pairs of angles are

$$T(\alpha,\beta)=(\gamma,\delta),\quad T(\alpha,\pi/2-\beta)=(\tau,\sigma),\qquad T(\delta,\gamma)=(\pi/2-\tau,\sigma) \tag{1}$$

and the $T(\mu_1,\nu_1)=(\mu_2,\nu_2)$ transformation is defined by

$$\mu_2=\operatorname{arctg}\left(\operatorname{tg}\mu_1\cdot\operatorname{cosec}\nu_1\right),\qquad \nu_2=\arcsin\left(\cos\mu_1\cdot\cos\nu_1\right) \tag{2}$$

Let a pulse compressor consist of two arbitrarily oriented gratings (Fig.2). The input beam is given by the angles of α_1 and β_1 while the beam location at the second grating is described by α_2 and β_2. The letters without or with prime mean the quantities before or after the diffraction due to the grating marked by the figure subscript. Thus, the appropriate grating equations are

$$\sin\beta_i+\sin\beta_i'=\frac{j_i\lambda}{d_i\cos\alpha_i},\qquad \sin\alpha_i'=-\sin\alpha_i,\quad i=1,2$$

where j_i is the interference order, λ is the wavelength and d_i is the groovewidth.

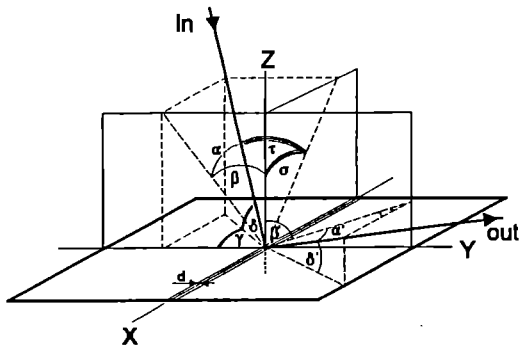

Figure 1 Diffraction of light from a grating in general case

To analyse the system α_2 and β_2 should now be derived explicitly from the parameters of the beam diffracted by the first grating taking into account the arbitrary location of the second grating. The position of the second grating with respect to the first can be specified by three rotations and one translation (Fig.2): around the X_2 axis with an angle $\Delta\xi$, around the Y_2 axis with an angle $\Delta\upsilon$ and around the Z_2 axis with an angle $\Delta\zeta$.

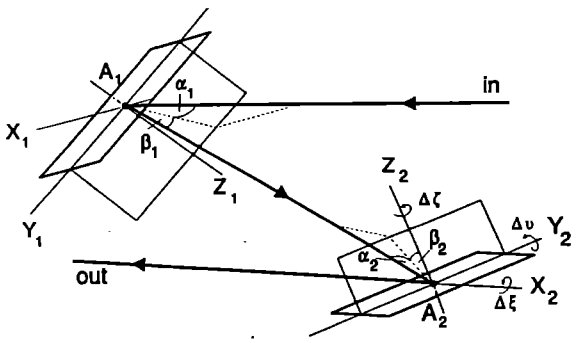

Figure 2 Light beam propagation through a grating pair. The non-parallel position of the grating planes is built up from three rotations: $\Delta\xi$, $\Delta\upsilon$ and $\Delta\zeta$.

Starting from the case of strictly parallel grating planes the initial values of α_2 and β_2 are $\alpha_2^*=\alpha_1'$ and $\beta_2^*=\beta_1'$. The tilt of the plane X_2Y_2 around the axes X_2, Y_2 and Z_2 can be expressed by

$$\left(\alpha_{2x}=\alpha_2^*,\beta_{2x}=\beta_2^*-\Delta\xi\right),\ \left(\tau_{2y}=\tau_{2x}-\Delta\upsilon,\ \sigma_{2y}=\sigma_{2x}\right),\qquad \left(\gamma_{2z}=\gamma_{2y}-\Delta\zeta,\ \delta_{2z}=\delta_{2y}\right) \tag{4}$$

where the subscript x, y, and z refer to the appropriate angles after the rotations around X_2, Y_2 and Z_2, respectively. Combining now (1)-(4), expressions for α_2 and β_2 are obtained[4].

In a rigorious treatment the direction of the output beam is given with respect to the input beam. Since the angular dispersion of the rays is more important than their absolute deviation we determine the position of the output beam with respect to the second grating by the angles α_2' and δ_2'. Taking derivatives the angular dispersion is

described along two directions each perpendicular to the output ray as well as to each other.

RESULTS

In our CPA system[5,6] a 13 ps chirped pulse at 248.6 nm should be compressed down to 100 fs by a pair of 3600mm^{-1} gratings. The laser beam with a diameter of 10 cm is less than three times diffraction limited. Because of the geometry of the target chamber the angle between the incident and diffracted rays is 4.5°.

Assuming first, that there is no deviation in the incident beam (α_1=0, β_1=24.73°) Figure 3.a and b shows the angular dispersions of $d\alpha_2'/d\lambda$ and of $d\delta_2'/d\lambda$, respectively. The solid lines refer to case of $\Delta\upsilon$ tilt with different parameters of $\Delta\zeta$ while the dashed curves give the $\Delta\zeta$ dependence. The structure of these curves is pretty much the same at different values of $\Delta\xi$, that is, the position of the C point is given by the $\Delta\xi$ dependence of the angular dispersions. The value of $d\alpha_2'/d\lambda$ varies between ±0.13 μrad/nm when $|\Delta\xi|$<35 mrad and, therefore, they have no strong effect on the beam quality but $d\delta_2'/d\lambda$ changes quite dramatically (Fig.4).

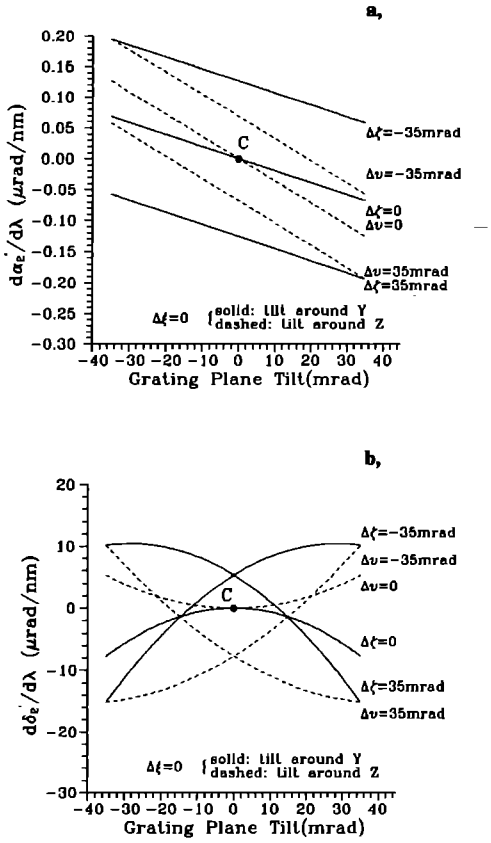

Figure 3 Angular dispersion in the plane of reflexion (a) and of diffraction (b). The C point of the curves give the $\Delta\xi$ dependence (see Fig.4)

Any uncertainity in the incident angles (α_1,β_1), moreover, results in angular dispersions, too. It is worth noting that $d\delta_2'/d\lambda$ is more sensitive to a variation of α_1 than β_1 though it stays within ±20 μrad/nm for $|\alpha_1|$<35 mrad.

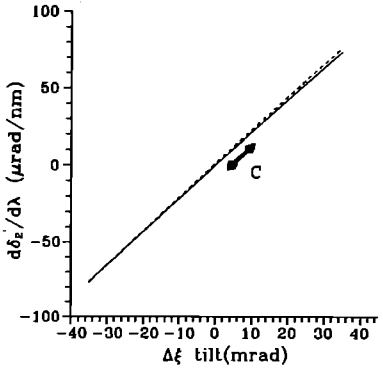

Figure 4 Angular dispersion in the plane of diffraction vs. $\Delta\xi$ tilt around the X axis. Solid line: $\Delta\upsilon$=0; dashed line: $\Delta\upsilon$=35mrad

The practical tolerances of the compressor alignment can be deduced from two restrictive conditions as spectral lateral walk off and pulse front tilt. The beam leaving the compressor exhibits spectral divergence which in the example chosen should be kept below 7 μrad in order to not double the size of the focal point of the three-times diffraction limited beam. This corresponds to less than ≅4 mrad deviation of the grating plane parallelism. The temporal effects of residual angular dispersion on the pulse length require a tighter condition for the alignment[4]. In our 100 fs system the tolerance on $\Delta\xi$ is 0.40 mrad to restrict the pulse broadening in the focus to 25 fs.

SUMMARY

The light diffraction in a grating pair compressor has been described for the most general case, which includes any position of the grating planes with respect each other as well as any pointing instability of the input beam. Practical tolerances have been calculated to ensure optimum fidelity in the recompressed pulse. It has been shown, that in a CPA system the dispersion and pulse front tilt accumulated before the compressor can be compensated in the compression by proper 'misalignment' of the grating pair.

REFERENCES

1. E B Treacy, IEEE J.Quant. Electr., **QE-5** 454 (1969)
2. T R Gosnell, A T Taylor (eds.), *"Ultrafast Laser Technology"*, SPIE **MS44**, Sect.6, 1991
3 O E Martinez, J.Opt.Soc.Am.B **3** 929 (1986)
4 K Osvay, I N Ross, Opt.Commun. **105** (1994) 271
5 I N Ross et al, submitted to Opt. Commun.
6 M J Shaw et al, EQEC'93, September 10-13 1993, Firenze, Italy, paper LDSa12

MODELLING THE KRF AMPLIFIER CHAIN IN THE TITANIA LASER SYSTEM

D C Wilson, A K Kidd, M H Key and M J Shaw

INTRODUCTION

The final design stage of the proposed KrF based Titania laser system is now well under way, and construction and installation are due to begin within the next year. In order to aid the design and in an attempt to predict the performance of the system, a computer code has been developed to model the amplification of a train of pulses in a chain of e-beam pumped KrF amplifiers. The model used here assumes a simple, single-state upper laser level. The main results obtained using this code and their implication for the system design are discussed in this report. In addition, the current development of a slightly more complex two-state upper level model is mentioned briefly.

THE TITANIA LASER SYSTEM

The original design for the Titania laser system comprised a chain of three double-passed e-beam pumped KrF amplifiers: Goblin and Sprite, which are present in the current Sprite system plus Titania, a new 42cm aperture amplifier. The front end of the system will deliver a train of four pulses to the input of a twelve-way multiplexer, resulting in 48 pulses separated by 1.5ns being delivered to the input of the first e-beam pumped amplifier. A two way multiplexer after Sprite splits each of the 12 beams out of Sprite into two, to yield 24 beams with 96 pulses for amplification in Titania.

THE SINGLE-STATE UPPER LEVEL COMPUTER MODEL

The code used to model the KrF amplifier chain is a 1D code based on that used previously to model the Sprite system [1-4]. The original code, which has been described in detail elsewhere [1], has been modified to include the new Titania amplifier, a x2 multiplexing stage between Sprite and Titania and to enable modelling of long pulse (1ns) amplification.

The code models the amplification of a train of pulses in a chain of e-beam pumped, double-passed KrF amplifiers. The equations governing the gain dynamics of the laser medium assume a single-state upper laser level [1]. Losses due to linear and nonlinear absorption in the inter-stage optics, unpumped fluorine absorption and absorption in the amplifier windows are taken into account. Amplified spontaneous emission (ASE) gain depumping is also included in the model, though the contribution arising from ASE coupling between amplifiers has previously been found to be negligible, and is not included. After each amplifying stage the energy of each pulse is calculated, and this enables the input/output characteristics of each amplifier, and of the system as a whole, to be derived.

The code has been run with pulse lengths of 10ps, 30ps, 100ps, 300ps and 1ns, with a pulse separation of 1.5ns in each case. In the case of the 1ns pulses a Gaussian pulse envelope was assumed and in all other cases a top-hat profile was used. Initially a system, consisting of the 3 KrF amplifiers, Goblin, Sprite and Titania was modelled for input energies to Goblin of between 1pJ and 100μJ per pulse. A second system with Goblin excluded has also been modelled.

The input energy to these model systems was a variable. In practice, the present front end produces a KrF energy of about 2.5mJ which, after pulse stacking and multiplexing, would correspond to an energy of 30μJ per pulse at the input to the KrF chain. With the proposed modifications to the front end of the system [5], the input energy per pulse should increase to about 100μJ.

AMPLIFIER PARAMETERS

Table 1 lists the values of the significant amplifier parameters which have been used in the model to obtain the results discussed below.

Table 1-Amplifier parameters

Amplifier	Goblin	Sprite	Titania
Aperture diam.	8	27	40
Amp. length	40	100	150
o/p window area	50	575	1257
o/p window thickness	1	2	1.5
i/p lens thickness	.5	.5	n/a *
o/p lens thickness	.5	.5	n/a *
beam dia. at i/p lens	2	2	n/a *
beam dia at o/p lens	2	9	n/a *
duration of e-beam	150ns	150ns	150ns
upper state lifetime	2ns	2ns	1ns
gain-length product	4.2	7.35	8
gain/loss ratio	10	10	10
unpumped F2 length (front)	10	57	30
unpumped F2 length (back)	25	25	25

Dimensions in cm

* Reflective optics to be used

nb. Fluorine absorption coefficient is taken to be 0.1%/ cm. in Goblin and Sprite and 0.2%/cm in Titania.

RESULTS

One of the main purposes of developing and running this code was to characterise the input / output behaviour of the Titania laser system. Originally it was envisaged that the KrF system beyond the front end would comprise Goblin and Sprite, the two amplifiers currently in operation, and Titania, a new 42cm aperture amplifier. Figures 1 to 3 show the predicted output pulse energy as a function of input pulse energy for each of the individual amplifiers, with the system operating in this configuration. The pulse used in these graphs was the 16th in the train of 24 input pulses, and it was chosen to represent a 'typical' pulse. It occurs at a point in the pulse train where the gain has settled down to a steady value in each amplifier. Figure 4 shows the overall gain characteristics of the system. The system output pulse energy is plotted against pulse energy into Goblin. The shapes of the graphs in figures 1 to 3 differ due to the different levels of saturation in each amplifier. While Goblin is hardly saturated even with the highest energy input pulse, Sprite and especially Titania are saturated even for quite low initial pulse energies. Ideally we would like to run the system with Goblin and Sprite operating in the small signal regime and with Titania just reaching saturation. Avoiding saturation in the first two amplifiers will reduce unwanted effects such as pulse sharpening between the oscillator and the target.

As expected, the highest output energy is achieved with the longest pulse length. The code predicts that for a 10ps pulse of energy greater than about 1μJ input into Goblin an output energy of between 6 and 7 J will be achieved; and this increases to almost 10 J for a 1ns pulse. A significant part of the difference in energies obtained at different pulse lengths is accounted for by two photon

absorption in the Titania output window. This is negligible for 1ns pulses but can be up to 8% for 10 ps pulses.

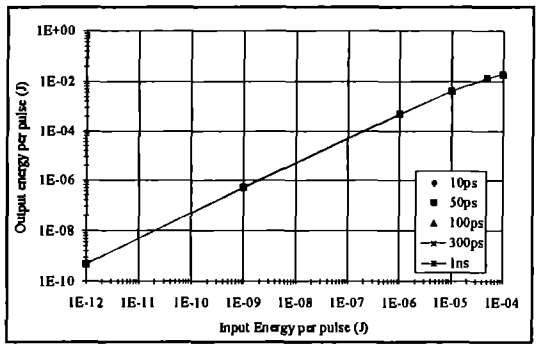

Figure 1: Goblin input / output characteristics

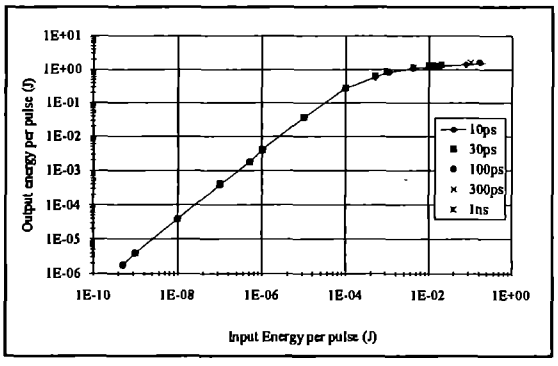

Figure 2 Sprite input/output characteristics

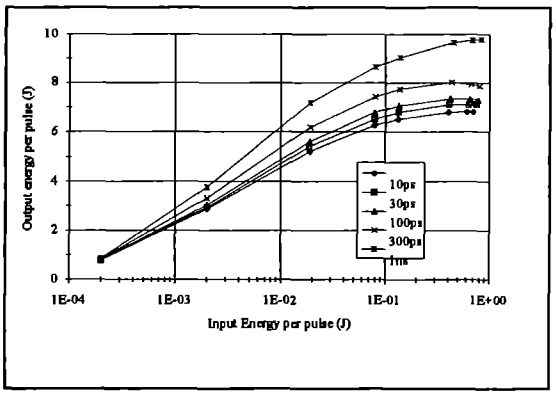

Figure 3 Titania input / output characteristics

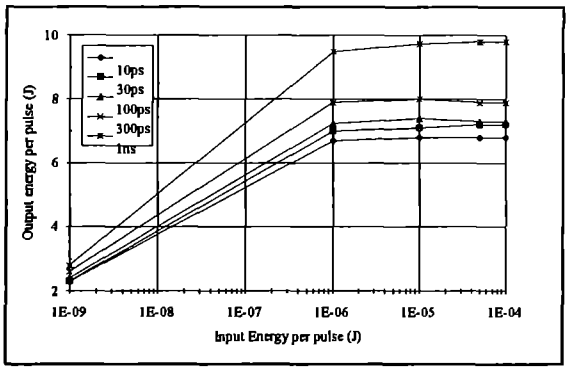

Figure 4 System input output characteristics

As was mentioned earlier, a typical pulse energy into Goblin is currently about 30 μJ, and from the graphs in figures 1 to 3, this will produce enough energy to almost saturate Sprite. It would be desirable to run Sprite below saturation and this will mean reducing the energy in the initial stages of the system. The most efficient way to do this may be to dispense with Goblin altogether and to run the system with just Sprite and Titania. From figure 3, an input pulse energy of approximately 100-150mJ is sufficient to saturate Titania, and this represents an output from Sprite of 200-300mJ per pulse. This is achieved well below saturation, for an input pulse energy to Sprite of approximately 70-100μJ. Figure 5 shows the predicted input / output characteristics of the system with Goblin removed. The output pulse energy from Titania is shown as a function of pulse energy into Sprite.

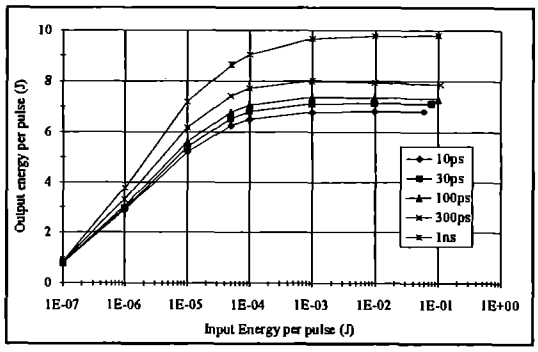

Figure 5 System input/output characteristics without Goblin

As can be seen, a pulse energy greater than about 70μJ at the entrance to Sprite should be enough to weakly saturate Titania, at least in the short pulse regime, and 100 to 200μJ will move the system well into the region of saturated operation for pulse durations of up to 300ps. Indeed the system would be weakly saturated even for a 1ns pulse. In reality we would expect a significant increase in the amount of energy available at the entrance to Sprite as the pulse length is increased, due to improved operation of the front end high gain amplifier at long pulse durations, so it should be possible to run the system with Titania saturated for pulse durations up to at least 1ns. It appears then, that with the introduction of the upgraded front end to the KrF system, it should be possible to run this system without the Goblin amplifier. This will greatly simplify the design and operation of the final system.

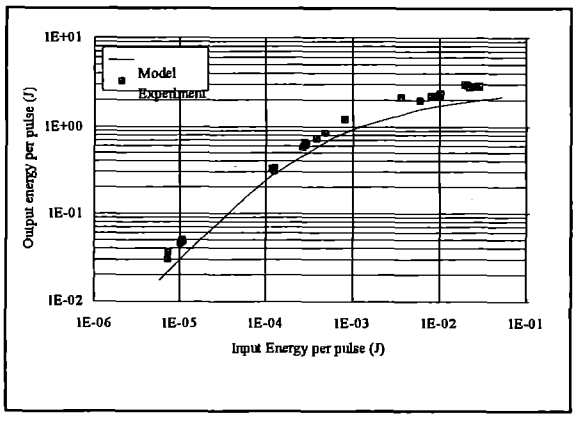

Figure 6: Sprite single shot data and prediction

To lend some credence to the code predictions discussed above, figure 6 shows a comparison of some experimental input / output data from Sprite, and the corresponding code predictions. The data shown were recorded with Sprite operating in single shot mode with a pulse length of 40 ps. Figure 6 shows that, if anything, the code

predictions are pessimistic as the experimentally measured gain was slightly higher than the code would suggest.

THE TWO-STATE UPPER LEVEL COMPUTER MODEL

The model used to generate the results discussed above assumes a single state upper energy level in the KrF laser transition. Under this assumption, the gain recovery equation is [1]

$$g(z, t+dt) = g_0 + [g(z,t) - g_0]\exp(-dt/\tau_b), \qquad (1)$$

which describes the repopulation of the upper laser level after the passage of a gain-depleting laser pulse. Here g(z, t) is the local gain at time t and is proportional to the population of the upper laser level, g_0 is the pumped small signal gain coefficient ($g_0 = R\tau_b$ where R is the pump rate into the upper laser level), and τ_b is the collisionally quenched upper state (B state) lifetime. The important point to note is that the gain recovery depends on just one time constant, τ_b. This lifetime is dependent on factors such as the gas mix used in the laser, and it is typically of the order of 1 to 5 nanoseconds. Using this single state model, we see the gain recover exponentially with a nanosecond time constant. The steady state ASE depumped gain of the amplifier will be determined by g_0 and τ_b, both of which are input parameters in the code.

Figure 6 demonstrates that with the appropriate choice of g_0 and τ_b, this single state model does give good agreement with experimental data in the single shot case. However, certain experimental observations have been made which cannot be explained using the single state model. For instance, Szatmari and Schafer used a picosecond pulse-probe technique to measure the short time gain recovery characteristics of a single pass KrF discharge laser, and they found that the gain recovery actually followed a double exponential curve [6]; in addition to the long term (~ns) recovery, governed by τ_b, they found an initial rapid recovery of the gain to about 20-25% of its steady state value. This rapid recovery was attributed to the fact that, in reality, under steady state conditions, the KrF* population is distributed between the upper level of the laser transition (the B state) and many other higher-lying energy levels. When the B state is extracted by a saturating laser pulse, the equilibrium conditions are broken and this results in a rapid decay of the population of the higher-lying states to the B state, replenishing the gain. There is no mechanism for this rapid initial gain recovery in the single state model since there it is assumed that the total KrF* population is in the B state and is accessible to the laser transition.

In order to take account of the experimental observation of a fast initial gain recovery, and to model the real situation more accurately, a two-state model is being developed in which, as well as the B state, we assume the presence of a higher-lying excited state in the KrF* molecule. This higher-lying state represents all energy levels in the KrF* molecule apart from the B state, which is the upper level of the laser transition. We assume that the KrF* molecules are initially formed in the upper excited state and that the B state is populated by collisionally induced or spontaneous decay from the upper state. In the two-state model the collisionally quenched lifetime of the upper excited state with respect to the B state determines the time constant of the fast initial gain recovery observed experimentally, and the steady state distribution of the population between the two excited states determines the level to which the gain initially recovers.

Using the new two-state model, we have attempted to simulate the experiment of Szatmari and Schafer, in which they first observed this fast initial gain recovery. The observed initial recovery of 20-25% implies a steady-state B state to upper state population ratio of 3-4. The measured time constant for the fast recovery was about 60ps and this corresponds to τ_{ub}, the lifetime of the upper state with respect to the B state, in the model. Figure 7 shows a comparison of the model prediction with the observed gain recovery behaviour. Also shown is the behaviour predicted by the single state model. Clearly the two-state model is far better able to account for the observed behaviour.

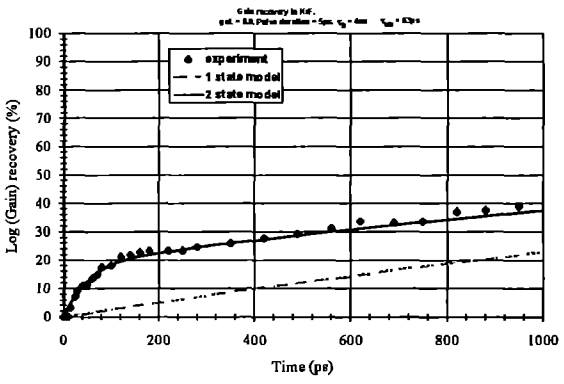

Figure 7 Picosecond gain recovery behaviour in a KrF laser. Values for g_0l and the lifetimes τ_b and τ_{ub} used in the model were set equal to the values measured in the experiment. Experimental data are taken from reference 6.

Further comparisons between predictions of the two-state model and experimental results are underway. Of particular interest at present is the behaviour predicted by the two-state model in the cw limit. Experimental observations have shown that in this limit the extractable gain of a KrF laser is somewhat less than that predicted by the one state model for a given KrF* formation rate. This can again be attributed to the fact that under steady state conditions some of the KrF* population is trapped in levels other than the B state and is therefore not accessible to the laser photons.

REFERENCES

[1] E C Harvey, C J Hooker, M H Key, A K Kidd, J M D Lister and M J Shaw *Picosecond gain and saturation measurements in a KrF laser amplifier depumped by amplifier spontaneous emission.* J. Appl. Phys. 70 p.5238 (1991).

[2] M H Key and A K Kidd *Analysis of the Performance Capabilities of the Sprite Laser Sysytem and of Options for its Optimisation.*CLF Annual Report 1990 p96

[3] A K Kidd and M H Key *Supersprite Gain Staging Analysis* CLF Annual Report 1991 p93

[4] A K Kidd RAL Internal Report *Titania Gain Staging Analysis and ISI*

[5] S Angood *et al. Specification for the TITANIA KrF Laser System* RAL report no. RAL-94-014

[6] S Szatmari and F P Schafer *Comparitive Study of the Gain Dynamics of XeCl and KrF with Subpicosecond Resolution* J. Opt. Soc. Am. B4 (1987) 1943

PERFORMANCE OF THE UPGRADED SPRITE RAMAN LASER

C J Hooker, E J Divall, K N Drodge, J A C Govans, S Hancock, G J Hirst, J M D Lister, A J MacKinnon[1], M J Shaw and D C Wilson[1]

Rutherford Appleton Laboratory
[1] Blackett Laboratory, Imperial College, London

INTRODUCTION

The upgrade to the Sprite Raman system which was described in last year's Annual Report has now been completed successfully. During initial tests and the first experimental run, the performance of the laser has improved broadly in line with expectations. The energy from Sprite available for pumping the Raman amplifiers has increased by about 65% to a typical level of 16 J. The new RA3 is more efficient than before, leading to Stokes energies of up to 10.6 J. The far-field quality of the Stokes beam is as good as before, typically 1.4 times the diffraction limit, and the near-field is smoother as a result of greater intensity-averaging with eleven pump beams. As far as possible, the changes made to the system have been such that components purchased for the upgrade can be incorporated into the Titania laser over the next two years. As detailed designs for the mirror frames and the VSF were developed during the year, the layout changed from that shown in last year's Annual Report. Figure 1 represents the final configuration as installed in the multiplexing area.

MODIFICATIONS TO THE SPRITE SYSTEM

The principal changes to the KrF chain were the reduction of the beam multiplexing interval to 3 ns, and the increase in the number of multiplexed beams from eight to twelve. As Sprite is quite heavily saturated, the energy in each pulse is the same as before, making the total energy 50% greater. A reduction in B integral in the path to RA3 was achieved by increasing the beam diameter from 8 cm to 10 cm, allowing the higher pump energy to be transported to the amplifier with less distortion of the spectrum by self-phase modulation. New input and output optics and a new back mirror were installed on Sprite to change the beam size. This has led to a modest increase in the external efficiency of the amplifier.

Other changes were aimed at improving the quality of the KrF beams. This is particularly advantageous when the laser operates in CPA mode, but the improvements in the near-field profile also benefit the Raman mode, as there is less likelihood of either imprinting of hot-spots or of localised spectral broadening. The KrF oscillator beam is now spatially filtered as it enters the multiplexing area. The pinhole diameter is a few times the diffraction limit, but nevertheless does improve the near-field of the KrF beam at the entrance to RA3. This spatial filter is filled with helium at atmospheric pressure, to avoid the spectral distortion that would occur if air was present. The introduction of positive lenses at the input to Sprite has resulted in greatly improved image relaying between Goblin and Sprite, which also helps to maintain a smooth near-field profile. As with the spatial filter, the Sprite beam pipe is filled with atmospheric-pressure helium to avoid spectral distortion occurring at the foci of the lenses.

The effect of timing jitter on Sprite has been reduced by using the fourth KrF pulse to pump the Raman preamplifier, RA2, rather than the first pulse as in the original system. A misfire of Sprite by a few nanoseconds no longer results in such low gain in RA2 that the output of RA3 is seriously reduced; the shot-to-shot variation in output energy is thus substantially smaller than before.

The configuration of the pumping array for RA3 has been changed from a circle to a cross pattern, which according to computer simulation is preferable for maintaining a Gaussian beam profile. It has the additional advantage that the pump beams are reflected only from the faces of the lightguide, thus avoiding the imprinting of lines on the pump profile due to imperfections in the corners. However, the intensity averaging of the pump beams now takes place in only two directions, which leads to some horizontal and vertical structure on the Stokes near-field profile.

The changes to the Raman system were directed at improving the beam quality in both the near and far fields. The only new component in the Raman beamline is a diffraction-limited spatial filter between RA2 and RA3, introduced to control the profile of the beam into the final amplifier. To maximise the lifetime of the pinhole, the focal lengths of the lenses were chosen to be as large as possible in the available space, and a

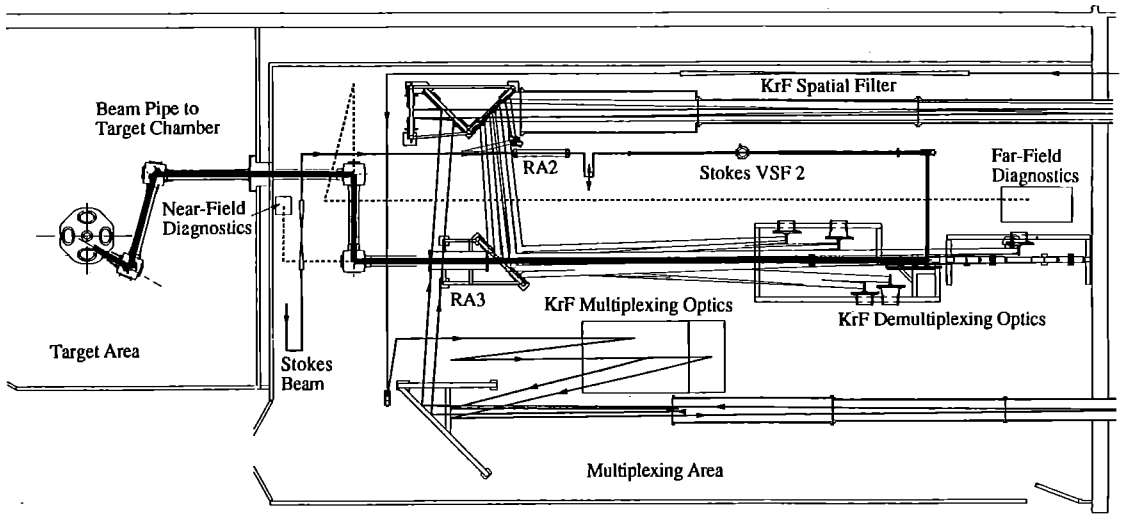

Figure 1. Final layout of the upgraded Sprite Raman system.

special telephoto combination was designed for the output lens using a ray-tracing program. This lens recollimates the beam before it enters RA3, allowing the calcium fluoride collimating lens which was formerly the output window to be replaced by a 0.6 mm thick silica window, significantly reducing the B integral. The quality of the output beam is largely determined by this VSF, and hence the lifetime of the pinhole is an important issue. It was decided to experiment with laser-drilled pinholes in diamond substrates, as the erosion of diamond by the beam should be extremely slow, thereby increasing the pinhole lifetime. The first of these was installed at the start of the commissioning period, and there is qualitative evidence that the lifetime is significantly longer than for metal pinholes.

As described in last year's Annual Report, a completely new mechanical design was developed for the RA3 lightguide, to allow the cross-section of the guide to be changed from a 10 cm square to a 10 x 12 cm rectangle for two-beam multiplexing. Although the delay to the upgrade has meant that this particular option will not be used, the new mechanical design has proved to be far superior to the old, which makes us confident that it can be scaled up to the 16 x 16 cm required for the large Raman amplifier in the Titania system.

The beam pipe enclosing the output beam from RA3 to the target area is constructed from low-cost plastic pipe sections and commercially-available boxes. These were modified to accept either windows, electrical ports for the control cables to the motor drives on the mirror mounts or flanges which hold the ends of the pipes. It was also decided to fill the beam pipe with argon rather than helium, for reasons of cost and also because of the difficulty of making the pipe entirely leakproof. The non-linear refractive index of argon is one-fifth that of air, so in fact the B integral in the path to the chamber is reduced to an acceptable level.

BEAM DIAGNOSTICS

Obtaining accurate diagnostics of the output Stokes beam is a problem when the power is in the terawatt range. Any beamsplitter that is inserted into the beam to deflect a small fraction to a diagnostic station will, if it is thick enough to ensure flatness, introduce an unacceptably large B integral and may degrade the target beam. Such degradation will not be detected by the diagnostic. The alternative is to perform beam diagnosis on the fractions transmitted through turning mirrors, and this was the method chosen for the upgraded laser. In any case, enclosing the output beam in a pipe to the target area makes the use of split-off fractions impractical. The ports behind the two mirrors in the multiplexing area were used to obtain near- and far-field beam profiles and for energy monitoring. The positions of the diagnostic stations are shown in Figure 1. The only turning mirrors that were available have very low transmission: the low intensity of the transmitted beam caused difficulties while setting up the diagnostics, and reduces the accuracy of the measurements, particularly of the far-field. New mirrors with "leaky" coatings on high-quality substrates have been ordered, and will allow us to have more confidence in the diagnostics.

SYSTEM PERFORMANCE

The installation and commissioning of the new system, and the first experiment, were carried out using 10 ps pulses. During this period a total of 406 shots were fired, with a peak energy of 10.6 Joules and an average of about 8 Joules. The next experiment required longer pulses, of 60 ps and 25 ps duration, which were obtained by installing different GTI dispersion compensating devices in the Tsunami oscillator. At 60 ps, energies in the KrF were 2.4 Joules per beam, or a total of 24 Joules, and Stokes energies of 11.6 Joules were recorded during the setup period. At the time of writing, the output of the system at 25 ps has not been evaluated.

Typical near- and far-field images are shown in Figure 2. The central spot in the far field shows a divergence of approximately 1.4 times the diffraction limit, with relatively small amounts of energy lost to the surrounding halo. The near-field image shows a certain amount of horizontal and vertical structure corresponding to the transverse motions of the pump beams across the Stokes. The overall shape of the beam is reasonably circular as a result of the change of shape of the pump array: the corners of the lightguide are relatively weakly pumped, so the Stokes beam has less tendency to become square.

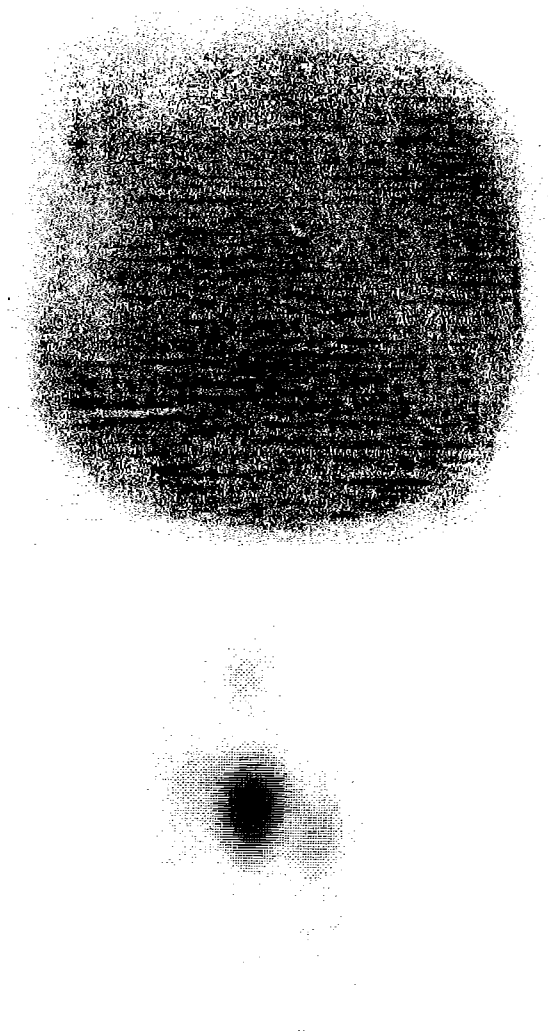

Figure 2. Near-field (upper) and far-field (lower) images of the Stokes beam. The central spot in the far-field corresponds to 1.4 times the diffraction limit. Note the structure on the near-field due to the two directions of intensity-averaging in the guide.

SUMMARY

The upgraded Raman system has achieved its design aims at 10 ps in terms of enhanced energy. The beam quality is as good as before, and there is a significantly smaller B integral in the optical path to the target chamber as a result of piping the beam in argon. The beam brightness has exceeded 10^{20} W cm^{-2} sr^{-1}, yielding intensities on target greater than 10^{19} Wcm^{-2}.

TWO-DIMENSIONAL RAMAN CODE MODELLING

G.H.C. New, D.C. Wilson, C. Moreira and K.E. Hill[1]

Department of Physics, Imperial College, LONDON, SW7 2BZ

[1]Department of Physics, The Open University, Walton Hall, Milton Keynes, MK11

INTRODUCTION

A computer code has been developed that models the final Raman frequency conversion stages in the Sprite laser system. In the real laser, multiple pump beams, roughly evenly spaced around the axis, interact with a single Stokes beam in a square cross-section waveguide[1]. The previous computer model attempted to take account of the complicated angled geometry that this implies by introducing a speed differential between the Stokes pulse and a single co-propagating pump[2]. The "one-dimensional" code embodying this procedure produced useful results, but there were significant differences of behaviour depending on whether the pump was assumed to travel faster than the Stokes, or vice versa.

Arguments could be advanced for either assumption. Clearly, for pump beams travelling at an angle θ to the axis, the average speed over a complete reflection cycle within the waveguide is $v_s\cos\theta$ where v_s is the speed of the Stokes; over short distances, on the other hand, the effective axial speed of the pump envelope is $v_g/\cos\theta$. These two options can be termed the "slow pump" and "fast pump" cases respectively. Both would appear to represent severe approximations to the real situation, providing a strong incentive for extending the analysis to two dimensions.

COMPUTER MODEL

The two-dimensional code has been constructed as a natural development of its one-dimensional forbear; the two programs have large sections in common and work from the same data file. In the 2D model, two pump pulses, angled symmetrically about the waveguide axis in the plane of incidence, interact with a Stokes pulse travelling along the axis. The code has been set up to allow the shape of the waveguide cross section to be varied while the cross-sectional area remains fixed. This allows the specifically two-dimensional features of the problem to be introduced progressively so that the performance of the code can be checked and the 2D effects isolated.

This approach has immediately yielded a significant result. For typical parameter values, as the transverse dimension of the waveguide (in the plane of incidence) is shrunk to zero, the one-dimensional result *for the case where the pump travels slower than the Stokes* is recovered. On the other hand, as the transverse width is increased to its actual value (corresponding to a square cross-section waveguide), the energy conversion efficiency falls, the fall being greater the shorter the duration of the pump pulse. Overall, the results provide a surprising degree of support for the 1D code in the "slow pump" case.

A comparison of results generated by the two codes, demonstrating this important conclusion, is shown in Fig. 1. Pulse profiles from the 1D code in both the "slow" and "fast" options are displayed together with the corresponding result from the 2D code. It is clear that, in the 1D case, the temporal positions of the peaks and troughs in the profiles of both the

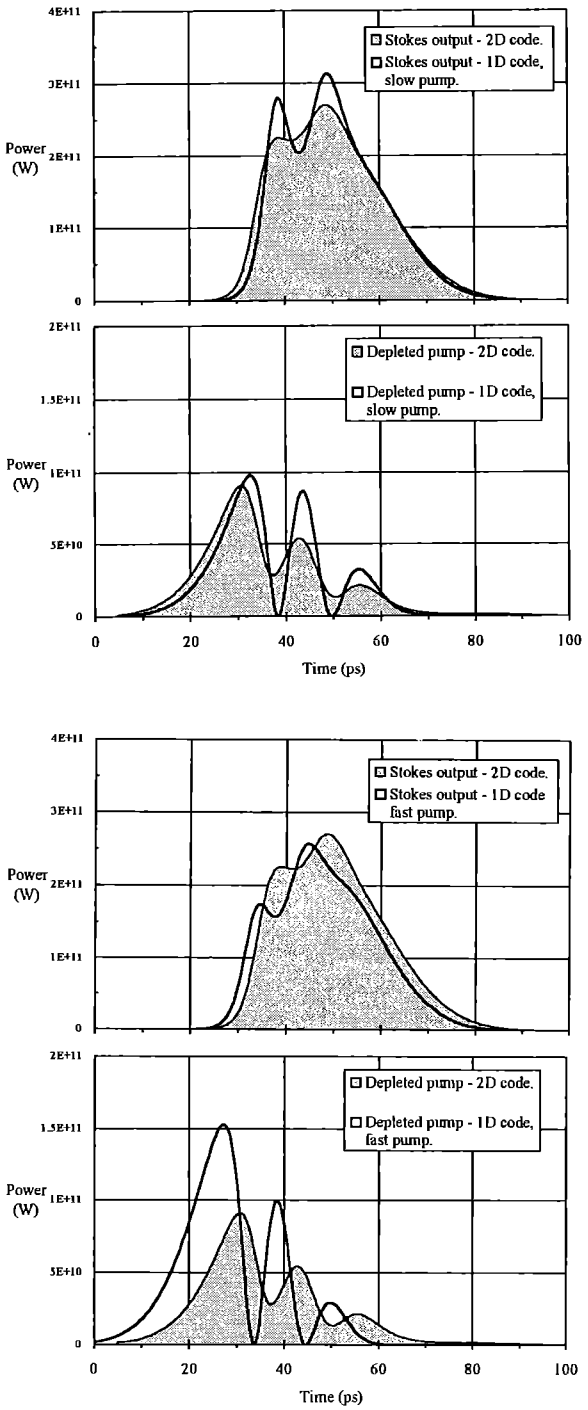

Figure 1 Comparison of 1D and 2D Raman code predictions. The temporal profiles of the output Stokes and depleted pump pulses are shown. The input pulses were all transform limited Gaussians with FWHM = 30ps.

Stokes and the depleted pump pulses correspond most closely to their positions in the 2D case if we stipulate a "slow pump". Furthermore, the conversion efficiency in the "slow pump" 1D case is 74.6%, while the "fast pump" model yields an efficiency of only 66.9%. The 2D code, in accordance with the 1D "slow pump" model, predicts a conversion efficiency of 74.5%.

When temporal phase fluctuations were introduced on to the pump pulse in the 1D code, it was found that the Raman conversion eficiency was severely reduced for pulses in the transient regime (where the pulse duration is comparable to the dephasing time of the Raman medium), and that temporal intensity fluctuations were induced in the Stokes output. Now, with the 2D code, it has been possible to investigate the effect of the presence of *spatial* phase fluctuations on the pump pulses. These spatial phase fluctuations occur in the real world as a result of aberrations arising in the optical paths of the KrF pump beams.

Transverse energy profiles obtained with the 2D code are presented in Fig. 2. Spatial phase noise is present in the input pump beams but there is no amplitude noise. Fig 2a shows a smooth final Stokes energy profile, demonstrating that spatial phase noise on the pump beams does not induce any amplitude fluctuation in the Stokes output. In fact, results suggest that the presence of transverse phase noise on the pump wavefront has absolutely no effect on the Raman process, even in the strongly transient regime. Although slightly counter-intuitive, this result is explained by considering the phase of the pump seen at each individual point in the Raman medium. At any given position, this phase does not change during the passage of the pump so there is, in fact, no mechanism for imprinting spatial phase noise from the pump onto the Stokes pulse.

Figures 2(b, c) show the depletion of the pumps as they move down the lightguide. The discontinuity, which moves across the guide in each of these figures, is a result of the reflection of the pumps at the guide walls. In figure 2(b), for example, the portion of the profile to the right of the discontinuity represents the unreflected part of the pump beam that was originally travelling from left to right accrss the guide. The portion to the left of the discontinuity arises from the reflected part of the other pump beam, which was originally travelling right to left, but which travels left to right after reflection.

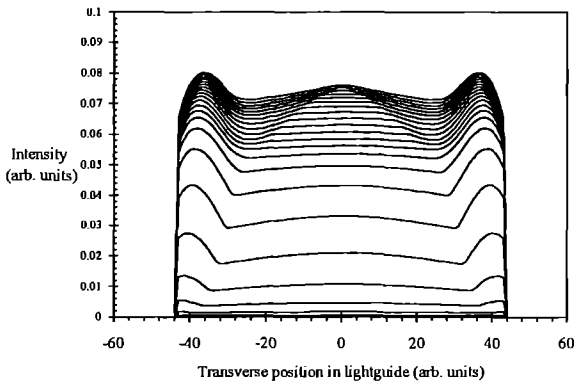

(a) Stokes intensity profile. The bottom curve shows the profile at the entrance to the lightguide, and the top curve shows the profile at the exit end of the lightguide, after amplification.

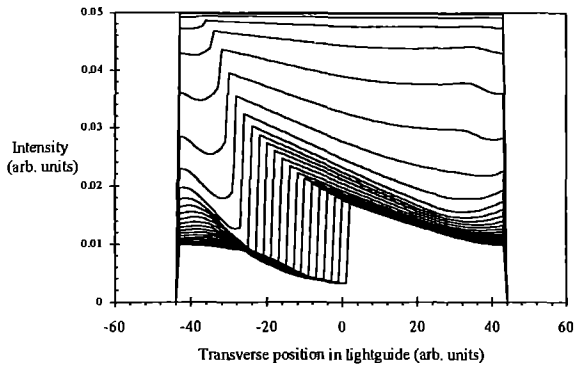

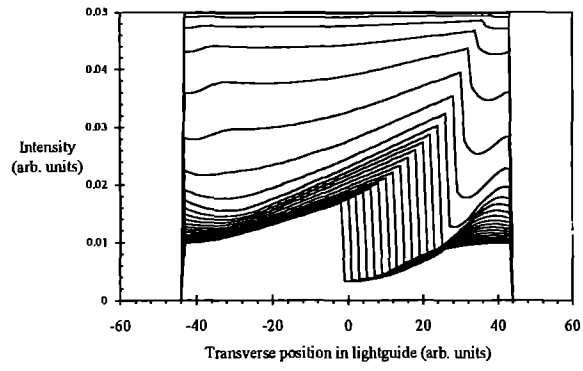

(b) and (c) Profiles of the 'left to right' and 'right to left' moving pumps respectively. The top curves show the profiles at the entrance to the lightguide and the bottom curves show the depleted pumps at the exit end of the guide.

Figure 2 Transverse intensity profiles of the pump and Stokes pulses. The figures show the amplification of the Stokes and the depletion of the two pumps as they propagate down the lightguide.

Having considered the effect of phase fluctuations in the input pump beams, the effect of intensity fluctuations (in both the longitudinal and transverse dimensions) now needs to be examined and this will be the subject of future study.

REFERENCES

1. I.N. Ross, M.J. Shaw, C.J. Hooker, M.H. Key, E.C. Harvey, J.M.D. Lister, J.E. Andrew, G.J. Hirst and P.A. Rodgers, Opt. Commun., **78** (1990) 263.

2. K.E. Hill, G.H.C. New, P.A. Rodgers and K. Burnett, Opt. Commun., **87** (1992) 315.

ULTRABROAD BANDWIDTH MULTILINE STIMULATED RAMAN SCATTERING

G S McDonald[1], G H C New[1], L L Losev[2], A P Lutsenko[2] and M J Shaw[3]

[1]Blackett Laboratory - Optics Section, Imperial College, London SW7 2BZ.
[2]P.N. Lebedev Physical Institute, Leninsky Prospekt 53, 117924 Moscow.
[3]Rutherford Appleton Laboratory, Chilton, Didcot OX11 OQX.

INTRODUCTION

Multiple high Stokes and antiStokes orders are frequently observed in stimulated Raman scattering (SRS). In the vast majority of cases the higher orders are the result of parametric 4-wave processes occuring under phase-matched conditions. This phase matching requires that the various orders are generated at widely differing angles and the resulting multifrequency beam is not focusable to a single spot. The much more interesting case is where higher orders are generated with a phase mismatch but are collinear. Such a beam may have application to laser fusion [1,2]. The rotational transitions in gases have been extensively used in Raman amplification and, recently, multiple components of comparable amplitude spanning a broad bandwidth have been generated using both hydrogen and nitrogen [3,4]. Previously, it has been thought that it would not be possible to switch on bandwidth on a timescale much shorter than the T_2 time of the medium and that this delay would severely limit the usefulness of the generated spectrum [1,2]. Experiment has tended to support this conclusion [4].

Multiseed SRS with identical pump and 1st Stokes pulse envelopes (symmetric bichromatic pumping) has not, to our knowledge, been investigated in the transient regime where turn on effects are important. It is precisely in this regime that we report the generation of more than 40 Stokes orders having intensity greater than 10% of the peak [5]. In addition to this, we demonstrate that, with an appropriate choice of experimental parameters, ultrabroad bandwidths may be turned on in a time much less than the T_2 time of the Raman medium [5]. The central motivation for this research is the optimisation of collisional absorption in high energy laser-target coupling experiments. Specifically, we are investigating powerful high bandwidth sources which may effectively raise thresholds for the competing parametric backscattering processes [1]. The benefits of increased bandwidth are many and may include improved efficiency of the laser fusion process and a significant increase in the number of alternative experimental configurations [4]. Since the underlying mechanisms involved in this work are fundamental, there may be a much wider range of applications.

MODEL AND RESULTS

To model SRS we have expanded the total electric field in terms of constituent plane waves (the pump and Raman sidebands). Each wave has a complex envelope varying in both longitudinal space and time and has a carrier frequency which is given by the pump frequency plus an integer times the Stokes shift. This integer may be positive or negative and is referred to here as the component number. To study the essential physics and scaling laws of the multiline generation process, we have recast the standard equations which describe multiwave interactions [6] in terms of dimensionless variables [5]. The amplitude of each line has been normalised to the peak value of the pump pulse and time has been scaled to its width, t_p. Propagation distances, z, have been scaled so that one deals directly with the gain-length product of the interaction, $Z = \gamma I z$, where I is the peak input intensity of the pump pulse. We consider symmetric bichromatic pumping as the initial condition at $Z = 0$. In this case the input pulses are synchronous, collinear, coherent and have equal amplitude and pulse length. All other components are set initially to zero.

Results are presented for stimulated rotational Raman scattering in H_2 gas where the Stokes shift is $587cm^{-1}$. The pump beam considered is a second harmonic of Nd:YAG which has frequency

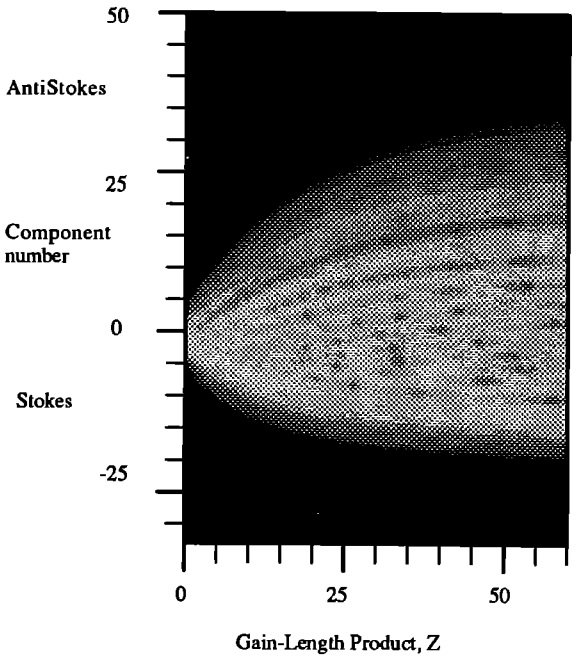

Figure 1(a). Variation of the steady-state multiline spectrum as a function of the gain-length product Z as it varies between 0 and 60. The Raman lines are separated by integer multiples of the Stokes shift. The effects of dispersion are neglected.

$18900cm^{-1}$. We choose the steady-state Raman gain coefficient to be unity, $\gamma I = 1cm^{-1}$ ($\gamma = 0.5cmGW^{-1}$ and $I = 2GWcm^{-2}$, for example), so that one can interpret Z as simply the cell length in centimetres.

It is instructive firstly to consider the multiline generation process without transient effects. Results for this case, valid for relatively long input pulses, are shown in Figure 1. In part (a) the output spectrum generated from the input beams (pump and 1st Stokes, with component numbers 0 and -1) is shown as a function of the gain-length product. For higher Z the multiline interaction becomes saturated and the output spectrum remains unchanged. In Figure 1(b) the effect of high gas pressure is demonstrated. Here, approximately the same output bandwidth is generated but it is shifted down to lower frequencies.

In steady-state calculations, such as those shown in Figure 1, cw or quasi-cw variables are assumed. However, when the durations of the input pump and Stokes pulses approach the dephasing time of the polarisation grating, T_2, transient effects can no longer be neglected. We now report on more general considerations involving multiline generation with *pulses* of input light and allowing for transient effects by solving a dynamic equation for the polarisation wave.

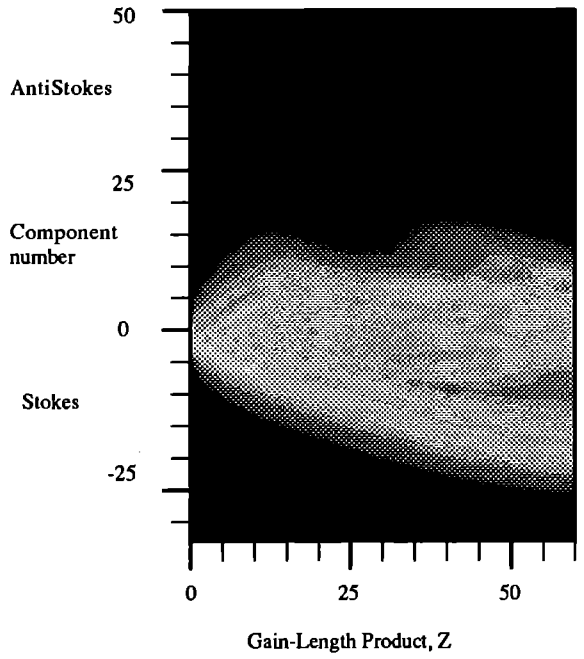

Figure 1(b). As part (a) but with a significant level of dispersion (approximately 3.6 atmospheres of H_2).

Figure 2 shows the output generated after propagation through a gas cell of length z = 200cm. The intensity profile of the output pulse at each Raman frequency has been integrated over time to show the generated power spectrum. To demonstrate the magnitude of this bandwidth one can calculate that the visible section of this spectrum only spans around 18 Stokes shifts.

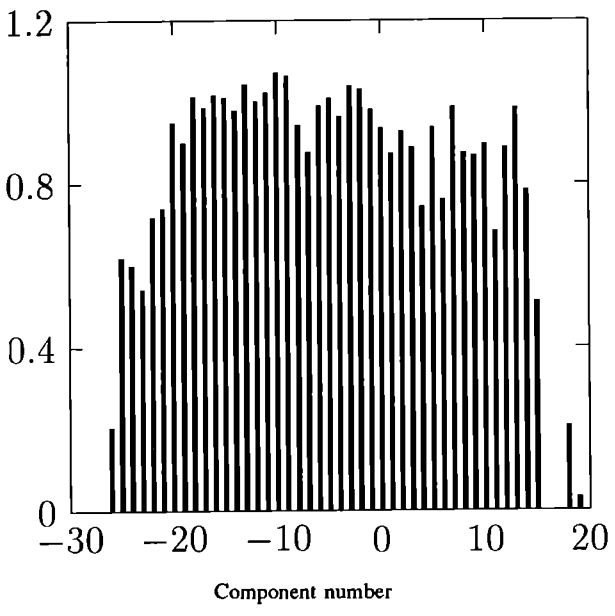

Figure 2. Time-integrated intensities of the generated Raman lines ($\log_{10}$ scale). Parameters are: $t_p/T_2 = 1$, $\gamma l = 1 cm^{-1}$ z = 200cm and the gas pressure is 0.66 atmospheres H_2.

In Figure 3 the results from a large number of simulations are summarised to outline the role of dispersion. For each value of t_p/T_2 considered, a suitably large gain-length product is specified to minimise z-dependent variation in the output bandwidth. In part (a) the variation of 10% bandwidth of the time-integrated spectra is shown. This definition of bandwidth corresponds to the width of the output spectrum within which the integrated-intensities of the lines are greater than 10% of their peak values. For t_p/T_2 values of 1 and 8 with low dispersion the generated bandwidths are slightly lower than their maximum values. It is possible that this effect is related to the gain suppression of phase matched interactions which has been quantified previously in models of three-wave coupling [6]. Also for low dispersion, one may observe an enhancement of the output bandwidth due to transient effects. This may be attributed to a longer interaction length which results from the longer life of the polarisation grating. With high gas pressures dispersion tends to inhibit the generation of ultrabroad bandwidths when transient effects are strong. Thus, for fixed steady-state gain, there exists an optimum gas pressure for maximising the output bandwidth.

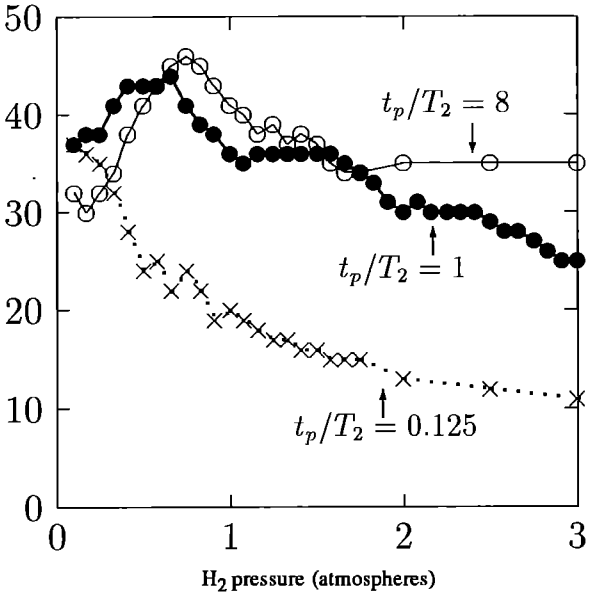

Figure 3(a). The characteristics of the time-integrated output as a function of gas pressure for 3 ratios of input pulse width to polarisation dephasing time: t_p/T_2 = 0.125, 1 and 8. 10% bandwidths, in units of the Stokes shift, are plotted.

As one might expect, instantaneous bandwidths (at particular values of local time) may exceed those of the time-integrated spectrum and can be greater that 50 Stokes shifts. In Figure 3(b) the points in time for maximum (instantaneous) bandwidth are shown. While changes in the global parameter of time-integrated bandwidth tend to saturate at large z, the switch-on time is more local and remains sensitive to z. The overall trends and level of sensitivity can be interpreted from correlating the results of a large number of simulations. Generally, with decreasing t_p/T_2 the switch-on time is seen to increase. However, the delays shown are still less than the input pulse width, t_p. When t_p/T_2 = 0.125, increasing the gas pressure tends to halt the generation of ultrabroad bandwidth. It is thus not surprising that switch-on times for these smaller bandwidths do not greatly increase with gas pressure and, instead, stay of the same order. When T_2 is less than t_p ultrabroad bandwidth may be switched on essentially instantaneously or even during the local rise time of the input pulses.

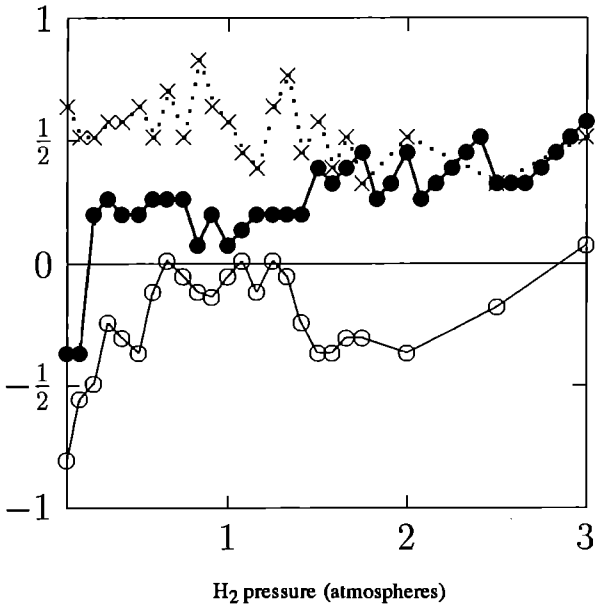

Figure 3(b). Points in the local time frame for maximum bandwidth (in units of t_p). Values of t_p/T_2 are as indicated in (a).

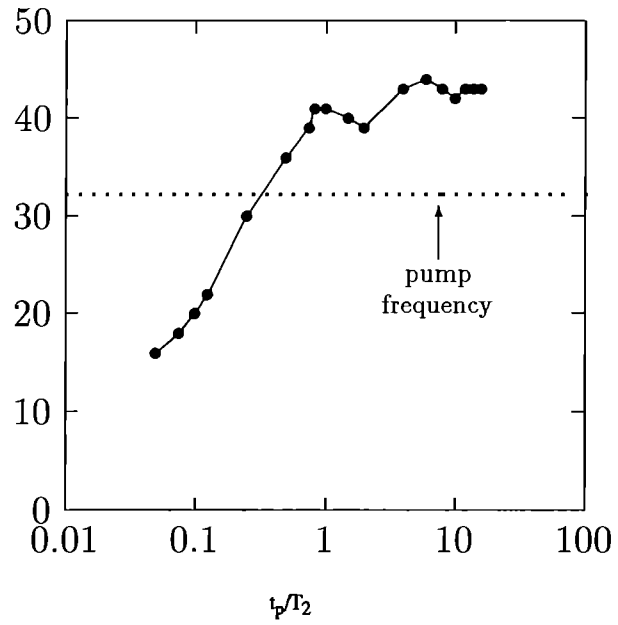

Figure 4. Variation of the generated bandwidth with t_p/T_2 for z = 500cm and 0.66 atm. H_2. 10% bandwidths and the magnitude of the pump frequency, in units of the Stokes shift, are shown.

In Figure 4 the variation of bandwidth with t_p/T_2 is shown for fixed gas pressure and gain-length product. In the direction of the extreme transient limit, $t_p<<T_2$, the suppression of ultrabroad bandwidth, that was indicated in Figure 3(a), is seen to continue while towards the steady-state regime, $t_p<<T_2$, bandwidth can be maximal. It is also in this latter regime where switch on time can be minimal [5]. Even while t_p/T_2 varies over two orders of magnitude, symmetric bichromatic pumping leads to significant bandwidth which coincides (temporally) with the pumps to within one pulse width.

SUMMARY

In summary, we have demonstrated that in stimulated rotational Raman scattering in hydrogen gas, output bandwidths greater than the pump frequency may be generated when symmetric bichromatic pumping is implemented. Previous research has shown that long transients may occur before bandwidths of more than a few components can switch on and that such transients may limit the usefulness of the generated spectrum. Here we have demonstrated that, with the correct choice of experimental parameters, *ultrabroad* bandwidths may be generated essentially instantaneously. It is expected that the principles underlying these results for linearly polarised light will have consequences in other polarisation geometries. Work is in progress to generalise these results through the systematic inclusion of asymmetries in the bichromatic pumping scheme and also to considerations of other nonlinear media such as nitrogen. Studies with more complex models to determine limiting factors that could suppress the generation of such ultrabroad bandwidth need to be undertaken. The experimental realisation of even a small fraction of the predicted bandwidth would be a very significant result.

ACKNOWLEDGEMENTS

This research was supported in part by SERC grant no. GR/J04746. Two of us (L.L. and A.L.) wish to acknowledge financial support from the Royal Society under part of a Joint Project on Raman Lasers.

REFERENCES

1. D. Eimerl, W.L. Kruer and E.M. Campbell, Comments Plasma Phys. 15, 85 (1992).

2. D. Eimerl, R.S. Hargrove and J.A. Paisner, Phys. Rev. Lett. 46, 651 (1981).

3. M. Hermann, M. Norton, D. Twede and L. Hackel, CLEO, Baltimore, May 1993.

4. D. Eimerl, D. Milam and J. Yu, Phys. Rev. Lett. 70, 2738 (1993).

5. G.S. McDonald, G.H.C. New, L.L. Losev, A.P. Lutsenko and M. Shaw, "Ultrabroad Bandwidth Multifrequency Raman Generation" (submitted to Optics Letters).

6. A.P. Hickman and W.K. Bischel, Phys. Rev. A37, 2516 (1988).

DESIGN SPCIFICATION AND CURRENT STATUS OF THE TITANIA KRF LASER SYSTEM

S Angood, A R Damerell, C N Danson, C B Edwards, P Gottfeldt S Hancock, G J Hirst, C J Hooker, M H Key, A K Kidd, J M D Lister, C Moreira*, D Neely, G H C New*, P A Norreys, C J Reason, I N Ross, M J Shaw, W T Toner, D C Wilson* and B E Wyborn.

Rutherford Appleton Laboratory
*Imperial College, London

INTRODUCTION

During the past year a "Task Force" comprising the authors of this paper has been looking at the design of the proposed new Titania KrF laser system. The outcome of these deliberations has been a specification for the design and construction of the system and this has been published as a RAL report[1]. In this paper the main conclusions of that report will be summarised and the present status of the construction will be presented.

OBJECTIVES

The construction of Titania has been constrained by a very tight budget and the rate of funding has controlled the phasing of the plan. The aim has been to minimise the down time of the operational laser facility in the transformation of Sprite into Titania. Another objective has been to create a facility which has the potential for future development. In order to minimise costs, maximum reuse has been made of the present Sprite system including its building. Incorporation of an adjacent building (R7) into the new system has enabled a low cost expansion to the Titania configuration and will provide space for future upgrades.

Titania will provide 4 Raman beams which together generate one hundred times more energy than the present Sprite Raman beam. It will also provide a single CPA beam with an energy capability six times greater than that of Sprite, of which an increasing fraction will be deliverable to target as compression grating technology improves. Titania will produce UV light which has many advantages for laser plasma experiments. It will be unique in the world in its Raman mode and will produce higher brightness than any other laser in the UV, it will also be unique in its CPA mode which promises to provide the highest brightness and shortest pulse of any high power laser worldwide.

PERFORMANCE

Perhaps the most significant aspect of the existing Sprite laser system is that it has demonstrated that KrF lasers can offer users some major advantages (compared with glass) which accrue from short wavelength, high repetition rate and exceptional brightness. The Sprite system was however not constructed for the most efficient extraction of the basic energy of the KrF amplifier, the number of multiplexed pulses being too small and intended only for proof-of-principle of the KrF laser-pumped Raman-laser concept.

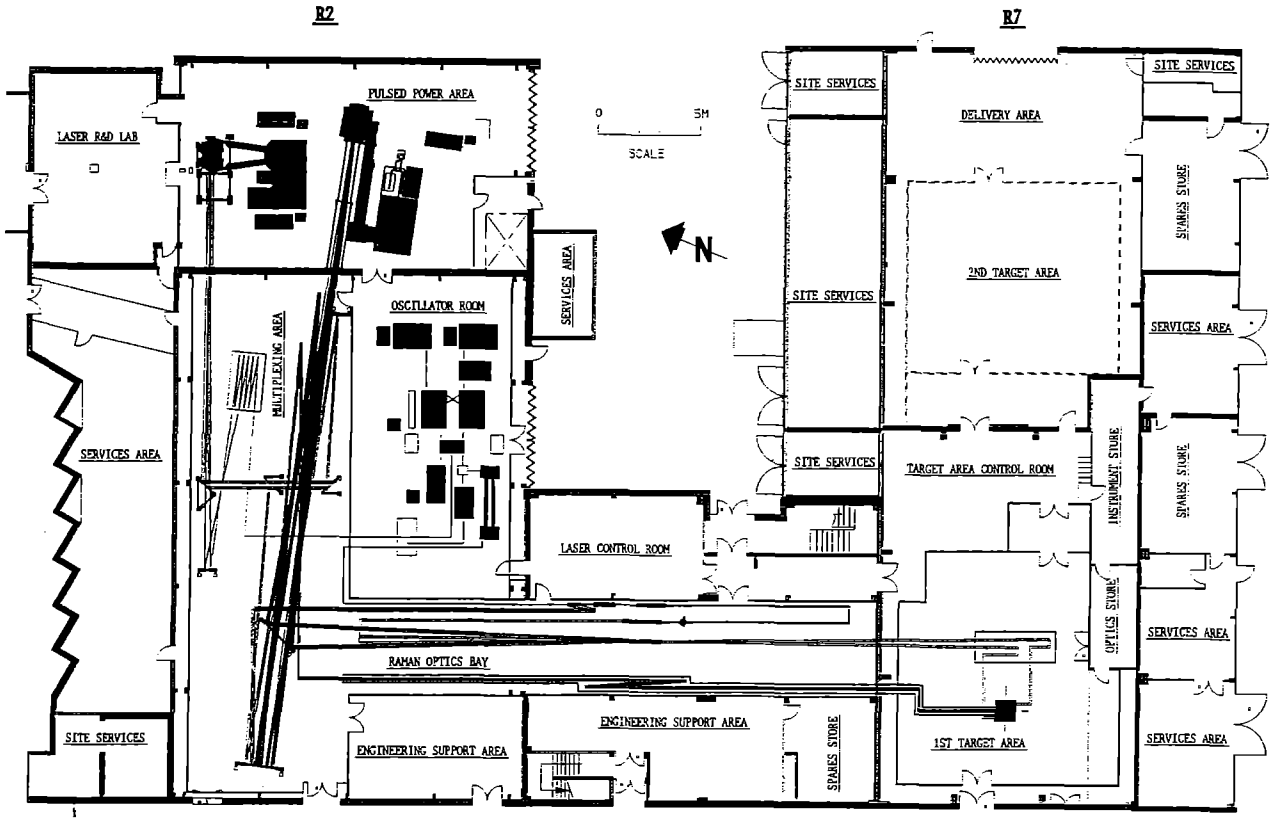

Fig. 1. Layout of the Titania Laser System

The new Titania system has been designed to provide a major upgrade in performance by increasing the number of multiplexed pulses (from 8 to 88), the final aperture (from 270 mm to 420 mm) and the final module run time from 60 ns to 170 ns. These changes will give about a one hundred-fold increase in the energy available to target (to over 360 J in the Raman mode) whilst the beam brightness is expected to be a factor of 10 higher than the existing Sprite Raman beam.

In the CPA single pulse mode of operation the ultimate improvement in energy capability and brightness could be over twentyfold, but here the grating damage threshold is the limiting factor with improvements expected from use of dielectric coatings rather than aluminium as at present. Pulse length reduction to 150 fs will also improve the brightness. Potentially, brightness approaching 10^{22} W cm^{-2}sterad^{-1} could be obtained.

Auxiliary beams in a glass laser system are added simply by increasing the number of parallel channels. In a KrF multiplexed system more channels can be added in series if sufficient amplifier run time is available. Two such auxiliary KrF channels have been incorporated in the design to provide short pulse probe beams or long pulse uniform irradiation at low intensity. Table 1. gives a summary of the on-target performance of the various modes of operation of the new laser system.

1. Raman Mode	
Number of beams	4
Beam diameter	150 mm
Wavelength	268 nm
Bandwidth	Transform Ltd
Pulselength range	30 - 500 ps
Maximum energy on target	365 J (Tp > 300 ps)
Maximum power on target	7.6 TW (Tp = 30 ps)
Beam divergence	< 3 μRd (1.7xDL)
Beam brightness	10^{21} W cm^{-2} st^{-1}
Focal irradiance (per beam f/4 optics)	5 x 10^{19} W cm^{-2}
Repetition Rate	20 shots per hour

2. CPA Mode	
Number of beams	1
Beam diameter	150 mm
Wavelength	248 nm
Minimum pulselength	150 fs
Maximum energy on target*	2.5 J
Peak power on target	> 15 TW
Beam brightness	5 x 10^{21} W cm^{-2} st^{-1}
Focal irradiance (f/4 optics)	3 x 10^{20} W cm^{-2}
Repetition Rate	10 shots per hour

3. Auxiliary Beams	
a. KrF probe beam (narrow band or chirped)	$\Delta\nu$ > 100 cm^{-1} chirped
Pulselength	30 - 500 ps
Energy	5 - 8 J
b. KrF broadband	$\Delta\nu$ > 60 cm^{-1}
Pulselength	1 - 6 ns
Energy	10 - 40 J

*CPA energy limit assumes a factor of 3 increase in the damage threshold of gratings.

***Table 1.** Predicted on-target performance of the Raman, CPA and auxiliary beams available from the Titania laser system.*

SITE

The proposed site for the new Titania laser system is shown in Fig 1 and will occupy the whole of the presently used building R2, the ground floor of the link building between R2 and R7 and most of building R7. The bulk of the laser is accommodated in R2 with the pulsed power amplifier modules at the East end as at present . A new oscillator room and extended multiplexer room occupy the remainder of the building. The Raman system is housed in the link building together with the laser control room and support areas.

This leaves the whole of building R7 available for target areas. Initially a single target area is proposed together with a control room. The floor area of the proposed new target area is comparable to the Vulcan TAE and TAW areas. The target area and laser control rooms are adjacent for ease of communication. The area in R7 on the east side is available for expansion as an additional target area. The area to the South of R7 is not built on and is available for future expansion of the whole system

THE LASER SYSTEM

The new laser system is based on technologies which have already been demonstrated and performance is a reasonable extrapolation, using bench marked codes, from the existing state-of-the-art .

In the front end it is proposed to operate two oscillators at 746 nm simultaneously (and eventually synchronously) to provide short (CPA) and long (Raman) pulses. A new solid state 746 nm amplifier is proposed to obtain much higher energy than at present before tripling and provide sufficient UV output at 10 Hz rep. rate for alignment of the main optical systems.

In modelling the KrF amplifier chain it has been found that sufficient drive for the Titania output module can be obtained from Sprite alone and so the present Goblin amplifier stage is not required thus reducing the system complexity and reducing ASE. The two e-beam-pumped KrF modules fit easily into the existing R2 bay with the Sprite amplifier remaining in its present position.

Energy is extracted from the final KrF amplifier module in 24 beams. Two beams provide the CPA channel and the KrF probe channel, two beams pump the Raman preamplifier and 20 beams pump the final Raman amplifier. Each of the KrF pump beams contains a four-pulse train and so energy is efficiently extracted from the final KrF amplifier by a continuous train of 88 pulses with a 1.5 ns separation. The final Raman amplifier is pumped four times with extraction on four Stokes beams each carrying up to 100 J energy.

The four Raman beams propagate to the target area in helium or argon-filled pipes which are necessary to reduce B-integral effects in the propagation path. A number of illumination geometries are envisaged including same side line focus or cluster and opposite side line focus or cluster.

The single KrF CPA beam will be the first beam to be amplified in the Titania module and after separation from the other beams will enter a vacuum pipe which will relay an image from the early part of the amplifier chain onto the compressor gratings. These will be situated close to the target area in the east end of R7. The chamber will be designed to be capable of accommodating both long and short focal length experiments with this very bright beam.

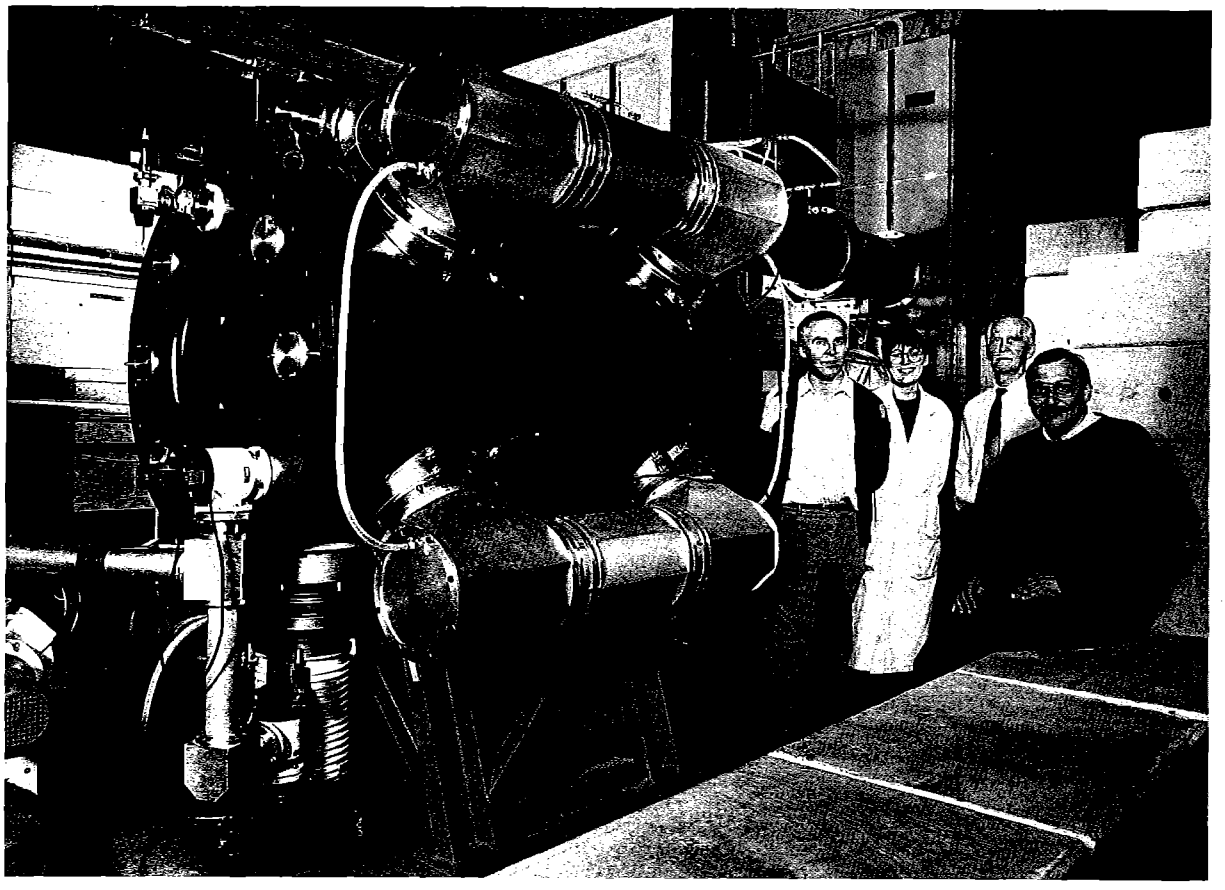

Fig. 2. Titania module under assembly in R7

PROGRAMME

The build programme for the Titania system is limited by the CLFs funding, by the the requirement to maintain operation of Vulcan during the build phase and the need to minimise the KrF facility shut down. It is therefore planned to extend the development of Titania over a further two years after the start of partial operation at the originally planned date of April 1996.

In FY 1994/95 Sprite will continue to operate as a user facility and the majority of expenditure will go on building the new target area and completing the Titania KrF amplifier module.

In FY 95/96 Sprite will be shut down and the installation of the major part of the new system will proceed. At the end of this financial year Titania will provide the CPA beam to target. In FY1996/97 half of the multiplexer optics will be installed and the Raman beams will be brought on stream operating at half power over a limited pulselength range. In FY1997/98 the remainder of the KrF optics will be installed and the oscillator upgraded to provide synchronous short and long pulses.

PRESENT STATUS (APRIL 1994)

The bulk of work to date has been on the new e-beam-pumped module and more recently on buildings. Fig 2 shows the present position with the big amplifier. The pulsed power system up to and including the laser triggered switches has been thoroughly tested up to full operating voltage (1200kV). The laser vessel has been foiled and tested under vacuum in the diode vessel. Current and voltage monitors have been constructed and calibrated. New radiation shielding is in place ready for the first e-beam shots. In the next year the diodes will first be tested shooting into inert gases to measure the diode-to-gas transfer efficiency. Following this laser gases will be used with the module running as a long pulse oscillator. An output energy of about 1.5 kJ is expected in this mode. It is hoped that a reasonably large number of test shots can be put on the module in this mode before strip down prior to moving to R2.

Thanks to allocation of some funds from the RAL Lab reserve rapid progress on the provision of buildings for Titania has been made. The whole of R7 has now been taken over by the CLF. The buildings on the south side have been completely refurbished and brought up to a suitable specification for use as storage or service areas. The target area has been roofed and most of the 4 metre high partition walls are in place. The wall between the link building and R2 in the line of the demultiplexed beams has been removed and various doors between R2/R7 and the link building have been put in. Installation of the partitioning for the demultiplexing area awaits the move of its present occupants.

REFERENCES

1. S Angood et al. *Specification for the Titania KrF Laser System*. Rutherford Appleton Laboratory Report RAL-94-014 February 1994

PERFORMANCE OF THE TITANIA LASER TRIGGERED SWITCHES

A K Kidd and M J Shaw

Rutherford Appleton Laboratory

INTRODUCTION

The Titania PFL switches are based on the radial diaphragm design that has been successfully tested at larger size on the Oberon pulsed power system. However, due to the lower line impedance and shorter pulse duration, a much lower inductance is required without increasing the electrical stress on the insulator surfaces.

The Titania switch is shown in Figure 1. The maximum operating pressure is 4 bar of SF_6 and the anode-cathode spacing is 50mm. Two alumina-loaded epoxy diaphragms support the pressure load. Shock isolation from the electrodes is obtained by spring washer stacks.

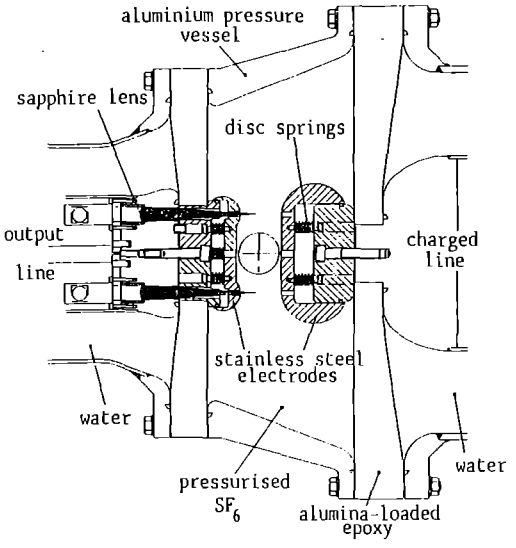

Figure 1: Cross-section through the PFL output switch.

The electric field distribution is calculated using the Magnet code[1]. The peak cathode field is 285kVcm^{-1} and the peak field on the insulator on the gas side is 95kVcm^{-1} for a charge voltage of 1200kV. The cathode breakdown field at 60psia SF_6 and 1.5μs charge time is calculated to be 320kVcm^{-1}.

TITANIA SWITCH PERFORMANCE

The switches were tested in self-break and laser-triggered mode up to the operating voltage of 1200kV. Figure 2 shows results of over 100 self-break shots performed on the switches. The self-break curves were obtained by adjusting the Marx charge voltage at each value of switch pressure such that the switch self-broke at the same point on the PFL charging waveform. Apart from three shots for which the switches self-broke early (possibly due to pre-ionization due to contaminants), all the data points within +/-3.0% of the best-fit curve. Above 40 psia SF_6, the self-break voltage increases less rapidly with SF_6 pressure.

Initial laser triggering tests have been performed at around 600kV on a single PFL switch incorporating Wollastonite-loaded epoxy diaphragms. Manufacturing problems resulting in small voids in the diaphragms caused failure on two of the four lines at a PFL voltage of 900kV. Two laser triggering channels are used since significant

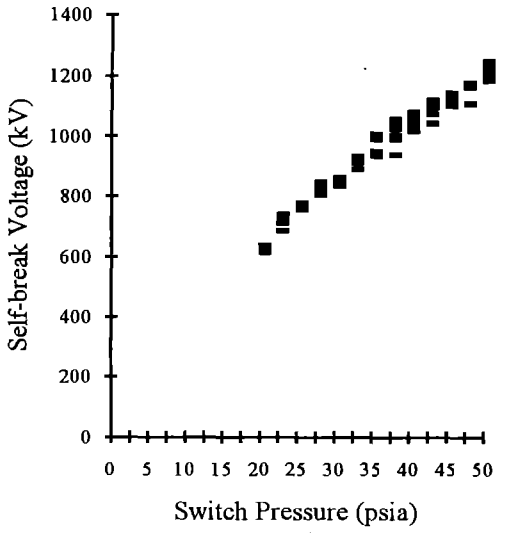

Figure 2: Self-break curve for the output switches

improvement in rise-time can be obtained this way. It is calculated that the effective insertion inductance of the switch is 110nH for a single channel and 60nH for two channels. A Lambda Physik EMG150 KrF discharge laser is used to deliver 25mJ of energy in each of two trigger laser beamlets to each spark channel. Each beamlet passes through a quartz window located in the output section of the PFL and is turned by a prism to be focussed by a 15cm focal length sapphire lens into the spark gap. Figure 3 shows two-channel laser triggering at 22.5psia. The switch was successfully triggered in two channels on 100% of shots.

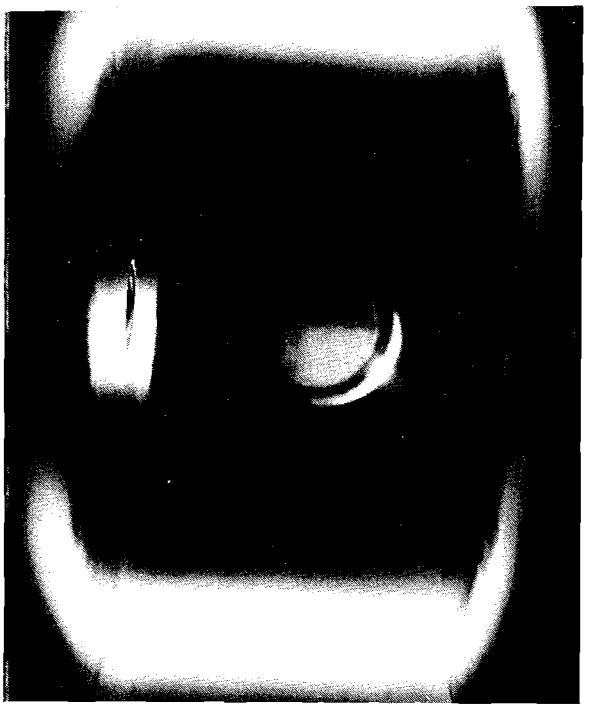

Figure 3: Two-channel laser-triggered operation of the Titania output switch at 22.5psia.

The arcs appear to be equally bright, suggesting that they carry equal currents. This results in a drop in switch inductance compared with one-channel operation. Figure 4 shows the PFL voltage measured at the switch cathode for two-channel operation. The load voltage risetime (10-90%) is reduced to 15ns compared with 25ns for one-channel operation. The system has been modelled with the BERTHA transmission line code which indicates the risetimes to be 15ns and 28ns. These results confirm the improvement in switch inductance by two-channel operation.

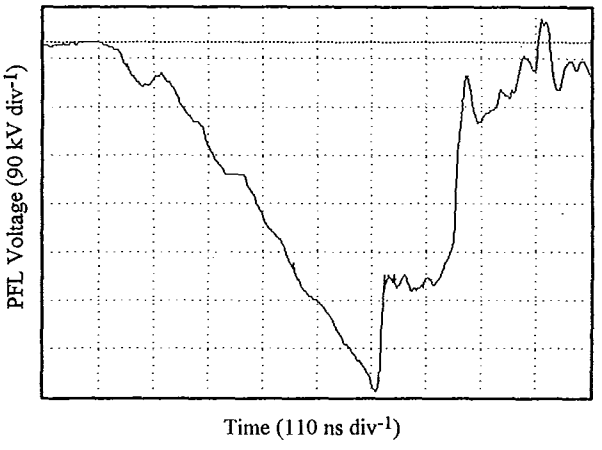

Figure 4: PFL voltage measured at the switch cathode for two-channel laser-triggered operation at 22.5psia.

The dependence of switching delay on the percentage of self-break voltage at which the switch was triggered is shown in Figure 5 for a SF_6 pressure of 35 psia. The self-break voltage is 1MV. The delay is defined as the period of time between the initiation of the laser pulse in the gap and the start of cathode voltage collapse. The experimental data indicates that the switching delay is a minimum of 10ns at 95% of self-break voltage, increasing to 95ns at 30%. The theoretical delay times τ (ns) are obtained from T H Martin's formula:

$$\rho\tau = 9.78x10^{13}\left(\frac{E}{\rho}\right)^{-3.44} \qquad (1)$$

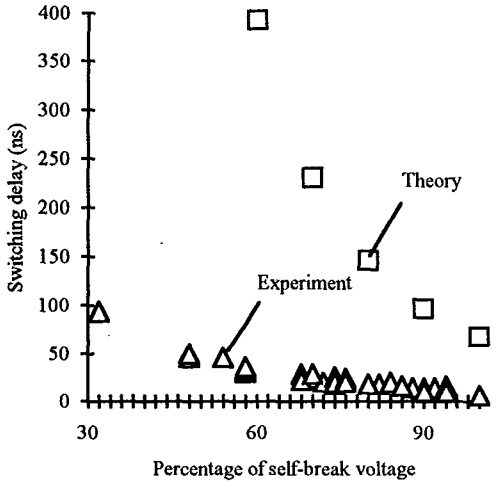

Figure 5: Switching delay as a function of percentage of self-break voltage.

where ρ is the gas density (g cm^{-3}) and E is the average electric field in kVcm^{-1}.

We are able to obtain delays which are 80-90% shorter than those predicted by equation (1) since the laser beams short out a large fraction of the inter-electrode gap during triggering, hence increasing the average electric field, E. Switch jitter was measured at 85-95% of self-break voltage to be 2ns (1σ) over 10 shots. This figure increased to 3ns at 70-80% of self-break voltage.

CONCLUSIONS AND PROGRAMME

The present status (April '94) of the Titania amplifier development is that the Marx, four PFLs and four switches have been tested up to the full design voltage of 1200kV in both self-break and laser-triggered mode into four resistive loads. The diode vessel has been installed. In the Spring of '94, the transport of the electron beams into the gas vessel will be tested. When satisfactory performance and foil longevity is obtained, the laser optics can be installed and full energy tests conducted (Summer/Autumn '94). In the Spring of '95, the pulsed power components can be stripped down in readiness for incorporation into the Titania laser system which begins operations in April '96.

References

1. S Angood, R Bailly-Salins, G J Hirst and M J Shaw.
Design of the Titania amplifier module.
Annual Report to the Laser Facility Committee, RAL-92-020, pp138-140 (1993).

SOLID RESISTOR TESTS

A K Kidd, H Medhurst, P S Carr[1] and M J Shaw

Rutherford Appleton Laboratory
[1]University of Portsmouth

INTRODUCTION

In order to reduce servicing time for the Titania system Marx generators, it is proposed to replace the existing copper sulphate resistors with solid ones. These are stacked linear disc element resistors supplied by HVR International Ltd[1]. Each resistor is a 32mm dia. x 25.4mm long ceramic carbon composite with metallised contacts. The resistors comprise a number of these elements held together by an insulating tie rod. In the resistors supplied by HVR, this tie rod was of 10mm diameter fibre glass. This was replaced by a 10mm diameter "Torlon" (Polypenco) rod for these measurements. Torlon is thought to be more suitable at high fields. Good electrical contact between discs, and between disk and aluminium alloy support, is achieved with a spring-loaded assembly (Figure 1).

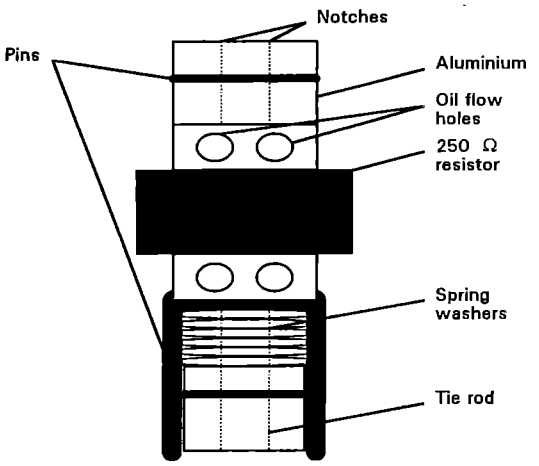

Figure 1: Construction of the solid resistor and compression-loaded assembly

Using data supplied by HVR, the breakdown electric fields are calculated to be 12.5 $kVcm^{-1}$ in air and 23.2 $kVcm^{-1}$ in SF_6. However, E-fields in excess of 30 $kVcm^{-1}$ will be encountered in oil in the Titania Marx.

SOLID RESISTOR TESTS

The single 240Ω resistor element to be tested is placed in series with a 33Ω (both measured on a Marconi LCR bridge) series protection copper sulphate resistor at the output of the trigger Marx generator. The Titania trigger Marx is a 10-stage Marx bank which is able to provide up to 500kV (ten capacitors, 50kV per capacitor).

Initial tests were performed on six individual 250Ω resistors with chamfered edges. The average breakdown voltage of the solid/copper sulphate resistor combination was around 200kV. There was no significant improvement in this figure by replacing the fibre glass rods as supplied with Torlon rods.

In a more detailed series of tests, a total of 426 shots were fired on 28 solid resistors with Torlon rods. The resistors and support structure were modified progressively to increase the voltage hold-off capability. The trigger Marx charge voltage was initially 14.5kV and is increased in 0.5kV steps until the resistors failed. The output voltage is 10 times the charge voltage. Figure 2 shows the voltage appearing on the copper sulphate/solid resistor combination for the case of an initial charge on the trigger Marx capacitors of 18.0kV.

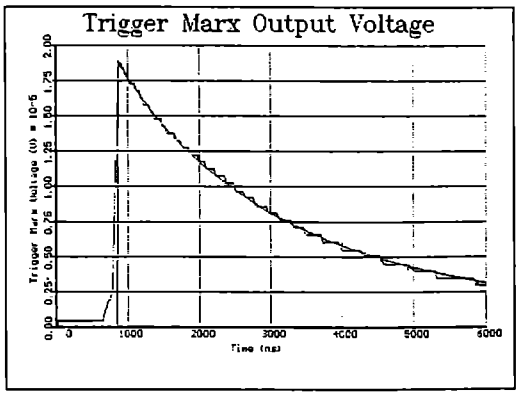

Figure 2: Voltage appearing on the trigger Marx output for an erected trigger Marx voltage of 193.8kV. Also shown is the modelled decay curve.

The peak voltage appearing across the resistor stack is 193.8kV; the rise-time (10-90%) of the applied pulse is 75ns and the FWHM is 1.67μs. The RC decay time constant is calculated from the best-fit curve (also shown) to be 2.5μs with a peak voltage of 195.0kV. For an erected capacitance of 22nF, the resistance of the combination of charging resistors (455Ω) and 33Ω copper sulphate/solid Resistor F combination is thus 169Ω, implying a solid resistance of only 136Ω. However, the solid resistor is measured on a Marconi LCR bridge to have a value of 240Ω (the nominal value is 250Ω). The discrepancy between the measured value and that obtained from the best-fit curve (Figure 2) is explained by the fact that the resistance is a strong function of electric field strength, E: the E-field dependent coefficient of resistance, α, is specified in the manufacturers' data sheet to lie within the range -1.0 to -7.5%/$kVcm^{-1}$.

The solid resistance $R_s(E)$ was remodelled assuming a functional form:

$$R_s(E) = R_0 \exp(-\alpha E) \qquad (1)$$

where R_0 is the solid resistance with zero applied E-field. At each step, the value of $R_s(E)$ is calculated iteratively from (1) so that the resistance and electric fields are self-consistent. The best-fit curve for the voltage appearing on the copper sulphate/solid resistor combination is shown in Figure 2. The E-field dependent coefficient of resistance, α, used is -2.0%/$kVcm^{-1}$ for which the theory and experimental curves agree closely. R_s increases from 80Ω to 205Ω over 6μs, during which time the voltage across the solid/liquid resistor combination decreases from 200kV to 25kV. At the upper range of voltage applied across the solid/liquid resistor

combination (237.9kV), the true solid resistance is only 30% of the zero-field value.

A series of modifications were made to the original resistor structure in order to increase breakdown voltage. The principal investigations involved the effect on breakdown voltage of the following modifications:

(1) Notches in the support structure to allow the flow of oil
(2a) The application of an anti-tracking coating
(2b) The removal of the chamfers
(2c) Radiusing of the resistor edges
(3) The addition of field shapers
(4) Vacuum oil impregnation
(5) A more elaborate aluminium structure to allow greater flow of oil
(6) The removal of the resistor from the oil for various periods prior to positioning in the trigger Marx tank

The average breakdown field of solid resistors with chamfers was found to be 56 $kVcm^{-1}$. A resistor was tested with notches drilled along the length of the aluminium support assembly; the maximum E-field developed across the resistor without breakdown, E_{max}, was 50 $kVcm^{-1}$. A further resistor broke down at 37 $kVcm^{-1}$, although it is believed that this resistor was tracked prior to the present testing. Resistors were tested without notches drilled in the aluminium support assembly; E_{max} lay within the range 43-45 $kVcm^{-1}$. For resistors which are coated with an anti-tracking coating and which have the chamfers removed; with no notches drilled in the aluminium assembly, E_{max} lay within the range 42-48 $kVcm^{-1}$, which is comparable to the values obtained with the coated resistors with chamfers. If the rough edges on the circumference of the resistor are removed, and the support assembly has notches, then there is an improvement in E_{max} of 5-10% to 46-50 $kVcm^{-1}$. Without the removal of the rough edges, E_{max} is 46 $kVcm^{-1}$. Field shapers in the form of grading washers were placed on the ends of an uncoated resistor to inhibit breakdown; E_{max}, was 55 $kVcm^{-1}$. In the case of a coated resistor, E_{max} is 50 $kVcm^{-1}$.

Small increases in E_{max} of around 10% have been achieved with these modifications. Larger increases are, however, achievable by impregnating the resistors with transformer oil under vacuum. Uncoated resistors were removed from the oil impregnation bath and immediately placed under oil in the trigger Marx. Notches were drilled in the support structure and E_{max} was found to lie in the range 57-66 $kVcm^{-1}$ - an improvement of up to 38% over the original chamfered resistor. Field shapers were placed on the ends of the resistors; under these conditions, E_{max} lies in the range 64-66 $kVcm^{-1}$. Impregnated resistor elements having anti-tracking coatings were found to have breakdown voltages around 10% lower than for the uncoated elements.

In view of the success achieved with the removal of trapped air from the assembly, a more elaborate aluminium structure to allow greater flow of oil was constructed (Figure 1). The collars are fitted at both ends of the resistor and are push button guards with 5mm holes drilled through the periphery. Uncoated resistors S and U were not vacuumed and placed directly in the trigger Marx tank with the new aluminium structure. E_{max} dropped to 46-54 $kVcm^{-1}$.

It is important that the benefits gained from vacuum impregnation are not lost if the resistor is exposed to air for any length of time following installation in the Marx tank. A number of resistors were fitted with the new aluminium structure, vacuum impregnated and removed from the oil for various periods of time prior to insertion in the trigger Marx.

There is in general little deterioration in E_{max} for resistors without field shapers that have been removed from the oil for about 1 day (65$kVcm^{-1}$) and those that have been removed for 11 days (62$kVcm^{-1}$). For resistors with field shapers, there is actually a slight increase from 60 to 62$kVcm^{-1}$.

The results of the solid resistor tests are illustrated graphically in Figure 3. The dotted line represents E_{max} = 56 $kVcm^{-1}$. It can be seen that *all* resistors with E_{max} below 56$kVcm^{-1}$ are those that have not been vacuum impregnated (LHS of the graph), whereas not one of the resistors that have been vacuumed failed below this value (RHS). The average value of E_{max} for all non-vacuumed resistors (12 resistors) is 47.9 $kVcm^{-1}$, whereas for vacuumed resistors, the value is 61.5 $kVcm^{-1}$ (14 resistors), an improvement of 28%.

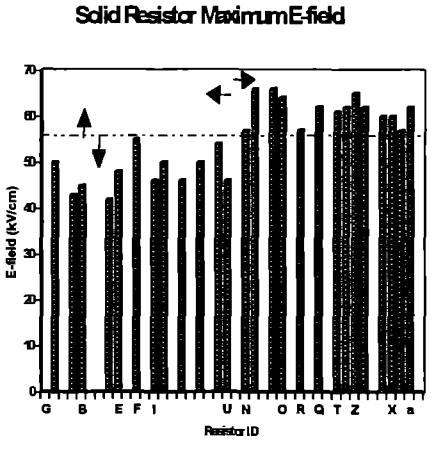

Figure 3. Solid resistor maximum E-fields

It is interesting to note that in all resistor tests except those evacuated under oil, the resistors shattered on failure, usually into three or more pieces. However, for evacuated resistors M and N, there was no shattering but evidence of surface tracking and erosion and evidence of a radial crack. For all resistors tested, the shot which caused failure was accompanied by a loud bang. However, for resistors that were vacuumed, the shot preceding the failure was accompanied by a quieter noise. There appears to be no difference between the failure trace of this resistor and that of vacuumed resistors.

CONCLUSIONS AND FUTURE WORK

It has been demonstrated that vacuum oil impregnation of solid resistors reliably produces E_{max} in excess of 55$kVcm^{-1}$. The resistors are unchamfered, uncoated and without field shapers, simplifiying their construction. Removal from oil for periods of up to 11 days has been shown to have little effect on E_{max}. The average value of E_{max} for all non-vacuumed resistors (12 resistors) is 47.9 $kVcm^{-1}$, whereas for vacuumed resistors, the value is 61.5 $kVcm^{-1}$ (14 resistors). It is thus recommended that solid resistors may be used to replace copper sulphate resistors in the Titania and Sprite Marx tanks where resistors may be stacked to increase resistance and voltage hold-off capability. It is however essential to model the performance of the Marx with particular attention to the dependence of the values of solid resistances on the applied E-field.

Reference

1. HVR International Ltd, Bede Industrial Estate, Jarrow, Tyne and Wear, NE32 3EN. England.

TITANIA DIODE CURRENT AND VOLTAGE MONITORS

M J Shaw, H T Medhurst, A K Kidd and S Angood

Rutherford Appleton Laboratory

INTRODUCTION

Accurate measurements of the current and voltage at the TITANIA diodes are extremely important in that they allow the diode power and energy to be calculated which in turn is required for calculation of the efficiency of the laser system. In a departure from previous practice on Sprite it was decided to use purely differential monitors for these functions due to their simplicity of construction and the ease of numerical integration from digitised voltage waveforms.

B-DOT MONITORS

The four 4 Ω output lines after the PFL switch each bifurcate into two 8 Ω lines for feeding into the diode vessel. The sum of the currents flowing into each vacuum insulator is a good measure of the total diode current. For a matched load we expect a peak current of 75 kA per insulator (600 kV in 8 Ω) with a rise time of about 25 ns.

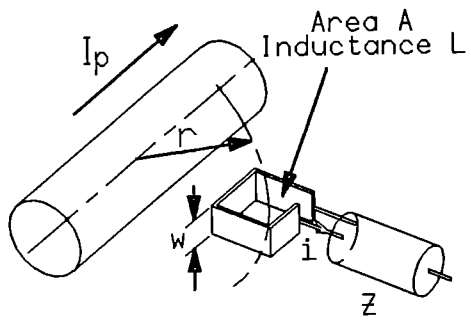

Fig. 1. Schematic diagram of a B dot loop

Fig. 1 shows a pick up coil situated inside a coaxial line carrying a current I_p at a radius r from the axis. If the area of the coil is A and it is oriented to link the azimuthal B field then the mutual inductance between the primary coaxial current and the secondary coil is given by flux in secondary/current in primary ie.

$$M = \frac{\mu_0 A}{2\pi r} \qquad (1)$$

The equation giving the current i in the secondary is:

$$L\frac{di}{dt} + iZ = -M\frac{dI_p}{dt} \qquad (2)$$

where L is the self inductance of the pick up coil and Z is the current viewing impedance (usually 50 Ω). For the coil to operate purely in the differential mode (ie as a B dot loop) it is necessary that the first term is small compared with the second. This is true if $L/Z \ll t_p$ where t_p is the pulsewidth. In this case the voltage across the load impedance approximates to

$$u = -M\frac{dI_p}{dt} \qquad (3)$$

and if the output voltage is integrated we get

$$\int u\,dt = -MI_p \qquad (4)$$

The sensitivity of the B dot loop is thus simply M volt secs/amp which is also the unit of inductance viz Henry. For the simple coaxial system in question the sensitivity is 2A/r (nH) where A and r are in cm. The neglected di/dt term introduces an e-folding risetime of $\tau = L/Z$ and so fast response requires a low inductance coil. For a strip coil of width w (cm) the inductance is given by L = 12.6A/w (nH) and so L can be reduced by increasing the width of the strip.

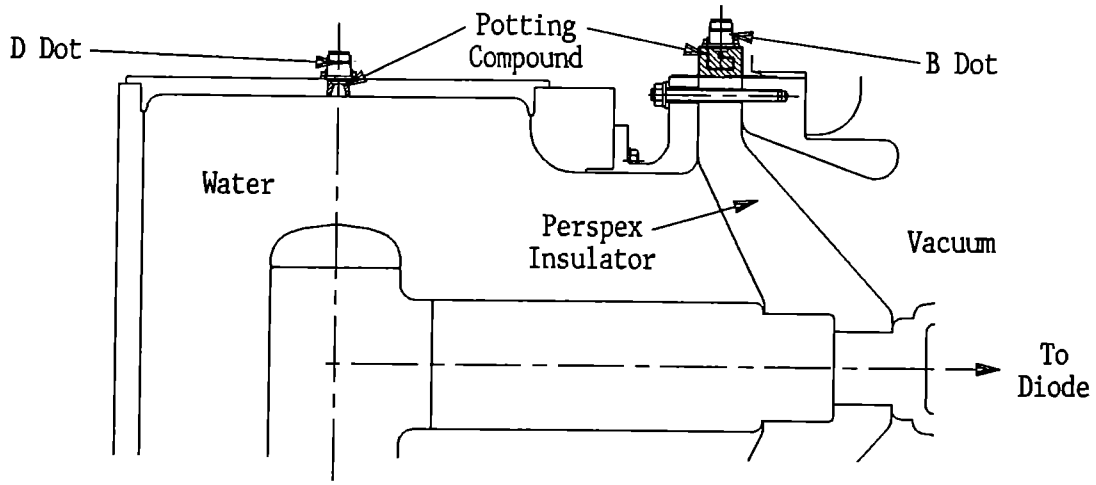

Fig. 2. Section through TITANIA vacuum feedthrough.

Fig 2 shows a section through the actual B dot monitor. The bolts holding the line outers to the laser vessel are insulated and the return current flows in a 100 μm copper sheet held in contact with the flange ends by large hose clips. The B dot loop is mounted inside a "blister box" about 10 cm long constructed from the same copper sheet with soldered joints. A slot is cut in the current sheet so that the return current flows outside the coil. The inside of the box is filled with epoxy potting compound (ε = 5.5) to maintain dimensional stability.

The area of the coil is 2.2 cm and its width is 1 cm. This gives a self inductance of 28 nH and a monitor risetime of 0.55 ns, much faster than the expected diode current risetime. The mutual inductance to the coaxial line is 0.2 nH ie a calibration factor of 200 nVs/kA. The space between the coil and the case can be regarded as a transmission line having an impedance of about 80 Ω and a transit time of 2 ns. The reasonably good match into 50Ω appears to prevent any high frequency ringing. The coil when excited by a fast (3ns rise) pulse integrated to give a faithful reproduction of the test pulse.

The coils were calibrated in-situ on the TITANIA vacuum insulator by discharging two 200 ns pulselength 50 Ω cables in parallel into the 4 Ω Tee piece and short circuiting the line on the vacuum side of the feedthrough. The cables could be charged to 25 kV giving a peak current of 1 kA. The calibration was done without water in the lines giving a current risetime of about 100 ns. By 150 ns the current was in the steady state and a good calibration could be arrived at. The monitor could be moved around the perimeter of the feedthrough and this showed that the current was not quite azimuthally symmetric being about 10% more for the shortest current return path compared with the longest. A position (halfway between the top dead centre bolt and the next bolt towards the middle of the vessel) was found which appeared to read the mean current and this was used for calibrating each of the monitors. Eight monitors were constructed and calibrated. The sensitivities ranged between 70 and 100 nVs/kA and could be reproduced to about 2%. The discrepancy between the calculated and calibrated factors is presumably due to the non-coaxial nature of the current flow in the shielding "blister". Under normal operating conditions the peak monitor voltage will be about 300 V and the cable and oscilloscope attenuators need to be chosen accordingly.

D DOT MONITORS

Fig 2 also shows the location and a section through the D dot monitor which measures the voltage on the domed end of the feed line just before the vacuum insulator. This is the nearest convenient place to the diode to measure the voltage and the end plate is removable in case changes need to be made. The measured voltage can be related to the actual diode voltage by a knowledge of the current flowing (given by the B dot monitor) and the inductance of the diode feed which amounts to about 60 nH per feed.

The D dot monitor takes the form of an insulated "button" mounted flush to the wall of the water line directly connected to a coax cable. If C_w is the capacitance between the high voltage(V) feed and the probe, then a current $i = C_w\, dV/dt$ will flow into the cable giving rise to a voltage $u = ZC_w\, dV/dt$ where Z is the cable impedance. Hence integration of u will give the required high voltage. In practice the actual situation is more complicated than this and Fig. 3 gives the appropriate circuit diagram. R_w is the resistance of the water between the high voltage line and the probe which has a capacitance C_p to ground. Considering current flowing in the two arms gives:

$$C_w\frac{dV}{dt}+\frac{V}{R_w} = -(C_w+C_p)\frac{du}{dt}+u\left(\frac{1}{R_w}+\frac{1}{Z}\right) \qquad (5)$$

For the probe to act correctly as a differential monitor it is important that the second term on the LHS is small compared to the first. This will be true if the water resistivity is high enough so that $R_wC_w >> t_p$ ie the pulse length to be measured is very much less than the self discharge time constant of the water. In our case this means working with about 1 MΩ-cm water (R_wC_w = 7μs) compared to our pulselength of 170 ns. Neglecting terms involving R_w eqn (5) can be integrated giving a response to a step function of amplitude V of:

$$\int u\,dt = ZC_wV\left[1-\exp\left(-\frac{t}{Z(C_p+C_w)}\right)\right] \qquad (6)$$

The risetime of the integrated signal thus depends on the sum of the water and probe capacitances but the integration time constant is just ZC_w as in the simple analysis.

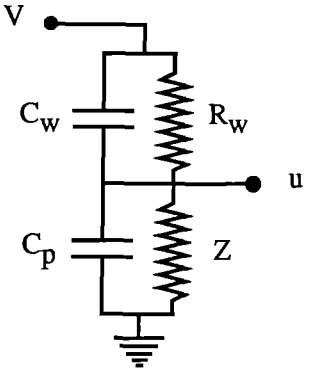

Fig. 3. Equivalent circuit for the D dot monitor

For the TITANIA probe C_w is in a somewhat unusual location and the capacitance is best estimated from a knowledge of the electric field at the end plate. The capacitance is then calculated from Gauss's Law viz. $CV = \varepsilon\varepsilon_0 \mathbf{E}.d\mathbf{S}$. The field is best approximated to the field between concentric cylinders

$$E_b = \frac{Va}{b(b-a)} \qquad (7)$$

where b is the larger and a the smaller radius. In this way the capacitance was estimated to be 0.3 pF. The capacitance of the probe to ground is more directly calculated to be 3 pF and Z is 50 Ω. The rise time is thus 150 ps which is much less than the estimated risetime of the voltage pulse (25 ns). The integration time constant is 15 ps giving a calibration factor of 15 nVs/kV. The peak differential voltage expected on the coax cable is about 400V. The probes need to be calibrated in-situ with high resistivity water against a known voltage pulse. This calibration remains to be done.

LASER BEAM SPATIAL INTENSITY CONVERSION WITH BINARY PHASE ZONE PLATE ARRAYS

D A Pepler[1], T H Bett[2], C N Danson[1], I N Ross[1], R M Stevenson[2]

[1]Rutherford Appleton Laboratory
[2]Atomic Weapons Establishment (A), Aldermaston, UK

INTRODUCTION

The Fresnel binary phase zone plate (PZP), laser-beam smoothing technique[1], has shown considerable improvements to the data from laser/plasma interaction studies and development has continued on the design and manufacture of these devices.

The PZP consists of an array of binary phase Fresnel zone plates, where each zone plate behaves as a lens, similar to the array of Deng *et al*[2], but with multiple foci corresponding to each of the diffractive orders. The principle of the beam smoothing scheme can be explained by a simple geometric optics analysis, shown in Figure 1. The PZP is positioned near a principal refracting lens of focal length F_P that focuses each positive 1st order beamlet onto a surface corresponding to the focal length of the combination of F_Z and F_P.

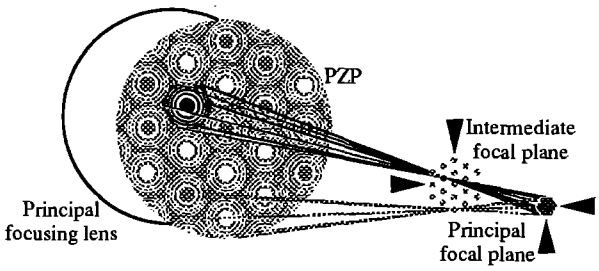

Figure 1 PZP focusing scheme

Each diffraction order result in a zone plate focal length inversely proportional to the order number, hence there are similar combination surfaces corresponding to both the positive and negative higher orders also. This is illustrated schematically in Figure 2 but with only the +/- 1st and +/- 3rd orders shown. The positive and the negative orders respectively focus before and after the principal focal plane. In the principal plane, all the diffracted beamlets are concentric with the optic axis, and the beamlet overlaps are the same size for each pair of orders, but scale with the order number. The superposition of the beamlets is the basis for the intensity averaging to produce the final distribution, which is not dependent on the input beam intensity distribution provided a sufficiently large number of beamlets are produced.

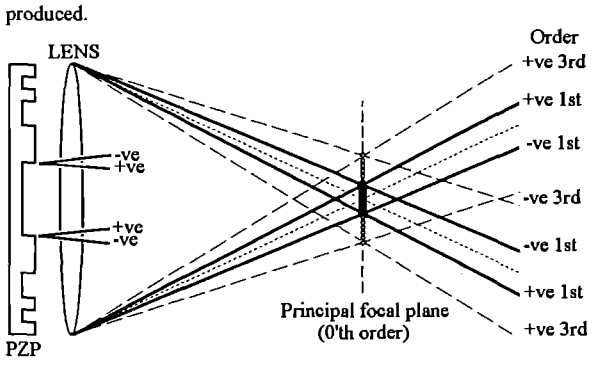

Figure 2 Intermediate focal planes for +/- 1st and +/- 3rd orders

From simple geometry the beam spot size W_S on the target positioned in the plane of the principal focal lens can be calculated for the two cases of the PZP before or after the lens and separated by a distance δ.

When the PZP array of 1st order focal length F_Z is before the lens of focal length F_P, the geometric spot size is independent of δ and is directly given by.

$$W_S = W_Z \frac{F_P}{F_Z} \qquad (1)$$

When the PZP array is positioned between the lens and its focal plane the expression above requires an additional correction term, and the geometric spot size then becomes

$$W_S = W_Z \left(\frac{F_P - \delta}{F_Z} \right) \qquad (2)$$

In the focal plane of the principal lens there are a number of interactions taking place that must be taken into account. Firstly, the diffraction pattern from each of the elements makes up the underlying distribution from each of the cells. Secondly, each of the foci at the combination focal surface from the positive 1st order acts as a point source for the generation of a fixed multi-beam interference pattern. Thirdly, any residual undiffracted or 0'th order light is focused and produces a central intensity spike.

THEORETICAL PZP DIFFRACTION EFFICIENCY

Two approaches have been taken to investigate the efficiency of the elemental zone plate cell. The first uses a Fourier analysis whilst the second relies on the fact that the intensity distribution of interest lies in the far-field of a lens and a Fraunhofer diffraction approximation may be applied.

The complex amplitude transmittance function of a single phase zone plate may be represented by a periodic square wave function, of period 2π, and a Fourier series expansion can then be used to determine the amplitude distribution in the various diffraction orders. When $\delta = \pi$ as in a standard phase zone plate this yields

$$F_P(\theta) = i\frac{2}{\pi}\sum_{n=-\infty}^{\infty} e^{-in\theta}\frac{\sin(n\frac{\pi}{2})}{n} \qquad (3)$$

Examination of this expression quickly shows that the theoretical diffraction efficiency into each of the even orders is zero, and only odd orders are present. Assuming monochromatic plane wave illumination, the fractional intensity into each odd order may be calculated. Table 1 shows the fraction of the incident flux that goes into each order (inclusive of both positive and negative order contributions). Since the various order spots overlap in the principal

Order	Fraction of incident flux	Total into each order	Total within order area	Total in 1st order area
1	$4/\pi^2$	0.8106	0.8106	0.8106
3	$4/(3\pi)^2$	0.0901	0.9007	0.8206
5	$4/(5\pi)^2$	0.0324	0.9331	0.8219
7	$4/(7\pi)^2$	0.0165	0.9496	0.8222
9	$4/(9\pi)^2$	0.0100	0.9596	0.8224

Table 1

lens focal plane, contributions from higher orders to the lower orders need to be included. For example, since the 3rd order spot is 3x larger than the 1st order spot, and hence 9x higher area, only 1/9th of the total energy from the 3rd order should be included. The total bounded by the 1st order area is shown in the final column.

The diffraction analysis of a single phase zone plate structure follows that of Ross[3]. Circular symmetry is assumed and the plate is treated as a series of annular zones with the amplitude disturbance, U(P), from the plate calculated at a point P in the principal focal plane as a summation of the contributions from each of the zones. The amplitude disturbance, U(P), is then given by

$$U(P) = 2\pi a^2 Ci\left(N\frac{2J_1(kw\sqrt{N}a)}{kw\sqrt{N}a} + 2\sum_{n=1}^{N-1}(-1)^n n\frac{2J_1(kw\sqrt{n}a)}{kw\sqrt{n}a}\right) \quad (4)$$

where C is a constant, $k = 2\pi/\lambda$, $w = r/f$, where r is the radius in the focal plane of the lens focal length f, J_0 is a Bessel function of the 1st kind, and the intensity, $I(P) = |U(P)|^2$

The intensity at each point is computed as a function of radius r in the focal plane then numerical integration of the radial intensity is used to produce Table 2 for comparison with the Fourier analysis.

Order	Total within order area
1	0.805
3	0.928
5	0.960
7	0.975
9	0.983

Table 2

Reasonable agreement is achieved with the ~ 2% difference believed to be due to numerical approximations of the Bessel functions and numerical integration errors.

The Bessel analysis was also used to investigate the effects of varying the number of zones in the zone plate to determine an optimum structure. It was noted that increasing the numbers of zones within a cell resulted in higher spatial frequency structure which would be more suitable for averaging multiple elements, and that a minimum of 4 zones was required. The structure of the zone plate rings was varied and the most significant effect was found to have a half width zone on the outer edge of the cell and / or to reduce the size of the central zone, the results of which were to reduce the intensity of the central spike to the same general level as the main part of the intensity distribution. Figure 3 shows a lineout where a cell of 10 zones with a half width outer zones is used.

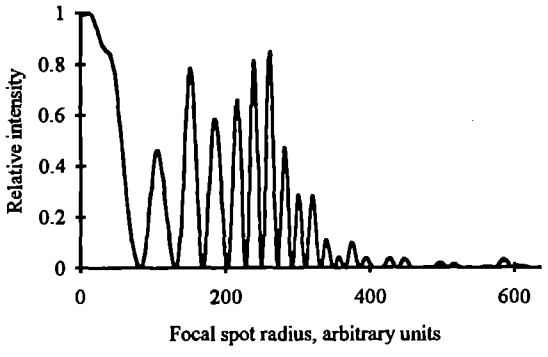

Figure 3 Bessel function analysis of 10 zone Fresnel cell, with a half-width outer zone

FABRICATION TOLERANCE

Errors in the fabrication process increase the intensity of the central spike and can manifest themselves in two ways :-

1) the photo-resist layer thickness does not produce exactly a π phase step
2) the 0 and π phase areas are not exactly the same

Both these situations can be investigated through the Fourier series expansion method used earlier. An incorrect thickness can be investigated through a non π phase step δ and the effects of over or under exposure can be considered through using a non $\pi/2$ angle ϕ at which the phase step occurs. These are considered in turn.

Assuming that $\phi = \pi/2$ and the zones have equal areas then the Fourier series expansion of the complex amplitude transmission function for a phase step δ reduces to

$$F_P(\theta) = \cos\frac{\delta}{2} + i\frac{2}{\pi}\sin\frac{\delta}{2}\sum_{n=-\infty}^{\infty} e^{-in\theta}\frac{\sin(n\frac{\pi}{2})}{n} \quad (5)$$

From this the 0'th order amplitude term is squared to convert it to intensity and then plotted against the relative phase step δ, centered on the minimum angle, π, in Figure 4.

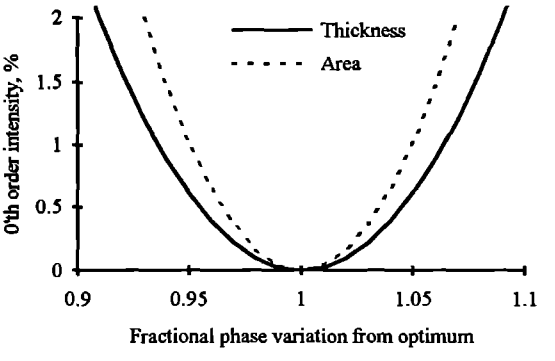

Figure 4 Graph showing 0'th order intensities produced from fabrication errors

The fabrication accuracy on thickness has been found to be approximately 5% from measurements made on several samples. Therefore layer thickness deviation from the optimum results in less than 1% of the light into the 0'th or undiffracted order.

In the case of a zone area error, it is assumed that $\delta = \pi$ and the Fourier expansion is taken as a function of ϕ. This results in the following expression.

$$F_P(\theta) = i(\frac{2\phi}{\pi} - 1) + i\frac{2}{\pi}\sum_{n=-\infty}^{\infty} e^{-in\theta}\frac{\sin(n\phi)}{n} \quad (6)$$

Again the 0'th order amplitude term is squared to convert it to intensity and is also plotted in Figure 3, against relative ϕ. In this case the optimum phase is $\pi/2$ and a 5% error produces about 1% into the 0'th order.

POINT DESIGN PROCEDURE

Several approaches can be taken in any given situation to determine the PZP array parameters. However in general the focal length of the principal lens F_P, the wavelength and the focal spot size W_Z are pre-defined and effectively only W_Z and F_Z need to be calculated. From

the equality $W_S/W_Z = F_P/F_Z$ of equation 1 it can be seen that in principal W_Z and F_Z can be any value. In practice W_Z is chosen to be as small as possible to get a large number of beamlets for good averaging, but large enough in order that sufficient zones are present within a cell for high spatial frequencies to be obtained.

The design procedure outlined here starts from the assumption of W_Z and from simple manipulation of equation 1, the calculation of F_Z. The number of zones within each cell is then calculated, to ensure that there are more than the minimum of four. From the text book equation for a zone plate, it follows that the highest number of zones in a cell of size W_Z, is given by,

$$m_{max} = \frac{W_Z^2}{4\lambda F_Z} \qquad (7)$$

If this value is less than the minimum, then by setting the value of m to the required number of zones, a modified value of W_Z' is obtained, given by,

$$W_Z' = 4\lambda m \frac{F_P}{W_S} \qquad (8)$$

F_Z is then modified to F_Z' to maintain the equality $W_S/W_Z' = F_P/F_Z'$.

MASK DESIGN

Trial PZPs were fabricated where all cells had identical focal lengths, and where cells in any one plate had random variations of 1%, 3% and 10% in focal lengths. When placed in a green HeNe laser at 543 nm the best performance was achieved with the plate with a 1% variation in focal lengths and this was chosen for the subsequent plates. A 3% difference in wavelength being within the manufacturing tolerance of the surface layer.

The flexibility of design allows the cell structure to be easily modified to produce different focal spot shapes, Jaroszewic *et al*[4]. This aspect has begun to be explored through the generation of zones within square cells, as shown in Figure 5. The result of the square cell

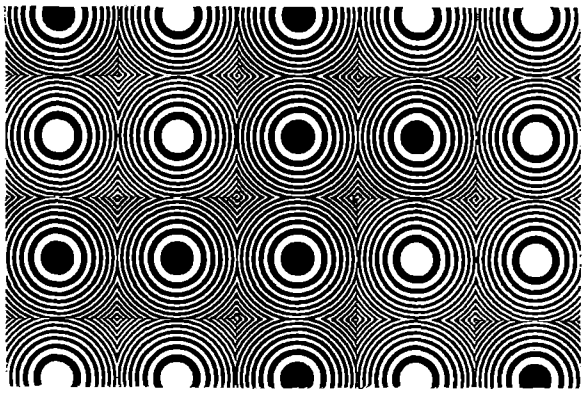

Figure 5 PZP mask to generate a square focus

boundaries is to produce a square focus, since the Fresnel zone within each cell is simply imaged into the target plane. To date PZPs with only one cell size have been used, but by varying both the size of cell and the focal length to obtain the same size focal spot, plates can be constructed with combinations of cells with various number of zones, as shown in Figure 6. Because of the different spatial frequency structure that results from each cell, an enhancement of the beam smoothing is expected.

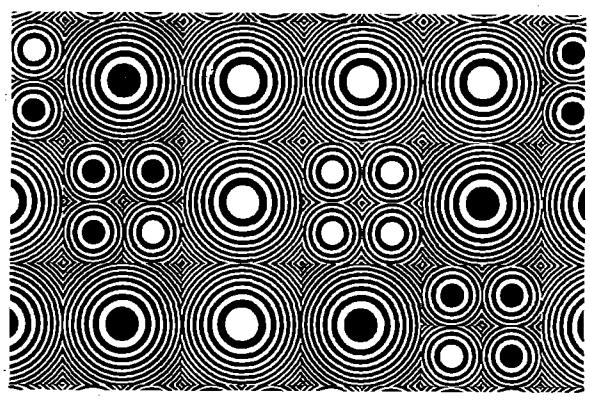

Figure 6 Combination PZP mask to generate a square focus with enhanced beam smoothing

In principle it is also possible to build up more complex foci using a mosaic of various shaped cells with the Fresnel zones of different focal lengths and / or of different axial positions within those cells. Figure 7 shows a simple application of this, with each Fresnel zone being masked by a shape of a 'H'. Due to this shape being rotational symmetric through 180°, this shape is imaged in both the positive and negative orders. Thus this mask produces a focus which is also a 'H'.

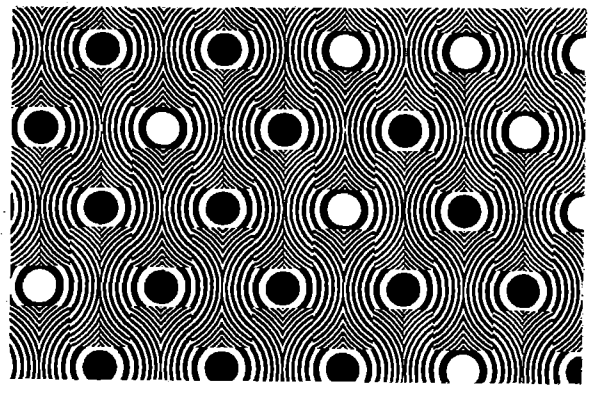

Figure 7 PZP mask to generate a 'H' shaped focus

The PZP plates are not specific to a particular near field intensity pattern provided several elements can be encompassed by the beam and therefore may be relevant to other laser applications requiring uniform beams on a target, provided high spatial frequencies are not detrimental to the laser absorption process.

Ideally, 100% diffraction efficiency into the 1st order is required to place all the energy into the focal spot and the PZP would behave in a similar way to the Deng lens array. This is possible in a diffractive component through increasing the number of phase levels. With a continuous phase transition the device becomes a Fresnel lens array which although possible to fabricate, is significantly more difficult than a binary phase plate. This will be assessed in future work and alternative non-periodic binary structures will be further investigated.

The PZP combines the simplicity of design and fabrication of the random phase plates with the advantage of near field target placement.

REFERENCES

1. R M Stevenson *et al*, Optics Letters **19**, No 6, 363-365 (1994)
2. X Deng *et al*, Applied Optics **25**, 377- 381, (1986)
3. I N Ross, Optics Communication (In press), (July 1993)
4. Jaroszewicz *et al*, J Mod Optics **4**, 601-612, (1993)

STUDY OF THE FAR-FIELD INTENSITY DISTRIBUTION OF A RANDOM-PHASED BEAM

T.Ceccotti, S. Bastiani, A.Giulietti, D.Giulietti[1], C.Danson[2].

Istituto di Fisica Atomica e Molecolare via del Giardino, 7 - 56127 Pisa, Italy.

[1]Dipartimento di Fisica, Università di Pisa
[2]Central Laser Facility, Rutherford Appleton Laboratory, Chilton, Didcot, UK.

INTRODUCTION

Random Phase Plates (RPP) are currently used as smoothing devices for high power laser beams. They are very easy to employ and effective to reduce undesired effects of far field non-uniformities once they have been properly designed for a given application and a given focusing optics. In fact the diffraction from each phase cell reduces large-scale perturbations in the focal spot, but small-scale perturbations are enhanced by the interference between a large number of phase cells.

The intensity distribution in the far field of a beam of diameter D focused with a focal length f, can be roughly represented as a set of randomly distributed beamlets, each having a cross section of $2\lambda f/D$ and a depth of $4\lambda(f^2/D^2)$, both zero to zero intensity[1]. The whole focal region has a cross section $2\lambda f/d$ and depth of $4\lambda(f^2/Dd)$, where d is the size of the dephasing structures. The first point is that the use of RPP increases the overall spot size and consequently limits the available irradiance on target. Higher intensities can be achieved with larger cells, but if the number of cells involved is too small, the large-scalelength smoothing is no longer effective.

Both transversal and longitudinal dimensions of the small scale intensity structures produced by RPP are relevant for many applications, including ICF. In fact most of the laser stimulated plasma instabilities in the coronal plasma surrounding a fusion target, have a distinct spatial grow-length along the beam, which has to be compared with the depth of the RPP generated microstructures. In what concerns filamentation, the minimum size of the intensity modulations that are able to grow against diffraction, have to be compared with the transversal size of the microstructures. In both cases f/numbers as small as possible are convenient to avoid the instability growth, but it is also necessary to account for the local increase in intensity due to the multi-cell interference. To improve the knowledge of the RPP action on the spot of powerful laser beams, we performed a series of measurements at IFAM, Pisa, in collaboration with CLF. RPP's were supplied by CLF. This work can also clarify some relevant results[2] we obtained in a previous experiment on laser interaction with preformed plasmas, performed at CLF[3].

FAR-FIELD IMAGING

We studied the far field of a 1.064 μm, nanosecond laser beam, produced by a Nd YAG oscillator and three amplifiers. The rod diameter of the last amplifier is 2.5cm and the beam divergence is three times the diffraction limit. The following measurements were obtained with only the oscillator operating and amplifiers switched off. The laser beam crossed all the optical elements of the chain, and resulted in an aberrated focal spot as the one in Fig. 1a, which was produced with an f = 240 cm lens and detected by a 1/2" sensor CCD camera *grabber* .

Fig.1 compares the aberrated focal spot (a) with the far-field intensity distribution (b) obtained with a 1mm squared cell RPP, and a f = 24 cm lens, in order to have a spot of comparable zero order size. The four first-order features are also clearly visible.

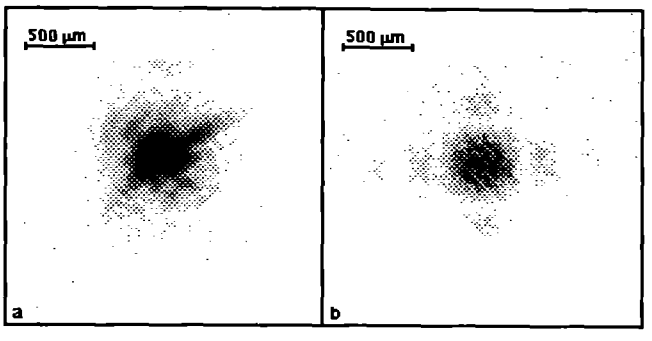

Fig. 1 - RPP smoothing of the far-field spot. (a) Focal spot without RPP, f=240cm. (b) Focal spot with 1 mm sq. RPP, f=24cm.

Four 0 - π dephasing (at 1.064 μm) RPP's were studied. Two of them were *squared* with cell size of 1mm and 2mm respectively. The two others will be conventionally called *circular* in the following, and had cells of 2mm and 3mm respectively. In this case the random dephasing was achieved by generating concentric circles of the required element spacing and then filling each annuli with an integral number of sub-elements, calculated by dividing the area of the annuli by the area of each 'square' sub-element[4]. Furthermore, the far field effect was studied of some *wrong* RPP's, including 1mm squared 0- π/2 RPP, 1 mm squared 0 - 0.86π RPP, and 1/2mm squared 0 - 0.93π RPP.

The Table summarises some of the measured parameters of the far field intensity distributions obtained with the four 0 - π plates, focusing the beam with the f = 240 cm lens. The first row shows the analogous parameters measured in the far field of the aberrated beam, without any RPP. The measured overall spot sizes are compared with the simple $2\lambda f/d$ theoretical evaluation. The standard deviation σ_{rms} of the intensity distribution was found to be slightly higher than 50%. The ratio $I_{max}/\langle I\rangle$ was evaluated, where $\langle I\rangle$ was obtained by numerical integration of the intensity in the area where its value lies between $I_{max}/10$ and I_{max}, divided by the area itself.

Particularly interesting for applications are the data reported in the last column, where the surface area whose intensity is higher than two times the mean intensity is reported for each RPP. They show that with respect to a

highly aberrated beam spot (No RPP case), the RPP's not only spread out the intensity maximum into a number of beamlets, but also reduce the overall involved surface.

RPP	Spot size (mm)	σ_{rms}	$\frac{I_{max}}{<I>}$	Spot surface with $I \geq 2 <I>$
No RPP	~ 0.7	~ 66%	2.5	10.6%
❑ 1mm	th =4.92 exp=4.32	~54%	3.1	6.7%
❑ 2mm	th =2.46 exp=2.31	~53%	2.7	3.6%
○ 2mm	th =2.46 exp=2.48	~ 55%	2.6	6.4%
○ 3mm	th =1.64 exp=1.74	~ 54%	2.6	4.1%

Table I. Summary of measured parameters of the far field intensity distributions obtained with the four 0 - π plates (see text).

Accurate statistical measurements were necessary to evaluate the mean size of the beamlet cross section (speckle size). A rather large number of speckles were analysed, and their size was measured from the contour plot obtained at different percentage of the maximum intensity of each speckle. A large spread in the speckle size distribution was found. Fig. 2 shows data obtained with the 1mm squared RPP and the their best fit obtained with a $(sinc)^2$ function. This function corresponds to the diffraction of a beam of diameter 1.75 cm in place of the experimental value of 2.5 cm.

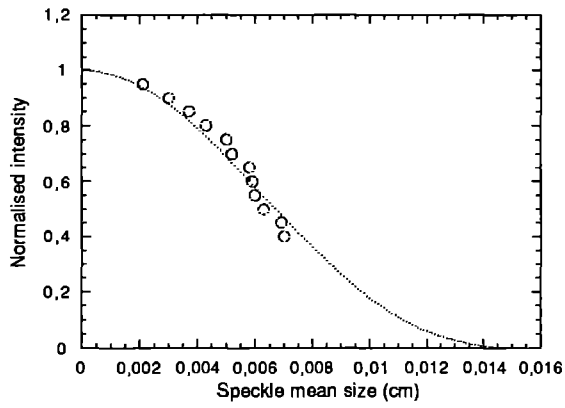

Fig. 2 Speckle size averaged over a large number of speckles, measured from the contour plot obtained at different percentage of maximum intensity of each speckle. The theoretical curve is a $sinc^2$ function.

BEAM APERTURING AND FAR FIELD PATTERN

For each RPP studied, a series of far-field images were collected with apertures of different diameter on the beam axis. The speckle size was found to increase regularly, as due to the decreasing diffraction angle. The contrast ratio, I_{max} /<I>, was found to be approximately constant

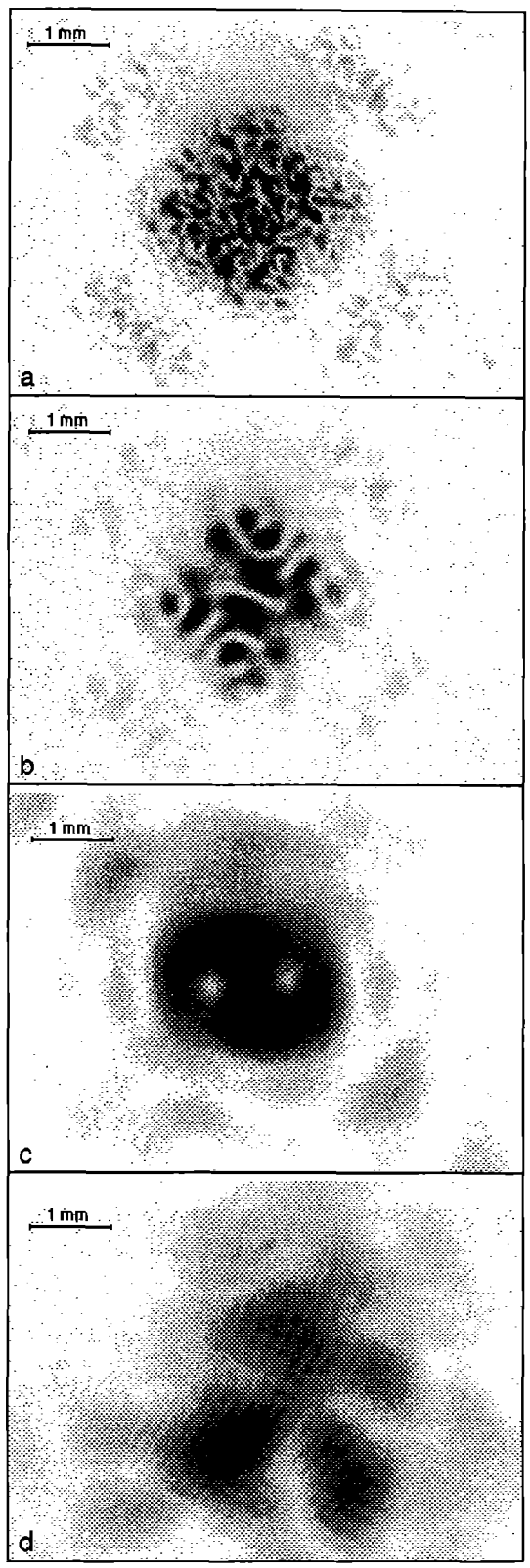

Fig. 3 Beam size reduction effects on far field intensity pattern. (a) Without aperture; (b) with the 1.2 cm diameter aperture; (c) with the 0.4 cm diameter aperture; (d) with the telescope.

until the number of cells involved was greater than 30. By further decreasing the number of cells acting on the beam, the contrast ratio gradually decreases, as expected from the interference of a decreasingly small number of sources.

Another interesting effect is that decreasing the aperture diameter, the far field pattern is more and more clearly centro-symmetric. This effect was found to depend just from the aperture size regardless the cell size of the RPP. This behaviour is expected because, by reducing the aperture diameter on the beam axis, we select a higher coherence portion of the beam. On the contrary, if we reduce the beam cross section with a telescope, though the number of involved RPP cells is still small, the symmetry is no longer clear, because the degree of coherence is the same of the original beam. The effect described above is illustrated for the 2mm squared RPP in Fig. 3. While the symmetry is not apparent with no aperture on the beam as in (a), it becomes evident for apertures of diameter smaller than 2 cm, as in (b) and (c) cases.

When the beam cross section is reduced with a telescope, the same "symmetrisation" effect does not occur, as shown by the picture (d).

"WRONG" RPP EFFECT

When the cell-to-cell dephasing is different from 0 to π, the expected pattern in the far-field of the of the original laser beam (which is less deep than the far-field of the dephasing cells) is a superposition of the usual random speckle pattern and the aberrated spot of the untreated laser beam. This is dramatically evident with a 0 - $\pi/2$ dephasing RPP, as shown in Fig. 4, with 1 mm squared cells.

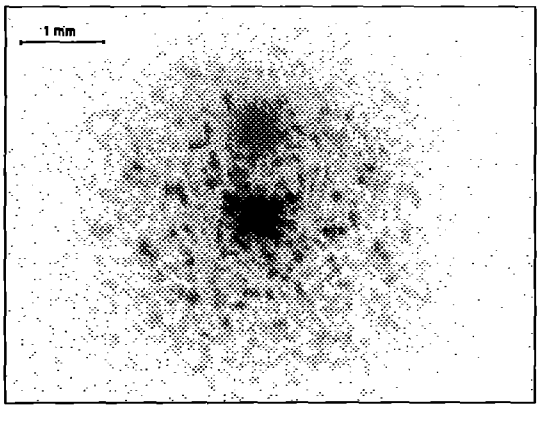

Fig. 4 Far-field pattern obtained with the 0-$\pi/2$ dephasing 1 mm cell RPP.

In this case the dephasing is very far from the correct 0 - π value and the result is an almost unperturbed spot (compare with Fig. 1a), taking about 50% of the laser energy, merged in a tenuous random pattern. On the contrary this effect is very weak when the dephasing is not far from 0 - π, as we found with the 0 - 0.93π 1/2 mm squared cell RPP.

No effect at all we were able to detect with the 0 - 0.86π 1 mm squared cell RPP. In this latter case the random pattern did not show any memory of the aberrated beam spot. Of course this kind of effect can be easily avoided, at least for dephasing not far from π, operating in the region which is far-field for the dephasing cells, but quasi-near-field for the whole beam, as actually we verified.

In conclusion we performed an accurate experimental analysis of the far field effects of RPP's devices on an aberrated beam. A complete description of the results will appear elsewere[5]. In general they appear in reasonable agreement with both theory and simulation[6], and confirm the need of an accurate design of the RPP cell structure for each experimental application.

Authors acknowledge the creative contribution of A.Barbini for the implementation of the CCD camera set-up, useful discussions with V. Biancalana, and relevant suggestions by D.Batani.

REFERENCES

[1] Y.Kato *et al.*, Phys. Rev. Lett., **53**, 1057 (1984)
[2] A.Giulietti *et al.*, Annual Report to the Laser Facility Committee 1993, **RAL-93-031**, Rutherford Appleton Laboratory, page. 38.
[3] L.A.Gizzi *et al.*, *Characterization of laser plasmas for interaction studies*, accepted for publication , Phys. Rev. E (1994).
[4] D.A.Pepler *et al.*, SPIE Proc., **1870**, 77 (1993)
[5] T. Ceccotti, Thesis, University of Pisa (1994).
[6] V. Biancalana *et al.*, *Handling of quasi-Gaussian beams by phase plates: far field simulation* In publication in Applied Optics (1994)

SHORT PULSE TEMPORAL PROFILE DIAGNOSTICS USING TWO PHOTON ABSORPTION

I N Ross, C J Hooker and J R Houliston

Rutherford Appleton Laboratory, Chilton, Didcot, OXON, OX11 0QX, England

INTRODUCTION

There has been a great deal of attention paid to the temporal characterisation of short pulses (1-15). There are now many demonstrated techniques, almost invariably using auto- or cross-correlation, which can measure a wide range of pulse durations, and even time dependence of amplitude and phase, from infrared to ultraviolet. In the ultraviolet the absence of efficient second harmonic crystals restricts the range of usable techniques, and it is particularly difficult to measure high contrast ratios because of the limited dynamic range of the nonlinear processes so far demonstrated. The need for measurements of high contrast ratios in the ultraviolet and for a simpler way to monitor pulse duration has led us to develop the two techniques described and demonstrated below. Both use two photon absorption as the nonlinear process because its measurement requires only simple calorimetry and because in silica TPA is the dominant nonlinear process at the KrF wavelength. Silica has good optical and damage characteristics in the UV, but suitable two photon absorbers can be found for most wavelengths making these techniques more generally applicable.

MEASUREMENT OF PULSE DURATION

The characteristic equation for two photon absorption in a parallel beam is:

$$I_T = \frac{I}{1+\beta I \ell} \tag{1}$$

where I and I_T are incident and transmitted intensities, b is the TPA coefficient and ℓ is the material length.

For a converging beam

$$I_T dA_T = dP_T = \frac{I dA_o}{1+\left(\frac{L}{L-\ell}\right) I\beta\ell} \tag{2}$$

where L is the distance to the beam focus.
Thus the energy transmitted,

$$E_T = \int P_T dt = \int_t \int_A \frac{I dA_o dt}{1+\left(\frac{L}{L-\ell}\right) I\beta\ell} \tag{3}$$

and the energy transmission

$$T = \frac{E_T}{E} = \frac{\iint \frac{I dA_o dt}{1+\left(\frac{L}{L-\ell}\right) I\beta\ell}}{\iint I dA_o dt} \tag{4}$$

Assume the spatial and temporal distributions do not change. Then:

$$T = fn(I) = fn(E/\tau) \tag{5}$$

where τ = pulse width in time.

If this function cannot be calculated or measured then to a reasonable approximation over a limited range of T:

$$T \approx \frac{1}{1+k\left(E/\tau\right)}$$

$$\therefore \tau = \frac{kET}{1-T} \tag{6}$$

Let the pulse be stretched by some means (for example using group velocity dispersion (GVD) in a block of glass) and let this time stretch be τ_s $\left(= \frac{t}{c}\frac{d^2n}{d\lambda^2}\lambda\Delta\lambda \text{ for the glass block}\right)$. The resultant pulse duration t is given, for a Gaussian distribution and assuming the initial pulse is not chirped and has a pulse duration t_0, by:

$$\tau = \sqrt{\tau_o^{\,2} + \tau_s^2} \tag{7}$$

Equations (6) and (7) can be combined to give

$$\tau_o = \frac{\tau_s}{\sqrt{\left(\frac{E_2}{E_1}\left[\frac{T_o^{-1}-1}{T_s^{-1}-1}\right]\right)^2 - 1}} \tag{8}$$

where T_S and T_0 = energy transmission for the stretched and unstretched pulse, respectively and E_2 and E_1 are pulse energies with and without the stretch.

Since E_1, E_2, T_0 and T_S are all measured and τ_s can be calculated (requiring only a measurement of the spectral width), this equation determines the pulse duration from two laser shots.

Apart from the measurement error there are uncertainties due to the approximations made in equations (6) and (7). As an example, for a pulse which is Gaussian in both space and time and if $T_o \approx 0.4$ and $T_s \approx 0.6$ then the pulse duration is overestimated by ~ 20%.

Improved accuracy can be obtained if more laser shots are used, by finding two energies E_1 and E_2 such that the transmission of a stretched pulse of energy E_1 is the same as that of an unstretched pulse of energy E_2. Equation (8) now becomes:

$$\tau_o = \frac{\tau_s}{\sqrt{\left(\frac{E_2}{E_1}\right)^2 - 1}} \tag{9}$$

In this case the method does not require knowledge of the type of nonlinear absorption process in operation. If the initial pulse is chirped, τ_o can still be found by making a third measurement using a different degree of stretch.

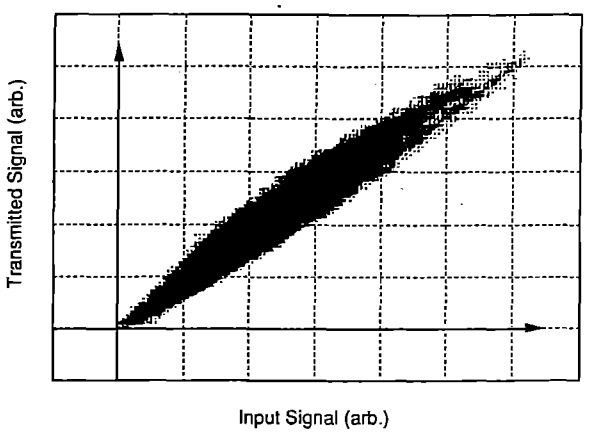

Figure 1 Experimental data showing the pulse transmission characteristics of the two photon absorber. Two photodiodes monitoring the incident and transmitt ed pulses are connected to the X and Y plates of an oscilloscope. Each laser pulse gives a linear trace. The figure shows the superposition of traces of a number of pulses with varying energy.

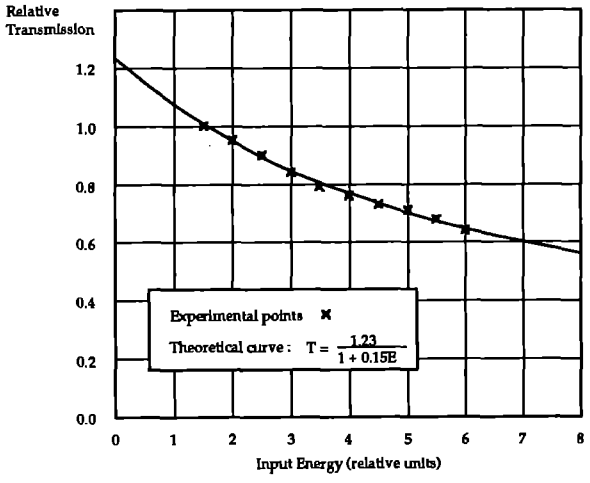

Figure 2 The transmission of the two-photon absorber as a function of incident energy. Plotted points are mesurements taken from figure 1. The curve is an analytical fit with appropriate constants in equation 6.

Figure 1 shows the raw data obtained when using this technique to monitor the pulse incident on target from a KrF laser using the scheme of chirped pulse amplification (CPA) and recompression. A silica plate of a few millimetres thickness was placed near the focus of the beam from an off-axis paraboloid. Incident and transmitted energies were monitored using integrating photodiodes, the two signals being connected to the X- and Y-plates of an oscilloscope. The resulting trace for a single laser pulse is a straight line with a slope proportional to the absorber transmission. The laser front end was operated at 8 Hz with large shot-to-shot variations. A number of shots are shown superimposed in Figure 1 and it can be seen that (as expected) the transmission, given by the slope, varied from a high value for low energies to a low value for high energies. Using the data in figure 1, figure 2 plots the transmission as a function of input energy. An analytical curve, using equation 6, shows a good fit to this experimental data. The slope (or transmission) for a given energy was consistent to within 10%. The device was primarily used to adjust the laser and CPA system for minimum recompressed pulse duration (minimum slope on the oscilloscope trace) and was found to be as accurate for this purpose as a more conventional autocorrelator. It is also a great deal simpler, quicker and more sensitive and can be used near the plane of interest. Approximately 1 μJ was incident on the silica plate and transmissions as low as 20% were obtained in the beam focus. An estimate was made of the minimum pulse duration by introducing a known amount of stretch at the grating pulse stretcher to give a transmission increase of 20-30%. This yielded a calculated pulse duration of ~ 400 fs in reasonable agreement with a measurement using a single-shot autocorrelator.

For the KrF wavelength of 249 nm TPA is probably the most sensitive of the nonlinear processes that can be used for pulse length measurements. From equation (1) and using b = 0.07 cm/GW for silica at 249 nm we find that T = 0.5 for $I\ell = 14GW/cm$. For a thickness ℓ = 0.5 cm, which results in less than 3% increase in the duration of a 100 fs pulse due to GVD, I = 28 GW/cm^2. Since the absorber plate can be placed near a focus where the beam may be less than, say, 100 μm in diameter over the plate length, the power required is less than 2 MW, corresponding to an energy of less than 1 μJ in 500 fs.

PULSE CONTRAST RATIO

In the absence of a high dynamic range nonlinear process at 249 nm with which to construct a high-contrast-ratio measurement correlator, an alternative approach has been considered and a possible solution is proposed. The principle of the technique is to reduce the contrast ratio to the level at which it can be measured. A simple way of doing this is to preferentially attenuate the short pulse using a nonlinear absorber such as silica at 249 nm. Figure 3 shows a possible scheme in which the beam is brought to a focus in a block of absorber.

The power absorption in the element $d\ell$ is given by:

$$\frac{dP}{P} = \frac{dI}{I} + \frac{dA}{A} = -\beta I d\ell \qquad (10)$$

where b is the TPA coefficient.

As an example let the focusing geometry be given by:

$$A = \frac{(A_o - A_{MIN})}{L^2}(L-\ell)^2 + A_{MIN} \qquad (11)$$

and let the beam have a 'top hat' profile.
Combining these equations and integrating gives:

$$\frac{1}{P_T} - \frac{1}{P_o} = \frac{1}{IA} - \frac{1}{I_o A_o} = \frac{\beta L}{\sqrt{A_{MIN}(A_o - A_{MIN})}}$$

$$\left[\cos^{-1}\sqrt{\sum} - \cos^{-1}\sqrt{\frac{A_{MIN}}{A}}\right] \qquad (12)$$

Maximum attenuation occurs for ℓ = L (focus at the exit plane of block). Assuming $A_{MIN} << A_O$, then

$$\frac{1}{P_T} = \frac{1}{IA} \approx \frac{\pi\beta L}{2\sqrt{A_o A_{MIN}}} \qquad (13)$$

or

$$P_T \approx \frac{2\sqrt{A_0 A_{MIN}}}{\pi\beta L} \qquad (14)$$

The transmitted power is independent of the input power, and the power attenuation factor is given by:

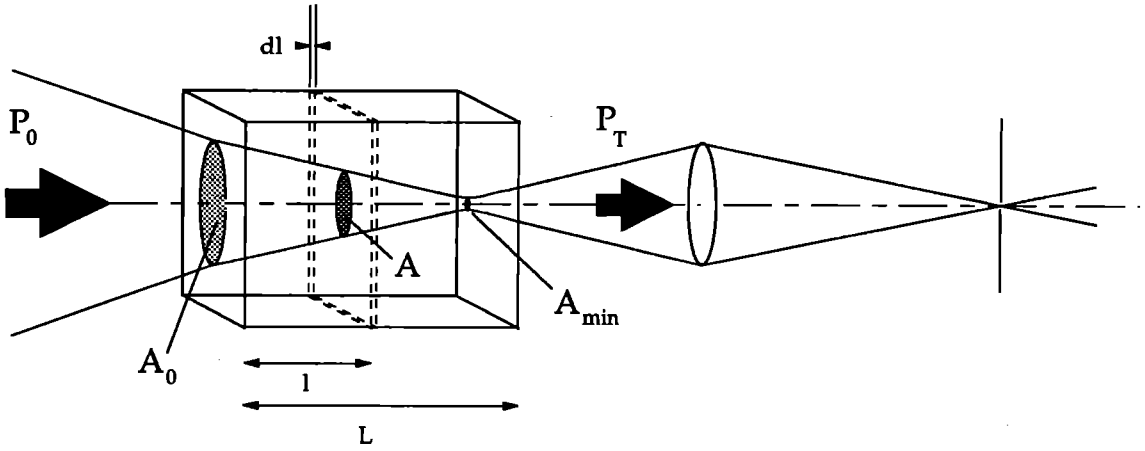

Figure 3 Geometry of the two photon absorber as used in the measurement of pulse contrast ratio

$$\frac{P_o}{P_T} = \frac{\pi}{2}\sqrt{\frac{A_o}{A_{MIN}}}.\beta I_o L. \qquad (15)$$

For example, for silica β = 0.07 cm/GW, so

if: $A_o = 1cm^2; A_{MIN} = 10^{-6}cm^2; L = 5cm,$

then $P_T = 1.8MW.$

Consequently if P_o = 100 GW, the attenuation factor is 0.55 x 10^5. This represents a useful suppression of the short pulse with very little suppression of background intensity, provided the latter is below the level of P_T: (attenuation factor = 2 for intensity = P_T).

To demonstrate the large suppression factors possible using TPA, the arrangement of figure 3 was set up using a silica rod of length 25 cm and spatial filtering using a pinhole of size approximately equal to the diffraction limit. An incident laser pulse of 0.1mJ in 500 fs having a diameter of 5 mm was attenuated by a factor 0.4 x 10^3 by the silica rod. The transmitted power was measured to be 0.2 MW. These measured values compare with the calculated values, using equations 15 and 14 respectively, of 1.6 x 10^3 and 0.1 MW. Given that the beam is not diffraction limited and that there is some ASE background this represents reasonable agreement between measurement and theory.

For very short pulses the attenuation factor of the TPA suppressor is reduced by the effects of GVD in the material of the suppressor. The reduction is significant if the GVD stretch is similar to the expected transmitted pulse duration in the absence of GVD. TPA itself causes this latter pulse duration to be longer than that of the input pulse (for example by a factor 4 for a Gaussian pulse in the above example). The shorter the length of material the better, although the minimum length will be restricted by material damage. In an optimised design the fluence has its maximum permissible level on the input face and at the focus, and will then not exceed this value elsewhere in the material. Such a design analysis leads to a material length dependent upon the required suppression ratio. In our example, assuming a maximum allowable fluence of ~ 1 J/cm^2 at 1 ps, the TPA suppresser must be at least 3 cm long.

For most effective use of the suppressor the output beam should be spatially filtered as shown in Figure 3 to obtain maximum suppression factor. The output of the spatial filter can then be fed into a device for measurement of the pulse contrast ratio. The suppression factor of the TPA block can be measured to the accuracy needed for contrast ratio measurements by measuring its energy transmission ratio. If this is repeated with the input attenuated a correction can be made for a significant level of background energy and a useful estimate made of the energy contrast ratio of the pulse.

REFERENCES

1) R. Wyatt and E. E. Marinero, App. Phys 25 (1981) 297
2) N. Morita and T. Yajima, App. Phys B 28 (1982) 25
3) D. M. Raynor, P. A. Hackett and C. Willis, Rev. Sci. Instr. 53 (1982) 537
4) J. Janszky, G. Corradi and R..N. Gyuzalian, App Phys B 33 (1984) 79
5) J.C.M. Diels, J.J. Fontaine, I.C. McMichael and F. Simoni, App. Opt. 24 (1985) 1270
6) F. Salin, P. Georges, G. Roger and A.. Brun, App. Opt. 26 (1987) 4528
7) M.H.R. Hutchinson, I.A. McIntyre, G.N. Gibson and C.K. Rhodes, Opt. Lett. 12 (1987) 102
8) G. Szabo, Z. Bor and A. Muller, Opt. Lett. 13 (1988) 746
9) N. Sarukura, M. Watanabe, A. Endoh and S. Watanabe, Opt. Lett. 13 (1988) 996
10) I.N. Ross, D. Karadia and J.M. Barr, App. Opt. 28 (1989) 4054
11) H. Schulz, H. Schuler, T. Engers and D. von der Linde, IEEE J.Q.E. 25 (1989) 2580
12) A. Tunnermann, H. Eichmann, R. Henking, K. Mossavi and B. Wellegehausen, Opt. Lett. 16 (1991) 402
13) S. P. LeBlanc, G. Szabo and R. Sauerbrey, Opt. Lett. 16 (1991) 1508
14) R. Trebino and D.J. Kane, JOSA (A) 10 (1992) 1101
15) J.L.A. Chilla and O.E. Martinez, Opt. Lett. 16 (1991) 39

CCD IMAGING FROM 20eV TO 8keV.

A. G. MacPhee, C.L.S. Lewis, J.E. Scott, J.Warwick.

Department of Pure and Applied Physics
The Queens University of Belfast, BT7 1NN

INTRODUCTION

The soft x-ray range of coverage for an active 2D detector system has been extended from 800eV to less than 20eV. Sensitivity and dynamic range at 182 Angstroms has been enhanced over that attainable using photographic emulsions by a factor of 8 and 300 respectively. The CCD based system has been calibrated for x-ray sensitivity at 33.74Å and 182Å. The detector employs a high efficiency, small grain, rare earth phosphor scintillator to convert uv and soft x-rays to visible photons matched to the sensitivity peak of EEV 15-11 series, ultra-low dark current inverted mode CCDs[1]. The phosphor is coupled to the CCD via 6μm channel diameter, proximity focused fibre bundles. A 150mm×70mm fibre faceplate coated with the phosphor isolates the vacuum system and provide a large area of acceptance for the incident flux. The integral fibre faceplate of the CCD is butt coupled to the region of interest on the phosphor plate for data capture. Software control of the transfer clock phases enables the detector to spatially integrate one dimension on the chip for a further increase in the signal to noise ratio.

An absolute calibration of the 700eV-8keV detector system[1], performed at 1.49keV, has been shown to agree with a calculation of sensitivity based on photo-absorption data.

DETECTOR CALIBRATION

The soft x-ray system was calibrated for sensitivity at 33.74Å and 182Å against a pre-calibrated[2] photographic emulsion (Ilford Q-plate), using hydrogenic carbon resonance emission generated at QUB with a 10Hz, 2J/7·5ns, injection seeded Nd:YAG laser operated at 2ω. The signal was spectrally resolved with a flat-field grazing incidence spectrometer, using a mean 1200 grooves/mm grating with a 200μm entrance slit set 75mm from the source. Films were analysed using a JL Automations MK6 microdensitometer, with matched influx and efflux optics with NA=0.25 and a 5μm × 50μm slit with the long edge parallel to the spectral lines. The optical density was measured at 2μm intervals in the spectral direction, with a separation of 5μm between adjacent scans. The density values were converted to intensity using the fit obtained in (2) to the semi-empirical model of Henke et al[3].

Fig.1 shows a typical single shot emission spectrum snatched from the real time display of the CCD output, where the signal has been spatially integrated on chip between shots and read out at 10Hz.

For the calibration, comparison was made between the signals recorded on each detector, within 1Å of both the third order of the Lyman-α and first order of the Balmer-α emission, integrated along 135μm of each line for 10 shots (table 1).

	33.74Å	182.17Å
$N_{photons}$ (film)	142489	38802
N_{counts} (CCD)	38935	8605

Table 1. Soft X-ray calibration data.

The film calibration employed was based on 33.74Å photons. Hence the above number quoted for the measured 182Å signal on film is the *equivalent* number of 33Å photons necessary to produce the *recorded* density. The film sensitivity is not necessarily independent of photon energy, hence a correction must be made: The phosphor output is known to increase ~linearly with incident photon energy[4]. From table 1, the ratio of the number of *counts* obtained on the CCD for the 33Å and 182Å emission is 4.52, so in terms of the number of incident *photons*, this ratio becomes 0.723. On the film, the same ratio expressed using the quoted *equivalent* number of 33Å photons is 3.67, hence the film sensitivity to 182Å photons is 0.723/3.67≈0.2 that for 33Å, which is reasonable to expect from a film of this type. The magnification of the system from the scintillator to the CCD is ×1, so with 27μm × 27μm pixels, the sensitivity at 182Å:

$$\frac{38802 \text{ (33Å photons)} / 729\mu m^2}{0.2 \text{ (33Å to 182Å conversion)} \times 8605 \text{ (CCD counts)}}$$

$$= 0{\cdot}03 \text{ photons}/\mu m^2/\text{count}.$$

The film fog density was measured to have a standard deviation equivalent to an incident 182Å photon intensity of 0·37 photons/μm², so that a signal of 1·1 photons/μm² would be within 3 standard deviations of the mean. For the CCD system, with standard deviation 1.8 counts (16-bit digitisation), 6 counts corresponds to 0·18 photons per square micron. This calibration is thought to be accurate to within a factor of ~4, based on our knowledge of the sensitivity of the photographic emulsion. The absolute QE of the phosphor alone at 182Å (within 10%)[4], would indicate that for optimum coupling, the sensitivity of the system could be enhanced by a factor of three over our measurement.

The kilovolt system was calibrated against absolutely calibrated (within 15%) Kodak DEF x-ray film[5], using helium like resonant emission from an aluminium plasma. The x-ray film was positioned so as to mask one half of the spectrum falling onto the CCD in a Bragg crystal spectrometer. The emission lines were uniformly continuous across the film / CCD interface, as verified in spectra recorded over the entire device. The number of photons integrated over an area in the vicinity of the interface on the film, was compared to the number of electrons generated in the depletion region of the CCD over an identical area for the same exposure. The standard deviation in the DEF fog density measured over 100 25μm×25μm pixels was equivalent to a 1·49keV photon intensity 0·025 photons/μm², so that an incident signal of 0·075 photons/μm² would be within 3 standard deviations of the mean. For the CCD, again with standard deviation 1.8 counts, 6 counts corresponds to 4.8×10^{-4} photons per square micron. Therefore at 1.49keV, the CCD system has 200 times the sensitivity of DEF. The number of 3 standard deviation signal increments required to bring the DEF film density to the shoulder of the HD curve at roughly OD 5, is 250. The well size of the CCD pixels has recently been increased by a factor of 4, to 1 million electrons, so that the corresponding number of 3 standard deviation increments for the 16-bit CCD system is 10800, which is 43 times that of DEF. On this basis, with a system gain of 15 electrons per count, 63% of the incident 1·49keV photon flux generates collectable photo-electrons in the depletion region of the device (at 3·65eV / e^-), compared to ~68%[5] from theory, which is well within the tolerance of the calibration data.

REFERENCES

[1] A.G. MacPhee, C.L.S. Lewis, 'CCD imaging from 0·7keV to 8keV with Multi-Pinned Phase technology.', SERC Central Laser Facility, Ann. Rept., 135-136, (1993).

[2] J. Krishnan *et al*, 'Film calibration for soft X-ray wavelengths', SERC Central Laser Facility, Ann.Rept., 22-23, (1992).

[3] B.L. Henke *et al*,, 'Low energy x-ray response of photographic films.', J.Opt.Soc.Am.B,1, 818-849 (1984)

[4] D.E. Husk, S.E. Schnatterly, 'Quantum efficiency and linearity of 16 phosphors in the soft X-ray regime', J.Opt.Soc.Am.B, 9(5), (May 1992)

[5] D. Mather, AWE Aldermaston, private communication.

[6] C. Castelli *et al*, 'Soft X-ray Response of Charge Coupled Devices', NIM A310, 240-243 (1991)

ACKNOWLEDGEMENTS

The authors wish to thank Andor Technology LTD (10 Malone Rd., Belfast, BT9 5BN), for their provision of the imaging systems and many useful discussions.

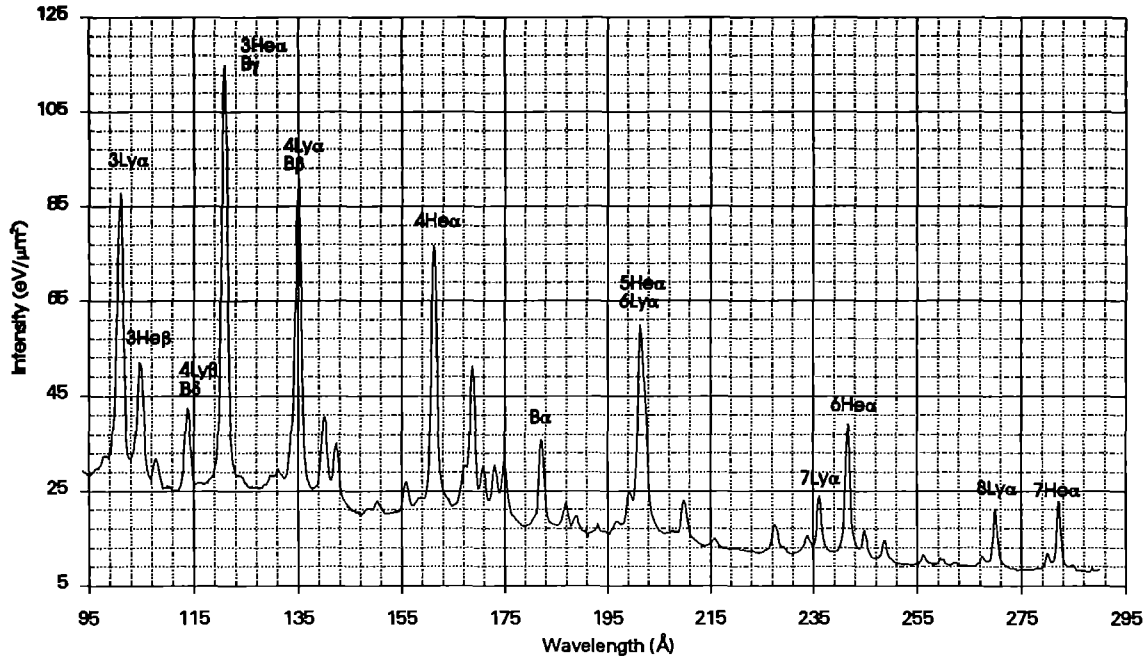

Fig.1 Typical single shot, carbon emission spectrum snatched from the real time display of the CCD output, where the signal has been spatially integrated on chip between shots and read out at 10Hz.

VULCAN OPERATIONAL STATISTICS

DA Pepler and CN Danson

Rutherford Appleton Laboratory

During the year 1993 / 1994 a record number of 8976 VULCAN shots were fired. Of these shots, 5452 were to the target areas, with Chart 1 indicating the relative breakdown of the shots per area. These shots included 1722 full disc shots to the main target areas and 1070 target shots to TA4, full details of which are given in Table I. These figures are approximately 25% higher than last year, with the shot failure rate continuing to be low at < 5 %.

The chirped pulse amplification (CPA) facility, was in constant demand and was upgraded mid-September, with the installation of a LMA oscillator to provide sub-picosecond operation with 35 TW and $> 10^{19}$ Wcm^{-2} to target.

Chart 1 Relative number of shots per area

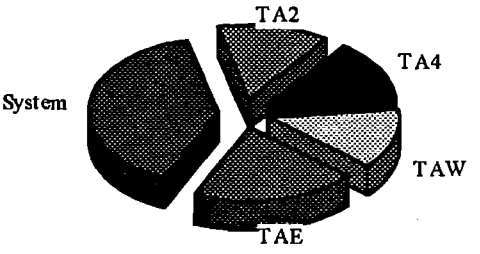

EXPERIMENTAL PERIOD	EXPERIMENT (Number of target shots)			
	TA EAST	TA 2	TA WEST	TA 4
22 Mar - 4 Apr	Setup	Setup		
5 Apr - 2 May	Short wave RT instabilities (106)	Ionisation fronts in Au (100)		Laser shocked quartz (142)
10 May - 16 May		Setup	Setup	
10 May - 20 Jun		Fracture strength (142)	CPA X-ray production (96)	
21 Jun - 18 Jul			CPA plasma plumes (116)	Biological imaging (59)
2 Aug - 15 Aug	Setup		Setup	
16 Aug - 13 Sep	X-ray laser (68)		Recombination X-ray laser (84)	Biological imaging (72)
14 Sep - 20 Sep			Facility development	
27 Sep - 31 Oct	X-ray laser (123)		CPA target experiment (82)	Confined foils (125)
8 Nov - 21 Nov	Setup	Setup		
22 Nov - 27 Dec	Direct / Indirect drive (100)	Opacity measurements (208)		Confined foils (494)
10 Jan - 16 Jan	Setup	Setup		
17 Jan - 13 Feb	RT instability & population redistribution	3D imaging (109)		Biological imaging (178)
14 Feb - 21 Mar	(289)		Tunnel ionisation (99)	
TOTAL NUMBER OF TARGET SHOTS	686	559	477	1070

Table I VULCAN statistics for the year to March 1994

SPRITE OPERATIONS

G J Hirst, E J Divall, K N Drodge and J M D Lister

Rutherford Appleton Laboratory

INTRODUCTION

This section summarises the Sprite scheduled programme, with more detailed reports of external-user experiments and development projects appearing elsewhere.

SHOT STATISTICS

The total number of Sprite system shots fired in this reporting year was 2612. Of these 1513 were target shots (i.e. were delivered to the Target Area during scheduled external-user experiments) and the rest were test shots, used for development and optimisation of the laser. These data are compared with those from recent years in figure 1. The slight fall in this year's total shot number was a consequence of the implementation of two major upgrades (CPA and Raman). Time was taken both for the installation of new hardware and for the fine-tuning of the systems' performance once they were operational. The tuning is now almost complete and users are already taking advantage of the increased power and the much wider range of available pulse lengths.

SCHEDULED OPERATIONS

The allocations of laser time this year were: 30 weeks for external users (an increase of 9% on 1992/93), 13 weeks for system development and 9 weeks for maintenance, changes to the laser configuration and planned shutdowns.

The external-user experiments are summarised briefly in Table 1. Further details can be found in Section I of this Report. The dates shown for each experiment include the standard one or two-week set-up period, in which target shots are not usually fired.

For the first time this year records were kept of unplanned Sprite shutdowns during external-user experiments. They were only noted if i) they lasted for at least half a day and ii) they actually affected the experimental programme so, for example, component failures were not included if they could be rectified before the components were needed. In total 9½ experimental days and 6 set-up days were lost to unplanned shutdowns. These figures represent 9% of the scheduled experimental time and 13% of the set-up time.

Development work was confined to completion of the CPA project, which took 6 weeks and 235 shots in April and October, and the Raman Upgrade, which was carried out in seven weeks around Christmas and which used 200 shots.

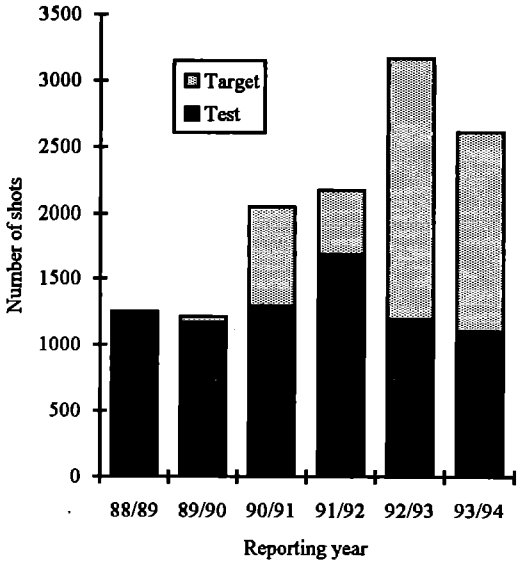

Figure 1 Annual numbers of Sprite test shots and target shots

INFRASTRUCTURE AND HARDWARE

In advance of the Titania installation, due to begin in one year's time, a number of infrastructure improvements have been made in the Sprite building, R2. These include the commissioning of the second chiller unit for the laser cooling system, modification of the overhead crane for remote operation and various structural alterations to allow the Titania beams to pass from R2 to R7. Meanwhile the Sprite final amplifier has continued to operate in its usual trustworthy fashion. We expect to fire the 18,000th system shot before the end of the reporting year and the last 8,500 of those will have been fired without changing the foils which surround the Sprite laser cell. Given that these are only 35 μm thick and that they must support a pressure difference of more than 1 atmosphere *and* withstand pulsed currents of 35 A cm^{-2} their durability is quite remarkable.

ACKNOWLEDGEMENTS

Once again it is a pleasure to acknowledge the support of the CLF Engineering staff, who make an invaluable contribution to the reliable operation of the Sprite system.

Experiment	Institution(s)	Dates (inc. Set-up)	Laser Configuration	Pulse Duration	Typical Energy	Target Shots
Multiphoton ionisation	Oxford-Alberta-Imperial College	7.6.93 - 9.7.93	KrF-CPA	300 fs	0.1-0.3 J	402
XUV harmonics	Oxford-Imperial College	12.7.93 - 20.8.93	KrF-CPA	300 fs	0.1-0.3 J	215
OFI ionisation	Imperial College	6.9.93 - 1.10.93	KrF-CPA	300 fs	0.1-0.3 J	349
Energy transport	Essex-RAL	18.10.93 - 19.11.93	KrF-CPA	300 fs	0.1-0.3 J	125
Heat transport	Imperial College	24.1.94 - 4.3.94	Raman	12 ps	0.5-10 J	346
Water-window XUV lasers	Oxford-Belfast-RAL X-Ray Laser Consortium	7.3.94 - 15.4.94	Raman	60 ps, 25 ps	(8-10 J)	(76)

Table 1 Summary of external-user experiments (bracketed figures are those for this reporting year)

SPRITE SYSTEM PERFORMANCE

J M D Lister, E J Divall, K N Drodge and G J Hirst

Rutherford Appleton Laboratory

INTRODUCTION

The beginning of the reporting year saw the completion of the Sprite CPA project, followed by four user experiments. At the end of 1993, the upgraded Raman system was implemented, and the second experiment to use this system is now in progress.

CPA SYSTEM

The initial CPA tests were completed on Sprite in April '93. The gain narrowing in the KrF amplifier chain was greater than expected, giving a recompressed pulse duration of 300fs. Further spectral measurements have been made which are discussed elsewhere in this report. The maximum energy delivered to target was 300mJ, giving a potential focused intensity on target of greater than 10^{19} W cm^{-2}. In practice, the intensity was less due to aberrations in the first order of the compressor gratings.

Some time was allocated during the year to optimising the performance of the CPA system. The pulse stretcher was moved from between the two passes of the discharge laser (as reported last year) to just before the first pass. This made it possible to operate the stretcher in a four-pass geometry (previously two-pass). In this configuration, there is no residual dispersion in the output beam, and the beam size can be reduced. The off-axis angle of the discharge laser could then be reduced slightly to increase the gain.

Further improvement in the beam quality has been achieved, but it was found that the size of the amplified focal spot increases dramatically when the laser is fired at high shot rates (more than 12 shots per hour). This is due to insufficient circulation of the laser gas between shots, and it is expected that this problem will be overcome with the installation of a new gas handling system later this year.

The maximum energy available from the CPA system is still limited by the efficiency and damage threshold of the recompressor gratings. At present, the first of the two gratings lasts for between 1 and 2 experiments before the damage reaches an unacceptable level. The second grating sees only 70% of the energy incident on the first, but at a shorter pulse duration. This grating shows little sign of damage, suggesting that the threshold is largely energy rather than intensity dependent. It is hoped that improvements in grating technology (particularly overcoating) will increase both the efficiency and the damage threshold sufficiently to allow full use of the single pulse energy available from Sprite (~1.4J).

RAMAN SYSTEM

This year has seen the implementation of the Raman upgrade, first described in last year's Annual Report. Details of the initial experiments are given elsewhere in this report.

The most significant improvements are in the energy delivered to target, and in the percentage of shots with near diffraction limited focal spots. The energy has been increased by about 60% with a maximum to date of 11 J in 12 ps. The beam divergence is not greatly improved over the old system, but the increase in beam diameter from 8cm to 10cm gives an increase in intensity at the focus of some 50% for the same energy (the F-number of the focusing optic is reduced from 4.2 to 3.4). In addition, the good quality focal spots are more reproducible, due to the new spatial filter before the final Raman amplifier.

Far-field measurements were made both using a CCD camera and by measuring the fraction of energy transmitted through a pinhole. The beam divergence at FWHM was as low as 4 μrad (1.4 times the diffraction limit) and the energy contained within the central spot was at least 25% of the total. This gives a figure for the intensity on target of greater than 10^{19} W cm^{-2}.

Measurements were made of the far-field of the oscillator beam in the chamber, which agreed with those taken from the diagnostic channel. As part of the upgrade, the output beam from the final Raman amplifier is now piped in argon to the target chamber, and there is only one (CaF_2) transmissive optic, so there should be no significant non-linear effects not seen by the diagnostic channel. As a result we now have far greater confidence that the focal spots measured by our monitor are an accurate representation of the focus in the target chamber. Table 1 summarises the performance of the 12ps Raman system before and after the upgrade.

	Old Raman system		Upgraded system	
	Max.	Typical	Max.	Typical
Pump energy (J)	11	9	20	16
Input energy (mJ)	200	80	30	5
Output energy (J)	5.6	3.5	11	8
Gain	1000	40	4000	1600
External efficiency (%)	60	45	65	45
Divergence (μrad)	5.0 (min)	7.0	4.0 (min)	5.0
Brightness (W cm^{-2} sterad^{-1})	>1x 10^{20}	4 x 10^{19}	2 x 10^{20}	1 x 10^{20}

Table 1 Raman system performance at 12ps (RA3) before and after upgrade

CONCLUSIONS

This year has seen the completion of the Sprite CPA system and the use of the 300fs, 1TW pulses in four user experiments. The Raman upgrade has been implemented and has largely achieved the predicted performance. 60ps and 25ps Gires-Tournois Interferometers (GTIs) have been purchased for the Tsunami oscillator to allow operation of the Raman system at longer pulse durations. One user experiment has been completed at 12ps and a second is now in progress using 60ps Raman pulses. The Sprite system can now deliver very high brightness pulses of up to 60ps duration, at powers of around 1TW for 300fs and 12ps durations.

LASER SUPPORT FACILITY PROGRAMME

W T Toner

INTRODUCTION

The contributions in this section range from the study of UV mutagenesis in scrapie through many fields of chemistry, biology and physics to coastal engineering and come from 36 user groups of whom 8 are new to the facility. Although the main focus is basic science there is much work of direct biomedical, environmental and industrial relevance.

The laser loan pool continues to have a wide geographical spread from Rennes to Belfast, Edinburgh and Leicester. The loan pool output is low for the second year running as a consequence of the reduction in size of the Pool as old lasers are retired. There was welcome news at the end of the year of a major grant to enable a 3-year upgrade and replacement programme. Users of the facilities at DRAL are now making full use of the provisions for fluorescence, transient absorbance and time resolved Raman spectroscopy on timescales down to sub-picosecond and covering the UV to near infrared spectral range.

Scientific highlights include:-

further results from a major study of the ultra-low temperature kinetics of molecular and radical reactions; the first detailed thermodynamic analysis of the separation of a geminate ion pair in an electron transfer reaction; the first observation of anti-Stokes population relaxation in photoexcited S_1 trans-Stilbene; the first spectroscopic observation of the zinc ethyl radical Zn C_2H_5; photolithography of 0.18 μm features for silicon FET devices; the production of an intense soft X-ray beam from a laser plasma source;

Many of the research programmes continue over several years and report encouraging progress: the work on electron transfer reactions is being extended now into the picosecond time domain; several studies of UV and X-ray induced damage to DNA, both in vitro and in vivo are making excellent progress; the studies of antioxidants have been extended to Probucol; a first study of UV mutagenesis in scrapie has shown an unexpected resistance of the organism to UV irradiation at 249 nm.

ANTI-STOKES AND STOKES PICOSECOND TIME-RESOLVED RESONANCE RAMAN SPECTRA OF THE SINGLET EXCITED TRANS-STILBENE

M Towrie[1], D L Faria[2], R E Hester[2], P Matousek[1], J N Moore[2], A W Parker[1], W T Toner[1]

[1]Rutherford Appleton Laboratory
[2]Department of Chemistry, University of York

INTRODUCTION

While the overall mechanism of *trans*-stilbene (tS) photo-isomerisation has been established[1], recent studies indicate that the detailed nature of the intramolecular processes and the role of the solvent require further investigation[2,3,4].

After photoexcitation into the S_1 state tS undergoes isomerization about the central olefinic C_0=C_0 bond on a time scale of c. 90 ps in n-hexane at room temperature. The process leads to a twisted intermediate which relaxes rapidly onto the S_0 surface to produce either cis- or trans-stilbene in the ground electronic state.

Picosecond time-resolved resonance Raman spectroscopy (ps-TR^3) has been applied successfully to the study of S_1 tS and results revealed the existence of mode-specific solvent-dependent changes occurring on a c. 10 ps timescale following photoexcitation. In this study, the ps-TR^3 apparatus has been used to probe S_1 tS to obtain the first ps-TR^3 anti-Stokes spectra enabling measurement of vibrational relaxation times and revealing further details of the relaxation mechanisms.

EXPERIMENTAL

The ps-TR^3 arrangement has been described earlier[5]. The sample solution was flown through a 0.5 mm open jet and kept at a temperature 25 °C. Pump (6 ps, FWHM) and probe (6 ps, FWHM) beams were focused into the sample to spot sizes with diameters of *c.* 40 μm and *c.* 65 μm, respectively. The concentration of tS in all solutions was 1 x 10^{-3} mol dm^{-3}. The fitting code described elsewhere[6] has been applied to the Raman spectra.

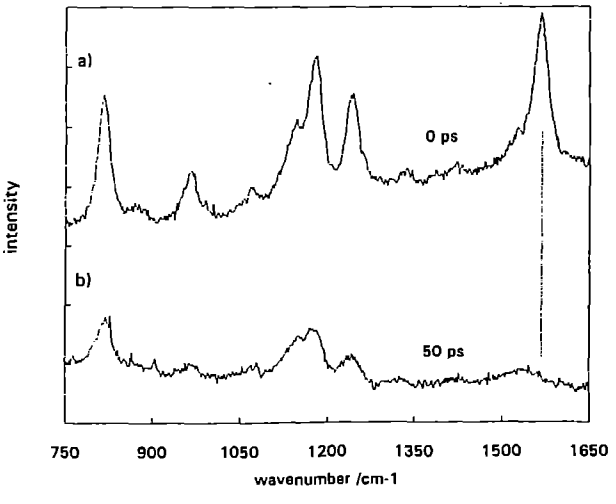

Fig 1 Anti-Stokes ps-TR^3 spectra of trans-stilbene in n-hexane a (a) 0 ps and (b) 50 ps time delay.

ANTI-STOKES SPECTRA

We obtained high quality, detailed anti-Stokes ps-TR^3 spectra of S_1 tS. Fig 1 shows the anti-Stokes spectra measured at time delays of 5 and 50 ps at pump (1.2 μJ) and probe (1.3 μJ) wavelengths of 305 and 610 nm, respectively. No correction for S_1 decay has been included.

The kinetic data of the anti-Stokes Raman band intensities were measured at the pump (0.2 μJ) and probe (0.45 μJ) wavelengths of 295 and 590 nm, respectively, with 10 min accumulation times. At the same time the Stokes spectra in the C_0=C_0 (1570 cm^{-1}) region were measured by changing spectrometer wavelength between the Stokes and anti-Stokes spectral regions. Therefore full information on the corresponding kinetic perturbations to the Stokes Raman spectra was available. The spectra were fitted to Lorentzian functions.

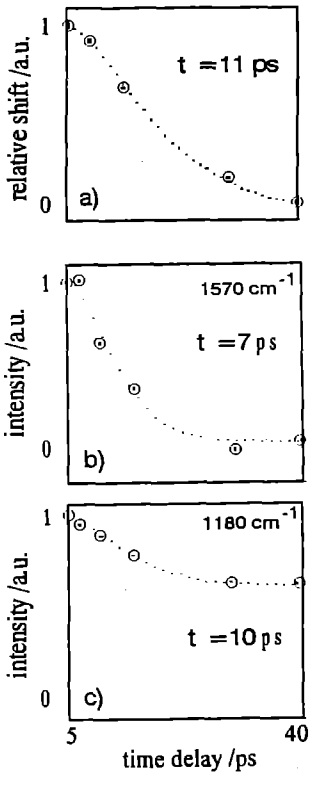

Fig 2 Time dependence (a) of the shift of the 1570 cm^{-1} band in the Stokes region and (b and c) the ratios of the anti-Stokes to Stokes intensities for the 1570 and 1180 cm^{-1} bands respectively.

The data were fitted to exponential functions taking into account the effect of the convolution of the pump and probe pulses. The 1570 and 1180 cm^{-1} intensity data fit to a single exponential with characteristic time constants 7 and 10 ps, respectively (see Fig. 2). The transient relative shift of the 1570 and 1180 cm^{-1} bands in the Stokes region fit to a double exponential function with a characteristic decay time of 11 ps.

The anti-Stokes signal scaled linearly with pump and probe power, but was found to be over an order of magnitude larger than expected and showed no temperature dependence. Consequently, the full interpretation of the data requires some caution. However, these results clearly indicate that the decay kinetics of the anti-Stokes bands matches that of the observed band width/position changes occuring in the Stokes tS bands.

NEW BANDS IN THE STOKES REGION

Several new ps-TR^3 bands of S_1 tS were observed in the Stokes region from 1600 to 3000 cm^{-1} at pump and probe wavelengths of 295 and 590 nm (see Fig. 3). These bands are believed to be combination and overtone bands. The Table 1 lists their positions.

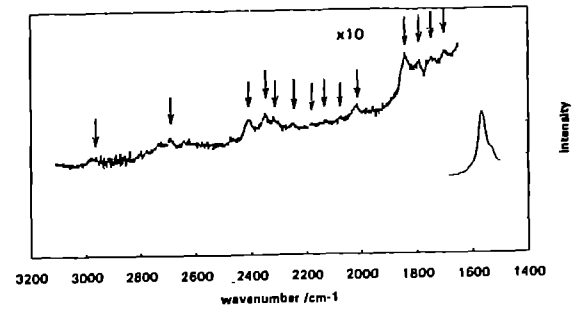

Fig 3 Combination and overtone ps-TR^3 bands of S_1 tS in n-hexane. Accumulation time was 600 s and the time delay 10 ps. Arrows indicate the positions of the new bands listed in table 1.

Table 1 New bands observed in the Stokes ps-TR^3 spectra

band position / cm^{-1}
1705
1752
1798
1845
2019
2078
2138
2182
2252
2318
2353
2412
c. 2731
c. 2974

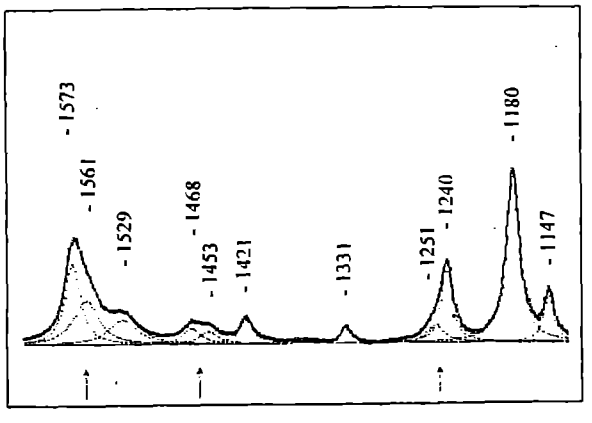

Fig 4 New Raman bands resolved into individual components in the Stokes ps-TR^3 spectrum at low temperature experiment (t = -35°C). The accumulation time was 300 s and the time delay 10 ps. The bands were fitted to Lorentzians and their positions are given in wavenumbers.

An experiment carried out at low temperature (tS in n-hexane, t = - 35 °C) resolved new bands at 1453 and 1468 cm^{-1} (see Fig. 4) and probably at least two bands in the 1245 cm^{-1} and 1570 cm^{-1} region. The experiment was carried out using pulse energies of 0.2 and 0.45 μJ for the pump (295 nm) and probe (590 nm) beams respectively.

CONCLUSIONS

A possible mechanism for the observed mode-selective dynamics is as follows. Photoexcitation of S_0 tS creates S_1 tS in an initially "hot" state with a wide range of vibrationally excited modes. The degree of excess energy will be dependent on the photoexcitation wavelength. Intramolecular vibrational energy redistribution (IVR) occurs, resulting in creation of vibrationally "hot", highly anharmonic, low frequency (deformation) modes which distort the molecular geometry. The proposed role of vibrationally "hot" low frequency modes is consistent with the fact that raising the temperature of the tS solution produces similar results to those observed at 10 ps on increasing the excess energy in the photoexcitation pulse[4]. This proposed mechanism is supported by our observation that the decay kinetics of the anti-Stokes band intensities in the C_0=C_0 region (1570 cm^{-1}) are on a similar timescale as the transient shifts observed in the Stokes region.

In summary we presently conclude from our work that the energy of the newly born excited state is initially stored in high lying vibrational modes and this becomes dissipated into lower lying vibrational modes - predominantly those which are coupled to them (combination bands may provide a clue here). The activated low modes could then perturb the high lying modes through this same coupling mechanism. The process is ultimately followed by complete intra-molecular vibrational energy redistribution or inter-molecular vibrational energy redistribution, EVR, (with solvent molecules) on the time scale of *c.* 10 ps.

REFERENCES

1. D H Waldeck, Chem.Rev. **91**, 415 (1991).

2. W L Weaver, L A Huston, K Iwata, T L Gustafson, J.Phys.Chem. **96**, 8956 (1992).

3. K Iwata, H Hamaguchi, Chem.Phys.Lett. **196**, 462 (1992).

4. R E Hester, P Matousek, J N Moore, A W Parker, W T Toner, M Towrie, Chem.Phys.Lett., **208**, 471 (1993).

5. P Matousek, R E Hester, J N Moore, A W Parker, D Phillips, W T Toner, M Towrie, I C E Turcu, S Umapathy, Meas.Sci.Technol. **4**, 1090 (1993).

6. P Matousek, A W Parker, W T Toner, M Towrie, Numerical Analysis of Raman Spectra, Central Laser Facility Annual Report, RAL-93-031, 1993.

PICOSECOND TIME RESOLVED RESONANCE RAMAN SPECTROSCOPY OF PHOTOCHROMIC SPIRO-INDOLINO-NAPHTHOXAZINES

J. Hobley[1], P. Matousek[2], A.W. Parker[2], M. Towrie[2], F. Wilkinson[1]

1 University of Technology, Loughborough, Leicestershire
2 Rutherford Appleton Laboratory

INTRODUCTION

Spiro-indolino-naphthoxazines (SINO's) undergo the following isomerisation reaction when irradiated with light in the ultra violet region of the spectrum[1].

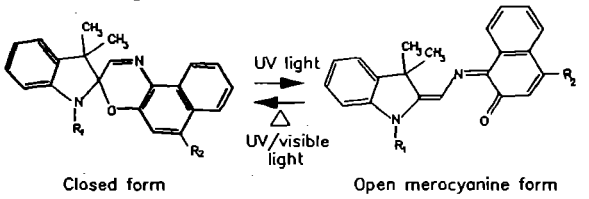

Closed form Open merocyanine form

The final photoproduct resulting from irradiation of the closed form is coloured and has a structure resembling that of a merocyanine dye.
Previous work has shown the presence of two transient species with lifetimes of 30ps and 1.4ns, following ultra violet irradiation of SINO5, on which R_1 is a hydrogen and R_2 is a piperidine group, in solutions of 1-butanol[2]. No transient having a lifetime extending into the nanosecond time regime was observed in solutions of SINO5 in cyclohexane, however a single species having a lifetime of around 70ps was observed[2].
Although these transients have been observed it had not been conclusively shown they directly lead to the merocyanine form. The present study has aimed to determine whether or not the transient species observed do lead directly to the final merocyanine forms.
For these picosecond TR[3] studies a pump wavelength of 290nm was used to excite solutions of SINO5 in cyclohexane and 1-butanol. The probe wavelength used was 580nm. The pump and probe powers were 0.9 and 2mW (4.46 kHz) respectively with a pulse width of 6ps.

RESULTS AND DISCUSSION

No evolution in the relative intensities of the Raman bands of transient spectra collected was observed in the case of SINO5 in cyclohexane after 10ps. The 0ps spectrum is different to any of the subsequent spectra collected. However due to the size of the signal this result needs confirmation. Figure 1 shows the time evolution of SINO5 in cyclohexane. When SINO5 is irradiated in 1-butanol the relative intensities of the transient Raman bands measured at different time delays do evolve with time up to the 1.5ns delay available on this apparatus. The 1.5ns spectrum closely resembles that of the merocyanine form measured in a 1-butanol solution present in a steady state thermal equilibrium with the closed form. Figure 2 shows the time evolution of the SINO5 Raman bands as a function of delay. This figure reveals that there are a minimum of two components combining to form the observed spectrum, these components are growing in with different rate constants. It was not possible to determine the exact rate constants for the growth of each component under the conditions of this experiment. The presence of at least two components in the evolution of these spectra is possibly due to different merocyanine isomers forming from a single cis isomer. It is interesting to note that two components were observed in the femtosecond pump probe experiments mentioned above[2].

(1) F. Wilkinson, D. J. McGarvey, J. Hobley, D. R. Worrall, A. Langley, W. Shaikh and W. Noad, Annual report to the Laser Facility Committee, Rutherford Appleton Laboratory Report RAL-93-031, 1993, 156-157.
(2) J. Hobley, A. J. Langley, W. Shaikh, P. Taday, D. R. Worrall, F. Wilkinson, Femtosecond Pump-Probe Laser Flash Photolysis Studies On Photochromic Spiro-indolino-naphthoxazines, This Report.

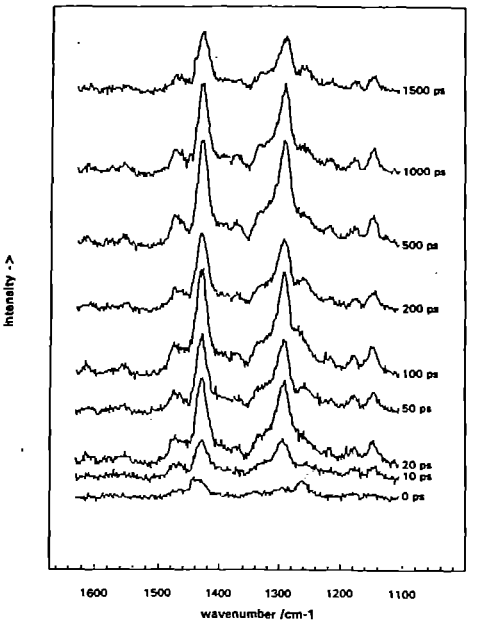

Figure 1
Picosecond TR[3] spectra of SINO5 in cyclohexane.

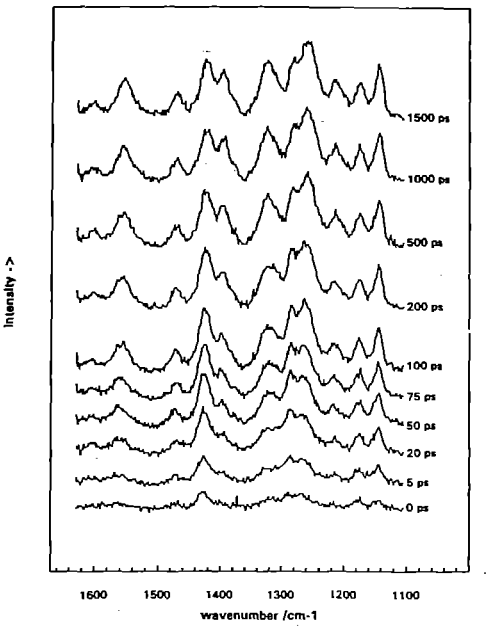

Figure 2
Picosecond TR[3] spectra of SINO5 in 1-butanol.

FEMTOSECOND PUMP-PROBE LASER FLASH PHOTOLYSIS STUDIES ON PHOTOCHROMIC SPIRO-INDOLINO-NAPHTHOXAZINES AND CHARGE TRANSFER INTERACTIONS BETWEEN AROMATIC HYDROCARBONS AND OXYGEN.

J. Hobley[1], A.J. Langley[2], W. Shaikh[2], P. Taday[2], D.R. Worrall[1], F. Wilkinson[1], D. J. McGarvey[1] and G. G. Sturley[1]

1 University of Technology, Loughborough, Leicestershire
2 Rutherford Appleton Laboratory
3 Keele University, Keele, Staffordshire

INTRODUCTION.

Spiro-indolino-naphthoxazines (SINO's) have been reported to undergo the following isomerisation reaction when irradiated with light in the ultra violet region of the spectrum.

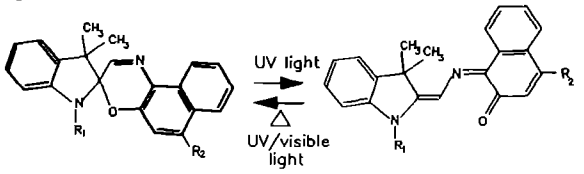

The final photoproduct resulting from irradiation of the closed form is coloured and has a structure resembling a merocyanine dye. The above reaction is both photochemically and thermally reversible and hence SINO compounds fit into the category of photochromic compounds.
The primary photochemical step in this isomerisation reaction occurs on the femtosecond timescale and is followed by a series of steps resulting in the formation of the final coloured merocyanine form of the molecule[1]. Previous work has been carried out on compounds SINO1, SINO2 and SINO3, see table 1.

Compound	R1	R2
SINO1	iso-butyl	indoline
SINO2	methyl	indoline
SINO3	methyl	hydrogen
SINO4	methyl	2-methyl-indoline
SINO5	methyl	piperidine

Table 1.

This work showed the presence of a transient state in the photoreaction of SINO1 and SINO2, when irradiated in 1-butanol, which lasted of the order of nanoseconds[1]. The lifetime of this state was not affected by changing the substituent R_1 from a methyl to a an iso-butyl group. No such transient was observed for SINO3 when irradiated in 1-butanol or for SINO1 when irradiated in cyclohexane.
Another result of this work was that the kinetics of the first 20 picoseconds the isomerisation reaction were very similar for all three compounds when irradiated in 1-butanol.
The experiments reported here have extended the work described above to include further changes in the substituent R_2, see table 1, and to increase the diversity of solvents used so that the effects of viscosity and polarity could be investigated as well as the effect of changing from a protic to a non-protic solvent.

The parameters of the individual solvents used in this study are summarised in table 2.

Solvent	Viscosity/cp	Dielectric constant
1-propanol	1.9	20.5
1-butanol	2.5	17.5
1-decanol	10.9	8.1
acetonitrile	0.4	36.0
cyclohexane	0.9	2.0

Table 2.

All solvents used were distilled and dried over calcium hydride and stored under dry nitrogen prior to their use.

RESULTS AND DISCUSSION

The results described here were obtained using sub picosecond laser pulses generated by a Tsunami titanium-sapphire laser being pumped by an argon ion laser. The resulting train of pulses were amplified using a Spectra Physics PDA1 three stage dye amplifier pumped Q-switched YAG laser at 532nm. The amplified pulse was frequency doubled using a BBO crystal to provide a pump beam of 369nm with an energy of ~1uJ per pulse and a pulse duration of ~800fs. The probe beam was generated by mixing 1064nm pulses from the YAG with 736nm light from the Tsunami in a KDP crystal to produce a probe wavelength of 435nm.
The presence of the long, nanosecond lifetime, transient in the photoisomerisation resulting after irradiation of SINO1 and SINO2 in 1-butanol with light in the ultra violet region of the spectrum has been confirmed by this study. This transient has so far only been detected for solutions of SINO compounds in 1-propanol, 1-butanol, 1-decanol and acetonitrile. The kinetics observed for SINO1 in acetonitrile show a faster picosecond transient as well as a the long lived nanosecond transient. Similar bi-exponential kinetics are seen for SINO5 in 1-butanol, however for SINO5 in cyclohexane only a short picosecond component is observed.
SINO1 SINO2 and SINO4 show simple first order kinetics in the alcoholic solutions studied. These results are summarised in table 3. Where τ_1 and τ_2 are the transient decay lifetimes following the initial rise in absorption.

Compound	Solvent	τ_1/ps	τ_2/ps
SINO1	1-propanol	560	-
SINO1	1-butanol	790	-
SINO1	1-decanol	1100	-
SINO2	1-butanol	790	
SINO4	1-butanol	1000	-
SINO1	cyclohexane	-	-
SINO1	acetonitrile	50	1600
SINO5	1-butanol	30	1400
SINO5	cyclohexane	70	-

Table 3.

Apparent from table 3 is the effect of increasing the alkyl chain length in the homologous series of alcohols used. The longer the chain length the longer the measured lifetime of the nanosecond transient.

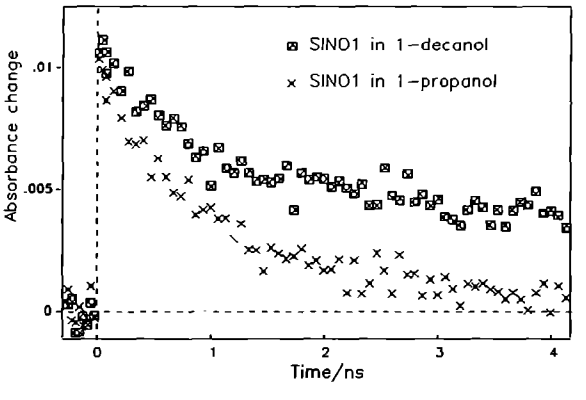

Transient decay kinetics for SINO1 in 1-propanol and 1-decanol.

This effect is most likely to be a viscosity effect rather than a polarity effect since increasing the alkyl chain length decreases the polarity of the alcohol. Decreasing the solvent polarity would be expected to decrease the transient lifetime in view of the results observed for SINO1 in acetonitrile and cyclohexane and SINO5 in 1-butanol and cyclohexane. If the observed effect of increasing the alkyl chain length is due to solvent viscosity then it is not unreasonable to assume that the transient is due to an isomerisation reaction, possibly a charge separated cisoid isomer rotating to form the final merocyanine products. Bohne et al measured a transient absorption spectrum of a cis type species resulting from the ultra violet irradiation of 2'-methyl SINO3. This species showed a large absorption band at ~450nm which is not prominent in the final merocyanine spectrum[2]. It is interesting to note that there is no effect on the lifetime of the long lived intermediate upon changing R1 from a methyl to an iso-butyl group, even though in the thermal reverse reaction the rate of ring closure is slowed when R1 is replaced by larger alkyl groups[3]. This may imply that the photochemically induced ring opening isomerisation is occurring on the excited state potential energy surface rather than the ground state surface as must be the case with the thermally activated ring closure reaction. The nanosecond transient lifetime increases in the order SINO2<SINO4<SINO5 due to changes in the substituent R2. It is not clear as to the exact cause of this phenomenon and more experiments are required to clarify this effect. It is likely that the electron donating characteristics of the R2 group are responsible for the changes observed. Once again the ordering of these lifetimes does not follow the order of the thermally activated ring closure reaction which goes in the order SINO5<SINO2<SINO4 at 298K[4].

NAPHTHALENE-OXYGEN COMPLEXES.

Oxygenated hydrocarbon solutions often exhibit additional absorption features in their UV-vis absorption spectra which are absent when either the oxygen or hydrocarbon is removed. These absorption features have been attributed[5] to the presence of an equilibrium population of hydrocarbon-molecular oxygen contact complexes, ($M..O_2\ ^3\Sigma_g^-$), which give rise to various electronic transitions including charge transfer (CT) transitions.—

$$M+O_2\ ^3\Sigma_g^- <=> {}^3(M..O_2\ ^3\Sigma_g^-) + h\nu \rightarrow {}^3(M^+.O_2^-) \qquad (1)$$

Our recent studies[1,6] of the dynamics of excited charge transfer complexes involving hydrocarbons and molecular oxygen, have revealed interesting solvent dependencies of the fate of these complexes, particularly with respect to the yield of hydrocarbon triplet state and singlet oxygen,$O_2\ ^1\Delta_g$.

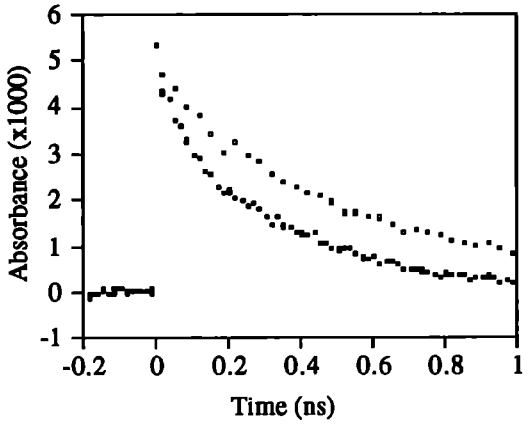

Figure 1: Decay of the triplet state of 1-methoxynaphthalene in CCl_4 at oxygen pressures of 50 atm and 80 atm following 373nm excitation into the CT absorption band of the 1-methoxynaphthalene-O_2 ground state complex. Probe wavelength; 436nm. [1-methoxynaphthalene]; 0.1 mol dm^{-3}.

However, because of multiphtonic induced transient absorbances we have been unable to observe the decay of the initially populated CT state involving substituted naphthalenes. As this was thought to be a consequence of the large hydrocarbon concentrations employed (~1.5 mol dm^{-3}) experiments have now been carried out using a high pressure absorption cell which permits lower hydrocarbon concentrations to be used(~0.1 mol dm^{-3}) at pressures of 50-80 atm oxygen. Unfortunately, this did not solve the problem of multiphoton-induced absorptions occurring on picosecond timescales. However, at such elevated pressures it is possible to observe the dynamic quenching of the hydrocarbon triplet state by oxygen following dissociation of the CT state. Figure 1 shows the effect of oxygen pressure on the triplet state decay for 1-methoxynaphthalene in CCl_4.

ACKNOWLEDGEMENT.

We are grateful to Professor T.G. Truscott for the loan of the high pressure cell.

REFERENCES.

(1) F. Wilkinson, D. J. McGarvey, J. Hobley, D. R. Worrall, A. Langley, W. Shaikh and W. Noad, Annual Report to the Laser Facility Committee, Rutherford Appleton Laboratory Report RAL-93-031, 1993, 156-157

(2) C. Bohne, M. G. Fan, Z. J. Li, Y. C. Liang, J. Lusztyk and J. C. Scaiano,
J. Photochem. and Photobiol. A: Chem., 66, 1992, 79-90

(3) J. C. Crano, W. S. Kwak and C. N. Welch, Applied Photochromic Polymer Systems ISBN 0-216-93140-1, 1992, 52-53.

(4) F. Wilkinson, J. Hobley and M. Naftaly, J. Chem. Soc. Faraday Trans., 88, 11, 1992, 1511-1517.

(5) Evans, D.F. J. Chem. Soc., 345 (1953).

(6) McGarvey, D.J.,F. Wilkinson, D.R. Worrall, J.Hobley and W. Shaikh, Chem. Phys. Letters, 202, 528,(1993).

MOBILITY, AGGREGATION AND DEACTIVATION PATHWAYS OF AROMATIC HYDROCARBONS ON SILICA SURFACES

F. Wilkinson[1], D.R. Worrall[1], S.L. Williams[1], D.J. McGarvey[2], A.J. Langley[3] and P. Taday[3]

[1]University Of Technology, Loughborough, Leicestershire LE11 3TU
[2]Keele University, Keele, Staffordshire
[3]Rutherford-Appleton Laboratory

INTRODUCTION

When adsorbed onto silica (60-100 mesh, 60 angstrom pore size) and excited at 355nm, anthracene shows both triplet state and cation radical formation. The emission spectrum shows both prompt and delayed fluorescence (produced from Triplet-Triplet anihilation), and two furthur emissions. One is broad and structureless centred at around 470nm, while the second has a very sharp short wavelength edge and a maximum at 530nm (figure 1). Both emissions rise promptly within the time resolution of our nanosecond flash photolysis apparatus (10ns) and decay by complex kinetics. The emission at 470nm is assigned tentatively as the singlet sandwich excimer on the basis of data obtained in a methylcyclohexane glass[1]. The emission at 530nm has not previously been reported for anthracene adsorbed on silica. Assignment of these emissions requires data on both the kinetics of decay of the normal prompt emission and of the rise and decay of the emissions at 530nm and 470nm, at a range of anthracene surface loadings.

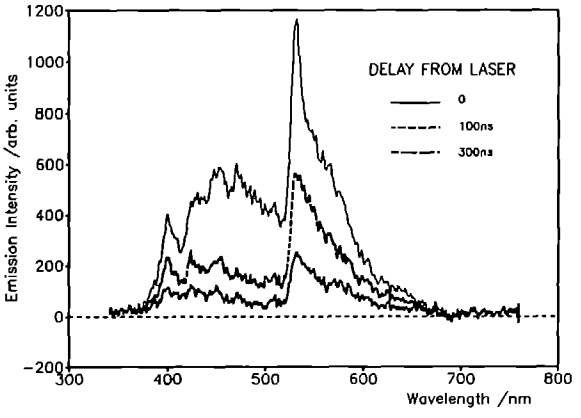

Figure 1: Anthracene emission from a silica surface excited at 355nm

EXPERIMENTAL

Samples were prepared by adsorbing anthracene from dry n-hexane solution onto silica gel previously pre-treated at 120°C and 10^{-5} mbar to remove physisorbed water. Following equilibration the solvent was decanted off and the sample dried under vacuum to 10^{-5} mbar before being sealed into quartz cuvettes.

Single photon timing data were obtained by exciting the sample at 313nm with the frequency doubled output of rhodamine 6G in a cavity dumped dye laser synchronously pumped by a mode-locked Nd:YAG laser. Data was collected for each sample at a range of emission wavelengths from 400 to 540nm. As anticipated for highly scattering samples, polarisation has no effect on the data obtained.

RESULTS AND DISCUSSION

Analysis of single photon timing data for aromatic hydrocarbons adsorbed on silica gel has been the subject of several practical and theoretical studies (see for example reference [2]). Each of these proposes a distribution of rate constants for the experimental data, the precise nature of the distribution depending upon a number of factors such as surface porosity, nature of the hydrocarbon etc.. In addition, analysis of the data in terms of distributions of rate constants requires experimental data with very high signal-to-noise along with careful choice of the fitting criterion. For the data obtained here the analysis has so far, for reasons of time constraints, been of a largely qualitative nature. Fitting of the data has been performed as the sum of three (or sometimes four) exponentials, with the reduced chi squared value being the fitting criterion. However, even with this initial analysis, certain trends in the data have appeared which correlate with the spectral data obtained using nanosecond flash photolysis.

At analysing wavelengths shorter than 450nm, the distribution of decay times is dominated by short time components, i.e. lifetimes of the order of 5ns which is the mean lifetime in this wavelength region measured by us using a nitrogen laser/avalanche photodiode combination. At wavelengths longer than 450nm, the emission intensity becomes significantly weaker and the decay time distribution becomes biased to longer lifetimes (>20ns). It is interesting to note that a plot of the ratio of >20ns to <5ns components as a function of wavelength (figure 2) reveals a shape similar to that shown in figure 1 except that the 470nm peak is much reduced. This difference in intensity may be explained in terms of the absorption by the emitting species at the exciting wavelength since we have demonstrated that both emissions are produced by a monophotonic process. This result lends further weight to the evidence gathered from nanosecond data which suggests that the excimer emission originates predominantly from small aggregates on the silica surface, since the absorption of such aggregates is bathochromically shifted from the monomeric form. The change in lifetime distribution with increasing wavelength confirms results obtained using nanosecond techniques, which clearly show that the longer wavelength emissions occur on timescales much longer than the "normal" anthracene emission.

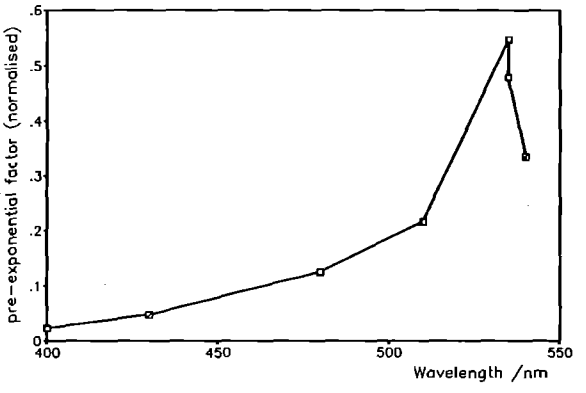

Figure 2: Ratio of <5ns component to >20ns component for a surface loading of 0.3% of a monolayer

A further important point to note is that the emission at 530nm is prompt, demonstrating that this is from a species directly excited on the surface and not one formed from diffusional processes. The fact that the decay time distribution appears independent of sample loading in the range employed (0.1 to 1% of a monolayer) is supportive of the hypothesis that diffusional processes do not play a large role in the singlet state decay.

The emission intensity at longer times in the 470nm region is too weak, for the reasons stated above, to determine its rise time. In order to study this emission in detail we require excitation wavelengths greater than 320nm. Longer excitation wavelengths are required to study other emission phenomena, for example excitation of the samples with wavelengths greater than 390nm causes profound changes in the observed emission spectra, probably due to excitation of further aggregates, the singlet state lifetime distributions of which have not yet been determined.

REFERENCES

1. M. Hoshino, H. Seki and M. Imamura, Chem. Phys. Lett., 104(4), 369-372 (1983)
2. W.R. Ware, Y.S. Liu and P. de Mayo, J. Phys. Chem., 97, 5980-6001 (1993)

THE ORIGIN OF THE ANOMALOUS FLUORESCENCE FROM METHYL 4-*N,N*-DIMETHYLAMINOBENZOATE

Robert Clark and Robert G. Brown

Chemistry Department, University of Central Lancashire

INTRODUCTION

The fluorescence properties of 4-(*N,N*-dimethylamino)- and 4-(*N,N*-diethylamino)- benzoic acid, various of their esters and their nitriles are anomalous in that two fluorescence bands are observed. One of these bands (the one at shorter wavelength) may be ascribed to "normal" fluorescence from the Franck-Condon excited state whilst the origin of the long wavelength band is controversial. Twisted intramolecular charge transfer (TICT) states[1,2] have been invoked to account for the observed dual fluorescence in the 4-(*N,N*-dialkylamino)benzonitriles[3]. The different relative orientations which can be adopted by the donor (4-(*N,N*-dialkylamino) group) and acceptor (nitrile group) parts of the molecule give rise to excited states which can be identified with "normal" and TICT fluorescence. The dual fluorescence from the methyl and ethyl esters of 4-(*N,N*-dimethylamino)- and 4-(*N,N*-diethylamino)- benzoic acid has also been ascribed to TICT state formation[4-7]. This assignment has been challenged by various other research groups including Visser *et al*[8] and Howell *et al*[9] who conclude that the dual fluorescence is due to solute-solvent exciplex or excimer formation respectively.

RESULTS AND DISCUSSION

We have been studying the fluorescence properties of 4-(*N,N*-dimethylamino)-benzoic acid and its methyl ester as part of a wider programme of work on the photophysics of the amino- and *N,N*-dimethylamino- benzoic acids. We confirm the presence of dual fluorescence in the 4-(*N,N*-dimethylamino) compounds in polar solvents and find that the spectra are concentration dependent for both the ester[10] and the acid[11]. Fluorescence lifetime measurements at the CLF have considerably enhanced the data that is available to us and back up our previous conclusions for these two compounds that the anomalous fluorescence originates in ground state dimerisation. A parallel set of measurements on 4-(*N,N*-dimethylamino)-benzonitrile reveals that the fluorescence decay of this compound is <u>not</u> concentration dependent (unlike the ester and acid), suggesting, in line with the literature, that a different mechanism for the dual fluorescence pertains in this compound.

A further series of measurements have looked at the fluorescence properties of the acid and its ester in non-polar hexane with small amounts of added acetonitrile. Once again we observe anomalous fluorescence. The spectra and decay kinetics depend on the amount of acetonitrile which is present but **do not** depend on the concentration of the solute (unlike in pure acetonitrile). The position of the second fluorescence band in the mixed solvents lies intermediate in wavelength between the normal fluorescence and the anomalous band observed in pure acetonitrile which suggests that we may be observing a different species. The variation of the fluorescence spectra with acetonitrile concentration appears to be in agreement with an exciplex mechanism as suggested by Visser *et al* for 4-(N,N-dimethylamino)-benzonitrile with acetonitrile[8] and by de Lange *et al* for this compound with benzene and toluene[12]. In this latter paper the authors have been able to decompose their spectra to show that the position of exciplex fluorescence varies with solvent composition. We are undertaking the same method of analysis for our data and will be preparing it for publication as soon as this is complete.

The fluorescence decay profiles of methyl 4-*N,N*-dimethylaminobenzoate in hexane also vary with the concentration of added acetonitrile. The normal ester fluorescence decays exponentially in pure hexane but the profile becomes increasingly non-exponential as acetonitrile is added (Figure 1). At least two exponential components are required to fit the decay profile as would be expected on the basis of reversible exciplex formation[13]. At longer wavelengths where the anomalous emission occurs, the observed decay profiles are very different (Figure 2).

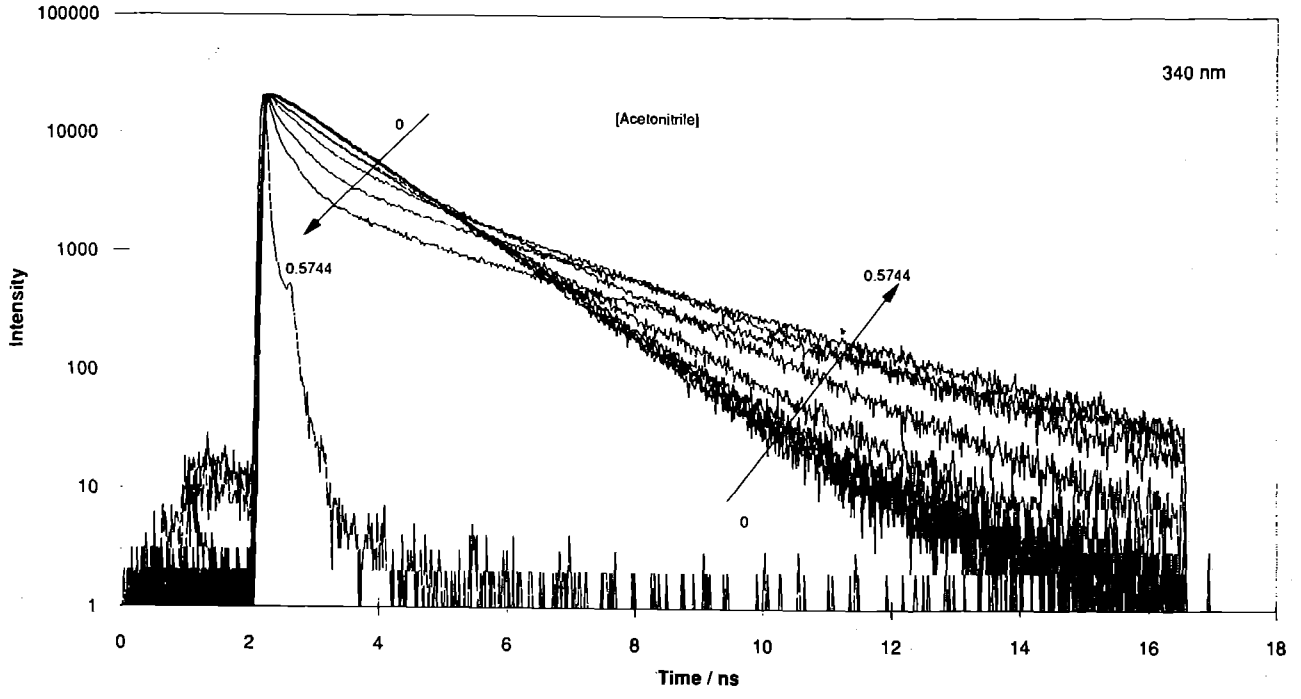

Figure 1: Fluorescence decay profiles (observed at 340 nm) of methyl 4-*N,N*-dimethylaminobenzoate in hexane as a function of added acetonitrile concentration.

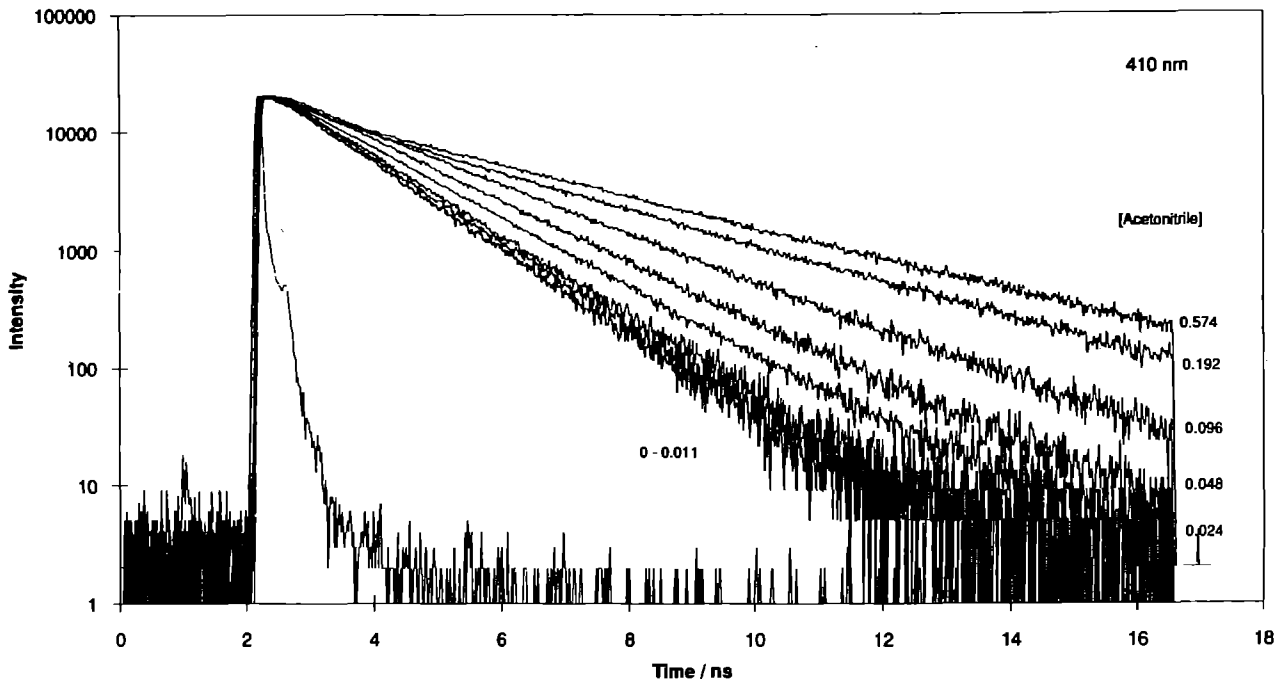

Figure 2: Fluorescence decay profiles (observed at 410 nm) of methyl 4-*N,N*-dimethylaminobenzoate in hexane as a function of added acetonitrile concentration.

Once again the decay becomes biexponential as acetonitrile is added and the lifetime of the longer of the two components matches that of the longer component observed at 340 nm. The agreement between the shorter lifetime components at the two wavelengths is less good and we do not observe the risetime for the anomalous fluorescence predicted by the exciplex model. However, this may simply be due to the presence of some normal ester fluorescence at 410 nm which masks the risetime. At even longer emission wavelengths (*e.g.* 450 nm) a risetime which is of the same order as the fast decay at 340 nm is observed for the highest acetonitrile concentrations used. However, the weakness of the emission often renders measurements at longer wavelength impossible and it is difficult to entirely isolate the exciplex emission from the quenched Franck-Condon fluorescence.

If our interpretation of our data is correct we are observing anomalous fluorescence from two different species, the nature of which is determined by solvent composition. In other words, there seems to be a solvent-induced switching between the different emitting states. Unfortunately, we are unable to study this phenomenon over the whole range of solvent composition in hexane/ acetonitrile because the two solvents are only miscible at the extremes of composition (up to about 0.5 mol.dm^{-3} of one solvent in the other). We are therefore not observing the changeover from exciplex to excited dimer emission as this lies in the region of solvent composition where the two solvents are incompletely miscible. We are therefore currently investigating the miscibility properties of mixtures such as hexane and hexanenitrile with the goal of studying the switch between the two emitting species.

REFERENCES

1. W Rettig, Angew Chem Internat Ed Engl, 25, 971, 1986.
2. W Rettig in "Modern Models of Bonding and Delocalisation" (Molecular Structure and Energetics, vol 6) eds J Liebman and A Greenberg, VCH-Publishers, New York, 1988, s229.
3. M van der Auweraer, Z R Grabowski and W Rettig, J Phys Chem, 95, 2083, 1991.
4. Z R Grabowski, K Rotkiewicz, A Siemiarczuk, D J Cowley and W Baumann, Nouv J Chim, 3, 443, 1979.
5. G Wermuth, W Rettig and E Lippert, Ber Bunsenges Phys Chem, 85, 64, 1981.
6. E Lippert, Ber Bunsenges Phys Chem, 92, 417, 1988.
7 . D J Cowley, P J Healy and A H Peoples, J Photochem, 9, 240,1978.
8. R J Visser, P C M Wiesenborn and C A G O Varma, Chem Phys Lett, 113, 330, 1985.
9. R Howell, A C Jones, A G Taylor and D Phillips, Chem Phys Lett, 163, 282, 1989.
10. J A T Revill and R G Brown, Chem Phys Lett, 188, 433, 1992.
11. J A T Revill and R G Brown, J. Fluorescence, 2, 107, 1992.
12. M C C de Lange, D Thorn Leeson, K A B van Kuijk, A H Huizer and C A G O Varma, Chem Phys, 174, 425, 1993.
13. W. R. Ware, J. D. Holmes and D. R. Arnold, J. Amer. Chem. Soc., 96, 7861, 1974.

PICOSECOND TIME RESOLVED RESONANCE RAMAN SPECTROSCOPIC INVESTIGATIONS OF EXCITED STATE ELECTRON TRANSFER REACTIONS - A PRELIMINARY REPORT

Anthony W. Parker[1], David Phillips[2], Eric Vauthey[3], Stuart Lawson[1], Michael Towrie[1] and Pavel Matousek[1]
[1]Rutherford Appleton Laboratory, [2] Imperial College, [3] University of Fribourg

In our other article this year we report our recent investigations on the structure of intermediates produced during electron transfer (e.t.) reactions using ns-TR^3. By choosing a medium polar solvent, 1,1,2,2-tetrachloroethane (TCE), it has been possible to study the rate of separation of a geminate ion pair into solvated ions. The following empirical equation[1] has been used by us to relate the rate of separation of a geminate ion pair into solvated free ions with the solvents' dielectric constant[2];

$$k_{diss}^{exc} = \frac{2.3 \times 10^9}{\eta}(cPs^{-1}) \exp\left(-\frac{e^2}{\varepsilon_s kT}\left(\frac{1}{d}-\frac{1}{a}\right)\right)$$

Where η is the solvent viscosity, ε_s is the static dielectric constant, and a and d are the acceptor-donor distance in the exciplex and geminate ion pair respectively. For the geminate ion pair separation to free solvated ions d is taken as ∞. Using a=7.5 Å k_{diss}=2.5 x 10^5 s^{-1} for TCE. This is slow enough to be followed using ns laser techniques (10 ns pulse widths). However, changing the solvent to MeCN makes k_{diss}=7 x10^8 s^{-1} and this is too fast to be followed by ns-TR^3. Thus, in order to progress our experiments into more polar solvents ps-time resolution is required. At present the existing wavelength range currently available on the ps-TR^3 system prohibits directly extending our work on the anthraquinone/1,2,4-trimethoxybenzene system into the faster time regime (λ_{pump}=350 nm and λ_{probe}=460 nm). This report outlines our efforts to find new donor/acceptor systems amenable to the current ps-TR^3 wavelengths. Using this faster time resolution it is hoped not only to test out e.t. theories in the more polar environments but also investigate excited singlet state e.t. reactivity and intramolecular e.t. reactions. Also, there is a particular interest in determining whether or not there are any structural differences in the intermediates produced from excitation of a ground state charge transfer complex and a diffusional encounter complex. Whilst much work has been performed using conventional ps time-resolved techniques (both absorption and fluorescence) these investigations are able to give little, if any structural information on the intermediates. For example; is the triplet exciplex produced from a triplet excited state encountering an electron donor/acceptor a real entity or is it actually a geminate ion pair? Our work to date[2] using ns-TR^3 has been unable to produce any evidence supporting the existence of the exciplex but faster time resolution is necessary before making any final conclusions. The existence of singlet exciplexes has been established from their fluorescence properties[3].

In the diffusion limit the e.t. intermolecular rate constant is given by;

$$k_{e.t.} = k_{diff}[Q]$$

where [Q] is the concentration of the ground state quencher. The diffusion rate constant, k_{diff} equals 1.9 x 10^{10} mol^{-1} dm^3 s^{-1} for acetonitrile @ 293 K. Therefore with [Q]=0.1 mol dm^{-3} the quenching rate constant is at most 1.9 x10^9 s^{-1}. This means that at this concentration one can not expect to see any ions until 500 ps after excitation. With the current ps-TR^3 apparatus the maximum pump/probe time delay is *c.* 1.5 ns meaning that realistically higher concentrations are necessary to increase the bimolecular reaction rate and ensure that an ample concentration of intermediates are available for probing. This reasoning also applies if the lifetime of the excited state is much shorter than the reaction time. In this case much higher quencher concentrations are again necessary to ensure reaction before the excited state decays. For these experiments it is important that efficient and very specific excitation by the pump laser occurs, e.g. the pump laser only produces excited state acceptor(donor) molecules. The high concentrations needed combined with the limited range of pump wavelengths makes experimental design very strict and with [Q] > 0.1 mol dm^{-3} the choice of reactant molecules which do not absorb the uv pump laser is very limited.

EXPERIMENTAL AND DISCUSSION

A. FLUORENE/CHLORANIL

Figure 1 shows the ps-TR^3 spectra of fluorene in acetonitrile at various time delays. We believe the spectra correspond to singlet excited state fluorene (bands marked with asterisks) and fluorene radical cation produced by pump laser photoionization. The radical cation assignment is based on our observing the intensities of these bands varying with pump power, see spectrum marked "low/100 ps" obtained using 6-times lower pump pulse energy and performing the experiment in the non-polar solvent gave only excited state singlet bands. This spectrum gives a linear decrease in singlet excited state bands with a corresponding non-linear decrease in bands assigned to the radical cation. Addition of the electron acceptor chloranil also produced similar spectra with no obvious time dependent shifts in band positions. An important observation of these results is that the band intensities of fluorene alone in MeCN does not grow after 100 ps. However, the addition of chloranil (10 mmol dm^{-3}) results in spectra of similar appearance but with different kinetic behaviour. The radical cation spectrum grows in on a time scale of 100 ps due to e.t. to chloranil. As this is an order of magnitude faster than expected for a diffusion controlled reaction at the Smoluchowski limit other, presently unknown, factors need to be considered.

B. METHYL VIOLOGEN

Excitation of MV^{2+} (10 mmol dm^{-3}) in water using 305 nm excitation and 610 nm probe produced a transient believed to be $^1MV^{2+}$. Addition of powerful electron donor DABCO (0.1 mol dm^{-3}) did not produce the expected $MV^{\cdot+}$ signal. Providing the electron process takes place on a time scale shorter than 1000 ps this product should be observable. This latter point was demonstrated by producing $MV^{\cdot+}$ chemically by adding the

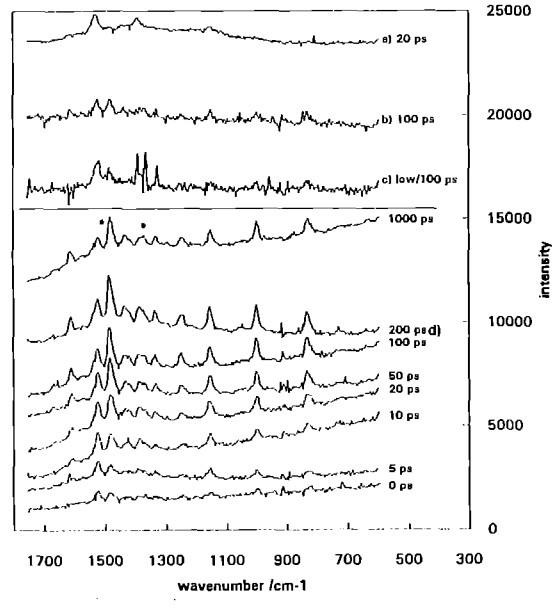

Figure 1: TR^3 spectra of fluorene (30 x10^{-3} mol dm-3) excited at 305 nm and probed at 610 nm: a) in hexane; b) in acetonitrile with chloranil (10 x10^{-3} mol dm^{-3}); c) in acetonitrile pumped with 6 times lower intensity; d) in acetonitrile: bands marked with stars are assigned to fluorene singlet excited state and unmarked bands to fuorene radical cation. Time delays are shown on the right. The ground state and solvent bands have been subtracted.

Table: Positions of transient Raman bands of fluorene in acetonitrile at $\Delta t = 200$ ps

band cm^{-1}	tentative assignment
1613	cation
1527	singlet
1484	cation
1433	cation
1383	singlet + cation
1335	cation
1250	cation
1157	cation (+ singlet)
1002	cation
832	cation

reductant $Na_2S_2O_3$ to an aqueous solution of MV^{2+}. Excellent Raman spectra (not shown) were recorded using the 615 nm probe laser.

Another way to perform bimolecular chemistry is to constrain the two reactants inside a micelle. Under favourable circumstances this effectively eliminates the diffusional processes, a trade off can be that the separation process is hampered (*cf.* non-polar solvents) leading to a diminished free ion yield. It does, however, enable the easy formation of ground state charge transfer complexes and should provide a means for studying such complexes. Recently, Hubig[4] has investigated the compact ion pairs formed between naphthalene (and fluoro-, chloro-, bromo- and cyano-naphthalenes) in SDS micelles with methylviologen. As SDS is an anionic surfactant the positively charged MV^{2+} adheres to the micelle surface and is able to form a charge transfer complex with the guest naphthalene as shown by the solution having an absorption band tailing to about 430 nm. The ps-TR^3 experimental results are given in Figure 2. The $MV^{\bullet+}$ bands decay rapidly over 100 to 200 ps. In aqueous solutions $MV^{\bullet+}$ can have very long lifetimes (dependent on oxygen concentration) indicating that charge separation does not occur in these systems. Interestingly the complex could also be formed in ethanol where similar spectra were observed but the sample degraded very quickly. We have been able to produce similar micellar charge transfer complexes with *trans*-stilbene which again yield $MV^{\bullet+}$ upon photolysis. Markel *et al.*[5] have obtained the Raman spectrum of hexamethylbenzene/ tetracyanoethylene charge transfer complex. The work identifies a 165 cm^{-1} band as the donor-acceptor intermolecular stretching mode. Whilst such low modes are at present not within the capabilities of the existing ps-TR^3 system they also observe higher modes producing overtones with this band indicating that such information should be possible.

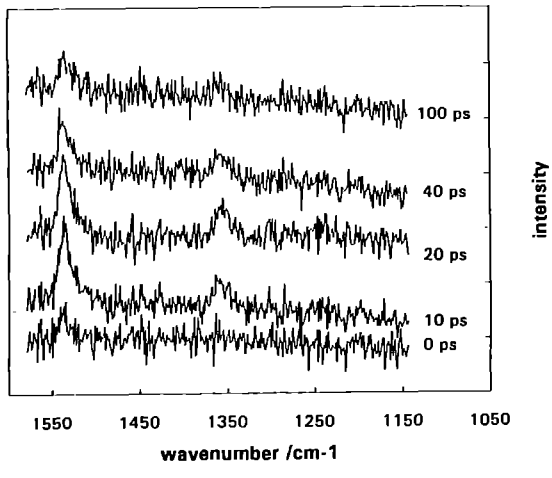

Figure 2: TR^3 spectra of a (0.08 mol dm^{-3}) aqueous micellar SDS solution of naphthalene (8 x 10^{-3} mol dm^{-3}) in the presence of MV^{2+} (2.3 x 10-3 mol dm^{-3}) solution excited at 305 nm and probed at 610 nm after various time delays. The ground state and solvent bands have been subtracted; all the bands are assigned to $MV^{\bullet+}$.

C. ANTHRAQUINONE/TEA and DABCO

Using both these donors and 285 nm and 570 nm for the pump and probe wavelengths failed to produce the expected resonance Raman spectrum of $AQ^{\bullet-}$. This result was rather surprising given the ease with which this species can be detected by ns-TR^3 using a probe wavelength of 540 nm even allowing for the weaker absorbance *c.* 3 times less @ 570 nm. This was investigated further using a single ns-laser operating at 570 nm and frequency doubling to produce a 285 nm probe pulse. Whilst this technique does not yield time resolved information it has the advantage of being easily setup. As can be seen from Figure 3a excellent quality data were obtained. At present we are uncertain as to why we have not observed $AQ^{\bullet-}$. A possible explanation is excessive sample degradation from the increased peak powers of the 6 ps laser pulses. Certainly with 1 mol dm^{-3} quencher concentration one would expect the reaction to be well established after 1.5 ns and $AQ^{\bullet-}$ should be observable by ps-TR^3. Figures 3b and 3c further demonstrate the use of a single laser to obtain Raman spectra of intermediates, the spectra of SINO5 (a spiro-indolino-naphthooxaazine) can be compared with those illustrated in the ps-TR^3 report on this compound found elsewhere in this report.

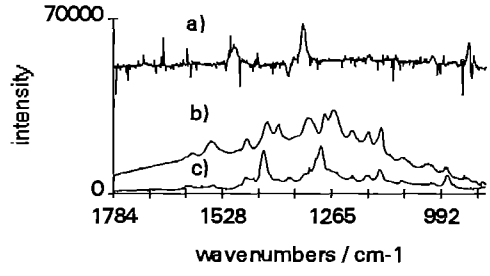

Figure 3: Transient resonance spectra produced using excimer pumped dye laser operating at 570 nm. This output was used as probe beam and the frequency doubled output (285 nm) as pump beam, producing zero time delay resonance Raman spectra. a) Anthraquinone (1 x 10^{-3} mol dm^{-3}) in the presence of TEA (0.1 mol dm^{-3}) in acetonitrile; b) SIN05 in butanol; c) SIN05 in cyclohexane.

REFERENCES

1) A. Weller, Pure Appl. Chem. (1982), 54, 1885
2) E. Vauthey, D. Phillips and A. W. Parker, J. Phys. Chem. (1992), 96, 7356
3) See for example T. Förster, The Exciplex; M. Gordon and W. R. Ware Eds., Academic Press: New York, (1975), 1 and references therein.
4) S. M. Hubig, J. Phys. Chem. (1992), 96, 2903
5) F. Markel, N. S. Ferris, I. R. Gould and A. B. Myers, J. Am. Chem. Soc., (1992), 114, 6219

ACKNOWLEDGEMENT

We thank F. Wilkinson and J. Hobley for providing SINO5

RATE OF SEPARATION OF GEMINATE ION PAIR INTO FREE IONS IN A MEDIUM POLAR SOLVENT

Anthony W. Parker[1], David Phillips[2], Bohdana Nohova[2], Eric Vauthey[3]
[1]Rutherford Appleton Laboratory, [2] Imperial College, [3] University of Fribourg

Solution phase electron transfer processes are of paramount importance in chemistry and in nature, and the enhancement of oxidation and reduction potentials in the electronically excited states of molecules makes excited state electron transfer of especial interest[1]. To date photo-induced electron transfer has been widely studied using conventional time-resolved absorption and fluorescence techniques and much has been established concerning the general reaction pathway. During the course of the electron transfer process an excited state donor/acceptor molecule collides with the ground state acceptor/donor molecule to form a precursor state known as an encounter complex. This provides a means by which an electron localised on the donor molecular orbital transfers to a molecular orbital localised on the acceptor molecule to form a geminate ion pair. Once this has occurred the geminate ion pair can separate and the ion become solvated. Data produced from transient absorption techniques are not capable of distinguishing the subtle structural changes taking place during this process and chemical systems where it is proposed the intermediates are produced do not show any spectral differences which differentiate them. We have recently reported our use of nanosecond time-resolved Raman spectroscopy to investigate the electron transfer between triplet anthraquinone (^{3}AQ) and 1,2,4-trimethoxybenzene (TMB) in solvents of differing polarity[2]. This work demonstrated that the frequency of the aromatic C-C stretch of $TMB^{\cdot+}$ was environment dependent. In 1,1,2,2-tetrachloroethane (TCE) a solvent of medium polarity, where the rate of separation of the geminate-ion pair into free ions, k_{sep}, is expected to be within the time resolution of the ns-TR[3] apparatus the frequency shifts from 1607 cm^{-1} at early time delays to 1590 cm^{-1} after 1 μs. These bands have been assigned to the $TMB^{\cdot+}$ C-C stretch within the geminate ion pair and freely solvated $TMB^{\cdot+}$ respectively. We now report direct measurement of the kinetics of the geminate ion pair separating into free ions and our establishment of the thermodynamics for this process.

RESULTS AND DISCUSSION

Figure 1 shows the resonance Raman band located around 1600 cm^{-1}. This band can be fitted by the convolution of two gaussians

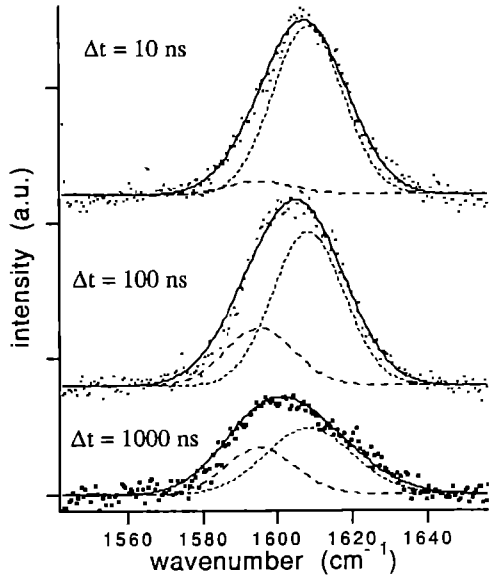

Figure 1: Time evolution of the shape of the resonance Raman band *c.* 1600 cm^{-1} obtained by pumping at 351 nm and probing at 460 nm a solution of AQ and TMB at -5°C. The dotted and dashed gaussians correspond to the C-C stretching of the $TMB^{\cdot+}$ in the geminate ion pair and free solvated ions respectively. The solid line is the convolution of two gaussians.

whose intensities vary with the time delay of the pump and probe laser. The overall process is shown in the scheme below which can be modelled mathematically to the kinetics of typical coupled system as used to describe delayed fluorescence[3]. The analysis was simplified by assuming the hyperfine coupling constant, k_{hfc}, is much smaller then k_{sep} and k_{rec} was approximated to first order rate constant (this of course being a second order process). Using this approach k_{sep} has been determined over the temperature range -5 to 35 °C. The Arrhenius plot for this data is given in Figure 2 and from this plot activation energy for the separation is calculated to be 0.16 eV (3.7 kcal mol^{-1}). As the separation into free ions is in essence a diffusional process, one part of this activation energy is associated with the temperature dependence of the solvent viscosity. Taking this into account the intrinsic activation enthalpy associated to the separation of the geminate ion pair into free ions, $\Delta H^{\neq}_{sep}$, equals 0.04 eV (2.7 kcal mol^{-1}). Thermodynamically, the energy of the geminate ion pair state and of the free ion state can differ through the electrostatic energy between the two ions and the solvation energy. The solvation energy for the geminate ion pair can be calculated from solvation of a dipole in a spherical cavity with two opposite charges separated by the ionic radii, r[4]:

$$E^{IP}_{solv} = -\frac{(2re)^2}{2a^3}\cdot\frac{2(\varepsilon-1)}{2\varepsilon+1} \approx -\frac{e^2}{r}\cdot\frac{2(\varepsilon-1)}{2\varepsilon+1}$$

where ε is the dielectric constant of the solvent, and a is the cavity radius. For the approximation the radius a of the sphere equals that of the two ions of radius r. On the other hand, the solvation of the free ions can be calculated from the Born equation[5]:

$$E^{FI}_{solv} = -\frac{e^2}{r}\cdot\left(1-\frac{1}{\varepsilon}\right)$$

The above two equations predict that in a very polar solvent the solvation energy of a geminate ion pair is the same as that of two free ions. However, in a medium polar solvent, such as TCE (ε=8.2 at

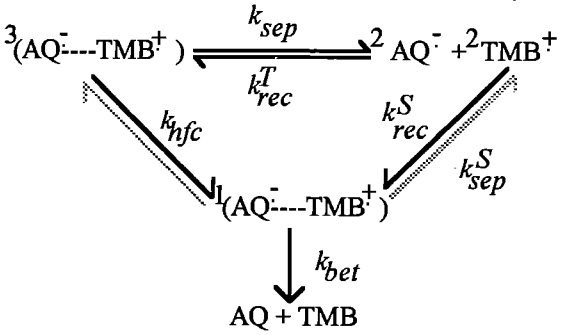

Scheme

20 °C), the solvation energy is slightly larger for the free ions than for the geminate ion pair , $E^{IP}_{solv}/E^{FI}_{solv}$ = 0.94. Taking the ions as spheres having the average molecular volumes AQ and TMB gives an ionic radius of 3.4 Å. The solvation energy difference between the free ions and the geminate ion pair using our approximations is about -0.19 eV. The Coulomb term accounting for the electrostatic stabilisation is given by:

$$C = -\frac{e^2}{d\varepsilon}.$$

For a loose ion pair with separation d = 7.5 Å[6], the electrostatic stabilisation equals -0.23 eV in TCE. If one considers the geminate

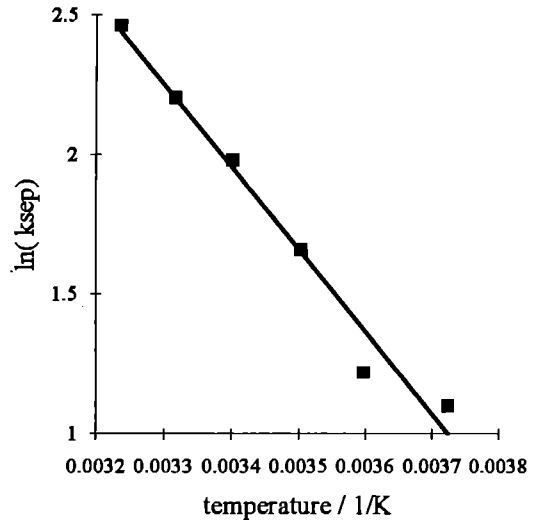

Figure 3: Temperature dependence of the rate constant of separation of the geminate ion pair into free ions

ion pair as a tight ion pair with a typical interionic distance of 3.5 Å[6] then the Coulombic stabilisation increases to -0.52 eV. Of course for free ions there is no electrostatic interaction because the average distance between the two ions of opposite charge is to large for any effect. From the above calculations the enthalpy difference between the free ions and the geminate ion pair, ΔH_{sep}, is about 0.04 eV for a geminate ion pair with interionic distance of 7.5 Å and 0.33 eV for a tight ion pair. In the latter case the separation is very endothermic with entropy strongly driving separation. Also, the equilibrium between geminate ion pair and free ions would favour the geminate ion pair contrarily to our experimental observations. We conclude that a realistic interionic distance within the geminate ion pair is 7.5 Å.

The separation of the geminate ion pair involves two opposite contributions. The loss of electrostatic stabilisation which requires an increase in the systems energy and as the separation proceeds some solvent molecules penetrate between the two ions with the solvation energy helping to stabilise the system and compensate for the loss in electrostatic stabilisation. The activation energy which has to be given to the ion pair to separate enough to allow solvent to penetrate is given by:

$$\Delta H^{\neq}_{sep} = \frac{e^2}{\varepsilon}\left(\frac{1}{d} - \frac{1}{d^{\neq}}\right)$$

where $d^{\neq}$ is the interionic distance in the transition state, the temperature dependence of ε can be neglected. Taking our measured value for $\Delta H^{\neq}_{sep}$ as 0.04 eV and a value for 2r as 7.5 Å, the interionic distance at the transition step is 9.5 Å. The molecular radius of TCE calculated from the method the Van der Waals increments[7] is around 2.8 Å. Thus the interionic distance appears to be just large enough for a solvent molecule to fit between the ions. In this state the solvation energy is larger and attenuates the loss of Coulomb energy. It is worth noting that for a tight ion pair the interionic distance within the transition state would be about 3.7 Å, which is only 0.2 Å larger than in the ion pair and this is unrealistic. Our measurements indicate the interionic distance within the geminate ion pair is 7.5 Å and **not** solvent separated. This latter point is concluded firstly from if this were not so then the solvation energy difference would be almost zero and secondly, if the geminate ion pair was solvent separated there would be no noticeable change to its environment after separation and our band shift would not be observed. Another point of reasoning could be that the ion pair structure is loose enough to allow partial penetration of solvent molecules. Indeed, if the interionic space was completely unaffected by the reaction field of the solvent, the dielectric constant of the solvent should be removed from the calculation and replaced by the polarisability of the ions[8]. In such a case the coulomb stabilisation would be *ca.* 4 times larger with a corresponding increase in the activation enthalpy.

Figure 4 shows a schematic diagram of the energy levels involved in the separation of the geminate ion pair. Considering the size of the activation enthalpy, $\Delta H^{\neq}_{sep}$, and the enthalpy difference ΔH_{sep}, it appears that there is no intrinsic activation barrier for the back reaction, i.e. free ions recombination. This is in good agreement with the equation developed by Debye[9] and Eigen[10] to describe the diffusion rate constant for two charged species.

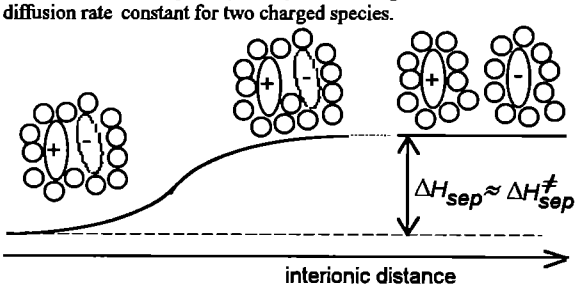

Figure 4: Artistic representation of the geminate ion pair at different stages of separation into free ions

We are now turning our attention to try and understand the nature of the environmental effect observed for the *c.* 1600 cm^{-1} band of $TMB^{+\cdot}$. To date we have only observed this effect with TMB. At present we believe that the changes in the Raman Spectra are due to some solvent induced structural change of the $TMB^{+\cdot}$ causing a change in the electronic coupling of the methoxy group π-lone pair with the aromatic ring. The Table summarises our findings to date, it is interesting to note that other methoxybenzenes do not give this effect. We are now investigating systems such as 2,5-dimethoxytoluene/ anthraquinone and other quinones or charge transfer complexes of chloranil.

Donor	Acceptor	Solvent	Comment
TMB	AQ	MeCN	shift too fast for kinetics
		TCE	kinetics temp dependence, solutions went blue
		1-octanol	fluorescence
		BuCN	solvent impurity
	duro-quinone	TCE	probably some shift
	benzo-quinone	TCE	probably some shift
2,3,5-trimeth-oxytolune	AQ	MeCN TCE	no shift
1,3-dimeth-oxybenzene		TCE MeCN	weak signal no shift
1,4-dimeth-oxybenzene		TCE	probably no shift
1,3,5-dimeth-oxybenzene		TCE	fluorescence
2,4-dimeth-oxytoluene		TCE	weak signal, probably no shift, solution went pink

REFERENCES

1) M.A. Fox and M. Chanon, 'Photoinduced Electron Transfer', Elsever, Amsterdam, (1988).
2) E. Vauthey, D. Phillips and A.W. Parker, J. Phys. Chem., **96**, (1992),7356.
3) J.N. Demas, 'Excited State Lifetime Measurements', Academic Press, New York, (1983), 59.
4) L. Onsager, J. Am. Chem. Soc, **58**, (1936), 1486.
5) M. Born, Z. Phys., **1**, (1920), 45.
6) A. Weller, Pure & Appl. Chem., **54**, (1982), 1885.
7) J.T. Edward, J. Chem. Educ., **4**, (1970), 261.
8) P. Suppan, J. Chem. Soc. Far. Trans. I, **82**, (1986), 509.
9) P. Debye, Trans. Electrochem. Soc., **82**, (1942), 265.
10) M. Eigen, Z. Phys. Chem.,(Wiesbaden), **1**, (1953), 176.

ACKNOWLEDGEMENT

We thank Pavel Matousek for his help with the computer programme.

TIME RESOLVED RESONANCE RAMAN OF CAROTENOID RADICAL ANIONS AND CATIONS

S M Tavender[1], J H Tinkler[2], A W Parker[1], R Goyal[2], L Mulroy[2] and T G Truscott[2],
[1] Laser Support Facility, Rutherford Appleton Laboratory, Chilton, DIDCOT Oxon, OX11 OQX
[2]Department of Chemistry, University of Keele, KEELE, Staffs ST5 5BG

INTRODUCTION

Carotenoid radicals have been implicated in the anti-cancer effect of dietary polyenes, the electron transfer reactions in photosynthesis and the vision process[1]. Whilst the radicals have been characterised using pulse radiolytic methods[2] this technique has only been able to identify their transient absorption spectra and has done little to establish their structure and indeed their reactivity. The absorption maximum of carotenoid radical anions and cations tends to be in the near infra-red, from 700-900 nm. As such, TR[3] spectroscopic studies have only recently been possible following the development of sensitive detectors which are capable of operating in this spectral region.

This project can be divided into two parts. Firstly, ns-laser flash photolysis experiments were performed to establish efficient photochemical methods for the generation of the carotenoid radical anions and cations. This is crucial as the biologically important carotenoids are only soluble in non-polar solvents where the photochemical generation of ions is unfavourable. Secondly, after the photochemistry is established, it must be applied within a TR[3] experiment to obtain the vibrational spectra of the intermediates. For the latter part the C_{20} retinoid, *all-trans* retinal was the first polyene studied. This was chosen because it can be dissolved in methanol, a polar solvent favouring ion formation. In this solvent the retinal anion and cation absorption maximum is at 390 nm and 435 nm respectively, allowing investigation using the existing TR[3] Triplemate set-up. After this a less polar solvent can be selected and the work repeated using the new near infra-red TR[3] spectrograph and CCD camera described elsewhere in this report. We also report preliminary results using this system for 7,7'-dihydro-β-carotene.

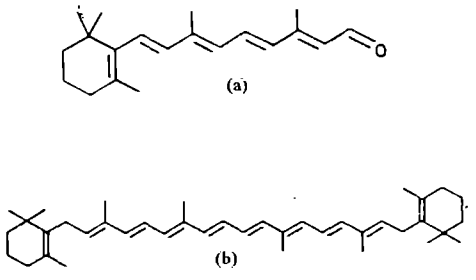

Fig 1. Structures of (a) *all-trans* retinal and (b) 7,7'dihydroβ-carotene

EXPERIMENTAL

Pulse radiolysis experiments on *all-trans* retinal ($3x10^{-4}$ mol dm^{-3}) in methanol have identified two bands, one immediately after the pulse at 435 nm and a second after 2 us at 390 nm[2]. These are assigned to the *all-trans* retinal radical cation and anion respectively. However, in alkali methanol only a single transient was observed with an absorption maximum at 410 nm assigned to the radical anion. The results imply that in neutral methanol an acid-base equilibrium is occurring.

All-trans retinal has a triplet quantum yield of only 0.12 and in order to generate higher concentrations sensitisation experiments using triplet naphthalene were tried. The radical anion can then be formed by triplet retinal capturing an electron from the photoionised naphthalene. Using alkali methanol as solvent, it is possible to generate only the radical anion. This was confirmed to be the anion by bubbling the sample with nitrous oxide which scavenges solvated electrons, oxidising them to •OH and so prevents anion formation. The proposed reaction scheme is as follows:

1) $Nap \xrightarrow{248nm} {}^3Nap$

2) $Nap \xrightarrow{248nm} Nap^{\bullet+} + e^-_{(solv)}$

3) $Nap + Ret \longrightarrow {}^3Ret + Nap$

4) ${}^3Ret + e^-_{(solv)} \longrightarrow Ret^{\bullet-}$

and in the presence of N_2O equation (5) follows equation (2)

5) $N_2O + e^-_{(solv)} \rightarrow [N_2O]^- \xrightarrow{H+} N_2 + {}^{\bullet}OH$

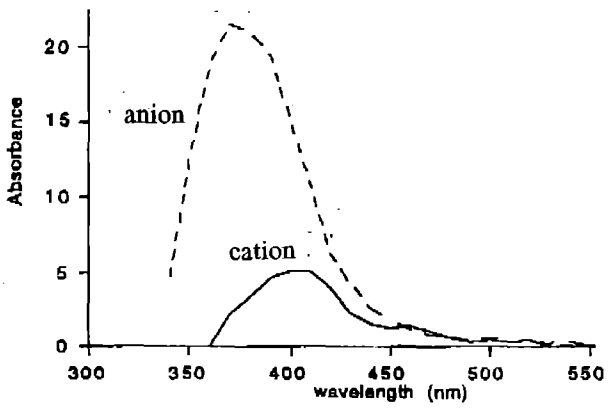

Fig 2. Nanosecond Flash Photolysis of *all-trans* retinal in methanol

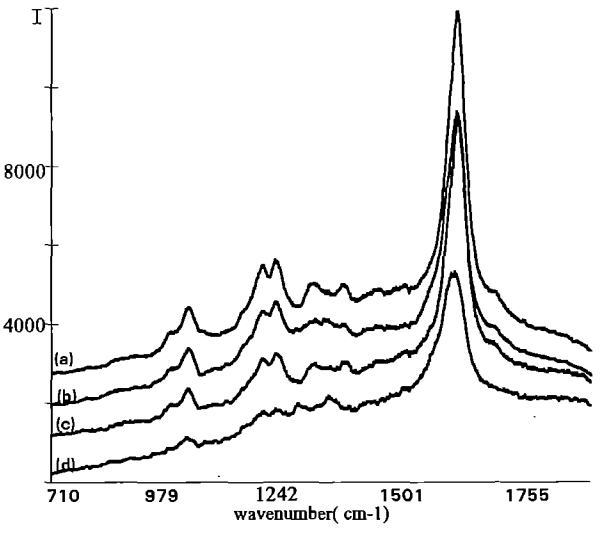

Fig 3. *All-trans* retinal + naphthalene in alkali methanol. (a) Probe only +N_2O,(b)Pump/probe +N_2O. (c) Probe only and (d) Pump/probe. Pump 248 nm, probe 425 nm. All spectra are solvent subtracted. Spectra produced from 6000 laser shots. Pump-probe time delay 2μs

Table 1. Raman assignments of *all-trans* retinal + naphthalene in alkali methanol

Band (cm^{-1})	Probe-only bubbled with N_2O	Pump/probe bubbled with N_2O	Probe-only	Pump/probe-	Assignment
965	m		m	m	g.s. C-H stretch
1007	s	s	s	m	g.s.C-H stretch
1164	s	s	s	m	g.s. C-H stretch
1195	s	s	s	m	g.s.C-H stretch
1241		w		s	Triplet
1272	s	m	s		g.s. C-H stretch/C-C bend
1304	w	s	w	s	Triplet
1337	m	w	s		Triplet nap/g.s. C-C stretch
1407	m	w	w		CH_3 deformation
1562				s	Anion
1572	vs	s	s		g.s.C=C stretch

Figure 3 shows the spectra produced from extending the flash photolysis work to ns-TR[3] experiments. The Raman spectra clearly show a shift in the ground state C=C double bond stretch at 1568 cm^{-1} and this is ascribed to the radical anion. This band shift is not observed when N_2O is present. The Raman assignments are given in Table 1.

All-trans retinal has ground state absorption from 250-410 nm and triplet absorption from 350-530 nm so the 425 nm probe is in resonance with both these species as well as the radical anion. The ground state and triplet Raman bands agree with other published data[3]. The subtracted spectra (Pump/probe minus probe only) are shown in Fig. 4. The major difference is the shift in the ground state C=C stretch band at 1585 cm^{-1}. The lowering of this band by 22 cm^{-1} in the anion spectrum indicates that there is a weakening of the conjugated system. Interestingly, a weak band appears at 1648 cm^{-1} which is in the region for a C=O stretch and where localisation of the electron may be expected. However, because of the weakening of the conjugated system and the greater aldehyde character in the anion spectrum we believe the electron to be located on the terminal carbon of the *all-trans* retinal.

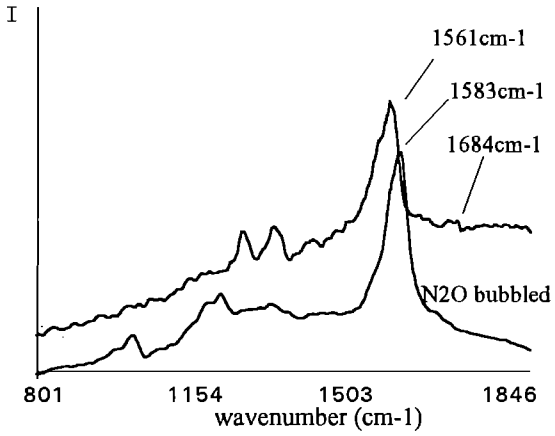

Fig 4. Subtracted spectra (pump/probe - probe only) showing differences between solutions with and without N_2O.

EXPERIMENTS USING THE CCD

Using the thinned, back illuminated liquid nitrogen cooled CCD detector our studies have been extended into the near infra-red region where the longer chain carotenoid ions come into resonance. Using 308 nm radiation two-photon ionisation of the 7,7'-dihydro-βcarotene (7,7DH) in hexane ($5x10^{-5}$ mol dm^{-3}) produced the 7,7DH radical anion. The yield of cation was increased by using tetranitromethane (TNM), an electron scavenger, which also prevents the formation of the anion allowing identification of the cation and anion Raman bands.

The ns-TR[3] spectra obtained from a Raman probe at 760 nm, which is in resonance with both the cation and anion is illustrated in Figure 5 and 6. Spectra shown were collected for 140 s. The time delay between pump and probe was 250 ns. The proposed reaction scheme is as follows:-

6) $7,7DH \xrightarrow{308nm} {}^1 7,7DH$

7) ${}^1 7,7DH \xrightarrow{308nm} 7,7DH^{\bullet +} + e^-_{solv}$

8) ${}^1 7,7DH + e^-_{solv} \longrightarrow 7,7DH^{\bullet -}$

and when TNM is present:

9) $TNM + e^-_{solv} \longrightarrow TNM^-$

The main features in the pump/probe spectra shown in Figure 5 are a new band at 1186 cm^{-1} and the appearance of three bands at 1508, 1539 and 1551 cm^{-1}. These are assigned to the cation. Comparing the pump/probe spectra with and without TNM shown in Figure 6, these features, although slightly weaker, are still present but the most dramatic difference is the additional band at 1242 cm^{-1}, a weak band at 933 cm^{-1} and a broadening of the ground state band at 1453 cm^{-1}. These are assigned to the anion.

Two bands at 733 cm^{-1} and 767 cm^{-1} are seen in all the excited state spectra. In the spectra without TNM they are slightly more intense indicating they could be cation bands. Further work is now underway to fully assign these bands.

Our assignments to the Raman bands are given in Table 2.

Table 2: Assignments of 7,7'dihydrobetacarotene in hexane

Band cm^{-1}	pump/probe	+ TNM probe only	+ TNM pump/probe	Assignment
733	s		s	C-H stretch, triplet
767	s		s	C-H stretch, triplet
826	s	s	s	solvent
871	s	s	s	gs C-H stretch
898	s	s	s	gs C-H stretch
933	w			Anion
1008		m	s	TNM
1042	s	s	s	gs C-H stretch
1081	m	s	s	solvent
1144	m	m	m	gs C-H stretch
1162	s	m	s	gs C-H stretch
1186			s	cation
1242	s			anion
1302	s	s	s	gs C-C stretch
1360	w			CH_3 deformation
1372	w		broad	CH_3 deformation
1387	w	w		CH_3 deformation
1453	broad	s	s	gs C=C stretch. Anion
1508	m		m	cation
1539	s		s	cation
1551	m		m	cation

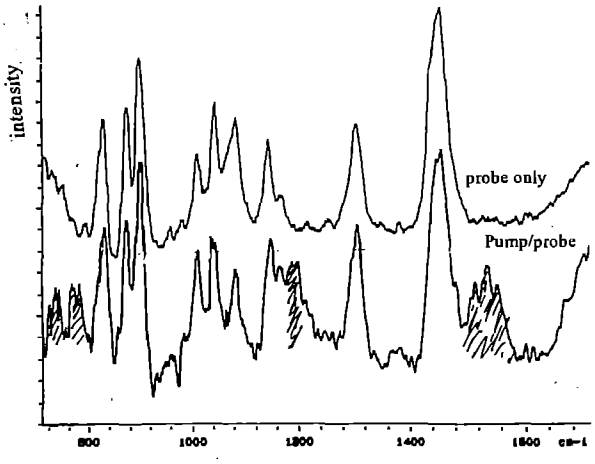

Fig 5. Pump/probe and probe only spectra for 7,7'dihydroβ-carotene in hexane + TNM. Note: the TNM degraded the carotenoid (going colourless) and so the solution was not recycled.

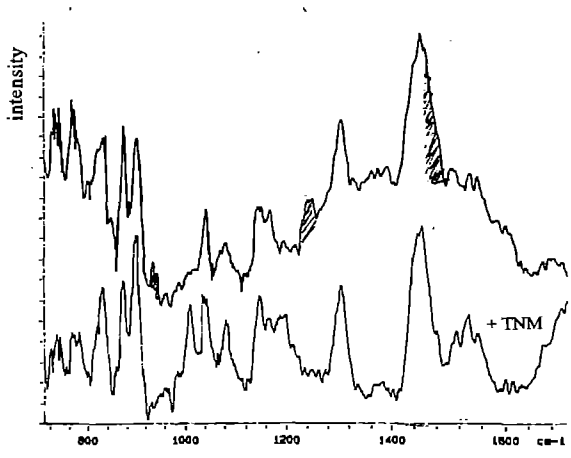

Fig 6. Pump/probe with and without TNM. Delay 250 ns

CONCLUSIONS

The radical anion of *all-trans* retinal has been photochemically produced and its Raman spectrum recorded. Results indicate the electron is situated on the terminal carbon. The ns-TR[3] work has been extended to the infra-red region where 7,7'-dihydro-β-carotene has been probed and both its radical cation and anion Raman spectra have been obtained and tentatively assigned. It is hoped to extend this work with power dependence experiments (both reaction mechanisms are two-photon processes), to use different time delays to study the lifetimes of the radical ions and also to use different solvents (more polar) to enhance the formation of the radical ions.

References

1. A Kropf and R Hubbard, Photochem. Photobiol. 12, p249 (1990) and J M Donahue and WH Waddell, Photochem. Photobiol. 40, No.3 p399 (1984)

2. R V Bensasson, E J Land and T G Truscott. Flash Photolysis and Pulse Radiolysis, Pergamom Press, 1983

3 H Hashimoto, Y Mukai, Y Koyama CPL 152 No4.5, p319 1988

RESONANCE RAMAN SPECTROSCOPY WITH A TI-SAPPHIRE LASER : PROBING AVERAGE-VALENCE SITES IN DI-COPPER AZACRYPTANDS

A H R Al-Obaidi[1], J J McGarvey[1], J Nelson[1,2], Lu Qin[1] and S E J Bell[1]

[1]School of Chemistry, The Queen's University of Belfast, Belfast, BT9 5AG

[2]The Open University (Northern Ireland).

INTRODUCTION

The proposal that the electron-transfer site in nitrous oxide reductase[1] and cytochrome c oxidase[2] contains an average-valence dicopper site [$Cu^{1.5}$-$Cu^{1.5}$] has rekindled interest in the possible existence of such a site in small molecule models. Recently, three dicopper-azacryptand complexes with an average-valence [$Cu^{1.5}$-$Cu^{1.5}$] site (**1-3**) have been structurally characterized[3,4,5]. All three complexes exhibit an intense UV absorption band near 330 nm together with a more complex feature in the red/near infrared (700-1100 nm) with an asymmetric profile suggesting the involvement of at least two electronic transitions over this wavelength range.

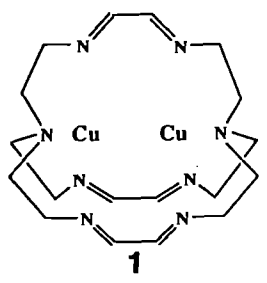

1

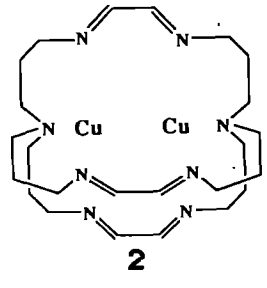

2

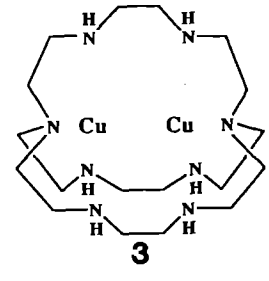

3

In the 1993 RAL report we presented preliminary data on low frequency modes in the range 200 - 500 cm^{-1} derived from Resonance Raman (RR) spectra of complexes 1 and 3 generated at 750 nm with the Ti-sapphire laser as excitation source. As a result of a second loan during the present session we have been able to carry out an extensive investigation of these interesting systems. Here more detailed RR data on all three complexes, including polarization studies, are reported. More importantly, by exploiting the tunability of the Ti-sapphire laser, excitation profiles over the range 700 - 900 nm for several low frequency modes have been constructed.

RESULTS AND DISCUSSION

Resonance Raman scattering from (3) recorded at 363.8 nm (in resonance with the ultraviolet band) showed a very similar Raman spectrum (Figure 1) to that recorded at 780 nm, but with the intense features at 165 cm^{-1} and 273 cm^{-1} notably absent. Excitation at wavelengths within the range of the average valence electronic transitions would be expected to enhance both ν(Cu-Cu) and ν(Cu-N) vibrational modes. Features in the frequency range 240 - 500 cm^{-1} can be assigned[5] to symmetric (Cu-N) stretches (Cu-N_{axial} or Cu-$N_{equatorial}$). Interestingly, for complex (3) none of these bands undergoes a shift in D_2O solution, suggesting that (N-H) stretching or bending motions do not make any significant contribution to these modes.

The prominent band appearing near 165-185 cm^{-1} in the spectra of all three complexes is assigned to ν(Cu-Cu), based on the expectation[5] that modes involving mainly Cu-Cu motion should occur below 200 cm^{-1} . It is evident from Figure 1 that the most intense features in the spectra are the bands due to ν(Cu-Cu) at 165-185 cm^{-1} and ν(Cu-N) at 250-300 cm^{-1}, thus supporting the earlier tentative assignment of the electronic transition at 780 nm.

The disappearance of the bands at 165 and 273 cm^{-1} in (3) (Fig. 1) suggests that the uv. transition in these complexes does not involve Cu-Cu bonding or antibonding orbitals.

The RR spectra of (1-3) in Figure 2 recorded at an excitation wavelength of 780 nm show several moderate to intense Raman bands in the region < 900 cm^{-1}, all polarized, confirming their assignment to symmetric vibrational modes.

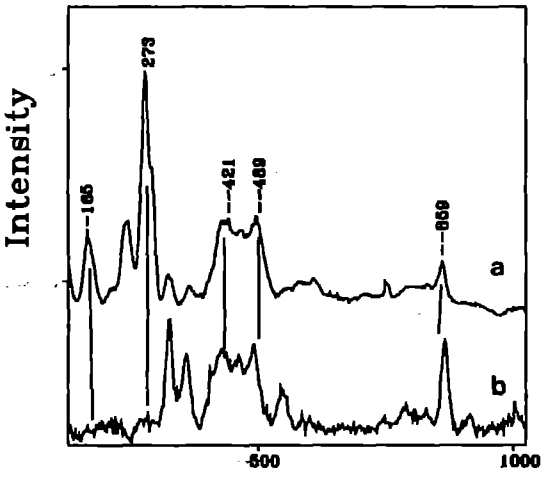

Fig. 1 Comparison of RRS of (3) recorded at excitation λ (a) 780 nm and (b) 363.8 nm

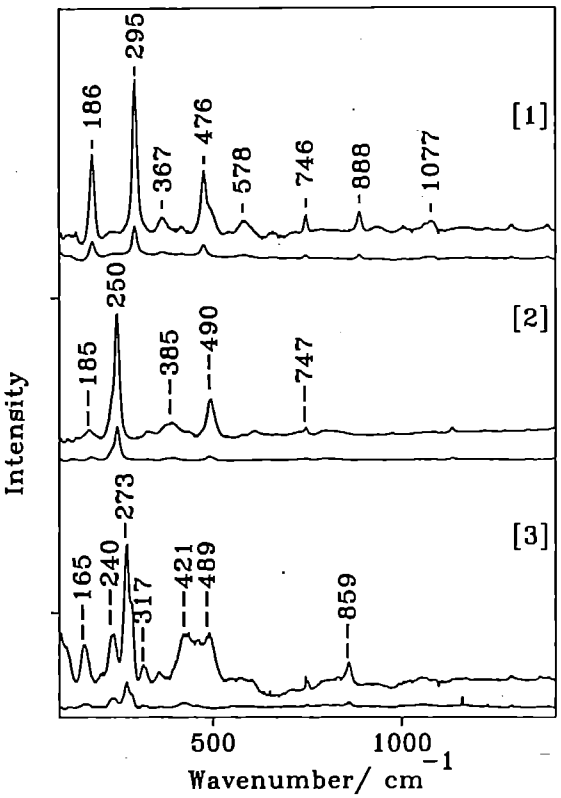

Fig.2 RRS of complexes (1-3) in aqueous solution (10^{-3} M) recorded at 780 nm excitation; parallel polarization (upper), perpendicular (lower).

The unusual asymmetry of the near red absorption band prompted a study of the excitation profiles of several of the low frequency modes. The stability of complex (1) (and to some extent, (2)) in aqueous solution is low but (3) has sufficient long term stability in aqueous media to enable the excitation profiles of several modes to be recorded on a single sample over the range 700-900 nm. The profiles for (3) shown in Figure 3 for the bands at 165 cm^{-1} and 273 cm^{-1} peak near 760 and 820 nm respectively, indicating that at least two transitions contribute to the absorption intensity in the range investigated, 700-900 nm. These results are supported by magnetic circular dichroism (MCD) measurements[6].

As can also be seen from Figure 3 the maximum in the excitation profile for the ν(Cu-Cu) mode at 165 cm^{-1} does not coincide with the 750 nm absorption band maximum. This indicates that the major contribution to the 750 nm absorption band for (3) is not the Cu-Cu transition but instead appears to involve excitation to an orbital with significant Np_z character. The fact that the excitation profile of the ν(Cu-N) mode at 273 cm^{-1} peaks near the 750 nm band maximum is consistent with this conclusion.

The wide tunability (675-1100 nm) of the CW Ti-sapphire laser has been a key factor in obtaining the present data on an important group of biosite model complexes. The work will be presented at the forthcoming International Conference on Raman Spectroscopy (Hong Kong, August 1994) and a paper

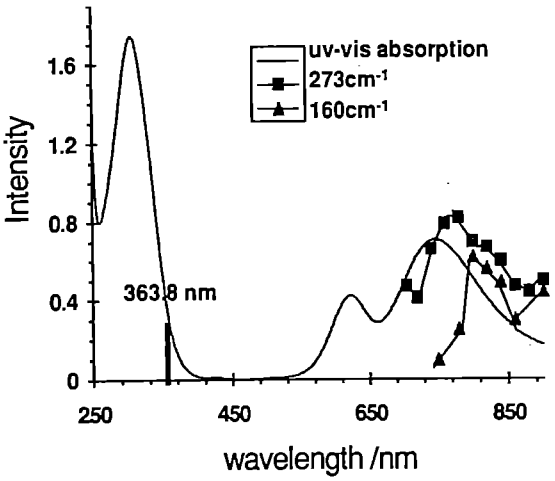

Fig. 3 Excitation profile of complex (3) recorded at excitation 700-900 nm, using $NaNO_3$ band at 1050 cm^{-1} as standard.

is in preparation[6]. To our knowledge a Ti-sapphire laser appears not to have been used previously to record RR excitation profiles in the red/near infrared region.

ACKNOWLEDGEMENTS

We thank the SERC for support (Grant GR/G00310) and Dr M. Towrie at the Laser Loan Pool for technical advice.

REFERENCES

1. W G Zumft, A Dreusch, S Loechelt, H Cuypers, B Friedrich and B Schneider. . J. Biochem., 208, 31 (1990).
2. B G Malmstroem and R Aasa. FEBS Lett., 325, 49 (1993).
3. C Harding, V McKee and J Nelson. J. Am. Chem. Soc., 113, 9684 (1991).
4. M E Barr, P H Smith, W E Antholine and B Spencer. J. Chem. Soc., Chem. Commun., 1649 (1993).
5. J E Pate, P K Ross, T J Thamman , C A Reed, K D Karlin, T N Sorrell and E I Solomon. J. Am. Chem. Soc., 111, 5198 (1989).
6. J A Farrar, V McKee, A H R Al-Obaidi, J J McGarvey, J Nelson and A J Thomson, to be submitted to Inorg. Chem.

THE PHOTOCHEMISTRY OF DIBENZOYLMETHANE; AN ENOLISED 1,3-DIKETONE

Andrew Beeby[1] and A.W. Parker[2]

1 Dept. of Chemistry, University of Durham, South Road, Durham, DH1 3LE
2 Laser Support Facility, Rutherford Appleton Laboratory, Chilton, Didcot Oxon. OX11 0QX

INTRODUCTION

The aim of this study is to characterise the photoproduct distribution of a range of enolised aromatic 1,3-diketones which are currently used as sunscreens and photostabilisers of polymers. These compounds exist almost entirely as the cyclic, hydrogen bonded enol form, (I), and the parent dibenzoylmethane, DBM, has strong absorption bands extending to 370nm. Substitution of the aromatic rings allows the fine tuning of the absorption maxima; for example the methoxy-derivative has bands extending to 410nm. These enolised 1,3-diketones have a variety of facile relaxation pathways available to their excited electronic states, allowing them to relax back to their ground electronic state, harmlessly dissipating the excitation energy as heat to the surroundings [1]. A number of possible reactions may occur, giving rise to a number of chemically distinct compounds and the relatively few studies reported have been somewhat contradictory. For example, it has been reported that irradiation of DBM produces both the enol and the keto form [2,3]. Furthermore it has been reported that these compounds do not generate singlet oxygen, $^1\Delta_g$, O_2, [4] although recent experiments have demonstrated that the triplet states have sufficient energy [5] and that its formation is strongly solvent dependent.

The excited state of DBM can undergo a number of isomerisation reactions. Thus, a non-hydrogen bonded enol can be formed by two distinct routes; cis-trans isomerisation about the double bond or breaking of the hydrogen bond followed by rotation about the C=O/α-C single bond leading to compounds IIa and IIb respectively. There are literature examples of both processes in analogous compounds. An alternative reaction is the formation of the keto form, III, by a [1,3]-sigmatropic shift of hydrogen and again there is precedence for this reaction. The products of these three pathways all have reduced conjugation, leading to a blue shift in their spectra relative to the hydrogen bonded enol form. Model compounds, locked into the ring opened enol and the keto form provide supporting evidence for this. Finally, DBM can undergo a [1,5]-hydrogen shift, resulting in no overall change in structure. These reactions are summarsied in scheme 1.

Preliminary experiments had shown that irradiation of DBM in degassed ethanolic solution produced a bleach of the ground state and the immediate formation of a transient absorbing at *ca* 290nm. This decayed with a lifetime of *ca.* 70μs to produce a new species identified by its absorption at 390nm, which in turn decayed back to the starting point with a lifetime of ≈ 1.5ms. Aerated solutions had shown rather different behaviour exhibiting only the 390nm transient [6]. Cyclohexane solutions of DBM behaved in a similar manner but showed considerably longer transient lifetimes. The aim of the work presented here was to identify the intermediates formed upon irradiation of DBM and to study the role of oxygen and of the solvent type. The production of singlet oxygen was also be investigated in these solvents.

RESULTS AND DISCUSSION

(i) LASER FLASH PHOTOLYSIS

Laser flash photolysis was used to probe the production of the transient species produced in ethanolic solutions of DBM. The LSF apparatus was used comprising a continuous Xe lamp as a probe source and the probe wavelength selected by the 0.5m monochromator. An R955 photomultiplier was used to monitor the light intensity and the time response of the system selected by the choice of load resistor; the fastest response with a FWHM of *ca.* 50ns is obtained with 50Ω termination.

Upon irradiation of an aerated solution of DBM at 355nm two transients were detected and characterised by their absorption bands at 290 and 390nm respectively. The time resolved spectra obtained at t=1μs and t=100μs are shown in figure 1. The absorption spectra of the parent DBM and the locked enol and keto species (O-methyl DBM and C-methyl DBM) are shown in figure 2 for comparison. The behaviour of the solution after degassing was found to depend strongly upon the nature of the degassing process. Thus, if samples were degassed by a conventional freeze-pump-thaw procedure little change was observed in the behaviour of the system. However, if the sample was degassed by argon sparging the lifetime of the 390nm transient increased considerably. Surprisingly, sparging the solution with oxygen gave the same result but purging the solutions with CO_2 lead to a marked change in the behaviour; a solution saturated with CO_2 the lifetime of the 290nm transient remained at 100μs and that at 390nm could not be detected. This observation suggested that the formation of the transient species absorbing at 390nm is strongly influenced by the presence of an acid. In ethanol traces of CO_2 lower the pH of the solution sufficiently to either prevent the formation of the 390nm species or vastly increase the rate of its removal. Cyclohexane solutions of DBM showed the formation of the 290 and 390nm transient species but there was little change upon bubbling with air, argon or CO_2. However, the observed kinetics were very sensitive towards the presence of traces of protic solvents and to the concentration of DBM. Solutions of DBM in acetic acid and pyridine were examined in order to further explore the role of acidic and basic solvents. In acetic acid there was an instantaneous bleach of the ground state and the formation of the 290nm transient. This decayed following first order kinetics with a lifetime of 5μs. The decay was not affected by the concentration of DBM and there was no evidence for the formation of the transient absorbing at 390nm. In pyridine solution there was an immediate bleach of the ground state and the rapid grow in of the transient at 390nm. This had a very long lifetime, >10ms.

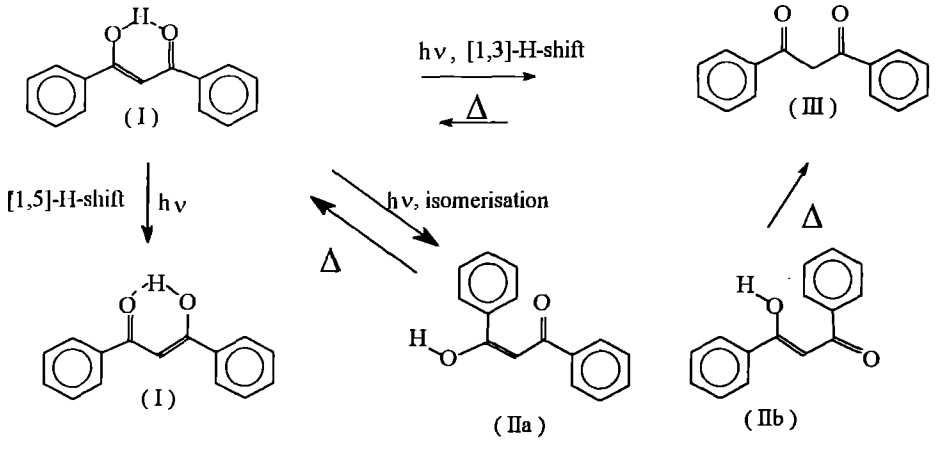

Scheme 1

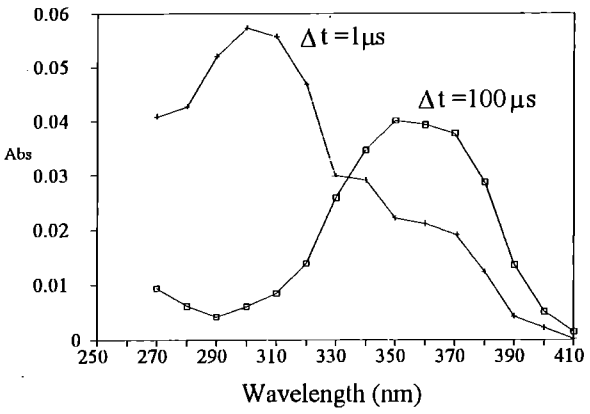

Figure 1. Transient Spectra obtained upon irradiation of aerated, ethanolic DBM.

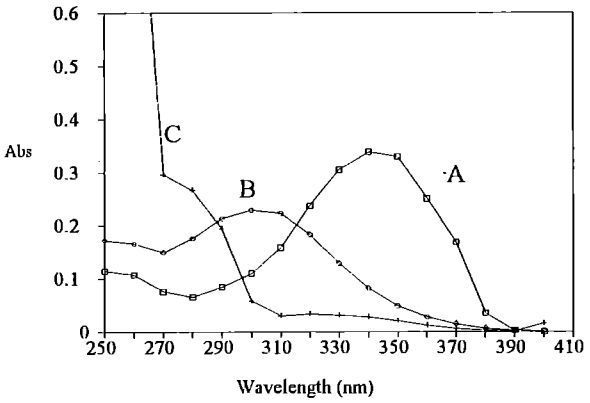

Figure 2. Absorption Spectra of (A) DBM, (B) O-Methyl DBM and (C) C-Methyl DBM

Steady state absorption spectra of DBM in acidic and basic solution indicate that the spectra of the DBM anion is virtually identical to that of the transient at 390nm. Furthermore the transient at 290nm is similar to that of the O-methyl DBM, a locked, non H-bonded enol form. therefore the reaction pathway illustrated in scheme 2 is believed to occur. Irradiation of the ground state DBM leads to the formation of an excited electronic state which rapidly undergoes isomerisation to a non-H-bonded enol form. (<50ns). This isomer can then isomerise back to the ground state, a reaction facilitated by a protic solvent, or ionise to give the dibenzoylmethane anion. This anion in turn can pick up a proton from the solvent to reform the H-bonded enol. A number of questions remain to be answered; the identity of the electronic state is not known and it is not clear which non H-bonded isomer is formed.

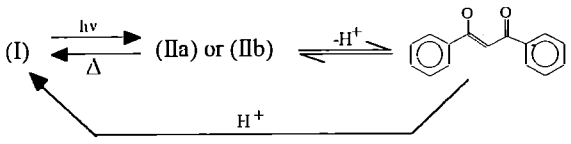

Scheme 2

(ii) SINGLET OXYGEN FORMATION

Singlet oxygen was detected by its luminescence at 1270nm following irradiation at 355nm. Singlet oxygen could only be detected in cyclohexane solutions of DBM, Φ_Δ =0.03; irradiation in ethanol, acetic acid, acetonitrile, pyridine and toluene produced no detectable luminescence.

(iii) GROUND STATE RESONANCE RAMAN SPECTRA

Good quality ground state resonance Raman spectra of DBM in cyclohexane and ethanol solution were obtained using the 363.8nm Ar^+ line. The spectrum obtained from a cyclohexane solution is shown in figure 3. Neutral ethanolic solutions produced a similar spectrum, but significant changes were observed in basic ethanol solution. Tayyari et al have reported that the vibrational frequencies of the 6-membered ring of the enol are strongly influenced by the strength of the H-bond [7], and we have demonstrated that the Q_4 mode of this ring has a strong Raman band (1280cm^{-1}) and there is a large shift induced by solvent deuteration (1100cm^{-1} in EtOD). It was not possible to measure Raman spectra of the locked keto and enol forms; due to their blue shifted absorption bands relative to the available Ar^+ lines no resonance enhancement is obtained and therefore the solvent spectrum dominates. It is anticipated that future scheduled ns-TR^3experiments will allow the study of the Raman spectra of the transient species absorbing at 290nm, and thus it will be possible to identify the structure of this species by comparison with the locked cis and trans enol species.

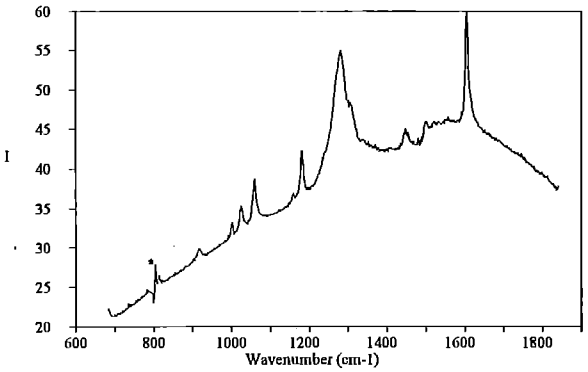

Figure 3. Resonance Raman spectrum of DBM in cyclohexane, excitation wavelength 363.8nm

REFERENCES

1 J. Catalan *et al*, J. Amer. Chem. Soc. (1992) **112** 747-59
2 P. Yankov, S. Salteil, I. Petkov and P. Markov, *Bulg. J. Physics* **12** 629-632 (1985)
3 D. Veierov, T. Bercovici, E.Fischer, Y. Mazur and A. Yogev, *J. Amer. Chem. Soc.* **99** 2723-29 (1977)
4 D. Guangson *et al*, *Youji Huaxue* **2** (1987) 115-18
5 H. Gonzenbach, T.J Hill and T.G. Truscott, J. Photochem. Photobiol B (1992) **16** 377-79
6 A. Beeby, in *Annual Report to Central Laser Facility* (1993) p160-161, RAL-93-031
7 S.F. Tayyari, T. Zeegers-Huyskens and J.L. Wood, *Spectrochimica Acta* (1979) **35A** 1265-76

FLASH PHOTOLYSIS OF PHTHALOCYANINE SENSITISERS FOR PDT PART 1 - SULPHONATED ALUMINIUM PHTHALOCYANINES IN REVERSED MICELLES

S Dhami & D Phillips

Department of Chemistry, Imperial College of Science, Technology & Medicine, South Kensington, London, SW7 2AY

INTRODUCTION

Photodynamic therapy (PDT) is the treatment of malignant tumours with laser-generated light following the systematic administration of a tumour-localising photosensitiser. The phototoxicity of these sensitisers is believed to be mediated via the triplet state. The presence of oxygen is vital for cell death to occur and it is widely believed that this is due to the formation of the cytotoxic species singlet oxygen. The sulphonated aluminum phthalocyanines, $AlPcS_n$ (n =0-4), show excellent photobiological activity.[1] The degree of sulphonation is known to affect cellular uptake and phototoxicity due to the differences in lipid solubility and aggregation properties.[2,3] The photophysics of $AlPcS_n$ are known to be solvent dependent due to the ability of ligands to co-ordinate to the central metal of the macrocycle and alter the rate of internal conversion from S_1, the first excited singlet state.[4] In biological systems, however, these sensitisers bind to various proteins and membranes, resulting in complex photophysical behaviour which bears little resemblance to the behaviour in homogeneous environments. In order to begin to understand the action of these sensitisers *in vivo* it is necessary to perform studies in more 'biologically relevant' media such as reversed micelles. These systems can be regarded as an accessible, though oversimplified, working model for biological assemblies.

In this study the triplet state properties of di- and tri-sulphonated aluminium phthalocyanine in cationic reversed micelles of benzyl ammonium hexadecyl chloride (BHDC), at varying [water]/[surfactant] ratios (R) are reported. These particular phthalocyanines were chosen as they do not aggregate in this reversed micellar system.[5] The production of singlet oxygen has also been studied and is reported here.

EXPERIMENTAL

Triplet state studies were carried out using the nanosecond laser flash photolysis system developed by Beeby *et al.*[6] Pump wavelengths of 355 and 670 nm were used with typical energies of 10-500μJ per pulse. Quantum yields were determined by the relative method using zinc tetraphenyl porphyrin (Φ_t = 0.84, ε_t = 74,000 $M^{-1}cm^{-1}$ at 470 nm)[7] and anthracene (Φ_t = 0.72, ε_t = 46,000 $M^{-1}cm^{-1}$ at 430 nm)[7] in toluene as standards. The production of singlet oxygen was monitored by near infra-red time-resolved singlet oxygen luminescence studies, using a North Coast EO-817P liquid-nitrogen cooled germanium photodiode and amplifier combination. Relative quantum yields were determined using standards zinc tetraphenyl porphyrin (Φ_Δ = 0.73), anthracene (Φ_Δ = 0.61) and benzophenone (Φ_Δ = 0.30) in benzene.[8]

The reversed micelles were prepared by dissolving BHDC in benzene to produce a 0.05M solution. The necessary volumes of water or deuterium oxide were then added to obtain the desired values of R. The clinical disulphonated phthalocyanine is a mixture of a least eight components which are believed to be individual $AlPcS_2$ regioisomers.[9] The cis-isomer used has both sulphonate groups substituted to the same side of the molecule.

RESULTS AND DISCUSSION

From Table 1, it can be seen that the triplet quantum yield does not depend on the water content within the reversed micelles. Little effect is observed when D_2O is used instead of H_2O. This indicates that the phthalocyanines do not interact significantly with the inner water pool of the reversed micelles. The triplet quantum yields, Φ_t, for both the H_2O and D_2O systems are considerably greater than in a homogeneous environment i.e. 0.33±0.04 compared to 0.17±0.02 in water and 0.24±0.03 in methanol.[10] The average value of Φ_t for $AlPcS_3$ is 0.27±0.04 which does not deviate considerably from a homogeneous environment.

	Φ_t (±0.05)			
$AlPcS_n$	R = 5.3	R = 10.6	R = 16.0	R = 23.1
n = 2 (cis-isomer)	0.32	0.33	0.35	0.32
n = 2 (clinical)	0.33	0.36	0.27	0.28
n =2 (D,O)	0.35	0.31	0.31	0.34
n = 3	0.26	0.22	0.32	0.28

Table 1 Triplet Quantum yields of $AlPcS_n$ at different water ratios R in BHDC/benzene reversed micelles

From previous studies, the fluorescence decays of cis-$AlPcS_2$ were single-exponential and bi-exponential for $AlPcS_3$.[5] For triplet studies, all decays could be described well by single exponential decay functions. The triplet lifetimes were, however, difficult to measure as it was impossible to de-oxygenate the samples completely without damaging the reversed micelles. The singlet oxygen quantum yields for the $AlPcS_2$ systems were also higher than those obtained in homogeneous solutions with Φ_Δ = 0.22±0.02 compared to 0.17±0.02 in water.[10] The singlet oxygen quantum yields are lower than the triplet quantum yields which could be due to a proportion of the singlet oxygen produced not being detected. This may be caused by trapping of oxygen within the reversed micelles which would also explain the problems encountered when attempting to completely de-oxygenate the samples. It has been demonstrated previously that the sensitivity of detection of singlet oxygen luminescence depends upon the overall composition of the medium, which is predominantly hydrocarbon for reversed micelles, and not on the local environment of the sensitiser.[11] The rapid partitioning of singlet oxygen between aqueous and non-aqueous phases on a time-scale faster than the decay of singlet oxygen in either phase results in monoexponential decays. As the partition favours the non-aqueous phase it is this phase which determines the behaviour of singlet oxygen resulting in longer singlet oxygen lifetimes compared to those obtained in water (τ_Δ = 4μs).[12] Lifetimes of 30±5μs were measured which is characteristic of the singlet oxygen lifetime in a pure solvent of benzene. As τ_Δ is known to be longer in deuterated solvents the reversed micelles were also prepared in a solvent of benzene-d_6. The lifetimes were seen to increase to a value of 350±50μs. On the other hand, the addition of D_2O instead of H_2O had no effect on the overall singlet oxygen lifetimes detected.

REFERENCES

1. W.S. Chan, J.F. Marshall, R.K. Svenson, J. Bedwell, I. Hart, *Canc. Res.* (1990)50 4533
2. B. Paquette, H. Ali, R. Langlois, J.E. Van Lier, *Photochem. Photobiol.*47(1988), 215-220
3. K. Berg, J.C. Bonner, J. Moan, *Cancer Letts.*44(1989), 7-15
4. A. Beeby, A.W. Parker, M.S.C. Simpson, R.K. Svenson, D. Phillips, *J. Photochem. Photobiol.,B,*16(1992), 73-81
5. S.Dhami, J.J. Cosa, S.M. Bishop, M.S.C. Simpson, D. Phillips, *Photodynamic Therapy of Cancer,* Vol. 2078, 475-482, G.Jori, J. Moan , W.M. Star, (1993)
6. A. Beeby, A.W. Parker, D. Phillips, *SERC CLF Annual Report* (1991) RAL-91-025 193
7. 2. I Carmichael, G.L. Hug, *J. Phys. Chem. Ref. Data* (1986) 15 1
8. F. Wilkinson, W.P. Helman, A.B. Ross, *J. Phys. Chem. Ref. Data* (1993) 22 1
9. A. Beeby, S.M. Bishop, B.J. Khoo, A.J. MacRobert, D.Phillips, *Photodynamic Therapy & Biomedical Lasers*, (1992), 780-83
10. S. Bishop, PhD Thesis (1993), University of London
11. R.W. Redmond, *Photochem. Photobiol.* 54(4) (1991), 547-56
12. P.C. Lee, M.A.J. Rodgers, *J. Phys. Chem.* 87 (1983), 4894-98

FLASH PHOTOLYSIS OF PHTHALOCYANINE SENSITISERS FOR PDT
PART 2 - TRIPLET STATE PHOTOPHYSICS OF NOVEL PHTHALOCYANINE SENSITISERS

S Dhami[1] D A Mayes[2] A Beeby[3] D Phillips[1] D A Russell[2] M J Cook[2]

[1]Department of Chemistry, Imperial College of Science, Technology & Medicine, South Kensington, London, SW7 2AY
[2]School of Chemical Sciences, University of East Anglia, Norwich, Norfolk, NR4 7TJ
[3]Department of Chemistry, University of Durham, South Road, Durham, DH1 3LE

INTRODUCTION

The triplet state photophysics of some highly substituted lipophilic zinc phthalocyanines are reported. These compounds exhibit an intense absorption band in the region 690-710 nm ($\varepsilon = 2 \times 10^5$ M^{-1} cm^{-1}). Figure 1 shows the general phthalocyanine structure. In this case, X = Zn and eight alkyl chains occupy positions 1,3,5 and 7. Photobiological studies on the octa-decyl zinc phthalocyanine show promising results for the use of these sensitisers in the photodynamic therapy of tumours.[1] The length of the alkyl chains has been varied to obtain a structure (i.e. peripheral substituent) - activity relationship. In order to elucidate further the effects of substituent groups on the photophysics of these molecules two more compounds were studied. From figure 1, these were 1) positions 1,5,7 = C_9H_{19}, 3 = $(CH_2)_5OH$ & 2) positions 1,3,5,7 = OR (R = iso-pentyl oxy-), 2,4,6,8,= Cl. The photophysical parameters ,τ_t, Φ_t and Φ_Δ, have been obtained for each of these compounds to enable the separation of their photodynamic efficiency and tumour-localising properties.

EXPERIMENTAL

See Part 1. Samples were prepared in a 1% pyridine in toluene solution, to prevent aggregation, with an optical density of 0.2-0.3 at the excitation wavelength. Samples were pumped at 355nm for triplet and singlet oxygen studies and at 710nm for the self-quenching rate constants and monitored at 550nm. Quantum yields were determined by the relative method using zinc tetraphenyl porphyrin ($\Phi_t = 0.84$, $\varepsilon_t = 74{,}000$ $M^{-1}cm^{-1}$ at 470 nm)[2] and zinc phthalocyanine ($\Phi_t = 0.58$, $\varepsilon_t = 36{,}000$ $M^{-1}cm^{-1}$ at 490 nm)[3] for triplet studies and zinc tetraphenyl porphyrin ($\Phi_\Delta = 0.73$)[4] and anthracene ($\Phi_\Delta = 0.61$)[4] in toluene for singlet oxygen studies.

RESULTS AND DISCUSSION

Table 1 shows the dependence of the triplet lifetime, τ_t, triplet quantum yield, Φ_t, and the self-quenching rate constant, k_q, on alkyl chain length. The triplet lifetimes of the alkyl substituted phthalocyanines are considerably shorter than that of the parent (non-substituted) molecule, although the triplet quantum yields are higher. The self-quenching of the triplet state by ground state sensitiser is also reduced compared to the non-alkylated phthalocyanine. This is believed to be a result of the steric hindrance induced by the bulky side chains. The presence of the alkyl chains may provide an increase in the non-radiative deactivation pathways due to an increase in the vibrational modes available. This would indeed explain the observed triplet quantum yields and lifetimes. Alternatively, these observations may be due to the inductive effect of the eight alkyl groups which would increase the electron density in the phthalocyanine core.

The singlet oxygen quantum yields (Φ_Δ) were also found to be higher than the parent in accordance with the triplet yields. Values of 0.6-0.7 were obtained, which did not vary considerably with chain length, as compared to 0.54 for the parent phthalocyanine.

Alkyl chain length	τ_t/μs	Φ_t	k_q/ x $10^8 M^{-1}s^{-1}$
0	330±30	0.58±0.08	3.5±0.4
1	150±20	0.65±0.08	1.1±0.3
4	50±10	0.71±0.09	1.9±0.3
5	45±10	0.80±0.09	0.87±0.2
6	51±10	0.76±0.09	0.41±0.2
8	49±10	0.81±0.09	0.91±0.2
10	51±10	0.74±0.09	3.3±0.4

Table 1 Variation of, τ_t, Φ_t, and k_q, with alkyl chain length

As would be expected compound 1) (as described above) showed similar photophysical properties to the longer chain alkyl phthalocyanines with τ_t = 49±10μs and Φ_t = 0.65±0.08. Compound 2) exhibited similar properties to the octa-methyl phthalocyanine with τ_t = 144±20μs and Φ_t = 0.55±0.08.

Figure 1 General phthalocyanine structure

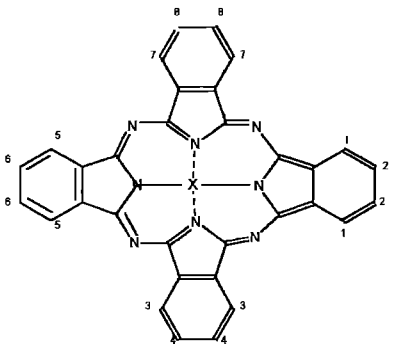

REFERENCES

1. M.J. Cook, C. Fabris, C. Orietto, D.A. Mayes, G. Jori, J. McMurdo, C. Milanesi, D.A Russell, *Photodynamic Therapy of Cancer*, Vol. 2078, 539-546, G.Jori, J. Moan , W.M. Star,
2. I Carmichael, G.L. Hug, *J. Phys. Chem. Ref. Data* (1986) 15 1
3. S. Bishop, PhD Thesis (1993), University of London,
4. F. Wilkinson, W.P. Helman, A.B. Ross, *J. Phys. Chem. Ref. Data* (1993) 22 1

REMPI STUDIES OF THE DISSOCIATIVE DESORPTION DYNAMICS OF ALKYL NITRITES ADSORBED ON DIELECTRIC SURFACES

C.J.S.M. Simpson[1], P.T. Griffiths[1] and M. Towrie[2].

[1] Physical Chemistry Laboratory, Oxford
[2] Rutherford Appleton Laboratory

INTRODUCTION

There is a widespread interest in the field of photodissociation. For the most part, recent studies have concentrated on laser induced gas phase dissociation. It was the purpose of our work to examine how the dynamics of such processes are modified by adsorption on a dielectric surface.

Alkyl nitrites are excellent candidates for such a study. There is a large body of experimental and theoretical work on gas phase photodissociation. They are model systems of vibrational predissociation and in addition, are easily handled.

Resonance Enhanced Multi-Photon Ionisation spectroscopy (REMPI) was used to characterize the nascent NO. This allows a complete characterization of the NO(v,J) produced. In addition, Time Of Flight (TOF) spectroscopy allows the translational energy of a selected quantum state to be measured. The detection system used has been previously described and is extremely sensitive, capable of detecting concentrations of NO of 10^4 molecules per quantum state per cm^3.

The dielectric MgF_2 was again employed as substrate. Many previous investigations have employed metal and semi-conductor surfaces [1,2]. Electron transfer from the substrate has been shown to occur in several cases [3]. In addition, absorption of desorption laser energy by the surface can result in extensive thermal desorption of the molecule of interest [4]. The use of a dielectric surface, transparent to laser radiation, avoids these effects and allows a study of the photochemical processes occurring within the molecule and how they are modified by the presence of the substrate.

Ultraviolet spectra of alkyl nitrites show two bands, the frequency of the observed transitions varying from molecule to molecule. A broad, structureless feature around 220 nm, is attributed to a ($\pi \rightarrow \pi^*$) transition. Excitation is to a repulsive surface, with the molecule promptly dissociating. Around 320nm a structured absorption is seen, corresponding to the $X^1A' \rightarrow A^1A''$ transition, approximately an ($n \rightarrow \pi^*$) transition, of an electron associated with the terminal oxygen atom, with concomitant excitation of the υ_3 vibration of the nitrite. *Ab initio* calculations predict a potential surface with a shallow well along the N-O coordinate which traps the excited molecule for a few vibrational periods before dissociating, producing the observed vibrational structure [5].

In this work, tert- and iso-butyl nitrite were chosen for study, the isomeric compounds showing similar properties of adsorption. Iso-butyl nitrite shows a similar ultraviolet absorption spectrum to methyl nitrite but has the advantage of being considerably easier to handle, being a volatile liquid. Figure 1 shows excitation of the adsorbed molecules by 351 nm radiation.

EXPERIMENTAL

The apparatus used in this work has been described previously [7]. Briefly, a Lambda Physik 105i excimer laser, operated as an XeF laser at 351 nm, was used to initiate desorption. The incident power on the crystal face was controlled via a NO_2 attenuating cell, and the most even portion of the beam was selected. In this work, fluences of around 5 mJ cm^{-2} were used. In previous work, it has been established that there is negligible thermal heating of the crystal face.

The ionisation laser used was a Lambda Physik 3032 dye laser pumped by a Lumonics 105 XeCl excimer laser. Various coumarin dyes were used for the different vibrational bands. The dye laser output was frequency doubled using a β-barium borate crystal.

REMPI spectra of the (0,0), (0,1), (0,2) (1,3) and (0,3) bands of NO were taken. TOF spectra were taken for each band. These were obtained by varying the delay between desorption and REMPI lasers.

Temperature Programmed Desorption spectra were taken before and after desorption laser shots to investigate the percentage of adsorbed molecules desorbed during an experiment.

In this work, approximately monolayer coverage of the crystal face was employed, allowing a direct investigation of the presence of the surface on the dissociation dynamics.

RESULTS AND DISCUSSION

TPD spectra taken showed that there had been negligible change in surface coverage during the scans, allowing the experiments to be performed without redosing of the crystal face.

Gas phase studies of methyl and tert-butyl nitrite at 351 nm show NO produced with approximately 4000 cm^{-1} translational energy. An approximately Gaussian distribution of rotational states, peaking around J=30, with energy of around 1800 cm^{-1} is seen. The vibrational distributions show that the initial vibrational excitation is largely preserved in the NO product [6].

Analysis of the TOF spectra showed that the NO is produced with approximately 500 cm^{-1} translational energy, and that there is little variation in this energy between vibrational levels and between molecules.

For the rotational spectra, peak integrals were first corrected for the Hönl-London line strength factors, and then Boltzmann plots were produced in order to determine rotational temperatures. A Boltzmann plot is for the (0,3) band of tert-butyl nitrite is shown in Figure 2. The best fit lines of the different branches do not lie on the same line due to the factors of intermediate state alignment and saturation not being included in the full analysis [8]. The rotational of the desorbed NO is calculated to be approximately 250 cm^{-1}

The translational and rotational energies are therefore far lower in this work than in similar gas phase studies. Most strikingly, a Boltzmann distribution of rotational states is seen, in contrast to the inverted distribution seen in gas phase work.

Excitation of tert-butyl nitrite at 351 nm produces an excited complex with 3 quanta in the NO stretch. Similarly, excitation of iso-butyl nitrite produces 2 quanta in the NO stretch. Gas phase experiments have shown that this excitation is largely preserved in the NO product.

A complete vibrational analysis of the NO product is still in progress, but a first estimation of the relative vibrational population of the desorbed NO has been made. In the case of butyl nitrite, the observed populations are in the ratio $<0.05:0.2:0.4:0.4$ of $(v=0):(v=1):(v=2):(v=3)$. This is in close agreement with the gas phase ratio 0.05:0.37:0.42:0.20. A different vibrational distribution is seen in the case of iso-butyl nitrite, yet it is similar to that seen in the gas phase studies of methyl nitrite.

From these results, it is clear that the presence of the dielectric substrate has indeed modified the dynamics of this dissociation process. The results show a marked deviation, not only in the energy, but in the nature of the distribution of energies. Previous work on the photolysis of NO dimers has shown that the dielectric substrate causes a change in the dissociation process, and that fragment translation and rotation may arise via a different route than vibration.

ACKNOWLEDGEMENTS

We thank Sue Tavender and Irene Gray at the Rutherford Appleton Laboratory for their help during this work, and G.J. Wilson and M.L. Turnidge for their assistance with the analysis of data.

FIGURE 1 DETAIL OF 350 nm SECTION OF ELECTRONIC SPECTRUM

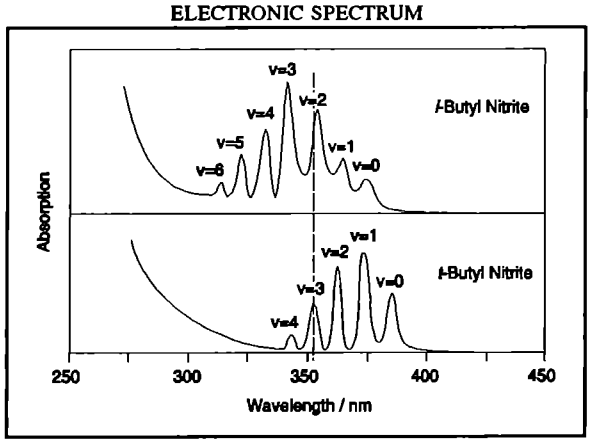

FIGURE 2 BOLTZMANN PLOT FOR THE (0,3) BAND OF NO FORMED BY THE DISSOCIATION OF TERT-BUTYL NITRITE ON AN MgF_2 SURFACE AT 351 nm

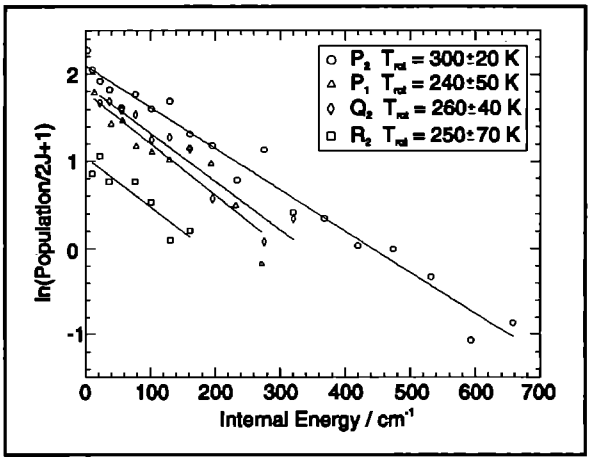

REFERENCES

1 L.J. Richter, S.A. Buntin, D.S. King and R.R. Cavanagh,
State-resolved studies of the laser induced desorption of NO from Si(111)7x7: Low coverage results.
J. Chem. Phys. 96, 2324, (1992).

2 D. Weide, P. Andresen and H.-J. Freund,
UV laser-stimulated resonant desorption from metal surfaces : NO/Ni(100).
Chem. Phys. Letters, 136, 106, (1987).

3 S.A. Buntin, L.J. Richter, D.S. King and R.R. Cavanagh,
State-resolved evidence for hot carrier driven surface reactions : laser induced desorption of NO from Pt(111)

4 K. Domen and T.J. Chuang,
Laser induced photodissociation and desorption. I CH_2I_2 adsorbed on Al_2O_3.
J. Chem. Phys. 90, 3318, (1989).

5 M. Nonella, J.R. Huber, A. Untch and R. Schinke,
Photodissociation of CH_3ONO in the first absorption band : A three-dimensional classical trajectory study.
J. Chem. Phys. 91, 194, (1989).

6 H. Reisler, M. Noble and C. Wittig,
in: Molecular Photodissociation Dynamics, eds. M.N.R. Ashfold and J.E. Baggot (Royal Society of Chemistry, London, 1987) p 162.

7 C.J.S.M. Simpson, J.M. Curry, A. Takami, K.R. Yoxall, A.W. Parker and M. Towrie, in preparation.

8 D.C. Jacobs, R.J. Madix and R.N. Zare,
Reduction of 1+1 resonance enhanced MPI spectra to population distributions : Application to the NO $A^2\Sigma^+ \rightarrow X^2\Pi$ system.
J. Chem. Phys. 85, 5469, (1986)

ELECTRONIC SPECTROSCOPY OF INVOLATILE, HEAVIER ELEMENT COMPOUNDS FORMED IN A FREE JET EXPANSION

J.M. Brown[1], I.R. Beattie[2], N.M. Lakin[1], M.P Barnes[1], D.M. Goodridge[1], A. Lukyashko[1]

[1] The Physical Chemistry Laboratory, Oxford University.

[2] The Department of Geology, Southampton University.

i. INTRODUCTION

High temperatures are required to produce sufficient vapour pressure of involatile solids. Under these conditions however, gas phase spectroscopy yields little information because the spectra are broad and featureless. In our experiment, molecules are formed in a heated alumina nozzle and are seeded into an inert gas stream (usually argon) at high pressure. The system will operate up to 1000°C. The gas mixture undergoes a free jet expansion through a small orifice (250μm in diameter) into a rapidly pumped vacuum chamber. As a result, the vibrational and rotational degrees of freedom are considerably cooled, to about 100K and 10K respectively and greatly simplified spectra are obtained. The focussed beam from a narrow band tunable dye laser is used to excite molecules in the jet and the resultant fluorescence is recorded (laser excitation spectroscopy). We have made use of the EMG 101E excimer and Lambda Physik FL3002 dye laser combination from the LSF loan pool to record the spectra of a number of interesting molecules. In November 1993, this laser was replaced by a JK Hyper Nd:YAG and Spectron PDL2 dye laser combination.

During the period covering this report, we have been able to extend our measurements of InOH, In_2O and $CuCl_2$. We have also recorded a new spectrum of YbCl and have searched unsuccessfully for the electronic spectrum of GaOH between 320 and 360nm.

ii. INDIUM HYDROXIDE

Three distinct electronic transitions of InOH have now been identified, lying close together in the near ultra-violet. We have extended our previous observations of InOH and InOD, formed by the reduction of In_2O_3 by H_2 or D_2 to higher wavenumbers to follow out vibrational progressions in the upper electronic states. We have also observed some hot bands at lower wavenumbers by expanding in He rather than Ar. In addition, we have recorded the corresponding spectrum of $In^{18}OH$ starting from a specially prepared sample of $In_2^{18}O_3$. The isotopic shift in vibrational wavenumber confirms the assignment to the In-O stretching and the bending vibrations. The O-H stretching vibration does not appear to be active. Several individual bands have been recorded at the highest possible resolution, with the intracavity etalon included giving a laser linewidth of about 0.08cm^{-1}. An example is shown in figure 1. Careful measurement of the vibrational spacings in these bands has enabled us to record the J=1←0 rotational transition in the ground state for InOH, InOD and $In^{18}OH$ with a pulsed microwave spectrometer. These very accurate measurements in turn provide a reliable method for the calibration of the etalon scans.

The analysis of the spectrum of InOH has made good progress. It is clear that the molecule is non-linear in all the states involved in these observations. Combination of the data from the different isotopes has permitted a determination of the r_0 geometry. The bond angle in the ground state is 131° and in the excited state is 105°.

The dispersed fluorescence spectrum of InOH is also very complicated. It can be interpreted in terms of quasi-linear behaviour in the ground state; the height of the barrier to the linear conformation corresponds to about 3 bending quanta. It is not yet clear if the upper states of the three electronic transitions identified are the three components of a triplet state i.e. that the transition observed is a triplet-singlet transition which is expected at these wavelengths by comparison with InF and InCl. The measured radiative lifetimes for InOH in these states (>2.4 μs) is consistent with such an assignment. A paper reporting the essence of our observations has been submitted[1].

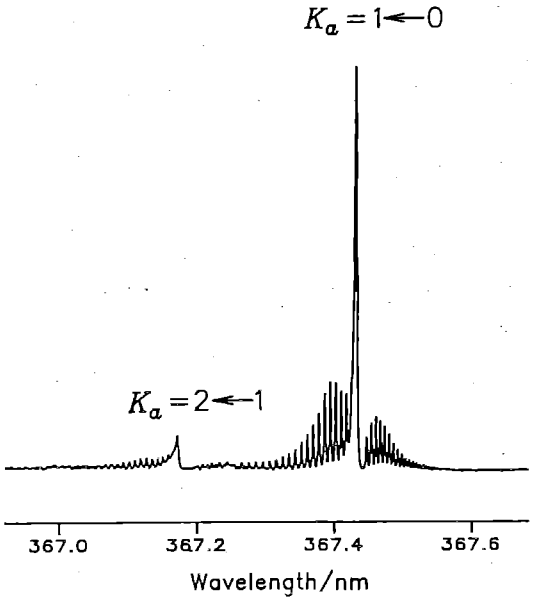

Fig 1. Detailed rotational structure of a vibrational band in the spectrum of InOH. The P, Q and R branch structure can be clearly seen.

iii. INDIUM SUB-OXIDE

One or more band systems have been observed between 390 and 370 nm from the products of the reduction of In_2O_3 by In at 950°C. Although vibrational structure is clearly seen, it has not been possible to resolve rotational structure, even with the etalon in the laser cavity. These observations are all consistent with the carrier being In_2O. We have extended the observations to $In_2^{18}O$ using the isotopically enriched sample of $In_2^{18}O_3$. All of the intervals in the spectrum change on isotopic substitution but the ratio does not support a linear geometry in both states. We are investigating the possibility that the spectrum can be explained if the molecule is non-linear in one or both states. Dispersed fluorescence spectra have been obtained. They show only two features close to the excitation band, about 100cm^{-1} and 230cm^{-1} below it.

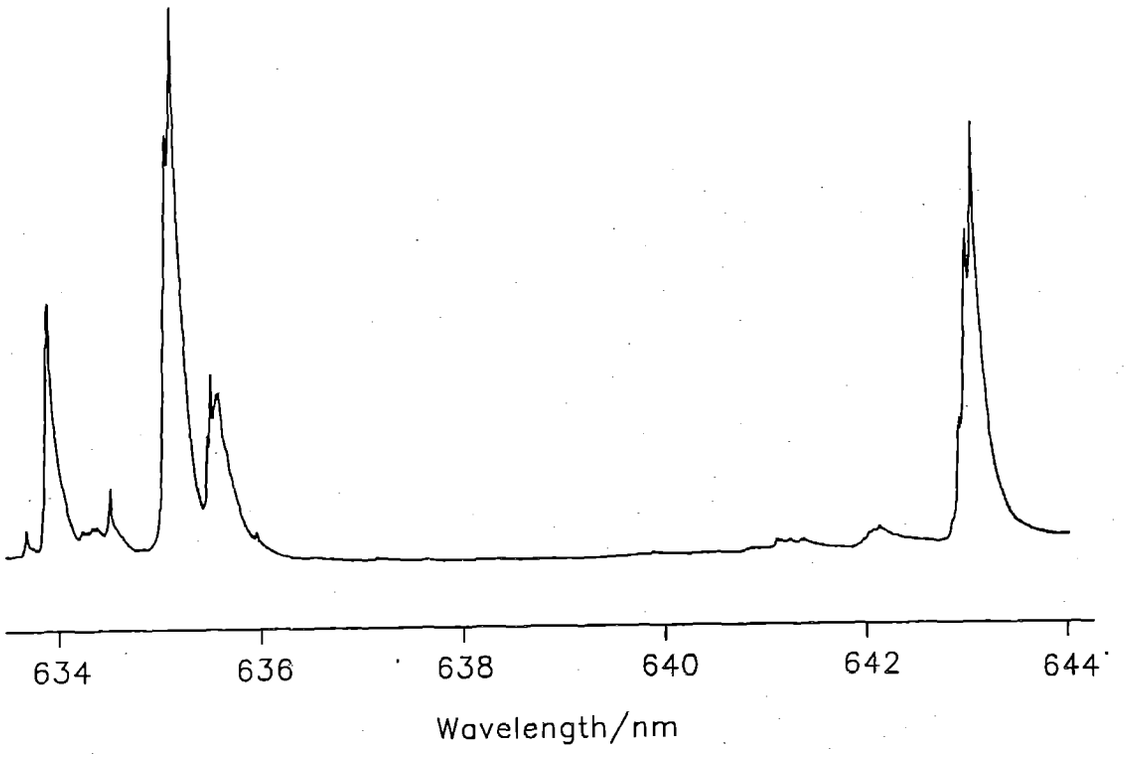

Fig. 2. The electronic spectrum of $CuCl_2$ in the region of the (0,0) band of the $^2\Pi_u \leftarrow ^2\Pi_g$ transition. The bands for three of the six possible isotopomers can be seen at the short wavelength end. The bands near 643nm are hot bands (this spectrum was recorded with a supersonic expansion in helium).

iv. COPPER DICHLORIDE

Copper dichloride has a very extensive band system in the red and yellow part of the spectrum. A paper on the analysis of some of the bands near 600nm has been published[2]. We have now recorded the excitation spectrum out to longer wavelengths and identified the origin band at about 643nm. This assignment is based on the absence of bands at longer wavelengths (under cold expansion conditions) and on the Cu and Cl isotope structure. The bands in this part of the spectrum are shown in Figure 2. We plan to study them at higher resolution. Some lifetime measurements have been made for bands at shorter wavelength. the values obtained are around 350ns but are erratic, suggesting considerable perturbation of the upper state levels.

v. YTTERBIUM CHLORIDE

We have recorded some bands around 558nm for a species produced in the high temperature reaction between ytterbium metal and chlorine at about 700°C. The carrier is almost certainly YbCl and the transition is $A^2\Pi_{\frac{1}{2}} - X^2\Sigma$; both (0,0) and (1,1) bands have been detected. The spectrum will be recorded at higher resolution to confirm this assignment and to provide structural information.

vi. GALLIUM HYDROXIDE

Searches have been carried out for the electronic spectrum of GaOH, formed in the high temperature reaction between gallium metal and water vapour. No bands have been seen in the region 320 to 360nm although it is apparent that a reaction is occurring. It is probable that the electronic transition analogous to that of InOH described above is at somewhat shorter wavelengths.

REFERENCES

1. N.M. Lakin, J.M. Brown, I.R. Beattie and P.J. Jones, J. Chem. Phys., submitted.
2. M.P.Barnes, R.T. Carter, N.M. Lakin and J.M. Brown, J. Chem. Soc., Faraday Trans., 89, 3205 (1993).

ULTRA-LOW TEMPERATURE KINETICS OF OH- AND CH-RADICAL REACTIONS

Bertrand R Rowe,[1] Ian R Sims[2] and Ian WM Smith[2]

[1]Université de Rennes 1
[2]University of Birmingham

INTRODUCTION

There is considerable interest in the rates of gas-phase, neutral-neutral reactions at ultra-low ($T \leq 77$ K) temperatures, both from fundamental[1] and astrochemical[2] standpoints. Despite this interest, the experimental database of thermal rate constants for neutral reactions in the gas phase is extremely sparse at temperatures below 200 K, and was non-existent below 77 K before the advent of the technique described here. The reasons for this deficiency lie principally in the difficulties encountered when the two usual methods of cooling are applied to chemical kinetics measurements. Cryogenic cooling, while suitable for the study of a number of species down to temperatures as low as 80 K,[3] becomes impractical at lower temperatures due to the rapidly diminishing vapour pressures of the reagent species. The gaseous reactants simply freeze out on the walls of the cell. The standard tool of the chemical physicist for cooling gaseous species to ultra-low temperatures, the free jet expansion or molecular beam, is not well suited to the study of reaction kinetics and other collisional processes due to the very low gas density and lack of collisions in the cold expansion, as well as the resultant lack of thermalisation and the loss of any meaningful concept of temperature.

Recently we have developed a new method for studying reaction kinetics of gas-phase neutral species at temperatures down to 13 K,[4,5] by combining the PLP-LIF (Pulsed Laser Photolysis – Laser Induced Fluorescence) technique for observing gas phase reactions of radical species with the ultra-cold, yet collisional and fully thermalised environment provided by the CRESU (Cinétique de Réaction en Ecoulement Supersonique Uniforme) technique. The new method has been applied at temperatures ranging from 295 K to as low as 13 K to the reactions of the CN radical with O_2,[4(a),4(b)] NH_3,[4(b)] and C_2 hydrocarbons,[4(c)] and most recently to the reactions of the OH radical with some butene isomers[5(a)] and HBr,[5(b)] as well as preliminary studies on the reaction of the astrochemically important CH radical.

EXPERIMENTAL

The CRESU technique and its adaptation to the study of neutral-neutral reactions (in particular those of the CN radical) by means of the PLP-LIF technique has been described in detail elsewhere.[4(b),5(a)] A schematic diagram of the apparatus may be found as Fig. 1 of ref. 4(b). Here, we will give a brief summary of the method as applied to measurements at ultra-low temperatures on the reaction of OH radicals with HBr.

The CRESU technique provides, via the isentropic expansion of gas through a Laval nozzle, a 'collimated' flow of ultra-cold gas which is uniform in temperature, density and velocity. The expansion and subsequent cooling are rapid enough that heavily supersaturated conditions may prevail, avoiding the major problem of condensation associated with the use of cryogenically-cooled cells. However, in contrast to free jet expansions and molecular beams where the concept of temperature is not really valid, the relatively high gas density (10^{16}—10^{17} molecule cm^{-3}) in the uniform supersonic flow ensures that frequent collisions take place during the expansion and subsequent flow, maintaining thermal equilibrium at all times. Several nozzles were employed in the present work, each providing a particular temperature and density for the selected carrier gas. Flow conditions have been verified previously by impact-pressure measurements, as well as by independent determination of the temperature via spectroscopic measurements on the (0,0) band of the ($B^2\Sigma^+$–$X^2\Sigma^+$) system of CN.[4(b)]

OH radicals were generated by the pulsed laser photolysis of H_2O_2 at 266 nm, and detected by LIF, exciting the (1,0) band of the OH($A^2\Sigma^+$-$X^2\Pi$) system at ~282 nm, and detecting off-resonance fluorescence from the (1,1) band – and any in the (0,0) band resulting from vibrational relaxation in the electronically excited state – at ~310 nm. Kinetic data were gathered using the strongest available rotational line, usually the $Q_1(1)$ line at 282 nm.

RESULTS AND DISCUSSION

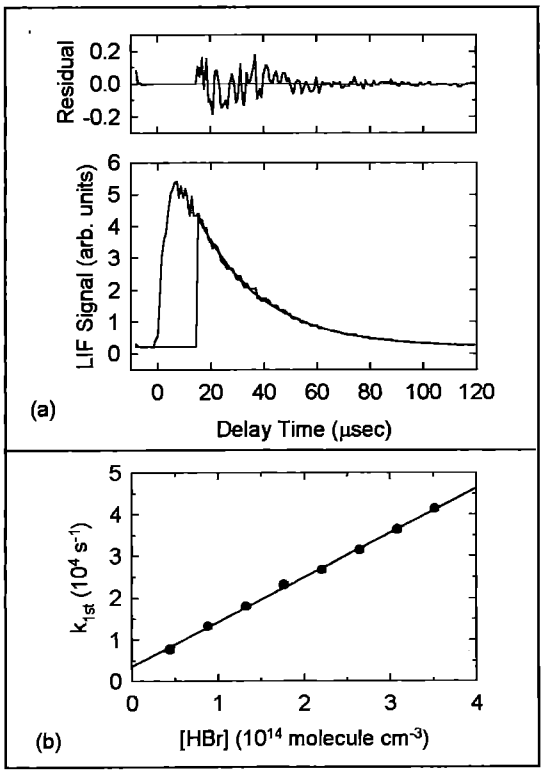

Figure 1 (a) First-order decay of LIF signal from OH in the presence of 3.5×10^{14} molecule cm^{-3} of HBr at 23 K in He, fitted to a single exponential decay with residuals shown above (b) First-order decay constants for OH at 23 K in He plotted against the concentration of HBr

In contrast to our measurements on the reactions of the CN,[4] where near-threshold photolysis of NCNO at 583 nm produced rotationally and vibrationally cold CN radicals, photolysis of H_2O_2 at 266 nm yields OH which, while still vibrationally cold, has a rotational temperature of 1500—1700 K.[6] Owing to the somewhat wide rotational level spacing in OH, rotational relaxation is comparatively slow, and so this must be taken into account in any studies of OH kinetics at ultra-low temperatures. LIF spectra of the OH radical at

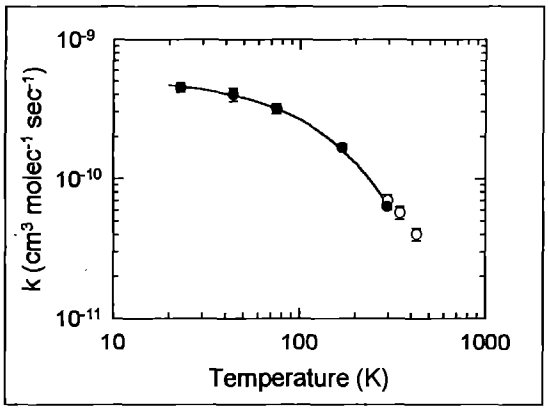

Figure 2 Rate constants for the reaction of OH with *trans*-but-2-ene at different temperatures The filled circles show the results of the present measurements in the CRESU apparatus and the line represents the exponential fit described in the text while the open circles show the results of Atkinson and Pitts[7] at temperatures between 298 and 424 K

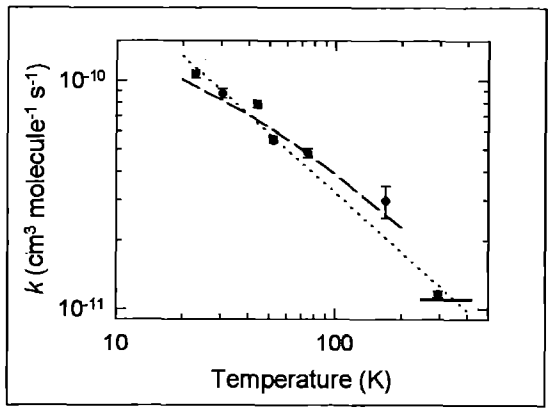

Figure 3 Rate constants for the reaction of OH with HBr at different temperatures The filled circles show the results of the present measurements in the CRESU apparatus between 23 and 295 K The horizontal, solid line represents the recommendation of Atkinson *et al.*[8] at temperatures between 249 and 416 K The dashed line shows the single parameter fit deduced from quantum scattering calculations while the dotted line shows a two parameter fit to a simple T^n dependence

different delay times[5(a)] provided an indication of the time taken for complete rotational and spin-orbit relaxation and the consequent delay necessary before kinetic decays were analysed, generally of the order of 10—20 μs.

An example of a trace of the LIF signal decay from OH of the kind used to extract values of the first-order rate constant k_{1st} by standard non-linear least squares analysis is displayed in Figure 1, and its quality is typical of those obtained in the present experiments. The delay before the signal reaches its maximum value, as rotational and spin-orbit relaxation occurs, is clearly visible on this trace. The values of k_{1st} obtained at a particular temperature were plotted against the concentration of HBr as shown in Figure 1(b).

This method has yielded rate constants for the reactions of OH with but-1-ene, *cis*-but-2-ene and *trans*-but-2-ene at temperatures down to 23 K.[5(a)] The rate constants for all three reactions increase monotonically as the temperature is lowered and this dependence of the rate constants on temperature can be fitted to an empirical expression of the form $(k/10^{-10}$ cm^3 molecule^{-1} s$^{-1}) = ae^{b(T/298\,K)}$ with a and b equal to 5.2 and −2.8 for but-1-ene, 4.7 and −2.1 for *cis*-but-2-ene and 5.4 and −2.1 for *trans*-but-2-ene. In Figure 2 we display the results obtained for the reaction of OH with *trans*-but-2-ene along with the previous high temperature results of Atkinson and Pitts.[7]

The first determination of the rate of reaction of OH radicals with HBr at temperatures below 249 K is also reported.[5(b)] Rate constants measured from 295 to 23 K increase monotonically with decrease in temperature and are faster than has previously been thought at the temperatures present in the mid and low stratosphere. The observed negative temperature dependence is well predicted by a simple formula deduced from quantum scattering calculations employing the rotating bond approximation. Our experimental results are displayed in Figure 3, and compared with a single parameter fit to this formula, as well as a two-parameter T^n dependence. The recommendation of Atkinson *et al.*[8] is also shown.

Preliminary work has also been performed on the reactions of the astrochemically important CH radical, produced by 266 nm multi-photon photolysis of $CHBr_3$. Results were obtained for the reactions of CH with D_2, O_2, NO and NH_3 at temperatures from 295 K to 13 K. Furthermore, some exploratory work was performed on the feasibility of studying the kinetics of formation of van der Waals complexes in the CRESU apparatus, concentrating on the well-characterised aniline-argon complex.

REFERENCES

1. D.C. Clary, Ann. Rev. Phys. Chem. 41, 61 (1990).
2. See *Rate Coefficients for Astrochemistry*, edited by T.J. Millar and D.A. Williams (Kluwer, Dordrecht, 1988).
3. (a) I.R. Sims and I.W.M. Smith, Chem. Phys. Lett. 151, 481 (1988); (b) I.R. Sims and I.W.M. Smith, J. Chem. Soc. Faraday Trans. 89, 1 (1993); (c) M.J. Frost, P. Sharkey and I.W.M. Smith, Faraday Discuss. Chem. Soc. 91, 305 (1991); (d) P. Sharkey and I.W.M. Smith, J. Chem. Soc. Faraday Trans. 89, 631 (1993).
4. (a) I.R. Sims, J.-L. Queffelec, A. Defrance, C. Rebrion-Rowe, D. Travers, B.R. Rowe and I.W.M. Smith, J. Chem. Phys. 97, 8798, (1992); (b) I.R. Sims, J.-L. Queffelec, A. Defrance, C. Rebrion-Rowe, D. Travers, P. Bocherel, B.R. Rowe and I.W.M. Smith, J. Chem. Phys. 100, 4229 (1994); (c) I.R. Sims, J.-L. Queffelec, D. Travers, B.R. Rowe, L.B. Herbert, J. Karthauser and I.W.M. Smith, Chem. Phys. Lett. 211, 461 (1993).
5. (a) I.R. Sims, P. Bocherel, A. Defrance, D. Travers, B.R. Rowe and I.W.M. Smith, J. Chem. Soc. Faraday Trans., in press; (b) I.R. Sims, I.W.M. Smith, D.C. Clary, P. Bocherel and B.R. Rowe, J. Chem. Phys., submitted.
6. (a) S. Klee, K.-H. Gericke and F.J. Comes, J. Chem. Phys. 85, 40 (1986); (b) K.-H. Gericke, S. Klee, F.J. Comes and R.N. Dixon, J. Chem. Phys. 85, 4463 (1986); (c) G.J. Germann and J.J. Valentini, Chem. Phys., Lett. 157, 51 (1986).
7. R. Atkinson and J.N. Pitts, Jr., J. Chem. Phys., 63, 3591 (1975).
8. R. Atkinson, D.L. Baulch, R.A. Cox, R.F. Hampson, Jr., J.A. Kerr, and J. Troe, J. Phys. Chem. Ref. Data 18, 881 (1989).

LASER PHOTOIONISATION TIME-OF-FLIGHT MASS SPECTROMETRY OF LASER DESORBED POLYCYCLIC AROMATIC HYDROCARBONS FROM CLOUD WATER AEROSOL FILTRATES

M J Dale, O H J Downs, K F Costello, C R Redpath, S J Wright and P R R Langridge-Smith
Department of Chemistry
The University of Edinburgh

INTRODUCTION

Polycyclic aromatic hydrocarbons (PAHs) make up a significant fraction of the atmospheric aerosols of anthropic origin. These compounds arise from the combustion of fossil fuels (fuel-oil, coal, petrol etc.) and are abundant in aerosols derived from urban environments [1]. Aerosol materials can be translated over very long distances; they are found in a wide range of atmospheric media, such as oceanic media [2] and polar atmospheres [3]. In such zones, remote from pollution sources, they are mainly associated with particulate matter. As these compounds are mutagenic or carcinogenic their presence in such particulates represents a potential environmental health hazard [4]. The fine particulates can enter the respiratory system and be deposited in the lung. It is, therefore, of major importance to be able to assay for their polyaromatic components.

The most widely used analytical methods for the determination of PAHs are based on sample extraction and chromatographic separation followed by mass spectrometry [5]. However, due to the low volatility and the poor solubility of PAHs, the detectable mass range using GC/MS is limited to around 300 amu. Futhermore, the low concentration of PAHs often requires that pre-concentration and purification steps are employed prior to analysis. The combination of all these procedures means that each analysis can take from hours to days to complete.

The technique of laser desorption laser photoionisation time-of-flight mass spectrometry (L^{2}TOFMS) has previously been shown to circumvent many of the difficulties inherent in hydrocarbon analysis from environmental matrices [6,7]. A pulsed CO_2 laser is used to desorb the material under investigation as intact neutral species. A pulsed ultraviolet laser is then used to ionise these gas-phase species. Photoionisation is achieved via a resonance enhanced multiphoton ionisation (REMPI) process. PAHs are a class of compounds which can be efficiently ionised using REMPI and show virtually no fragmentation at low incident laser fluences.

The advantages of the technique are (i) laser desorption of the target molecules directly from their environmental matrices (*in situ* analysis), (ii) soft ionisation of the desorbed species leading to mass spectral simplification, (iii) semi-selective ionisation of target molecules possessing a significant absorption cross section at the chosen ionisation wavelength , and (iv) highly sensitive detection of PAHs. Therefore, it is possible to directly analyse trace quantities of target compounds, contained in complex mixtures, without recourse to time-consuming and expensive sample extraction, separation or preconcentration steps.

In the present work, we report the results of an investigation into the analysis of PAHs associated with the particulates contained in cloud water aerosols. The purpose of the investigation was to demonstrate the ability of L^{2}TOFMS to determine the polyaromatic components of cloud water particulates directly from the bulk particulate matter.

EXPERIMENTAL

Collection and preparation of cloud water samples

The cloud water samples were provided by J N Cape at the NERC Institute of Terrestrial Ecology, Penicuik, Midlothian. The cloud water collector consisted of a conical passive Harp-wire device strung with polypropylene filament (0.55 mm diameter) and draining to a polypropylene bottle [8]. A polypropylene faced lid 1200 mm in diameter was supported over the cloud collector to reduce rainfall contamination of the cloud water sample; this excluded raindrops larger than 0.5 mm in diameter at wind speeds up to approximately 5 ms^{-1}. A 100 ml sub-sample of each of the cloud water samples was filtered through a polycarbonate membrane (Nucleopore, Costar, U.K.). The membrane, loaded with solid particles, was dried to a constant weight in a vacuum desiccator over phosphorus pentoxide.

Mass spectrometric analysis of particulate material

The L^{2}TOFMS instrument used in the experiments described here consisted of two differentially pumped vacuum chambers: the desorption/ionisation chamber and the reflectron time-of-flight mass spectrometer. A schematic of the instrument is shown in Figure 1.

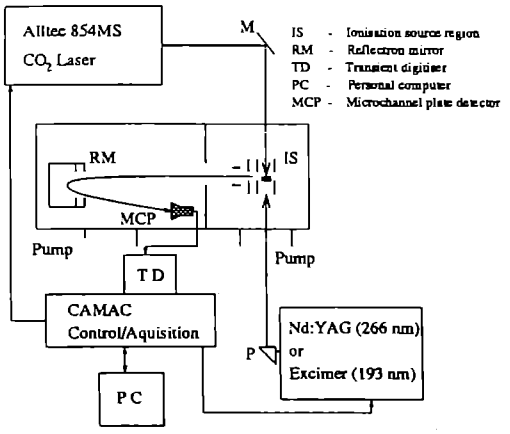

Figure 1 Schematic diagram of L^{2}TOFMS instrument

The sample filters were attached to a Macor sample probe in the desorption/ionisation chamber. This probe was connected to an externally mounted XYZ vacuum compatible manipulator to enable various locations on the sample filter to be interrogated. Sample desorption was carried out using a pulsed TEA CO_2 laser (Alltec 854MS). This was focussed to ca. 1 mm^2 using a 30 cm focal length NaCl lens. Typical desorption power densities were ca. 2 MWcm^{-2}. The desorbed neutral molecules were photoionised directly above the surface of the sample. The sample probe - ionisation laser separation was typically 5 mm. Photoionisation was performed using 193 nm laser radiation. This was generated using the ArF line of a Questek Model 2740 excimer laser. A typical ionising power density was ca. 1.3 MWcm^{-2} at 193 nm. This power density was selected as it provided good detection sensitivity with minimum laser induced fragmentation of the molecular ions. The photoions were mass analysed using a reflectron time-of-flight mass spectrometer. The ions were

detected using a tandem microchannel plate detector, the output of which was fed to a Joerger 200 MHz transient digitiser (TD).

RESULTS AND DISCUSSION

The L²TOF mass spectrum obtained using 193 nm laser photoionisation is shown in Figure 2. This was obtained using a 40 ns sampling interval for the TD. This sampling frequency degrades the ultimate resolution of the mass spectrometer but enables a larger mass window to be examined in a single experiment. There are two principal regions of interest in the mass spectrum. At the low mass end, below 100 amu, there are a number of relatively intense peaks which correspond in mass to a number of metal cations. The masses 23, 27, 39 and 56 can be attributed to the presence of sodium, aluminium, potassium and iron in the sample. However, it is the higher mass region which is of more interest. Above mass 160 amu, all the notably intense mass peaks can be attributed to the molecular ions of parent PAH molecules. The signals at 202, 252, 276, 300, 326 and 350 amu can be assigned to pyrene, benzo[a]pyrene, benzo[ghi]perylene, coronene, dibenzo[a,ghi]perylene, and benzo[a]coronene, or their isomers, repectively. The peak marked with an X is a background signal derived from the diffusion pump oil. The identities of the base peak, at 149 amu, and the relatively intense peak at 105 amu, are at present undetermined.

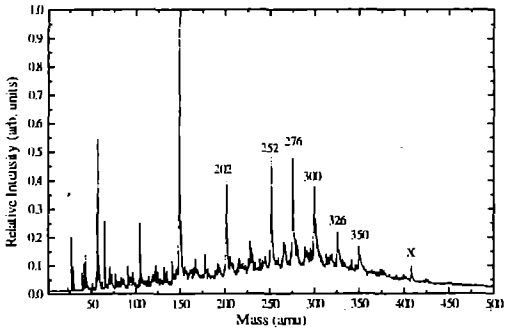

Figure 2 L²TOF mass spectrum of PAH contaminated cloud water particulates obtained using 193 nm laser photoionisation

It is possible to achieve an improved mass resolution by changing the sampling interval on the TD to 20 ns. Doing this restricts the observable mass window but substantially increases the amount of information the mass spectrum contains. Figure 3 shows the mass spectrum obtained with improved resolution. Again background peaks are labelled with an X. Inset in this figure is an expansion of the region around mass 252. As in Figure 2, the major peaks again correspond in mass to PAH species. There are, however, a number of notable differences. In Figure 3, peaks are observed to higher mass than those in Figure 2. The highest assignable mass peak is observed at 448 amu. This can be attributed to benzo[a]ovalene and its isomers. Other assignable peaks are present at 374 and 424 amu, corresponding to dibenzo[a,bc]coronene and benzo-napthocoronene, respectively.

A more detailed examination of the mass spectrum (see insert in Figure 3) reveals that there are other peaks present which can be related to PAHs, e.g. 252, 266 and 280 amu. It is possible that these peaks correspond to the presence of successively alkylated benzo[a]pyrene or its isomers. A similar series of peaks can be observed for other PAH parent skeletons, e.g. coronene at 314 and 328 amu.

It is clear from these mass spectra that L²TOFMS has unique potential as a technique for screening aerosol particulates for their polyaromatic components. We have also demonstrated that laser desorption facilitates the analysis of the increasingly involatile and high mass components that can not readily be examined by alternative techniques.

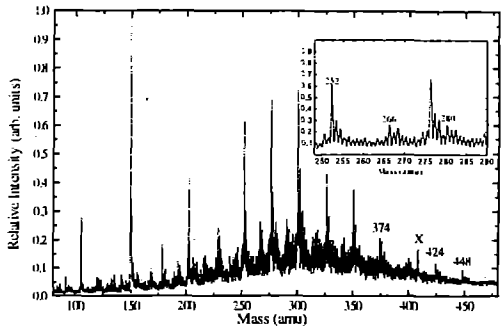

Figure 3 High resolution L²TOF mass spectrum of PAH contaminated cloud water particulates obtained using 193 nm laser photoionisation (Insert: region from 248 to 290 amu)

REFERENCES

1. P Masclet, G Mouvier, K Nikolaou.
Relative Decay Index and Sources of Polycyclic Aromatic Hydrocarbons.
Atmos. Environ., 20, 439 (1986)

2. P Masclet, P Pistikopoulos, S Beyne, G Mouvier.
Long Range Transport and Gas/Particle Distribution of Polycyclic Aromatic Hydrocarbons at a Remote Site in the Mediterranean.
Atmos. Environ., 4, 639 (1988)

3. J -L Jaffrezo, P Masclet, M P Clain, H Wortham, S Beyne, H Cachier.
Transfer Function of Polycyclic Aromatic Hydrocarbons from the Atmosphere to the Polar Ice - I: Determination of Atmospheric Concentrations at Dye 3, Greenland.
Atmos. Environ., 27A, 2781 (1993)

4. G G Grimmer (Ed.).
Environmental Carcinogens: Polycyclic Aromatic Hydrocarbons. Chemistry, Occurrence, Biochemistry, Carcinogenicity.
CRC Press, Inc. Boca Raton, FL, 1983.

5. W H McClennen, W S Arnold, K A Roberts, H L C Meuzelaar, J S Lightly, E R Lindgren.
Fast, Repetitive GC/MS Analysis of Thermally Desorbed Polycyclic Aromatic Hydrocarbons (PAHs) from Contaminated Soils.
Combust. Sci and Tech., 74, 297 (1990)

6. M J Dale, A C Jones, S J Pollard, P R R Langridge-Smith, A G Rowley.
Application of Two-Step Laser Mass Spectrometry to the Analysis of Polynuclear Aromatic Hydrocarbons in Contaminated Soils.
Environ. Sci. Technol., 27, 1693, (1993)

7. M J Dale, A C Jones, S J Pollard, P R R Langridge-Smith.
Direct Determination of Polycyclic Aromatic Hydrocarbons from Environmental Matrices using Two-Step Laser Desorption Laser Ionization Mass Spectrometry.
The Analyst, in press.

8. A Crossley, D B Wilson, R Milne.
Pollution in the Upland Environment.
Environ. Pollut., 75, 81 (1992)

NEGATIVE ION AND NEUTRAL PHOTODETACHMENT FROM SURFACES

H. Rieley, S. M. Reeman and D. J. Colby

Department of Chemistry, University of Liverpool

INTRODUCTION

The photochemistry of surface bound species is a relatively young field, and offers the possibility for many new and interesting phenomena. The presence of the surface has been found in many cases to alter the photochemical cross-section of the adsorbed species by many orders of magnitude from those in the gas phase, and it is now established that photon-induced processes which are well known in the gas-phase and on many insulator surfaces can compete effectively with quenching on metal substrates [1,2,3].

While direct absorption of a photon by the adsorbed species has been observed, in a number of cases, to be the initial reaction step, it is becoming increasingly apparent that the dominant mechanism driving photoprocesses at metal surfaces involves photoexcited substrate electrons [4]. Reaction is initiated by tunnelling of the electron into an energy level associated with the adsorbate, which excites the adsorbate/substrate system onto an electronically excited state. In most cases, the system will typically decay back to the ground state within 10^{-14}s, during which time the adsorbate may have gained enough energy, by propagation on the excited state, for reaction to occur.

A second type of reaction, and one that is central to this work, can occur when the attaching electron causes direct reaction i.e. excitation onto a highly repulsive electronic state. In this case the electron does not return to the metal by quenching, and energetic ionic products are formed, for example in the CCl_4/Ag(111) system where photo-produced Cl- ions have been observed [5]. It is the detection of these ionic products that provides direct evidence for photoelectron driven processes.

EXPERIMENTAL

All the experimental studies were carried out in an ultra-high vacuum system where base pressures of 10^{-10} torr were regularly obtained by the combination of turbo- and titanium sublimation pumps. The metal sample was held within the chamber on a sample mount which allowed both vertical axis and azimuthal rotation, as well as x,y,z translation. Liquid nitrogen cooling allowed the sample to be maintained at a base temperature of 110K from which it could be heated either resistively or by electron bombardment to a maximum of ~1000K. The sample temperature was measured using K-type thermocouples held in contact with the metal crystal by clamps.

Sample cleaning was performed by Argon ion bombardment using a commercial ion gun (VG Scientific Instruments). The sample was heated to ~600K after bombardment to allow the damaged surface to reorder back to its equilibrium geometry. Sample cleanliness was monitored by Low Energy Electron Diffraction (LEED) and Auger spectroscopy (VG Scientific Instruments).

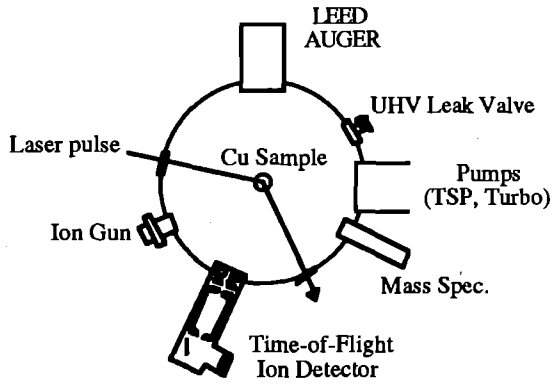

Figure 1 : Vacuum Apparatus

The Methyl Bromide experiments described in this report were performed using a pulsed Nd:YAG laser, which produced ~10ns pulses of light at selected wavelengths of 1064, 532, 355 or 266 nm. The photon flux/pulse was measured using a laser power meter, and could be attenuated using a number of beam splitters. The laser beam was directed into the chamber through a quartz window by a series of prisms. Detection of neutral photo-products was performed using the amplified signal from a commercial quadrupole mass spectrometer (VG Micromass PC).

Photo-production of negative ions was investigated using a negative ion time-of-flight detection system which was developed 'in house'. Figure 1 below shows the ion detector design. The majority of this work was performed using an excimer laser with ArF gas fill, producing 193 nm light in approximately 12 ns pulses.

In a typical experiment, the metal sample was first cleaned and then cooled to 110K. The species of interest was dosed onto the sample through a UHV leak valve (VG Scientific Instruments). The laser was then switched on, and any photo-products monitored using the quadrupole mass spectrometer (QMS) or ion detector. Post-irradiation studies, utilising the LEED/Auger unit and the QMS for temperature-programmed desorption, were carried out to detect products remaining on the surface.

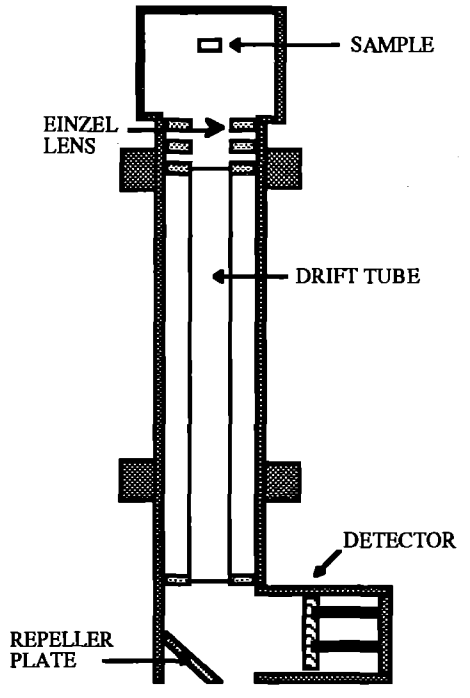

Figure 2 : Negative ion detector

RESULTS

(1) Methyl Bromide/Copper.

Photodissociation of CH_3Br on copper was investigated using 266 nm from the Nd:YAG laser. On irradiation, methyl fragments were observed to leave the surface by time-of-flight mass spectrometry (TOF-ms). An example of a typical time-of-flight spectrum is shown in figure 3 below. The photoreaction was investigated by varying the photon flux, methyl bromide coverage and irradiation angle. As yet no conclusions concerning the mechanism and dynamics of the reaction have been drawn.

However preliminary study shows that the results obtained so far compare qualitatively with studies presented in the literature for photodissociation of methyl bromide on a passivated nickel surface, where photoexcited electrons were identified as the species responsible for the reaction [6]. Any quantitative statements concerning CH_3Br on copper would be premature until an in-depth analysis of the data has been completed.

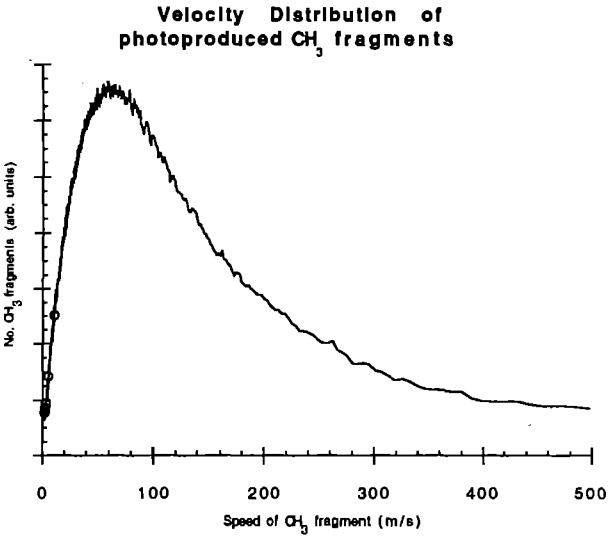

Figure 3

(2) CCl_4/Cu(100)

Preliminary studies of the photodissociation of CCl_4 on the Cu(100) surface were carried out using the 266 nm wavelength output from the Nd:YAG laser mentioned previously. No chlorine ions could be detected. However, previous work by Dixon-Warren et al on the CCl_4/Ag(111) system [5] indicated that at this wavelength the cross-section for Cl- ejection is ~$10^{-28}cm^2$, clearly unfavourable. In an attempt to solve this problem, potassium was dosed onto the copper surface prior to CCl_4 adsorption in an effort to decrease the workfunction of the system and hence increase the flux of photo-produced electrons at the metal surface with energies above the limit for Cl- ejection. However, upon irradiation with 266 nm laser light, no Cl- ions could be detected leaving the surface. This is probably due to a combination of two effects. Firstly, the presence of potassium on the surface is likely to cause dissociation of CCl_4, and hence the surface density of molecular CCl_4 capable of producing Cl- is decreased. Secondly, the potassium adatoms cause the metal surface to be more attractive to the photo-produced Cl- ions, greatly reducing the probability that once the ion is formed it will be able to escape and be detected.

Work on the CCl_4/Cu(100) system was continued using 193 nm radiation from the excimer laser. Using Auger Electron Spectroscopy (AES), a rise in surface coverage of chlorine is observed following irradiation of the surface, although no chloride ions are detected leaving the sample. This rise in chlorine coverage indicates that photodissociation of CCl_4 is indeed taking place, since it stems from exited chloride ions which fail to escape the surface image charge and are recaptured. Discussions with Dixon-Warren and others indicate that fine tuning of the ion detection system is vital for success, and it is felt that with further time this problem can be solved.

References

[1] J. Kiss, D. Lennon, S. K. Jo, J. M. White, *J. Phys. Chem.*, **95**, (1991), 8054

[2] Z. -M. Liu,S. A. Costello, B. Roop, S. R. Coon, S. Akhter, J. M. White, *J. Phys. Chem.*, **91**, (1989), 7681

[3] Ph. Avouris, B. Persson, *J. Phys. Chem.*, **88**, (1984), 837

[4] J. W. Gadzuk in "Laser Spectroscopy and Photochemistry on Metal Surface", Ed. W. Ho, *to be published*

[5] St. J. Dixon-Warren, E. T. Jensen, J. C. Polanyi, *Phys. Rev. Lett.*, **67(7)**, (1991), 2395

[6] E. P. Marsh, F. L. Tabares, M. R. Schneider, J. P. Cowin in "Chemically Modified Surfaces", Vol. 2, Ed. D. Leyden, Gordon & Breach, New York (1988)

Acknowledgements

We would like to thank the Royal Society for a Research Grant award which allowed the purchase of a digital oscilloscope, the SERC for financial support of the other equipment described and for studentships for SMR and DJC. Finally, of course, we are indebted to RAL and the Laser Support Facility Panel for the allocation of a laser loan.

LASER SPECTROSCOPY OF ORGANOMETALLIC INTERMEDIATES

I. M. Povey, A. Bezant, G. C. Corlett and A. M. Ellis
Department of Chemistry, University of Leicester, Leicester LE1 7RH

INTRODUCTION

Spectroscopic studies of molecular free radicals can provide detailed information on the properties of these highly reactive species. In addition, observation of their spectra during a chemical reaction can provide crucial evidence for elucidating reaction mechanisms. Many organic and inorganic radicals have been extensively studied in the gas phase by the spectroscopic community but organometallics have, by comparison, received scant attention. Organometallic intermediates, including radicals, can be prepared in the gas phase by a number of methods including UV photolysis of a volatile precursor [1] or by a synthetic route employing laser ablation of metals [2]. There are, alas, difficulties with each of these approaches. In the case of photolysis, suitable volatile precursors are all too rare while for both the photolysis and laser ablation methods an expensive laser system is required to generate the radicals.

We have experimented with a pulsed electrical discharge as a means of mimicking laser production of radicals but at a much lower cost. Pulsed electrical discharges have been used by several groups in recent years to generate highly reactive molecules [3-6]. Our aim was to generate organometallic radicals by one of two means:

(1) Fragmentation of an organometallic precursor in the discharge. This is analogous to UV photolysis, although mechanistic details will differ.
(2) Synthesis of organometallic radicals by metal + organic reactions. As indicated in (1), a pulsed discharge can cause fragmentation of organic molecules to produce fragments such as methyl or ethyl radicals. In addition, cathode sputtering can produce metal atoms and these can combine with the organic fragments to produce novel organometallic species.

The focus of our attention is on the simplest possible organometallic intermediates of formula M-R, few examples of which are known. Although at a preliminary stage, this work has already met with some success.

EXPERIMENTAL

The discharge nozzle is based on a simple design by Bondybey and co-workers [5] and is illustrated schematically in Figure 1. It consists of a teflon fixture mounted on the faceplate of a commercial pulsed valve and within the fixture are two metal electrodes at a distance of about 1mm apart. The nozzle is mounted inside a vacuum chamber and a continuous voltage in the range 500-1500 V is applied between the electrodes. On opening of the pulsed valve, gas flows between the electrodes and a discharge self-ignites. Subsequently, the gas mixture flows into vacuum to form a supersonic jet and is probed using laser-induced fluorescence (LIF) spectroscopy.

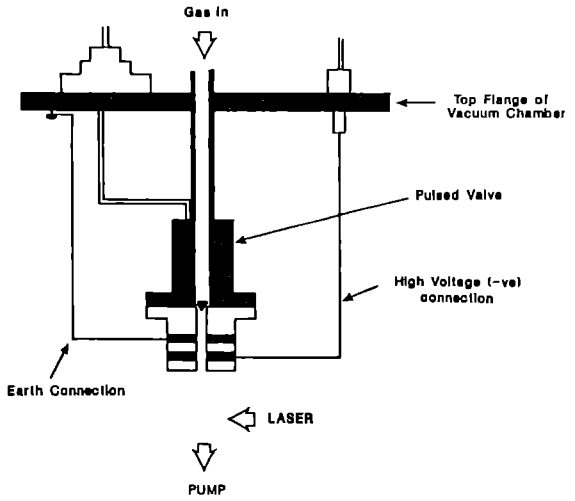

Figure 1. Schematic illustration of pulsed discharge nozzle.

RESULTS AND DISCUSSION

A. Metal atom sputtering

In order to employ method (2) above to prepare organometallics, copious metal atom production must be achieved in the discharge. To investigate this, a pulsed discharge across indium electrodes in the presence of pure argon was employed. Indium atoms are a convenient diagnostic since they have a strong absorption line close to 22160 cm^{-1} (^2P-^2S) which can be detected *via* fluorescence from the ^2P excited electronic state. As shown in Figure 2, a strong In signal was observed in the experiments for voltages exceeding 1.2 kV. Clearly, extensive metal atom sputtering from the cathode is possible.

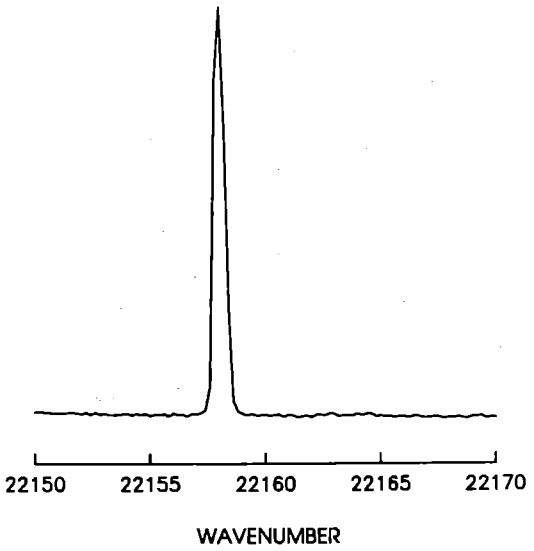

Figure 2. Laser excitation spectrum of atomic indium.

B. Production of organometallic radicals by sputtering approach

To test the feasibility of this approach, attempts were made to prepare the $ZnCH_3$ radical by method (2). $ZnCH_3$ has already been studied in detail by one of the authors (AME) and co-workers in laser photolysis experiments and is known to have a strong LIF spectrum [1]. A number of unsuccessful experiments were undertaken involving zinc electrodes and several potential methyl radical precursors including acetone, methyl iodide, and butyl peroxide. However, $ZnCH_3$ was observed when $Al(CH_3)_3$ was employed as the methyl radical precursor, as can be seen in Figure 3. This excitation spectrum shows the $\tilde{A}^2E-\tilde{X}^2A$, 0_0^0 band of $ZnCH_3$ and clearly demonstrates the potential of the discharge sputtering method for preparing novel organometallic intermediates.

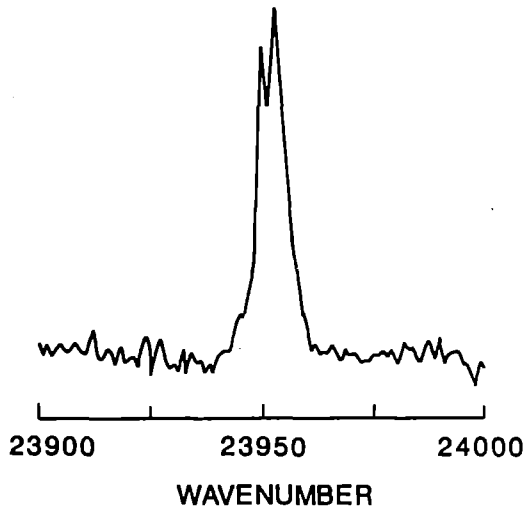

Figure 3. Excitation spectrum of jet-cooled $ZnCH_3$ radical produced by sputtering of zinc electrodes in presence of $Ar/Al(CH_3)_3$.

C. Observation of a new organometallic radical, ZnC_2H_5

There have been a number of recent studies of the photolysis of $Zn(C_2H_5)_2$. This dialkyl complex is, like several other metal alkyls, an important precursor to metal deposition in the semiconductor fabrication industry. The indications are that on absorption of a UV photon, $Zn(C_2H_5)_2$ dissociates to ZnC_2H_5 and C_2H_5 but the zinc ethyl radical is sufficiently vibrationally excited that it undergoes rapid dissociation itself. Nevertheless, indirect measurements at high gas pressures by Jackson [7] indicate that ZnC_2H_5 can be collisionally stabilised by V→T transfer. Jackson attempted to observe the LIF spectrum of ZnC_2H_5 but was unsuccessful, concluding that the radical probably has a low fluorescence quantum yield.

We have attempted to record the excitation spectrum of ZnC_2H_5 by pulsed discharge of $Zn(C_2H_5)_2$ vapour seeded in helium or argon carrier gas. Under similar conditions using $Zn(CH_3)_2$ precursor, a strong $ZnCH_3$ signal was observed. For $Zn(C_2H_5)_2$, a strong excitation spectrum was also obtained as shown in Figure 4. Apart from clearly identifiable sharp ZnH lines at high wavenumber, we believe the remaining bands are due to ZnC_2H_5. This radical is identified as the carrier for a number of reasons, including the absence of the features in Figure 4 when employing $Ga(C_2H_5)_3$ or $B(C_2H_5)_3$ precursors. Work is now underway to produce a specific assignment of the observed bands.

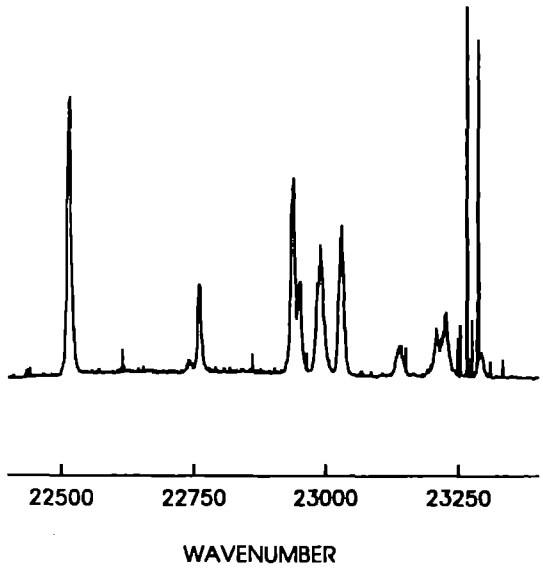

Figure 4. Laser excitation spectrum showing ZnC_2H_5 and ZnH features.

CONCLUSIONS

We have shown that a pulsed electrical discharge nozzle can be used to achieve 'gentle' fragmentation of organometallic precursors to produce organometallic radicals. In addition, synthesis of intermediates by metal + ligand reactions has been demonstrated in which metal atoms sputtered off the electrode surface combine with organic fragments produced in the discharge. This preliminary work has also allowed the first spectroscopic observation of the zinc ethyl radical, ZnC_2H_5.

REFERENCES

[1] Robles, E. S. J., A. M. Ellis and T. A. Miller, Chem. Phys. Letters, 178, 185 (1991).

[2] Ellis, A. M., E. S. J. Robles and T. A. Miller, J. Chem. Phys., 94, 1752 (1991).

[3] Sharpe, S. and P. Johnson, Chem. Phys. Letters, 107, 35 (1984).

[4] Bramble, S. K. and P. A. Hamilton, Chem. Phys. Letters, 170, 107 (1990).

[5] Schlachta, R., G. Lask, S. H. Tsay and V. E. Bondybey, Chem. Phys., 155, 267 (1991).

[6] Rosser, K. N., Q.-Y. Wang and C. M. Western, J. Chem. Soc., Faraday Trans., 89, 391 (1993).

[7] Jackson, R. L., J. Chem. Phys., 96, 5938 (1992).

THE INTERACTION OF THE RESTRICTION ENDONUCLEASE ECO RV WITH DNA: A STUDY USING RESONANCE RAMAN SPECTROSCOPY OF OLIGODEOXYNUCLEOTIDES CONTAINING 4-THIOTHYMIDINE

Harry Thorogood[1], Timothy R. Waters[2], Anthony W. Parker[3], Christopher W. Wharton[4] and Bernard A. Connolly[1]

[1]University of Newcastle upon Tyne
[2]University College London
[3]Rutherford Appleton Laboratory
[4]University of Birmingham

The restriction endonuclease Eco RV recognises GATATC sequences in double-stranded DNA and cuts between the central T and dA bases. The most noteworthy feature of this enzyme is its extremely high selectivity. Sequences that differ from the cognate GATATC site by one base are cut 10^6-10^8 times more slowly. X-ray structures of this protein complexed to DNA are available and figure 1 shows that the enzyme is dimeric and that the DNA is bound in a deep cleft that is formed between the two sub-units. DNA that contains the GATATC is extremely distorted when it is bound to the enzyme. Figure 2 shows the conformation of the bound DNA. The DNA is bent almost through 90° with the distortion being centred on the central T and dA bases in the GATATC site (i.e. at the scissile bond). All the base pairs are buckled, twisted and rolled, sometimes severely, when compared with typical base pair parameters seen for B-DNA in solution. These crystal structures, together with a variety of solution kinetic data, have led to the following proposal for how Eco RV achieves high selectivity. Cognate GATATC sequences form twelve hydrogen bonds to the enzyme. These are not used to strengthen substrate binding but rather to drive the distortion of the DNA substrate. This moves the scissile phosphate into the catalytic site and simultaneously assembles the binding site for Mg^{2+} (an essential cofactor). This cation binds and hydrolysis takes place. Sequences lacking GATATC sites do not form the twelve hydrogen bonds to the enzyme. However, they bind just as tightly as substrate DNA. As the hydrogen bonds are not formed no nucleic acid distortion occurs and so no hydrolysis takes place.

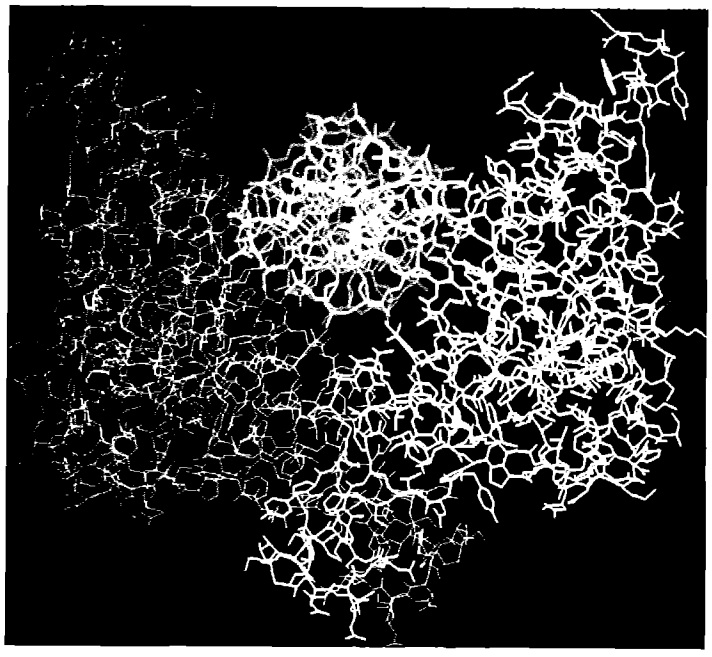

Figure 1. The Eco RV endonuclease dimer (orange/yellow) containing bound DNA (blue)

The conformation of DNA bound to the endonuclease has been investigated by resonance Raman spectroscopy. The base 4-thiothymidine (figure 3) is a close structural analogue of thymidine and has a sulphur atom at the four position rather than an oxygen. this base absorbs light at 340 nm (rather than the 260 nm seen with the four normal bases) and is a strong Raman scatterer. The absorption maximum at 340 nm means this base can be excited without inducing electronic transitions in the four standard bases. Thus measuring the resonance Raman spectrum of oligonucleotides containing 4-thiothymidine using 363.8 nm light gives signals that are only due to this base and reasonably free of any other transitions.

Three oligodeoxynucleotides d(GACGA[^{4S}T]ATCGTC), d(GACGATA[^{4S}T]CGTC) and d(GACC[^{4S}T]ATAGGTC) have been used with this study. The first two contain a modified GATATC site (in which the T's are replaced with 4-thiothymidine) and the third is a control that lacks this site. Only the sequence d(GACGA[^{4S}T]ATCGTC) is a substrate for the endonuclease.

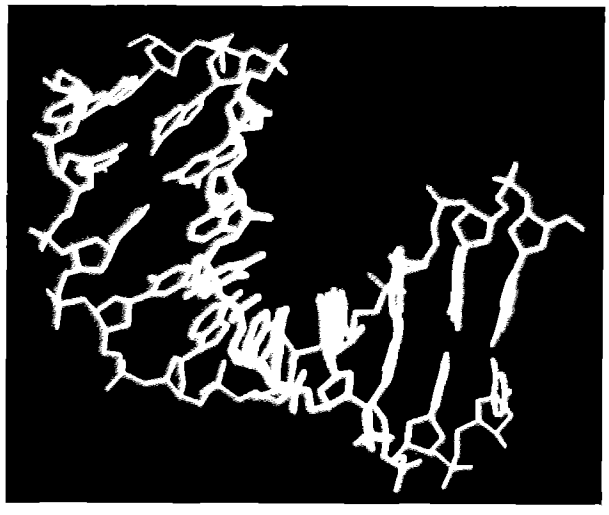

Figure 2. The structure of GATATC containing DNA bound to Eco RV

Obviously the control is not turned over but d(GACGATA[^{4S}T]CGTC) is also not a substrate as the T to ^{4S}T alteration prevents catalysis. The reasonance Raman spectra of all three oligonucleotides both free in solution and bound to Eco RV are shown in figures 4a, b and c. The identification of each peak to a particular transition (based on model compounds) is given in figure 5. The presence of Eco RV has a significant effect on the spectrum of the substrate d(GACGA[^{4S}T]ATCGTC) but little influence on those of the non-substrate d(GACC[^{4S}T]ATAGGTC)

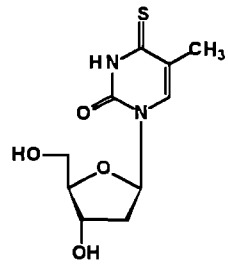

Figure 3. The structure of 4-thiothymidine

and the control d(GACGATA[^{4S}T]CGTC). This is what we would expect from the crystallographic data which suggests that non-substrate oligonucleotides are not distorted by the endonuclease and remain in B-like conformation, whereas substrates are severely distorted. Experiments showed that under the conditions used for recording the spectra, all three oligonucleotides were completely bound to the enzyme. The different interaction of the specific oligonucleotide with Eco RV is evident, if not totally understood. The 704 cm C=S peak moves back towards that of 4-thiothymidine, indicating a pseudo-non-duplex structure (as seen in the crystal structure). The most dramatic effects are seen in the upper region of the spectrum. Both the C5=C6 vibration and C5-methyl stretch undergo large shifts. The methyl group is embedded in a hydrophobic pocket within the protein according to the crystal structure and the C5-C6 region of the base is also buried in a hydrophobic area. Attempts are currently being made to interpret these spectral changes in a rational manner (especially by comparison with the crystal structure) and to come up with a dynamic solution model for the interaction of RV with its cognate sequence.

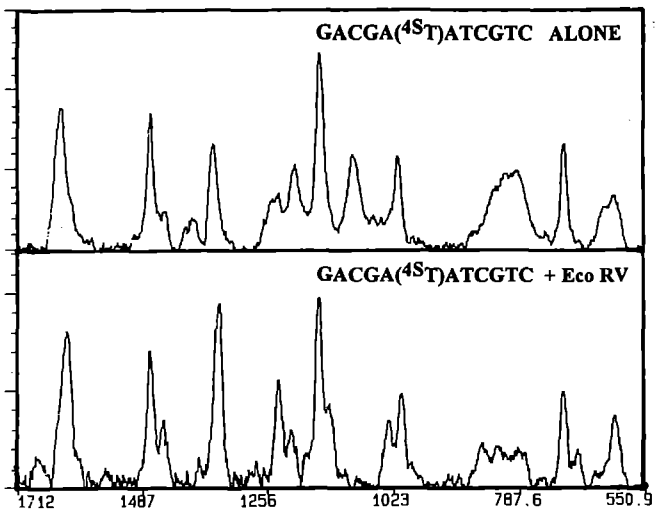

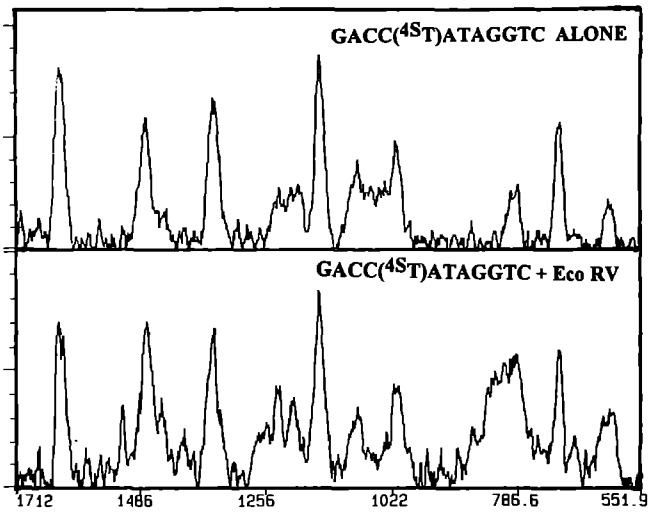

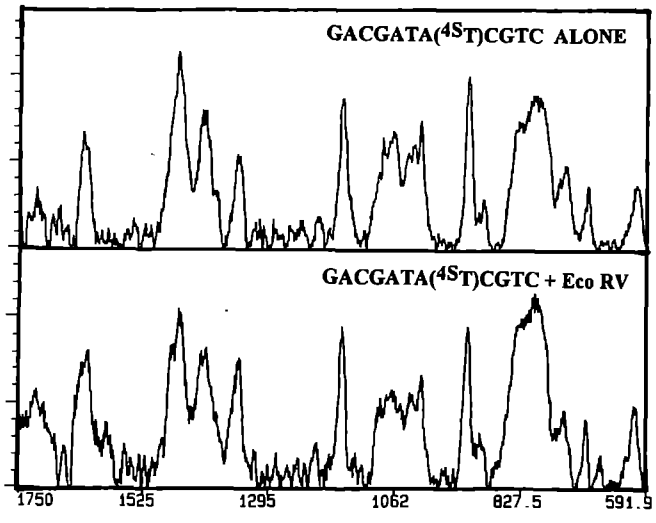

Figure 4A (top left), 4B (bottom left) and 4C (top right) The Raman spectra of the three oligonucleotides used in this study either alone or complexed to the Eco RV endonuclease. The y axis is intensity and the x wavenumber in all cases.

MODE	4-THIOTHYMIDINE	GACGA(4sT)ATCGTC with Eco RV in brackets	GACGATA(4sT)CGTC with Eco RV in brackets	GACC(4sT)ATAGGTC with Eco RV in brackets
ring stretch ν_h^6(C5=C6)	1631	1636 (1625)	1632 (1632)	1632 (1634)
ring stretch ν_a^6	1478	1471 (1471)	1462 (1462)	1476 (1473)
ring streeth $\nu\delta a^6$ coupled with N1-C1 stretch	1351	1409 & 1392 (1383)	1413 (1413) & 1389 (1390)	1404 (1404)
C5 Methyl stretch	1351	1355 (1345)	1351 (1350)	1350 (1350)
unknown		1249 (1235)	1235 (1236)	1231 (1233)
Kekule	1231	1206 (1212)	1202 (1203)	1208 (1205)
Ring Br^6 coupled with C=S stretch	1156	1157 (1161)	1158 (1157)	1156 (1157)
Ring stretch $\nu\delta b^6$ plus PO_2^- stretch		1096	1083 (1083)	1085 (1085)
Ring stretch $\nu\delta b^6$	1087			
Ring deformation Tr	1016	1014 (1009)	1014 (1011)	1015 (1015)
unknown	864			
C=S stretch coupled with ring breath Br^6	709	704 (706)	705 (705)	705 (705)
Ring deformation δa^6	630	630	631	(622)
unknown	609	610.(609)	612 (612)	614.(608)

Figure 5. The identification of each of the peaks seen in Figures 4A, 4B and 4C.

TIME-RESOLVED RESONANCE RAMAN SPECTROSCOPY AND FLASH PHOTOLYSIS INVESTIGATIONS OF ANTIOXIDANT REACTIONS

Roger H Bisby[1] and Anthony W Parker[2]

[1]Department of Biological Sciences, University of Salford
[2]Rutherford Appleton Laboratory

INTRODUCTION

Constant oxidative stress endured by aerobic organisms, including man, is countered by a range of defences. These include the enzymes superoxide dismutase, catalase and glutathione peroxidase as well as a range of low molecular weight antioxidants such as α-tocopherol (vitamin E), ascorbate (vitamin C), thiols and uric acid[1]. We have previously used nanosecond laser flash photolysis to study one-electron transfer reactions involving antioxidant radicals and have shown than in membrane systems recycling of the α-tocopheroxyl radical by ascorbate is extremely rapid[2,3]. Time-resolved resonance Raman spectroscopy (TR^3S) was also used to characterise the α-tocopheroxyl and related radicals and to demonstrate that the effectiveness of α-tocopherol is as an antioxidant is related to electron delocalisation in the α-tocopheroxyl radical[4].

Lipids are a particularly sensitive to oxidation, and in the blood low density lipoprotein (LDL) can be readily damaged by free radical reactions[5]. Oxidative modification of LDL leads to its enhanced uptake by macrophage cells in the blood vessel wall[6]. This is the initial stage of a sequence of events which lead to atherogenesis and coronary heart disease. Antioxidants associated with the LDL particle, particularly α-tocopherol, protect against LDL oxidation. Recent epidemiological surveys have indicated that dietary supplementation with vitamin E may reduce the risk of heart disease by up to 40%[7]. The cholesterol-lowering drug probucol has been found to inhibit oxidation of LDL[8] suggesting that it acts similarly to α-tocopherol, although its free radical chemistry remains largely unexplored.

Oxidative stress may be initiated by a range of reactive oxygen species including the superoxide and hydroxyl radicals as well as excited singlet oxygen ($^1O_2$). Singlet oxygen may be produced not only by photosensitization, involving energy transfer from a photo-excited state of an organic molecule, but also in "dark" reactions such as autoxidation and enzymic reactions which yield excited carbonyl products[9,10]. α-Tocopherol is known to be a particularly effective singlet oxygen quencher, but the chemical reactivity of antioxidants suggests that they may also suppress singlet oxygen damage by reduction of the precursor triplet states. The present investigations have used laser flash photolysis and singlet oxygen phosphorescence decay measurements to investigate the kinetics of these reactions, and TR^3S to study their mechanisms.

REACTIONS OF ANTIOXIDANTS WITH TRIPLET STATES

Second order rate constants for reaction of duroquinone (π,π^*) and benzophenone (n,π^*) triplet states were obtained by flash photolysis from the rates of decay of the triplets as a function of antioxidant concentration. The results are shown in the Table. α-Tocopherol and probucol were found to react with both triplet states with rate constants close to the diffusion-controlled limit. The two thiols, N-acetyl cysteine and dihydrolipoic acid, were substantially less reactive and the food antioxidant, palmitoyl ascorbate, possessed intermediate reactivity. Taking into account the difference in solvents, the difference between the rates of reaction of ^3DQ and ^3BP increased as the overall reactivity decreased and is especially marked with N-acetyl cysteine. For ^3DQ similar rate constants were obtained from measurements of singlet oxygen yield (see below). The similarity between the reactivities of α-tocopherol and probucol strongly supports the contention that probucol may be an effective antioxidant in vivo.

THE PROBUCOL RADICAL

Laser flash photolysis (308nm) of Probucol (4-4'-[1-methylethylidine)*bis*(thio)]*bis*[2,6-*bis*(1,1-dimethylethyl)]phenol) led to a weakly absorbing intermediate with λ_{max}=550nm, the intensity of which increased on repeated exposure to the laser. This is therefore unlikely to be the phenoxyl radical which is the putative intermediate formed during the reaction of probucol as an antioxidant. In contrast, oxidation of probucol by both ^3DQ and ^3BP gave a strong transient with λ_{max}=500nm, similar to that observed on one-electron oxidation of probucol in pulse radiolysis experiments. The TR^3 spectrum of this radical is shown in Figure 1. In ethanol the spectrum is very similar to those of other phenoxyl radicals, with a peaks at 1520 cm^{-1} and 1575 cm^{-1} attributed to C-O and C=C stretching vibrations respectively. Also apparent is the C-H bending vibration at 1125 cm^{-1}. In octanol and Triton micelles there is evidence for another band at 1550cm^{-1} which has not been assigned. The inability to directly photoionise probucol to the phenoxyl radical has prevented direct measurement of the rate constant for reaction of this radical with ascorbate. When ^3DQ is used as the oxidant, no reaction faster than the direct oxidation of ascorbate by ^3DQ could be observed, showing that the second order rate constant for reaction of probucol radical in Triton micelles with ascorbate is $<10^5$ dm^3 mol^{-1} s^{-1}.

TABLE:- Rate constants for quenching of triplet benzophenone (^3BP), duroquinone (^3DQ) and singlet oxygen by antioxidants (AH).

ANTIOXIDANT (AH)	k(AH + ^3DQ) [^3DQ decay]	k(AH + ^3BP) [^3BP decay]	k(AH + ^3DQ) [$^1O_2$ yield]	k(AH + $^1O_2$) [$^1O_2$ decay]
Probucol	$(3.1\pm0.2)\times10^9$	$\sim10^9$	$(2.9\pm0.1)\times10^9$	$<10^6$
α-Tocopherol	$(2.8\pm0.2)\times10^9$	$(5.7\pm0.7)\times10^9$	$(3.7\pm0.1)\times10^9$	$(2.01\pm0.01)\times10^8$
Palmitoyl ascorbate	$(1.8\pm0.1)\times10^9$ $(3.5\pm0.3)\times10^9$ ‡	$(1.1\pm0.1)\times10^9$	$(1.9\pm0.1)\times10^9$	$(9.9\pm2.5)\times10^5$
N-Acetyl cysteine	$(1.5\pm0.1)\times10^8$	$\leq5\times10^6$	$(1.9\pm0.1)\times10^8$	$<2\times10^4$
Dihydrolipoic acid	$(7.9\pm0.4)\times10^8$	$(4.2\pm0.1)\times10^7$	$(9.4\pm0.1)\times10^8$	$(5.7\pm0.9)\times10^5$

Values for ^3DQ and singlet oxygen quenching in ethanol except for ‡acetonitrile; values for ^3BP quenching in acetonitrile. Rate constants in units of dm^3 mol^{-1} s^{-1}.

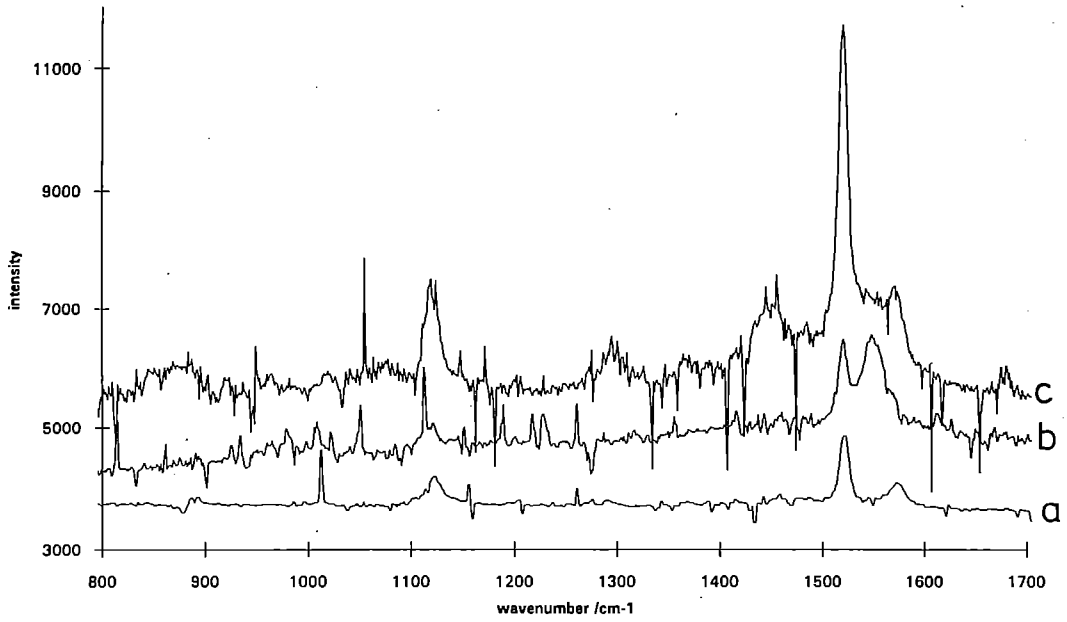

FIGURE 1 Time-resolved resonance Raman spectra of the probucol radical in a) ethanol; b) octanol; and c) Triton X-100 (reduced) micelles in aqueous solution at pH 7. The oxidation of probucol was sensitised with duroquinone, excited at 355nm. The probe pulse was at 500nm, delayed 1 μs after the pump pulse.

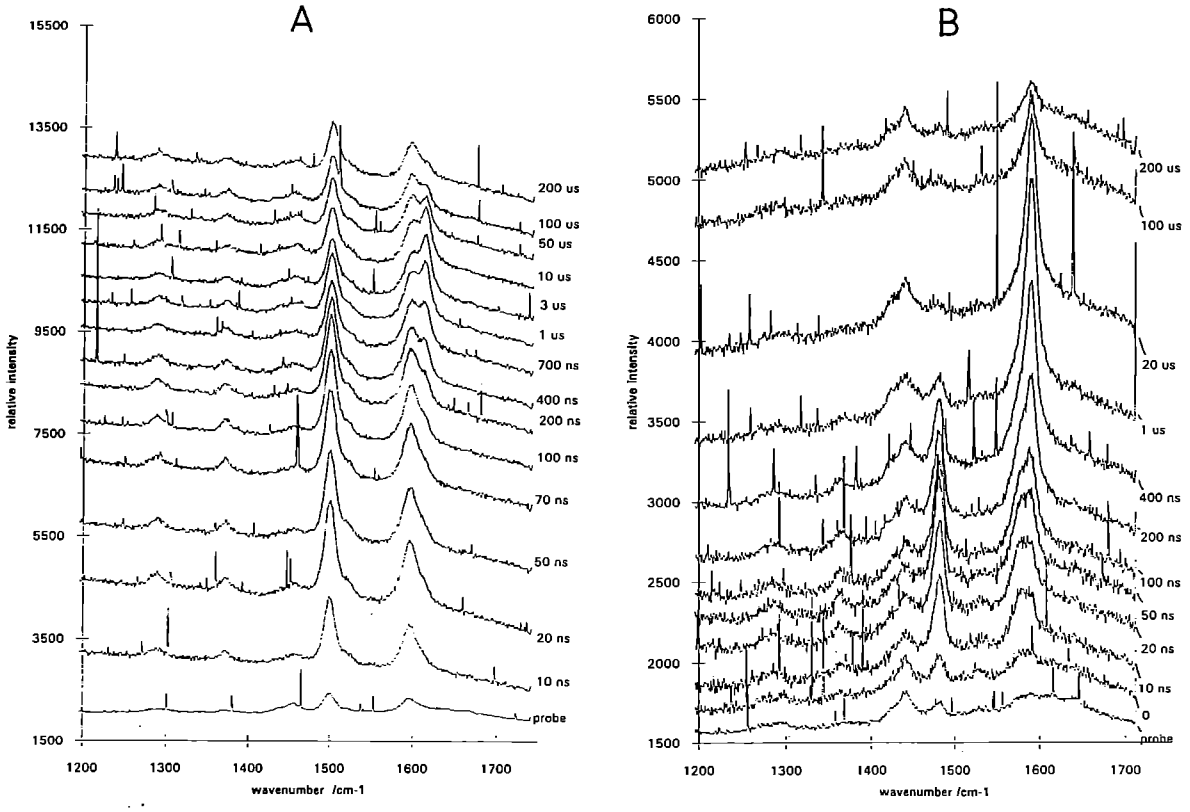

FIGURE 2 Time-resolved resonance Raman spectra from the reaction between triplet duroquinone and α-tocopherol (A) and palmitoyl ascorbate (B) in SDS micelles at pH 7.0. The pump pulse was at 350nm, and the probe pulse at 425nm, delayed by the indicated times.

MECHANISM OF REACTION BETWEEN TRIPLET DUROQUINONE AND ANTIOXIDANTS

The preference of triplet ketones to react with phenols by hydrogen atom transfer rather than electron abstraction is well known. Figure 2A confirms that this is the case for reaction between ^3DQ and α-tocopherol in an aqueous micellar solution of sodium dodecyl sulphate (SDS) at pH 7. Immediately after the pump pulse (350nm), producing ^3DQ, probing at 425nm reveals peaks in the Raman spectrum at 1504 and ~1590 cm^{-1}. These represent the unresolved spectra of both the tocopheroxyl radical and the neutral duroquinone radical (DQH·), formed by hydrogen atom transfer:-

$$^3DQ + \alpha\text{-}T\text{-}OH \rightarrow DQH\cdot + \alpha\text{-}T\text{-}O\cdot$$

Over the timescale of about a microsecond, the neutral DQH· radical diffuses out of the micelle and deprotonates to form the radical anion (DQ^{-}·) which has a Raman band at 1612 cm^{-1}. This subsequently decays over hundreds of microseconds, leaving the spectrum of the persistent α-tocopheroxyl radical. Kinetic analysis shows that the rate constant for exit of DQH· from the micelle is approximately $2x10^6$ s^{-1}.

Since at pH 7 ascorbate exists as a monoanion ($AscH^-$), there is the possibility that ^3DQ may react with ascorbate either by hydrogen atom or electron transfer:-

$$^3DQ + AscH^- \rightarrow DQ^{-}\cdot + AscH\cdot$$
$$^3DQ + AscH^- \rightarrow DQH\cdot + Asc^{-}\cdot$$
$$AscH\cdot \rightleftharpoons Asc^{-}\cdot + H^+ \qquad (pK=-0.4)$$

Figure 2B shows TR^3S from the reaction between ^3DQ and palmitoyl ascorbate ($pK_a=5.1$) in Triton micelles at pH7. In this case only the duroquinone radicals are in resonance at the probe wavelength. Again the spectra indicate an initial hydrogen atom transfer reaction to give DQH· followed by protonation/deprotonation steps leading to DQ^{-}·.

QUENCHING OF SINGLET OXYGEN YIELDS AND LIFETIMES BY ANTIOXIDANTS

Reaction of an antioxidant with triplet duroquinone (rate constant k_q) will compete with internal conversion of the triplet state (rate constant k_d) and energy transfer to oxygen (rate constant k_t).

$$^3DQ + AH \xrightarrow{k_q} DQH\cdot + A\cdot$$

$$^3DQ + {}^3O_2 \xrightarrow{k_t} DQ + {}^1O_2$$

$$^3DQ \xrightarrow{k_d} DQ$$

According to this scheme, the quantum yields for singlet oxygen in the absence and presence of antioxidant (ϕ_o and ϕ respectively) are related to the rate constants by:-

$$\frac{\phi_o}{\phi} = 1 + \frac{k_q[AH]}{k_d + k_t[O_2]}$$

Relative quantum yields for singlet oxygen formation were determined from time-resolved singlet oxygen phosphorescence decays, measured at 1260nm using a cooled germanium diode, extrapolated to the centre of the laser pulse and corrected for fluctuations in laser intensity. Plots of ϕ_o/ϕ such as in Figure 3 were found to be linear. Using values of k_t and k_d recently published by Darmayan and Foote[11], estimates of k_q were obtained and are included in the table. These compare very well with values of k_q measured directly from the rate of triplet decay as a function of antioxidant concentration.

The rate of singlet oxygen quenching by the antioxidant was determined from the rate of singlet oxygen phosphorescence decay. α-Tocopherol is well known as a singlet oxygen, and the present value compares well with those in the literature[12]. The other antioxidants studied, even probucol as a related phenol, were very poor singlet oxygen quenchers compared with α-tocopherol, showing values of k_q between two and three orders of magnitude lower. This difference between α-tocopherol and probucol may be useful as a probe for the involvement of singlet oxygen in causing oxidative damage.

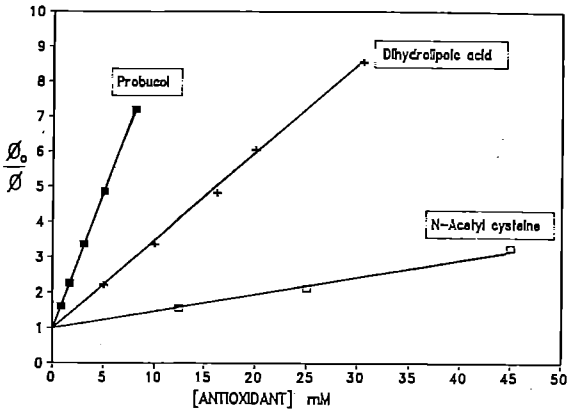

FIGURE 3 Effect of antioxidant concentration on the yield of singlet oxygen in air-saturated solutions of duroquinone (5 mmol dm^{-3}) in ethanol, photolysed with a 355nm laser pulse.

REFERENCES

1. G R Buettner. The pecking order of free radicals and antioxidants: lipid peroxidation, α-tocopherol and ascorbate. Arch.Biochem.Biophys., 300, 535 (1993).
2. R H Bisby and A W Parker. Reactions of the α-tocopheroxyl radical in micellar solution studied by nanosecond laser flash photolysis. FEBS Lett., 290, 205 (1991).
3. R H Bisby and A W Parker. Radiation-induced free radical reactions. In "Free radicals: from basic science to medicine" (Eds E Albano and M Dianzani) Birkhauser, Basel, pp.31-37 (1993).
4. A W Parker and R H Bisby. Time-resolved resonance Raman spectroscopy of the α-tocopheroxyl and related radicals in solvent, micellar and membrane systems. J.Chem.Soc., Faraday Trans., 89, 2873 (1993).
5. H Esterbauer, J Gebicki, H Puhl and G Jurgens. The role of lipid peroxidation and antioxidants in oxidative modification of LDL. Free Rad.Biol.Med., 13, 341 (1992).
6. D S Leake. Oxidised low density lipoproteins and atherogenesis. Br.Heart J., 69, 476 (1993).
7. E B Rimm, M J Stamper, A Ascherio, E Giovannucci, G A Colditz and W C Willett. Vitamin E consumption and the risk of coronary heart disease in men. New Engl.J.Med., 328, 1450 (1993).
8. M Kuzuya and F Kuzuya. Probucol as an antioxidant and antiatherogenic drug. Free Rad.Biol.Med., 14, 67 (1993).
9. N Duran and E Cadenas. The role of singlet oxygen and triplet carbonyls in biological systems. Rev.Chem.Intermed., 8, 147 (1987).
10. E Cadenas. Generation of electronically excited states during electron transfer of quinones. Chemica Scripta 27A, 113 (1987).
11. A P Darmayan and C S Foote. Solvent effects on singlet oxygen yield from n,π^* and π,π^* triplet carbonyl compounds. J.Phys.Chem., 97, 5032 (1993).
12. A A Gorman. The bimolecular reactivity of singlet molecular oxygen. Adv.Photochem., 17, 217 (1992).

ELECTRON TRANSFER IN DNA AND POLYDEOXYNUCLEOTIDES: MIGRATION OF OXIDATIVE DAMAGE TO THE MOST EASILY OXIDISED BASE.

P. Cullis,[1] M.C.R. Symons,[4] M.E. Malone,[1] A.W. Parker,[2] P. O'Neill,[3] S. Botchway,[3] T. Melvin,[3]
Leicester University[1], Rutherford Appleton Laboratory,[2] MRC Radiobiology Unit,[3] Essex University.[4]

INTRODUCTION

Ionising irradiation causes a diversity of damage to deoxyribose nucleic acid (DNA)[1]. The lethal and mutagenic effect of the radiation leads to cell malfunction and cell death through strand breaks (sb). The insult of ionising radiation on the DNA is via radical formation. Ionisation can occur either within the DNA (the direct effect) or with the environment, usually water. Damage also stems from attack on the DNA by the reactive water species that have been produced by the radiation. Both direct and scavengeable damage mechanism leads to strand breakage within the DNA molecule. The reactions of the water derived molecules have been studied extensively, however, as yet, information regarding the direct reaction of ionising radiation with DNA is scarce. This direct interaction of ionising radiation with DNA results in the formation of a nucleic acid base radical cation and an electon. It is argued that the primary radical cations produced upon ionisation migrate in the DNA and become trapped at the purines, primarily guanine[2]. Similarly, the ejected electrons migrate within the DNA, becoming trapped at the pyrimidines. In frozen aqueous systems where the effective target is glassy DNA, the major radicals observed are thymidine and guanine type radicals.[2,3].

Another method of producing the radical cations of purine and pyrimidine nucleotides in aqueous solutions involves generating powerful oxidant, $SO_4^{\cdot-}$ by pulse radiolysis. Unfortunately this oxidant not only reacts by an electron transfer pathway but also an addition pathway and as a result the interpretation of the results is complicated[4].

The use of pulsed high intensity laser light has aided in the study of the direct effect since 'clean' primary DNA radical cations are generated selectively. Irradiation of aqueous DNA and its base constituent with high energy laser light (193nm) yields a hydrated electron (e_{aq}^-) and the radical cation of the nucleic acid base. Based on the ionisation potentials one would predict on purely theoretical grounds, that hole migration within DNA to the most easily ionisable base, guanine will occur. Reactions of the radical cations and their resulting neutral radical may produce strand breaks (sb) in nucleic acids[5]. The guanine radical cation, $G^{\cdot+}$ is formed by the action of the ionising radiation with DNA. It is therefore necessary and important to understand the role of this radical in the strand break processes.

We report here experiments that are designed to determine whether hole migration occurs upon 193 nm laser light irradiation of mixed polymers and oligonucleotides to the most easily oxidised site.

DOES ELECTRON TRANSFER OCCUR ALONG SINGLE STRANDED OLIGODEOXYNUCLEOTIDES?

Laser flash photolysis experiments using 193nm laser light with optical detection were performed using a series of specifically prepared *single-stranded* oligodeoxynucleotides to assess the migration of oxidative damage to the most easily oxidised base. The efficiency of photoionisation to each nucleic acid base component with a mixed oligonucleotide is dependent on the quantum yield of photoionisation and the relative extinction coefficients of the nucleic acid bases at 193nm. As determined previously, the quantum yield of photoionisation is inversely proportional to the ionisation potential.[5] For a large percentage of the primary radical species to be formed on the least easily oxidised nucleic acid base, oligodeoxynucleotides were prepared with the least easily oxidised nucleic acid base species present in the greatest abundance.

Short oligodeoxynucleotides were prepared with an oligonucleotide synthesiser and purified by HPLC (to remove any impurities, such as small traces of protecting groups that had been used during the oligonucleotide synthesis). These consisted of nucleic acid bases in a ratio of 2:1 with the least easily oxidised species present in excess. Transient absorption spectra following flash photolysis were obtained from oxygen saturated solutions of these oligodeoxynucleotides. The quantum yields for their photo-ionisation were determined from dependence of the yield of electrons (as measured at 650nm for nitrogen saturated samples), on the laser intensity and comparison from this dependence obtained for sodium chloride solutions assuming $\phi(e)_{NaCl}=0.46$).

Quantum Yield of Photoionisation.

Oligodeoxynucleotide	Quantum Yield of Electrons
Adenine/Guanine	0.059
Thymine/Adenine	0.041
Cytosine/Adenine	0.041

The theoretical yield of radical cations of purines:pyrimidines is of the order of one:one when the less easily oxidised nucleic acid base neighbours a purine nucleic acid base. The transient spectrum for the single stranded polydeoxynucleotide composed of adenine/guanine composition is shown in figure 1. In this instance the guanine is expected to be more readily oxidised component, and therefore the oligodeoxynucleotide was prepared with the adenine composition greater than the guanine component. The primary percentage of guanine radical cations is estimated to be 64%[6]. Electron transfer, if it takes place, will result in the transient optical spectrum of the guanine radical cation, or its deprotonated state. This spectrum obtained is similar to that for the deprotonated guanine radical cation.[4,7] The transfer of an electron occurs within times less than a few microsec.

Figure 1. Absorption spectrum recorded after 193nm irradiation of an oxygen saturated aqueous solution of the adenine/guanine oligodeoxynucleotide.

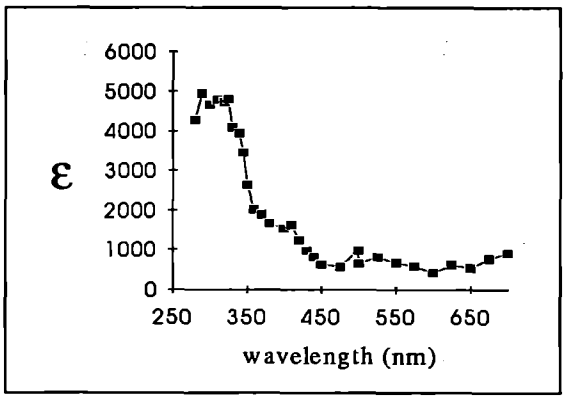

Therefore, transfer of charge occurs from adenine to guanine in this oligodeoxynucleotide. The positive hole is located ultimately on the more readily ionised purine.

DOES INTER AND INTRA STRAND ELECTRON TRANFER OCCUR IN DOUBLE STRANDED POLYDEOXYNUCLEOTIDES?

Laser flash photolysis experiments with 193nm irradiation were performed using a series of polydeoxyribonucleotides to assess whether electron migration from the most easily oxidised base occurs in double and single stranded polynucleotides and polydeoxynucleotides in aqueous solutions. The migration of the oxidative damage could theoretically occur via both *inter* and *intra*-strand processes and experiments were designed to assess this. An *inter* strand electron transfer process is a transfer of an electron from a more easily oxidised nucleic acid base to a radical cation that is located on a PAIRED strand. Intra strand electron transfer is the transfer of an electron from a more easily oxidised nucleic acid base to a radical cation that is located on the SAME strand. (shown schematically in figure 2)

Figure 2 Showing the types of electron transfer (oxidative damage) using a schematic representation of double stranded DNA

Inter strand electron transfer		Intra strand electron transfer	
X---Y	X---Y	X---Y	X---Y
$Y^{+\cdot}$---X→	Y---$X^{+\cdot}$	$Y^{+\cdot}$---X→	Y---X
X---Y	X---Y	X---Y	$X^{+\cdot}$---Y
Y---X	Y---X	Y---X	Y---X

X=more easily oxidised nucleic acid base, Y=less easily oxidised nucleic acid base

The mixed polynucleotides that were studied contained the bases guanine/cytosine (polyG.polyC, polydG.polydC, polydGdC.polydGdC) and adenine/thymine (polydA.polydT, polydAdT.polydAdT). A proportion of the photo ionisation event is expected to occur on both of the nucleic acid base sites. Electron transfer from the purine to the pyrimidine radical cation, if it occurs, must compete with the decay processes, usually deprotonation or reaction with water, of the pyrimidine radical cation species.

These transient laser flash photolysis experiments were restricted to the assessment of the photo ionisation damage in the microsecond time range following reaction of e^- with oxygen. Determination of the rate of electron transfer was not attempted at this point. The purine radicals have very distinctive UV spectral features and the comparison of the spectra that were obtained for each of the polydeoxynucleotides allowed us to determine whether electron transfer had taken place or not. Our results indicate that only *intra*-strand charge migration occurs effectively to the purines leading to hole stabilisation at this site. Unexpectedly our data reveals further information about the fate of the radical species formed whereby the pyrimidine, thymine, interferes with the *intra*-strand migration of charge complication the situation compared to cytosine. This requires more detailed studies to assess the involvement of irreversible pathways leading to thymine damage. The interaction with neighbouring base species within the polydeoxynucleotide strand may play a role. For polymers where only interstrand migration can occur figures 3a & b, where for polydG.polydC two different spectral components were identified, a longer lived species, with a spectral maximum at 310nm (open diamonds), due to the guanine radical, and a second shorter lived species with a maximum at 350nm, which is most likely due to a product of the cytosine radical cation. Convertion of the shorter lived species to the longer lived one within this time scale does not appear to occur.

Figure 3a Absorption spectra obtained after 193nm irradiation of an oxygen saturated solution of Poly dG.Poly dC at (i) filled squares ~ 40μs, (ii) open squares = 75μs, (iii) filled diamonds = 150μs and (iv) open diamonds = 350μs.

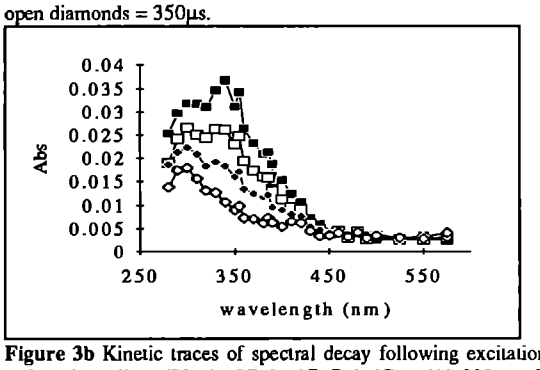

Figure 3b Kinetic traces of spectral decay following excitation with 193nm laser light (20ns) of Poly dG. PolydC at (A) 300nm, 350nm and 450nm.

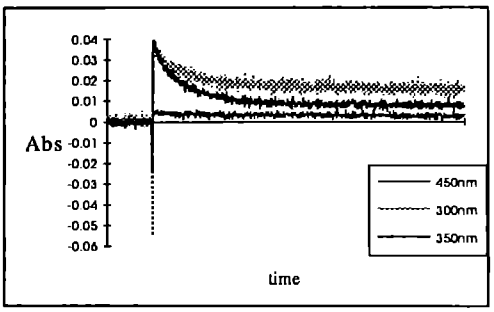

In conclusion, the transfer of charge occurs predominantly via an intra strand migration. With the purines, electron transfer occurs from guanine to the adenine radical with localisation of the damage at guanine. If the strand contains pyrimidine bases, the situation becomes more complicated as thymine interfers with intra strand transfer.

EPR SPECTROSCOPY TO CHARACTERISE THE PRODUCT RADICALS OF PHOTOIONISATION

EPR spectroscopy was used to characterise the electron loss radicals generated by photo-ionisation of DNA and its constituents. EPR spectral evidence for a number of radical products, that had been previously predicted to be formed from the radical cation of thymidine, was obtained .[8] For thymine, electron loss results in the normal Π -radical cation but this rapidly undergoes proton loss, probably from the N^1-H group. The EPR spectrum is well defined and characteristic of this radical. This species was detected in perchlorate matrices and there was no evidence of electron capture by thymine. However in pure aqueous systems, $TH^{\cdot}$ radicals, possibly formed by electron capture followed by protonation, were detected. In contrast, for N^1 substituted species such as TMP, the Π -radical cations were not detected by EPR spectroscopy. Instead there were comparable yields of $TCH_2^{\cdot}$ radicals in which one of the methyl radicals had been lost. These give rise to a characteristic quartet splitting from hyperfine coupling to the $-CH_2$- proton, together with the C^6H- proton which gives about the same splitting. Only in the case of alkaline perchlorate glasses, when the N^3-H proton is removed, was the electron lost from the Π system to give the neutral Π radical. The ribonucleosides of cytosine and uracil were found to give rise to sugar radicals but not base radicals, presumably from a hydrogen shift. Tentative assignment of the radicals of the purine and pyrimidine products has been made

PRELIMINARY EXPERIMENTS TO DETERMINE THE SITE OF STRAND BREAKAGE CAUSED BY PHOTOIONISATION

A number of preliminary strand breakage studies on double stranded oligodeoxyribonucleotides at room temperature using 193nm light were performed. These indicate contrary to earlier reports[9], that there is insignificant prompt strand breakage. However sugar damage leading to latent strand breakage does occur on treatment of the photolysed DNA sample with hot piperidine, an indication of base damage being converted to a strand break. The important question relates to whether charge migration occurs from guanine and if damage at this purine site leads ultimately to a strand breakage at this site by a 'prompt' mechanism.

REFERENCES

1.D. Goodhead, *Can.J.Phys.*, 1990, **68**, 872-886.

2.P.Cullis,M.R.C.Symons,*Radiat.Phys.Chem.*,1986,**27**, 93-100.

3.W.A. Bernhard,*J.Phys.Chem.*, 1989, **93**, 2187-2194.

4.P. Wolf, G.D.D. Jones, L.P. Candeias, P. O'Neill, *Int. J. Rad. Biol.*,1993,**62**,1-11.

5.E.Bothe,H.Goemer,J.Opitz,D. Schulte-Frohlinde,A. Siddiqui, M.Wala, *Photochem. Photobiol.*,1990, **52**, 949-959.

6. S.Botchway, P.O'Neill, A.W. Parker, M.C.R. Symons, SERC Central Laser Facility Annual Report 1992.

7. Calculated using data obtained by L.P. Candeias, S. Steenken, *J.Am.Chem.Soc.*,**114**, 699, 1992.

8. M.E.Malone,M.C.R.Symons, A.W.Parker, *J.Chem.Soc. Perkin Trans 2*, 1993, 2067- 2075.

9. D.T. Croke, W. Blau, C. OhUigin,J.M. Kelly, D.J. McConnell, *Photochem.Photobiol.*,1988,**47**,527-536.

ATTEMPTS TO MUTATE SCRAPIE AGENT: A BIOLOGICAL APPROACH TO MOLECULAR IDENTITY?

H Fraser[1] and A W Parker[2]

[1]AFRC & MRC Neutopathogenesis Unit, Institute for Animal Health, Edinburgh
[2]Rutherford Appleton Laboratory

INTRODUCTION

The chemical identity of the scrapie agent is unknown. Some of its biological properties are consistent with an agent containing conventional genomic information. For instance there are many stains of the causal agent, and strain-characteristic properties are not host-directed. Wild-type scrapie strains can mutate when infection is passed within or between species. The wild-type 87A- strain of scrapie has been isolated frequently by transmissions to C57BL mice from the brains of sheep with naturally occurring scrapie. In the same transmissions, another strain, 87V, has consistently been isolated in VM mice; 87A and 87V are probably mutants, arising and selected in the mice infected with a field strain of scrapie in these sheep. When 87A is sub-passaged at high infective dose in C57BL mice, spontaneous mutation to the ME7-strain is common, and 87A can only be maintained by sub-passage at low dose or limiting dilution. The ratio of 87A:ME7 in some samples of 87A infected mouse brain is approximately $1:10^4$, and the mutation rate is likely to be lower[1] than this because ME7 has a faster replication rate than 87A, thus, in C57BL mice, ME7 has survival advantage over 87A.

Mutations in conventional biology arise when survival advantage is gained following chemical modification of nucleic acid genome. The chemical modification can occur spontaneously or be induced with physical or chemical mutagens. Such mutation can be induced in DNA with UV or ionising radiation, and the conditions for obtaining conventional mutations, such as in DNA, are well defined. It was proposed that, if the frequency of mutation could, or not, be altered in 87A-scrapie agent, using conditions used in conventional mutagenesis, this would provide evidence for or against a nucleic acid genome in the scrapie agent. The strains are easily distinguished from one another on the basis of incubation period and neutopathology in C57BL mice; 87A produces a dose-dependent incubation period after intracerbral injection of 350-600 days, with ME7 this is 150-300 days.

We report here our initial attempt to induce mutation in 87A agent by exposing a crude brain homogenate, or PrP protein from this homogenate, prepared from six terminally-affected 87A-infected C57BL mice. Bioassay of the samples revealed that the level of ME7-agent was very high, such that no 87A-agent was detectable even in the unexposed samples. Thus our original objective was unobtainable. However, there was no loss of the residual ME7-infectivity in any of the samples, even in those exposed to ~200,000 J/m^2 laser UV at a wavelength of 248 nm (5 Hz and 100 Hz). (Tables 1 and 2).

Table1. Incubation periods (days, mean ± standard error) of C57BL Mice Injected Intracerebrally with ME7-Scrapie Brain Homogenate Exposed to Laser UV.

Wavelength (nm)	351		248		Un-Exposed
Dose (J/m^2)	217728 (100 Hz)	16125 (5 Hz)	193536 (5 Hz)	193536 (100 Hz)	
	184±3	191±3	197±3	189±2	188±4

Table 2. Details as for Table 1. Mice injected with PrP preparations from brain homogenates.

Wavelength (nm)	351		248		Un-Exposed
Dose (J/m^2)	217728 (100 Hz)	16125 (5 Hz)	193536 (5 Hz)	193536 (100 Hz)	
	215±6**	248±6	236±6	227±4*	249±6

**p,0.001
*p,0.01
two-tailed t-test

CONCLUSION

The failure to produce any apparent loss of biological activity with exposure of ME7 scrapie agent to these very high doses of irradiation is difficult to interpret in molecular terms. It is certainly significant that 248 nm irradiation which is known to damage DNA and proteins did not affect infectivity. There is the remote possibility of some unrecognised molecular repair mechanism in neurons which are post-mitotic, operating over the long intervals offered by the scrapie incubation period measured in hundreds of days, compared with a more usual biological generation times in mammalian cells, bacteria, viruses or 'phage, of a few hours or days. The significance of the shortened incubation periods in mice injected with irradiated PrP protein cannot be assessed without further work.

REFERENCE

1. M E Bruce and A G Dickinson
J Gen Virol, 68, 79, (1981).

STUDIES OF DAMAGE TO PLASMID DNA USING 248 nm LASER PULSES

K.M. Prise[1], B.D. Michael[1], R.A. Meldrum[2] and C.W. Wharton[2]

[1]CRC Gray Laboratory, PO Box 100, Mount Vernon Hospital, Northwood, Middlesex, HA6 2JR, UK.
[2]School of Biochemistry, University of Birmingham, Birmingham B15 2TT, U.K.

INTRODUCTION

Pulsed laser sources in the UV and soft X-ray regions can be used to probe the mechanisms of DNA damage induction. We have carried out a preliminary study with the 248 nm krypton fluoride laser and pBR322 plasmid DNA. Using gel electrophoresis, induced damages such as single- and double-strand breaks (ssb, dsb), conformational alterations and plasmid-plasmid crosslinks can be readily assayed. Plasmids can be exposed in aqueous solution or under dry, evacuated conditions, allowing the damage-modifying influence of water to be examined. By varying intensity, the contribution of biphotonic processes can be determined. This provides a ready means of investigating excitation levels that cannot be easily induced monophotonically using other lower intensity sources because of absorption and penetration problems.

RESULTS

Data from initial experiments are shown in Figures 1 and 2. Induction of ssb results in loss of the supercoiled form of the plasmid (Figure 1) and comparison of curves A and B shows that for plasmids irradiated in suspension the responsiveness increases with intensity, indicating a biphotonic contribution. Dry plasmids, irradiated under vacuum, show a further increase in responsiveness which indicates that water has a substantial protective action. Induction of dsb produces the linear form (Figure 2) and the effects of intensity and of water are broadly similar to those found for ssb induction. For dsb, however, there appears to be a predominantly quadratic dependence on dose when the plasmids are irradiated in suspension, indicating that pairs of separate events (ssb) may be required to form a dsb.

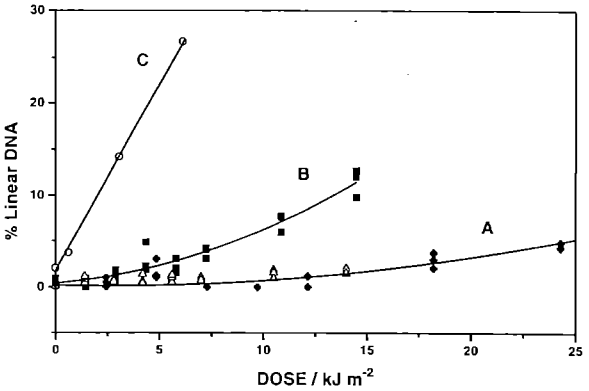

Figure 2. Induction of double-strand breaks in pBR322 plasmid DNA. Curves A and B in aqueous suspension, curve C under dry evacuated conditions. Intensities during pulse: ■ 724; △ 70; ♦ 12; ○ 615 J m^{-2}.

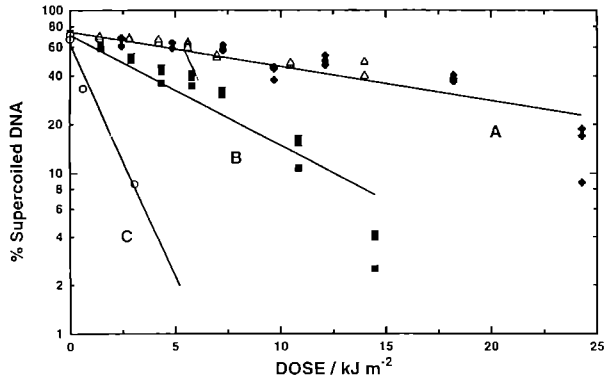

Figure 1. Induction of single-strand breaks in pBR322 plasmid DNA. Curves A and B in aqueous suspension, curve C under dry evacuated conditions. Intensities during pulse: ■ 724; ▵ 70; ♦ 12; ○ 615 J m^{-2}.

KINETIC STUDIES OF THE REPAIR OF 248 nm UV LASER-INDUCED DNA DAMAGE IN MAMMALIAN CELLS

R Meldrum, W Meaking, S Ward and C Wharton

School of Biochemistry, Univeristy of Birmingham, Edgbaston, Birmingham B15 2TT, England

INTRODUCTION

In previous reports we have described how a 'panic' synthesis of DNA of apparently low fidelity follows shortly after 248 nm UV laser damage to cellular DNA. The low fidelity 'bad' DNA exists only transiently and is rapidly degraded to make way for the synthesis of high fidelity DNA; this step represents 'correct' repair. We have been able to simulate experimental observations using the kinetic scheme shown in Fig.1. This scheme incorporates an incision step at which the DNA is cut immediately adjacent to the site of damage, assumed to be a thymidine dimer or a 6:4 photoadduct. More recent evidence from alkaline elution studies reported last year indicate that the repair we have observed is related to biphotonically induced direct single strand breaks in the DNA. The kinetic model is quite insensitive to the inclusion of this incision step, since it is characterised by the same rate constant as the subsequent 'bad' DNA polymerisation step. Thus it is apparent that kinetic modelling cannot help us to make the decision as to whether direct breaks are the objects that are targeted by the repair apparatus at early times after damage by UV laser pulses. The alkaline elution experiments have shown that the repair response is correlated with the induction of direct breaks but the repair of a small subset of the forms of damage induced at low intensities (and at high intensities in large numbers) cannot be ruled out. This report details some further experiments that have been directed to establishing the nature of the UV laser induced panic response.

RESULTS AND DISCUSSION.

In the 1993 Annual Report we described some preliminary modelling studies which have now been used to make predictions concerning the rates at which the various components of the system are released as the repair process takes place.

Fig. 1 shows predictions for the release of pyrophosphate and nucleotide monophosphate during the course of repair. The pyrophosphate [PPi] arises on the transformation of (di)deoxynucleotide triphosphate [(d)dNTP] to (di)deoxy-nucleotide monophosphate [(d)dNMP] as a result of polymerisation to form part of the DNA chain. If the (d)dNTP is labelled with ^{32}P in the α position this is retained in the DNA and not lost in the PPi (see Fig. 1). The (d)dNMP is subsequently released when 'bad' DNA is degraded to allow synthesis of the final high fidelity DNA. It is seen that a distinct lag phase is predicted in the release of the (d)dNMP as compared with the release of the PPi. Shown in Fig. 1 are experimental points for the determination of the the ^{32}P retained in the DNA and the ^{32}P-ddAMP released as the 'bad' DNA is broken down.

The analysis of the ^{32}P in DNA has previously been described. The ^{32}PddAMP was isolated by using HPLC. Standards of unlabelled tri-, di- and monophosphates were run on the HPLC, being detected by absorption at 260 nm, and the radioactivity that coincided with the species to be analysed was collected and counted. It is clear that the experimental points, which were taken from a single experiment, broadly follow the predictions and this provides strong support for the validity of the model.

The data shown refer to repair events trapped and labelled by ddATP which is a chain termination inhibitor. A similar experiment which employed dTTP (a natural component of DNA) gave essentially the same results and so again supports our contention that the transiently synthesised DNA is of low fidelity. The 'natural' nucleotide would not be excised if it were paired with the correct base.

It is notable over a large number of experiments that the excision phase is of a similar magnitude when measured using either ddATP or dTTP. Since ddATP is a chain termination inhibitor only a single molecule can be incorporated at any one repair site, although several unlabelled bases could be incorporated prior to this until a thymidine residue (which requires dA or ddA as a partner) is reached in the template strand. This implies that only a single dTTP molecule is incorporated and that the patches of low fidelity DNA in each case are of similar length.

The above findings may be explained in two possible ways. The low fidelity DNA is synthesised by a polymerase that does not have an operational exonuclease (the error checking enzyme often carried by the polymerase that excises incorrectly paired bases to ensure fidelity). After ca. 30 seconds the polymerase recruits an exonuclease and starts 'editing' the DNA. This recruitment may be a specific response to damage but the low fidelity synthesis is likely to have an evolutionary value in maintaining strand continuity and hence the reading frame of the DNA during a period of heavy damage.

The alternative, less likely explanation, involves an effect on replication polymerisation, which is active in HL60 cells used for most experiments. Here the polymerase may encounter damage and stall. In order to allow access of the repair system the polymerase would have to 'back off' the damage site and reverse the last part of the chain just synthesised; the exonucleases achieve this. This latter explanation is regarded as less likely since as reported last year we have observed the panic response in contact-inhibited V-79 cells that are not replicating.

The transient incorporation of ddAMP into low fidelity DNA and its subsequent excision

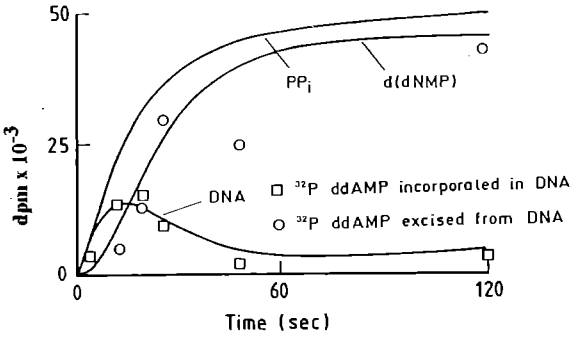

$$\text{Damaged DNA} \xrightarrow{10s^{-1}} \text{Incised DNA} \xrightarrow{10s^{-1}} \text{'Bad' DNA + PPi}$$

$$\text{'Bad' DNA} \xrightarrow{15s^{-1}} \text{Excised DNA + d(dNMP)}$$

$$\text{Excised DNA + d(dNTP)} \xrightarrow{0.02s^{-1}} \text{'Good' DNA + PPi}$$

References:

C W Wharton, R A Meldrum, C Reason, J Boone and W Lester (1993) An Automated programmable apparatus for studies of fast events in DNA repair. Biochem. J. 293,825-828.

R A Meldrum, W Meaking and C W Wharton (1994) Kinetics & mechanism of the repair of UV damage in mammalian cells. Nucleic Acids Research in press.

THE NATURE OF SOFT X-RAY DAMAGE TO MAMMALIAN CELLULAR DNA AND ITS REPAIR

R Meldrum, I C E Turcu*, A R Damerell*, S Ward and C Wharton

School of Biochemistry, Univeristy of Birmingham, Edgbaston, Birmingham B15 2TT, England
*Rutherford Appleton Laboratory, Chilton, Didcot, OXON, OX11 0QX, England

INTRODUCTION

In last years report we described some preliminary experiments which used the alkaline elution method to detect DNA strand breakage as a result of soft X-ray irradiation. This work has now been extended somewhat and the results have been quantified. Further progress has been made in defining the effect of varying the dose of soft X-rays on the induction of the 'panic' response.

RESULTS AND DISCUSSION

Fig. 1 shows the relationship between the strand scission factor (SSF) and the dose of X-rays.

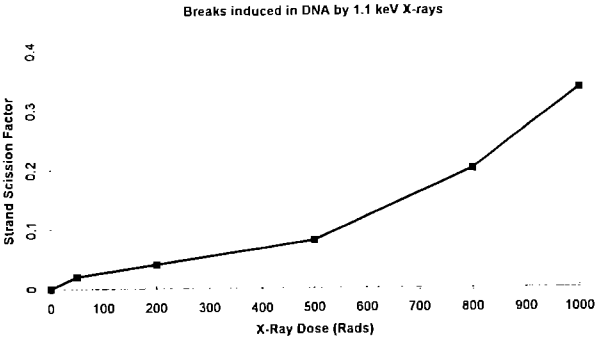

The SSF is directly related to the number of breaks induced in the DNA and indicates that some 3600 breaks are formed at 1000 rads. It is notable that the number of breaks appears to be proportional to greater than the first power of the dose. This is suggestive of biphotonic behaviour but may also arise from a changing ratio of single to double strand breaks as the dose is increased. It has been noted that low energy X-rays are more efficient in killing cells than are high energy γ-ray photons. It has been proposed that this arises because the photons are arrested and cause ionisations in a more restricted area (5-10 nm) as compared with high energy rays, where the ionisations are clustered along tracks. The effect may be linked to damage being concentrated within a nucleosome which is ca. 10 nm in diameter and may lead to unrepairable damage.

In parallel with the alkaline elution experiments we have made further efforts to characterise the kinetics of the repair of breaks induced in cellular DNA by soft X-rays. We have examined the effects of various doses of soft X-rays on the nature of the 'panic' response which is provoked. This has been done using several different reagents to trap and label breaks transiently induced in the DNA. Fig. 2 shows such a result when ^{3}H-thymidine, which requires no electroporation to enter cells is used.

Fig.2. 3H-thymidine uptake. circles 250 rads,squares 1000 rads,triangles control.

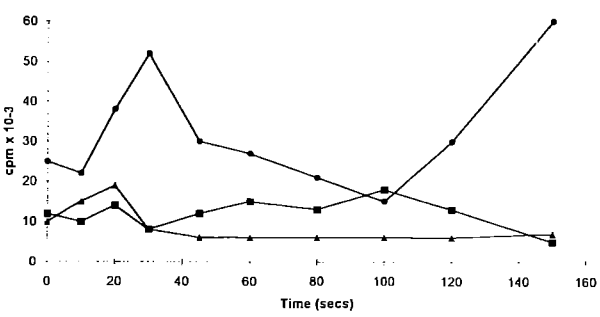

A strong response is induced at 250 rads but this is inhibited at 500 rads.

When 32P-ddATP is used as the trapping agent a different response is seen (Fig. 3). Here a fast transient (max. at 10 secs) is induced at 500 rads while 1000 rads induces a later transient (max. at 25 secs). Notably 250 rads induces no transient.

Fig. 3. 32P-ddATP uptake. Triangles 250 rads, circles 500 rads,squares 1000 rads.

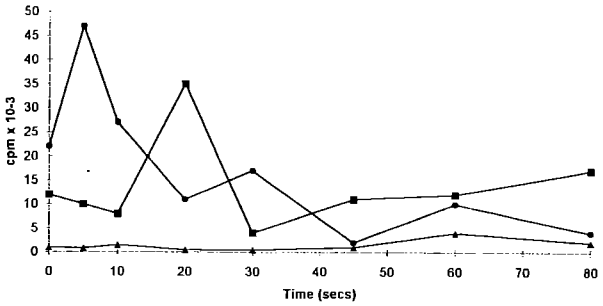

This behaviour may be the result of an electroporation-induced desensitisation towards repair of radiation damage. This effect has been observed in less detail previously. In some experiments a dual transient is seen. At present we have no explanation for this but suspect it may be related to the state of the cells as these experiments are very sensitive to the 'health' of the cell monolayers. Any 'curling up' of the cells will remove them from the region where they will absorb the expected X-ray dose. Several of our experiments have been adversely affected by this and show apparent extreme radiation resistance of the cells. For quantitative purposes it is clear that only experiments done on cells grown together as a batch of dishes can be compared in detail.

Fig. 4 shows the results of an experiment in which pyrophosphate (PPi) has been included in the assay. Incorporation of deoxynucleotide triphosphates into DNA gives PPi as a product and so this would be expected to inhibit the polymerisation phase of the repair process. PPi indeed appears to be a potent inhibitor.

Fig. 4. Pyrophosphate Inhibition of 32P-TTP uptake. Circles minus PPi, Squares plus 0.5 mM PPi. 250 rads X-rays.

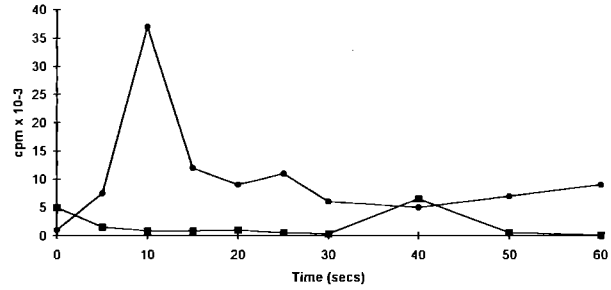

One of the main aims of future work will be to demonstrate that the 'panic' response to X-rays follows the same mechanism that we have proposed for the repair of UV laser induced damage.

TIME RESOLVED FLUORESCENCE MEASUREMENTS OF FIREFLY LUCIFERIN

R S Chittock[1], N S Parkinson[2], D G Lidzey[2], N Berovic[2], M Towrie[3], P Matousek[3], C W Wharton[1], J B Jackson[1], T D Beynon[2]
*S Szatmari,

[1]School of Biochemistry, University of Birmingham, Edgbaston, Birmingham B15 2TT
[2]School of Physics and Space Research, University of Birmingham, Edgbaston, Birmingham B15 2TT
[3]Rutherford Appleton Laboratory, Chilton, Didcot, OXON, OX11 0QX

Introduction

The heterocyclic compound luciferin (I) is one of the substrates used by the enzyme luciferase to produce light. During the course of the reaction with the other substrates ATP and O_2 the luciferin is converted to an excited state of the product oxyluciferin (II).

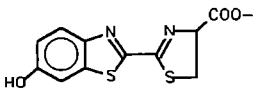

IA

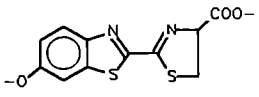

IB

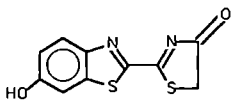

II

Bioluminescence occurs when this product returns to the ground state by emitting a photon (λ_{max} = 560 nm). An understanding of the electronic states of luciferin will be necessary to describe luminescence.

The steady state fluorescence spectrum of luciferin has been described by Morton *et al* (1969).

Figure 1. Proposed Electronic States of Luciferin

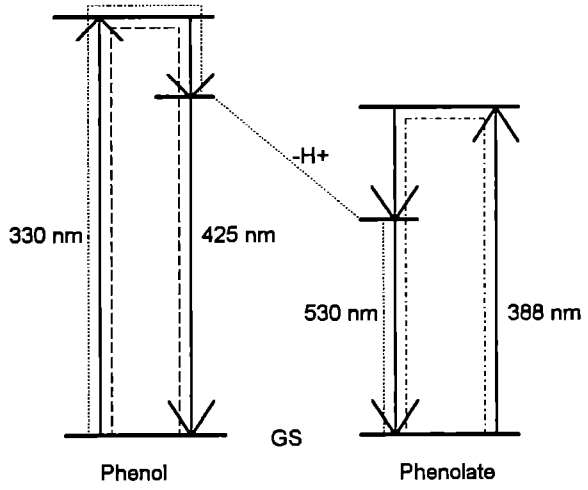

Since luciferin can exist in either phenol (IA) or phenolate (IB) forms both absorbance and excitation fluorescence spectra are pH dependent (pK=8.6). However the emission fluorescence spectra of both forms are identical. Morton explained this by proposing the model shown in Fig.1, in which the transition from the phenol excited state to the ground state is forbidden so fluorescence only occurs when the molecule looses a proton to form the phenolate form.

Additional evidence for the model is that in organic solvents, where proton loss cannot occur, low quantum yield fluorescence with λ_{max} = 425 nm is observed. Also the fluorescence quantum yield of the phenol form is less than that of the phenolate form suggesting the phenol excited state is long lived than that of the phenolate.

This model makes several predictions of luciferin fluorescent lifetimes.

① Fluorescence lifetime of the phenolate form should be limited by the k_{off} rate constant of phenol → phenolate conversion. Assuming the k_{on} rate constant is diffusion limited and given the pK of 8.6, the fluorescence lifetime of the phenol form should be in the range 1-10 ns.

② In D_2O the leaving moiety of the phenol → phenolate transition will be a deuteron rather than a proton, so the observed fluorescence lifetime should increase by a factor of 2.5.

③ In an organic solvent such as ethanol proton loss to form the phenolate form cannot occur so the phenol form is forced to return to the ground state by the 'forbidden' blue emission. This fluorescent lifetime should be slow relative to that observed in acidic aqueous solution.

④ Under alkaline conditions luciferin exists as the phenolate form, so no proton loss will be involved in the fluorescence. The fluorescence lifetime should be fast relative to that in acid aqueous conditions and unaffected by D_2O.

This report describes the use of the LSF time-resolved single photon counting apparatus to measure the fluorescent lifetimes of luciferin under a variety of conditions. To date a single week's feasibility study has been performed. We hope to extend the work to the true luminophore oxyluciferin in future visits.

Effect of Solvent

The effect of solvent on the fluorescent lifetime of luciferase is summarised in Table 1 and Fig. 2. All lifetimes were measured at the peak emission wavelength using 305 nm excitation wavelength. The

system was cross-calibrated using the standard dyes anthracene and coumarin 307 which both produced the expected single exponential decay curves. For biexponential lifetimes, the relative amount of the fast component is measured using the factor F_{fast}, the fraction of the fast component in the fluorescence decay.

Table 1 Effect of Solvent on Luciferin Fluorescence Lifetimes

Solvent	τ_1(ns)	τ_2(ns)	F_{fast}	λ_{max}(nm)
A D_2O pD 10	5.97	-	-	532
B H_2O pH 10	4.95	-	-	532
C D_2O pD 4	5.76	0.85	0.06	532
D H_2O pH 4	4.72	0.52	0.05	532
E Ethanol	2.46	0.34	0.10	426

Figure 2. Effect of Solvent on Luciferin Fluorescence Lifetime.
Fluorescence is normalised to peak height.
A=D_2O, pD 10; B=H_2O, pH 10; C=D_2O, pD 4; D=H_2O, pH 4; E=Ethanol

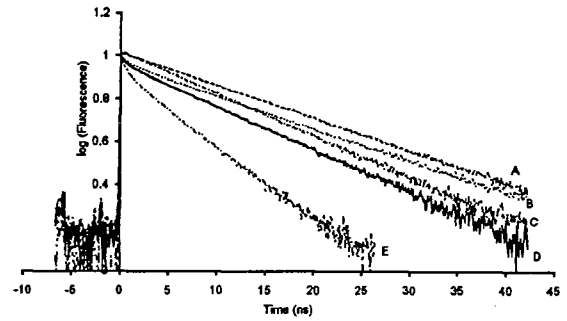

As predicted by the Morton model, luciferin at pH 4 in aqueous solution had a fluorescent lifetime of 4.7 ns. There was also a minor fast component. In D_2O at pD 4 the major component is slower, but not by the predicted factor of 2.5.

At pH 10 in H_2O the fluorescence decay was a single exponential but the lifetime was significantly longer than at pH 4, while the model predicts a much shorter decay. In D_2O at pD10 a single exponential was also observed but with a longer lifetime than in H_2O. The model predicts that lifetimes should be identical in D_2O and H_2O under alkaline conditions.

In ethanol the model predicts that the fluorescence lifetime should be much longer than aqueous solution at pH 4. In fact the observed lifetime was faster than aqueous solution and a biexponential.

Effect of Wavelength

The relation between emission wavelength and fluorescence decay for luciferin in aqueous solution at pH 4 is summarised in table 2 and Fig.3.

At all wavelengths the decay was a biexponential with an identical slow component within experimental error but the fast component increased from 0.104 ns to 0.645 ns as emission wavelength increased from 470 nm to 570 nm.

Table 2. The Effect of Emission Wavelength on Luciferin Fluorescent Lifetimes

λ_E(nm)	τ_1(ns)	τ_2(ns)	F_{fast}
426	3.90	0.087	0.99
440	5.25	0.342	0.59
460	4.91	0.092	0.62
470	4.84	0.104	0.36
480	4.70	0.133	0.14
490	4.71	0.170	0.09
510	4.87	0.620	0.08
530	4.85	0.725	0.07
532	4.86	0.783	0.07
550	4.82	0.684	0.07
570	4.82	0.645	0.08

Figure 3 Relation between Emission Wavelength and Fluorescence Lifetime. Fluorescence is normalised to peak height. A=532nm; B=510nm; C=480nm; D=460nm.

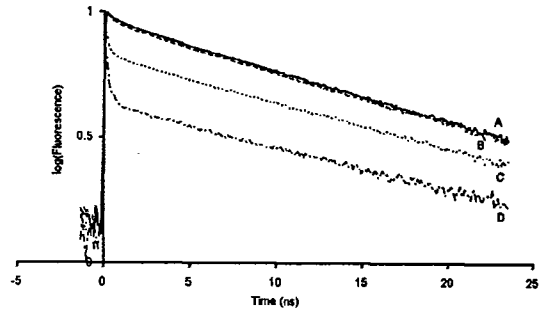

Conclusions

These results show several deviations from the predictions of Morton's model.

① Fluorescence lifetimes are longer in D_2O than H_2O under both acid and alkaline conditions.

② Fluorescence lifetime is shorter in ethanol than in aqueous solution.

③ The fluorescence decay under aqueous acidic conditions is a biexponential. The proportion of the fast component is function of emission wavelength.

These discrepancies suggest that more electronic states participate in luciferin fluorescence than suggested by Morton's model. It is probable that one or more of the crossovers between these states is slower than the rate of proton loss from the excited state of the phenol form. We shall investigate this further in future visits to the Facility.

References

R.A. Morton *et al* Biochemistry **8** 1598-1607 (1969)

INDUCED ABSORPTION CHARACTERISATION OF INFRARED SENSITIVE PHOTOREFRACTIVE $BaTiO_3$.

Robert W Eason and Graeme W Ross

Department of Physics and Optoelectronics Research Centre,
Southampton University

INTRODUCTION

Photorefractive materials such as $BaTiO_3$, have been extensively researched over the last fifteen years, and have shown themselves to be very efficient for generation of novel self-pumped and mutually pumped phase conjugate geometries. So far, most attention has been focussed on the visible spectral region, where the efficiency has tended to be highest, and the speed of response fastest. More recently however, interest has turned towards the near-infrared spectral region, due to the increasing availability and technological importance of very efficient solid-state laser diode sources operating at the ~800nm region. Such infrared active $BaTiO_3$ crystals have been supplied for our use by Sandoz Huningue, and we have been investigating their unique properties for self-pumping, mutual pumping and two-beam coupling[1]. The question of why these crystals, which are deep blue in colour, behave so well at these longer wavelengths is still open for discussion, but it undoubtedly involves their multiple dopant, many level impurity states which in turn involve both deep and shallow traps[2].

We have characterised their behaviour therefore using simultaneous excitation from two different wavelength laser sources: a He-Ne, and a tunable Ti:sapphire, operating at ~800nm to simulate typical diode laser operation. This characterisation, together with a two-level model developed at Imperial College London, has allowed us to evaluate the relevant material parameters for these blue crystals, thus generating feedback for the crystal growers who seek to improve the material response out to beyond 1μm.

EXPERIMENTAL WORK

The first experiments to test photoinduced absorption involved measuring the transmission of o-polarised He-Ne light as a function of the laser intensity. Figure 1 shows a plot of the maximum change in the absorption coefficient as a function of the log. of the incident intensity. The upper intensity limit was restricted by the maximum He-Ne power available, and powers less than 10μW proved extremely hard to measure reliably. The form of the graph resembles a saturable absorption characteristic, implying two absorption levels with different cross-sections. The solid line is the best fit obtained using a numerical simulation of the shallow trap model. The parameters used for the fitting are listed in table 1.

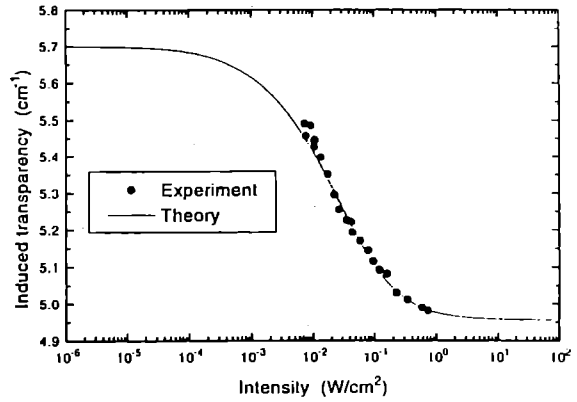

Figure 1. Induced transparency in blue $BaTiO_3$, as a function of incident He-Ne laser intensity.

	Deep traps	Shallow traps
Total density of species	$N_D=N+N^*=1\times10^{18}cm^{-3}$	$M_T=M+M^*=1.3\times10^{18}cm^{-3}$
Effective trap density	$N_{t(eff)}=N_D-N_a$ $=N_D/50=2\times10^{16}cm^{-3}$	$M_{t(eff)}=M_T$
Photoexcitation coefficient at λ_R = 633nm (red)	$s_R=17.8cm^2J^{-1}$	$s_{sR}=5.9cm^2J^{-1}$
Photoexcitation coefficient at λ_{IR} = 800nm (infrared)	$s_{IR}=5.2cm^2J^{-1}$	$s_{sIR}=7cm^2J^{-1}$
Recombination rate	$\gamma=5\times10^{-8}cm^3s^{-1}$	$\gamma_s=1.2\times10^{-8}cm^3s^{-1}$
Thermal excitation rate	$\beta=4\times10^{-5}s^{-1}$	$\beta_s=0.4s^{-1}$

Table 1. Materials parameters used in fit to experimental data.

Additionally, light induced absorption has also been observed as well as the light induced transparency of figure 1. The crystal was first exposed to a 1mm diameter, 6.7mW o-polarised He-Ne beam, whose intensity was held constant throughout the experiment, at a point near the saturation limit of figure 1. The He-Ne transmission was then monitored as a function of the intensity of a second, near infra-red beam from the Ti:sapphire laser, which was also o-polarised to minimise photorefractive grating effects. As seen in figure 2, an increase in the absorption experienced by the He-Ne beam of up to 0.2 cm^{-1} is observed when the crystal is simultaneously exposed to both laser wavelengths. Although the 800nm light appears to have a slightly more significant effect than the 750nm light, this may not be true when one considers that the bulk absorption coefficient at 750nm is greater than for 800nm, hence more light is absorbed at 750nm before it overlaps spatially with the He-Ne laser beam. The solid curve again shows a theoretical fit, using the same parameter set in table 1.

Both light induced absorption and transparency were observed in the last experiment, which again used dual wavelength excitation. As previously, o-polarised light from both lasers was arranged to overlap within the crystal. For this arrangement, the intensity of the infra-red laser was held constant at 1.3 Wcm^{-2}, and the transmission of the He-Ne probe laser was monitored as a function of intensity. These results indicate the role of the excitation wavelength in exciting and filling the deep and

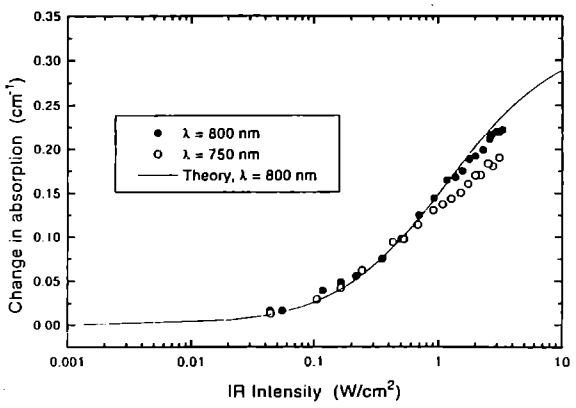

Figure 2. Light induced absorption at He-Ne wavelengths induced by simultaneous illumination with infra-red light at 750nm, and 800nm respectively.

shallow levels. Figure 3 shows that for intensities greater than ~0.02Wcm^{-2}, light induced absorption occurs, while for lower intensities, light induced transparency prevails. Once again the solid line is a theoretical fit based on the same common set of parameters listed in table 1.

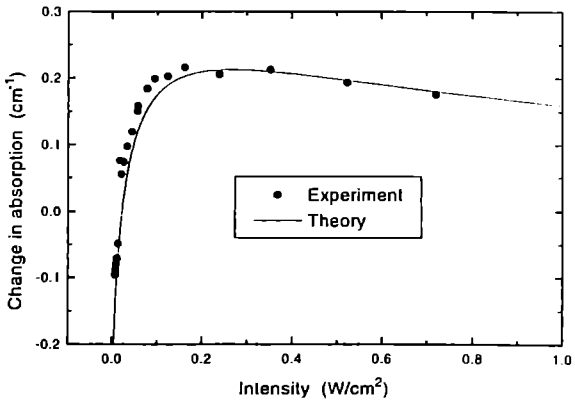

Figure 3. Light induced absorption and transparency at He-Ne wavelength, for a constant intensity incident infra-red intensity.

CONCLUSIONS

The simultaneous illumination technique used for this infra-red sensitive $BaTiO_3$ has allowed detailed modelling of the relevant materials parameters. It is clear that both deep and shallow traps are required to explain the absorption/transparency characteristics, and this in turn goes some way to explain the characteristic infra-red sensitivity of this crystal. No information can be extracted at this stage concerning the exact nature of the traps involved, and this would require a separate spectroscopic analysis. However, the important fact is that the dual wavelength technique allows parameters such as total trap density, and photoexcitation coefficient to be evaluated. Further work is in progress on evaluation of similar parameters in ion-beam implanted waveguides which have been grown in these crystals, where evidence shows a gain direction reversal has occurred.

ACKNOWLEDGEMENTS

Thanks to Mark Garrett and Daniel Rytz of Sandoz Huningue S.A., France, and to Mike Damzen, Reuben Ramos-Garcia and Roger Troth of Imperial College, London, for collaborative research efforts.

REFERENCES

1. P.Yeh, Proc.IEEE **80**, 436 (1992)
2. P.Tayebati and D.Mahgerefteh, J.Opt.Soc.Am.B **8**, 1053 (1991)

COMMISSIONING OF 3D LDA FOR UK COASTAL RESEARCH FACILITY AT HR WALLINGFORD

I Shepherd, L Smith and R Whitehouse

HR Wallingford Limited

INTRODUCTION

Laser Doppler Anemometry has been a very valuable research tool in hydraulics for many years. During the last 10 years fibre optic systems have evolved and become very popular for measurements in locations where access for conventional laser optics is difficult. This is especially relevant to experiments performed on the newly commissioned UK Coastal Research Facility where access to the measuring point through side windows, for example, is not practical and measurements require the use of an immersible probe. The basin which has a fixed bed moulded from mortar is being used to make measurements of the interaction between simulated wind waves and longshore coastal currents.

LASER SYSTEM

A 3 component LDA probe system using fibre optic transmission as shown in Figure 1 has been installed. This allows point measurements of the 3 components of the turbulent flow field to be made at a sampling rate of up to about 70 Hz. Considerable development of conventional LDA systems by the manufacturer and HR was involved in the instrument.

The requirement was for the smallest practical single point mounting three component underwater probe. The probe has a 6 beam optical system producing a single measuring point about 60 mm from the probe face, and in operation it is tilted at 45° to the horizontal. This maximises the sensitivity to all 3 components of flow and minimises the potential for interference from eddy shedding. This last point is particularly important because it is not always possible to predict the direction of the dominant flow.

The laser light, which is generated by a 5 watt Argon-Ion laser supplied by RAL, is transmitted from the control room along a 60 m fibre to the optics which are located at the end of a traversing bridge which allows the probe to be positioned accurately within the 20 m by 15 m working section of the basin. The system includes colour separation, frequency shift and transmission optics for the 20 m long polarisation preserving fibres to the probes. One probe produces 2 colour, 4 beam outputs and the other 1 colour 2 beam outputs. The beams are focused at the measuring point, and the scattered light from one probe is collected by the other. Validity of the data relies upon the sophisticated processor that establishes time coincidence between the three signals produced by the photomultipliers. Software computes the vector components of the flow from a knowledge of the geometry of the optical system and the probe orientation.

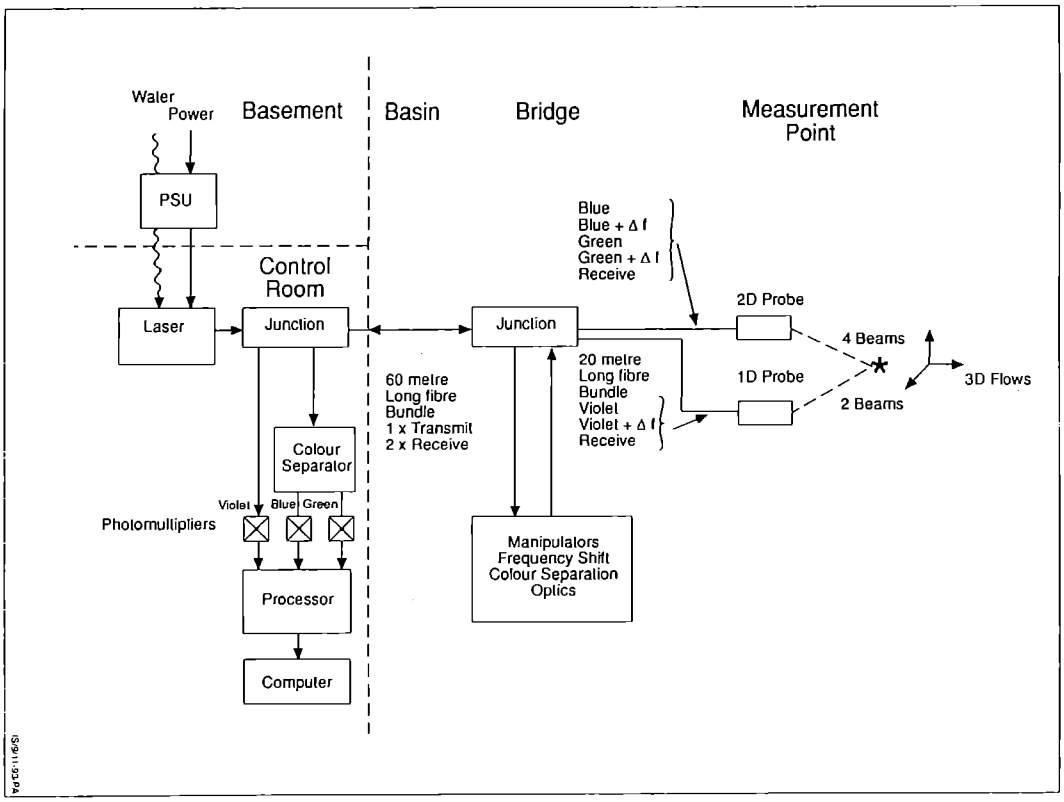

Figure 1 3D Laser Doppler Anemometer

X-RAY LITHOGRAPHY FOR 0.18 MICRON SILICON FET TECHNOLOGY

C M Reeves, I C E Turcu, P Lake, J T M Stevenson, A W S Ross, A M Gundlach, P Prewett, P Anastasi, B Cook and P Mitchell

Rutherford Appleton Laboratory, Chilton, Oxon OX11 0QX, England
University of Edinburgh, Mayfield Road, Edinburgh EH9 3JL, Scotland

INTRODUCTION

This article describes an experiment in which a KrF excimer based plasma X-ray source is used for 0. 18 micron X-ray lithography for silicon FET device fabrication. The experiment is based on a five way collaboration involving the Laser Support Facility, Edinburgh University, King's College London, Central Microstructure Facility (also at RAL) and Leica Cambridge Ltd. The development of 0.18 micron industrial lithography is of particular importance for future 1Gbit DRAM technology and its logic derivatives.

LITHOGRAPHY OPTIONS

There are several alternative industrial lithography options for future silicon FET manufacture at 0.18 micron dimensions. The most important of these options are optical, x-ray and e-beam techniques. The work presented here follows the X-ray lithography option based around a plasma X-ray source. This provides an interesting alternative to the electron storage ring X-ray approach which is being investigated by IBM.[1]

X-RAY SOURCE

For this X-ray lithography experiment, the KrF excimer based plasma X-ray source was configured as shown in Ref 2. A modelocked YAG laser is used to generate a 5psec pulse at a wavelength of 746nm and repetition rate of 5OHz. The pulse is passed through three XeF laser pumped dye amplifiers and then frequency tripled to 248nm. Next the pulse is temporally multiplexed to produce a train of eight pulses which are further amplified by two passes through a KrF amplier. The resulting output pulse train has an energy of l4OmJ. This output is focused onto a moving copper tape. X-rays are produced from the copper target at a wavelength of 1nm (copper L-shell transitions).

X-RAY MASK

Exposures were carried out using silicon nitride membrane X-ray masks. These membranes were 0.1 microns thick and were patterned with 0.3 micron gold absorber layers. Linewidths on the mask ranged from 0.3 to 0.2 micron. Mask fabrication involved Edinburgh, King's College and Leica Cambridge Ltd. Exposures were carried out by placing photoresist coated wafers close to the X-ray mask using a 12 micron mylar spacer ring. The wafer/mask combinafion was then placed at a working distance of 125mm from the plasma X-ray source. This exposure geometry is shown in Fig 1 and typical exposure times were 5-6 minutes.

WAFER EXPOSURES

A novolak based positive tone chemically amplified resist (AZPF514) was used in this experiment. The resist was found to have an exposure sensitivity of 20mj/cm2 at 1nm wavelength. With assistance from the Central Microstructrure Facility, a reliable procedure was developed for patterning 0.18 micron features.[3] Typical 0.18 micron lines on a 1.5 micron pitch are shown in Fig 2. Identical linewidths were patterned onto six silicon FET device wafers which had been prepared earlier in the CMOS processing laboratories at Edinburgh University. Three of the wafers were designed for n-channel operation and three were designed for p-channel operation. The device structure for the n-channel case is shown in Fig 3. The X-ray lithography step was used to define the gate electrodes. Other features in the device included 5nm gate oxides, gate sidewall spacers and ultrashallow source/drain extensions. These devices represent state-of-the-art silicon technology research and the device results from this experiment are to be presented at ESSDERC in September 1994.[4]

SUMMARY

A scheduled experiment in Laser Support Facility was carried out to demonstrate the use of a KrF excimer based plasma X-ray source for X-ray lithography at 0.18 micron dimensions. Exposure times were typically 5-6 minutes for patterning 0.18 micron gate electrodes onto silicon FET wafers. The experiment has demonstrated an important new industrial lithography option for IGbit DRAM technology and its logic derivative.

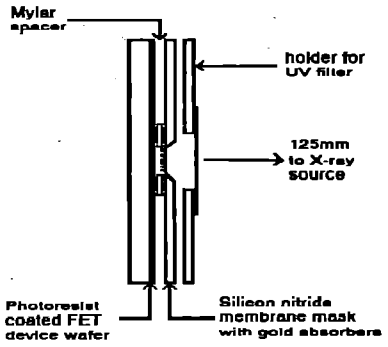

Fig 1. X-ray exposure configuration

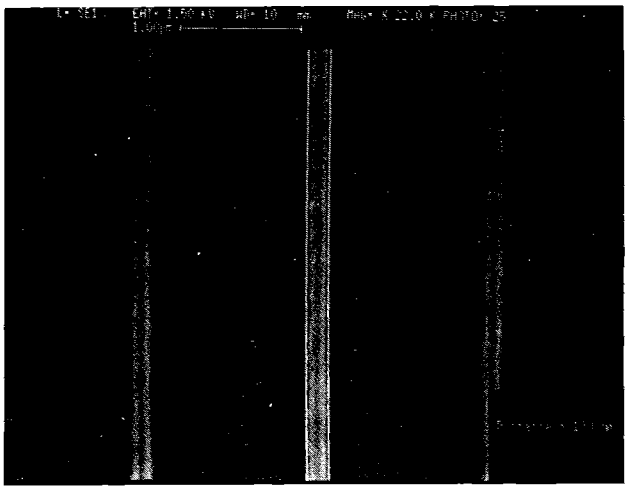

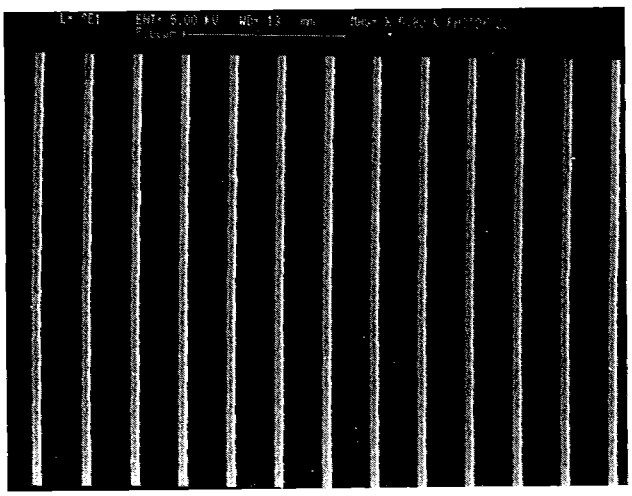

Fig 2. Electron micrographs showing 0.18 micron lines patterned into AZPF514 resist.

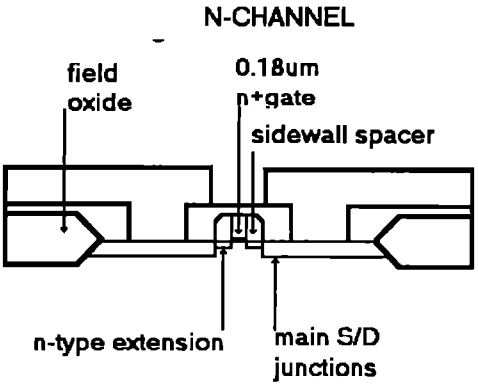

Fig 3. Diagram showing cross section of 0.18 micron FETs as studied in this experiment.

REFERENCES

1. R Viswanathan et al.,'Fabrication of high performance 512K static random access memories in 0.25 micron complementary metal oxide semiconductor technology using x-ray lithography', J Vac Sci Technol B, Vol 11, p2910, 1993.

2. I C E Turcu et al, 'Picosecond excimer laser-plasma X-ray source for microscopy, biochemisity and lithography', SPIE Vol 2015 'Applications of laser plasma radiation', paper, 2015-37, 1994. I C E Turcu et al., 'High Average Power 7 picosecond Krf Laser System for X-ray Generation', RAL Report RAL-93-031, 230 (1993).

3. C M Reeves, I C E Turcu, P Lake, J T M Stevenson, A W S Ross, A M Gundlach, P Prewett, P Anastasi, B Cook and P Mitchell, '0.18 micron device lithography using a KrF excimer driven plasma X-ray source', Submitted to Electronics Letters.

4. C M Reeves, I C E Turcu, A M Gundlach, J T M Stevenson, P Prewett, A J Walton and C D W Wilkinson, 'Application of optical, x-ray and e-beam lithography options to 0.18 micron silicon FET technology', Submitted for presentation at ESSDERC 1994.

FEMTOSECOND MEASUREMENTS OF OPTICAL NONLINEAR PROPERTIES OF Cd/Te/Cd/MnTe QUANTUM WELLS

N Cain, M O'Neill and J E Nicholls

University of Hull, Hull HU6 7RX

INTRODUCTION

The study of optical nonlinearities in III-V multiple quantum well systems is well established and much of the theory has been developed with reference to the standard GaAs/AlGaAs system. With the development of high quality MBE grown material, the theory can now be applied to II-VI quantum wells systems where the carrier-LO phonon interaction is stronger and excitons exist with higher binding energies. Studies of the ZnSe/ZnMnSe[1] and CdZnTe/ZnTe[2] have been made. The CdTe/CdMnTe multiple quantum well system grown on an InSb substrate forms a low strain structure and recently exciton resonances have been observed in its room temperature absorption spectrum[3]. This report describes nonlinear pump and probe transmission experiments, used to investigate the magnitude of nonlinear effects in CdTe/CdMnTe quantum wells at room temperature and to examine the dynamics of carrier transfer from the barriers to the wells and carrier relaxation in the wells. The experiments were carried out at the Central Laser Facility, Rutherford Appleton Laboratory. Optical pulses from a mode-locked Titanium-Sapphire laser were amplified to energies of several microjoules by a Q-switched Nd^{3+}:YAG pumped dye laser operating at 10 Hz. The amplified pulses were split in two components; the first was used as the pump to excite the sample, the second was focussed onto a rotating glass disc to generate a broad spectral continuum for the probe beam. The time resolution of the system was about 300 fs. Interference filters with a bandwidth of 10 nm were used to select probe wavelengths resonant with the exciton transition. The bandwidth of the exciton resonance at room temperature closely matches that of the filters. Three samples, each containing 15 wells separated by 150 Å barriers, were investigated. The well width of samples A and B was 75 Å and that of sample C was 50 Å. The barrier composition of sample A was $Cd_{0.85}Mn_{0.15}Te$ and that of samples B and C was $Cd_{0.92}Mn_{0.08}Te$. The InSb substrate of each sample was removed using an electrochemical etch[4].

DENSITY DEPENDENCE OF ABSORPTION

Let us consider the various mechanisms which contribute to nonlinear absorption in quantum well systems. Phase space filling[5], the filling of states out of which excitons are created, results from the Exclusion Principle and band-gap renormalization comes about from Coulombic screening[6]. Knox et al.[7] have shown that the latter effect, though very important in 3-D systems is significantly smaller in 2-D. Measurements of the valence and conduction band offsets of CdTe/CdMnTe quantum wells[8] suggest that, at room temperature, the samples discussed here are intermediate between 2-D and 3-D with electrons confined in the wells and holes delocalized in the wells and barriers. At room temperature, kT $\approx$ 26 meV and the exciton binding energy is about 20 meV so that at equilibrium, a population of excitons and "cold" free carriers, which have low kinetic energy, exists. This contrasts with room temperature conditions in GaAs/AlGaAs quantum wells where kT is much greater than the exciton binding energy resulting in "hot" free carriers with high kinetic energy and a very small exciton population. The time resolution of our nonlinear measurements is insufficient to distinguish between the nonlinear effects of free carriers and excitons, since, as indicated by linewidth measurements of the room temperature exciton resonance[3], exciton ionization by LO phonon scattering occurs on a timescale less than 100 fs. Figure 1 shows the absorbance at the exciton resonance as a function of carrier density for sample A.

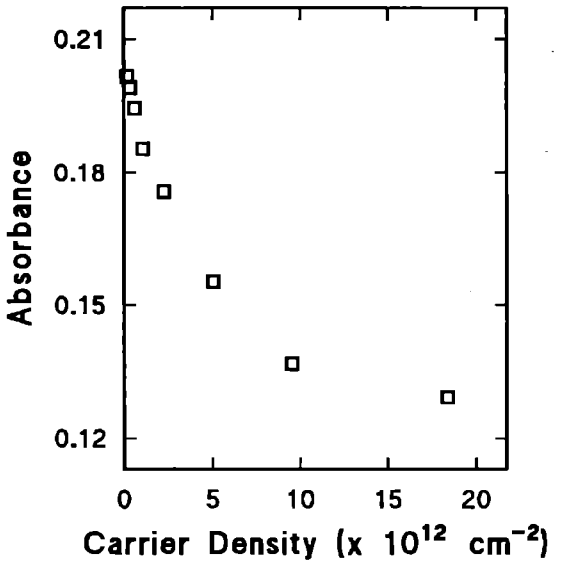

Figure 1: Carrier density dependence of absorbance at the exciton resonance of sample A.

The absorbance is observed to saturate as the carrier density is increased. Similar nonlinear changes in absorbance were found for the other samples. The saturation carrier density, N_s, is calculated by fitting the equation

$$\alpha(N) = \frac{\alpha_0}{1 + N/N_s} + \alpha_1 \qquad (1)$$

to the data. α_0 and α_1 are the saturable and nonsaturable linear absorbances and α(N) is the saturable absorbance when the carrier density per quantum well is N. α_1 includes the absorbance of the CdTe buffer layer and residual absorption from small islands of InSb which were not completely removed by etching. For reasons discussed below, low density data is used only in the fit. The results for the three samples are tabulated as follows.

Sample	N_s (cm^{-2})
A	2.5 – 5.1 x 10^{12}
B	6.5 – 9.5 x 10^{12}
C	4.8 – 8.8 x 10^{12}

The saturation carrier density due to phasespace filling, N_{psf}, can be evaluated by equation 1 in the limit of low carrier density[5]. Schmitt-Rink et al[6] have evaluated a theoretical expression for N_{psf}, which is correct within a factor

of two or three, given by

$$\frac{1}{N_{psf}^{ex}} = \frac{8}{7}\pi a_0^2 \qquad (2)$$

for excitons and by

$$\frac{1}{N_{psf}^{fc}} = 2\pi a_0^2 \qquad (3)$$

for free carriers at low temperatures. Our experimental conditions satisfy the low temperature criterion of equation 3 since "cold" free carriers with low kinetic energy exist at room temperature. Using experimental measurements of the exciton binding energy of similar CdTe/CdMnTe wells[8], a_0, the effective 2-D Bohr radius, is calculated to be 35 Å. Substitution of this value into equations 2 and 3 gives the saturation carrier density for excitons as 2.3 x 10^{12} cm^{-2} and the saturation carrier density for free carriers as 1.3 x 10^{12} cm^{-2}. These values agree quite well with the experimental results from sample A. Comparisons with results from samples B and C are less good. Both of these samples were excited into the barrier so that trapping of carriers in the barrier layers or recombination at the air and buffer layer interfaces may have occured. Consequently, the assumption of complete transfer of carriers from barrier to wells used in our density calculations may not be accurate. Alternatively, band-gap renormalization may also contribute to the observed nonlinearity. However, we do not have the spectral resolution to separate the effects of phase space filling and band-gap renormalization.

Carrier transfer and relaxation

The time dependence of nonlinear transmission was used to measure the timescale of carrier relaxation in the wells and carrier transfer from the barriers to the wells. Sample A was excited at 740 nm resonantly into the n=2 transition of the wells so that the rise-time of the nonlinear change in transmission at the exciton resonance, as shown in Figure 2, is a measure of the carrier relaxation time.

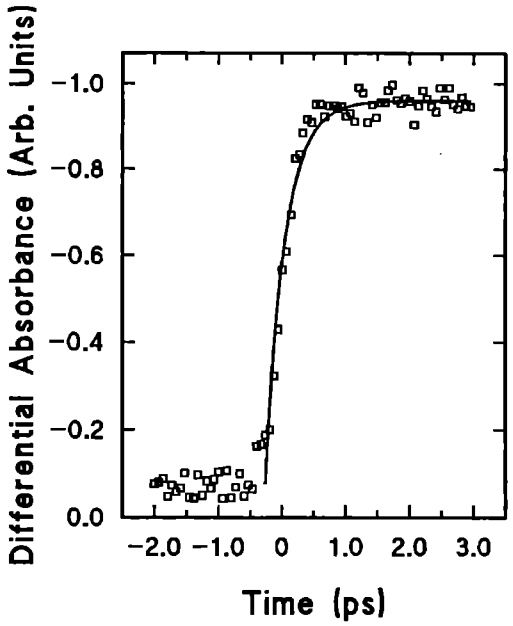

Figure 2: Differential absorbance at the exciton resonance of sample A as a function of delay between the pump and probe beam. The points are experimental data and the solid line is a single exponential fit giving a resolution limited rise-time of 300 fs.

A rise-time of 300 fs, limited by the time resolution of our experiment, is found. The experiment measures the relaxation time of electrons since, at room temperature, holes are delocalized between the barriers and wells. However, we cannot distinguish between the intersubband electron relaxation time from the n=2 to the n=1 level and the intrasubband relaxation of hot electrons in the n=1 level. Taking the conduction band offset as 66% of the total offset between the pump and probe, a lower limit for the electron relaxation rate of 1.56 x 10^{11} eV s^{-1} is found. Monte-Carlo calculations are in progress[9] to determine the scattering mechanism responsible for the relaxation. The pump wavelength of 740 nm was resonant with the barrier transition of samples B and C so that carriers were created both in the wells and barriers. The rise-time of nonlinear transmission is a measure of the electron transfer time from barriers to wells and the relaxation time to the bottom of the wells. In both cases, the measured rise-times are resolution limited and similar to that of sample A indicating that both the electron transfer and relaxation occur on a timescale less than 300 fs.

Conclusions

Nonlinear changes of transmission at the exciton resonance in CdTe/CdMnTe quantum wells can be explained by phase space filling by excitons and free carriers. The electron transfer time from the barriers to the wells and the relaxation time to the bottom of the wells occur in less than 300 fs at room temperature.

Acknowledgements

We would like to thank A. J. Langley, P. Taday and W. Shaikh of the Central Laser Facility, Rutherford Appleton Laboratory for their help in setting up the experiment. The work has been supported by the U. K. Science and Engineering Research council as part of the Low Dimensional Structures Initiative.

References

1 D.R. Anderson, L. A. Kolodiejski, R. L. Gunshor, S. Datta, A. E. Kaplan and A. V. Nurmikko, Applied Physics Latters, **48** 1559

2 P. C. Becker, D. Lee, M. R. X. de Barros, A. M. Johnson, A. G. Prosser, R. D. Feldman, R. F. Austin and R. E. Behringer, IEEE J. Quantum Electronics, **QE- 28** 2535 (1992)

3 M. O' Neill, M. Oestreich, W. W. Rühle and D. E. Ashenford, Physical Review B, **48** 8980 (1993)

4 R. J. Nicholas, Private communication.

5 D. S. Chemla, D. A. B. Miller, P. W. Smith, A. C. Gossard and W. Wiegman, IEEE J. Quantum Electronics., **QE 20** 265 (1984)

6 S. Schmitt-Rink, D. S. Chemla and D. A. B. Miller, Advances in Physics, **38** 89 (1989)

7 W. H. Knox, C. Hirlimann, D. A. B. Miller, J. Shah, D. S. Chemla and C. V. Shank, Physical Review Letters, **56** 1191 (1986)

8 S. R. Jackson, J. E. Nicholls, W. E. Hagston, P. Harrison, T. Stirner, J. H. C. Hogg, B. Lunn and D. E. Ashenford, *submitted to* Physical Review B.

9 W. E. Hagston, Private communication

A SEARCH FOR DIRECT (CORRELATED) TWO-ELECTRON EMISSION FROM URANIUM IN INTENSE LASER FIELDS

G M Cross, L J Frasinski, L Zhang†, P A Hatherly and K Codling

J J Thomson Physical Laboratory
Whiteknights, Reading RG6 2AF, UK

and

A J Langley and W Shaikh
Laser Division
Rutherford Appleton Laboratory
Didcot OX11 0QX, UK

ABSTRACT

A Ti:sapphire laser of focused intensity up to 2×10^{15} W/cm^2 has been used to search for direct (correlated) electron emission in atomic uranium using the molecule UF_6. The aim was first to use ion time-of-flight (TOF) spectroscopy to provide evidence of correlated emission and then to apply the electron-electron (EE) covariance mapping technique to confirm its existence. The ion TOF spectra did not provide sufficient encouragement to warrant proceeding with the EE coincidence experiment but suggested an approach that might be successful.

1. INTRODUCTION

There are two mechanisms by which an intense laser can multiply-ionize an atom; sequential (step-wise) or direct (correlated). Initially it was thought that the direct process must be important, because multiple ionization rates appeared much higher than predicted on the basis of single-electron, non-resonant transitions (Delone et al 1984). However, it was soon realised that other explanations could be found for this unexpected behaviour, see Lambropoulos (1985); Trainham et al (1992). One implication of the Lambropoulos work was that, when a laser of modest rise time is used, the production of single ions is bound to occur on the rising edge of the laser pulse, reducing significantly the possibility of the direct double ionization process.

The simplest experimental method of confirming the existence of direct double ionization is ion time-of-flight (TOF) spectroscopy. Plotting a graph of the logarithms of the ion count rate versus laser intensity should reveal the direct channel, if it exists. L'Huillier et al (1983) studied the multiple ionization of Xe using a laser of wavelength 532 nm, pulse length 50 ps and focused intensity in the range 10^{11}-10^{13} W/cm^2 and observed an initial rapid rise in the yield of Xe^{2+} ions that was attributed to direct double ionization. The direct process was assumed to terminate when the ground state population was depleted. Thereafter the Xe^{2+} yield increased at a lower rate, consistent with sequential ionization.

The direct double ionization process ought to be revealed much more definitively using electron-electron (EE) coincidence techniques. This is because the two electrons are expected to be correlated in energy and angular momentum. For example, if the photon energy is $\hbar\omega$ and N is the minimum number of photons required to overcome the total binding energy, E_b, of the two electrons (atom plus ion ionization potentials), then the kinetic energies of the two correlated electrons, E_1 and E_2, are given by the equation $E_1 + E_2 = N\hbar\omega - E_b$. The two electrons share the total energy in various ways, producing a continuous spectrum of energies that would be hard to recognise in a conventional electron TOF spectrum. (Electrons from a sequential process produce discrete peaks in the TOF spectrum.) However, correlated emission should produce a recognisable feature on an electron-electron covariance map (Frasinski et al 1992).

Trainham et al (1992) employed the EE covariance mapping technique to search for direct double ionization in Mg, using a laser of wavelength 615 nm and pulse length of 80 fs; they were unsuccessful. They pointed out that laser fluctuations created artificial correlations that overwhelmed the real single-atom correlations. More recently, Walker et al (1993) returned to Xe using a laser of wavelength 527 nm and pulse length 50 ps. They observed the same 'knee', or double rate, seen earlier by L'Huillier et al. They performed EE coincidence experiments and were able to put an upper limit on the direct events that was about two orders of magnitude lower than the Xe^{2+}/Xe^{+} ratio (itself less than 1/100). They concluded that a higher order *sequential* process was responsible for the knee structure seen in Xe^{2+}.

Clearly, if one wishes to convincingly demonstrate direct double ionization, one must find an atom where the ratio of double-to-single ionization is much more favourable. Ideally, one needs to produce experimental conditions such that the atom is found *only* in the doubly charged state; this would constitute strong evidence for the direct (correlated) process. We chose to study UF_6 because recent work by Armstrong et al (1993) had shown an interesting trend in the ratio of U^{2+}/U^{+} as a function of wavelength. At 266 nm, the 4th harmonic of the Nd:YAG laser, the U^{2+} signal was less than that of U^{+} at a threshold intensity of 10^9 W/cm^2. At the third harmonic (355 nm), the U^{2+} and U^{+} signals appeared almost equally strongly at a threshold intensity of about 10^{11} W/cm^2 and at the second harmonic (532 nm), the U^{2+} signal was considerably greater than the U^{+} signal at a threshold intensity of about 10^{12} W/cm^2. Moreover, the fragment ions UF_x^{+} (x = 1-3) that were evident at threshold at 266 and 355 nm, were missing entirely at 532 nm.

The TOF spectra obtained by Armstrong et al at 532 nm are shown in figure 1, the laser intensity varying from 1.1 x 10^{12} to 1.3 x 10^{13} W/cm^2. In fact, as the laser intensity increases, the ratio U^{2+}/U^{+} remains high (the U^{2+} signal saturates at the higher laser intensities) but the U^{3+} signal increases steadily. This situation must be avoided because one is looking to perform EE covariance mapping in order to conclusively recognise direct double ionization, and additional electrons associated with the production of U^{3+} ions could compromise such an experiment. The production of fragment ions, UF_x^{+}, is to be avoided for the same reason.

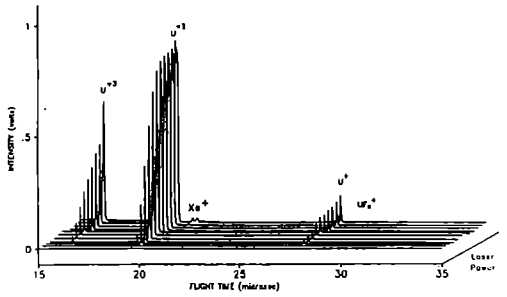

Figure 1 TOF spectra of UF_6 at a wavelength of 532 nm as a function of laser intensity, from Armstrong et al (1993). With kind permission of the authors.

Armstrong et al (1993) made measurements mainly at 266 nm but also at 355 nm and 522 nm using both ion TOF spectroscopy and photoelectron spectroscopy; they observed a continuum of very low energy electrons at all wavelengths investigated. They found it difficult to conceive of a step-wise neutral ladder mechanism leading to U^+ ions, followed by step-wise ionization to U^{2+}, that would explain the fact that the U^{2+} signals were so much greater than the U^+ signals. Usually, of course, the single ion yield far exceeds the double ion yield at most laser intensities, see L'Huillier et al (1983). They concluded that their results could be understood in terms of multiple excitation of a 'giant resonance' in the 12-14 eV region; this produced 'superexcited' states of UF_6 that dissociatively ionized via two channels:

$$UF_6 + N\hbar\omega \rightarrow [UF_6^{**}] \rightarrow U^{n+} + 6F + ne \quad (1)$$

$$UF_6 + N\hbar\omega \rightarrow [UF_6^{**}] \rightarrow UF_x^{n+} + (6-x)F + ne \quad (2)$$

Their results indicated that decay channel (1) was completely dominant. Whether such superexcited states are invoked or not, the two-electron ejection process (n=2) could be direct, with the two electrons sharing a specific energy.

Our aim, then, was first to study UF_6 multiple ionization using ion TOF spectroscopy at a wavelength of 750 nm, hoping that the trend of increasing U^{2+}/U^+ ratio with wavelength would continue, and to identify the conditions which maximised this ratio, while at the same time avoiding complications associated with UF_x^+, UF_x^{2+} and U^{3+} ions. We expected that the possibility of observing direct ionization would be enhanced by using a much shorter pulse length (~200 fs) than that employed by Armstrong et al (~5 ns). There are two arguments in favour of the shorter pulse (Trainham et al 1992). The faster the higher intensities are reached, the sooner the direct process wins over the first step of the sequential process. Furthermore, the shorter the pulse, the less 'sequential' the process becomes, in the sense that the two electrons are expected to be correlated both spatially and temporally.

Since we were obliged to work with U in the form of the molecule UF_6, it was important to ensure that the observation of U^{2+} ions was associated with double-electron ejection and not with negative ion production. The possible routes to U^{2+} production involving negative ions are the following:

$$UF_6 + N\hbar\omega \rightarrow U^{2+} + F^- + 5F + e^- \quad (3)$$

$$\rightarrow U^{2+} + 2F^- + 4F \quad (4)$$

The experiment must therefore be capable of detecting F^- ions; this was achieved by simply reversing the polarity of the appropriate potentials applied to the TOF system.

2. EXPERIMENTAL ASPECTS

The laser system consisted of an argon-ion laser pumping a passively mode-locked Ti:sapphire laser, producing pulses in the range 100 - 300 fs. A pulse, typically 100 fs in length, was stretched using a pair of prisms with negative group velocity dispersion (GVD) to give a pulse length of about 600 fs. These pulses were amplified at 10 Hz through a 3-stage amplifier pumped by a frequency-doubled, Q-switched Nd:YAG laser. The third stage was a Bethune cell, introduced to retain good beam uniformity and low wavefront distortion. The pulses were recompressed using a glass block to provide positive GVD. The amplified pulse duration (FWHM) after compression was typically 120 fs.

A laser diagnostic package consisting of single-pulse auto-correlator and grating spectrometer took 2% of the beam, see Langley et al (1994). Thus it was possible to determine the pulse duration and spectrum simultaneously and check that the pulses were close to their Fourier transform limit ($\Delta\nu\Delta t$ = 0.32 for $sech^2$ profiles). The beam passed into the experimental chamber which housed two identical doublet lenses, corrected for spherical aberration. The first pair focused the 20 mm diameter laser beam to an Airy disc about 4 μm in diameter. The second pair ensured that parallel light exited the chamber. The focal region was then projected by a simple optical system on to an appropriately placed aperture which allowed radiation from the Airy disc to fall on an energy meter. Thus the focused intensity was determined on a pulse-to-pulse basis to an accuracy of ±30%. It should be admitted that one disadvantage of using a doublet lens rather than a paraboloidal mirror to focus the laser beam is that this combination stretches the pulse (Bor and Horvath 1992). The rise time is hardly affected and inasmuch as the interesting physics is likely to occur at the leading edge, this stretching may not be too important.

The experimental chamber also housed two drift tubes lying co-axially either side of the laser-molecule interaction region. The first was only 25 mm in length and allowed almost all ions to be collected with 100% efficiency, regardless of their energy or charge state (Hatherly et al 1989). The second drift tube, 125 mm in length, could be used to improve the energy resolution, but usually at the expense of collection efficiency; this longer drift tube was used for the measurements reported here. If positive ion - negative ion (pair) production were to occur, the process could be studied using ion-ion covariance mapping.

3. RESULTS AND DISCUSSION

The results of a careful study of the variation of the TOF spectra of UF_6 with a laser of wavelength 750 nm at a number of intensities are shown in figure 2. From measurements with the single-pulse autocorrelator and spectrometer, the laser pulses were found to be 140 (±20) fs and to be close to Fourier-transform-limited. Passage through the doublet lens increased the pulse length to 200 (±20) fs. The intensities quoted are those within the central Airy disc.

At the highest laser intensity (2×10^{15} W/cm^2) the ratio of the peak heights (U^{2+}/U^+) is about 30 and it remains roughly constant down to about 10^{14} W/cm^2. This ratio is taken from the raw TOF spectra, but if one accounts for the different detection efficiencies for U^+ and U^{2+} and their different dispersions, it reduces to below a factor of 10. The vertical scales have been arranged so that the U^{2+} signal is the same height in all spectra and one sees that the U^+ signal hardly changes in this intensity range. The raw TOF data of Armstrong et al (1993) at 532 nm show a ratio of about 10. However, in contrast to the results of Armstrong et al (1993), there are many peaks associated with fragments such as UF^+, UF_2^+, UF^{2+}, UF_2^{2+} etc and these fragments persist at the lowest

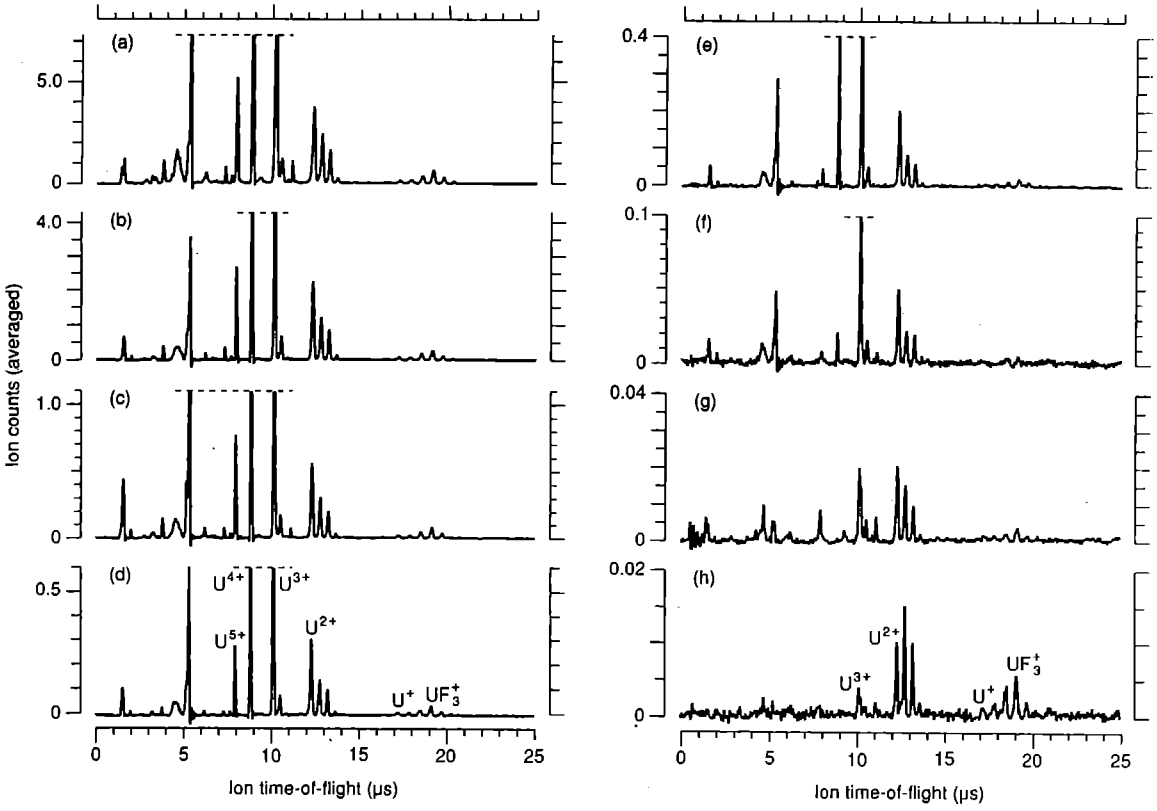

Figure 2 TOF spectra of UF_6 at a wavelength of 750 nm. The laser intensities are as follows (a) 2×10^{15} W/cm^2; (b) 1.3×10^{15} W/cm^2; (c) 8×10^{14} W/cm^2; (d) 5×10^{14} W/cm^2; (e) 2×10^{14} W/cm^2; (f) 1.3×10^{14} W/cm^2; (g) 8×10^{13} W/cm^2; (h) 4×10^{13} W/cm^2. The peaks below 6 μs are to be associated with ions such as H^+, F^+, HF^+ and F^{2+}.

laser intensities. The various UF_x^+ peaks (x=0-5) retain their relative intensities as the laser intensity is reduced but the UF_x^{2+} peaks (x=0-3) show some variations.

At the lowest intensity (4×10^{13} W/cm^2) the U^{2+} peak is still *larger* than the U^+ peak although the peaks associated with the fragments UF_x^+ are relatively more intense; the fragments UF^{2+} and UF_2^{2+} have also gained intensity relative to the U^{2+} ion. Moreover, a substantial U^{3+} peak is still observed. At the slightly lower intensity of 3×10^{13} W/cm^2 almost no ions are detected above background. This may seem surprising when Armstrong et al saw many ions at a peak intensity of 1.3×10^{13} W/cm^2. However, their focal volume was much greater, a pulsed nozzle enhanced the pressure in the molecular beam and a much longer pulse was used.

In order to determine the regime under which the present experiments were conducted, a plot was made of the logarithms of the U^{2+} and U^+ ion counts versus laser intensity, see figure 3. The slope of 3/2 shown in the figure is expected if one is in the saturation, or barrier suppression ionization (BSI) regime. In other words the focal volume in which a specific ion charge state is produced increases as the 3/2 power of the laser intensity. The U^{2+} data points fall on this line but the U^+ data points show a significant departure at low laser intensities. A recent calculation of ion yield versus laser intensity using a simple tunnel ionization model suggests that the BSI regime is reached at an intensity of about 10^{13} W/cm^2 and that the U^+ curve lies well *above* the U^{2+} curve at all laser intensities. (The model assumes dissociation of UF_6, followed by ionization of the U atoms.)

Therefore the unusual behaviour observed in UF_6 at a

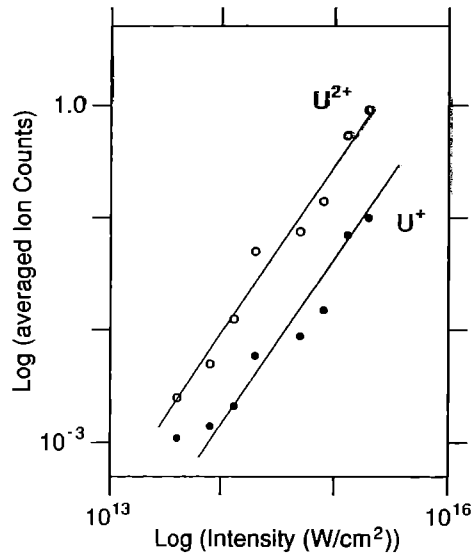

Figure 3 The ion yield curves for U^+ and U^{2+}, taken from the data of figure 2.

wavelength of 532 nm and pulse length of a few nanoseconds duration is repeated at 750 nm using a pulse length of 200 fs, in as much as the U^{2+}/U^{+} ratio is much greater than simple theory would predict. However, the existence of many UF_x^{+} and UF_x^{2+} ions at low intensities is disappointing; the large reduction in pulse length clearly has a major effect on the complexity of the TOF spectra. A modest increase in pulse length, from 200 fs to 600 fs (removal of the glass block providing the positive GVD) had no effect on the TOF spectra shown in figure 2.

The possible creation of negative ions was mentioned earlier. The TOF spectrometer was modified to search for such ions and none were found.

4. CONCLUSION

The aim of the experiment was to observe direct double ionization; this has not been achieved. The TOF spectrum at 750 nm did not show the same simple structure as had been seen earlier by Armstrong et al (1993) at 532 nm. The U^{2+} signal was greater than the U^{+} signal at 750 nm, but because many other fragments were observed, it did not appear worthwhile to perform an EE coincidence experiment. However, a double-pulse experiment should be performed. The first should be a long (~1 ns), weak pulse to completely dissociate the UF_6, the second a short, intense pulse to produce U^{2+} ions.

ACKNOWLEDGEMENTS

We are pleased to acknowledge the Science and Engineering Research Council (UK) for providing financial support and access to the Laser Support Facility of Rutherford Appleton Laboratory.

REFERENCES

Armstrong D P, Harkins D A, Compton R N and Ding D (1993) J. Chem. Phys. (in press).

Bor Z and Horvath Z L (1992) Optics Comm. **94** 249

Delone N B, Suran V V and Zon B A (1984) in "Multiphoton Ionization of Atoms", Ed S L Chin and P Lambropoulos (Academic: New York)

Frasinski L J, Stankiewicz M, Hatherly P A, Cross G M, Codling K, Langley A J and Shaikh W (1992) Phys. Rev. A **16** R6789

Hatherly P A, Frasinski L J, Codling K, Langley A J and Shaikh W (1990) J. Phys. B: At. Mol. Opt. Phys. **23** L291

Lambropoulos P (1985) Phys. Rev. Lett. **55** 2141

Langley A J, Noad W J, Ross I M and Shaikh W (1994) Appl.Opt. (in press)

L'Huillier A, Lompre L A, Mainfray G and Manus C. (1983) Phys. Rev. A **27** 2503

Trainham R, van Druten N J, Noordam L D, Muller H G, Breger P, Petit G, Mevel E, Agostini P and Antonetti A (1992) in "Coherence Phenomena in Atoms and Molecules in Laser Fields" Ed A D Bandrauk and S C Wallace (Plenum: New York)

Walker B, Mevel E, Yang B, Breger P, Chambaret J P, Antonetti A, DiMauro L F and Agostini P (1993) Phys. Rev. A**48** R894

THE SEARCH FOR DIRECT DOUBLE IONIZATION IN HE AND XE

G M Cross, L J Frasinski, A J Giles, P A Hatherly and K Codling

J J Thomson Physical Laboratory
Whiteknights, Reading RG6 2AF, UK

and

A J Langley and W Shaikh
Laser Division
Rutherford Appleton Laboratory
Didcot OX11 0QX, UK

The search for direct (non-sequential) double ionization in uranium (in the form of UF_6) is described in a recent publication (Cross et al 1994). As a first step, conventional ion time-of-flight (TOF) spectra were obtained, but the existence of many UF_x^+ and UF_x^{2+} ions meant that it would have been unproductive to use the electron-electron covariance technique to look for correlated two-electron emission. (The direct process should show up as a recognisable feature on an electron-electron covariance map.)

It has been thought for some time that evidence for direct double ionization exists in the work of L'Huillier et al (1983) on Xe. They used a laser of pulse length 50 ps, intensities in the range 10^{11}-10^{13} W/cm^2 and ion TOF spectroscopy. However, Walker et al (1993) have recently shown that a high order sequential process was responsible for the "knee" in the Xe^{2+} yield curve. The process of direct double ionization ought to be considerably enhanced if laser pulses of much shorter duration are used. We therefore decided to look again at Xe with the Ti:sapphire laser, where Fourier-transform-limited pulses of less than 200 fs duration were available. As in the case of uranium, an important first step was to determine the laser conditions that would optimise the Xe^{2+}/Xe^+ ratio, using ion TOF spectroscopy.

Experiments were performed where the Airy disc was continuously monitored in order to obtain accurate values of laser intensity. The optimum condition for the highest Xe^{2+}/Xe^+ ratio was found, which at the same time minimised the Xe^{3+} ion count; this was important since one wished to avoid additional electrons from 'spurious' ions. The best ratio achieved was 33% at a laser intensity of 2×10^{14} W/cm^2.

The most fundamentally interesting atom to study is undoubtedly He. Direct double ionization is known to occur in single photon experiments but so far there is very limited evidence in the multiphoton regime. Fittinghoff et al (1992) used ion TOF spectroscopy to obtain results which are claimed to indicate the nonsequential process. As in Xe, the He^{2+} data exhibit a feature that saturates in parallel with the He^+ signal. We optimised the He^{2+}/He^+ ratio but in this case the best ratio achieved was 3% at a laser intensity of 10^{15} W/cm^2.

Having found the conditions that optimised the double-to-single ion ratios in Xe and He, the electron-electron experiment was coupled to the Ti:sapphire laser system in January 1994. There were problems with detecting the electron signal; the pulse heights were considerably lower than in earlier runs. In consequence electron-electron covariance mapping could not be attempted. When the experiment was returned to Reading, it was found that one of the microchannel plates was cracked; this may well have been the cause of low electron pulse heights.

There has been a recent publication by Corkum (1993) suggesting that the double ionization observed by Fittinghoff et al (1992) could be understood in terms of correlated emission but in this case the initially ejected electron returns to the ion to eject a second electron in an "e-2e" scattering process. If this is the case, then the double ionization process should be critically dependent upon the states of polarization of the laser, whether linear or circular. We hope to study this phenomenon in the future using electron-electron covariance mapping.

REFERENCES

Corkum P B 1993 Phys. Rev. Lett. **71** 1994.

Cross G M, Frasinski L J, Zhang L, Hatherly P A, Codling K, Langley A J and Shaikh W J. Phys. B. (accepted).

Fittinghoff D N, Bolton P R, Chang B and Kulander K C 1992 Phys. Rev. Lett. **69** 2642.

L'Huillier A, Lompré L A, Mainfray G and Manus C 1983 Phys. Rev. A**27** 2503.

Walker B, Mevel E, Yang B, Breger P, Chambaret J P, Antonetti A, DiMauro L F, Agostini P 1993 Phys. Rev **A48** R894

X-RAY FOCUSING USING MICROCHANNEL PLATES (MCPs)

G W Fraser[1], A N Brunton[1], J E Lees[1] and I C E Turcu[2]

[1]Dept of Physics and Astronomy, University of Leicester, Leicester LE1 7RX
[2]Rutherford Appleton Laboratory, Chilton, Didcot, OXON, OX11 0QX

INTRODUCTION

Novel, lightweight, low-cost microchannel plate (MCP) X-ray optics manufactured from lead silicate glass have been under study at Leicester since 1990 [1-3] for future applications in hard X-ray astronomy. MCPs provide a new means of imaging the sky in the little-explored 10-100 keV energy band. Other, terrestial, applications proposed for MCP optics include collimation for projection X-ray lithography, flux concentration for X-ray fluorescence (XRF) studies and "relay-lens" operation for contact X-ray microscopy of biological specimens.

This report briefly describes the first study of microchannel plate X-ray focusing using the RAL picosecond pulse train excimer laser plasma X-ray source. The RAL source has a number of attractive features for the evaluation of MCP optics : (i) small effective source size (10 microns instead of 0.5 mm for the Leiecester laboratory X-ray source) (ii) high brightness (78 mW/sr) and (iii) the availability of a calibrated Si photodiode for the measurement of absolute focusing efficiencies.

A series of measurements was carried out using two MCP geometries, both previously tested at Leicester, and two X-ray wavelengths (7.76 Ångstroms from He-like Al XII and 33.7 Ångstroms - C VI Lyman alpha). The experiment took place in the period 10-21 January 1994, following the cancellation, due to laser problems, of an earlier run scheduled for August 1993. A paper describing our results in detail is in preparation [4].

MCP GEOMETRIES

Most data was obtained with a planar, square-pore microchannel plate [1,3] manufactured by Galileo Electo-Optics (Sturbridge, MA, USA). The channel side length was 86 microns and the inter - channel pitch was 122 microns. Thus, the plate thickness of 4.8 mm gave a channel aspect ratio of 55:1, leading to an optimum focusing efficiency at wavelengths around 20 Ångstroms. The active area of the plate was 30 mm in diameter. During manufacture, this MCP had been reduced in hydrogen, a process thought to reduce surface roughness in lead silicate glasses.

A limited number of images were also obtained using a Philips Photonics (Brive la Gaillarde, France) "spherically slumped" round-pore MCP capable of focusing a parallel beam to a point or of expanding a point source to a quasi-parallel output beam [2]. Analysis of these images is presently (March 1994) incomplete (as is the analysis of the photodiode signals for the planar, square-pore MCP), and will not be reported here.

RESULTS

In laboratory tests of the Galileo MCP prior to the laser run, the cruxiform image structure expected from a planar, square-pore plate in "point-to-point" focusing mode [1] was observed with an elliptical central focus 1.33 x 1.87 mm fwhm in extent at 7.1Å (Si K X-rays) and 1.35 x 2.30 mm fwhm for 44.7Å (C K X-rays).

In our laser plasma X-ray experiments, the source to MCP separation l_s was chosen for each wavelength so that the maximum angle of incidence to the channel walls was equal to the calculated critical angle of reflection from lead silicate glass (1.22 degrees for 7.76Å X-rays ; 2.68 degrees for 33.7 Å). Focused images were recorded on film placed a distance $l_f = l_s$ on the other side of the channel plate. Kodak Direct Exposure Film (DEF) [5] was used for the Al X-rays and Shanghai 5F no-supercoat XUV film to record the focused Carbon K-shell X-ray flux. Each film was preceded by a 1.0 micron thick polypropylene visible light filter supported by a wire mesh. Both MCP and film holders were free to move in an extension pipe connected to the main source chamber.

Figure 1 shows a typical Al K-shell X-ray image recorded on DEF film. Similar images were recorded, even for "single shot" laser operation (a diode charge of as little as 2nC). The expected cruxiform image structure is again clearly apparent : X-rays reflected once from channel surfaces parallel to the x-axis appear as a horizontal "line focus", while those reflected once from channel walls parallel to the y-axis give rise to a vertical line focus. The central, "true" focus is formed from X-rays which have been reflected from a pair of orthogonal channel walls. The "splitting" of the line foci appears to be due to a slight mispositioning of the channel plate (i.e. $l_s = l_f$). Since the film resolution (DEF grain size 1.3 microns) is very much smaller than the channel size, the "diffuse" component of the image - composed of photons

passing straight through the MCP - is clearly resolved into the projections of individual pores. The image may therefore serve as an informative diagnostic of MCP geometric regularity. Blocked channels and misorientated multifibres (the 2x2 mm^2 sub-units of the structure) are among the imperfections which are readily visible.

Preliminary scans of DEF film images with a Joyce Loebl Mark 3C microdensitometer at Leicester indicate maximum intensity gains (relative to the flux measured with the MCP absent) of ~21 times. The true focus at 7.76Å has a fwhm extent of 2.1 mm, although film optical densities (OD) in this region generally exceed 2.5 and are therefore right at the limit of published OD-to-exposure calibration curves [5]. The film measurements indicate that the X-ray intensity achievable by combining the laser plasma source and currently available MCPs is of order $2x10^7$ 7.76Å photons/sq.mm/s for a laser repetition rate of 100 Hz and a distance from the source of 1.29 m.

CONCLUSIONS

The high flux and small (10 micron diameter) effective size of the laser plasma X-ray source make it a perfect tool for the determination of channel -to- channel misalignments and glass surface microroughness in future generations of MCP X-ray optic. Conversely, the combination of the laser plasma X-ray source with MCP optics produces, at low cost, a low-debris, high intensity "beamline" which may find future applications in a number of ground based studies such as XRF. We hope to utilise the RAL facility to test future generations of MCP X-ray optic from which, as mechanical perfection is improved and pore sizes are reduced, we may expect to achieve in turn still higher focused intensities.

REFERENCES

1. G.W. Fraser, A.N. Brunton, J.E. Lees, J.F. Pearson and W.B. Feller, Nucl.Instr.Meth. A324 (1993) 404-7.
2. G.W. Fraser, A.N. Brunton, J.E. Lees and D.L. Emberson, Nucl.Instr.Meth. A334 (1993) 579-88.
3. G.W. Fraser, A.N. Brunton, J.E. Lees, J.F. Pearson, R. Willingale, D.L. Emberson, W.B. Feller, M. Stedman and J. Haycocks, Proc. SPIE 2011 (1993) 215-26.
4. I.C.E. Turcu, A.N. Brunton, J.E. Lees and G.W. Fraser, "High intensity focused X-rays from a repetitive laser plasma source", in preparation.
5. B.L. Henke, J.Y. Uejio, G.F. Stone, C.H. Dittmore and F.G. Fujiwara, J.Opt.Soc.Am. B3 (1986) 1540.

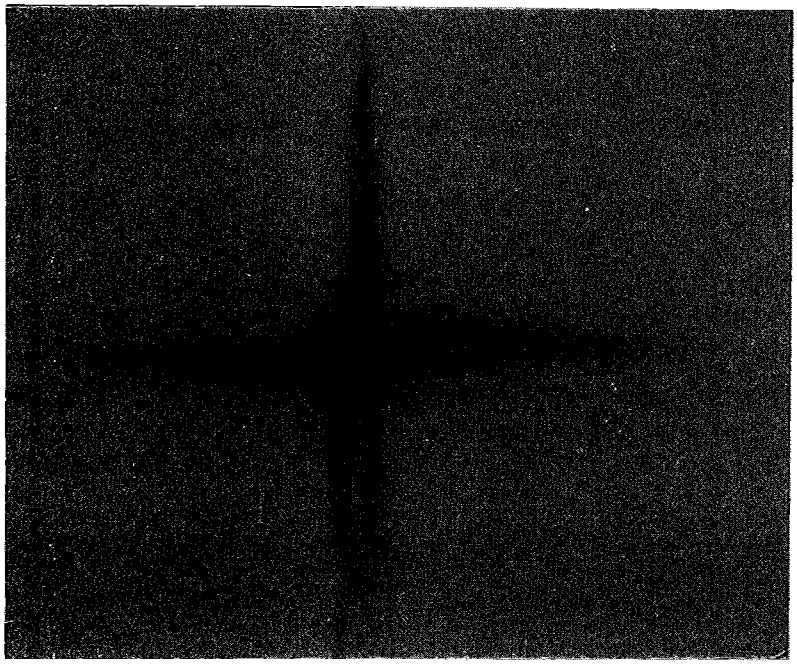

Fig.1 DEF image of focused 7.76Å X-rays. Source-MCP and MCP-film separations equal to 645 mm. Image magnification - times 2 (approx).

CALIBRATION OF X-RAY LASER DIAGNOSTICS AND CHARACTERISATION OF THE LSF X-RAY SOURCE

L. Dwivedi[1], G.J. Tallents[1], I. C. E. Turcu[2], P. Trenda[2]

[1]Department of Physics, University of Essex, Colchester CO4 3SQ, U.K.
[2]Central Laser Facility, Rutherford Appleton Laboratory, Didcot, OX11 0QX, U.K.

INTRODUCTION

The accuracy of the results that are obtained in x-ray laser experiments are highly dependent on the diagnostic equipment used. One important diagnostic commonly used in x-ray laser experiments is the flat field axial spectrometer. The main element of the flat-field spectrometer is a ruled diffraction grating[1]. These gratings have a variable d-spacing of ~ 833 nm (1200 lines/mm) and ~ 417 nm (2400 lines/mm) depending on the range of wavelengths being studied and as a result of the variable line spacing produce a flat focal plane. In order to obtain a more accurate value of the x-ray laser output obtained in the experiments, this instrument should be calibrated. X-ray film is extensively used as a medium on which spectral or other information of the plasma medium is recorded. It is also necessary to calibrate the film so that the optical density of the film exposure can be converted to the x-ray incident flux producing the exposure.

The laser plasma x-ray source in the Laser Support Facility (LSF) at the Rutherford Appleton Laboratory is ideal as an x-ray source for calibration at soft x-ray wavelengths mainly because the exposure on the film can be adjusted accurately by changing the exposure time. The krypton fluoride (KrF) laser used to create the plasma for these measurements can be run at repetition rates of 10-50 Hz with 20ns long pulse trains having individual pulses of 8 ps duration spaced at 2 ns intervals which means that the x-rays produced are quasi-continuous in nature. We describe here an experiment performed to measure the reflectivity of the flat field gratings and calibrate different types of x-ray film. In addition an x-ray streak camera was used to study the temporal behaviour of the x-ray source.

EXPERIMENTAL PROCEDURE

X-ray laser wavelengths of interest are in the soft x-ray region and hence it is necessary to calibrate the flat field gratings and film in that wavelength region. A mylar ($C_{10}H_8O_4$) tape target for the x-ray source was chosen. This target when irradiated in a spot focus by pulsetrains (20 ns duration) from the repetitive excimer (KrF) laser and produces a quasi-monochromatic x-ray source emitting chiefly in the water-window region (between 23 Å and 44 Å). The x-ray source has been described in more detail elsewhere[2]. A calibrated P-i-N silicon x-ray diode, filtered with 0.5 μm thick vanadium, was used to monitor and quantify the total x-ray flux emitted in the water window region.

The x-ray source in the Laser Support Facility is housed in a target chamber having a radius of 25 cm which made it impossible to mount the flat field spectrometer directly on the chamber wall. An adaptor flange was constructed which would allow a larger housing flange to be connected to the chamber wall. The flat field spectrometer was then bolted onto the end of this housing flange such that the horizontal entrance slit (10 mm long x 100 μm wide) along the source axis was at a distance of 56 cm from the source itself.

The same housing was used to mount the x-ray streak camera. Streak camera operation requires vacuum conditions better than ~10^{-4} Torr and so it was necessary to separate the target chamber (operated at 20 Torr pressure of helium typically to reduce the effect of target debris on the focusing lens) and the housing chamber for the streak camera using a parylene window so that the streak camera could be operated at a vacuum pressure of 10^{-4} Torr. The filtered x-ray streak camera had a ~80 μm wide entrace or timing slit oriented vertically and positioned behind the 1 mm wide vertical parylene window. A caesium iodide (CsI) coated photocathode was used for increased sensitivity.

Carbon spectra clearly showing the C VI Lyman-α, C VI Lyman-β and the C V $1s^2$-1s2p lines in the first and higher orders were obtained on UF-SH4 film using the flat field spectrometer. This was repeated for different x-ray exposures and spectra obtained on different x-ray film. The UF-SH4 film was chosen chiefly because it had been previously calibrated at the same wavelengths[3] and calibration curves showing optical density on film as a function of x-ray flux in units of photons / μm^2) were available for comparison. A densitometer trace of a typical spectrum from a mylar tape target recorded on Russian UF-SH4 x-ray film is shown in figure 1.

ANALYSIS OF RESULTS

The optical densities of the C VI Lyman α, C VI Lyman β and the C V $1s^2$-1s2p lines on film were measured by using a Joyce-Loebl densitometer for different values of x-ray exposure (photons / μm^2) measured by the x-ray diode. The measured values of x-ray flux incident on the spectrometer entrance slit and the known calibration of the x-ray film were used to determine the reflectivity of the diffraction gratings.

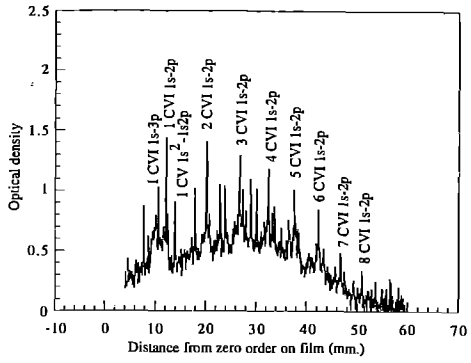

Figure 1:- Spectrum from the mylar tape target showing the C V and C VI spectral lines recorded using the flat field grating spectrometer.

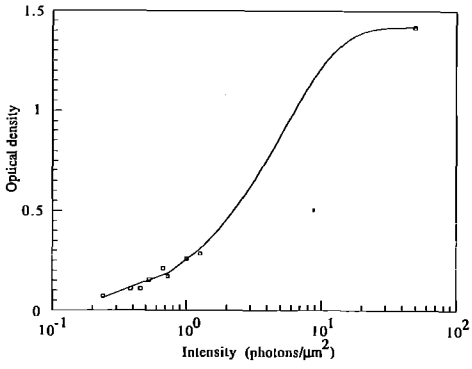

Figure 2:- Calibration curve for Kodak 104-02 soft x-ray film.

Henke has given an equation relating the photon flux on film to the optical density for monolayer emulsion-type films eg. Kodak 104-02 as

$$D = \{1 - \exp(-CI)\} D_{sat} \qquad \text{--- (1)}$$

where I is the intensity corresponding to a particular optical density D, D_{sat} is the saturation density on the film and C is a constant depending on the characteristics of the film such as grain size and emulsion thickness. A calibration for the Kodak 104-02 film was then obtained by fitting equation 1 above to the experimental data

(see figure 2). In the same way, by comparison to previous calibrations, calibration curves were obtained for UF-SH4 Shanghai 5F film and are shown in figures 3 & 4 respectively. The same 1200 lines / mm flat field grating was used for all the calibrations and a grating reflectivity ~ 14% obtained. Spectra were also obtained using a grating having a period of 2400 lines/mm. A higher grating reflectivity of ~ 21 %. was deduced for this grating by comparing the optical density corresponding to a particular value of x-ray flux to the absolute value obtained from a previous calibration curve as described in the case of the 1200 lines/mm grating.

A copper tape target irradiated by single shots from the KrF laser and providing 1.2 keV hard x-rays was used for time resolution studies. The streaked image was recorded on optical HP-5 film after the x-rays were converted to optical emission using a phosphor-image intensifier combination. Figure 5 shows a densitometer trace of a streaked image of x-rays from a copper target irradiated by a pulse train (20 ns long) comprised of individual 8 ps pulses from the KrF laser. The KrF laser was then set to provide single 8 ps pulses per shot and a streaked image of the x-ray emission obtained (see figure 6). It is clear that the x-ray emission is coincident with the laser pulses and that there is not additional emission per pulse with the pulsetrain. The duration of the x-ray emission from a single pulse was measured to be 55 ps (FWHM). However, this value does not give an accurate estimate of the duration of the x-ray emission as the CsI photocathode used has a fluorescence time which limits the temporal resolution of the streak camera. It is likely that the value of 55 ps deduced thus gives an estimate of the fluorescence time of the CsI photocathode and that the x-ray emission time is shorter.

CONCLUSIONS

The laser plasma x-ray source in the Laser Support Facility has been used to determine the reflectivities of flat field gratings and also to obtain calibration curves for different types of x-ray film. An x-ray streak camera was used to study the temporal behaviour of the x-ray source and a photocathode-limited value for the duration of the x-ray emission from a single pulse obtained.

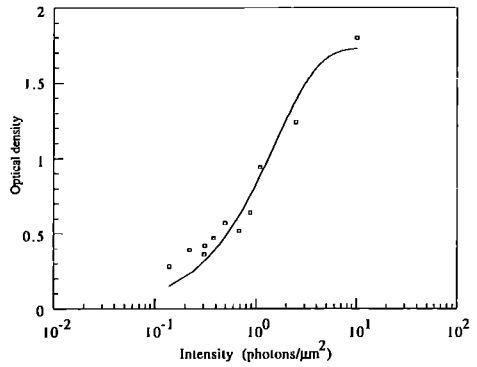

Figure 3:- Calibration curve for UF-SH4 soft x-ray film.

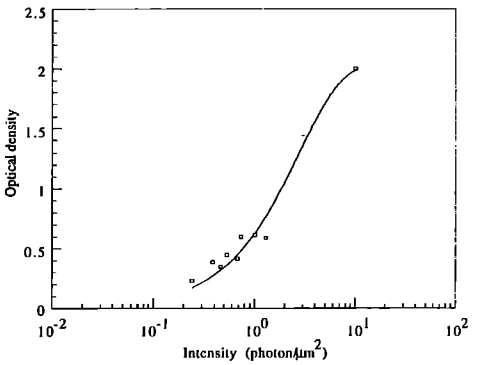

Figure 4:- Calibration curve for Shanghai 5F x-ray film.

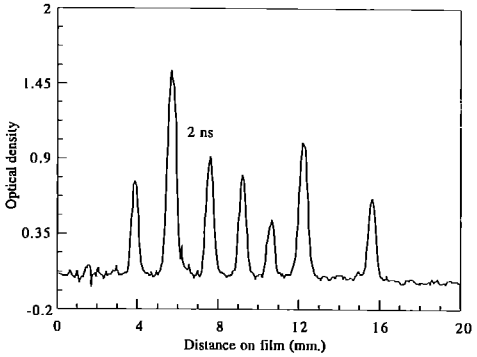

Figure 5:- Time resolved x-ray emission from a copper plasma created by a laser pulse train (20 ns long) comprised of individual pulses (8 ps long).

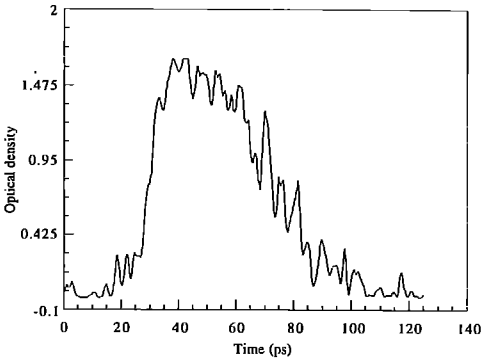

Figure 6:- Time resolved image of x-ray emission from a copper plasma created by a single 8 ps driving laser pulse.

REFERENCES

1. T. Kita et.al. 1983 Appl. Opt. 22, 512
2. F. O'Neill et.al. 1989 Appl. Phys. Lett. 55, p. 2603.
3. J. Krishnan et.al. 1992 RAL Annual Report (RAL-92-020), p. 22.

COLLISIONAL ALIGNMENT OF MOLECULES IN HIGH PRESSURE FLUID JETS

A.J.Bain, G.Butcher-Taylor and P.Chandna

Department of Physics, University of Essex

INTRODUCTION

Ordered molecular arrays and the mechanisms by which they are produced is an area of considerable scientific and technological interest. Both the linear and nonlinear optical responses of a medium are strongly influenced by the degree of ordering of its component parts. Second order nonlinear optical responses for instance are forbidden in centrosymmetric media[1] whilst the coupling between optical fields via $\chi^{(3)}$ in degenerate four-wave mixing and transient grating phenomena can be significantly enhanced by the presence of molecular ordering[2].

The imposition of order in an otherwise isotropic fluid is achieved by the application of external forces which act in opposition to the randomising effects of Brownian motion. The application of an external electric field to produce bulk orientation and alignment via dipole and induced dipole interactions is well known and forms the basis of Electric Field Induced Second Harmonic Generation (EFISH) technique[3] and electric dichroism and birefringence phenomena (Electro Optic Kerr Effect)[4]. The degree of anisotropy induced in these instances is small, the orientational distribution function for the dipolar array in polar coordinates being given by

$$P(\theta,\phi) = \frac{\exp(-\mu E / kT)\cos\theta}{\int_0^{2\pi} d\phi \int_0^{\pi} \sin\theta d\theta . \exp(-\mu E / kT)\cos\theta} \qquad (1)$$

where θ is the angle between the applied electric field and the permanent molecular dipole moment μ. Even for highly polar molecules (μ~20 Debye) practible values of (μE/kT) are small (c.a. 0.06) resulting in only weakly anisotropic arrays and as such (with the exception of liquid crystals) the technique has limited application.

An alternative approach is to generate molecular alignment via the shear (collisional) forces generated by laminar fluid flow, the observation of induced birefringence in flowing canada balsam by Maxwell in 1873 being the first experimental observation of the coupling between molecular ordering and the linear optical properties of a medium. Until recently the only application of these principles to fluid media has been the Couette technique in which a velocity gradient is used to align anisotropic solute molecules in a solution confined between counter rotating concentric cylinders[5-8]. The torques generated by such mechanical means are weak and consequently Couette flow has only been successfully applied to the alignment of macromolecules such as DNA.

EXPERIMENTAL

A recent series of pilot experiments by us at RAL has demonstrated that it is possible to produce highly ordered arrays of small to medium sized molecules (Resorufin and R6-G) at the exit face of 100μm and 500μm sapphire nozzles using ethylene glycol and polyethylene glycol jets[9,10]. Using a novel polarisation resolved picosecond time correlated single photon counting technique (TCSPC) we have been able to measure the intrinsic alignment of these arrays and to determine the nature of the angle dependent intermolecular potential responsible for the alignment (fig 2). Well depths as large as 0.7 kT have been measured yielding intrinsic alignment factors that are over an order of magnitude greater than those achievable by the imposition of strong DC electric fields. A further refinement of the technique involves variable excitation polarisation, enabling the photoselection of a range of non-equilibrium orientational

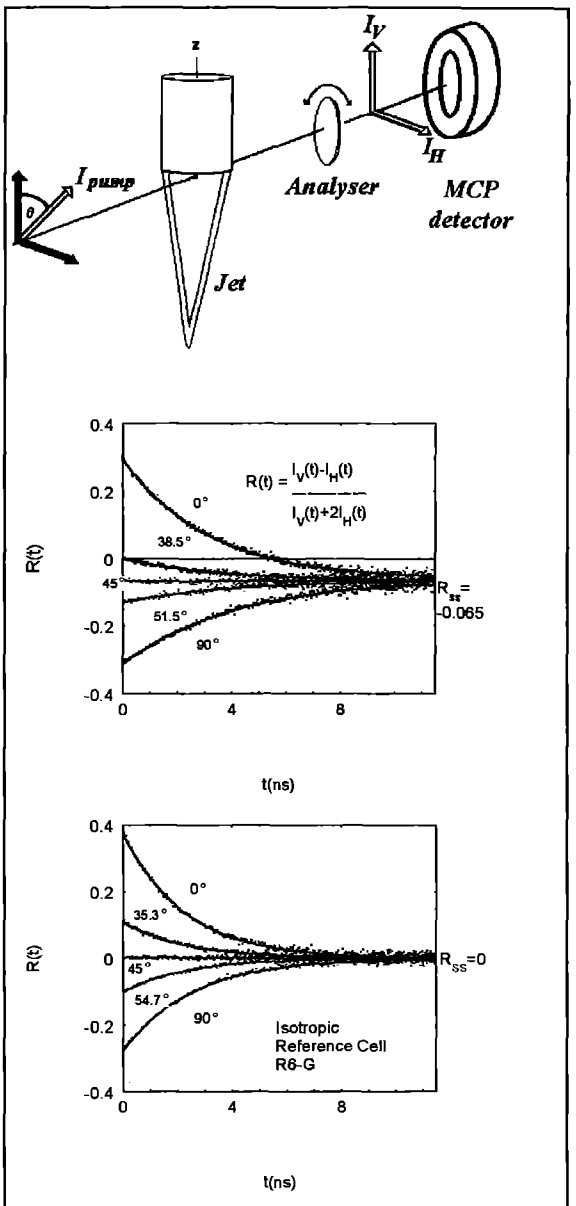

Figure 1 A schematic of the excitation and detection parameters involved in our pilot experiment. A jet of R6-G (1.4×10^{-4}M) is produced from a 100μm sapphire nozzle. Fluorescence is excited by cavity dumped dye laser pulses which are focused to ca 100μ m spot. The jet can be translated or rotated with respect to this position allowing the investigation of the spatial anisotropy inherent in the system. The excitation polarisation angle is varied from θ = 0° (parallel to the jet axis) to θ = 90° and the corresponding jet fixed fluorescence polarisation observables $I_V(t)$ and $I_H(t)$ are built up by repeated alternation of the computer controlled polarisation analyser between vertical and horizontal settings.
Irrespective of the excitation angle θ, the fluorescence anisotropy is seen to return to a steady state (or intrinsic) value R_{SS}.
Shown for comparison are the anisotropy decays measured by the same system for an identical but static solution of R6-G

distributions and the subsequent relaxation back to the equilibrium configuration (fig 1). The symmetry breaking presence of the aligning potential permits the observation of orientational processes forbidden in isotropic media (figs. 1 and 3).

The fundamental rate constants obtainable from these measurements together with those from an otherwise identical but isotropic system and the angle dependent potential surface, constitute the most complete picture now available of the directional nature of molecular collisions and the role of frictional forces at the molecular level.

ANALYSIS

The orientational probability distribution function for an ordered assembly of oriented molecules is most conveniently expressed as an expansion of spherical harmonics.

$$P(\theta,\phi,t) = \frac{1}{4\pi}\left(1 + \sum_{K\geq 0,Q} Y_{KQ}(\theta,\phi)\langle\alpha_{KQ}(t)\rangle\right) \qquad (2)$$

The moments $\langle\alpha_{KQ}(t)\rangle$ of the distribution contain all the information on the time dependent orientational dynamics of the system following laser excitation. Single photon electric dipole selection rules restrict the polarisation observables of any excited state distribution to the cylindrically symmetric $\langle\alpha_{20}\rangle$ and cylindrically asymmetric $[\langle\alpha_{22}\rangle + \langle\alpha_{2-2}\rangle]$ alignment moments[11]. The time dependent fluorescence anisotropy measured in the jet fixed axis system, R(t) is

$$R(t) = \frac{I_V(t) - I_H(t)}{I_V(t) + 2I_H(t)} = \frac{\frac{\langle\alpha_{20}(t)\rangle}{\sqrt{5}} - \frac{1}{\sqrt{30}}\left[\langle\alpha_{22}(t)\rangle + \langle\alpha_{2-2}(t)\rangle\right]}{1 + \frac{2}{\sqrt{30}}\left[\langle\alpha_{22}(t)\rangle + \langle\alpha_{2-2}(t)\rangle\right]} \qquad (3)$$

For excitation polarised at θ=45° to the jet axis the subsequent photoselection yields an excited array for which $\langle\alpha_{20}(0)\rangle, \langle\alpha_{22}(0)\rangle$ and $\langle\alpha_{2-2}(0)\rangle$ are extremely close to their equilibrium values. R(t) is constant (R_{ss}), yielding the intrinsic anisotropy of the system which can be measured downstream from the nozzle exit (fig 2). ϕ dependent R(t) data for θ = 0° and 90° are used to investigate the cylindrical ordering of the array. All the arrays so far produced are cylindrically symmetric and the R_{ss} data is then used to construct the angle dependent potential energy surface (E(θ)) for the equilibrium distribution. Variation of θ permits the photoselection of a range of non-equilibrium orientational distributions by changing the initial values of the excited state alignment moments. The relaxation of these distributions strongly depends on E(θ). One of the most striking features of the symmetry breaking due to the E(θ) is the direct observation of the collisional ordering of an initially "isotropic" array (fig 3).

The relaxation dynamics of the individual moments of the system are observed to be linear i.e.

$$\frac{\partial}{\partial t}\left[\langle\alpha_{KQ}(t)\rangle - \langle\alpha_{KQ}(ss)\rangle\right] = -\gamma_{KQ}\left[\langle\alpha_{KQ}(t)\rangle - \langle\alpha_{KQ}(ss)\rangle\right]$$

$$\left[\langle\alpha_{KQ}(t)\rangle - \langle\alpha_{KQ}(ss)\rangle\right] = \left[\langle\alpha_{KQ}(0)\rangle - \langle\alpha_{KQ}(ss)\rangle\right]\exp\left(-\gamma_{KQ}t\right) \qquad (4)$$

Under isotropic conditions each moment $\langle\alpha_{KQ}\rangle$ relaxes independently and the rate constants γ_{KQ} are related by simple symmetry factors[12]. An obvious consequence is that $\gamma_{20} = \gamma_{2Q}$. The effect of E($\theta$) is to break this restriction. Our primary results following a self-consistent R(t), θ analysis indicate that

γ_{20}(isotropic) = 4.5 x $10^8 s^{-1}$ > $\gamma_{2\pm2}$ (jet) = 3.8 x $10^8 s^{-1}$ > γ_{20} (jet) = 3.2 x $10^8 s^{-1}$

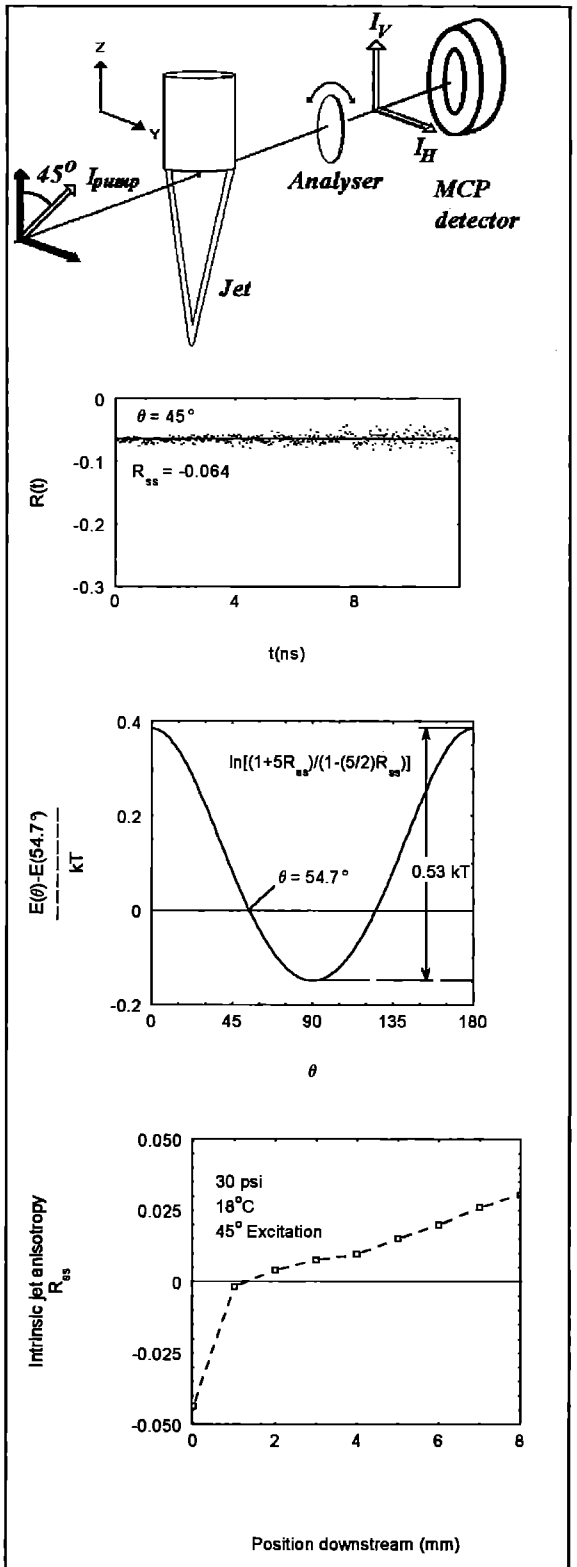

Figure 2 For the excitation polarised at θ = 45° to the jet axis, the excited state orientational distribution function suffers little disturbance from its intrinsic or steady state form. The fluorescence anisotropy R(t) is (to within experimental error) a constant R_{ss}. The R_{ss} date can be inverted to yield the angle dependent intermolecular potential generated by the shear flow. Translation of the jet with respect to the laser axis enables a picture of the spatial dependence of R_{ss} and hence E(θ) to be built up.

The physical reason for this behaviour is that different torques are exerted on the $\langle \alpha_{20}(0) \rangle$ and $\langle \alpha_{2\pm2}(0) \rangle$ moments. In addition, off diagonal relaxation due to the interconversion of photoselected but non-optically active moments (K'>2; Q'≠ 0,2) of the distribution is also possible.This can easily be seen from a simple treatment of Debye-type orientational relaxation in the presence of an external potential E(θ). In such instances, the time dependent orientational probability distribution function is given by P(θ,ϕ,t)[13]

$$\frac{\partial}{\partial t}\left[P(\theta,\phi,t)-P(\theta,\phi,ss)\right]=-\hat{H}\left[P(\theta,\phi,t)-P(\theta,\phi,ss)\right] \quad (5)$$

where P(θ,ϕ,ss) is the steady state or equilibrium distribution function and $\hat{H}$ is a Markovian relaxation operator of the form[14]

$$\hat{H}=-D\nabla^2-D\nabla^2\left(\nabla E(\theta)/kT\right) \quad (6)$$

where D is the molecular diffusion coeffecient for rotational motion perpendicular to the symmetry axis.
Expanding P(θ,ϕ,t) in terms of spherical harmonics as above, the time dependent moments $\langle \alpha_{KQ}(t) \rangle$ are given by[15]

$$\langle \alpha_{KQ}(t)\rangle-\langle \alpha_{KQ}(ss)\rangle=$$
$$(\exp-K(K+1)Dt)\sum_{K'}\langle KQ|\exp\left\{-D\nabla^2\left(\frac{\nabla E(\theta)}{kT}\right)t\right\}|K'Q\rangle$$
$$\times\left\{\langle \alpha_{K'Q}(t)\rangle-\langle \alpha_{K'Q}(ss)\rangle\right\} \quad (7)$$

The $\nabla E(\theta)$ term represents the gradient, or torque generated by the effective intermolecular potential E(θ) and plays the role of coupling the otherwise orthogonal moments of P(θ,ϕ,t).

Steady state, R_{ss}, and initial anisotropy measurements, R(0), can be used to determine the quadrupolar (K=2) and hexadecapolar (K=4) contributions to E(θ). The diffusion equation can then be numerically solved with this input to yield predicted γ_{KQ} values which can be directly compared with the experimental data obtained from our R(t) vs. θ measurements. This approach allows a test of fundamental theory in a manner not permitted by conventional time resolved fluorescence anisotropy and four wave mixing studies, which invariably observe molecular motion averaged over an isotropic collisional background[11].

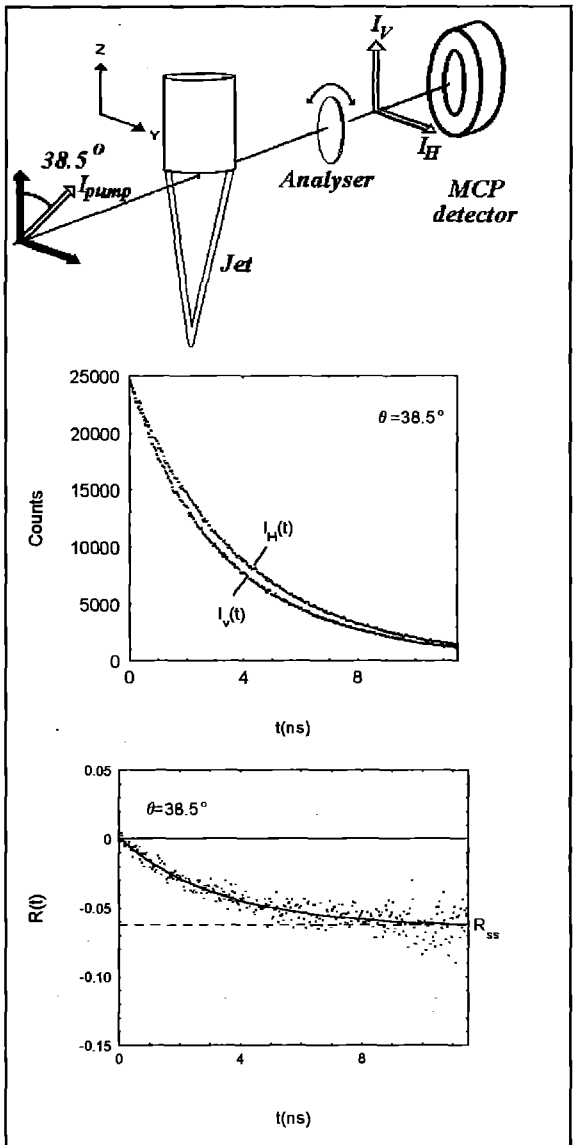

Figure 3 It is possible to find an excitation polarisation angle for which the initial excited state distribution appears isotropic $\left(\langle \alpha_{20}(0)\rangle=(1/\sqrt{6})\left[\langle \alpha_{22}(0)\rangle+\langle \alpha_{2-2}(0)\rangle\right]\right)$ and R(0) = 0.
The anisotropic torques generated by E(θ) result in the direct collisional ordering of this distribution to its steady state configuration.The R(t) vs. θ data produced from this and other experiments (figure 1) is then used to extract the γ_{20} and $\gamma_{2\pm2}$ relaxation rates for the system.

REFERENCES

1. Y.R.Shen, Principles of Nonlinear Optics, Wiley, New York, (1984).
2. W.R.Thompkin, M.S.Malcut, R.W.Boyd and J.E.Sipe, J. Opt. Soc. Am., 6, 757, (1990).
3. K.D.Singer and A.F.Garito, J. Chem. Phys., 75, 3572, (1981).
4. H.Benoit, Ann. Phys., 6, 561, (1951).
5. M.Couett, Ann. Chim. Phys., 21, 433, (1890).
6. J.T.Edsall, Adv. Colloid Sci., 1, 296, (1942).
7. A.Peterlin and H.A.Stuart, Hand u Jahrb, Chem. Phys., 8, Becher and Leipzig, (1943).
8. W.Heller, R.Tabibian, M.Nakagaki and L.Papazian, J. Chem. Phys., 52, 4294, (1970).
9. P.Chandna, A.J.Bain, A.J.Langley, M.Towrie and P.Matousek, RAL CLF Annual Report, 227, (1993).
10. A.J.Bain and P.Chandna, submitted to Nature.
11. A.J.Bain, D. Phil. Thesis, University of Sussex, (1984).
12. B.Berne and R.Pecora, Dynamic Light Scattering, Wiley, New York, (1976).
13. K.Blum, Density Matrix Theory and Applications, Plenum Press, New York, (1981).
14. G.R.Luckhurst, M.Setaka and C.Zannoni, Mol. Phys., 28, 49, (1974).
15. A.J.Bain and P.Chandna, to be published

LASER SUPPORT FACILITY: OPERATIONS AND DEVELOPMENT

A total number of 46 RAL-based user experiments were scheduled - an increase of 12% over the previous year - and 15 experiments were carried out in university laboratories using lasers from the LSF loan pool. The number of scheduled user experiments, and weeks of scheduled time, have increased at an average rate of 13% per year (Fig. 1). The distribution by subject is shown in Table 1.

Table 1

1993/94	Physics	Chemistry	Biology
Applications %	29	59	12

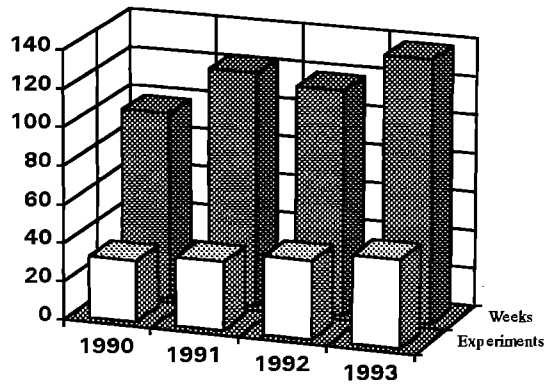

Figure 1

Major equipment currently available is shown in table 2. Funding has been obtained through Research Grants and external contracts to replace and upgrade the equipment in the Laser Loan Pool, the Picosecond Laboratory and the X-Ray Laboratory. Work will begin in the coming year.

FEMTOSECOND LASER LABORATORY

Andrew Langley, Waseem Shaikh, Phil Taday and Tanvir Alam

During the year there were 9 scheduled user experiments with the amplified 100 fs titanium sapphire laser. These are reported in more detail elsewhere within this year's annual report and include studies of excitons in multiple quantum wells, charge transfer complexes, the kinetic behaviour of photochromic materials, and experiments in multiphoton ionisation. Of the 41 weeks available on the system, 83% of this time was used for user experiments. The remaining time, i.e. about 3.5 days per month, was spent in preparing for these experiments i.e. installing and testing a new argon ion laser, building optical layouts, constructing and testing an autocorrelator, beam monitor and spectrometer. There was virtually no equipment down time during scheduled experiments apart from routine maintenance of about 3 hours per week.

A new Spectra-Physics 2080 argon-ion laser was acquired to pump the mode-locked titanium sapphire TiS laser (Tsunami), thus replacing the old 171 pump laser. This has resulted in improved stability and reliability whilst the increased power will allow us to respond to user demand to expand the wavelength capability of the TiS laser.

THE PICOSECOND LABORATORY

Mike Towrie and Pavel Matousek

This year there have been a total of 12 scheduled experiments, 9 using the time correlated single photon counting system and 3 using the picosecond time-resolved resonance Raman (ps-TR^3) apparatus.

The Picosecond Facility has received funding for an important upgrade. This will comprise of a broadly tunable high repetition rate picosecond laser system based on optical parametric oscillator technology and is to be built in a collaboration between RAL and the ORC in Southampton. The system will provide two independently tuneable outputs and access to spectrally important wavelengths in the blue and IR that cannot be obtained by the present apparatus. The high repetition rate will enable high statistics data to be obtained using lower peak intensities than at present and avoiding nonlinear effects

The time-correlated photon counting (TCSPC) apparatus has been used in a number of experiments in gas, solution and solid phase. An automated system for making accurate anisotropy measurements was developed by Bain, Chandna (Essex) and Noad (LSF) and used in their anisotropic flow studies . Wavelength selection of the fluorescence emission has been improved by the provision of a small monochromator.

Earlier ps- TR^3 studies on the early dynamics of S_1 trans-stilbene were extended into the anti-Stokes region. From very high quality spectra we have the first direct evidence of vibrational relaxation in the S_1 state of trans-stilbene following photo-excitation. The relaxation rates of the higher lying modes appear strongly correlated to the rate of the changes observed in the Stokes spectra.

The ps -TR^3 apparatus has also been used in a number of preliminary studies. For example in a scheduled experiment on ion formation and separation by Phillips (IC)/Vauthey (Fribourg)/Parker (LSF) and on the photoisomerism of spiro-oxazines by Wilkinson (Loughborough) which complemented their time resolved absorption studies using the Femtosecond Facility.

NANOSECOND LABORATORY

Anthony W. Parker and Susan M. Tavender

A total of 14 experiments were scheduled this year in the ns-laser lab. Lost experimental time caused by major equipment failures was one week.

During the first few weeks of the year the laser X-ray source was moved out of laser lab A. The new arrangement for labs A and B is shown in Figure 2. Lab A now houses the two Raman spectrographs and cw argon ion laser and provides a safe work station area for users of this equipment. The additional space in lab B provides better accommodation for experiments requiring the temporary installation of large pieces of user equipment. The separation of the lasers also allows small development projects to be carried out when only one area is occupied for a user experiment. Space has also been made available for the fluorescence/Raman microscope (funded grant Phillips/ MacRobert /Parker). to be purchased mid 1994.

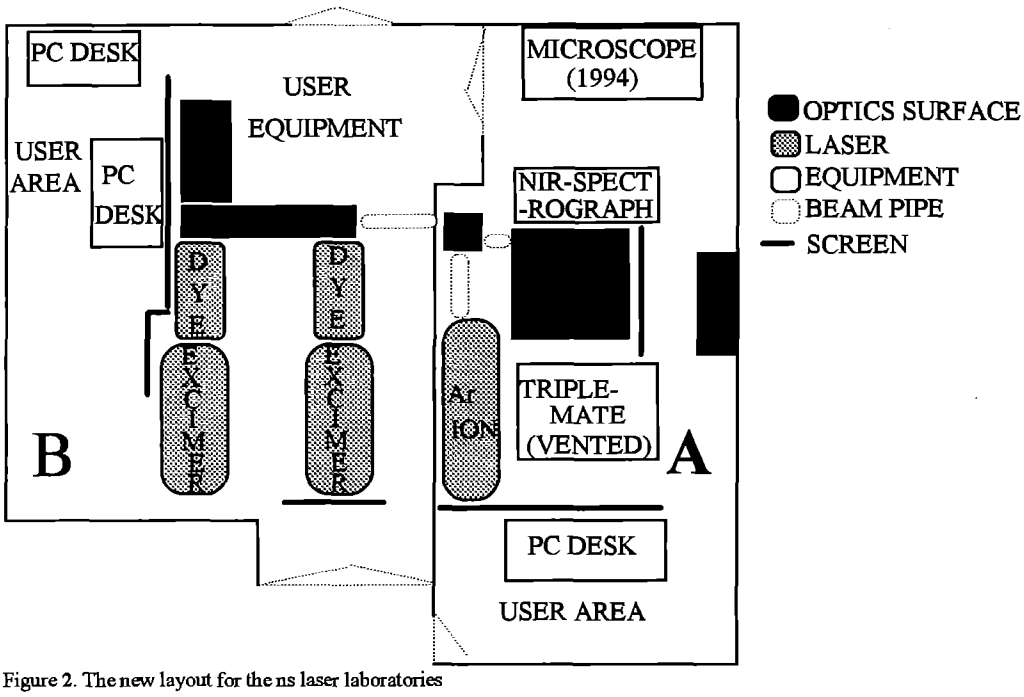

Figure 2. The new layout for the ns laser laboratories

On the science side the new CCD Raman detector has started to produce results for the Keele/RAL collaboration studying the resonance Raman spectra of carotenoid anion and cation radicals. The detector has also benefited other users, e.g. in studying 4-thiothymidine incorporated oligonucleotides (Connolly) and spectral quality has been much improved (*c.* 20 times signal-to-noise improvement) from the earlier work using the diode array. The phthalocyanine study by Phillips *et al.* (IC) has now started to investigate the photochemistry of alkyl substituted phthalocyanines in collaboration with Russell and Cooke (UEA). The geminate ion pair work (Vauthey/Phillips/Parker) has used ns-TR^3 to measure the intrinsic energy barrier for the separation of a radical cation and radical anion formed from a photochemical electron transfer reaction. This group has begun to develop suitable chemical systems for extending this work into the picosecond time regime where Marcus theory can be tested in more polar solvents.

Dr Simpson (Oxford) has continued his collaboration with Towrie on the photolysis of physisorbed $(NO)_2$ using REMPI and has shown that when the surface is MgF_2 the vibrational deactivation of nascent NO molecules is inefficient

LASER-PLASMA X-RAY LABORATORY
Edmond Turcu

The "High Average Power Laser-Plasma X-Ray Source" moved into a new, larger laboratory, which allows more space for the laser system, the X-ray source and the user experiments. This has improved substantially the safety of the laboratory in its complex, multilaser/multiwavelength mode of operation.

Ten experiments were performed in the laboratory in 1993, of which five have used the picosecond X-ray source and five, just the flourine excimer lasers. The DNA research continued successfuly both using UV and X-ray pulses. A new record was achieved in X-ray dose rate delivered to biological cells: 3.5KRad/s. Experiments in X-ray lithography have demonstrated good fidelity printing of 0.18μm lines with exposure times of 5min. Development of an X-ray beamline using MCP X-ray optics resulted in $\sim 10^{11}$photons/s focused in 1mm diameter spot, at $h\nu \sim 0.4$KeV photon energy.

The X-ray work resulted in eleven publications and was presented at a number of international conferences of which we mention: CLEO93, Microcircuit Eng 93 and Applications of Laser Plasmas. A scientific video was produced by the University of Birmingham and RAL: "How Do Cells Repair DNA?". A patent application was made on: Laser Excited X-Ray Sources.

LASER LOAN POOL
Mike Towrie

This year there has been a total of 12 chemistry and 3 physics based loans of six months. The lasers have been used in the study of gas phase reaction kinetics, photo-desorption processes, the spectroscopy of organo-metallic compounds, photorefractive waveguides and oceanic wave mechanics. Much of this work appears in this years Annual Report.

A grant has been awarded for the upgrade of the Loan Pool which was begining to suffer seriously from underinvestment both in the number of laser systems and in their quality. The User community has been consulted to help establish the specifications for new laser systems. The "Case for Support" stressed the new opportunities that have arisen from the recent developments in solid state laser technology (optical parametric oscillators) which give access to a broad spectrum of radiation from the UV to the infrared. The present status of the Loan Pool is given in Table 2.

Table 2: Major Laser Support Facility Equipment

	Laser (Wavelength range/max pulse energy/pulse length/max rep rate)	Main Uses
RAL BASED LASERS	Two excimer pumped dye lasers (200-950 nm/20 mJ/30 Hz)	ns-TR^3, Raman, fluorescence, laser flash photolysis, REMPI. Delays from ms to ns.
	Laser-plasma X-ray source (3, 1, 0.7 nm) 200 mW average power, 100 Hz, 3.5 krad/s dose rate at specimen	DNA damage and repair, lithography, microscopy, calibration.
	UV fluoride excimer laser (157, 193, 222, 248 nm/400 mJ/20 ns or 4 ps for 248 nm using YAG laser seed pulse 100 Hz)	DNA damage and repair, flash photolysis, singlet oxygen reactions, mutation studies.
	Argon ion (525, 514, 488, 457, 364, 353 nm/cw source)	Raman spectroscopy
	cw argon ion (all lines) pumped mode-locked titanium sapphire laser (100 fs, 10 nJ, 720-820 nm) seeding a Q-switched Nd:YAG pumped dye amplifier (740-800 nm/400 μJ 370-445 nm/30 μJ)	Transient absorption spectroscopy (using continuum generation), multiphoton-ionisation (10^{16} Wcm^{-2})
	Copper vapour pumped amplifier system (550-655 nm/55 μJ/6 ps/4.5 kHz)	ps-TR^3
	Modelocked Nd:YAG pumped cavity dumped dye laser (560-640 nm/20 nJ/4 ps/4 MHz)	Single photon counting
LASER LOAN POOL	Quanta Ray GCR-11 (1064 nm/320 mJ, 523 nm/155m J, 355 nm/70 mJ, 266 nm/30 mJ/10 Hz) with PDL-3 dye laser (400-900 nm/45 mJ/<0.08 cm^{-1} bandwidth)	Transient spectroscopy, photolysis and reaction kinetics
	JK Hyperyag 750 (1064 nm/700 mJ, 532 nm/200 mJ, 355 nm/40 mJ, 266 nm/10 mJ/20 Hz) with PDL-2 dye laser (400-900 nm/40 mJ/0.1 cm^{-1} bandwidth)	Transient spectroscopy, photolysis and reaction kinetics
	Spectron (1064 nm/580 mJ, 532 nm/180 mJ, 355 nm/35 mJ, 266 nm/10 mJ/10 Hz) with PDL-2 dye laser (400-900 nm/40 mJ/0.1 cm^{-1} bandwidth)	Transient spectroscopy, photolysis and reaction kinetics
	Spectra Physics 2025 Argon Ion (5 W visible/0.4 W UV single line)	Gas phase kinetics, particle image velocimetry and semiconductor science
	Spectra Physics titanium sapphire system (680-1040 nm/500 mW)	IR Raman studies, fibre amplifier and waveguide studies
	Fluorine Excimer laser (157 nm/10 mJ, 193 nm/400 mJ, 249 nm/600 mJ, 351 nm/300 mJ)	Photolysis source and laser ionisation
	RE-EQUIPMENT: SEE TEXT	

AMPLIFIED FEMTOSECOND LASER FACILITY DEVELOPMENT

T Alam, A J Langley, W Shaikh and P F Taday

Rutherford Appleton Laboratory

Last year[1,2] we reported on the development of a high brightness laser using a titanium sapphire oscillator and amplification in laser dyes to produce >0.3 mJ pulses of ≈100 fs duration at 740 nm. This system has been used to study[3] the dynamics of carrier relaxation in quantum wells, multiphoton ionisation of various atomic species and the fast photo physics of photochromic materials. Many of these experiments required the generation of short pulses in the UV and blue spectral region in addition to the near IR. The typical performance obtained is shown in the table below.

Wavelength / nm	Method	Amplified Energy / μJ	Pulse Length / fs
760	Fundamental	220	100
750	"	300	100
725	"	300	120
720	"	320	120
400-900	Continuum	>10 nJ / nm	-
436	Mixing 740 nm & 1064 nm YAG	1	-
370	Doubling 740 nm	40	-

PULSE CHARACTERISATION

Measurements to routinely characterise laser pulses are vital in ultra-short laser experiments. A new single-shot autocorrelator was developed which contained entirely non-dispersive optical components, apart from a 0.5 mm thick doubling crystal (BBO type I), in order to maximise the achievable temporal resolution. A plan of the autocorrelator is shown in figure 2. The incoming amplified pulses were split at a 50 % reflecting pellicle beam splitter. A corner cube retroreflector mounted on a micrometer adjusted slide acted as a variable optical delay line for calibration purposes. The beams were recombined at the 4.0 x 4.0 mm BBO crystal by focusing with a 250 mm focal length cylindrical mirror obtained by coating a 1000 mm focal length negative lens with aluminium. The UV generated at the crystal was filtered and imaged to a UV sensitive Pulnix TM 765 CCD camera. The estimated resolution of the autocorrelator is 30 fs which implies a 100 fs pulse can be measured to an accuracy of 5%. The autocorrelation image was transferred to a frame store (Oxford Framestores Applications Ltd) simultaneously with a single shot spectrum obtained from a second camera attached to a 0.25 m spectrometer.

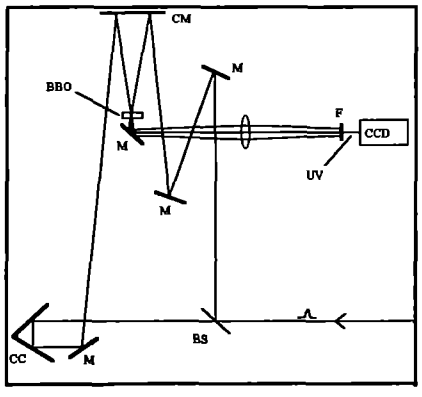

Figure 1 Plan of the single-shot autocorrelator. Pellicle beam splitter BS, mirror M, corner-cube retro-reflector CC, cylindrical mirror CM, filter F.

A single shot autocorrelation and spectrum of an amplified pulse are shown in figure 2 and give a the time-bandwidth product is 0.32 implying Fourier transform limited $sech^2$ pulses. Typically, amplified pulse durations were around 100 fs and the shortest pulses observed were 88 fs. These pulses were ≈20 % shorter than those reported previously[2] and this is consistent with our using a wider (30 nm fwhm) ASE attenuation filter in the dye amplifier rather than the 10 nm filter used earlier.

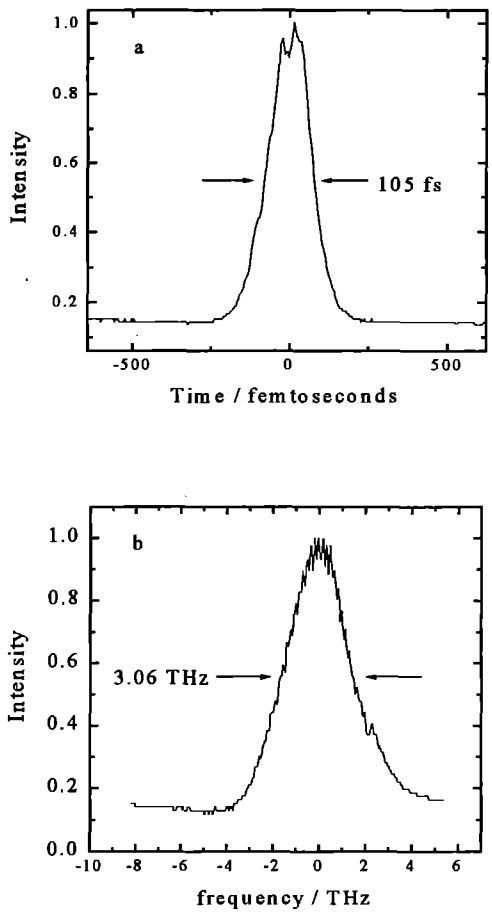

Figure 2 Single-shot autocorrelation (a) and spectrum (b) of an amplified laser pulse

The laser and diagnostics for pulse characterisation together with the wavelengths available are shown schematically in figure 3.

REFERENCES

1. A J Langley, W J Noad, I N Ross and W Shaikh. CLF Annual Report 221 (1993).

2. In press. A J Langley, W J Noad, I N Ross and W Shaikh. Applied Optics. (1994)

3. CLF Annual Report (1994)

AMPLIFIED 100 FEMTOSECOND LASER (10Hz)

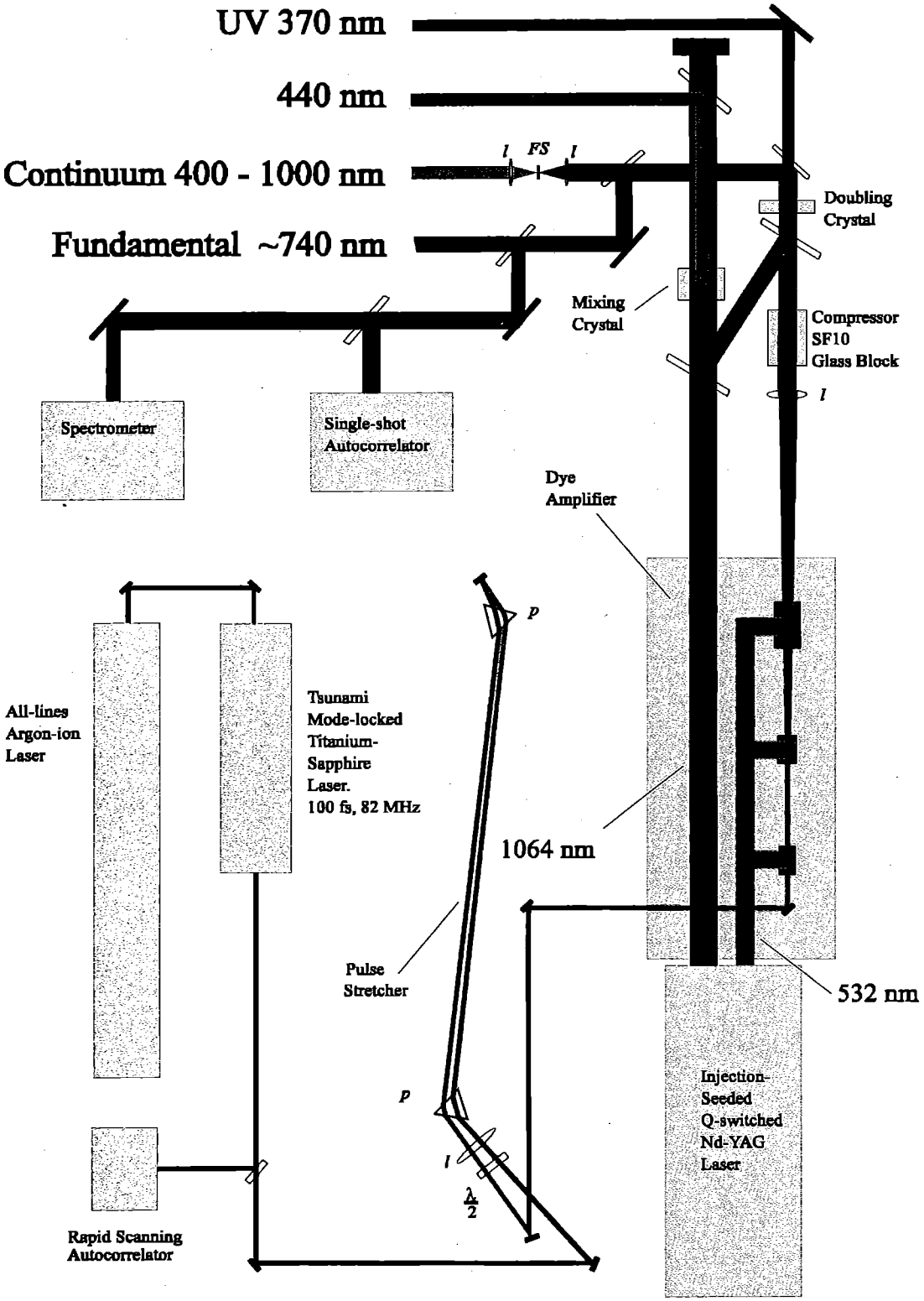

Figure 3 Plan of the 100 fs, > 300 μJ, near infra-red pulsed laser system available for user experiments, showing the short pulse oscillator (Tsunami), three stage dye-amplifier and other wavelengths generated. Key: half wave-plate λ/2, lens *l*, prism p, fused silica disk FS.

DEVELOPMENT OF A TRANSIENT ABSORPTION SPECTROMETER USING LASER PULSES OF 100 fs DURATION AND CCD DETECTION

A J Langley, W Shaikh and P F Taday

Rutherford Appleton Laboratory

INTRODUCTION

Good quality kinetic transient absorption measurements using short laser pulses and discrete probe wavelengths have been possible at the Central Laser Facility for some years[1]. There has been considerable interest in extending the system capability to obtain simultaneous multichanel spectral and kinetic transient information and we report here on a recently initiated development programme to achieve this.

INSTRUMENT DEVELOPMENT

The apparatus we are in the process of developing at RAL is shown schematically in figure 1. The laser source used in these measurements is described in the previous article and in more detail elsewhere[2]. The incoming 100 fs laser pulses, at a wavelength around 750 nm, were split at a pellicle beam splitter. The pump beam was relayed to the sample via an optical delay line consisting of a corner-cube retroreflector mounted on a computer controlled 760 mm long slide. The forward transmitted beam at the pellicle beam splitter was focused into a 3 mm thick fused silica disk to generate a "white light" continuum between 400-1000 nm as a probe. The disk was slowly rotated in a plane perpendicular to the beam axis to avoid thermal distortion of the probe beam. The probe was then split before reaching the sample to produce two beams, one to probe the pumped region of the sample and the other to act as a reference.

Excellent signal to noise has been achieved in earlier transient absorption kinetics experiments[1] with discrete probe wavelengths by careful splitting of the probe to ensure close similarity between the probe and reference beams. Signal-to-noise >100 with a background noise of $\pm 2\times10^{-4}$ in absorbance units was achieved averaging over 100 laser pulses. Splitting the beams in the current system was achieved by using a thin (thickness ≈3 mm) uncoated 5^{o} wedged beam splitter and two mirrors as shown in figure 2. The advantage of this method is that for a given wavelength λ the intensities of the two probe beams, $I_1(\lambda)$ and $I_2(\lambda)$, are nearly identical i.e.

$$I_1(\lambda) = I(\lambda)r_1(\lambda)r_2(\lambda)\{1 - r_1(\lambda)\}\{1 - r_3(\lambda)\} \qquad (1)$$

and

$$I_2(\lambda) = I(\lambda)r_3(\lambda)r_4(\lambda)\{1 - r_1(\lambda)\}\{1 - r_3(\lambda)\} \qquad (2)$$

where $I(\lambda)$ is the incident intensity whilst $r_1(\lambda)$, $r_2(\lambda)$, $r_3(\lambda)$ and $r_4(\lambda)$ are the surface reflectivities shown in figure 2. The probe and reference probe beams will have identical intensities if $r_1(\lambda)r_2(\lambda) = r_3(\lambda)r_4(\lambda)$. A disadvantage of this method is that it is very wasteful of light, though our continuum beam is sufficiently intense for this not to be a problem. For example from equation (1) if $r_1(\lambda) = r_3(\lambda) = 0.10$ then $I_1(\lambda) = 0.08r_2(\lambda)I(\lambda)$ and similarly the maximum value of $I_1(\lambda)$ is only $0.15r_2(\lambda)I(\lambda)$ when $r_1(\lambda) = r_3(\lambda) = 0.33$.

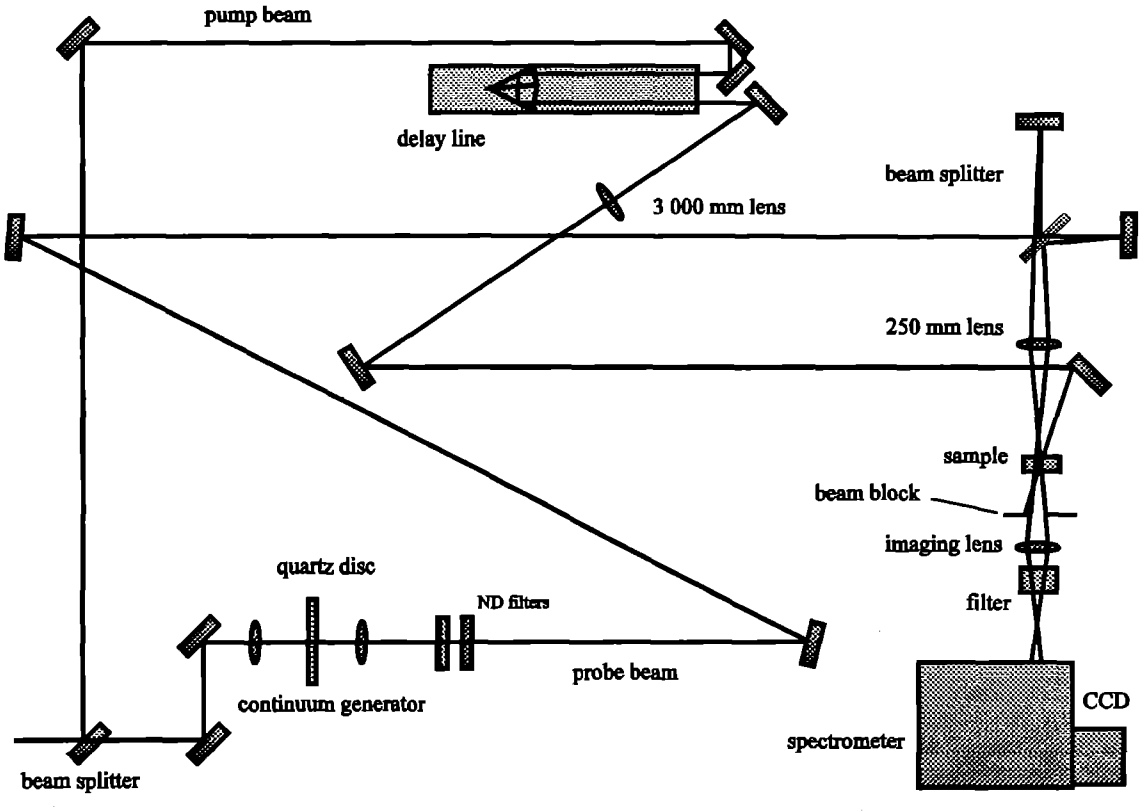

Figure 1 Femtosecond transient absorption apparatus

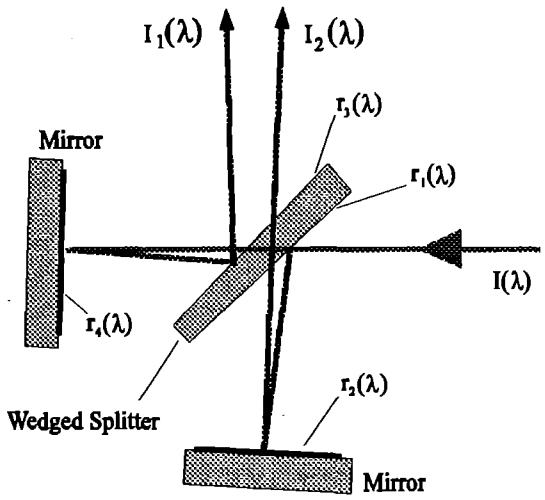

Figure 2 Probe splitter

We were concerned that the wedged beam splitter may introduce either positive or negative pulse chirp or a pulse front delay[3] across the 10 mm diameter beam. Autocorrelation measurements of the pulses after the wedge indicate no measurable stretch of the pulses at 740 nm. The chirp in the blue will be more significant but cannot be measured easily. However, the advantages of using the wedged splitter for the purposes of this development exercise outweighed the problems which anyway can be overcome by placing another identical wedged splitter in the outgoing beam to correct for pulse tilt.

The probe beam was filtered before the sample to reduce intensity near the laser wavelength and after the sample to reduce scattered pump light. The pump beam was blocked after the sample and the two probe beams were imaged, displaced from one another, onto the slit of a 270M SPEX imaging spectrometer. A spectrometer slit width of 0.8 mm was used together with a 300 lines/mm grating (blazed at 500 nm) to achieve a resolution of about 10 nm. The probe and reference spectra were measured with a Peltier cooled 15 bit (256x1024 pixel) Wrights Instruments CCD with a gain of 30 photoelectrons per count. The CCD signal was transferred to a 66 MHz 486 PC for analysis.

DATA ANALYSIS

The transmission as a function of wavelength of the *i*th probe pulse at the sample can be expressed as

$$T_1(\lambda)_i = \frac{{}^{P}P_r(\lambda)_i}{I_1(\lambda)_i} \quad (3) \quad \text{and} \quad T_2(\lambda)_i = \frac{{}^{o}P_r(\lambda)_i}{I_1(\lambda)_i} \quad (4)$$

where $I_1(\lambda)$ is the incident light intensity and ${}^{P}P_r(\lambda)$ and ${}^{o}P_r(\lambda)$ are the intensities of the probe spectra in the presence and absence of the *i*th pump pulse respectively. (See figure 3).

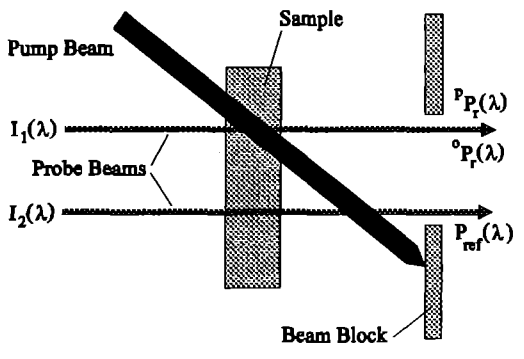

Figure 3 Pump and probe beams at the sample

The change in transmission induced by the *i*th pump pulse is

$$\Delta T(\lambda)_i = T_1(\lambda)_i - T_2(\lambda)_i \quad (5)$$

and so

$$\frac{\Delta T(\lambda)_i}{T_2(\lambda)_i} = \frac{{}^{P}p_r(\lambda)_i}{{}^{o}p_r(\lambda)_i} - 1 \quad (6)$$

We cannot of course know ${}^{o}P_r$ and ${}^{P}P_r$ simultaneously for the same laser pulse, but we have a reference probe pulse P_{ref} which we assume is related to ${}^{o}P_r$ by a constant k(λ) i.e.

$$P_{ref}(\lambda)_i = k(\lambda)_i {}^{o}P_r(\lambda)_i \quad (7)$$

The average value of k(λ) may be determined by averaging many measurements of the ratio $P_{ref}(\lambda)_j / {}^{o}P_r(\lambda)_j$ in the absence of pump pulses and can be defined as

$$\overline{k(\lambda)} = \frac{1}{m}\sum_{j=1}^{m}\frac{P_{ref}(\lambda)_j}{{}^{o}P_r(\lambda)_j} \quad (8)$$

where *m* is a large number of laser shots. The value of ΔT(λ)/T(λ) averaged over n shots is thus

$$\overline{\frac{\Delta T(\lambda)}{T(\lambda)}} = \frac{1}{n}\sum_{i=1}^{n}\left\{\overline{k(\lambda)}\frac{{}^{P}p_r(\lambda)_i}{p_{ref}(\lambda)_i} - 1\right\} \quad (9)$$

Similarly, the change in absorbance induced by the pump beam is given by

$$\Delta A(\lambda)_i = \log\frac{1}{T_1(\lambda)_i} - \log\frac{1}{T_2(\lambda)_i} \quad (10)$$

and so the value of ΔA(λ) averaged over n shots can be shown to be given by

$$\overline{\Delta A(\lambda)} = -\frac{1}{n}\sum_{i=1}^{n}\log\left\{\overline{k(\lambda)}\frac{{}^{P}P_r(\lambda)_i}{P_{ref}(\lambda)_i}\right\} \quad (11)$$

RESULTS

For the purposes of testing the transient absorption apparatus the laser dye HITCI (1,1',3,3,3',3'-Hexamethylindotricarbocyanine Iodide) was selected because it has a strong excited state absorption[4] near 500 nm probably due to the transition $S_4 \leftarrow S_1$. Figure 4 shows the transient absorption spectra of HITCI obtained at 133 fs time intervals relative to the pump pulse. The dye was pumped at a wavelength of 740 nm and the spectra were each obtained from an average of 500 laser shots using the data analysis described above. In addition to the bands near 500 nm we observed a fast transition at 595 nm with a lifetime <1 ps. We have found no mention in the literature of such a fast component and are uncertain of its origin. It is clear from these spectra that the probe pulse in the blue/green is severely chirped, although in principle this chirp can be removed. The chirp was measured in our experiment by using the optical Kerr effect[5] OKE in CCl_4 by placing a polariser, crossed with the probe polarisation, after the sample. The pump was polarised at 45° to the probe and pump-induced anisotropy of the refractive index was detected by an increase in probe transmission through the polariser. The transmission of the probe spectrum at 333 fs intervals with respect to the pump pulse is shown in figure 5 and the chirp or time delay as a function of wavelength is shown in figure 6. The OKE data can also be used to obtain a measure of the time resolution of the system as CCl_4 has been shown[5] to exhibit an instantaneous response to pulses of 75 fs FWHM, and an almost symmetrical signal of width < 150 fs. Figure 7 shows the OKE signal at the probe wavelength 530 nm which has a FWHM of 300 fs.

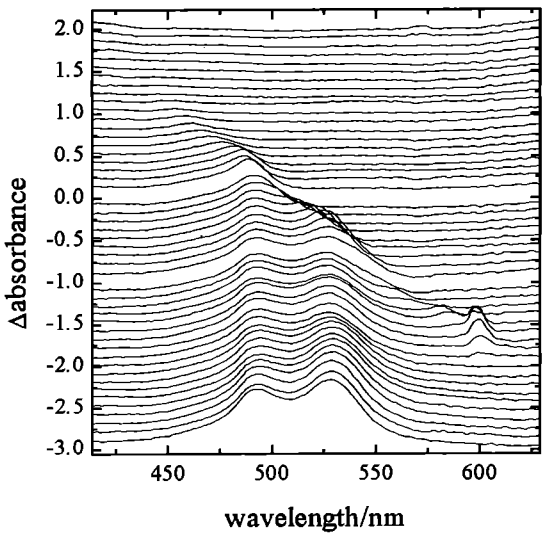

Figure 4 Transient absorption spectra of HITCI at 133 fs time intervals. Spectra off-set for clarity.

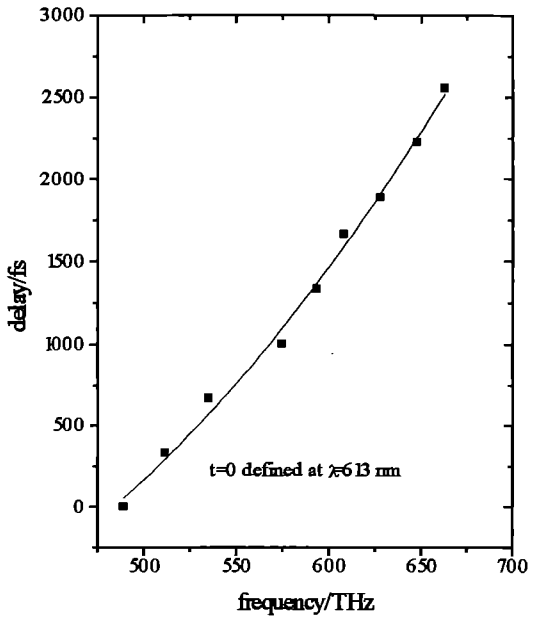

Figure 6 Delay versus frequency

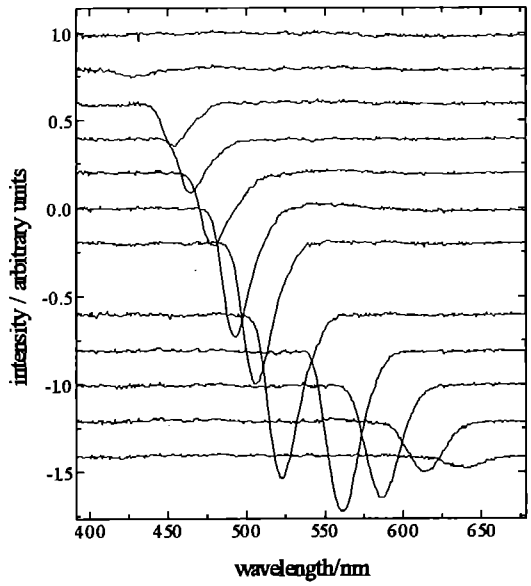

Figure 5 OKE signal as a function of delay. Spectra off-set for clarity.

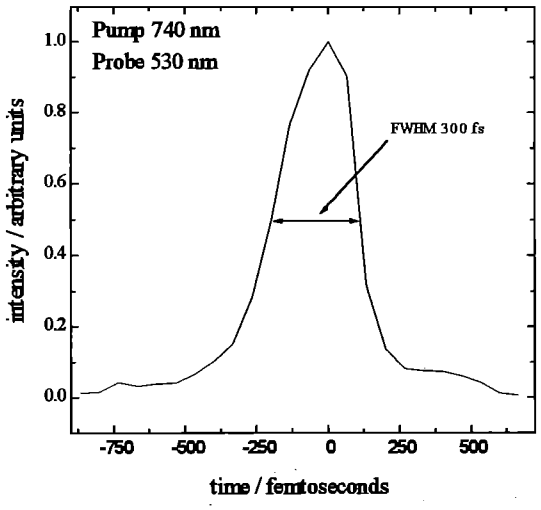

Figure 7 OKE signal

Another sample investigated were multiple quantum wells in the semiconductor material CdTe/CdMnTe. Kinetic and spectral data obtained at room temperature are shown in figure 8. The spectra were obtained at 66 fs time intervals. Each spectrum was averaged over 1000 laser shots by reading out the CCD every 10 s and averaging over 10 readouts. The baseline noise on the kinetic data was about $\pm 2 \times 10^{-3}$ rms. No smoothing methods were applied. CCD detectors obey Poisson statistics and the standard deviation in the calculated delta absorbance was estimated to be of $\pm 5 \times 10^{-4}$ for a mean readout value of 10^4 counts from the CCD detector. Thus about one quarter of the observed error in these data is due to shot noise at the CCD detector and should diminish in proportion to the square root of the number of readouts acquired. The remainder of the noise due to fluctuations in the background light or probe and reference beams warrant further investigation.

CONCLUSIONS

Within a period of a few weeks we have constructed and successfully tested an instrument for measuring transient absorption spectra using 100 fs laser pulses. We have demonstrated that spectral and kinetic data can be obtained with probe light both in the blue/green and near infrared regions of the spectrum. The best noise level for kinetic data was $\pm 2 \times 10^{-3}$ rms. The temporal resolution at 530 nm was about 300 fs.

ACKNOWLEDGEMENT

We thank Dr Mary O'Neill of the University of Hull for allowing us to present the quantum wells data.

REFERENCES

1. F Wilkinson, D Worrall, D McGarvey, A Goodwin and A J Langley. Kinetic spectroscopy of pyrazolotriazole azomethine dyes. J. Chem. Soc. Faraday Trans., 89(14), 2385-2390 (1993).

2 A J Langley, W J Noad, I N Ross and W Shaikh. High brightness femtosecond laser using titanium-sapphire technology and amplification in dyes. Applied Optics. In press.

3. Z Bor and B Racz. Group velocity dispersion in prisms and its applications to pulse compression and travelling-wave excitation. Opt. Comm. 54(3), 165 - 170 (1985).

4. A Muller, J Schulz-Hennig and H Tashiro. Excited state absorption of 1,1',3,3,3',3'-Hexamethylindotricarbocyanine Iodide: A quantative study by ultrafast absorption spectroscopy. Appl. Phys. 12, 333 - 339 (1977).

5. D. McMorrow, W T Lotshaw and G A Kennedy-Wallace. Femtosecond optical Kerr studies on the origin of nonlinear responses in simple liquids. IEEE J. Quantum Electron. QE24(2), 443 - 454 (1988).

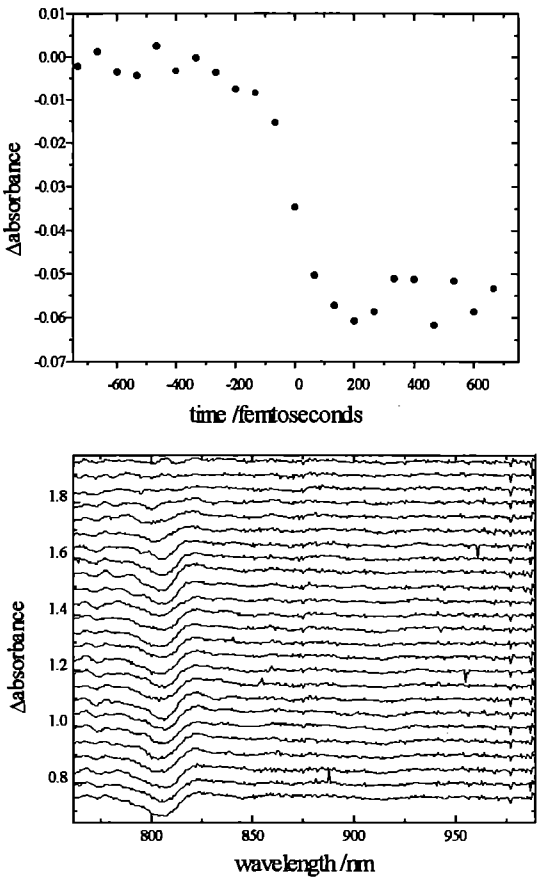

Figure 8 Kinetic and spectral data of CdTe/CdMnTe multiple quantum wells. Spectra off-set for clarity.

DEVELOPMENT OF A NEAR-INFRARED NANOSECOND RAMAN SYSTEM

S Tavender[1], J Tinkler[2], R Goyal[2], S Bates[1], A W Parker[1] and T G Truscott[2]
[1]Laser Support Facility, Rutherford Appleton Laboratory, Chilton, DIDCOT Oxon OX11 OQX
[2] Department of Chemistry, University of Keele, KEELE, Staffs ST5 5BG

INTRODUCTION

The nanosecond Time Resolved Resonance Raman (ns TR^3) has been extended into the near-infrared with the commissioning of a state-of-the-art near infra-red spectrograph and CCD camera. The system was purchased as part of the Grant GR/H59992 (Truscott/Parker/Land) to study the biologically important carotenoid radical ions which have absorption maxima in the near-infrared, mainly from 700-900 nm. The new system has enabled the first nsTR^3 spectra of the radical cation and anion of 7,7'-dihydrobetacarotene to be recorded.

CHOICE OF DETECTOR

For light detection in the near infra-red spectral region a detector choice must be made. The detectors available differ by the light sensitive material used. Popular substrates include indium/gallium/arsenide (InGaAs) and germanium. A first and obvious choice would be to choose the detector which is most sensitive over the widest spectral range. However, for Raman spectroscopy, other factors must be considered. For example. samples to be studied may fluoresce and this means accumulation times must be short to avoid saturation of the detector. Thus, for signal averaging a large number of chip read-outs must be performed and the signal-to-noise of the spectra will depend on the dynamic range, dark counts and read-out noise from the detector. Table 1. compares the specifications of three types of detector. The dead-space between each sensitive diode strip on the chip's array can also effect spectral resolution. InGaAs has 40% dead space compared with only 10%. for Ge. Whilst the Ge detector has the greatest sensitivity and the InGaAs the greater spectral range, the high dark charge and larger insensitive areas of these detectors make them less suitable for Raman spectroscopy. Hence, the thinned, back illuminated liquid nitrogen cooled CCD camera was chosen.

The detector chip selected for the CCD was the largest available - 1024 x 1024 pixels. This means a wide spectral range can be covered during data acquisition. The chip has an enhanced uv coating and is sensitive over the range 350 nm to 1050 nm. Whilst the uv coating does not directly benefit near infrared sensitivity, it acts as an anti-reflection coating for the higher wavelengths. Although the Raman probe beam is limited to *ca.* 900 nm by the sensitivity of the detector (i.e. 1700 cm^{-1} is at 1060 nm), this still enables the carotenoid ions to be studied. The quantum efficiency of the CCD detector is shown in Figure 3.

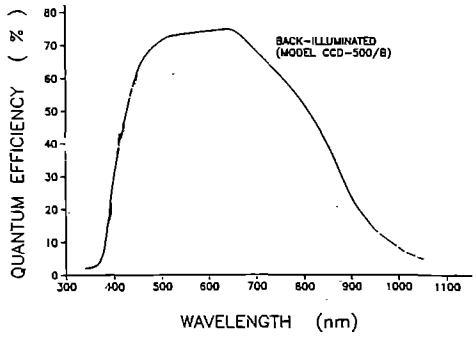

Figure 3. Quantum efficiency of CCD detector

SYSTEM APPARATUS

The detector is controlled by a Princeton Instruments model ST-130 controller which interfaces to CSMA software by means of a Del 486M p.c. The experimental set-up is shown in Figure 1. Detail of the sample chamber is shown in Figure 2. An Acton Research Corporation SpectraPro-500 single stage scanning spectrometer disperses the collected light and Rayleigh light is rejected using Holographic notch filters. A 2-stage lens collection system collimates the Raman light from the sample and images on to the spectrograph slit. The focal length of the lens were chosen to match the f/value (6.6) of the spectrometer. The sample is flowed through a jet nozzle as the pump power required to generate the intermediates needs to be high. This also minimises the Rayleigh scatter produced from the sample/glass interface.

DATA COLLECTION AND ANALYSIS

A Del 486M personal computer controls the detector and allows manipulation of peripheral devices via a software package, CSMA. The data is processed by the CSMA software which is written in 'spectrum basic'. Additional custom programs have been written to allow users to manipulate their data. For instance, there are now programs where a chosen number of frames can be selected, added together, normalised and stored in a new file. The subtraction of probe only from pump/probe spectra can now be run as a stand-alone program.

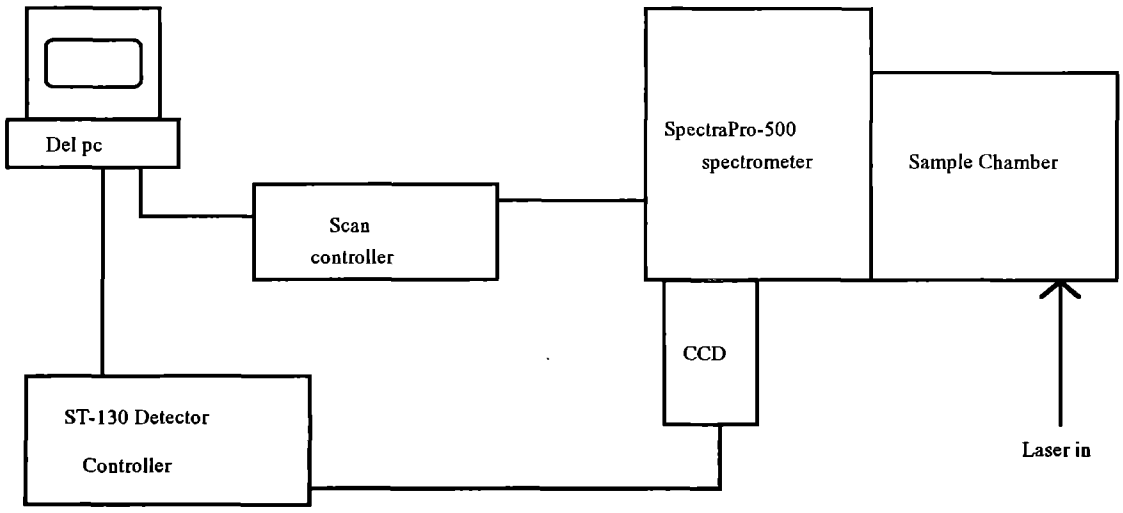

Figure 1. Experimental set-up

Table 1. Comparison of available CCD detectors

Type	Spectral Range(nm)	Sensitivity Photons/ct	Dark charge Cts/s	Read-out noise cts RMS	Dynamic range
Ge	500-1500	8000	250	2	16000
InGaAs	800-1650	2500	1500	1	10000
Thinned back-illuminated CCD	350-1050	55	11.5	1	62500

SYSTEM IMPROVEMENTS

Over the year, the system has continued to be developed. One of the biggest problems encountered with the system was the overlap of the pump (usually uv) and probe (infrared) beams as it was difficult to see both the uv and the infrared with the same optical viewing device. At first, a helium-neon laser was used to back-illuminate the CCD by means of a swing mirror which allowed the collimating and focusing lens to be aligned and define the sample position. This defines the point in space where the pump and probe beams must overlap. Problems arose when a combination of beams all of different colours, (uv/vis/ir) had to be seen. An improved alignment aid consisting of a micro-balloon,ϕ = 100μm, clamped to the back of the sample holder and able to be swung into the position of the sample, will be incorporated into the system. This will be used to define the focus of the collimating lens and so the sample position. The pump and probe beams can then be aligned and overlapped on this point.

A 760 nm laser diode has now been mounted on the back of the spectrometer. This means that the alignment laser is the same 'colour' as the probe laser and so aids alignment of the imaging optics with the sample of the collimating lens and so the sample position. The pump and probe beams can then be aligned and overlapped on this point.

SIGNAL-TO-NOISE

The typical noise count from the CCD detector is 130 cts/s. This compares to 340 cts/s from the diode array system. Typical spectra of the solvent toluene are shown in Figure 4(a) and (b).

CCD ON THE EXISTING SPECTROGRAPH

With its enhanced signal-to-noise, the CCD has been used on the Triplemate and has given greatly improved signal-to-noise on data. Several reports in this Annual Report e.g.Bisby/Parker, Phillips and Connolly bear witness to this improvement.

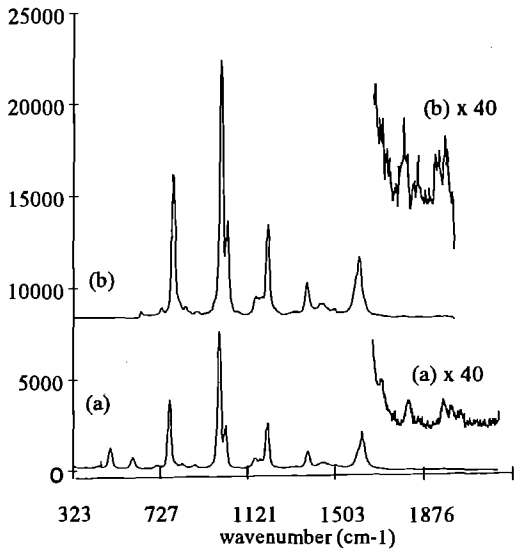

Figure 4. (a) toluene spectrum collected from CCD: 30 s accumulation. (b) toluene spectrum collected from diode array: 32 s accumulation. λ = 406 nm.

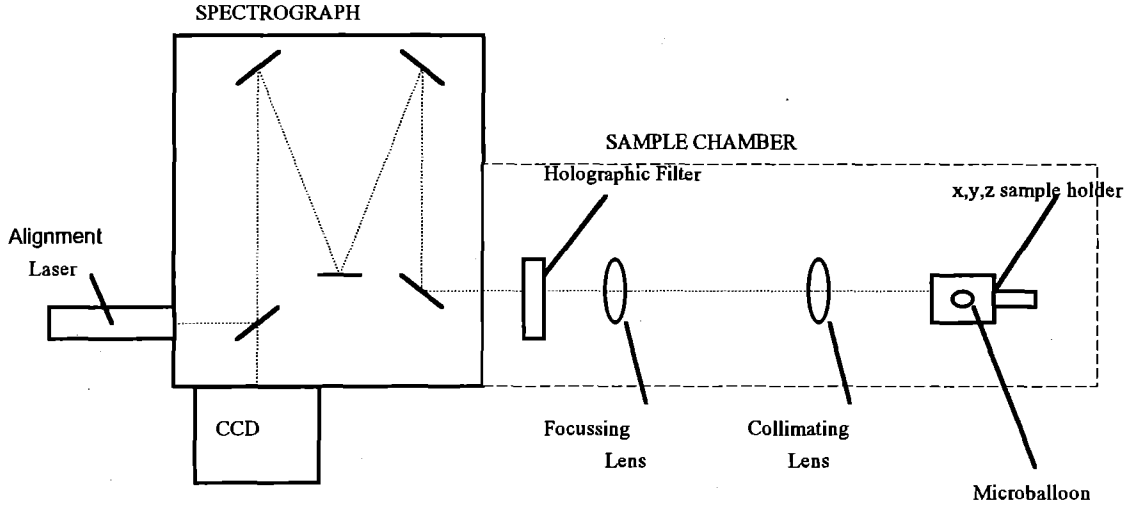

Figure 2. Sample chamber arrangement showing beam paths through chamber

HIGH BRIGHTNESS X-RAY SOURCE GENERATED BY A LASER-PLASMA

ICE Turcu, IN Ross, GJ Tallents, L Dwivedi, J Krishnan, H Goodson and M Schmidt

Rutherford Appleton Laboratory

Very high peak brightness X-ray emission can be obtained from plasmas generated with high power pulsed lasers. The intense X-ray emission is due to the extreme plasma temperature of around five million degrees centigrade. Large laser installations, like Vulcan at RAL, can generate line plasmas which emit laser radiation in the soft X-ray region, with the maximum peak brightness achieved in laboratory.

In the "Laser Plasma X-Ray Laboratory" in the Laser Support Facility we concentrate on using high repetition rate, low energy/pulse, commercial excimer lasers to generate high peak and average power plasma X-ray sources for applications in radiobiology, lithography, microscopy and calibration of X-Ray instruments[1].

In order to achieve the high laser power density on target, the excimer laser is used to amplify trains of picosecond pulses. In last year's report[2] we presented in detail this laser system and the dramatic improvements it brings in laser to X-Ray energy conversion efficiency[3] and in the reduction of target debris.

Presently the system repetition rate has been improved to 80Hz by the introduction of a new Bethune Cell dye amplifier in the picosecond laser generator and a new gas circulation system in the X-Ray chamber.

As a result of the improvement in system repetition rate, a record 200mW X-Ray average power was generated by the source at 1nm wavelength (Cu tape targets), as shown in Fig.1.

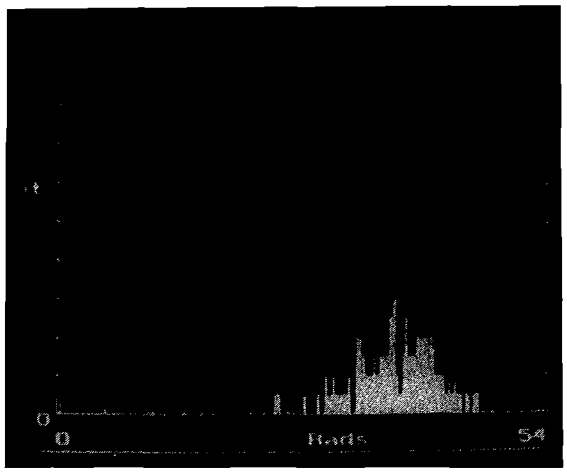

Figure 1 Histogram of X-ray signals recorded p-i-n diode measuring the dose of 1nm radiation reaching the biological cells in the DNA experiment carried out by the group from Birmingham University. A record 78mW/sr average X-ray power is emitted, coresponding to a record 3.5KRad/s dose rate delivered at the biological cells in water.

Figure 2. Spectral brightness of the laser-plasma source at 3.37nm (CVI L_α) is shown (◆) on the chart of X-ray sources, reproduced with permission from "X-Ray Data Booklet" published in 1986 by the "Centre of X-Ray Optics", Berkeley, CA, USA.

Fig. 2 shows the very high spectral brightness of the X-Ray source when operated with mylar tape target emitting radiation from hydrogen-like carbon ions, which is monochromatized efficiently (using nitrogen gas X-Ray filter) on the 3.37nm Lymann - α line of CVI.

REFERENCES

1. ICE Turcu, IN Ross, P Trenda, CW Wharton, RA Meldrum, H Daido, MS Schulz, P Fluck, AG Michette, AP Juna, JR Maldonado, H Shields, GJ Tallents, L Dwivedi, J Krishnan, DL Stevens, TJ Jenner, D Batani and H Goodson, "Picosecond excimer laser-plasma x-ray source for microscopy, biochemistry and lithography", Proc Soc Photo-Opt Instrum Eng "Applications of laser-plasma radiation", **2015**, 243-260 (1994).

2. ICE Turcu, IN Ross, AJ Langley, P Trenda, W Shikh, S Quayoum and H Goodson, "High Average Power, 7 Picosecond, KrF Laser System for X-Ray Generation", Rutherford Appleton Lab Report **RAL-93-031**, 230-1 (1993).

3. ICE Turcu, IN Ross and GJ Tallents, "Efficient KeV x-ray emission from plasmas generated with 4ps KrF excimer laser pulses", Appl. Phys. Lett. **63**, 3046-8 (1993).